

NASA
CP
2128
c.1

NASA Conference Publication 2128
FAA-RD-80-30

LOAN COPY: RE
AFWL TECHNICAL
KIRTLAND AFB,



Lightning Technology

Proceedings of a technical symposium
held at NASA Langley Research Center,
Hampton, Virginia, April 22-24, 1980



Page intentionally left blank

NASA Conference Publication 2128
FAA-RD-80-30

Lightning Technology

Proceedings of a technical symposium
sponsored by the National Aeronautics
and Space Administration, the Florida
Institute of Technology, and the
Department of Transportation and
held at NASA Langley Research Center,
Hampton, Virginia, April 22-24, 1980



National Aeronautics
and Space Administration

**Scientific and Technical
Information Office**

1980

Page intentionally left blank



PREFACE

The proceedings of the 1980 Symposium on Lightning Technology held at Langley Research Center April 22-24, 1980, are reported in this NASA Conference Publication. This Symposium was sponsored by the National Aeronautics and Space Administration, the Florida Institute of Technology, and the Department of Transportation.

The 1980 Symposium included papers in several facets of lightning technology including phenomenology, measurement, detection, protection, interaction, and testing. Papers identified in the Contents by an asterisk are a set organized as "New Thrusts in Lightning Electromagnetics." In addition to the presentation sessions, open forums were held on protection of ground systems and on simulated lightning testing. The NASA Langley Research Center lightning-instrumented F-106 aircraft was displayed and the instrumentation system was described during a conducted tour.

This publication was prepared from camera-ready copies of the conference presentations supplied by the authors. In order to prepare the proceedings for distribution at the meeting, the papers were printed as received from the authors. The material presented in this report was taken from a variety of sources; therefore, various units of measure are used. Use of trade names or names of manufacturers in this report does not constitute an official endorsement of such products or manufacturers, either expressed or implied, by NASA.

Felix L. Pitts

Page intentionally left blank

CONTENTS

PREFACE	iii
-------------------	-----

SESSION I - PHENOMENOLOGY OF LIGHTNING

Chairman: C. B. Moore

1. A WAVE GUIDE MODEL OF LIGHTNING CURRENTS AND THEIR ELECTROMAGNETIC FIELD	3
Hans Volland	
2. *CALCULATIONS OF LIGHTNING RETURN STROKE ELECTRIC AND MAGNETIC FIELDS ABOVE GROUND	21
M. A. Uman, Y. T. Lin, R. B. Standler, M. J. Master, and R. J. Fisher	
3. *SUBMICROSECOND RISETIMES IN LIGHTNING RADIATION FIELDS	29
C. D. Weidman and E. P. Krider	
4. *MEASUREMENT OF ELECTROMAGNETIC PROPERTIES OF LIGHTNING WITH 10 NANOSECOND RESOLUTION	39
C. E. Baum, E. L. Breen, J. P. O'Neill, C. B. Moore, and D. L. Hall	

SESSION II - LIGHTNING INSTRUMENTATION AND MEASUREMENTS

Chairman: B. L. Dove

5. *ELECTROMAGNETIC SENSORS FOR GENERAL LIGHTNING APPLICATION	85
Carl E. Baum, Edward L. Breen, John P. O'Neill, Charles B. Moore, and Gary D. Sower	
6. *EXPANDED INTERLEAVED SOLID-STATE MEMORY FOR A WIDE BANDWIDTH TRANSIENT WAVEFORM RECORDER	119
Robert M. Thomas, Jr.	
7. *BROADBAND ELECTROMAGNETIC SENSORS FOR AIRCRAFT LIGHTNING RESEARCH	131
Thomas F. Trost and Klaus P. Zaepfel	
8. *AIRBORNE LIGHTNING CHARACTERIZATION	153
Robert K. Baum	
9. MAGNETIC TAPE LIGHTNING CURRENT DETECTORS	173
Keith E. Crouch and W. Jafferis	

SESSION III - LIGHTNING DETECTION AND TRACKING

Chairman: Dale Vance

10. A STUDY OF THE COMPARATIVE PERFORMANCE OF SIX LIGHTNING
WARNING SYSTEMS 187
Richard L. Johnson, Donald E. Janota, and J. Edmund Hay
11. AN AUTOMATIC LOCATING SYSTEM FOR CLOUD-TO-GROUND LIGHTNING 205
E. Philip Krider, Alburt E. Pifer, and Martin A. Uman
12. RADAR-LIGHTNING RELATIONSHIPS FOR THUNDERSTORMS IN
FLORIDA AND OKLAHOMA (Paper unavailable at time of publication)
M. W. Maier
13. LIGHTNING WARNING AND TRACKING SYSTEMS (Paper unavailable at
time of publication)
R. A. Bent and T. Scheffler
14. A NETWORK OF AUTOMATIC ATMOSPHERICS ANALYSATORS 215
Josef Schafer, Hans Volland, Paul Ingmann,
Andrew J. Eriksson, and G. Heydt

SESSION IV - LIGHTNING INTERACTION AND SIMULATION

Chairman: C. E. Baum

15. *SHIELD TOPOLOGY IN LIGHTNING TRANSIENT CONTROL 229
E. F. Vance and F. M. Tesche
16. *THE SEM DESCRIPTION OF INTERACTION OF A TRANSIENT ELECTRO-
MAGNETIC WAVE WITH AN OBJECT 245
L. Wilson Pearson and Donald R. Wilton
17. *TRANSIENT CORONA EFFECTS ON A WIRE OVER THE GROUND 265
Kenneth C. Chen
18. *SIMULATION OF ELECTROMAGNETIC ASPECTS OF LIGHTNING 283
Carl E. Baum
19. *EXPERIMENTAL RESOLUTION OF SYSTEM RESONANCES PRODUCED
BY SIMULATED LIGHTNING EXCITATION (Paper unavailable
at time of publication)
W. G. Butters, K. P. Murphy, and D. W. Clifford

SESSION V - PROTECTION OF GROUND SYSTEMS

Chairman: Joseph J. Pizzicaroli

20. A UNIVERSAL PROCEDURE FOR EVALUATION AND APPLICATION OF
SURGE-PROTECTIVE DEVICES 303
Bernhard I. Wolff

21. CONDUCTIVE SURGE TESTING OF CIRCUITS AND SYSTEMS	327
Peter Richman	
22. IMPLEMENTATION AND EXPERIENCE WITH LIGHTNING HARDENING MEASURES ON THE NAVY/AIR FORCE COMBAT MANEUVERING RANGES (Paper unavailable at time of publication)	
J. E. Nanevich and E. F. Vance	
23. THE FAA LIGHTNING PROTECTION MODULES DESIGNED FOR LEADLESS DEVICES (Paper unavailable at time of publication)	
R. M. Cosel and M. Figueroa	
24. RESPONSE OF SURGE PROTECTION DEVICES TO FAST RISING PULSES	345
I. N. Mindel	

SESSION VI - LIGHTNING AND STATIC INTERACTIONS WITH AIRCRAFT
Chairman: P. F. Little

25. FURTHER THOUGHTS ON LOCATION OF LIGHTNING STRIKE ZONES ON AIRCRAFT (Paper unavailable at time of publication)	
J. A. Plumer	
26. DIRECT EFFECTS OF LIGHTNING ON AN AIRCRAFT DURING INTENTIONAL PENETRATIONS OF THUNDERSTORMS	363
Dennis J. Musil and John Prodan	
27. STATE-OF-THE-ART METHODS FOR COMPUTING THE ELECTROMAGNETIC INTERACTION OF LIGHTNING WITH AIRCRAFT	371
F. J. Eriksen, R. A. Perala, and John C. Corbin, Jr.	
28. PRECIPITATION STATIC IN GENERAL AVIATION AIRCRAFT (Paper unavailable at time of publication)	
W. G. Butters	
29. ANOTHER LOOK AT AIRCRAFT-TRIGGERED LIGHTNING	393
D. W. Clifford	

SESSION VII - OPEN FORUM ON PROTECTION OF GROUND SYSTEMS
Chairman: R. A. Bent

SESSION VIII - AIRCRAFT LIGHTNING PROTECTION DESIGN AND TESTING
Chairman: Gary DuBro

30. F-5F SHARK NOSE RADOME LIGHTNING TEST	421
George W. Scott	
31. LIGHTNING PROTECTION TECHNIQUES FOR RADOMES HAVING FORWARD MOUNTED PITOTS (Paper unavailable at time of publication)	
A. W. Hanson	

32. ANALYSIS AND MEASUREMENTS OF LOW FREQUENCY LIGHTNING COMPONENT PENE- TRATION THROUGH AEROSPACE VEHICLE METAL AND GRAPHITE SKINS	431
John D. Robb and Ta Chen	
33. FULL SCALE LIGHTNING TEST TECHNIQUE	449
Lawrence C. Walko and John G. Schneider	
34. THE ROLE OF FIELD CALCULATIONS IN LIGHTNING SIMULATION TESTS TO AIRCRAFT (Paper unavailable at time of publication)	
B. J. C. Burrows	

SESSION IX - OPEN FORUM ON SIMULATION AND TESTING
Chairman: J. A. Plumer

SESSION I - PHENOMENOLOGY OF LIGHTNING

Page intentionally left blank

A WAVE GUIDE MODEL OF LIGHTNING CURRENTS AND THEIR ELECTROMAGNETIC FIELD

Hans Volland
Radioastronomical Institute, University of Bonn

SUMMARY

Lightning channels are considered as resonant wave guides in which only standing resonant wave modes can be excited. Two types of discharging currents can develop. Type 1 is an aperiodic wave of the form described by Bruce and Golde. Type 2 is a damped oscillation. The electromagnetic radiation field of both types of currents is calculated and compared with the observation.

LUMPED CIRCUIT MODEL

The Bruce- Golde formula (ref. 1)

$$I = \bar{I}(e^{-\alpha t} - e^{-\beta t}) \quad (1)$$

($0 < \alpha < \beta$; α, β real) simulates well the observed temporal variation of the electric currents I at the base of return stroke channels. However, it will be shown in the following that most spheric wave forms observed at far distances from the stroke are related to lightning currents of the form

$$I = 2\bar{I} \sin \delta t e^{-\gamma t} \quad (2)$$

($0 < \gamma, \delta$; γ, δ real). Form (1) shall be called a type 1 current. Form (2) shall be called a type 2 current. With

$$\left. \begin{array}{l} \alpha \\ \beta \end{array} \right\} = \gamma \pm i\delta \quad ; \quad \bar{I} = - \frac{\alpha\beta}{(\beta-\alpha)} \bar{Q} \quad (3)$$

type 1 can be transformed into type 2. \bar{Q} is the total charge stored within the channel at time $t = 0$. For type 1, δ is imaginary. For type 2, δ is real.

Oetzel (ref. 2) has shown that in a parallel lumped circuit model with resistance R , capacitance C , and inductance L , a discharging current flows at time $t \geq 0$ which has the form of (1) or (2), and it is

$$\gamma = \frac{R}{2L} \quad ; \quad \delta = \sqrt{\frac{1}{LC} - \frac{R^2}{4L^2}} \quad (4)$$

Evidently, type 1 currents flow if $R > 2 \sqrt{L/C}$.

WAVE GUIDE MODEL

A more realistic model of lightning currents must take into account the finite diameter d and the finite length ℓ of the channel (approximated here by a vertical straight wire). At time $t = 0$, such wire has contact with the perfectly conducting earth in the case of return (R) strokes, or discharging starts at time $t = 0$ without contact to the earth in the case of intracloud (IC) strokes. The maximum spectral amplitude of return strokes is near 5 kHz (ref. 3). The corresponding wavelength $\lambda \approx 60$ km in free space is large compared with the channel length ℓ . Therefore, the propagation of electromagnetic waves in such channel must be treated by full wave theory.

The boundary condition are

1. zero vertical electric field at the top of the wire ($z = H + \ell$)
- 2a. zero horizontal electric field at the ground ($z = 0$) for R strokes
- 2b. zero vertical electric field at the bottom ($z = H - \ell$) for IC strokes
3. continuity of the horizontal fields of E and H at the surface of the wire
4. radiation condition fulfilled outside the wire.

For moderate electric conductivity within the wire ($\sigma \approx 10^4$ S/m), small diameters ($d < 5$ cm), and low frequencies, it can be shown that the current within the wire has the form (ref. 4)

$$I_n = -\bar{Q}_n (\gamma_n^2 + \delta_n^2) \frac{\sin \delta_n t}{\delta_n} e^{-\gamma_n t} \cos h_n (z-H) \quad (5)$$

for $(H-L \leq z \leq H+\ell)$. It is $H = L = 0$ for R strokes, H the center and $L = \ell$ for IC strokes. The vertical wave number

$$h_n = \frac{(2n-1)\pi}{2\ell} \quad (6)$$

is chosen such that the boundary conditions (1) and (2) are fulfilled. An infinite set of eigen frequencies

$$i\omega_n = \gamma_n + i\delta_n \quad (7)$$

can be found from the eigenvalue equation

$$u \ln u = - \frac{i \omega \kappa^2}{\mu_0 c^2 \sigma} \quad ; \quad u = \left(\frac{\kappa d}{4c} \right)^2 (c^2 h_n^2 - \omega_n^2) \quad (8)$$

with $\kappa = 1.781$ the Euler-Mascheroni constant (ref.5), c the speed of light, and $\mu_0 = 4\pi \times 10^{-7}$ H/m.

Eq.(5) is identical with (1) and (2) apart from the height structure function. It shows that the lightning channel behaves like a resonance cavity in which only standing modes can be excited.

From the equation of continuity of the current, one can derive a charge density within the wire of

$$q_n = h_n \bar{Q}_n \left\{ \cos \delta_n t + \frac{\gamma_n}{\delta_n} \sin \delta_n t \right\} e^{-\gamma_n t} \sin h_n (z-H) \quad (9)$$

The total energy dissipated within the wire by the n -th mode of R strokes is

$$P_{\text{diss}} = \frac{R}{\ell} \int_0^\ell \int_0^\infty I_n^2 dz dt = \frac{\bar{Q}_n^2}{4C_n} \quad (10)$$

where R is the total resistance of the wire and C_n its capacitance according to (4).

The eigenvalue equation (8) must be solved numerically. In Fig. 1, d is plotted versus a reduced channel length $\ell_n = \ell / (2n-1)$ as derived from (8) for a set of pairs (α, β) or (γ, δ) , respectively. The conductivity is assumed to be $\sigma = 10^4$ S/m. Transition from the (α, β) regime (type 1) to the (γ, δ) regime (type 2) occurs at the fat dash-dotted line where $\delta = 0$. Given the channel parameters ℓ and d , the reduced channel lengths ℓ_n are determined uniquely from (6) from which one finds the corresponding eigenvalues in Fig. 1. The larger the wave number n , the smaller the pulse length of the n th mode.

EXCITATION OF EIGENMODES

If the electric charge distribution just before discharging starts is $\bar{q}(z)$, matching of that distribution by the eigenmodes (9) yields for R strokes

$$\bar{q}(z) = \sum_{n=1}^{\infty} h_n \bar{Q}_n \sin h_n z \quad (11)$$

which gives

$$\bar{Q}_n = \frac{4}{\pi(2n-1)} \int_0^\ell \bar{q}(z) \sin h_n z dz \quad (12)$$

At time $t = 0$, all modes are excited simultaneously with amplitudes \bar{Q}_n . Although these wave modes are standing waves, their superposition gives the impression of the transport of a disturbance. Imagine that in an ideal straight wire of length l which is grounded at the bottom, one puts a negative point charge at the height z_0 . Just after the discharge process started (say, at time $t_1 = 1 \mu s$), the charge region has somewhat broadened, and currents flow from the environment into that region (Fig. 2a). A very small discharging current flows already through the bottom of the channel. At time $t_2 = 10 \mu s$, the pulse form is in full development (Fig. 2b). The higher order modes with their shorter pulse lengths have already died out. The vertical pulse form of the charge becomes broader and smoother. Two regions of disturbances of the current "propagate" toward the ends of the wire with finite "velocity". The discharging current through the bottom of the channel has nearly reached peak amplitudes. At $t_3 = 100 \mu s$ finally, (Fig. 2c) only the first mode remains while all other modes have decayed. In the case of a point charge originally at the top of the wire, only one "pulse" would travel downward. In the case of the point charge at the bottom, only one "pulse" would travel upward.

The "propagation" effect in Fig. 2 is due to the superposition of all standing wave modes which have different pulse lengths. Physically speaking, this is a diffusion effect rather than a propagation process because the type 2 waves are quasi-evanescent, the type 1 waves are evanescent with infinitely large phase velocities.

In an imperfect wave guide such as the tortuous lightning channel with branches etc., resonance loses its meaning for the higher order modes which have wavelengths small compared with the channel length ($n \approx 10$). These waves propagate like free waves. They are partially reflected at inhomogeneities and damped along their propagation path. They are generated all the time during a flash. However, they are ineffective for transporting electric charge because they interfere destructively. Their contribution to channel heating is probably of minor importance. This wave component is the quasi-continuous radio noise observed at frequencies $f \approx 100 \text{ kHz}$.

Waves of intermediate wave numbers ($3 \lesssim n \lesssim 10$) have wavelengths comparable with the large scale inhomogeneities of the channel. On the other hand, their wavelengths are too large to allow propagation as free waves. Therefore, these waves cannot develop to their full impulse form, and mode coupling from that range of wave numbers into the other wave modes is expected. The waves of lowest wave numbers ($n \lesssim 3$) are the only modes where resonance effects can lead to the full development of pulse forms like (5). In particular, the first mode ($n = 1$) has a wavelength of four times the channel length which is large even compared to the large scale inhomogeneities of the channel. It is that mode which most effectively transports and redistributes electric charge within the lightning channel and also heats the channel to temperatures where luminous events can be observed. A discharging process where the first mode is involved probably starts after the channel has reached some kind of stable configuration.

CHANNEL HEATING

The observations suggest and the theory outlined above strengthens the idea that it is mainly the first mode which transports charge during strokes. However, that mode is a standing wave starting simultaneously at all heights along the channel. This is in apparent disagreement with observations of luminous events where one sees a "wave front" propagating upward with velocities of the order of 1/3 of the speed of light (ref. 6). That discrepancy may be dissolved in the following manner: Luminous events can only be observed after the gas in the channel is heated to temperatures of the order of $T_m = 30\,000\text{ K}$ (ref. 6). That heating process is due to the dissipation of electric energy (Joule heating) of the first mode. For a very rough estimate, one can use the equation of energy in the form ($\rho \approx \text{constant}$)

$$\rho c_v \frac{dT}{dt} \approx \frac{RI^2}{V} \quad (13)$$

with ρ the gas density, c_v the specific heat at constant volume, T the temperature, R the total resistance of the channel, I the electric current of the first mode, $V = Fl$ the volume of the channel, and $F = \pi d^2/4$ its cross section. Since I_1 in (5) decreases with height by a cosine law, the threshold temperature where luminous events start is reached at later times t_m in greater heights:

$$z_m \approx \frac{2l}{\pi} \arccos \left\{ \frac{P_{\text{therm}}^{1/2}}{P_{\text{joule}}^{1/2}} \right\} \quad (14)$$

with

$$P_{\text{therm}} \approx \rho c_v (T_m - T_o) \approx 27 \text{ MJ/m}^3 \quad (15)$$

the thermal energy necessary to heat the channel to a temperature of T_m . T_o is the temperature of the channel just prior to the discharge. Furthermore,

$$P_{\text{joule}} = \frac{RI_1^2}{V} \int_0^{t_m} (e^{-\alpha_1 t} - e^{-\beta_1 t})^2 dt \leq \frac{2P_{\text{diss}}}{V} = \frac{Q_1^2}{2C_1 V} \quad (16)$$

with P_{diss} from (10). According to (14), the channel can never be illuminated up to its very top. Evidently, it must be $P_{\text{therm}} < 2P_{\text{diss}}/V$ in order that luminous events can be observed at all. According to (16), the degree of luminosity along the channel depends mainly on the ratio between total charge Q and channel volume V .

ELECTROMAGNETIC RADIATION

The vertical electric field E_z and the azimuthal magnetic field B_ϕ of a vertical lightning channel of a return stroke with a current configuration of (5) observed on the surface of a perfectly conducting earth is (ref. 4)

$$E_z = \frac{\mu_0 c^2 \bar{Q}_n}{2\pi \bar{R}^3} \int_0^{\ell'} \left\{ \sin^2 \theta' \frac{G_1}{D} + (1 - 3 \cos^2 \theta') \left(\frac{G_2}{D^2} + \frac{G_3}{D^3} \right) \right\} \cos h_n z' dz' + \text{residuum}$$

$$cB_\phi = - \frac{\mu_0 c^2 \bar{Q}_n}{2\pi \bar{R}^3} \int_0^{\ell'} \sin \theta' \left(\frac{G_1}{D} + \frac{G_2}{D^2} \right) \cos h_n z' dz' \quad (17)$$

with $G_m(t_r)$ from table 1, $t_r = t - R/c$ a retarded time, $R = \sqrt{\rho^2 + z'^2}$ the distance between a channel element at height z' and the receiver on the ground in a horizontal distance of ρ from the channel bottom, $\sin \theta' = \rho/R$, $\cos \theta' = -z'/R$, $D = R/\bar{R}$, and $\bar{R} = 1$ km a normalizing distance (see Fig. 3). It is

$$\ell' = \begin{cases} \sqrt{c^2 t'^2 + 2\rho c t'} & \text{for } ct' < \rho \\ \ell & \text{for } ct' > \rho \end{cases} \quad \sqrt{\rho^2 + \ell^2} - \rho \quad (18)$$

that height on the channel where the last signal reaches the receiver at the receiver time $t' = t - \rho/c$. At time $t' = 0$, the first signal reaches the receiver. At the channel time $t = 0$, the current starts to flow.

At large distances from the channel ($\rho \gg \ell$), the G_m and D in (17) are nearly independent of height, and it is $\theta' \approx 90^\circ$. Thus, a dipole approximation yields

$$E_z = 9\bar{M} \left(\frac{G_1}{D} + \frac{G_2}{D^2} + \frac{G_3}{D^3} \right) ; \quad cB_\phi = -9\bar{M} \left(\frac{G_1}{D} + \frac{G_2}{D^2} \right) \quad (19)$$

with

$$\bar{M} = 2(-1)^{n+1} \bar{Q}_n \bar{\ell}_n \quad \text{an electric dipole moment (in C m), and}$$

$$\bar{\ell}_n = 1/h_n \quad \text{an effective antenna length (in m).}$$

The residuum in (17) takes into account the finite charge stored at $t = 0$ on the channel.

Note that the z -axis is orientated positive upward and that by definition, the electric field disappears at $t \rightarrow \infty$. Thus, a transformation from that defined field to the field as usually defined in the literature (e. g. ref. 6) is necessary:

$$\Delta E_z = E_z(0) - E_z(t) \quad (20)$$

DISCUSSION

In table 1, the ratio between maximum and minimum of the radiation component G_1 , labelled as R_1 , and its crossover time t_c are given as functions of (α, β) and (γ, δ) , respectively. It is $R_1 \approx 7.4$ for type 1 currents, and < 7.4 for type 2 currents. The two parameters R_1 and t_c are useful for a quick decision whether observed spheric wave forms belong to type 1 or to type 2 currents.

The electromagnetic field of the first mode ($n = 1$) of a type 2 current from (5) with the parameters $Q_1 = -0.49$ C, $\ell = 18.7$ km, $\gamma_1 = 1.15 \times 10^4$ s $^{-1}$, $\delta_1 = 2.3 \times 10^4$ s $^{-1}$, $P_{diss} = 2$ MJ as calculated from (17) is plotted in Fig. 4 for three distances $\rho = 1$ km, 10 km, and 200 km (solid lines). The individual components $m = 1, 2$ and 3 in (17) are plotted as dashed curves in Fig. 4. The dotted lines are observed wave forms of a first return stroke reproduced from Lin et al. (ref. 7). The agreement between the observations and the model is excellent at 200 km distance. At 10 km, the theoretical amplitudes are somewhat smaller than the observed data, although the agreement between the wave forms is reasonable. In particular, the "ramp" due to the electrostatic component ($m = 3$) of the E-field and the "hump" in the B-field are clearly visible. The electrostatic component of the E-field is apparently too small to adequately reproduce the "ramp". The model also does not simulate the "initial peak" in the data.

In the case of 1 km distance, the calculated field strengths are one order of magnitude too small compared with the observations although again the wave forms are similar. This discrepancy may be not too surprising in view of the simplified model which can only simulate the vertical part of a real oblique and tortuous channel. The huge channel length of nearly 20 km already indicates that the channel must possess a significant horizontal extent, and it is well known that the horizontal part of an antenna near the ground does only significantly contribute to the electromagnetic field in the immediate environment of the antenna (ref. 5). This idea is supported by the behavior of the dipole approximation (the dash-dotted lines in Fig. 4). While a reasonable approximation at 200 km, it somewhat overestimates the observed field at 10 km, and it grossly overestimates the field at 1 km distance. On the other hand, the calculated field of the vertical channel underestimates the measurements. Hence, a vertical antenna having a dimension between $\bar{\ell} = 0$ (dipole) and ℓ would reproduce the magnitude of the measurements although the details are lost.

Lin et al. (ref. 7) maintain that their observed wave forms in Fig. 4 are typical for the first and for subsequent R strokes. In the case of subsequent strokes, their observed crossover time is of the order of 30 μ s. That crossover time corresponds to channel lengths of about 10 to 12 km and channel diameters of about 5 cm. The wave forms again point to type 2 currents. Measurements of Taylor (ref. 8) also indicate a predominance of type 2 currents (80 % of all cases). On the other hand, the Bruce-Golde formula (1) based on direct current measurements is of type 1. The question arises then why type 1 appears to be rarely seen in spheric wave forms. A possible answer may be the following: the channel parameters deduced from the numbers \bar{I} , α , and β (e. g.

from ref. 9) are $\ell = 8$ km, $d = 1.6$ cm, and $P^{\text{diss}} = 35$ MJ for the first R stroke, and $\ell = 8$ km, $d = 3.2 - 4.5$ mm, and $P^{\text{diss}} = 180 - 46$ MJ for subsequent strokes (ref. 4). Thus, the typical Bruce-Golde current has a relatively small channel volume, and the energy P^{diss} is larger than the critical thermal energy in (15). Therefore, a significant part of the channel is illuminated. On the other hand, the typical lightning channel associated with sferics has a large channel volume, and the dissipated energy is small. Therefore, that lightning may be at or even below the threshold of visibility.

Fig. 5 shows the radiation component ($m = 1$) of the first mode ($n = 1$) of a typical intracloud K stroke situated at a distance of 25 km from the observer and centered at a height of 5 km above ground. The channel parameters are $\bar{Q}_1 = 9.6$ mC, $2\ell = 4.3$ km, $\gamma_1 = 10^5 \text{ s}^{-1}$, and $\delta_1 = 2 \times 10^5 \text{ s}^{-1}$. That wave form simulates well observed K strokes (ref. 10). The solid line in Fig. 5 is the dipole approximation over a perfectly conducting earth. The dashed line takes into account the finite electric conductivity of the earth's surface, and the dotted line is derived from the exact formula (17).

SPECTRAL AMPLITUDES AND FINITE ELECTRIC CONDUCTIVITY OF THE EARTH

The spectral amplitude of E_z of the radiation component of the dipole approximation over a perfectly conducting earth is

$$\hat{E}_z = \frac{9\bar{M}\bar{R}^3}{2c} \frac{\alpha\beta}{(\beta-\alpha)} \left\{ \frac{\beta}{\beta-i\omega} - \frac{\alpha}{\alpha-i\omega} \right\} \frac{e^{i\omega\rho/c}}{\rho} \quad (21)$$

and a corresponding form for (γ, δ) . Maximum spectral amplitudes are at

$$\omega_0 = \begin{cases} \sqrt{\alpha\beta} \\ \sqrt{\gamma^2 + \delta^2} \end{cases} \quad (22)$$

The influence of the finite electric conductivity of the earth surface on the ground wave can approximately be taken into account by the transmission function (ref. 4)

$$W(\rho, \omega) = \frac{X^2 e^{i\omega\tau}}{(X-i\omega)^2} \quad (23)$$

$$\text{with } X = 2c\sqrt{2c\mu_0\sigma_E/\rho} \quad ; \quad \tau = \frac{\pi}{2X}$$

Thus, the spectral amplitude of the ground wave over an imperfectly conducting earth becomes

$$W(\rho, \omega) \hat{E}_z(\rho, \omega) \quad (24)$$

The magnitude of \hat{E}_z increases proportional to ω for $\omega \ll \omega_0$ and decreases proportional to $1/\omega$ for $\omega \gg \omega_0$. The magnitude of the product $\omega \hat{E}_z$ in (24) decreases proportional to $1/\omega^3$ for $\omega \gg X$, that is for frequencies $f \gtrsim 200$ kHz if $\sigma_E = 10^{-3}$ S/m. This can be seen in Fig. 6 where the spectral amplitudes of a series of model spheric wave forms are plotted versus frequency. The symbols "R" and "K" are related to the type 2 wave forms in Figs. 4 and 5. The symbols "R_{first}" and "R_{subs}" are related to type 1 currents derived from Bruce-Golde's formula (ref. 4). The dotted line in Fig. 6 has been calculated for a perfectly conducting earth.

The spectral amplitude of the type 2 R stroke peaks near 4 kHz in reasonable agreement with observations (ref. 11). The amplitude of the K stroke peaks near 35 kHz, and those of the type 1 R strokes peak near 10 kHz. The slow tail of the type 1 subsequent strokes is represented by the broad maximum with relatively large amplitudes at low frequencies in the curves "R_{subs}" in Fig. 6.

The imperfectly conducting earth modifies the wave forms in the time domain in such a manner that the maximum amplitude of the radiation component decreases and the rise time to that first maximum increases with increasing distance and/or decreasing electric conductivity of the earth's surface. The observed rise times of about 3 μ s in the case of R strokes is consistent with a conductivity of about $\sigma_E = 10^{-3}$ S/m (Fig. 4 and ref. 4). The rise time also depends on the pulse length. For K strokes with pulse lengths of the order of 20 μ s as in Fig. 5, the rise time is already 2 μ s at 25 km distance.

REFERENCES

1. Bruce, C. E. R.; Golde, R. H.: The Lightning Discharge. J. Inst. Electr. Engrs. 88, Part II, 487, 1941.
2. Oetzel, G. N.: Computation of the Diameter of a Lightning Return Stroke. J. Geophys. Res. 73, 1889, 1969.
3. Taylor, W. L.: Daytime Attenuation Rates in the Very Low Frequency Band using Atmospherics. J. Res. NBS 64D, 349, 1960.
4. Volland, H.: Low Frequency Radio Noise. Handbook of Atmospherics, H. Volland (ed), CRC Press, Boca Raton, FL, 1981.
5. Sommerfeld, A.: Lectures in Theoretical Physics, Vol.II and VI. Academic Press, New York, 1952.
6. Uman, M. A.: Lightning. McGraw Hill Comp., New York, 1969.
7. Lin, Y. T. et al.: Characteristics of Lightning Return Stroke Electric and Magnetic Fields from Simultaneous Two- Station Measurements. J. Geophys. Res. 84, 6307, 1979.
8. Taylor, W. L.: Radiation Field Characteristics of Lightning Discharges in the Band 1 kc/s to 100 kc/s. J. Res NBS 67D, 539, 1963.
9. Dennis, A. S.; Pierce, E. T.: The Return Stroke of the Lightning Flash to Earth as a Source of VLF Atmospherics. Radio Sci. 68D, 777, 1964.
10. Weidman, C. D.; Krider, E. P.: The Radiation Field Wave Forms produced by Intracloud Lightning Discharge Processes. J. Geophys. Res. 84, 3159, 1979.
11. Serhan, G. I.; Uman, M. A.; Childers, D. G.; Lin, Y. T.: The RF Spectra of First and Subsequent Lightning Return Strokes in the 1 - 200 km Range, Radio Sci. 84D, 1980 (in Print).

TABLE 1

	Aperiodic Wave (Type 1)	Damped Oscillation (Type 2)
G_1	$\frac{\alpha \beta \bar{R}^2}{(\beta - \alpha) c^2} \{ \beta e^{-\beta t} - \alpha e^{-\alpha t} \}$	$(\gamma^2 + \delta^2) \frac{\bar{R}^2}{c^2} \{ \cos \delta t - \frac{\gamma}{\delta} \sin \delta t \} e^{-\gamma t}$
G_2	$\frac{\alpha \beta \bar{R}}{(\beta - \alpha) c} \{ e^{-\alpha t} - e^{-\beta t} \}$	$\frac{(\gamma^2 + \delta^2) \bar{R}}{\delta c} \sin \delta t e^{-\gamma t}$
G_3	$\frac{1}{(\beta - \alpha)} \{ \alpha e^{-\beta t} - \beta e^{-\alpha t} \}$	$- \{ \cos \delta t + \frac{\gamma}{\delta} \sin \delta t \} e^{-\gamma t}$
R_1	$\frac{\alpha}{\beta} e^{2\beta t_c}$	$e^{2\gamma t_c}$
t_c	$\frac{1}{(\beta - \alpha)} \ln \left(\frac{\beta}{\alpha} \right)$	$\frac{1}{\delta} \arctan \left(\frac{\delta}{\gamma} \right)$

Wave forms of radiation component (G_1), of induction component (G_2), and of electrostatic component (G_3) to be included in Eq. (17). Note that the time t must be replaced by the retarded time t_r in (17). R_1 is the ratio between first maximum and first minimum of the radiation component G_1 . t_c is the time of crossover from positive to negative values of G_1 .

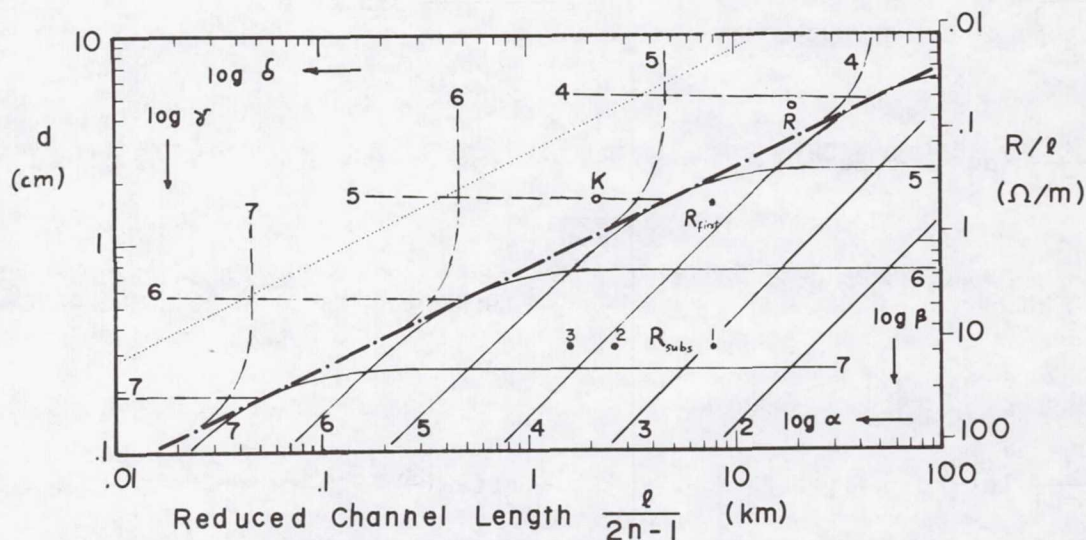


Figure 1.- Solutions of the eigenvalue equation (8). Isolines of α and β (solid lines) and of γ and δ (dashed lines), respectively, as functions of the reduced channel length ℓ_n and of the diameter d . The electric conductivity is assumed to be $\sigma = 10^4$ S/m. The fat dash-dotted line separates the (α, β) regime from the (γ, δ) regime. The (α, β) regime is related to aperiodic variations (type 1), the (γ, δ) regime is related to damped oscillations (type 2). The right ordinate is scaled according to $R/\ell = 4/(\sigma\pi d^2)$. The thin dotted line indicates the limit of validity of eq. (8). The solid dots give the locations of the parameters of the type 1 first return stroke and of the type 1 subsequent return stroke (lower series of dots). The circles give the locations of the type 2 return stroke (R) and of the type 2 K stroke (K).

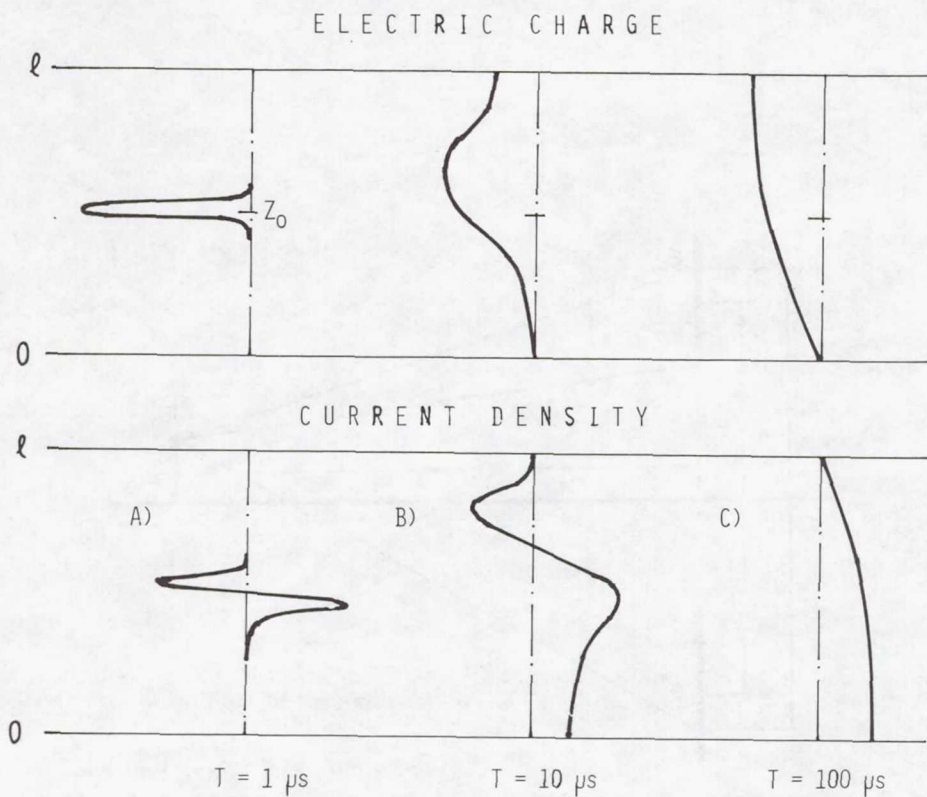


Figure 2.- Discharging of a point charge on an ideal grounded wire which is situated at height z_0 at time $t = 0$. Three different stages for the charge and the current configuration along the wire are shown (not to scale) at times $t_1 = 1 \mu s$, $t_2 = 10 \mu s$, and $t_3 = 100 \mu s$.

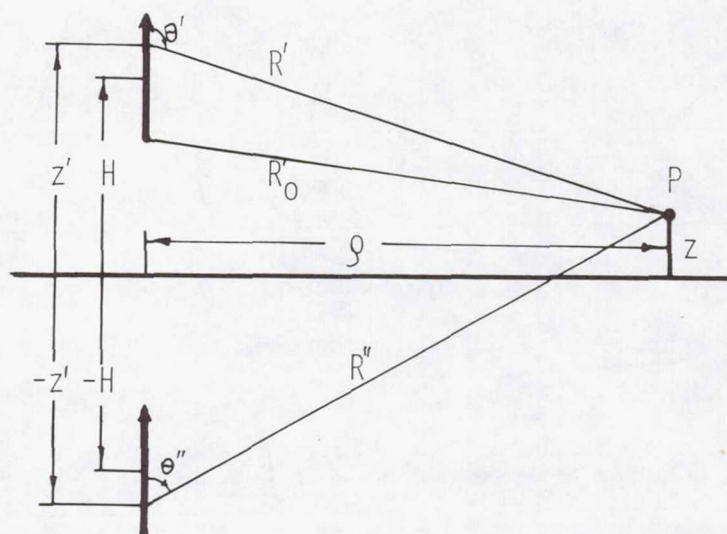


Figure 3.- Geometry of a vertical lightning channel and its image.

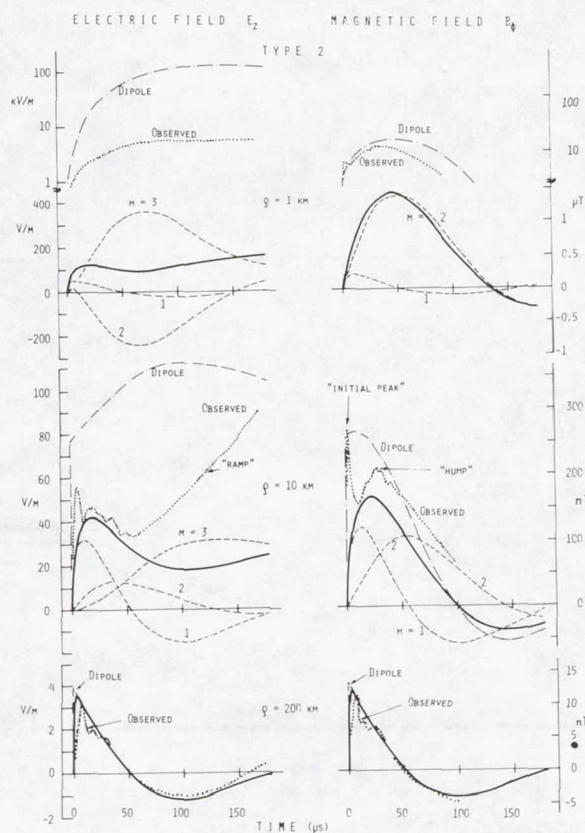


Figure 4.- Type 2 return stroke. Calculated vertical electric field (left) and azimuthal magnetic field (right) versus time at three different distances of 1, 10, and 200 km. Solid lines: total field. Dashed lines: radiation component ($m = 1$), induction component ($m = 2$), and electrostatic component ($m = 3$). Dash-dotted lines: total field of dipole approximation (eq. 19). The scaling on the right ordinate in μT ($=10^{-6}\text{T}$) and in nT ($=10^{-9}\text{T}$), respectively, equals the scaling on the left ordinate in Volt/m if the magnetic field is multiplied by the speed of light. The dotted lines are from observations (ref. 7). Note that the scaling of the dipole field and of the observations at 1 km distance is logarithmic.

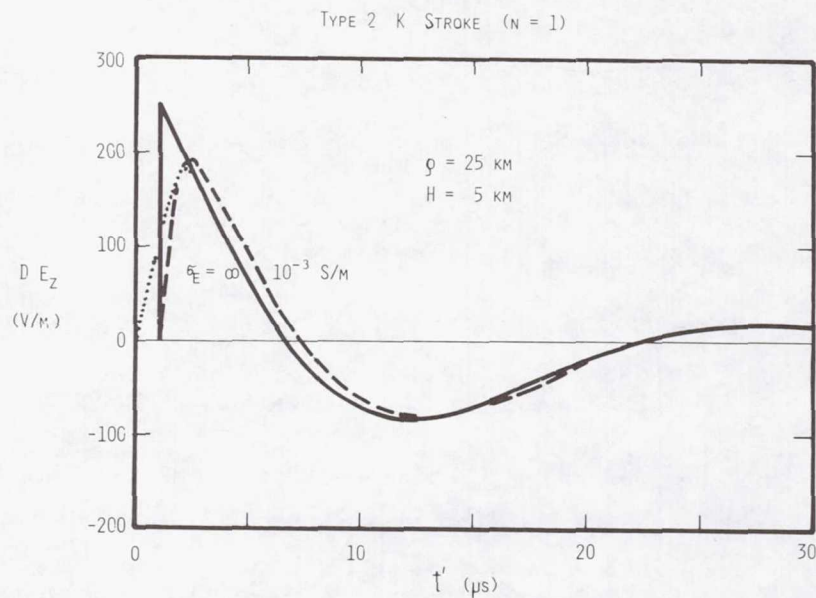


Figure 5.- Radiation component ($m = 1$) of a type 2 K stroke normalized to a distance of 1 km ($D = 1$). The distance from the lightning channel is 25 km, the center of the channel is at 5 km altitude. Solid line: dipole approximation over a perfectly conducting earth (eq. 19). Dashed line: dipole approximation over an imperfectly conducting earth with conductivity $\sigma_E = 10^{-3} \text{ S/m}$. Dotted line: exact calculation over a perfectly conducting earth (eq. 17).

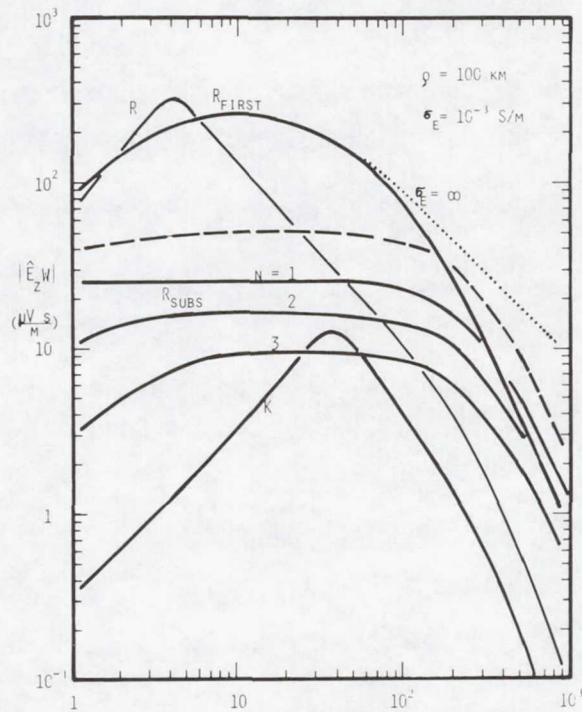


Figure 6.- Spectral amplitudes versus frequency of the dipole approximations of the radiation component ($m = 1$) of R and of K strokes at 100 km distance over an imperfectly conducting earth ($\sigma_E = 10^{-3}$ S/m). The dashed curve is the sum of the three modes ($n = 1, 2$, and 3) of the type 1 subsequent stroke. The dotted line gives the spectral amplitude of the type 1 first return stroke over a perfectly conducting earth.

Page intentionally left blank

CALCULATIONS OF LIGHTNING RETURN STROKE ELECTRIC
AND MAGNETIC FIELDS ABOVE GROUND

M. A. Uman, Y. T. Lin*, R. B. Standler**, M. J. Master
Department of Electrical Engineering
University of Florida
Gainesville, FL 32611

R. J. Fisher
Kaman Science Corporation
P.O. Box 7563
Colorado Springs, CO 80933

INTRODUCTION

Lin et al. [1] have recently introduced a new lightning return stroke model with which the two-station electric and magnetic fields measured at ground level by Lin et al. [2] can be reproduced. Here, we use that model to compute fields at altitudes up to 10 km and at ranges from 20 m to 10 km. These calculations provide the first detailed estimates of the return strokes fields that are encountered by aircraft in flight. With the advent of modern aircraft utilizing low voltage digital electronics and reduced electromagnetic shielding by way of structures containing advanced composite materials [3], these calculations are of considerable practical interest. Further, since airborne electric and magnetic field measurements are presently being attempted [4], a comparison of the calculations presented in this paper with appropriate experimental data, when they are available, will constitute a test of the return stroke model.

THEORY

We model the lightning return stroke current as contained in a thin vertical wire of height H above a perfectly conducting ground plane. The electric and magnetic fields at altitude z and range r from a vertical dipole at height Z of current $i(Z,t)$ are:

*Present address: Texas Instruments, Dallas, TX 75234

**Present address: Xerox Corporation, Rochester, NY 14580

Acknowledgement: This research has been supported in part by the Atmospheric Sciences Section of the National Science Foundation (ATM-76-01454) and the Office of Naval Research (N00014-75-C-0143). Additional funding has been made available by Electromagnetic Applications, Inc. via contract #F33615-79-C-3412 with the U.S. Air Force Flight Dynamics Laboratory.

$$\begin{aligned}
\vec{dE}(x,y,z,t) = & \frac{dZ}{4\pi\epsilon_0 R} \left[\left\{ \frac{3r(z-Z)}{R^4} \cdot \int_0^t i(Z,\tau - R/c) d\tau \right. \right. \\
& + \frac{3r(z-Z)}{cR^3} \cdot i(Z,t - R/c) + \frac{r(z-Z)}{c^2 R^2} \cdot \frac{\partial i(Z,t - R/c)}{\partial t} \left. \right\} \vec{a}_r \\
& + \left\{ \frac{2(z-Z)^2 - r^2}{R^4} \cdot \int_0^t i(Z,\tau - R/c) d\tau + \frac{2(z-Z)^2 - r^2}{cR^3} \cdot i(Z,t - R/c) \right. \\
& \left. \left. - \frac{r^2}{c^2 R^2} \cdot \frac{\partial i(Z,t - R/c)}{\partial t} \right\} \vec{a}_z \right] \quad (1)
\end{aligned}$$

$$\vec{dB}(x,y,z,t) = \frac{\mu_0 dZ}{4\pi R} \left\{ \frac{r}{R^2} \cdot i(Z,t - R/c) + \frac{r}{cR} \cdot \frac{\partial i(Z,t - R/c)}{\partial t} \right\} \vec{a}_\phi \quad (2)$$

where equations (1) and (2) are expressed in cylindrical coordinates; all geometrical factors involved in these equations are defined in Fig. 1. Equations (1) and (2) are obtained in a straightforward manner using an approach similar to that of Uman et al. [5]. The effects of the perfectly conducting ground plane are included by postulating an image current dipole beneath the plane. The electric and magnetic fields due to the image dipole may be obtained by substituting R_I for R and $-Z_I$ for Z in equations (1) and (2) above. The contributions to the fields from an elemental source at height Z and its image at $-Z$ are equal when the field point is on the ground [5]. Above ground level, the contribution of the image to the total field is smaller than the contribution of the source. Above ground and very close to the channel, the image contribution is negligible.

The model of Lin et al. [1] describes the current in the return stroke as being composed of the three components illustrated in Fig. 2 and 3: (a) a short-duration upward-propagating pulse of current associated with the upward-propagating return-stroke electrical breakdown and responsible for the peak current value; (b) a uniform current which may already be flowing (leader current) or may start to flow soon after the commencement of the return stroke; and (c) a "corona" current caused by the radially inward and then downward movement of the charge initially stored to the corona sheath around the leader channel and discharged by the return stroke wave front.

We calculate the electric and magnetic fields from equations (1) and (2) for a relatively large subsequent stroke. The parameters of the three current components are [1]:

- (a) peak breakdown current pulse: 50 kA; zero to peak risetime: 1.8 μ s;
fall time to half value: 3.8 μ s;
- (b) uniform current: 7000 A;

(c) corona current injected per meter of channel: $I_0 e^{-Z/\lambda} (e^{-\alpha t} - e^{-\beta t})$,
 with $I_0 = 50.41 \text{ A/m}$, $\lambda = 2700 \text{ m}$, $\alpha = 10^5 \text{ sec}^{-1}$, $\beta = 3 \times 10^6 \text{ sec}^{-1}$.

For this stroke, the initial leader charge is 1.2 C, and the total current at ground level is shown in Fig. 3. The return stroke velocity is chosen constant at $1 \times 10^8 \text{ m/sec}$ in a straight, vertical channel of 7.5 km length.

We examine only the subsequent stroke fields because subsequent strokes are more adequately modeled by the technique of Lin et al. [1] than are first strokes: subsequents have few, if any, branches [6], roughly constant luminosities and return stroke velocities with height [6], and are probably initiated at ground level rather than by upward-going leaders. For this reason, it is subsequent stroke fields with which Lin et al. [1] have primarily tested the model from which the fields presented in this paper are calculated. On the other hand, first and subsequent stroke measured fields at ground level are similar [2], and the modeling of first strokes can be successfully done with a constant return stroke velocity, even though this is probably the case only until the first major branch is reached [6], and with a corona current delay height about twice that typical of subsequent strokes [1]. Thus, one would expect the calculated airborne subsequent stroke fields to be qualitatively similar to those from first strokes. The subsequent stroke we have modeled is at the upper end of the peak current and charge transfer spectrum [1] and hence to that extent is similar to a first stroke.

The fields calculated from the current parameters given in the previous paragraph are adequate to produce reasonable fields at ground level, as shown by Lin et al. [1]. Further, the fields at ground level are not influenced much if the initial breakdown pulse has a current which decreases with height, as is certainly the case with first strokes. However, the fields above ground are influenced by the decrease of the breakdown current pulse with height, an effect we will discuss later.

RESULTS

Calculated vertical and horizontal electric are shown in Figs. 4a and 4b, respectively, and calculated magnetic fields in Fig. 4c. All indicated times are relative to the start of the return stroke current at ground level. The slanted lines in the figures indicate the time at which the return stroke wavefront passes each height. A number of features of the calculated waveforms are worthy of note.

1. At ranges less than about 200 m the electric and magnetic fields above ground reach peak value at about the time at which the return stroke breakdown pulse current is at the same altitude as the field point. The horizontal electric field rise time is about 1.8 sec with a $\frac{dE}{dt}$ of about 200 kV/m/ μs at 20 m.
2. At less than about 200 m range the vertical electric field above ground is bipolar due to the passage from below to above of the charge associated with

breakdown pulse current. As one moves farther away from the channel, or is near the ground, this effect is reduced.

3. At less than about 1 km range the peak value of the horizontal electric field above ground is much larger than the vertical electric field component. The horizontal and vertical fields above ground are roughly equal in magnitude in the 3 km range, and the vertical field is larger beyond about 10 km.

4. The magnetic field and the vertical electric field at about 10 km range and beyond are relatively weak functions of altitude so that measurements taken on the ground or in the air beyond 10 km should yield essentially similar results, thus providing a technique for calibration of the airborne measurements. The horizontal electric field above ground has a similar shape to the vertical electric field.

5. The field discontinuities associated with the idealized ends of the real and image channels are shown in Fig. 4a, b, c, but do not usually occur in nature [2].

DISCUSSION

The fact that the very close fields are similar as a function of height is related to the constancy with height of the upward-propagating breakdown current pulse. Further, the discontinuities in the waveforms at late times are due to this current pulse turning off as it reaches the end of both the source and image channels. It is likely that the actual breakdown current pulse will decrease with height, as has been shown to be the case for first strokes [6]. The result of incorporating a breakdown current pulse which decays with altitude in the electric and magnetic field calculations is to produce fields which, at close range, decrease with height, and which do not exhibit the late-time field discontinuities. Detailed calculations of fields for breakdown current pulses which decay with height will be published in the near future.

REFERENCES

1. Lin, Y.T., M.A. Uman, and R.B. Standler, Lightning Return Stroke Models, J. Geophys. Res., 85, Spring 1980.
2. Lin, Y.T., M.A. Uman, J.A. Tiller, R.D. Brantley, W.H. Beasley, E.P. Krider, and C.D. Weidman, Characterization of Lightning Return Stroke Electric and Magnetic Fields from Simultaneous Two-Station Measurements, J. Geophys. Res., 84, 6307-6314, 1979.
3. Corbin, J.C., Protection/Hardening of Aircraft Electronic Systems Against the Indirect Effects of Lightning, FAA-FIT Workshop on Grounding and Lightning Technology, March 6-8, 1979, Melbourne, FL, Report No. FAA-RD-79-6, pp. 97-103.
4. Pitts, F.L., M.E. Thomas, R.E. Campbell, R.M. Thomas, and K.P. Zaepfel, Inflight Lightning Characteristics Measurement System, FAA-FIT Workshop on Grounding and Lightning Technology, March 6-8, 1979, Melbourne, FL, Report No. FAA-RD-79-6, pp. 105-111.
5. Uman, M.A., D.K. McLain, and E.P. Krider, The Electromagnetic Radiation from a Finite Antenna, Amer. J. of Physics, 43, 33-38, 1975.
6. Schonland, B.F.J., The Lightning Discharge, Handbuch der Physik, 22, 576-628, Springer-Verlag, OHG, Berlin, 1956.

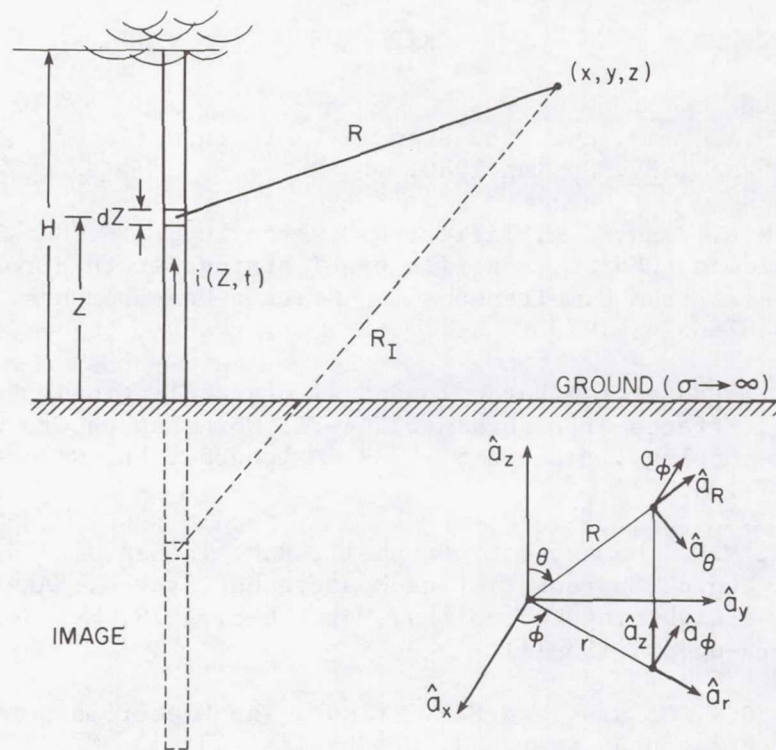


Figure 1.- Geometry for field computations.

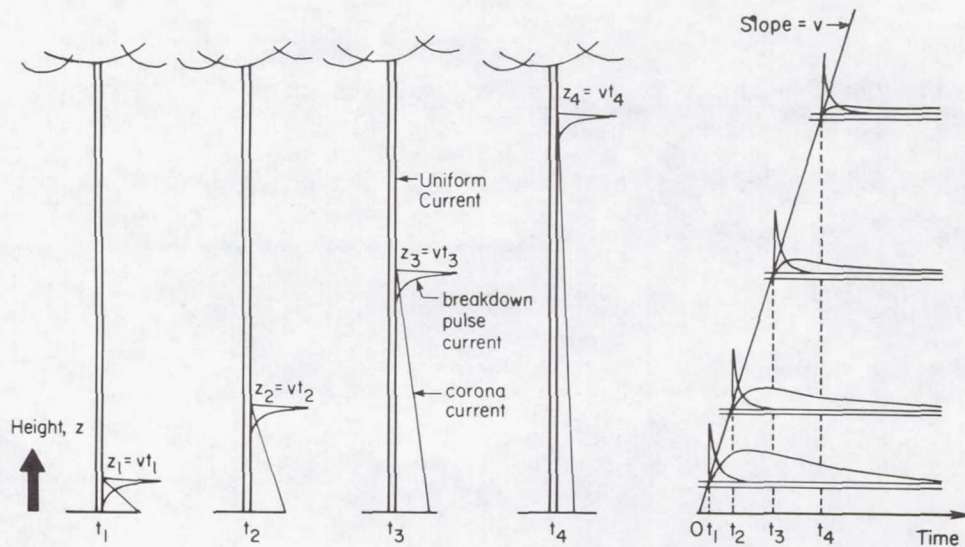


Figure 2.- Return stroke component currents.

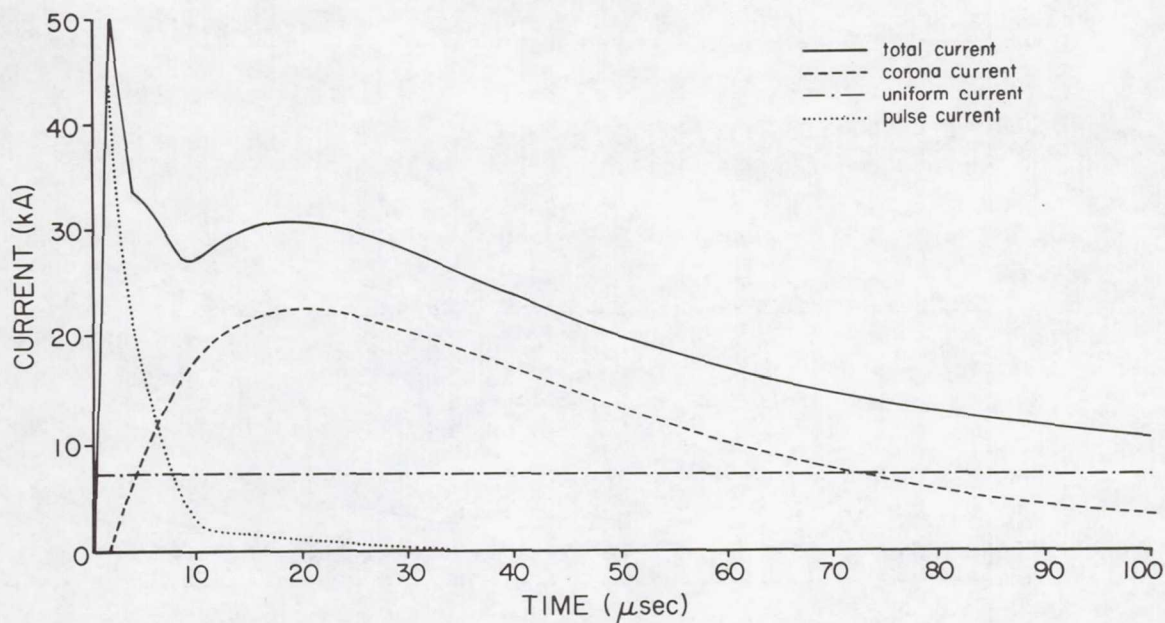


Figure 3.- Return stroke current at ground.

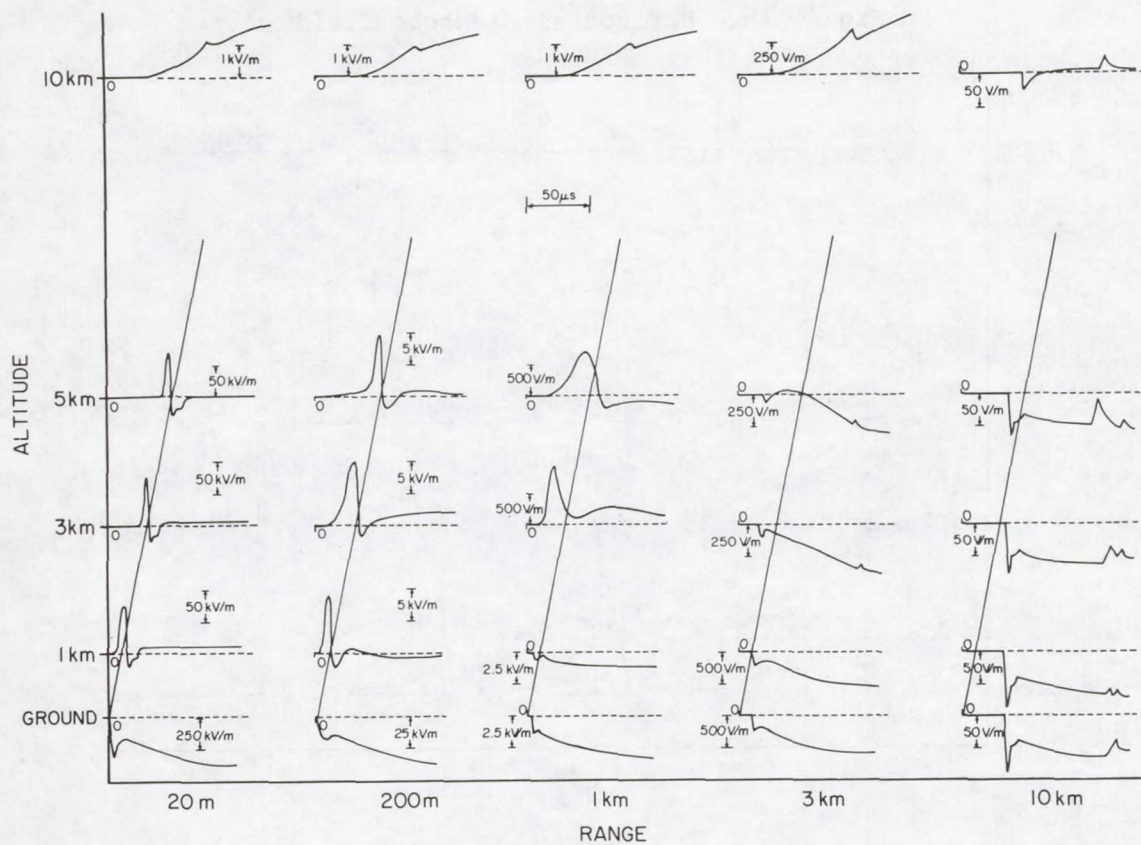


Figure 4a.- Vertical electric field.

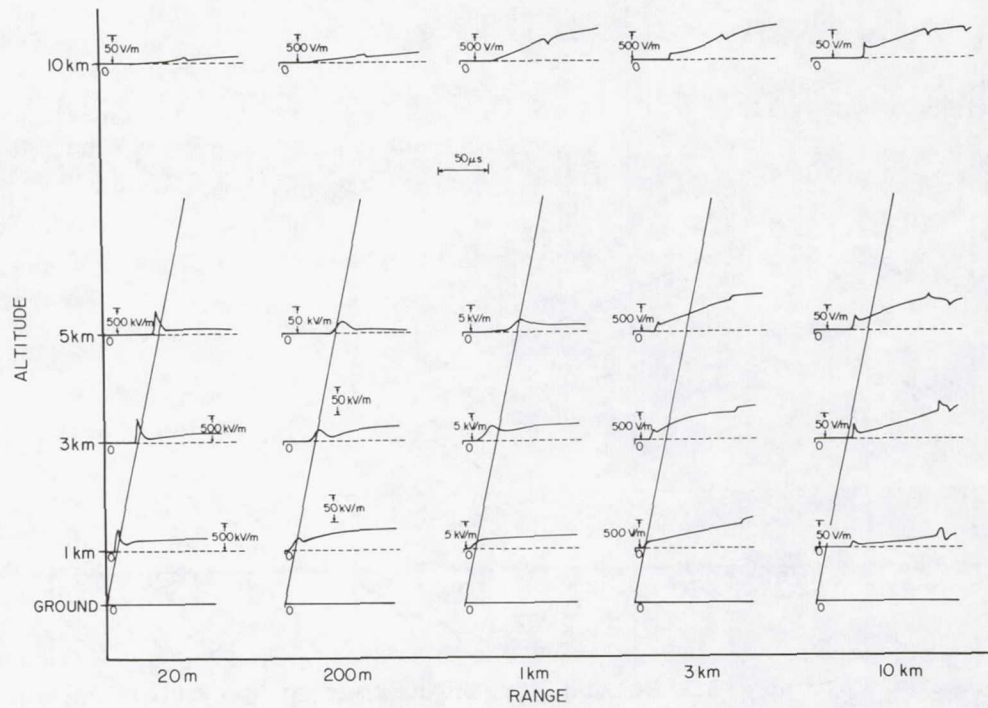


Figure 4b.- Horizontal electric field.

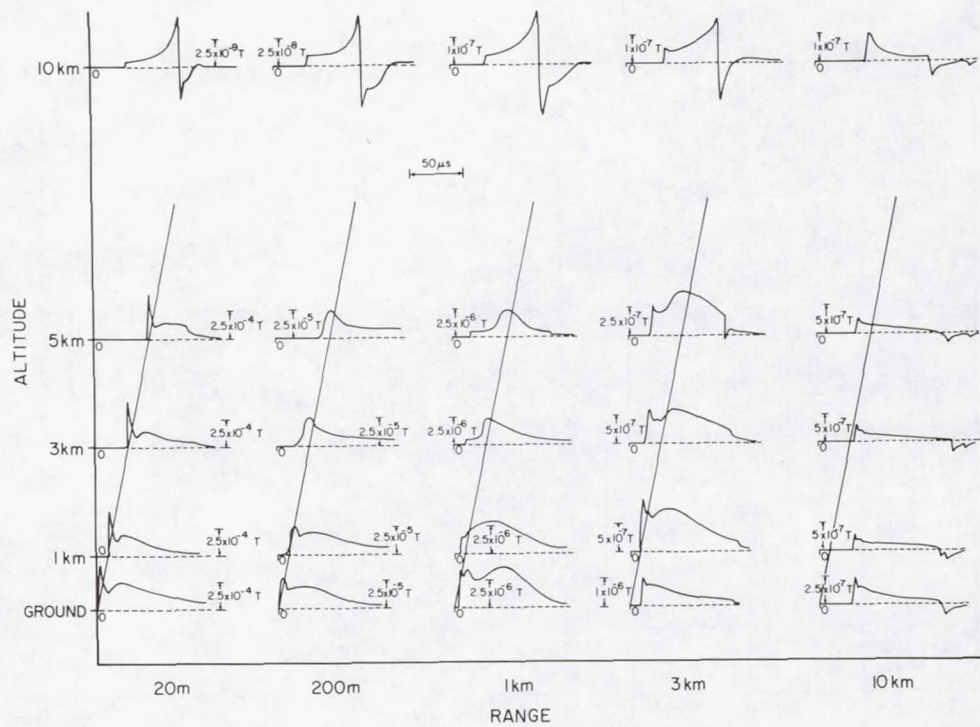


Figure 4c.- Magnetic field.

SUBMICROSECOND RISETIMES IN LIGHTNING RADIATION FIELDS

C. D. Weidman and E. P. Krider
Institute of Atmospheric Physics
The University of Arizona, Tucson, Arizona 85721
(602) 626-1211

SUMMARY

Measurements of lightning electric fields, E , and dE/dt signatures have been made near Tampa Bay, Florida, under conditions where the field propagation from the source to the detector was entirely over sea water. The fast transitions found on the initial portion of return stroke E waveforms have 10-90% risetimes ranging from 40-200 nsec, with a mean of 90 nsec. The maximum dE/dt values during these transitions range from 5-80 (V/m) μsec^{-1} , with a mean of about 30 (V/m) μsec^{-1} when normalized to a distance of 100 km. The initial risetimes of stepped-leader impulses that occur just prior to the first return stroke in cloud-to-ground flashes are very similar to the fast transitions in return strokes. The dE/dt values during leader steps range from 10-40 (V/m) μsec^{-1} with a mean of 20 (V/m) μsec^{-1} when normalized to 100 km. The fast impulses superimposed on large-amplitude intracloud waveforms have E risetimes and dE/dt values similar to those of the leader steps.

INTRODUCTION

In recent years, there has been increasing evidence that lightning radiation fields contain large, submicrosecond variations and that the corresponding lightning currents may be considerably faster than previously thought. Weidman and Krider (ref. 1) have found large, submicrosecond transitions in the fields produced by return strokes, the large current surges produced by discharges to ground. Krider et al. (ref. 2) have found submicrosecond risetimes in the stepped-leader impulses which precede return strokes; and Weidman and Krider (ref. 3) have also found large, submicrosecond components in the fields produced by cloud discharges. In all of the measurements referenced above, the field recording system was limited by a response time of about 150 nsec (ref. 2), and many field risetimes were essentially at this limit.

Since the interactions of lightning with aircraft, space vehicles, power systems, structures, etc., are critically dependent on the field and current risetimes, we have endeavored to make improved measurements of lightning field risetimes. A recording system was assembled which had a response time of about 10 nsec on the time-derivative of the electric field, dE/dt , and about 40 nsec or less on the electric field, E . Great care was taken to record the fields on several time scales simultaneously so that the type of lightning impulse and the time at which it occurred within the discharge could be accurately determined. The experiment was located in a region where the lightning locations

were known and where the fields would not be distorted by propagation before they reached the recording apparatus.

MEASUREMENTS

A block schematic diagram of the measuring equipment is shown in figure 1. Two circular flat plate antennas (0.2 m^2) with guard rings were mounted on the roof of a grounded metal bus that housed the recording apparatus. The vehicle was located approximately 10 m from a sea wall on the northeast edge of Anna Maria Island, which is at the southern entrance to Tampa Bay, Florida. From that location, any lightning field that originated within a broad area from 100 km to the northwest to about 50 km to the northeast would propagate entirely over sea water to the recording site. The left antenna in figure 1 was centered on the bus and horizontal, so that any electric field which might be produced by vehicle resonances would be a minimum. The bus was grounded to a salt-water ground plane (about 1 m below the sandy surface) by one copper-clad steel rod on each of the four sides of the bus. One end of a $10 \times 10 \text{ m}^2$ wire mesh ground plane was attached to the bus, and the other end was immersed in sea water.

To obtain a signal proportional to dE/dt , the output of the left antenna in figure 1 was connected directly to the input of a Tektronix 7834 storage oscilloscope through a short piece of coaxial cable that was terminated in the characteristic cable impedance (50Ω). The response time of the antenna, cable, and oscilloscope system was approximately 10 nsec, as shown in figure 2b. In order to obtain a signal proportional to E , the 50Ω terminating resistor could be replaced by $100 \text{ k}\Omega$, so that the combined capacitance of the antenna, cable, and oscilloscope preamplifier (250 pF total) acted as a passive integrator. Travelling wave effects in the antenna cable limited the system risetime in the E configuration to about 40 nsec, as shown in figure 2a. Normally, the storage oscilloscope was triggered internally whenever the dE/dt or E signal exceeded a preset threshold. The gate output from the storage oscilloscope triggered three Biomation waveform recorders that provided the electric field and the North-South and East-West components of the magnetic field on slower time scales. The Biomation outputs were displayed on two time bases simultaneously, using a Tektronix 555 dual-beam oscilloscope. The dual-beam oscilloscope was photographed using a streak camera. The storage oscilloscope was operated in a single-sweep mode with automatic reset and was photographed with a framing camera. With the above arrangement, both fast and slow lightning signals could be recorded with a time-synchronization of about 100 nsec.

In figures 3-6, we present examples of E and dE/dt signatures which were produced by (a) return strokes in lightning discharges to ground, (b) leader steps which precede return strokes, and (c) cloud discharge processes which precede ground flashes or which occur in isolation. The locations of the lightning in these figures were obtained from an LLP lightning locating system operated by the Tampa Electric Company (ref. 4) and/or by visual observations and flash-bang time delays.

Examples of return-stroke fields are shown in figure 3. Each signal is displayed on both a fast and a slow time scale, either 100 ns/div or 200 ns/div and 4 μ s/div, respectively. The fast record is shown above the slower trace, but the time scales have been shifted so that the field peaks are aligned vertically. The vertical gain on the fast record was about twice that of the slow record. The field-amplitude scale shown on the left reflects an absolute calibration which we believe is accurate to $\pm 15\%$.

To obtain the records in figure 3, the storage oscilloscope trigger level was set low, so that the system triggered on the slow initial portion of the field. (See ref. 1 for a discussion of the structure of return-stroke fields.) Note how all the return strokes in figure 3 show a fast rise to peak following a slow initial portion. The physical processes which occur between the last leader step and the onset of the return stroke are not well understood (ref. 1), but it is clear that large, submicrosecond fields are being radiated. The small pulse on the initial portion of figure 3b was a relatively frequent signature which we think may have been caused by a leader step field being superimposed on a slower return-stroke front. Note how the initial slope of the leader step is comparable to that of the return stroke. Figure 3c is an example of what is probably a return stroke subsequent to the first. Note how the rapidly varying initial field is similar to those of first strokes in figures 3a and 3b. Note also that the transition from the subsequent stroke front to the fast rise to peak is quite distinct even on the 100 ns/div time scale.

Examples of dE/dt signals produced by the fast-rising portions of return strokes are shown in figure 4. A 4 μ s/div E waveform is shown again as the lower waveform on each flash, and the vertical arrow shows the time at which the storage oscilloscope triggered. The dE/dt waveform is shown at the upper left on a time scale of 50 ns/div, and a computer integral of the dE/dt output is shown at the upper right. The location of the dE/dt baseline was recorded frequently during the data runs and has been drawn on each dE/dt record. The initial portion of the dE/dt waveform was interpolated smoothly back to zero to produce the computer-integrated trace. The peak dE/dt signals and the structure of the dE/dt integral curve are very consistent with the maximum slopes and shapes of the records shown in figure 3 after range normalization.

Figure 5 shows E, dE/dt , and B records for a stepped-leader impulse that preceded the first return stroke in a flash by about 130 μ sec. Here, the dE/dt signature is fast and narrow, and the 10-90% E risetime is about 50 nsec.

Figure 6 shows four examples of the electric fields radiated by cloud discharges. Waveforms such as these tend to be produced by the cloud breakdown that precedes flashes to ground (ref. 3), and they usually occur as part of a rapid sequence of pulses. It is clear from figure 6 that the fast components of cloud impulses also have submicrosecond risetimes, and that risetimes and slope values are similar to those of leader steps.

CONCLUSIONS

Measurements of the fast-field transitions found on the initial portion of 125 return strokes show 10-90% risetimes in the range from 40-200 nsec with a mean of 90 nsec, as shown in figure 7. Figure 8 summarizes measurements of the maximum slopes on E field records and the peak dE/dt signals for 97 return strokes. Maximum field derivatives range from 5-80 (V/m) μsec^{-1} with a mean of about 30 (V/m) μsec^{-1} when normalized to a distance of 100 km using an inverse distance relation. The risetimes of individual leader steps are similar to the fast portions of return strokes, and the dE/dt values of 18 steps range from 10-40 (V/m) μsec^{-1} , when normalized to 100 km, with a mean of 21 (V/m) μsec^{-1} . The fast pulses superimposed on large cloud impulses have risetimes and maximum dE/dt values similar to leader steps.

Since the submicrosecond variations in the lightning fields are large and since similar variations must be present in the lightning currents (ref. 1), these fields and the physical processes which produce them will be the objects of a continuing study.

REFERENCES

1. Weidman, C. D., and Krider, E. P.: The Fine Structure of Lightning Return Stroke Wave Forms. J. Geophys. Res., vol. 83 (C12), 1978, pp. 6239-6247.
2. Krider, E. P., Weidman, C. D., and Noggle, R. C.: The Electric Fields Produced by Lightning Stepped Leaders. J. Geophys. Res., vol. 82 (6), 1977, pp. 951-960.
3. Weidman, C. D., and Krider, E. P.: The Radiation Field Wave Forms Produced by Intracloud Lightning Discharge Processes. J. Geophys. Res., vol. 84 (C6), 1979, pp. 3159-3164.
4. Krider, E. P., Pifer, A. E., and Uman, M. A.: An Automatic Locating System for Cloud-to-Ground Lightning. Symposium on Lightning Technology. NASA CP-2128, 1980.

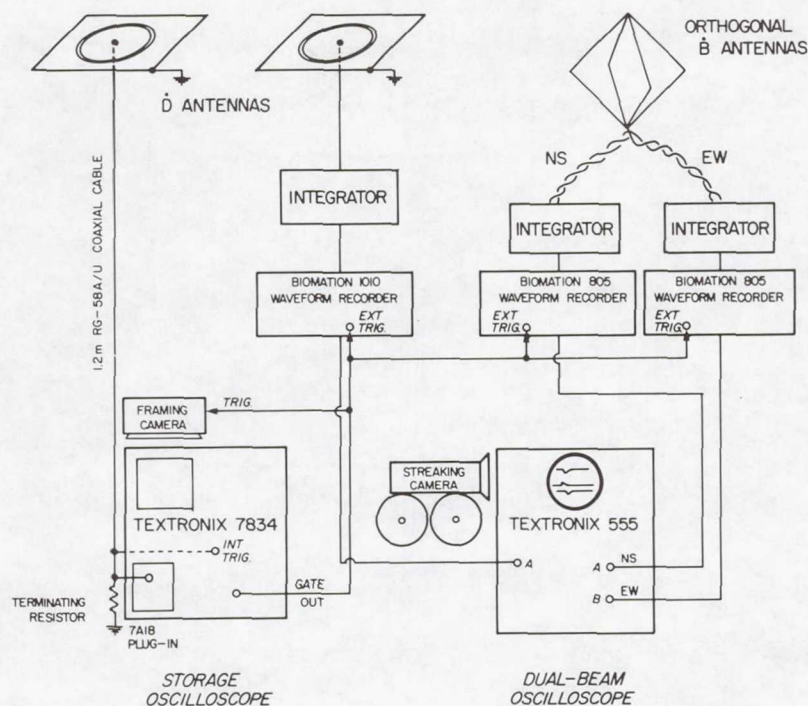


Figure 1.- A block diagram of the recording system.

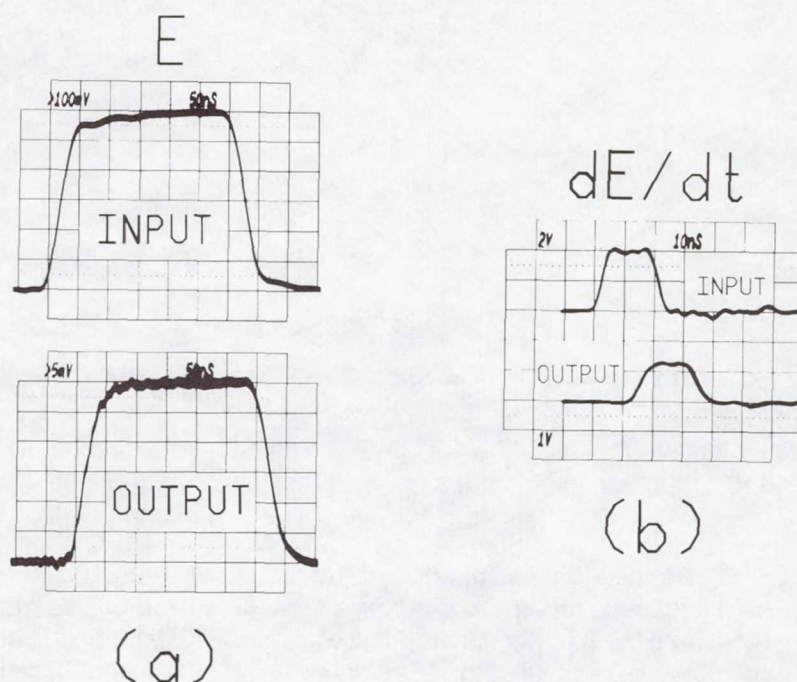


Figure 2.- the response times of (a) the E and (b) the dE/dt recording systems. The time scale in (a) is 50 nsec/div and in (b) is 10 nsec/div.

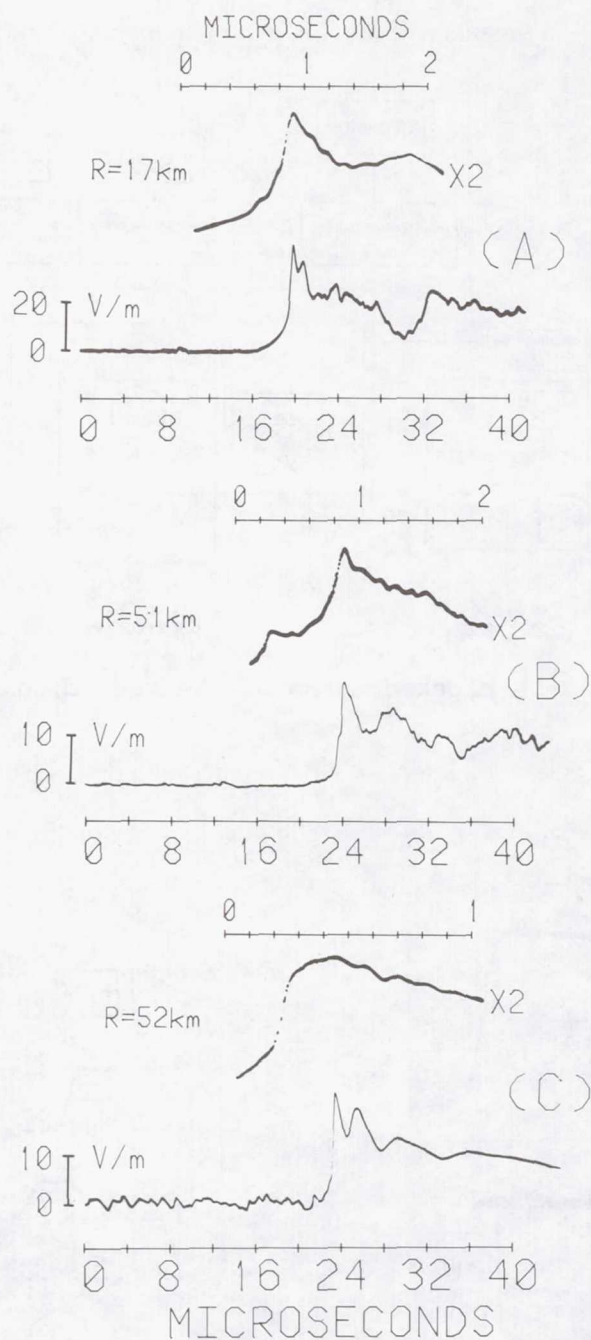


Figure 3.- Electric field waveforms produced by three lightning return strokes. The same waveform is shown on both a slow ($4 \mu\text{s}/\text{div}$) and a fast ($200 \text{ ns}/\text{div}$ in A and B, $100 \text{ ns}/\text{div}$ in C) time scale. The field amplitude is shown to the left of the lower record. The vertical gain of the upper trace is twice that ($\times 2$) of the lower trace. The range, R , to the lightning discharge is shown for each flash.

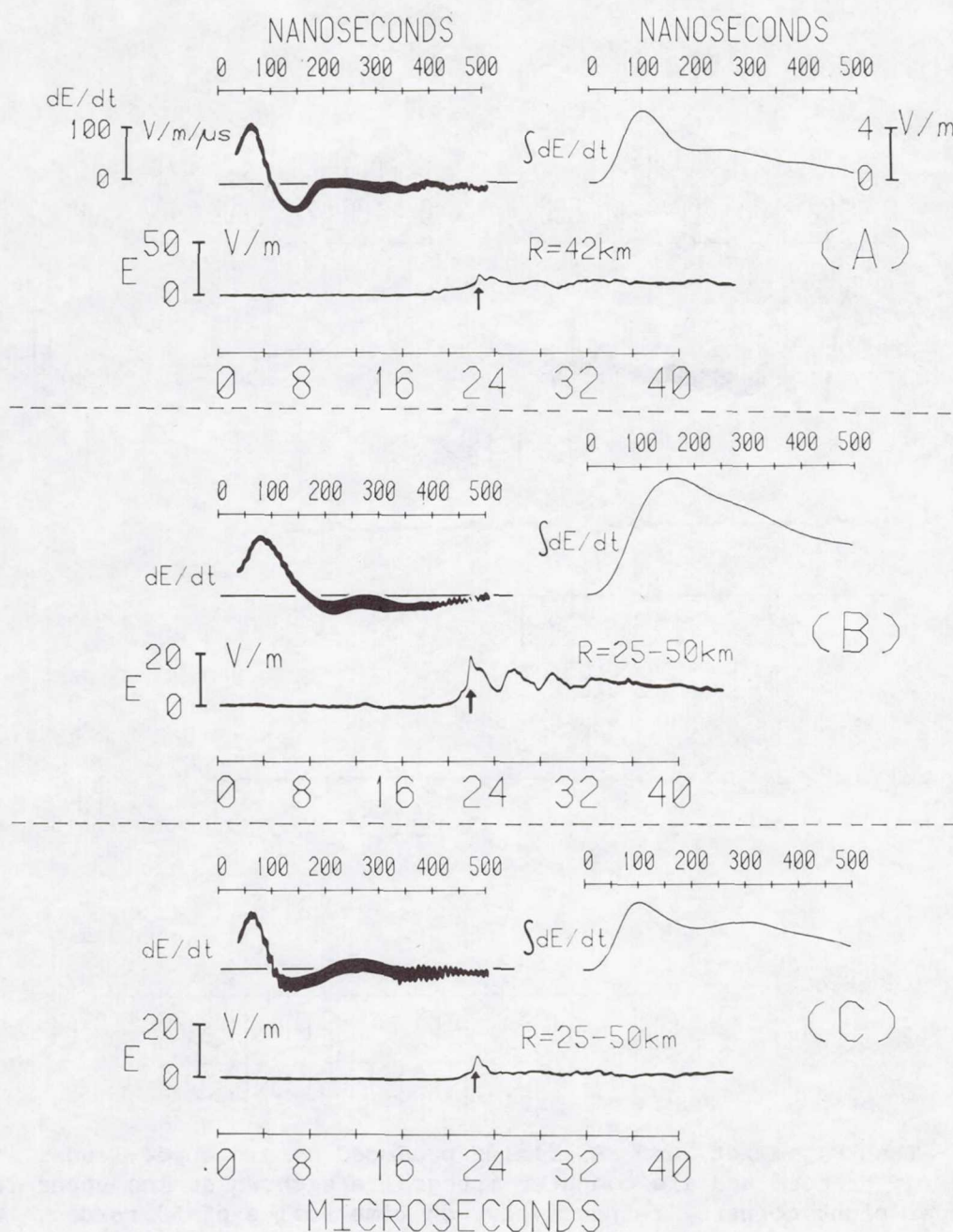


Figure 4.- Examples of E and dE/dt signals radiated by three return strokes. The dE/dt amplitude scale is shown at the top left of stroke A and is the same for all three discharges. All dE/dt records and their computer integrals are shown on a 50 ns/div time scale. The starting point of the dE/dt record has been indicated by a vertical arrow on the E record.

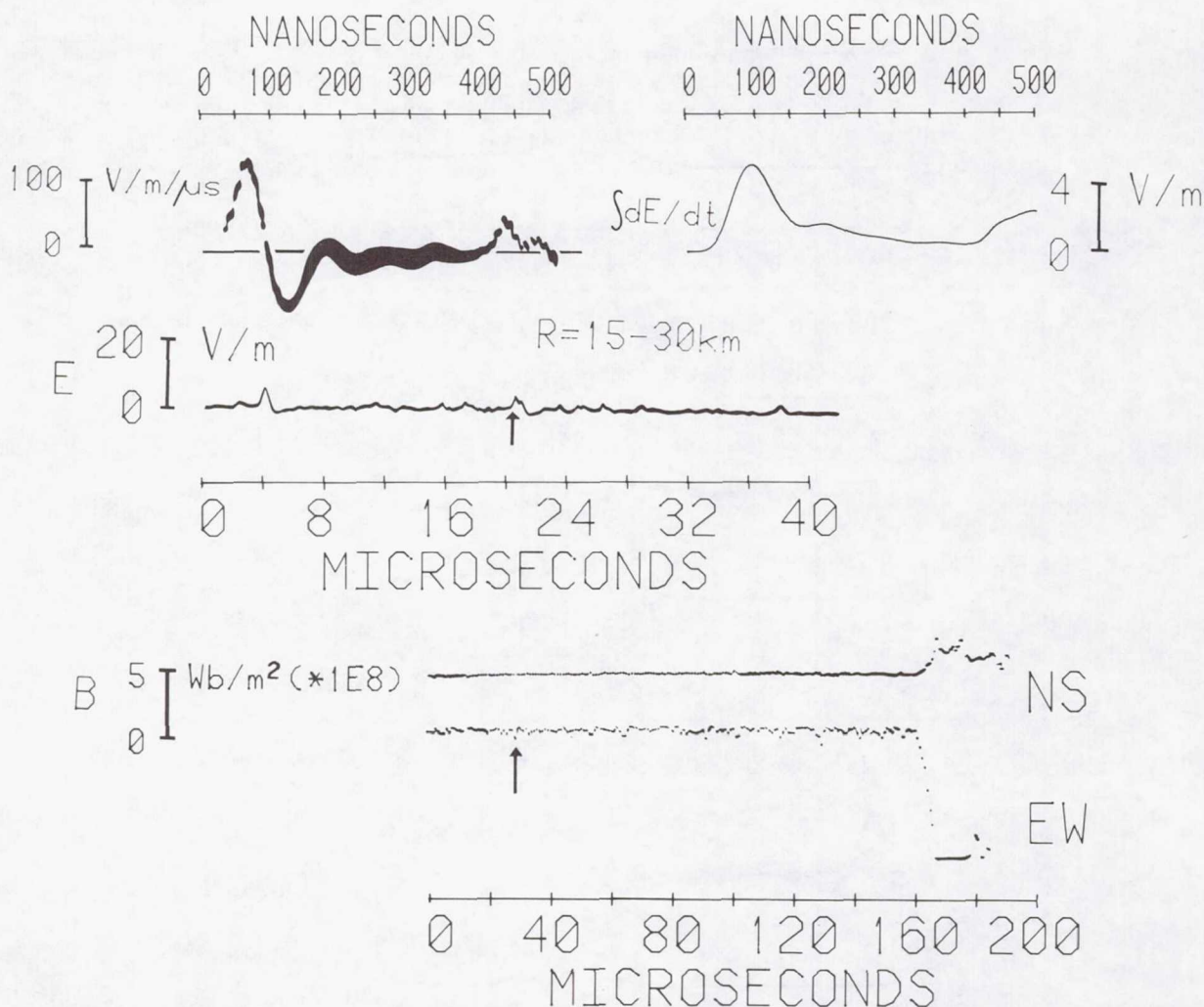


Figure 5.- The E , dE/dt , and B fields produced by a stepped-leader impulse. The dE/dt record and its computer integral are shown at the upper left and upper right corners, respectively, on time scales of 50 ns/div. The electric field and the NS and EW components of the magnetic field are shown below on time scales of 4 μ s/div and 20 μ s/div, respectively. The starting point of the dE/dt record is indicated by the vertical arrow on the slow electric and magnetic field records.

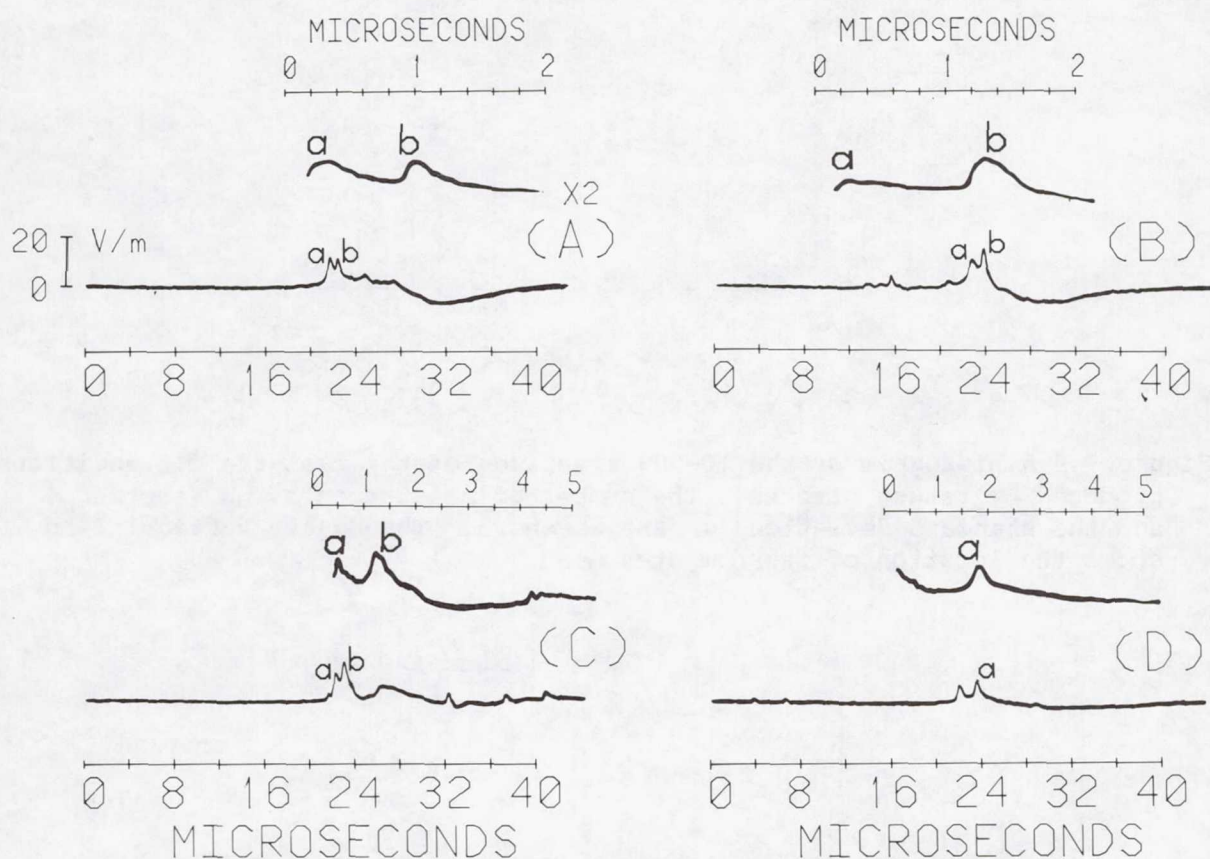


Figure 6.- E waveforms produced by four intracloud discharges. Each event is shown on a slow (4 μ s/div) and a fast (200 ns/div in A and B, 500 ns/div in C and D) time scale. The amplitude scale of all slow records is shown to the left of A. The vertical gain of the upper trace is twice that of the lower trace in each example. Corresponding peaks on each time scale have been identified with a lower case letter for each event. These discharges occurred over salt water approximately 15-25 km from the recording site.

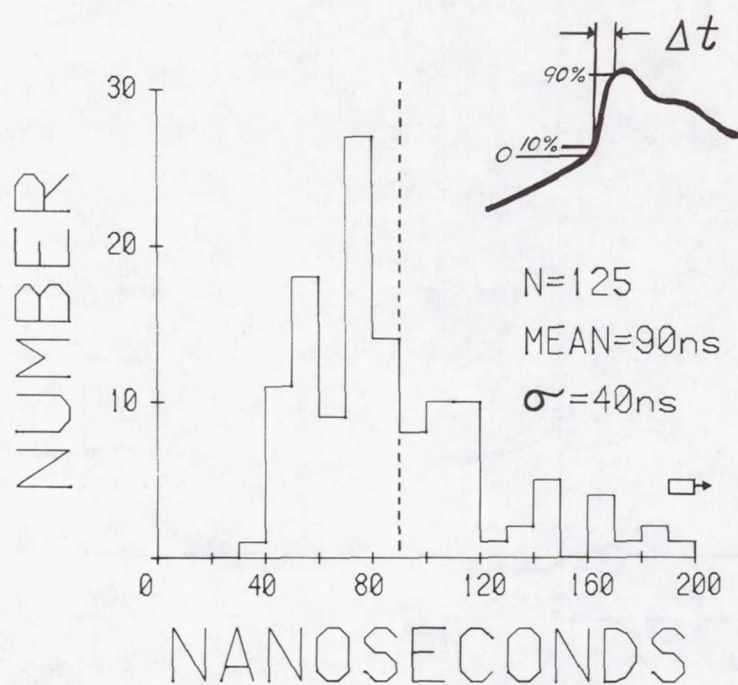


Figure 7.- A histogram of the 10-90% risetimes of the fast-field transitions produced by return strokes. The number of measurements, N , the mean, and the standard deviation σ are as shown. The dashed vertical line shows the location of the computed mean.

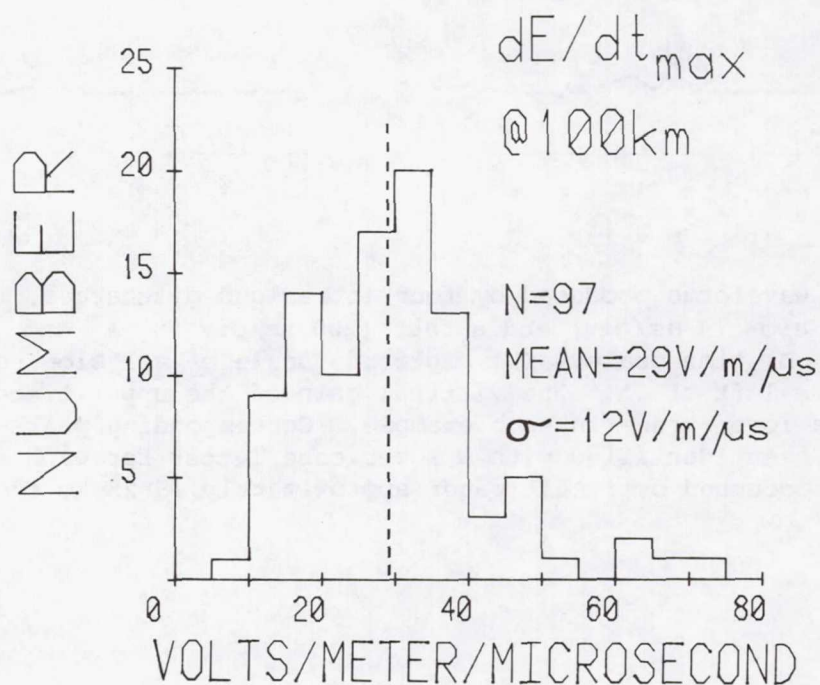


Figure 8.- A histogram of the maximum return-stroke dE/dt values normalized to a distance of 100 km.

MEASUREMENT OF ELECTROMAGNETIC PROPERTIES OF LIGHTNING WITH 10 NANOSECOND RESOLUTION

C. E. Baum, E. L. Breen, and J. P. O'Neill
Air Force Weapons Laboratory

C. B. Moore and D. L. Hall
New Mexico Institute of Mining and Technology

ABSTRACT

This paper presents electromagnetic data recorded from lightning strikes. The data analysis reveals general characteristics of fast electromagnetic fields measured at the ground including rise times, amplitudes, and time patterns. A look at the electromagnetic structure of lightning shows that the shortest rise times in the vicinity of 30 ns are associated with leader streamers. Lightning location is based on electromagnetic field characteristics and is compared to a nearby sky camera. The fields from both leaders and return strokes have been measured and are discussed.

The data were obtained during 1978 and 1979 from lightning strikes occurring within 5 kilometers of an underground metal instrumentation room located on South Baldy peak near Langmuir Laboratory, New Mexico. The computer controlled instrumentation consisted of sensors previously used for measuring the nuclear electromagnetic pulse (EMP) and analog-digital recorders with 10 ns sampling, 256 levels of resolution, and 2 kilobytes of internal memory.

I. INTRODUCTION

In the summers of 1978 and 1979 a set of measurements of the electromagnetic fields from natural lightning was made near the top of South Baldy peak (elevation 3275 m) which also houses Langmuir Laboratory near Socorro, New Mexico, U.S.A. As will be discussed in this paper the data consist of time waveforms of about 20 μ s duration at a 10 ns sample spacing for the three electromagnetic field components (one electric and two magnetic) which exist adjacent to a conducting ground plane on top of the "iron Kiva" (or Kiva) (our screen room buried in the top of the mountain) and the surrounding earth surface (see fig. 1.1). The details of the instrumentation system are discussed in another paper (ref. 5).

As background, these measurements resulted from some interest in the difference between lightning and the nuclear electromagnetic pulse. For nuclear detection purposes it is desirable to reliably detect a nuclear EMP event without false triggering by lightning. The ARGUS-1A detector system was designed with the high altitude EMP environment in mind (ref. 2). For this

purpose magnetic (loop) sensors were used to avoid the low-frequency electric field from lightning and local static charging effects. In addition the sensors respond to the derivative of the field to emphasize the high frequencies present in the high-altitude nuclear EMP. Essentially one is looking for a pulse with 10 ns to 100 ns important characteristic times.

In order to understand the sensitivity of the ARGUS-1A to lightning two things were done. First the detectors were placed on South Baldy peak and their response to lightning monitored. Second, and more important for this paper, the fast transient characteristics of the transient electromagnetic fields (in time-derivative form) were measured. It is these measurements and some analysis of them which are presented here.

The field sensors consist of two MGL-3 B-dot sensors and one ACD-5 D-dot sensor located on the roof (ground plane) of a buried shield enclosure (Kiva). The roof of the Kiva is flush with the earth surface and is electrically connected to the center of a 30 m \times 30 m wire-mesh ground plane. Data recording is accomplished by Biomation 8100 waveform recorders controlled by an HP 9825 calculator. A more complete description of the instrumentation is presented in reference 5.

At first we had little idea of what to expect. We made some measurements (section 2) which showed us some of the signal levels and patterns in the waveforms of the field time derivatives, and in the time integral of these waveforms. Based on the kinds of pulses observed and their time patterns it appeared that these related to individual fast pulses along some leader formation process. This led to a model (section 3) which with ranging information (section 4) allowed us to infer some of the characteristics of the current in the lightning streamer. Section 5 then applies this to some of the data obtained.

II. GENERAL CHARACTERISTICS OF OBSERVED ELECTROMAGNETIC FIELDS

With the instrumentation at the Kiva discussed in reference 5 measurements were begun in the summer of 1978. For use in our data analysis the $\partial \vec{B}/\partial t$ sensors (MGL-3) had $A_{heq} = 0.1 \text{ m}^2$, and the $\partial \vec{D}/\partial t$ sensor (ACD-5) had $A_{eq} = 1.0 \text{ m}^2$ for use in the formulas

$$V_h = \vec{A}_{heq} \cdot \frac{\partial}{\partial t} \vec{B} \quad (\text{open circuit voltage}) \quad (2.1)$$

$$I_e = \vec{A}_{eq} \cdot \frac{\partial}{\partial t} \vec{D} \quad (\text{short circuit current})$$

where the fields are those in the presence of the ground plane (i.e., including reflection). The response times (10-90 rise times of integrated output for step-function exciting field) into 50 Ω loads are short compared to our 10 ns sampling resolution and hence neglected.

The three sensors responded to the north and east components of $\partial \vec{B}/\partial t$ and to the vertical (up) component of $\partial \vec{D}/\partial t$. The signal from $\partial \vec{B}/\partial t$ north was attenuated a factor of 2 by a power splitter used to send this signal to an additional recorder for other purposes. These corrections and the equivalent areas are all removed for the displays of $\partial \vec{B}/\partial t$ and $\partial \vec{D}/\partial t$ in this paper. The \vec{B} and \vec{D} waveforms are determined by numerical integration of the digital data provided by the Biomation 8100 waveform recorders. Note that the integrated waveforms exhibit baseline slope which is at least partly due to errors in determining the baseline values for the original waveforms; this baseline shift is partly removed by estimating the baseline position near the beginning of the recording. The long-time variation of the integrated waveforms should not be trusted, nevertheless; the purpose of the integration is to see the shape and amplitude of the fast pulses which are more reliable.

A nice property of the Biomation 8100 waveform recorder is that one has a significant length of recording time before the pulse which triggers the system is recorded. This pretrigger data time was set at about 4 μs . The self trigger was used on all three channels with the first trigger level being exceeded triggering all the recorders. Triggering in this case means freezing the data stream and transferring the 20 μs of information to magnetic disk.

Since the recording is digital there is also some limitation in the signal amplitude (voltage) resolution. The full scale is 256 uniformly spaced levels with zero approximately centered. Typical signals deviated about one third from baseline (zero) to the full level on one side of zero.

For some preliminary information let us now consider two examples of the kinds of waveforms we have seen. Detailed analysis of such waveforms is considered in section 5. A representative example of a leader waveform is given in figures 2.1 and 2.2. A representative example of a return-stroke waveform is given in figures 2.3 and 2.4. In both cases only the east components of $\partial \vec{B}/\partial t$ and of \vec{B} are exhibited.

Consider the leader waveform in figure 2.1. Note the complex structure with many individual pulses indicating the progression of the leader as a sequence of impulsive events. The horizontal distance (by flash to bang) to this stroke was about 350 m.

Note the large pulse at about 4 μs which triggered the recording. The first 7 μs of the record is expanded in figure 2.2. From a printout of the digital data this pulse has the approximate characteristics:

pulse at 4.0 μs

$$\frac{\partial}{\partial t} B_E \left\{ \begin{array}{l} \text{peak} \approx 2.42 \text{ T/s} \\ \text{zero to peak rise} \approx 90 \text{ ns} \\ \text{10-90 rise} \approx 50 \text{ ns} \end{array} \right.$$

(2.2)

$$B_E \left\{ \begin{array}{l} \text{baseline to peak} \approx 0.169 \mu\text{T} \\ \text{baseline to peak rise} \approx 150 \text{ ns} \\ \text{10-90 rise} \approx 80 \text{ ns} \\ \text{width} \approx 500 \text{ ns} \end{array} \right.$$

$$\tau \approx 70 \text{ ns}$$

Here τ has been defined as a characteristic time for the rise portion of the waveform with the formula

$$\tau \equiv \frac{\text{waveform peak}}{\text{derivative waveform peak}} \quad (2.3)$$

Selecting a few more pulses from this waveform for comparison we have

pulse at $1.3 \mu\text{s}$

$$\frac{\partial}{\partial t} B_E \left\{ \begin{array}{l} \text{peak} \approx 1.48 \text{ T/s} \\ \text{zero to peak rise} \approx 50 \text{ ns} \\ \text{10-90 rise} \approx 30 \text{ ns} \end{array} \right. \quad (2.4)$$

$$B_E \left\{ \begin{array}{l} \text{baseline to peak} \approx .079 \mu\text{T} \\ \text{baseline to peak rise} \approx 100 \text{ ns} \\ \text{10-90 rise} \approx 60 \text{ ns} \\ \text{width} \approx 250 \text{ ns} \end{array} \right.$$

$$\tau \approx 53 \text{ ns}$$

and another

pulse at $12.9 \mu\text{s}$

$$\frac{\partial}{\partial t} B_E \left\{ \begin{array}{l} \text{peak} \approx -.86 \text{ T/s} \\ \text{zero to peak rise} \approx 60 \text{ ns} \\ \text{10-90 rise} \approx 30 \text{ ns} \end{array} \right. \quad (2.5)$$

$$B_E \left\{ \begin{array}{l} \text{baseline to peak} \approx -.03 \mu\text{T} \\ \text{baseline to peak rise} \approx 80 \text{ ns} \\ 10-90 \text{ rise} \approx 40 \text{ ns} \\ \text{width} \approx 160 \text{ ns} \end{array} \right.$$

$$\tau \approx 35 \text{ ns}$$

and another

pulse at 14.0 μs

$$\frac{\partial}{\partial t} B_E \left\{ \begin{array}{l} \text{peak} \approx -.547 \text{ T/s} \\ \text{zero to peak rise} \approx 40 \text{ ns} \\ 10-90 \text{ rise} \approx 30 \text{ ns} \end{array} \right.$$

$$B_E \left\{ \begin{array}{l} \text{baseline to peak} \approx -.014 \mu\text{T} \\ \text{baseline to peak rise} \approx 50 \text{ ns} \\ 10-90 \text{ rise} \approx 35 \text{ ns} \\ \text{width} \approx 70 \text{ ns} \end{array} \right.$$

(2.6)

$$\tau \approx 26 \text{ ns}$$

Comparing these individual pulses we have seen characteristic times for the rise ranging from about 70 ns to less than 30 ns. Also one can note that there seems to be a general trend in that smaller pulses have shorter characteristic times for the rise and shorter pulse widths. Pulse widths vary from about 500 ns to about 70 ns.

Now consider the return-stroke waveform in figure 2.3. The $\partial \vec{B} / \partial t$ structure is somewhat simplified by comparison to the previous leader example. The horizontal distance (by flash to bang) to this stroke was about 850 m. Comparing the peak derivative signals between return stroke (fig. 2.3) and leader (fig. 2.1) note that they are of comparable magnitude. Assuming that the leader is elevated somewhat above the ground, the inferred slant ranges to the sources for the two examples are crudely of the same order as well. It therefore seems that we may typically expect peak derivative waveforms from the larger leader pulses to have about the same strength as those for return strokes (at comparable distances).

The main pulse at about 4 μs which triggered the recording is expanded in figure 2.4 for the first 7 μs . Note the wide pulse characteristic of the return stroke as indicated in the east component of the \vec{B} waveform. From a

printout of the digital data this pulse has the approximate characteristics:

pulse at 4.0 μ s

$$\begin{aligned} \frac{\partial}{\partial t} B_E & \left\{ \begin{array}{l} \text{peak} \approx -2.81 \text{ T/s} \\ \text{zero to peak rise} \approx 110 \text{ ns} \\ \text{10-90 rise} \approx 35 \text{ ns} \end{array} \right. \\ B_E & \left\{ \begin{array}{l} \text{baseline to peak} \approx -.129 \text{ } \mu\text{T} \\ \text{baseline to peak rise} \approx 160 \text{ ns} \\ \text{10-90 rise} \approx 60 \text{ ns} \\ \text{width} \approx 1000 \text{ ns} \end{array} \right. \end{aligned} \quad (2.7)$$

$$\tau \approx 46 \text{ ns}$$

It does seem that return strokes can be somewhat fast. We have looked at other return strokes and noticed similarly small values of τ . For this type of pulse of \vec{B} the concept of width is somewhat problematical because of the current that continues in the arc after the fast part of the pulse has occurred.

III. FAST TRANSIENT ELECTROMAGNETIC FIELDS AT EARTH SURFACE RELATED TO INDIVIDUAL LIGHTNING CURRENT PULSES

Having seen some of the transient waveforms in section 2, and noting that many of the individual pulses are extremely fast with rise times of the order of some tens of ns, it appeared that one might be able to model these pulses as events somewhat localized in space. This concept uses the limitation of the speed of light on current propagation as compared to the distances of hundreds to thousands of meters from source to observer. As will appear later, this approach yields some valuable insight into the lightning streamer currents and propagation.

Let us begin by defining a spherical (r, θ, ϕ) coordinate system based on the Kiva as in figure 3.1A. For our purposes (r, θ, ϕ) signifies some position in space which is the source of the observed lightning signals at (near) $\vec{r} = \vec{0}$ (the Kiva). In addition to the spherical coordinates we have cylindrical (Ψ, ϕ, z) and cartesian (x, y, z) coordinates all related via

$$\begin{aligned} x &= \Psi \cos(\phi) = r \sin(\theta) \cos(\phi) \\ y &= \Psi \sin(\phi) = r \sin(\theta) \sin(\phi) \\ z &= r \cos(\theta) \end{aligned} \quad (3.1)$$

$$r^2 = \psi^2 + z^2$$

$$\psi^2 = x^2 + y^2$$

$$\frac{\sin(\phi)}{y} = \frac{\cos(\phi)}{x}$$

with x and y taking the signs of $\cos(\phi)$ and $\sin(\phi)$ respectively. As indicated in figure 3.1A the coordinate system is oriented so that

$$\begin{aligned} x &\text{ is north (geographical)} \\ y &\text{ is west} \\ z &\text{ is up} \\ \theta &\text{ is zenith angle} \\ \phi &\text{ is counterclockwise from north} \end{aligned} \tag{3.2}$$

Associated with these coordinate sets there are sets of unit vectors (right-handed) as

$$\begin{aligned} \vec{i}_x \times \vec{i}_y &= \vec{i}_z, \vec{i}_y \times \vec{i}_z = \vec{i}_x, \vec{i}_z \times \vec{i}_x = \vec{i}_y \\ \vec{i}_\psi \times \vec{i}_\phi &= \vec{i}_z, \vec{i}_\phi \times \vec{i}_z = \vec{i}_\psi, \vec{i}_z \times \vec{i}_\psi = \vec{i}_\phi \\ \vec{i}_r \times \vec{i}_\theta &= \vec{i}_\phi, \vec{i}_\theta \times \vec{i}_\phi = \vec{i}_r, \vec{i}_\phi \times \vec{i}_r = \vec{i}_\theta \end{aligned} \tag{3.3}$$

which are related by

$$\begin{aligned} \vec{i}_\psi &= \vec{i}_x \cos(\phi) + \vec{i}_y \sin(\phi) \\ \vec{i}_\phi &= -\vec{i}_x \sin(\phi) + \vec{i}_y \cos(\phi) \\ \vec{i}_r &= \vec{i}_\psi \sin(\theta) + \vec{i}_z \cos(\theta) \\ \vec{i}_\theta &= \vec{i}_\psi \cos(\theta) - \vec{i}_z \sin(\theta) \end{aligned} \tag{3.4}$$

In addition to the coordinates for the source point with respect to the observation point let us define a set of unit vectors for describing the wave propagation to the observer. These are a right-handed system

$$\vec{i}_1 \times \vec{i}_2 = \vec{i}_3, \vec{i}_2 \times \vec{i}_3 = \vec{i}_1, \vec{i}_3 \times \vec{i}_1 = \vec{i}_2 \tag{3.5}$$

which are related to our previously defined coordinate unit vectors as

$$\begin{aligned}
\vec{l}_1 &\equiv -\vec{l}_r \\
\vec{l}_2 &\equiv -\vec{l}_\phi \\
\vec{l}_3 &\equiv -\vec{l}_\theta
\end{aligned}
\tag{3.6}$$

Viewed from an observer at the Kiva one has the picture in figure 3.1B in which

$$\begin{aligned}
\vec{l}_1 &\equiv \text{direction of propagation} \\
&\equiv \text{pointing to observer} \\
\vec{l}_2 &\equiv \text{horizontal to right} \\
\vec{l}_3 &\equiv \text{"up" as modified by being perpendicular to } \vec{l}_1
\end{aligned}
\tag{3.7}$$

Note that \vec{l}_2 and \vec{l}_3 are polarization vectors for the wave. The plane of incidence is defined by \vec{r} and the z axis; it contains \vec{l}_1 and \vec{l}_3 as well as \vec{l}_r , \vec{l}_θ , \vec{l}_ψ , and \vec{l}_z ; \vec{l}_2 and \vec{l}_θ are perpendicular to the plane of incidence.

Next consider some distribution of current density $\vec{J}(\vec{r}, t)$ in free space. The electromagnetic fields from this can be represented as (ref. 1)

$$\begin{aligned}
\vec{E}_{\text{inc}}(\vec{r}', s) &= - \left\langle \vec{\tilde{Z}}(\vec{r}', \vec{r}''; s) ; \vec{\tilde{J}}(\vec{r}'', s) \right\rangle \\
\vec{H}_{\text{inc}}(\vec{r}', s) &= \frac{1}{s\mu_0} \left\langle \nabla \times \vec{\tilde{Z}}(\vec{r}', \vec{r}''; s) ; \vec{\tilde{J}}(\vec{r}'', s) \right\rangle
\end{aligned}
\tag{3.8}$$

with the subscript inc indicating incident at the observer at $\vec{r}' = \vec{0}$ and where \vec{r}', \vec{r}'' are now general coordinates (positions), s is the Laplace-transform variable (or complex frequency) with respect to time t (in general two sided) and the tilde \sim indicates a Laplace-transformed quantity. The impedance kernel is

$$\begin{aligned}
\vec{\tilde{Z}}(\vec{r}', \vec{r}''; s) &= s\mu_0 \vec{\tilde{G}}_0(\vec{r}', \vec{r}''; s) \\
\vec{\tilde{G}}_0(\vec{r}', \vec{r}''; s) &= \left[\vec{1} - \gamma^{-2} \nabla' \nabla' \right] \tilde{G}_0(\vec{r}', \vec{r}''; s) \\
&\equiv \text{dyadic Green's function of free space} \\
\tilde{G}_0 &= \gamma \frac{e^{-\zeta}}{4\pi\zeta} \quad (\text{for } \vec{r}' \neq \vec{r}'') \\
&\equiv \text{scalar Green's function of free space} \\
\gamma &\equiv \frac{s}{c} \equiv \text{free space propagation constant}
\end{aligned}
\tag{3.9}$$

$$c \equiv \frac{1}{\sqrt{\mu_0 \epsilon_0}} \approx 3 \times 10^8 \text{ m/s}$$

\equiv speed of light (in free space)

$$Z_0 \equiv \sqrt{\frac{\mu_0}{\epsilon_0}} \approx 377 \Omega$$

\equiv wave impedance of free space

$$\zeta \equiv \gamma |\vec{r}' - \vec{r}''|$$

The symbol \langle, \rangle indicates integration over the space coordinates common to the two terms (\vec{r}'' in (3.8)). The free-space dyadic Green's function has the explicit form

$$\begin{aligned} \tilde{G}_0(\vec{r}', \vec{r}''; s) = & \frac{\gamma}{4\pi} e^{-\zeta} \left\{ \left[-2\zeta^{-2} - 2\zeta^{-3} \right] \vec{1}_R \vec{1}_R \right. \\ & \left. + \left[\zeta^{-3} + \zeta^{-2} + \zeta^{-1} \right] \left[\vec{1} - \vec{1}_R \vec{1}_R \right] \right\} + \frac{1}{3\gamma^2} \delta(\vec{r}' - \vec{r}'') \vec{1} \end{aligned} \quad (3.10)$$

$\vec{1} \equiv$ identity dyad

$$\vec{1}_R \equiv \frac{\vec{r}' - \vec{r}''}{|\vec{r}' - \vec{r}''|} \quad \text{for } \vec{r}' \neq \vec{r}''$$

where the delta function is introduced so that the remaining part can be handled in (3.8) as a principal value integral with a small spherical zone of exclusion centered on $\vec{r}' = \vec{r}''$ (ref. 3).

For our present purposes we assume that the distance from source to observer is large compared to the size of the source, i.e.,

$$\begin{aligned} \vec{r}' &= \vec{0} \\ r'' \equiv |\vec{r}''| &\approx r \gg |\vec{r}' - \vec{r}''| \end{aligned} \quad (3.11)$$

where \vec{r} is taken as some effective center of the source. Furthermore we assume that frequencies of interest are sufficiently high that only the leading term for large r'' (the $|\vec{r}' - \vec{r}''|^{-1}$ or ζ^{-1} term in (3.10) need be included giving

$$\begin{aligned} \tilde{G}_0(\vec{r}', \vec{r}''; s) &\approx \frac{e^{-\gamma |\vec{r}' - \vec{r}''|}}{4\pi |\vec{r}' - \vec{r}''|} \vec{1}_t \\ &\quad \gamma \vec{1}_R \cdot \vec{r}'' \\ &\approx \frac{e}{4\pi r} \vec{1}_t \end{aligned} \quad (3.12)$$

$$\vec{l}_t \equiv \vec{l} - \vec{l}_R \vec{l}_R \equiv \text{transverse dyad}$$

Now referring to figure 3.1 we can approximate as

$$\begin{aligned} \vec{l}_R &\approx \vec{l}_1 = -\vec{l}_r \\ \vec{l}_t &\approx \vec{l} - \vec{l}_1 \vec{l}_1 = \vec{l} - \vec{l}_r \vec{l}_r \end{aligned} \quad (3.13)$$

This allows us to write (from (3.8))

$$\begin{aligned} \vec{E}_{inc}(0, s) &\approx -\frac{\mu_0 e^{-\gamma r}}{4\pi r} \vec{l}_t \cdot \vec{T}(s) \\ \vec{T}(s) &\approx s \int_V e^{\gamma(\vec{r} - \vec{l}_r \cdot \vec{r}'')} \vec{J}(\vec{r}'', s) dV'' \end{aligned} \quad (3.14)$$

In time domain we have

$$\vec{T}(t) \approx \frac{\partial}{\partial t} \int_V \vec{J}(\vec{r}'', t) + \frac{1}{c}(\vec{r} - \vec{l}_r \cdot \vec{r}'') dV'' \quad (3.15)$$

This \vec{T} can be thought of as a kind of effective source vector. Assuming that changes in \vec{J} propagate over the source volume at velocities slow compared to c we have

$$\begin{aligned} \vec{T}(s) &\approx s \int_V \vec{J}(\vec{r}'', s) dV'' \\ \vec{T}(t) &\approx \frac{\partial}{\partial t} \int_V \vec{J}(\vec{r}'', t) dV'' \end{aligned} \quad (3.16)$$

The magnetic field incident at $\vec{r}' = \vec{0}$ can be found by expanding from (3.8), or by simply noting that the far field ($|\vec{r}' - \vec{r}''|^{-1}$ term) has a plane-wave relation between the electric and magnetic field as

$$\begin{aligned} \vec{H}_{inc}(0, s) &\approx \frac{1}{Z_0} \vec{l}_1 \times \vec{E}_{inc}(0, s) \\ &\approx -\frac{e^{-\gamma r}}{4\pi r c} \vec{l}_1 \times \vec{T}(s) \end{aligned} \quad (3.17)$$

In time domain the fields are

$$\vec{E}_{inc}(0, t) \approx -\frac{\mu_0}{4\pi r} \vec{l}_t \cdot \vec{T}(t - \frac{r}{c}) \quad (3.18)$$

$$\vec{H}_{inc}(0,t) \approx -\frac{1}{4\pi rc} \vec{l}_1 \times \vec{T}(t - \frac{r}{c})$$

Near $\vec{r}' = \vec{0}$ the incident field is an approximate plane wave propagating in the \vec{l}_1 direction; it can be represented as

$$\begin{aligned} \vec{E}_{inc}(\vec{r}', t) &\approx E_h(t - \frac{\vec{l}_1 \cdot \vec{r}'}{c}) \vec{l}_2 + E_e(t - \frac{\vec{l}_1 \cdot \vec{r}'}{c}) \vec{l}_3 \\ \vec{H}_{inc}(\vec{r}', t) &= \frac{1}{Z_0} \left\{ E_h(t - \frac{\vec{l}_1 \cdot \vec{r}'}{c}) \vec{l}_3 - E_e(t - \frac{\vec{l}_1 \cdot \vec{r}'}{c}) \vec{l}_2 \right\} \end{aligned} \quad (3.19)$$

This decomposes the fields incident at the observer into two parts, an E wave (or TM wave) denoted by a subscript e, and an H wave (or TE wave) denoted by a subscript h. This decomposition is based on the polarization with respect to the z axis (i.e., a TM wave has the magnetic field perpendicular to the z axis, and a TE wave has the electric field perpendicular to the z axis).

Now when the incident fields reach the ground plane (the x,y plane), the conducting ground plane reflects the fields so that (at least at the higher frequencies because of the finite dimension of the ground plane on the earth) approximately we have

$$\begin{aligned} E_z &\approx 2\vec{l}_z \cdot \vec{E}_{inc} \\ H_x &\approx 2\vec{l}_x \cdot \vec{H}_{inc} = H_N = -H_S \\ H_y &\approx 2\vec{l}_y \cdot \vec{H}_{inc} = H_W = -H_E \end{aligned} \quad (3.20)$$

The remaining three fields components are approximately zero. Note the orientation of the cartesian coordinates with respect to the (geographical) compass positions (north \equiv N, east \equiv E, south \equiv S, west \equiv W).

On the ground plane we then have

$$\begin{aligned} E_z &= 2 \sin(\theta) E_e \\ H_\phi &= -H_2 = \frac{2}{Z_0} E_e \\ H_\psi &= -\cos(\theta) H_3 = -\frac{2}{Z_0} \cos(\theta) E_h \end{aligned} \quad (3.21)$$

Then construct

$$\frac{1}{2} E_z \approx \sin(\theta) E_e$$

$$\frac{Z_o}{2} H_\phi = \frac{Z_o}{2} \{-H_x \sin(\phi) + H_y \cos(\phi)\} = E_e \quad (3.22)$$

$$\frac{Z_o}{2} H_\psi = \frac{Z_o}{2} \{H_x \cos(\phi) + H_y \sin(\phi)\} = -\cos(\theta) E_h$$

From our measurements we have three pieces of information: E_z , H_x , and H_y . We have four unknowns: E_e , E_h , θ , and ϕ .

If we knew the source angles (θ, ϕ) , or at least one of these, then the two waves E_e and E_h could be constructed. Let us for the moment assume that θ and ϕ are known. From (3.18) and (3.19) together with E_e and E_h we can find

$$\begin{aligned} \vec{l}_t \cdot \vec{T}(t - \frac{r}{c}) &= -\frac{4\pi r}{\mu_o} \vec{E}_{inc}(0, t) \\ &= -\frac{4\pi r}{\mu_o} \{E_h(t) \vec{l}_2 + E_e(t) \vec{l}_3\} \end{aligned} \quad (3.23)$$

This shows that we can obtain the relative strength of the transverse (2 and 3) components of the source \vec{T} by comparing E_h and E_e . Referring to figure 3.1B one can plot on such a diagram an angle that \vec{T} makes with respect to say \vec{l}_3 as another vector on the plane perpendicular to \vec{l}_1 . Note that the 1 component of \vec{T} is not obtained in this technique since it does not appear in the far-field expansion at $\vec{r}' = \vec{0}$. If one knew r then the 2 and 3 components of \vec{T} would be completely known. Techniques for estimating r are discussed in another section of this paper. Having r then one can use (3.23) to find T_2 and T_3 ; this is used for later plots of the transverse part of \vec{T} .

Having $\vec{l}_t \cdot \vec{T}$ one can also make some estimates concerning currents in the fast pulses in the source region near \vec{r} by writing

$$\vec{T} \equiv \overrightarrow{(I v_{eff})} = \Delta \left\{ \frac{\partial}{\partial t} \int_{V''} \vec{J}(\vec{r}'', t) dV'' \right\} \quad (3.24)$$

Here Δ indicates the change in the quantity; for later plots this is the change from the ambient value before a fast pulse to the peak of the pulse. (This convention is employed for $\partial \vec{T} / \partial t$ also.) An effective streamer speed v_{eff} can be used to obtain some indication of the current I , or at least some rough bound on it.

Now consider the determination of θ, ϕ . Figure 3.2 shows a type of display of coordinates which is useful for our purposes. Superimposed on the cartesian directions and compass coordinates we have a polar plot in which θ is the radial coordinate with $0^\circ \leq \theta \leq 90^\circ$. The azimuthal coordinate is ϕ with $0 \leq \phi < 360^\circ$.

Returning to (3.22) our three measurements (E_z , H_x , H_y) can be used to find a relationship between θ and ϕ . Specifically the first two of (3.22) can be used to eliminate E_e giving

$$Z_o \left\{ -H_x \sin(\phi) + H_y \cos(\phi) \right\} = \frac{E_z}{\sin(\theta)} \quad (3.25)$$

as our θ, ϕ relation. Constraining $0 \leq \theta \leq 90^\circ$ and ϕ real gives a curve in the θ, ϕ "plane" of acceptable solutions of (3.25). For each pulse we can consider the change in the fields (ambient to peak) in (3.25) or some other aspect of the pulse waveforms. Besides the field change we have used the change in the time derivatives of the fields ($\partial E_z / \partial t$, $\partial H_x / \partial t$, $\partial H_z / \partial t$) in (3.25) to determine the θ, ϕ curves. Both the field changes and changes in field time derivatives (on the rise of the pulses) typically give comparable results, as will be seen later.

A special case is encountered if the incident field is a pure H wave (i.e., \vec{E} parallel to the ground plane). In this case $E_e = 0$. From (3.22) we have

$$\tan(\phi) = \frac{H_y}{H_x} \quad (3.26)$$

which has two solutions for ϕ separated by 180° . In the θ, ϕ "plane" in figure 3.2 this gives a locus of solutions a "straight line" passing through the zenith ($\theta = 0$).

Having a contour in the θ, ϕ "plane" resulting from a particular measured fast electromagnetic-field pulse (or its time derivative) one would like to find some point along that contour that represents the true angles θ, ϕ to the source. One way to do this uses an assumption that another pulse in a particular recording (about 20 μs wide in the presented data) comes from approximately the same source location. This is physically reasonable if one considers a leader propagating through the air to establish the lightning channel. If each pulse represents some brief extension of the arc channel, and if the distance the streamer propagates during the pulse is small compared to the distance to the observer, then the change in (θ, ϕ) is small. Furthermore, if the two pulses under consideration have different polarizations (different proportions of E and H waves) due to different directions of $\vec{l}_t \cdot \vec{T}$, then (3.25) will give in general different θ, ϕ contours for the two pulses. The intersection of the two contours can then be taken as an experimental determination of (θ, ϕ) for both pulses.

Going further, it will be observed in considering the data that the intersection of θ, ϕ contours is remarkably successful in determining (θ, ϕ) values. In some cases all the θ, ϕ contours (of the order of ten contours) can all pass quite near a common (θ, ϕ) approximate intersection. In other cases subsets of the contours for a particular waveform set form a few distinct approximate (ϕ, θ) values. Some cases are presented in the data illustrating some of the complexity that can be unravelled in this way.

Having determined the (θ, ϕ) values appropriate to particular pulses, and estimating the corresponding r , one goes back to (3.22) to find E_e and E_h (or their derivatives with respect to time). Then (3.23) gives the transverse components of \vec{T} for plots with respect to the \vec{l}_2 and \vec{l}_3 directions as in figure 3.1B.

IV. ESTIMATION OF RANGE TO LIGHTNING CURRENT PULSES

The electric field changes produced by lightning in this study were also sensed with a "slow antenna" field change meter and recorded onto FM magnetic tape, together with the IRIG B, 1 kHz time code that was distributed to coordinate the thunderstorm and lightning measurements. This time code was synchronized with Radio Station WWV and permitted the slow measurements to be correlated with a time resolution of 1 ms. A Globe 100 B microphone with an extended low frequency response was mounted on the metal mesh adjacent to the Kiva and was used to detect the arrival of thunder. The thunder signals were recorded on a second FM magnetic tape channel. In this manner, the time of occurrence, the nature of the lightning flash and the time from flash-to-thunder could be determined.

Two acoustic arrays, each consisting of three microphones at the vertices of 30 m, equilateral triangles were located in the meadow, south of the Kiva. (See Figure 1.1.) The time-difference of arrival of individual thunder peals across each of these triangular arrays permitted a determination of the direction cosines for the normal to the acoustic wave front. With these and the distance from each source to the array calculated from the speed of sound and the time interval from field change to peal arrival, a first estimate could be made for location of each source. Corrections were then made for the local winds and for thermal refraction in a second approximation for the source location using the technique described by Winn et al. (ref. 4).

In addition to the use of these acoustic techniques for the location of lightning, the flashes in the vicinity of the Kiva were video-recorded with a time resolution of 16 ms per TV frame. One TV camera recorded the view from an all-sky reflecting, parabolic mirror located on top of South Baldy peak about 50 m north of the Kiva, while another TV system located at Langmuir Laboratory recorded the view of lightning over South Baldy peak as seen from 2 km to the SSE.

These video recordings have been played back, frame by frame, onto a video monitor where they were photographed together with an output displaying the IRIG B time code that was also recorded on the audio tracks of the video tape recorders.

All of the flashes reported in this study were "cloud-to-ground" discharges. Our first approximation for the slant range from the Kiva to the lightning current element of interest is based on the assumption that the time from flash to thunder multiplied by the speed of sound in air gives the horizontal distance from the Kiva microphone to the closest part of the lightning channel (that is striking the earth approximately vertically).

From section 3, the zenith angle θ and the azimuth angle ϕ can be estimated for the current element from the electromagnetic signal that it produced.

The approximate slant range r from the Kiva to the current element is therefore given by

$$r \approx (336 \text{ m/s})(\Delta t)/\sin(\theta) \quad (4.1)$$

The cartesian coordinates of the current element are therefore

$$\begin{aligned} x &= (336 \text{ m/s})(\Delta t) \cos(\phi), \text{ toward the north} \\ y &= (336 \text{ m/s})(\Delta t) \sin(\phi), \text{ toward the west} \\ z &= r/\cos(\theta), \text{ above the Kiva} \end{aligned} \quad (4.2)$$

In the four cases to date in which we have compared the thunder source maps with current element coordinates, there has been a fair agreement between the two somewhat independent location systems. If the range chosen from the horizontal distance assumption is too small, a better estimate for the range can be extracted from the intersection of the vector \vec{r} --directed along the calculated values of θ and ϕ --with the thunder channels mapped by the acoustic technique.

V. ANALYZED WAVEFORMS

In this section the techniques discussed in sections 4 and 5 are applied to some example data sets for four selected waveforms.

A. Rocket-Triggered Lightning

Our first example is given in figures 5.1 through 5.8. It is a good example of leader-like behavior and is associated with a triggered lightning event. The lightning stroke was triggered by a wire-trailing rocket launched from the position indicated in figure 1.1 which is 350 m in horizontal range at an azimuth of $\phi = 155^\circ$ with respect to the Kiva. The rocket was launched approximately vertically. Based on visual observations its height was estimated as about 600 m above the Kiva when it initiated a lightning discharge. This corresponds to a zenith angle of $\theta \approx 30^\circ$ with respect to the Kiva. Based on the extreme electric-field enhancement at the rocket, it was expected that the streamer direction of interest was upward, beginning from the rocket. This polarity is assumed later in the data analysis.

Looking at figure 5.1 we see the leader-like behavior on the 20 μs waveform for the three derivative field components. For convenience 9 pulses are identified by numbers corresponding to their peak times of occurrence (within the record event) in microseconds; the north component of $\partial \vec{B}/\partial t$ had the generally largest pulses and was used for this labelling. Figure 5.2 results from the numerical integration of the digital data from which figure 5.1 was produced. Here the pulses are also identified (on the east component of \vec{B} in this case). Note the general drift in the baseline which may be partially due to a little offset in the recording of the derivative data, but probably is a result of a continuing current flowing up the channel initiated by the rocket.

Figure 5.3 shows the slow changes in the electric field, first from the rising of the grounded wire, followed by the emission of upward-going positive streamers. Also shown is a recording of the narrowband RF power received centered on 34 MHz, as measured by a different experiment (Hayenga) with a complex antenna pattern. For our purposes it is interesting to note that the RF power emissions began at about 0.6 s after rocket launch indicating some corona-like discharges before the main lightning event.

The acoustically determined (per section 4) thunder sources are displayed in figure 5.4. This indicates that the lightning discharge turned south and extended about 4 km at a height of about 2 km. This can be compared to the whole-sky video-tape photograph in figure 5.5B obtained at the balloon hanger (fig. 1.1) about 700 m south of the rocket launcher. This indicates the main streamer rising and propagating to the south near cloud-base level at a height of about 1 km. Figure 5.6B shows the same event at about 160 ms later. Note in the whole-sky photographs the TV camera in the center since it is above a paraboloidal mirror.

The θ, ϕ contours from the nine pulses identified for the derivative waveform in figure 5.1 are displayed in figure 5.5A. This shows a remarkably tight set of intersections in which all 9 contours pass through nearly the same point. The estimated angles from the Kiva to the source are $(\theta, \phi) \approx (30^\circ, 177^\circ)$. This is in quite good agreement with the estimated rocket position. The major difference is in azimuth (177° vs 155°), but there are uncertainties in the exact position of the rocket because it impacted to the south near the comet observatory (fig. 1.1), despite its near vertical aiming. The slant range is estimated as $r \approx 700$ m based on $\theta = 30^\circ$ and a horizontal distance of 350 m. The same contours, except now based on the field (numerically integrated) waveform are shown in figure 5.6A. Here the intersection is not so tightly clustered indicating that more accuracy is generally obtained from the derivative-format data. This is not surprising since the analysis is based on a high-frequency approximation and because the integration has some error. For comparison the estimated source location (based on the derivative data) is superimposed on the plot of acoustic source locations in figure 5.4.

Now we reconstruct the source. In figure 5.7 the derivative waveform with the estimated \vec{r} (as discussed) is used to find the peak values of the $\partial \vec{T} / \partial t$ pulses. Figure 5.7B shows the individual vector pulses (as seen from the Kiva) oriented to the right and slightly downward. Assuming that the streamer velocity \vec{v}_{eff} is parallel to \vec{J} and in the same direction for this case we have the effective reconstruction of the positive streamer in figure 5.7A. For this type of assumed positive streamer, denoted by $\vec{v}_{\text{eff}} \uparrow \uparrow \vec{J}$ we take the individual vector pulses in their order of occurrence and lay them out from the graph origin sequentially in a cumulative manner (tail of vector coincident with head of previous vector). Figure 5.8 does the same thing for the \vec{T} pulses from the field waveforms and gives a comparable picture.

While this lightning event was a positive-going streamer, it is interesting to note that the impulsive nature of the fields is similar to that of natural negative step leaders.

B. Midrange Leader(s)

Our second example is given in figures 5.9 through 5.21. As will be seen this is a case of significant branching. For sake of a label let us refer to this case as "midrange leader(s)." Figures 5.9 and 5.10 show the derivative fields and fields for the 20 μ s record indicating leader-like behavior.

Figure 5.11 shows the slow electric field and thunder microphone records from which a horizontal range of 400 m is estimated. Figure 5.12 gives the acoustic source reconstruction indicating an interesting streamer-path structure. Extending from about 3 km height, about 3 km to the east (slightly north of east), the pattern divides at about 2.5 km above the Kiva and descends to the mountain in at least three major channels. On this is superimposed three EM source locations determined from the derivative waveform.

The whole-sky video-tape photographs in figures 5.13B and 5.14B show these three channels quite clearly as seen from the Kiva. Figure 5.14B corresponds to 32 ms later than figure 5.13b.

Looking at the θ, ϕ contours in figure 5.13A from the derivative waveform in figure 5.9, we do not see all the contours passing near a common (θ, ϕ) . It appears that several sources are located above the Kiva. From figure 5.13A three (θ, ϕ) values were found as indicated on the figure. These angles are combined with the horizontal range of 400 m to give the estimated EM source locations in figure 5.12. As an aid in identifying the three sets of pulses corresponding to the three locations, the directions of $\partial \vec{T} / \partial t$ were considered so as to have all the $\partial \vec{T} / \partial t$ pulses in a particular set have the same general direction (as in figures 5.15 through 5.17).

Considering the field waveform in figure 5.10 the plot of θ, ϕ contours in figure 5.14A was made. Here four sets of pulses were identified. Sets 1, 2, and 3 correspond reasonably to those from the derivative waveforms as do the directions of the \vec{T} pulses as compared to the corresponding $\partial \vec{T} / \partial t$ pulses. Set 4 in figure 5.14A was defined based on a disagreement in the direction of \vec{T} pulses from those in set 1 as based on the directions in figures 5.18 and 5.21. However, noting the small θ values for this case the change in ϕ still corresponds to only a small distance change on the unit sphere, but a large rotation of the unit vectors \vec{i}_2, \vec{i}_3 . Identifying these set 4 \vec{T} pulses with the corresponding $\partial \vec{T} / \partial t$ pulses it appears that set 4 pulses likely belong combined with set 1.

Since set 1 corresponds to small θ an estimate of slant range based on 400 m horizontal range is likely in error because the lightning arc is not exactly vertical. Based on figure 5.12 the lower heights as in figure 5.15 for $\theta = 20^\circ$ are more reasonable. This is consistent with relying more on $\partial \vec{T} / \partial t$ data for θ, ϕ determination.

For this negative step leader we have $\vec{v}_{\text{eff}} \updownarrow \vec{J}$ (antiparallel). So in the effective streamer reconstruction in figures 5.15 through 5.21 the vectors for the sequential pulses are started from the graph origin with each vector head placed at the previous vector tail.

Note that values of \vec{T} pulses depend on choice of r . For sets 1 and 4 r is clearly overestimated indicating the true T values are somewhat less (by perhaps a factor of 2) than indicated in figures 5.18 and 5.21.

C. Nearby Leader

Our third example is given in figures 5.22 through 5.31. This is labelled "nearby leader." Figures 5.22 and 5.23 show the derivative fields and fields for the 20 μ s record.

Figure 5.24 shows the slow electric field and thunder microphone records, from which a horizontal range of 95 m is estimated. Figure 5.25 gives the acoustic source reconstruction indicating one principal streamer channel near the Kiva. Extending from about 5 km height there is some branching also collecting charge about 1.5 km a little north of west. On this is superimposed the location of the two EM sources which were very close together on this scale. Figures 5.26B and 5.27B show the same whole-sky video-tape photograph indicating a channel to the west. Noting that this whole-sky camera is not exactly at the Kiva, but about 50 m north of it on the highest point of South Baldy peak (see fig. 1.1) the several channel location techniques give quite good agreement.

Looking at the θ, ϕ contours for derivative data in figure 5.26A we find two approximate sets of contour intersections. This was aided by noting the direction of $\partial\vec{T}/\partial t$ pulses in figures 5.28 and 5.29. Figure 5.27A does the same for the field waveform pulses with good agreement, including the directions of the \vec{T} pulses in figures 5.30 and 5.31.

Noting the two sources approximately above and below each other, these appear to be on or near the same main channel. It is conceivable that the lower source is a positive streamer and the upper streamer a negative one with the two streamers heading toward each other. For the plots of the $\partial\vec{T}/\partial t$ and \vec{T} pulses in figures 5.28 through 5.31 we have chosen the convention $\vec{v}_{eff} \uparrow \downarrow \vec{J}$ since such an above possibility is difficult to confirm.

D. Return Stroke

Our fourth example is given in figures 5.32 through 5.39. This is labelled "return stroke" based on the wide (1 μ s) pulses as indicated in figure 5.33, as well as the sustained deviation of the later-time portions of the waveform. Figures 5.32 and 5.33 show the derivative fields and fields for the 20 μ s records.

Figure 5.34 shows the slow electric field and thunder microphone records, from which a horizontal range of 1775 m is estimated. Figure 5.35 gives the acoustic source reconstruction indicating two possible closures to ground. Extending from about 4 km height a little north of east of the Kiva the channel approaches the Kiva striking the ground about 2 km due east. On this is superimposed the estimated locations of the EM source, one each for the derivative waveform and the field waveform. Figures 5.36 and 5.37 show the same whole-sky

video-tape photograph indicating a channel to the east, in agreement with the acoustic source location.

Looking at the θ, ϕ contours for derivative data in figure 5.36A we find a single approximate contour intersection somewhat north of east and at a high elevation. Similar results are found from the field waveform pulses in figure 5.37A. These two (θ, ϕ) values are combined with the horizontal range to give the two estimates for the source location in figure 5.35. Note, however, that the lightning channel is not vertical and the true source location is likely to be farther to the east, and at a high elevation, unless some branching occurs back toward the west.

Figures 5.38 and 5.39 give the rough streamer reconstruction based on $\vec{\partial \vec{T}}/\partial t$ and \vec{T} respectively. The streamer is assumed positive, i.e., $\vec{v}_{eff} \uparrow \uparrow \vec{J}$, in keeping with the character of a return stroke. Note, however, the high elevation. This return-stroke corresponds to a large and wide current pulse in the clouds. A larger range (as is possible) would give larger $\vec{\partial \vec{T}}/\partial t$ and \vec{T} pulses than indicated in figures 5.38 and 5.39.

E. Some Comments

These four examples give representative characteristics of lightning near South Baldy peak. Many more recordings were obtained. It is anticipated that a significant fraction of these will be analyzed for future publication. These include both leader-like examples and return-stroke-like examples, including events near the horizon which appear to be more classical return strokes.

From the examples given the values of \vec{T} have magnitudes (from transverse components) of about 2×10^{12} Am/s for return strokes to about 5×10^{11} Am/s for leader-like sources (noting order of magnitudes and directions of streamers toward (or away from) the observer at the Kiva). Assuming a v_{eff} of about 10^8 m/s gives 20 kA for return strokes and 5 kA for leader-like pulses. These are very variable and the number is quite approximate. Further analysis of the data may shed more insight into such results.

For these data all the lightning events represent negative charge being, in effect, lowered to earth. It would be interesting to see what would occur in the rare event of positive charge being lowered to earth.

In the recordings for the three components of field time derivative at the Kiva the peaks did not occur at exactly the same time. The separation of the sensors on the ground plane was about 11 ns, and the difference in cable transit times was about 14 ns, giving a maximum time shift of about 25 ns. This resulted in peaks on the digital printout having a relative time displacement of up to three time intervals, or 30 ns, as was observed. For the present analysis the actual peaks of the individual components, regardless of time, were used.

Unfortunately the trigger signal for the Biomation recorders was not recorded on magnetic tape in 1979, whereas it had been so recorded in 1978. This would have given even more definitiveness to the interpretations of the

3-component 1979 data. However, analysis of 1978 waveforms does indicate that to the 1 ms tape resolution, the waveforms all correspond to the first return stroke or the leader-like anticipation of this return stroke.

VI. SUMMARY

As the foregoing data and associated data analysis has indicated, fast nuclear-EMP related sensors and appropriate fast transient recorders have much to offer for the measurement and associated understanding of lightning electromagnetic environments. The lightning and nuclear EMP phenomena have some similar characteristics because of their common nature as transient electromagnetic phenomena.

In this report we have discussed some of the results obtained concerning lightning environments from our measurements using such instrumentation on South Baldy peak. Three electromagnetic field components (one electric, two magnetic) were measured on a ground plane with 10 ns resolution for recording times of about 20 μ s. By comparing the three field components to each other, and by the use of acoustic ranging, the lightning electromagnetic sources were approximately located and their characteristics were studied.

The individual lightning waveforms yielded information concerning the temporal characteristics of leader electromagnetic fields. Pulse widths of the electromagnetic field individual pulses varied from about half a microsecond to less than 100 ns. Characteristic times for the rise (peak field divided by peak derivative) varied from something approaching 100 ns to something less than 30 ns; rise times were a little longer than these characteristic times for the rise.

Information was also obtained concerning the temporal characteristics of return-stroke electromagnetic fields. Pulse widths (of the magnetic field) of the order of 1 μ s were observed, and rise times less than 100 ns were also observed. Characteristic times for the rise of the order of 50 ns were observed.

Comparing the fast electromagnetic-field pulses from leaders and return strokes at comparable distances from source to observer shows that the return-stroke field waveforms have generally larger amplitudes than those for leaders. However, for the time derivatives of the electromagnetic fields, the amplitudes for leaders and return strokes are quite comparable.

Combining the three electromagnetic-field time-derivative waveforms (or their time integrals) one can obtain for each pulse a relation between θ and ϕ giving a contour in the θ, ϕ "plane." Intersections of such contours can give approximate (θ, ϕ) values for source location providing the corresponding pulses originate from nearly the same locations. With location, source orientation (current density transverse polarization) can then be determined. Acoustic data can be used to estimate distances to these sources. The source vectors $\vec{I}_t \cdot \vec{T}$ (their peaks or peak time derivatives) can then be plotted to see how the current

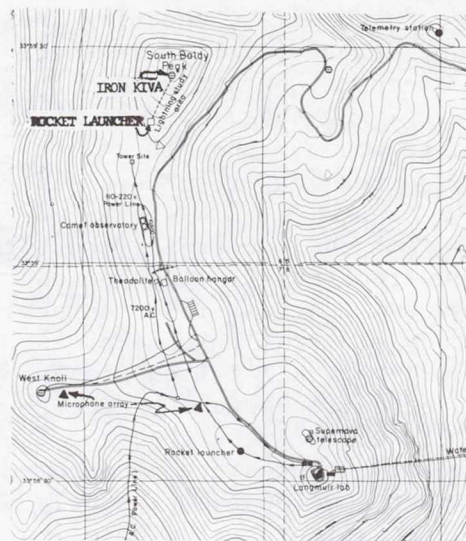
direction changes from pulse to pulse. Connecting these vectors end to end gives a crude picture of the tortuosity of the leader path. From the magnitudes of the components of \vec{T} one can obtain some information concerning currents and streamer speeds by giving these components the form I_{eff} . Typical current values of less than to greater than 10 kA are consistent with streamer speeds of the order of 10^8 m/s for leader strokes and return strokes respectively.

This data has some implications concerning the formulation of criterion lightning electromagnetic environment(s). The pulses encountered are significantly faster than a microsecond in their rise characteristics, even less than 100 ns. In terms of frequency spectrum this means much more high frequency content for the individual pulses. A detailed frequency spectral analysis of these kinds of pulses would be quite useful for the formulation of lightning electromagnetic criteria. One should note that these waveforms are not strictly applicable for direct-strike lightning since measurements were not made in such an environment. One may expect some of the presently observed environmental characteristics to apply in the direct-strike case, but this is not a full description.

The measurements reported here were made on South Baldy peak. Measurements at other geographical locations with different atmospheric conditions might reveal some differences in the electromagnetic waveforms from those obtained here. In the context of South Baldy peak more analysis of the existing data may reveal additional interesting features; additional waveforms are planned to be included in a future report. Future measurements may also obtain more complete lightning waveform information by finer time resolution, longer recording time windows, and/or additional and/or more accurate tie-ins with other physical phenomena.

REFERENCES

1. Baum, C. E.: Emerging Technology for Transient and Broad-Band Analysis and Synthesis of Antennas and Scatterers. Interaction Note 300, November 1976, and Proc. IEEE, November 1976, pp. 1598-1616.
2. Longmire, C. L.: On the Electromagnetic Pulse Produced by Nuclear Explosions. IEEE Trans. Antennas and Propagation, January 1978, pp. 3-13, and IEEE Trans. Electromagnetic Compatibility, February 1978, pp. 3-13.
3. VanBladel, J.: Some Remarks on Green's Dyadic for Infinite Space. IRE Trans. Antennas and Propagation, November 1961, pp. 563-566.
4. Winn, W. P., C. B. Moore, C. R. Holmes, and L. G. Byerley III,: Thunderstorm on July 16, 1975, Over Langmuir Laboratory: A Case Study. J. Geophysical Research, vol. 83, no. C6, June 20, 1978, pp. 3079-3092.
5. Baum, C. E., E. L. Breen, C. B. Moore, J. P. O'Neill, and G. D. Sower: Electromagnetic Sensors for General Lightning Application. Symposium on Lightning Technology, NASA, Hampton, Virginia, U.S.A., 22-24 April 1980.



Iron Kiva altitude: 3275m. m.s.l.
map contour decrements: 13m

Figure 1.1.- Top view of electromagnetic and related measurement layout around South Baldy Peak, New Mexico.

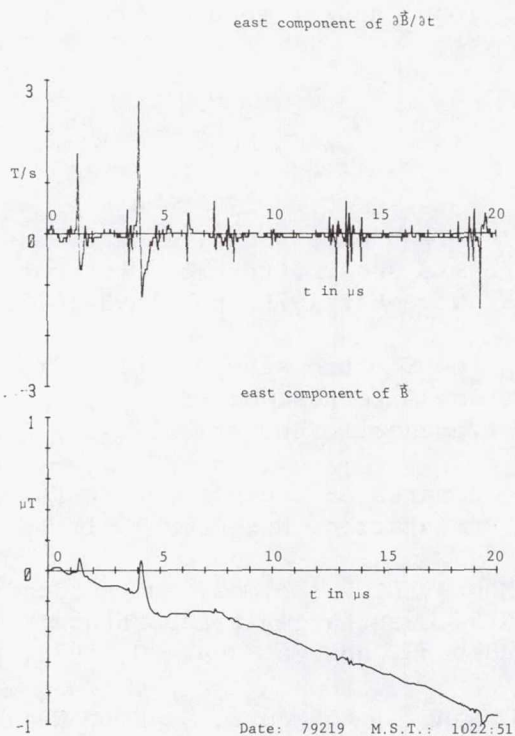


Figure 2.1.- Leader example: 20 μ s scale.

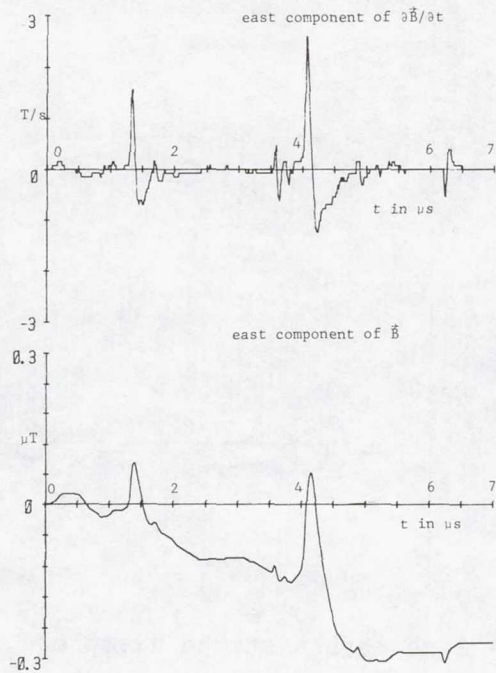


Figure 2.2.- Same leader example: 7 μs scale.

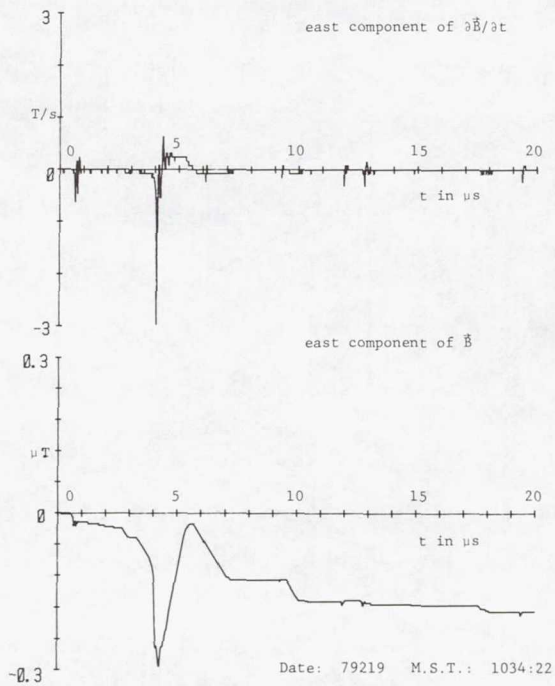


Figure 2.3.- Return-stroke example: 20 μs scale.

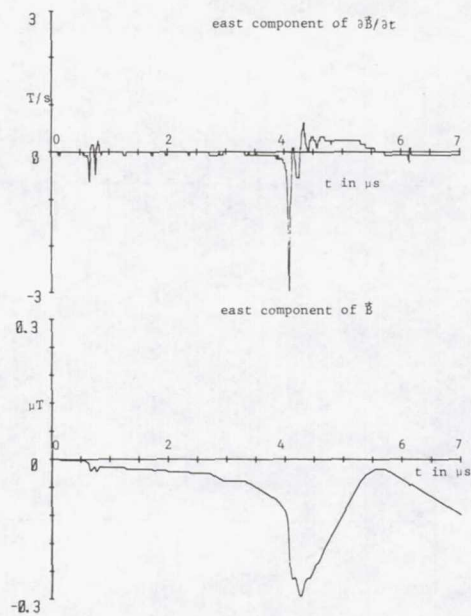
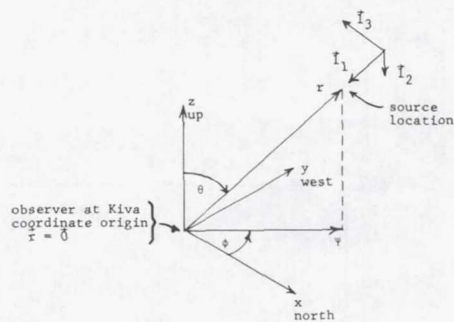


Figure 2.4.- Same return-stroke example: 7 μs scale.



A. Coordinate systems

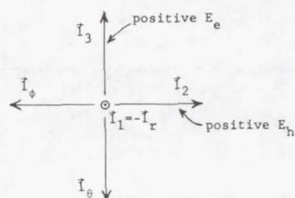


Figure 3.1.- Coordinates for lightning data analysis.

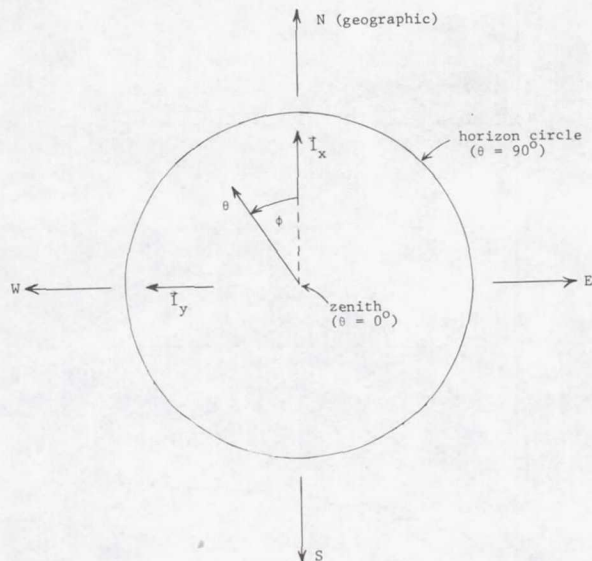
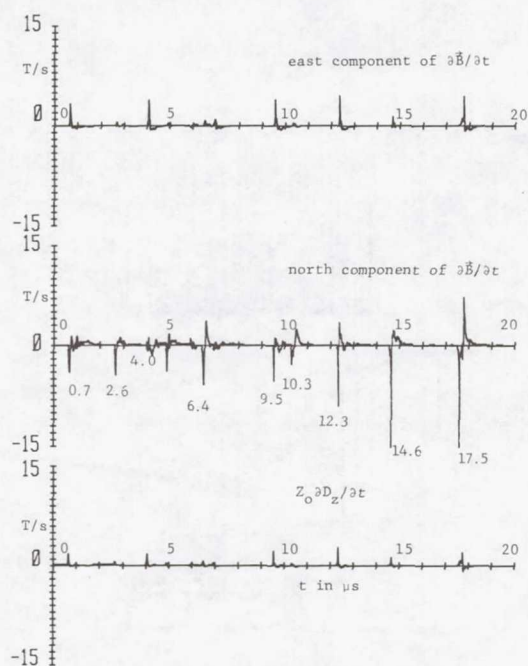
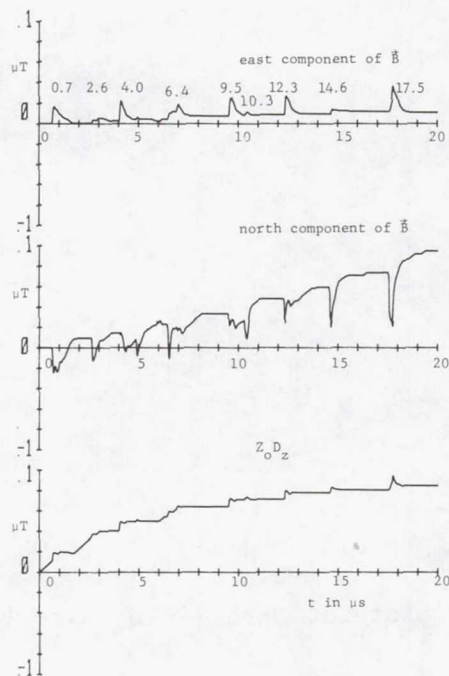


Figure 3.2.- Polar plot for determining direction to source.



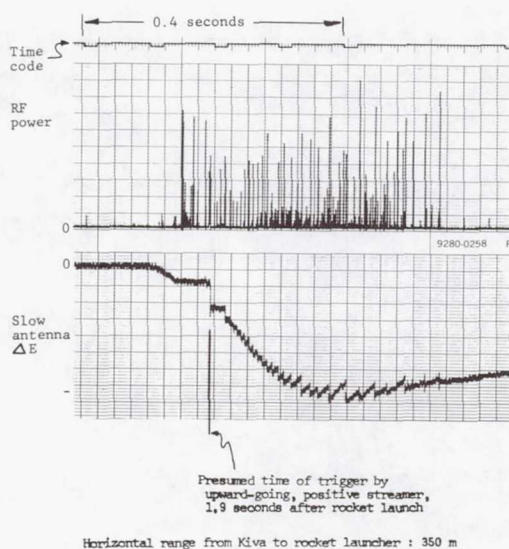
Date: 79228 M.S.T.: 1545:12

Figure 5.1.- Derivative fields from rocket-triggered lightning.



Date: 79228 M.S.T.: 1545:12

Figure 5.2.- Fields from rocket-triggered lightning.



Date: 79228 M.S.T.: 1345:12

Figure 5.3.- Slow electric field change and RF power received at 34 MHz from rocket-triggered lightning.

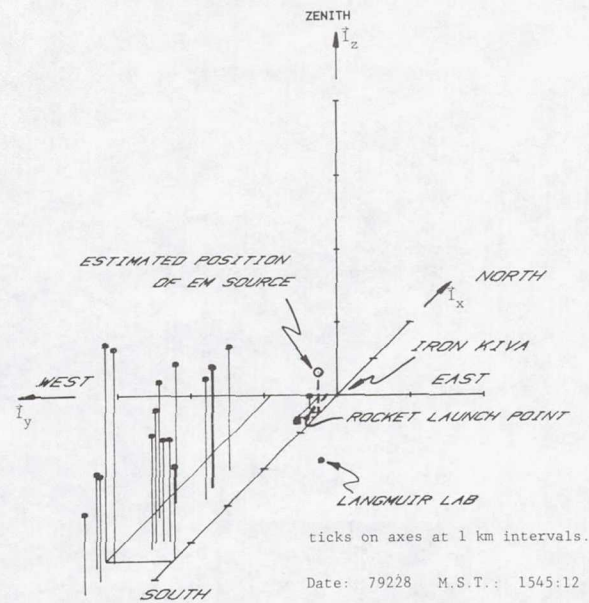


Figure 5.4.- Acoustic location of rocket-triggered lightning.

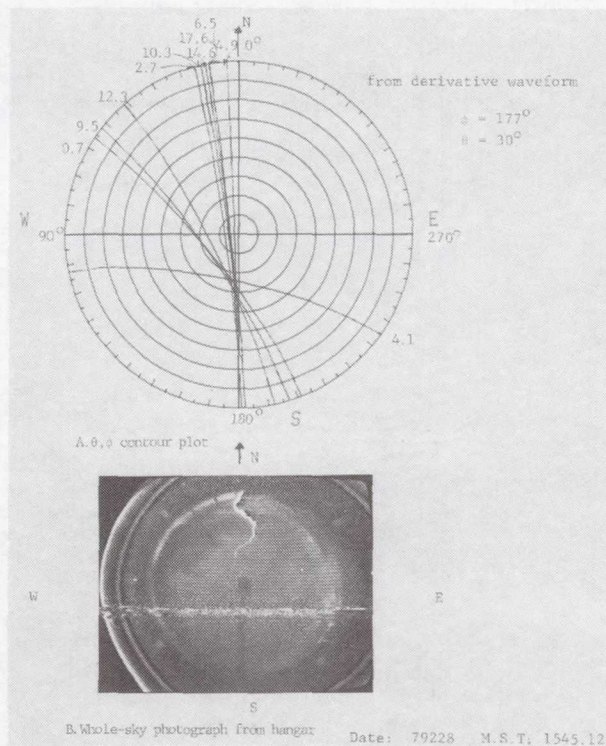


Figure 5.5.- θ, ϕ contours for rocket-triggered derivative waveform and whole-sky videotape photograph.

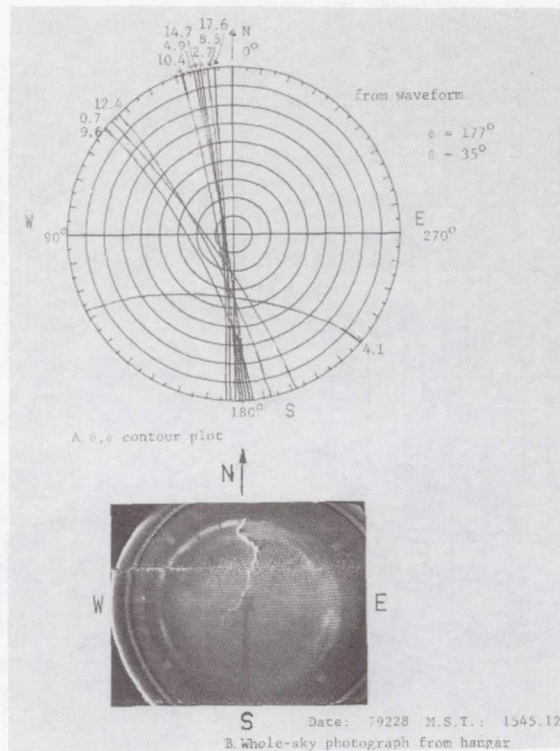
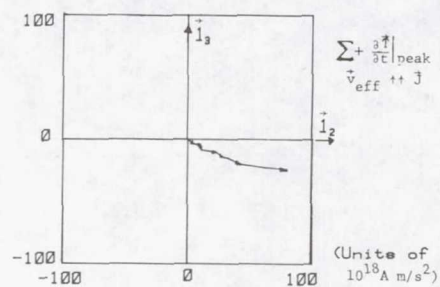
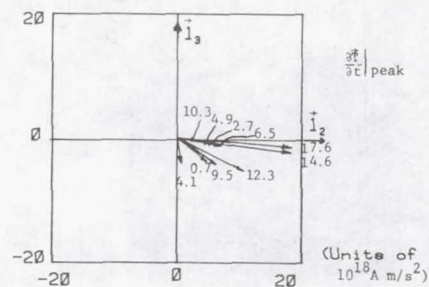


Figure 5.6.- θ, ϕ contours for rocket-triggered waveform and whole-sky videotape photograph.



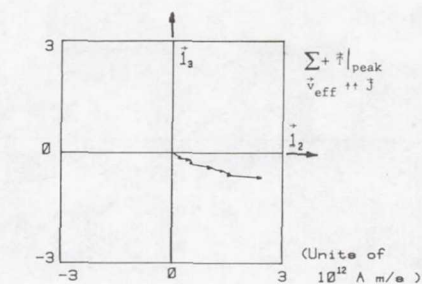
A. Effective reconstruction of positive streamer



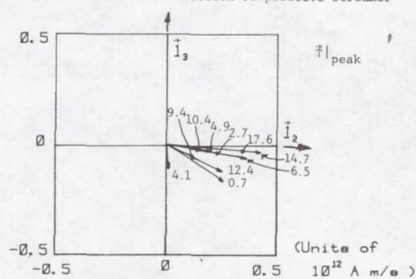
B. Peaks of $\frac{\partial T}{\partial t}$
 $\phi = 177^\circ$, $\theta = 30^\circ$, $r = 700\text{m}$

Date: 79228 M.S.T.: 1545:12

Figure 5.7.- $\frac{\partial T}{\partial t}$ for rocket-triggered lightning.



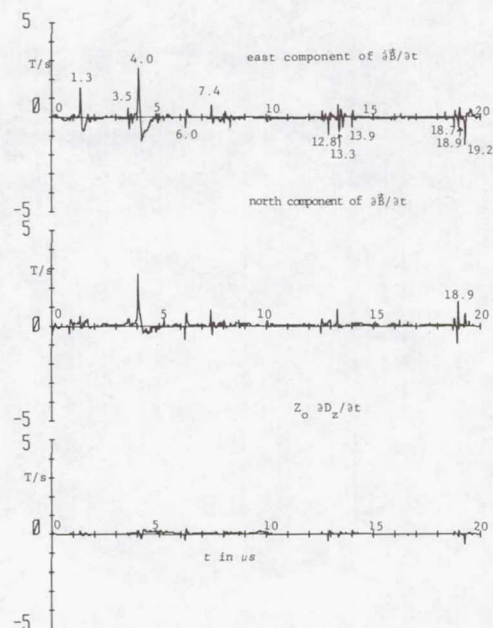
A. Effective reconstruction of positive streamer



B. Peaks of \vec{i}
 $\phi = 177^\circ, \theta = 35^\circ, r = 610\text{m}$

Date: 79228 M.S.T.: 1545:12

Figure 5.8.- \vec{T} for rocket-triggered lightning.



Date: 79219 M.S.T.: 1022:51

Figure 5.9.- Derivative fields from midrange leader(s).

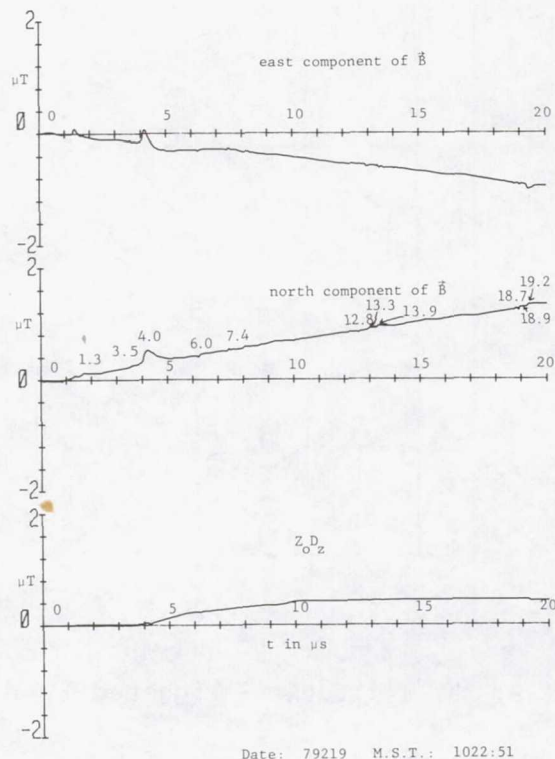


Figure 5.10.- Fields from midrange leader(s).

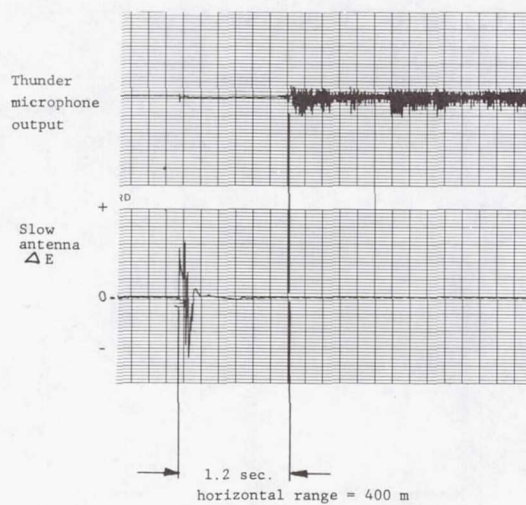
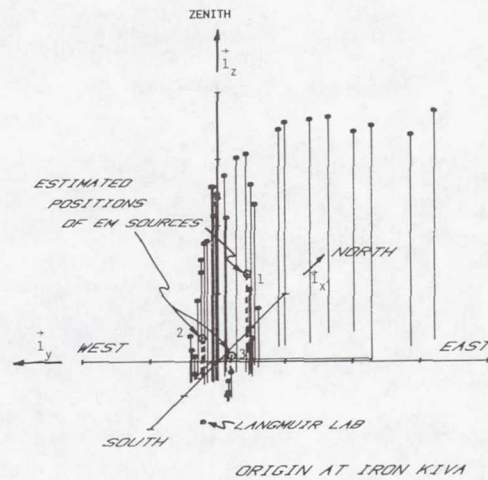


Figure 5.11.- Slow E field change and thunder microphone record of midrange leader.



ticks on axes at 1 km intervals.

Date : 79219 M.S.T. : 1022:51

Note: Three lightning channels to earth

1,2,3 indicate set numbers of $\partial \vec{r} / \partial t$ pulses.

Figure 5.12.- Acoustic location of midrange leader(s).

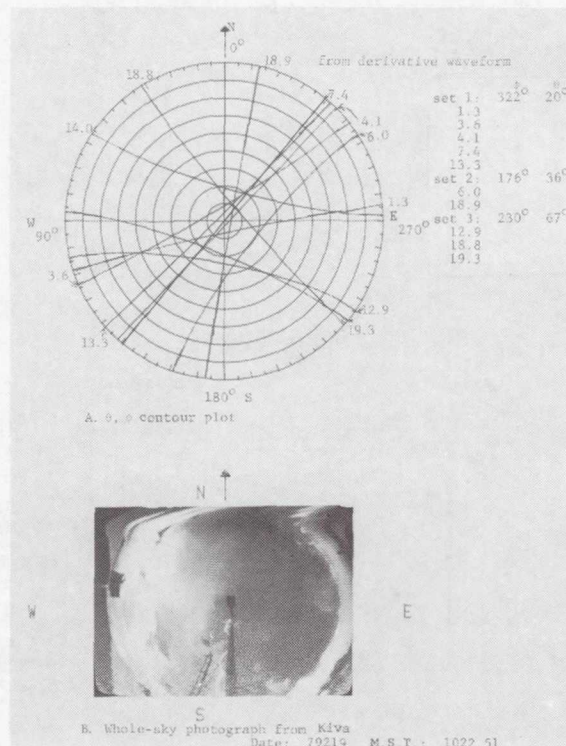


Figure 5.13.- θ, ϕ contours for midrange leader derivative waveform and whole-sky videotape photograph.

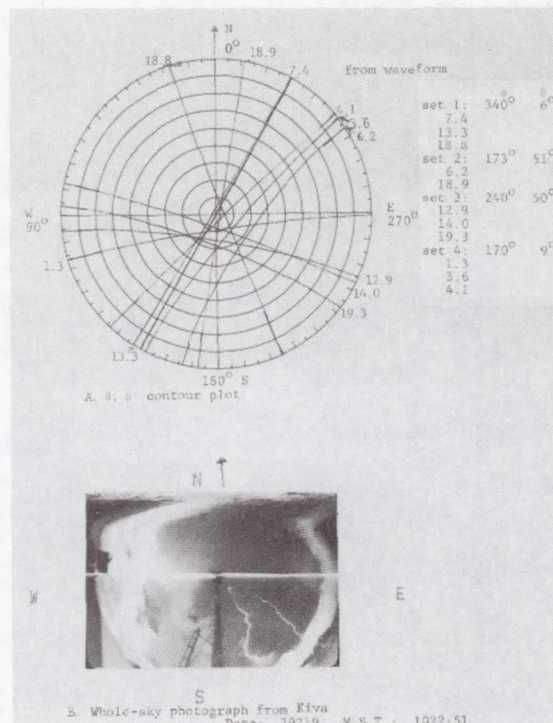


Figure 5.14.- θ, ϕ contours for midrange leader waveform and whole-sky videotape photograph.

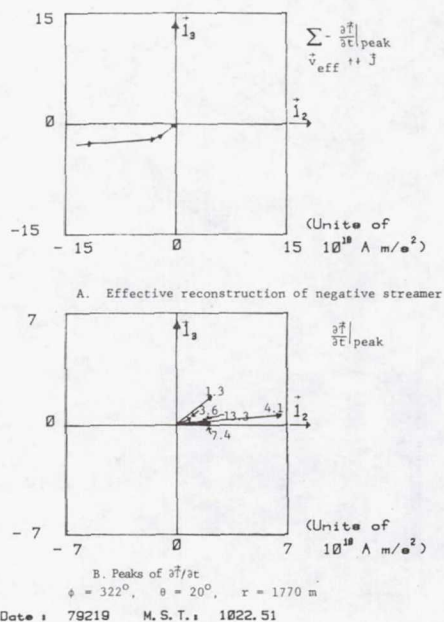
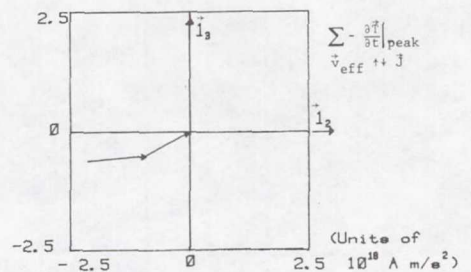
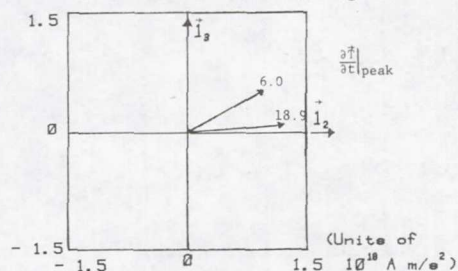


Figure 5.15.- $\partial \vec{T} / \partial t$ for midrange leader (set 1).



A. Effective reconstruction of negative streamer

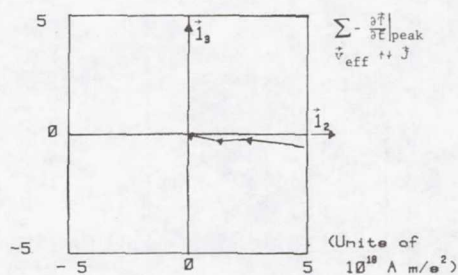


B. Peaks of $\partial \vec{T} / \partial t$

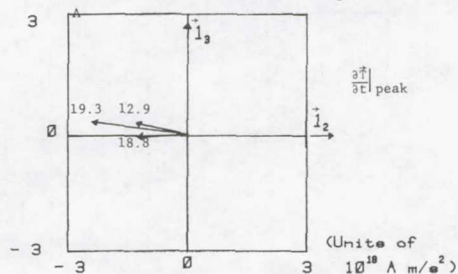
$\phi = 176^\circ$, $\theta = 36^\circ$, $r = 681 \text{ m}$

Date: 79219 M. S. T.: 1022.51

Figure 5.16.- $\partial \vec{T} / \partial t$ for midrange leader (set 2).



A. Effective reconstruction of negative streamer

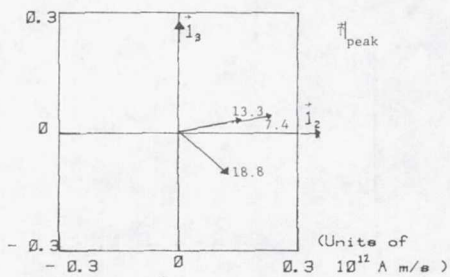
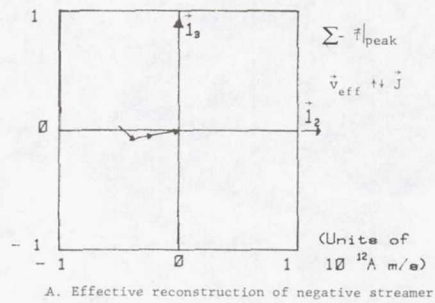


B. Peaks of $\partial \vec{T} / \partial t$

$\phi = 230^\circ$, $\theta = 67^\circ$, $r = 435 \text{ m}$

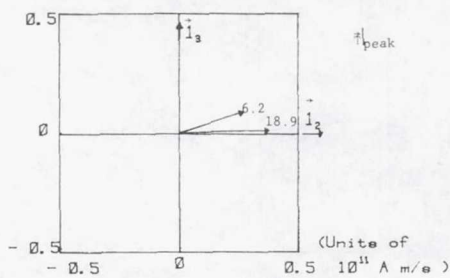
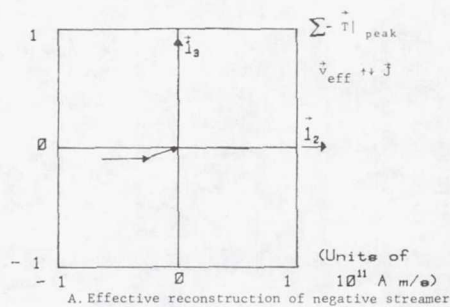
Date: 79219 M. S. T.: 1022.51

Figure 5.17.- $\partial \vec{T} / \partial t$ for midrange leader (set 3).



$\phi = 340^\circ$, $\theta = 6^\circ$, $r = 3827 \text{ m}$
 Date: 79219 M.S.T.: 1022.51

Figure 5.18.- \vec{T} for midrange leader (set 1).



$\phi = 173^\circ$, $\theta = 51^\circ$, $r = 515 \text{ m}$
 Date: 79219 M.S.T.: 1022.51

Figure 5.19.- \vec{T} for midrange leader (set 2).

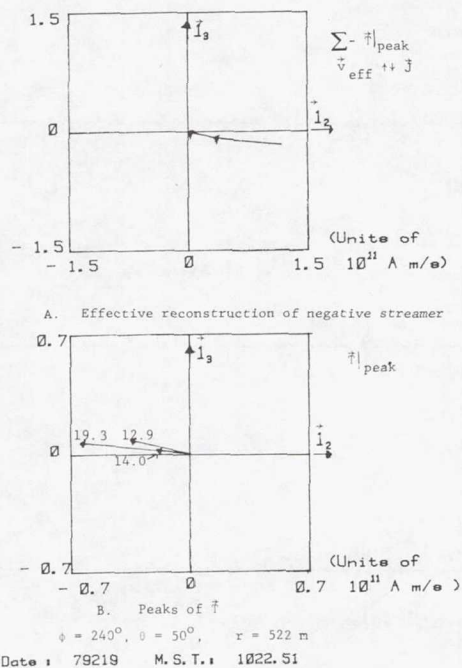


Figure 5.20.- \vec{T} for midrange leader (set 3).

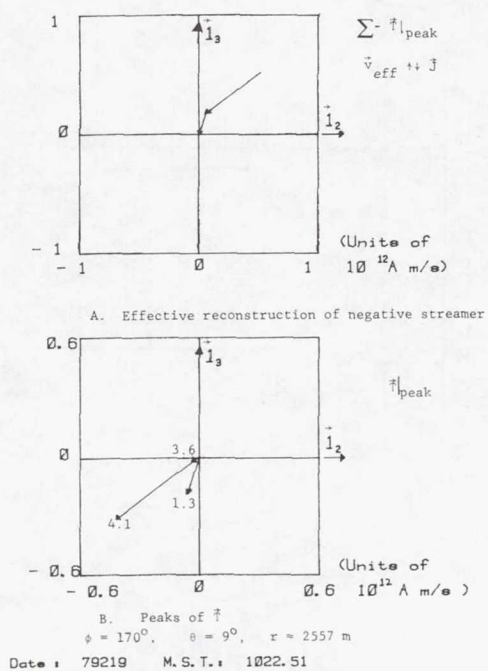


Figure 5.21.- \vec{T} for midrange leader (set 4).

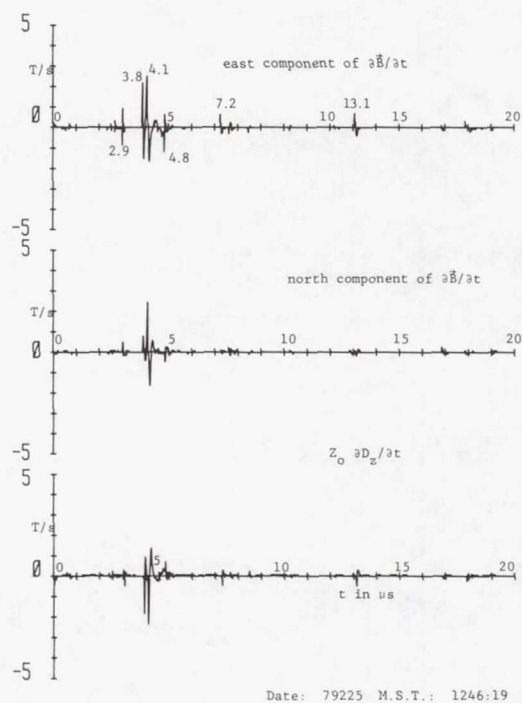


Figure 5.22.- Derivative fields from nearby leader.

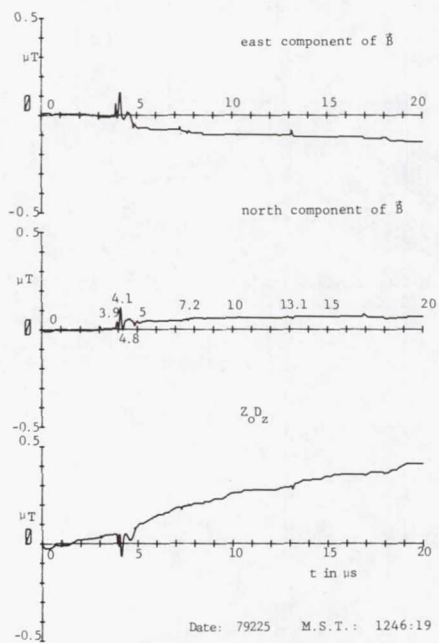
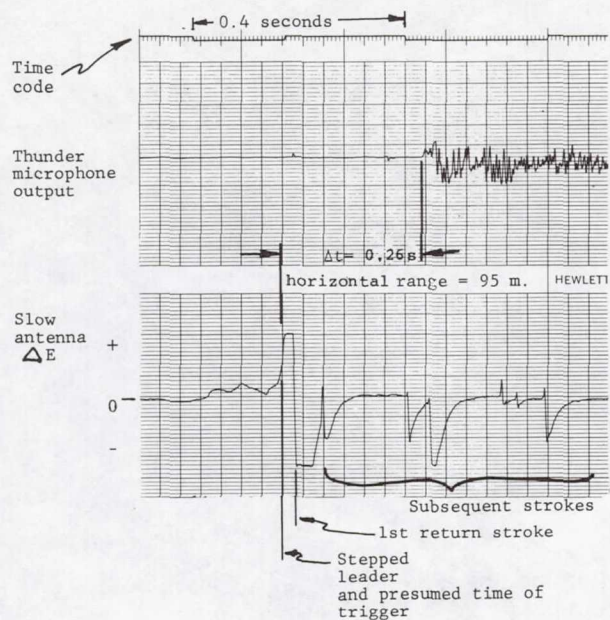
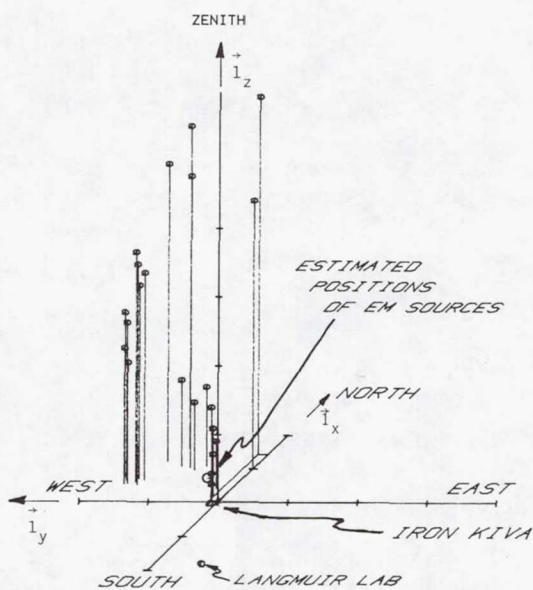


Figure 5.23.- Fields from nearby leader.



Date: 79225 M.S.T.: 1246:19

Figure 5.24.- Slow electric field change and thunder microphone record from nearby leader streamer.



ticks on axes at 1 km intervals

Date : 79225 M.S.T. : 1246:19

Figure 5.25.- Acoustic location of lightning with nearby leader streamer.

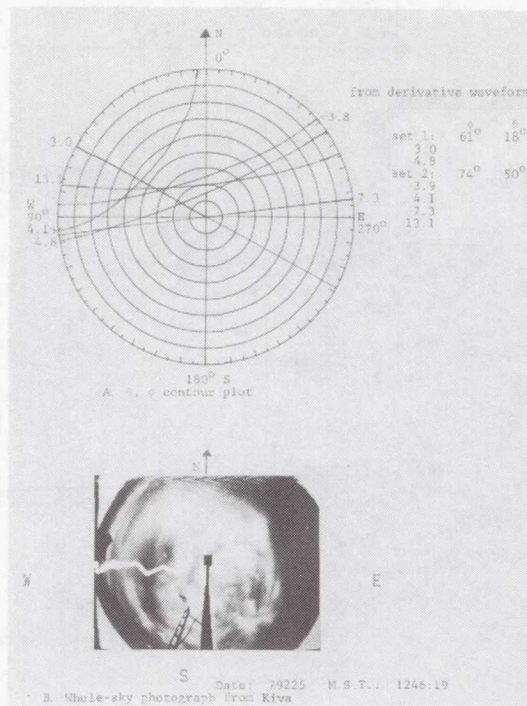


Figure 5.26.- θ, ϕ contours for nearby leader derivative waveform and whole-sky videotape photograph.

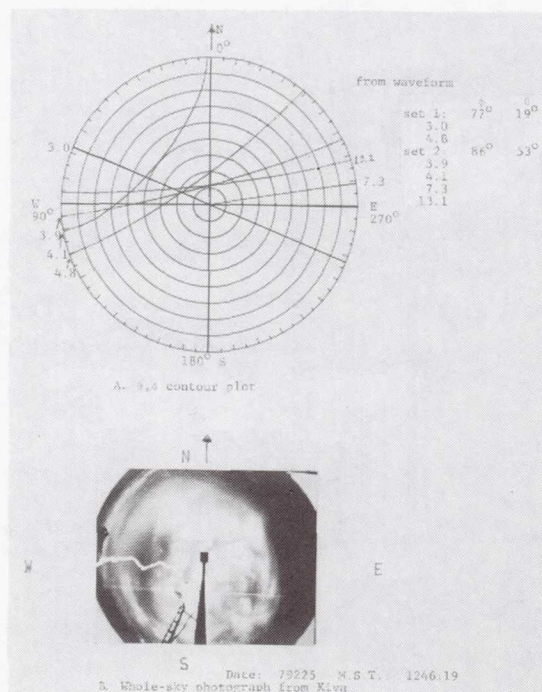
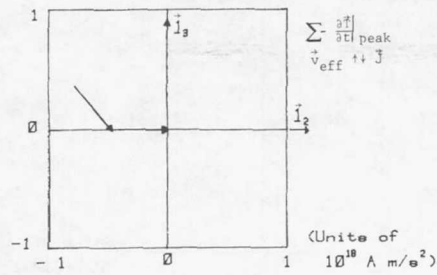
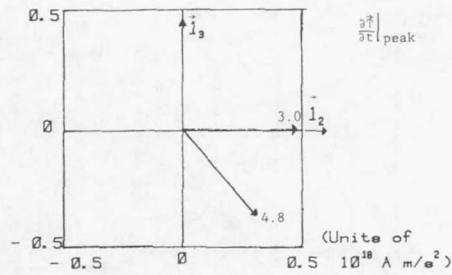


Figure 5.27.- θ, ϕ contours for nearby leader waveform and whole-sky videotape photograph.



A. Effective reconstruction of negative streamer

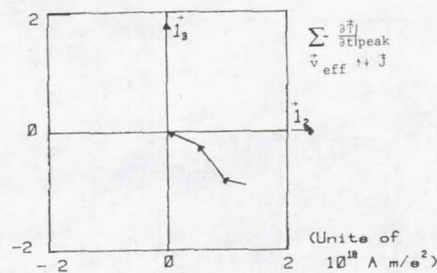


B. Peaks of $\frac{dI}{dt}$

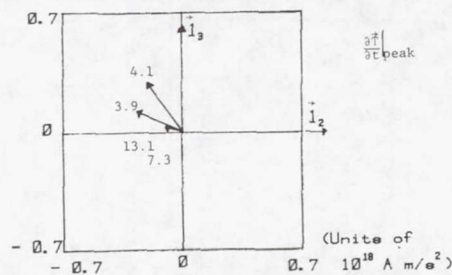
$\phi = 61^\circ$, $\theta = 18^\circ$, $r = 307 \text{ m}$

Date: 79225 M. S. T.: 1246.19

Figure 5.28.- $\frac{\partial T}{\partial t}$ for nearby leader (set 1).



A. Effective reconstruction of negative streamer

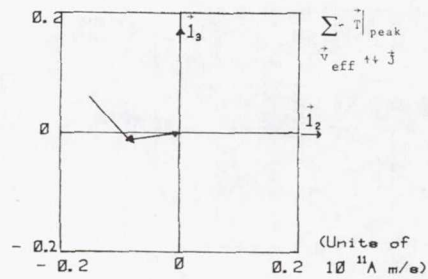


B. Peaks of $\frac{dI}{dt}$

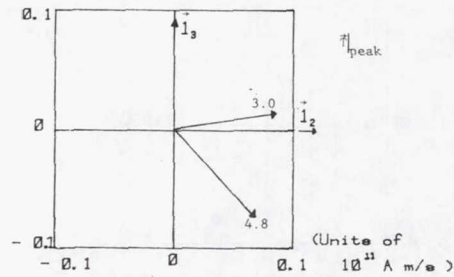
$\phi = 74^\circ$, $\theta = 50^\circ$, $r = 124 \text{ m}$

Date: 79225 M. S. T.: 1246.19

Figure 5.29.- $\frac{\partial T}{\partial t}$ for nearby leader (set 2).



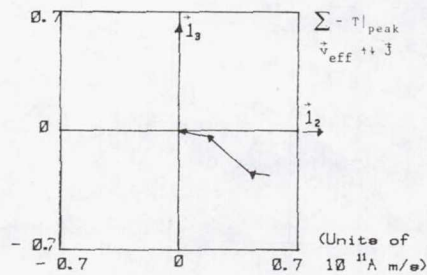
A. Effective reconstruction of negative streamer



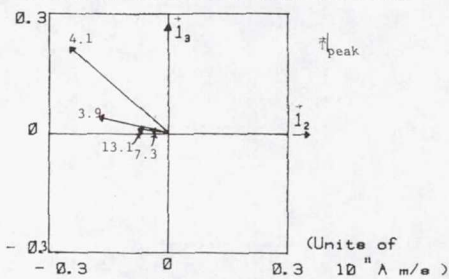
B. Peaks of T

$\phi = 77^\circ$, $\theta = 19^\circ$, $r = 292 \text{ m}$
Date: 79225 M.S.T.: 1246.19

Figure 5.30.- T for nearby leader (set 1).



A. Effective reconstruction of negative streamer



B. Peaks of T

$\phi = 86^\circ$, $\theta = 53^\circ$, $r = 119 \text{ m}$
Date: 79225 M.S.T.: 1246.19

Figure 5.31.- T for nearby leader (set 2).

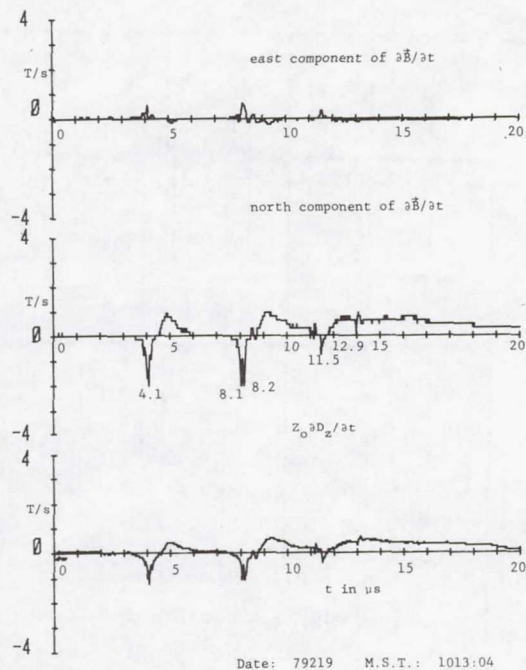


Figure 5.32.- Derivative fields from distant return-stroke.

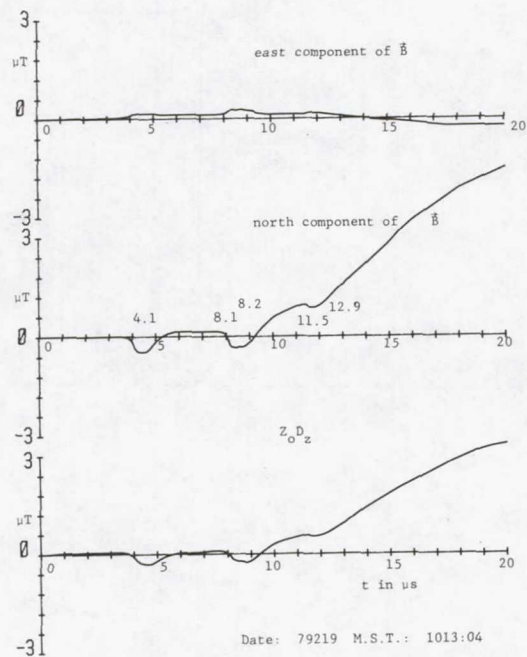


Figure 5.33.- Fields from distant return-stroke.

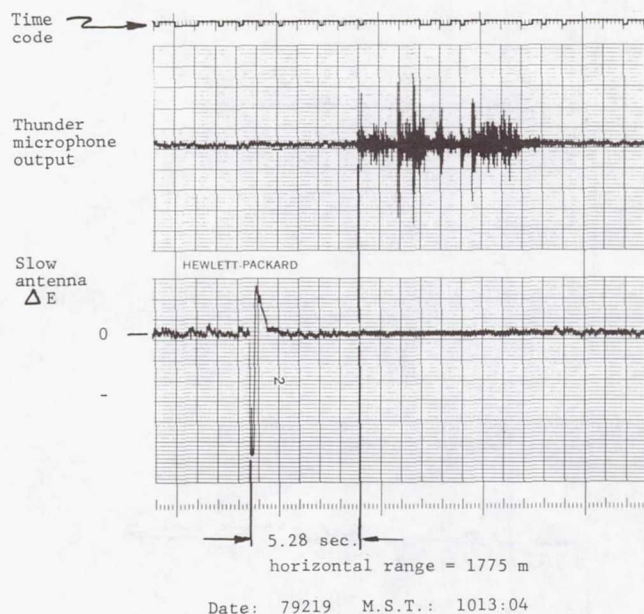


Figure 5.34.- Slow E field change and thunder microphone record of distant return-stroke.

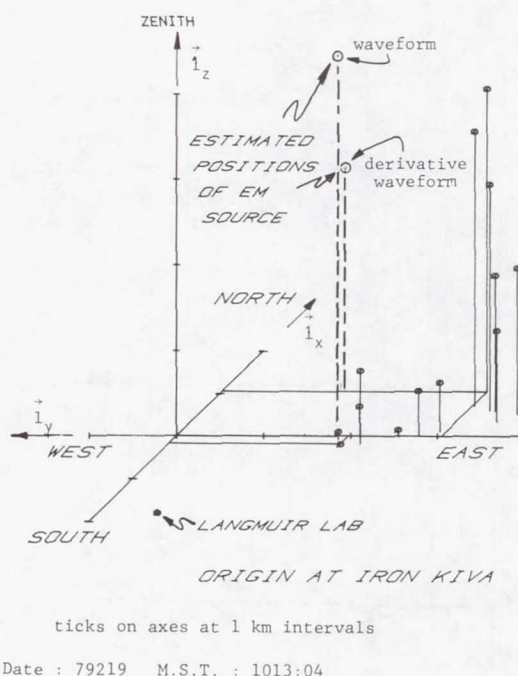


Figure 5.35.- Acoustic location of lightning with a distant return stroke.

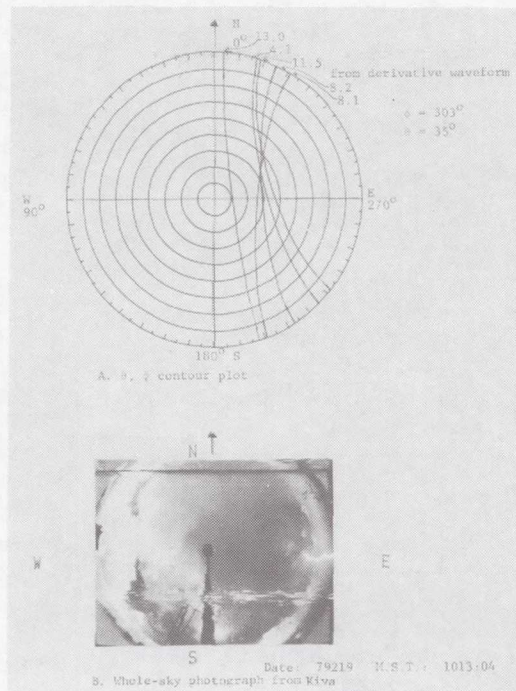


Figure 5.36.- θ, ϕ contours for distant return-stroke derivative waveform and whole-sky videotape photograph.

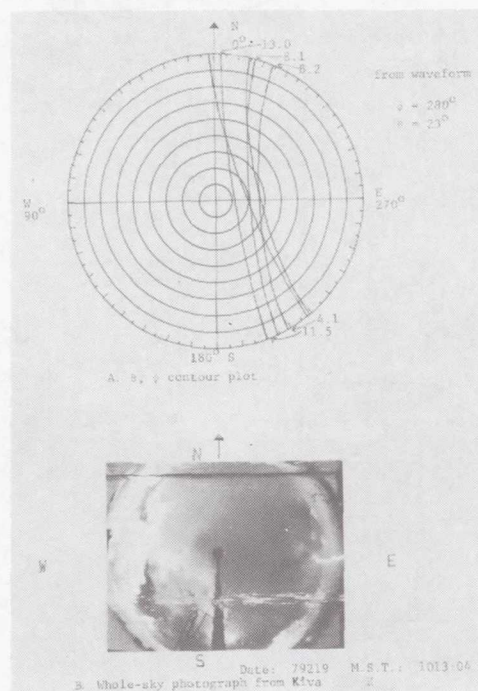
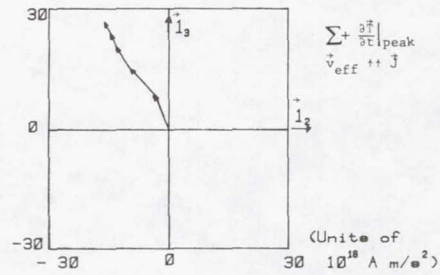
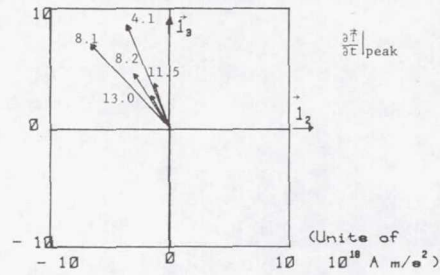


Figure 5.37.- θ, ϕ contours for distant return-stroke waveform and whole-sky videotape photograph.



A. Effective reconstruction of positive streamer

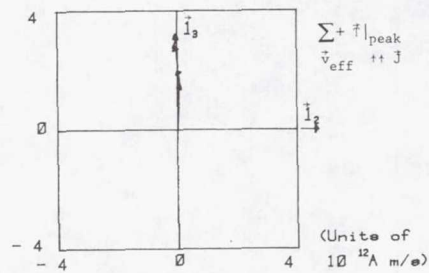


B. Peaks of $\partial \vec{T} / \partial t$

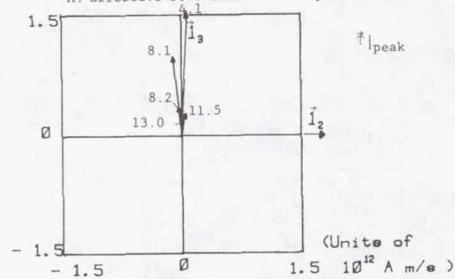
$\phi = 303^\circ$, $\theta = 35^\circ$, $r = 3138 \text{ m}$

Date: 79219 M.S.T.: 1013.04

Figure 5.38.- $\partial \vec{T} / \partial t$ for distant return stroke.



A. Effective reconstruction of positive streamer



B. Peaks of \vec{T}

$\phi = 280^\circ$, $\theta = 23^\circ$, $r = 4607 \text{ m}$

Date: 79219 M.S.T.: 1013.04

Figure 5.39.- \vec{T} for distant return stroke.

SESSION II - LIGHTNING INSTRUMENTATION AND MEASUREMENTS

Page intentionally left blank

ELECTROMAGNETIC SENSORS FOR GENERAL LIGHTNING APPLICATION

Carl E. Baum, Edward L. Breen, and John P. O'Neill
Air Force Weapons Laboratory

Charles B. Moore
New Mexico Institute of Mining and Technology

Gary D. Sower
EG&G Albuquerque, N.M.

ABSTRACT

This paper discusses electromagnetic sensors for general lightning applications in measuring environment as well as system response to the environment. This includes electric and magnetic fields, surface current and charge densities and currents on conductors. Many EMP sensors are directly applicable to lightning measurements, but there are some special cases of lightning measurements involving direct strikes which require special design considerations for the sensors.

The sensors and instrumentation used by NMIMT in collecting data on lightning at South Baldy peak in central New Mexico during the 1978 and 1979 lightning seasons will also be discussed. The Langmuir Laboratory facilities and details of the underground shielded instrumentation room and recording equipment will be presented.

I. INTRODUCTION

In measuring the lightning pulse, one has to often deal with distributed electromagnetic quantities such as electric and magnetic fields, current densities, charge densities, and conductivity, as well as integral quantities such as voltage and current. As indicated in Figure 1.1, there are four kinds of distributed quantities that are directly related by Maxwell's equations and constitutive equations. It is these quantities, a combination of them, or simple transformations of them that one wishes to measure. The sensor problem is then basically how to measure these. (See (1) for a discussion of sensors for EMP measurements.)

What then is a sensor? For purposes of this discussion, let us quote our definition of a sensor as a special kind of antenna with the following properties (1):

- 1) It is an analog device which converts the electromagnetic quantity of interest to a voltage or current (in the circuit sense) at some terminal pair for driving a load impedance, usually a constant resistance appropriate to a transmission line (cable) terminated in its characteristic impedance.
- 2) It is passive.
- 3) It is a primary standard in the sense that for converting fields to volts and current, its sensitivity is well known in terms of its geometry; i.e., it is "calibratable by a ruler". The impedances of loading elements may be measured and trimmed. Viewed another way it is in principle as accurate as the standard field (voltage, etc.) in a calibration facility. (A few percent accuracy is typically easily attainable in this sense.)
- 4) It is designed to have a specific convenient sensitivity (e.g., $1.00 \times 10^{-3} \text{ m}^2$) for its transfer function.
- 5) Its transfer function is designed to be simple across a wide frequency band. This may mean "flat" in the sense of volts per unit field or time derivative of field, or it may mean some other simple mathematical form that can be specified with a few constants (in which case more than one specific convenient sensitivity number is chosen).

For the measurement of local electric field and total-current-density quantities, we use an electric dipole sensor (dipole due to reciprocity between transmission and reception) as indicated in Figure 1.2. The equivalent circuits are for the case where the sensor is electrically small. If the medium is conducting, then a conductance G appears in parallel with the capacitance C . In a lightning source region in air, G is time dependent and a function of the electric field; there is a conduction as well as a displacement current density, and there is a source current density of high energy electrons. The Thevenin and Norton equivalent circuits correspond most conveniently to open circuit and short-circuit conditions where the magnitude of the load impedance Z_c

is large or small, respectively, compared to the magnitude of the source impedance $1/(sC)$, or better $1/(sC + G)$ where s is the complex frequency (Laplace transform variable with respect to time indicated by a tilde above a quantity). For open circuit purposes, the sensitivity is characterized by a constant equivalent length (or height) \vec{l}_{eq} (a vector) which samples the incident electric field in a dot product sense. For short circuit purposes, the sensitivity is characterized by an equivalent area \vec{A}_{eq} which samples the incident current density displacement current density in free space) in a dot product sense with conventions as in Figure 1.2. Note that \vec{l}_{eq} , \vec{A}_{eq} , and C are defined by the asymptotic form of the response in the electrically small sense. These parameters are not all independent but are related by

$$\vec{A}_{eq} = \frac{C}{\epsilon_0} \vec{l}_{eq} \quad (1.1)$$

with ϵ_0 as the permittivity of free space (or other surrounding uniform isotropic medium) (18). Note in Figure 1.1 that open and short circuit for such a sensor correspond to two of the four basic types of quantities from Maxwell's equations.

For magnetic quantities we use a magnetic dipole sensor (a loop) as indicated in Figure 1.3. The equivalent circuits for electrically small sensors are characterized by an inductance L (and perhaps some series resistance which is kept small), an equivalent area \vec{A}_{heq} for open circuit measurements for which $\partial \vec{B} / \partial t$ is sampled (with units V/m^2 or voltage density), and an equivalent length \vec{l}_{heq} for short circuit measurements for which \vec{H} is sampled. Open and short circuits correspond to the magnitude of Z_c (the load, usually resistive) large or small, respectively, compared to the magnitude of sL . These quantities are related by

$$\vec{A}_{heq} = \frac{L}{\mu_0} \vec{l}_{heq} \quad (1.2)$$

where μ_0 is the permeability of free space. Again, these parameters are defined by the asymptotic form of the response in the electrically small sense (18). In Figure 1.1, open- and short-circuit conditions correspond to the remaining two of the four basic types of quantities from Maxwell's equations.

An important question relating to these kinds of sensors is which type is best for a certain kind of application. Such questions are usually cast into an efficiency format in the sense of most output per unit input. Here one must recognize the broadband character of the measurement problem so that output should also include an appropriate bandwidth in its definition.

One concept of historical and technical interest is that of equivalent volume that has the formulas (18), (26) for electric

$$V_{eq} = \frac{\epsilon_0}{C} \vec{A}_{eq} \cdot \vec{A}_{eq} = \frac{C}{\epsilon_0} \vec{l}_{eq} \cdot \vec{l}_{eq} = \vec{A}_{eq} \cdot \vec{l}_{eq}$$

$$V_{heq} = \frac{\mu_0}{L} \vec{A}_{heq} \cdot \vec{A}_{heq} = \frac{L}{\mu_0} \vec{l}_{heq} \cdot \vec{l}_{heq} = \vec{A}_{heq} \cdot \vec{l}_{heq} \quad (1.3)$$

and magnetic dipole sensors, respectively. The equivalent volume is based on the energy extracted from the incident field and delivered to the load. This equivalent volume can be divided by a geometrical volume to give a dimensionless efficiency. This geometrical volume might be a specified volume into which the sensor is to fit; the better sensor design has the better efficiency. This type of definition is appropriate for cases in which the sensor is electrically small at all frequencies of interest, the critical frequency $1/(Z_c C)$ and Z_c/L (for constant resistance Z_c) is within the electrically small regime, and the basic limitation on the sensor design is size.

Several of the sensor types discussed herein are not constrained directly by physical dimensions but by upper frequency response (l_c or f_c which might be interpreted as a characteristic time t_c) for which the approximation of the response being proportional to the time derivative type of field quantity dotted into an equivalent area breaks down. The sensor size can be made as large as possible to obtain sensitivity for a given bandwidth. As the sensor size is increased, the approximation of an electrically small sensor breaks down at the highest frequencies of interest. One defines then the characteristic frequency or time according to when the ideal dot product and derivative response is in error by some specified amount. The resulting figure of merit is found to be

$$\Lambda_e = \left(\frac{Z_c}{Z_0} \right)^{1/2} \left| \vec{A}_{eq} \right| l_c^{-2} \quad \Lambda_h = \left(\frac{Z_0}{Z_c} \right)^{1/2} \left| \vec{A}_{heq} \right| l_c^{-2} \quad (1.4)$$

for electric and magnetic dipole sensors, respectively, where the wave impedance of free space is

$$Z_0 = \left(\frac{\mu_0}{\epsilon_0} \right)^{1/2} \quad (1.5)$$

and Z_c is the assumed frequency independent load resistance, typically the characteristics impedance of a transmission line. For this purpose, we have introduced a characteristic length (noting that the high-frequency limitation tends to be related to transit times on the structure) as

$$l_c = ct_c = \frac{c}{\omega_c} \quad (1.6)$$

where c being the speed of light, thus putting the bandwidth in length units. The figure of merit is of the form sensitivity times (bandwidth)², a quantity which is not a function of sensor size but only a function of the design, shape, and impedance loading distribution. The definition of this figure of merit is based on power delivered to the load Z_c which places electric and magnetic sensors on a common basis for comparison (40).

The various sensors in their free space designs can usually be mounted on ground planes by cutting them in half along an appropriate symmetry plane. The figures of merit for a given type of design are different in these two situations. In this paper we refer the figures of merit for each design type to their free space (full sensor) versions. Note that a particular sensor design in a ground plane version may have a different equivalent area and drive a different load impedance, although both are simply related to the free space versions.

Another common type of electromagnetic sensor is that used for measuring current or current density, specifically for measuring the time derivative of the current "through" the sensor via inductive coupling to the associated magnetic field (24). An alternate scheme for measuring the current density involves a short-circuit electric dipole as in Figure 1.2 (7). However, this has significant limitations in nuclear source region applications.

The inductive current sensor is shown schematically in Figure 1.4. It is characterized by a mutual inductance M relating the open circuit (OC) voltage to the time derivative of the total current I_t (including displacement current, i.e., surface integral of $\epsilon \partial E / \partial t$). Inherent to the sensor design is the equality of the line integral of the magnetic field around an area to the surface integral of the total current density through the area. The basic relations are

$$V_{oc} = M \frac{\partial}{\partial t} I_{t_{inc}} \quad I_{t_{inc}} = \vec{A}_{t_{eq}} \cdot \vec{J}_{t_{inc}} \quad (1.7)$$

The latter equation is used in the case that the total current density is to be measured; $\vec{A}_{t_{eq}}$ is the corresponding equivalent area. In this latter case there are two important sensitivity parameters, both of which must be considered for the accuracy of the sensor transfer function. Again, these parameters are defined by the asymptotic form of the response in the electrically small sense.

This type of sensor also has a self-inductance L which is in general not the same as M . One could modify the Thevenin equivalent circuit of Figure 1.4 into a Norton form. However, this would bring the self-inductance L (which is in general not as accurately known as M) into the sensor sensitivity when operated in the short-circuit mode.

II. SENSORS FOR USE AWAY FROM LIGHTNING ARCS AND CORONA

Electromagnetic sensors for use in measuring lightning phenomena at a distance sufficiently removed from the lightning stroke that arcs and corona are not present are very similar to sensors used for EMP measurements away from a nuclear source region. These sensors may be used in one of two ways, for measurement of the environment created by the lightning and for measurement of the response of a system to the environmental fields.

D-DOT SENSORS

The D-dot sensor is used to measure the time rate of change of electric flux density. The sensor's response is described by the Norton equivalent circuit of Figure 2.1. The frequency domain response of the sensor is given, for bandwidth limited by capacitance and not by transit times, by

$$\tilde{V}(s) = \frac{\epsilon s \vec{E}_{inc}(s) \cdot \vec{A}_{eq} Z_c}{1 + s Z_c C} \quad (2.1)$$

and for frequencies where $\omega \ll 1/(Z_c C)$ the response can be simply expressed as

$$\tilde{V}(s) = \epsilon s \tilde{E}_{inc}(s) \cdot \vec{A}_{eq} Z_c. \quad (2.2)$$

It is of primary importance that an accurate determination of sensor equivalent area can be made. For that reason, only sensor geometries with accurately calculable equivalent areas are used. Sensor capacitance as a design parameter need not be known so accurately, but it should be a low value as it shunts the load resistance and determines the high-frequency response. For very fast sensors, it should be small enough that the high frequency response is determined by transit-time effects.

Hollow Spherical Dipole (HSD)

The HSD sensor design (30), (34), (39), (45), (65) uses the geometry of a sphere with a narrow slot around the equator. The slot is resistively loaded by the signal cables. The sensor shown in Figure 2.1 is the HSD-S1A(R) for use on a conducting ground plane. It consists of a hemispherical shell mounted on a ground plate. Signal current from the hemisphere flows to the ground plate through four equally spaced 200- Ω strip lines. The four strip lines from the hemisphere join at the center of the base of the hemisphere and then continue along a 50- Ω coaxial cable to the output connector. The HSD-2A(R) is a balanced output version of the sensor for free-space measurements. It consists of two sensing hemispheres placed back-to-back with a thin ground plane between them. The two 50- Ω coaxial cables are contained inside the output stem which extends radially out in the plane of the center plate to a twinaxial connector. The signals from the two hemispheres produce a differential signal which is then carried by standard 100- Ω twinaxial cable (8), (66). The sensitivity of the HSD sensor is expressed as an equivalent area. The area is shown to be $|\vec{A}_{eq}| = 3\pi a^2$ where a is the sensor sphere radius (30), (34). The Λ_{10-90} figure of merit for this sensor is 0.078. HSD sensors have been fabricated with equivalent areas of 0.1 and 0.01 m² in both differential and single-ended versions.

Asymptotic Conical Dipole (ACD)

An improved sensor geometry from the standpoint of figure of merit is the ACD. The ACD sensor geometry is determined by a method described in (25), (65). The particular shape used to date is derived from a line charge $\lambda(z)$ on the z axis given by

$$\lambda(s) = \begin{cases} \lambda_0, & \text{for } 0 < z < z_0 \\ -\lambda_0, & \text{for } 0 > z > -z_0 \\ 0, & \text{for } z = 0 \\ 0, & \text{for } z > z_0 \end{cases} \quad (2.3)$$

$$\lambda_0 > 0, \quad z_0 > 0.$$

The potential distribution for the above charge distribution is solved for the electrostatic equipotentials surrounding it. The surface of the sensor corresponds to a particular equipotential surface which approaches a 100- Ω bicone at its base in its differential form. The ACD-5A(A) sensor is shown in Figure 2.2. The design details for this single-ended sensor are in (46). It consists of the sensor element attached to a 50- Ω coaxial cable which passes within the ground plane to the coaxial connector. The sensor element is supported by a thin dielectric cylinder which provides weather protection and mechanical support. The sensor has an equivalent area of $1 \times 10^2 \text{ m}^2$ and an upper frequency response $>75 \text{ MHz}$. Sensor element capacitance to ground is 17 pF. The Λ_{10-90} figure of merit is ≈ 0.2 (based on measurements on a scale model) which is comparable to the MGL B-dot sensors. The ACD sensors have also been fabricated with equivalent areas of 10^{-2} , 10^{-3} and 10^{-4} m^2 in both differential and single-ended versions (46).

Flush Plate Dipole (FPD)

The geometries of the HSD and ACD sensors cause electric field enhancement which is most pronounced at the top of the sensing element. The enhancement is three times for the HSD and larger for the ACD. The flush plate dipole minimizes field enhancement and chances for field distortion. The sensor geometry is shown in Figure 2.3. It is basically a conducting disk centered in a circular aperture in a conducting ground plane (17), (31), (32), (52), (65). The signal is taken from the sensor element at four equally spaced points around its circumference by 200- Ω strip lines. The strip lines feed two 100- Ω coaxial cables which are paralleled into a 50- Ω connector. The flat surface of the sensor is covered by a thin piece of mylar which acts as a weather cover. The bottom side of the sensor is covered by a conducting pan to provide a consistent electrical environment as well as to provide protection. Resistive loops are positioned inside the cover to absorb energy below to the sensor element. The equivalent area of the FPD is derived in (32) in which the area is given as a normalized area

$A = |\vec{A}_{eq}|/(\pi ab)$ where a and b are the radii of the sensor element and the circular aperture, respectively. For the FPD-1A $a = 0.0508$ m, $b = 0.0635$ m, $A = 0.988$, and $A_{eq} = 0.01$ m². The normalized capacitance is calculated (32) for various disk and aperture radii, and for the dimensions of the FPD-1A that value is 6.8 pF. This value of capacitance along with the 50- Ω cable impedance would give a frequency response of 468 MHz. The presence of the mylar sheet covering the sensor, the disk support structure, and the bottom cover add an additional 1.2 pF and reduce the frequency response to approximately 390 MHz. The Λ_{10-90} figure of merit is 0.08 related to a differential configuration.

MAGNETIC FIELD SENSORS

The inductance-limited transfer function of the magnetic field sensor of Figure 1.3 is given by

$$\tilde{V}(s) = \frac{s\tilde{\vec{B}}_{inc}(s) \cdot \vec{A}_{heq} Z_c}{sL + Z_c} \quad (2.4)$$

For frequencies where $\omega \ll Z_c/L$,

$$\tilde{V}(s) = s\tilde{\vec{B}}_{inc}(s) \cdot \vec{A}_{heq} \quad (2.5)$$

For frequencies where $\omega \gg Z_c/L$,

$$\tilde{V}(s) = \frac{\tilde{\vec{B}}_{inc}(s) \cdot \vec{A}_{heq} Z_c}{L} \quad (2.6)$$

Using the concept of equivalent length, the above can be expressed as

$$\tilde{V}(s) = \tilde{\vec{H}}_{inc}(s) \cdot \vec{l}_{heq} Z_c \quad (2.7)$$

Multigap Loop (MGL)

The MGL series of magnetic field sensors (20), (21), (43), (53), (55), (58), (59), (65) is used for high-frequency B-dot

measurements. The basic free-field MGL (full loop) sensor is built in the form of a right circular cylinder. The cylinder is formed from 1/16-in printed circuit board material which is etched to provide the gaps and 200- Ω strip lines which pick off the signal. The sensor is divided into four quadrants by axial shorting plates that connect to the cylinder midway between the gaps. The signals from quadrants one and three are combined to form one side of the differential output signal, and the signals from quadrants two and four combine to form the other. Combining the signals in this manner minimizes the E-field response. The gaps are formed with the proper angle to form a 200- Ω impedance which improves the sensor risetime. The cylindrical geometry of the MGL sensor permits an approximate determination (20) of the effects of the number of gaps, the cable impedance, the sensor length, and orientation of the gaps with respect to the magnetic field. The single-ended sensors are essentially one-half of the sensor described above except that they consist of two adjacent quadrants with signals connected in parallel. The MGL-3 (10⁻¹ m²) used for far-field lightning measurements is shown in Figure 2.4. MGL sensors have been built with equivalent areas of 10⁻¹, 10⁻², 10⁻³, 10⁻⁴, and 10⁻⁵ m². Equivalent area is maintained to an accuracy of +3 percent. The area accuracy considerations are discussed in (43). The Λ_{10-90} figure of merit is 0.24.

One-Conductor, Many-Turn Loop (OML)

A single-gap half-cylinder loop with four-turn wiring (12), (65), and an equivalent area of one square meter is available for measurements requiring more sensitivity. This sensor, designated the OML-1A(A), operates as a derivative output device at frequencies below 3.5 MHz and has a risetime of about 100 ns. Figure 2.5 shows the wiring diagram. Special triaxial cable with 25- Ω outer line and 50- Ω inner line is used. The gap voltage is picked off at four points and carried by the 25- Ω outer lines to two summing gaps in the 50- Ω internal lines. The two 50- Ω lines drive the 100- Ω differential output at the final gap in the cable. The four voltage pickoff points along the gap were selected experimentally to optimize frequency response.

Multiturn Loop (MTL)

The MTL-1 (16), (18), (27), (28), (49), (56) is a full-loop (free field) 50-turn sensor with an equivalent area of 10 m² and a B-dot upper frequency response of approximately 25 kHz. Above 25 kHz the sensor is self-integrating with its useful bandwidth extending to 3 MHz. Above this frequency, resonances within the

complex signal distribution network perturb the output signal. The sensor has an equivalent length of 0.02 m and a self-inductance of 6.3×10^{-4} H. The MTL-1 design employs several special features to achieve the 3.5 MHz bandwidth (12). It has four loop gap signal pickoffs and is wound in two identical 25 turn half-loops, each of which drives one side of the differential output. Figure 2.6 shows the sensor interior. A shield of resistively loaded loops can be seen on the outside of the coil. This shield is electrically connected to eight axial shorts which help break up resonances and keep out unwanted electric and magnetic field components. The 50-turn sensor loop is wound on a fiberglass coil form in a counter-wound manner with a sequence of over and under crossovers on diametrically opposite sides of the coil. The signal is developed across the loop gaps and transmitted through 25- Ω outer part of a triaxial cable to the summing junction where they add and are transmitted to the sensor output connectors on a 50- Ω inner part of a triaxial cable. The two 50- Ω half-loop output cables then combine to drive a 100- Ω differential output cable. The 25- Ω and 50- Ω signal cables are part of the sensor loop which is wound with 50/25- Ω triaxial cable. Midpoint grounds divide each half loop into two quarter loops. The midpoint ground structure consists of the sensor stem and connections to the loop structure at equipotential points, and do not affect the desired sensor response. They do, however, decrease the "electrical size" of the structure for undesired resonances and hence improve the high-frequency performance. Additional equipotential points are connected together to further improve the sensor response. Resistors are used in these "interwinding shorts" to dissipate the resonant energy. Final adjustments of the high-frequency response are made by adding a resistive shield around the outside of the coil to exclude the incident electric field at low frequencies. The quotient of equivalent volume divided by geometric volume is 1.3.

The MTL-2 has ten turns, an equivalent area of 10^{-2} m², an equivalent length of 10^{-2} m, a self-inductance of 1.25×10^{-6} H, and an upper frequency response of 12.6 MHz for B-dot operation. The quotient of equivalent volume divided by geometric volume is 0.56.

CURRENT SENSORS

Circular Parallel Mutual-Inductance Sensor (CPM)

This sensor is used to measure the time derivative of the total current through the aperture of the sensor. The CPM (24), (47), (48), (50), (65) is an inductive sensor of torodial shape as illustrated in Figure 2.7. The loop turns are oriented to be sensitive to the component of the magnetic field H with respect

to the measurement axis. This sensor has a cross section of width w , an inner radius r_1 , and an outer radius r_2 . The mutual inductance is

$$M = \frac{N \mu_r \mu_o w \ln\left(\frac{r_2}{r_1}\right)}{2\pi} \quad (2.8)$$

III. SENSORS FOR USE NEAR LIGHTNING ARCS AND IN CORONA

The environment inside the lightning arc and corona region is rather inhospitable for electromagnetic measurements. It differs from the nuclear source region in that we do not have a distributed source current density originating from Compton scatter of γ rays and photoelectric scatter of X-rays occurring in air and in the various materials of the sensor itself. We do have conduction effects associated with the surrounding air medium. The impact of the air conductivity is fundamentally different for electric (capacitive-conductive) and magnetic (inductive) devices. Since the air conductivity is a nonlinear effect (because of the dependence of the electron mobility on the electric field), it is imperative that an electric type sensor not significantly distort the local electric field so as not to change the conductivity (9). For a magnetic type sensor, the problem is somewhat different. Local changes in the air conductivity are not as significant; the magnetic field incident on the sensor is more governed by the currents in a volume of space with dimensions of the order of the radian wavelength (or skin depth) so that the local perturbations do not matter so much (at least for the lower frequencies) (15).

The problem of concern then is ionization of air, if present, which constrains electric sensor design to be nondistorting of the local electric field, and which loads the loop-gaps of magnetic sensors.

In reducing the deleterious effects in the lightning source region various general guidelines are useful.

1. For Magnetic Sensors

The gaps are encapsulated in dielectric to prevent a shunt conductivity across the gap.

2. For Electric Sensors or Current Density normal to a Conductive Surface

They must negligibly distort the electric field in the immediate vicinity to not perturb (significantly) the conduction current density.

Various designs of sensors for electric and magnetic fields and currents in lightning source regions have been developed and used, and are discussed here.

It is generally easier to construct lightning source sensors than it is to construct nuclear source region sensors. The latter is rich in high energy photons (γ and x-ray) and also possibly neutrons. This necessitates sensor elements being as sparse as possible, and also that all materials used be of as low atomic number as practical so that cross-sections to the irradiation are minimized. This also includes such items as output cables which are specially fabricated and delicate. For lightning sensors we can use more materials such as brass sheet metal and copper jacketed coaxial cables.

For mounting of lightning source region sensors on objects, such as airplanes, a few simple precautions are in order. The sensors should be as flush with the surface of the object as possible so as not to perturb the fields and possibly attract direct attachment to the sensors. Cables between sensors and recording equipment should be shielded as soon as possible, and the recording system enclosed inside a topological electromagnetic shield.

ELECTRIC FIELD SENSORS

As discussed in the previous section, the most severe effect of a lightning source environment on electromagnetic measurements is that on the electric field sensor in air. Effects associated with air conductivity alter the characteristic response of the sensor.

PARALLEL MESH DIPOLE SENSOR (PMD)

The parallel mesh dipole sensor (PMD-1) (1), (13), (63), (64) in Figure 3.1 reduces the effect of the air conductivity by means of having its sensing element constructed of fine wires as opposed to a solid plate of a parallel plate dipole, so that most of the conduction current is allowed to flow around the dipole conductors instead of through them. The mesh wire is suspended from nylon thread 0.5 cm above the ground plane. In the quasi-static case, the wire grid lies on an equipotential plane so that

the equivalent length of the sensor is also 0.5 cm. The output voltage of the E-field sensor is obtained by measuring, through a sensing resistor, the voltages across the capacitor/conductor formed by the wire mesh and the ground plane. The sensing resistor is in series with the terminated signal cable forming a resistive voltage divider (11). The voltage across the capacitor will decay with a time constant determined by the sensor capacity and the sensing resistor except for local conductivity. This time constant must be long compared to measurement times of interest.

MAGNETIC FIELD SENSORS

The maximum air conductivity limits the loop radius to the order of a skin depth or less at the highest frequency of interest. Below this frequency the air conductivity does not significantly enter into the loop response. Thus for such a loop the nonlinear and time varying character of the air conductivity is insignificant. However, sensors associated equipment such as cables in the air medium should generally be limited to the same dimensions to avoid magnetic field distortions which may couple into the loop. It is possible to minimize the conductivity related effects by the use of insulators with the loop structure. Also, the cable impedance which loads the loop can be chosen, together with the loop inductance, to give a frequency response of the order of the skin depth limitation. The problem of air conductivity is eliminated in these sensors by encapsulating the volume enclosing the sensing element gap with an epoxy resin.

CYLINDRICAL MOEBIUS LOOP SENSOR (CML)

A useful magnetic field sensors for lightning source environments is a loop structure (3), (5), (6), (15), (16), (38), (41), (42), (57), (60), (61) with the signal cables wired in a Moebius configuration designated as cylindrical Moebius loop (CML) sensors. This greatly reduces the common mode radiation noise currents found in the split shield loop type of sensors. A CML sensor can be shown to be a two-turn loop by tracking current flow from one twinaxial cable lead to the other (Figure 3.2). At frequencies where the magnetic field does not penetrate the shield of the gap-loading cables, the sensor acts as a single-turn cylindrical loop with a resistive gap load given by the total terminating cable impedance. The four gap loading coaxial cables in the sensor are properly terminated at the point of coax-to-twinax junction as depicted in Figure 3.2. A voltage V at the gap appears as a positive signal in one pair of 100- Ω

gap-loading cables and as a negative signal in the other pair. The signal from the gap arrives at the coax-to-twinax junction at the same time from all four gap cables, which produces a differential mode signal across the balanced twinax. For a differential signal, the twinax may be considered to be two resistors each of a value of 50Ω to ground that properly terminate the 50Ω parallel combination of the two 100Ω coaxial cables (from each side of the gap). For a given gap voltage, a signal voltage of twice the amplitude of the gap voltage appears at the balanced twinax output.

Four models of CML sensors have been designed and fabricated. They vary in equivalent area from $5 \times 10^{-3} \text{ m}^2$ to 0.02 m^2 , and have been built with encapsulation for use in conductive air measurements.

CURRENT SENSORS

Radiation hardened current sensors have been designed which are similar to the CPM series of I-dot probes (23), (24). These sensors are designed to be part of a specific structure in a way that they will not appreciably affect the current flow on that structure.

Outside Moebius Mutual Inductance (OMM)

Figure 3.3 shows three OMM-1A I-dot sensors assembled into a cylindrical antenna (54), (62). Surface current flowing along the cylinder axis must pass through the sensor's internal cavity. The changing magnetic field produced within the sensor cavity produces a voltage across the gap according to $(1/N)M \text{ dI/dt}$ where M is determined by (2.8). The signal is taken from the gap by four 100Ω cables in the same manner as shown in Figure 3.3 for the CML sensor. The signal cables are routed to the inside of the sensor for electrical purposes and radiation shielding. The sensor interior and gap are encapsulated with an epoxy material in much the same way as with the CML B-dot sensor. The differential signal from each sensor is transmitted by cables of equal length. The OMM-1A has a mutual inductance of $2 \times 10^{-9} \text{ H}$ and a $10\text{-}90$ risetime $<0.5 \text{ ns}$. It is 6.4 cm long and of a diameter for use with a 10-cm pipe (outside diameter). A much smaller OMM-2 sensor has been built to measure current in cable shields, conductors, or structural members. It has a mutual inductance of $2 \times 10^{-9} \text{ H}$ and a risetime of $<0.5 \text{ ns}$. It is 8.9 cm long and designed to use with a 2-cm pipe (outside diameter).

IV. SOUTH BALDY LIGHTNING ELECTROMAGNETICS INSTRUMENTATION

A program was initiated in 1976 by the Air Force Weapons Laboratory with the New Mexico Institute of Mining and Technology to test the Air Force ARGUS 1A system which is used for detection of the electromagnetic pulse from a high altitude nuclear weapon detonation. The objective of this test program is to record the performance of the ARGUS 1A when operated in a lightning electromagnetic environment and to determine the electromagnetic properties of nearby lightning of potential significance to such detectors. The measurements are made at the center of a 30m x 30m square wire mesh ground plane placed on a relatively flat surface of the earth near the crest of South Baldy Peak. Copper ground rods are connected at 3m intervals around the perimeter of the wire mesh and across its surface. The Kiva is buried at the center of the wire mesh with its roof flush with the earth and electrically connected to the mesh. Figure 4.1 shows the site viewed from the north.

The Kiva is a 4.25m diameter by 2.44m high welded tank made from 3mm (1/8") thick sheet steel. The top of the tank is extended about 1m in radius to provide an adequate mounting surface for the sensors as well as an access area for some of the penetrations into the Kiva. Figure 4.2 provides a closer view of the Kiva from the south. Access to the Kiva is by the stairway shown in the lower right of the photo. Shielding integrity of the Kiva is maintained by a "shielded room" door on the side of the tank.

Three ARGUS systems are shown in Figure 4.1. They are equally spaced on an 8m radius from the center of the Kiva. Each system is set at a different detection sensitivity.

Two MGL-3 B-dot sensors are shown in Figure 4.2. The MGL-3 has an equivalent area of 0.1m^2 . Its upper frequency response is down to 0.7 (3 dB down) at about 70 MHz. The sensor (B-dot East) on the upper right of the Kiva has its area vector pointing east and the sensor (B-dot north) to the left of the Kiva has its area vector pointing north. B-dot east has the significance that when B-dot is positive in the east direction, the voltage on the center conductor of the sensor output connector is positive, and similarly for B-dot north.

The ACD-5 D-dot sensor is shown at the front and center of Figure 4.2. It has an equivalent area of 1m^2 . Its frequency response is down to 0.7 (3 dB down) at about 75 MHz. The area vector for the ACD-5 is pointing toward zenith. A D-dot signal that is positive toward zenith will produce a negative voltage on the center conductor of the sensor output connector.

Each sensor is mechanically and electrically connected to the Kiva surface in several places around the edge of the sensor baseplate. The output signal from each sensor penetrates the Kiva top surface by going directly from the sensor output to a feedthru connector. RG-213 coaxial cable is used inside of the Kiva. The sensors are mounted on a 1.7 meter radius about the center of the Kiva. Because of the separation of sensors, arrival times for signals can vary by up to 11 ns depending on the azimuth and elevation of the signal source.

A block diagram of the lightning electromagnetics data acquisition system is shown in Figure 4.3. Each of the sensor signals is digitized with a Biomation model 8100 waveform recorder. This waveform recorder has eight bit resolution (256 levels). Each sampled voltage is accurate to 0.4 percent of full scale. The minimum sample interval is 10 ns. The pretrigger mode of recording is used to permit any desired part of the 2048 recorded samples to be those taken before the recorders are triggered. Typically about 20% of the samples are saved prior to trigger. The recorders are connected with their triggers in parallel. Triggering any recorder by signal causes all of them to trigger.

The recorders are controlled by one HP 9825 mini-computer controller. Upon completion of the recorder digitization, a signal is sent to the HP 9825 that then transfers the shift register data from each recorder, in turn, into the memory of the HP 9825. The HP 9825 then re-arms the recorders in preparation for acquisition of the next signals. After re-arming the recorders, the HP 9825 stores the first set of data on a magnetic disc for later analysis. In this mode of operation, an interval of about 25 milliseconds is required to collect a set of data from the four recorders and then to re-arm them for a possible second acquisition from the same lightning flash. By operating in this mode it is in principle possible to obtain data both on the initiating stepped-leader process and then, in the second acquisition, on a subsequent return stroke all in the same flash.

The B-field information for lightning is obtained by numerically integrating the digitized B-dot data. The baseline drift of the recorder and the inability to accurately determine the value of the drift results in a ramp error. For this reason an integrator with 100 μ s decay time constant has been connected to the B-dot north channel. The use of an integrator in the recording of the derivative signal will allow an accurate determination of the north component of the B field out to beyond 100 μ s. Integrators are not on the B-dot east and D-dot channels because of the limitations in the number of available recorders.

V. SUMMARY

The environmental fields from lightning are generally both slower and weaker (at moderate to large distances) than those from the nuclear EMP. However, the basic technology for measuring transient electromagnetic fields and related electromagnetic parameters is in general applicable to both. There are quantitative differences which can lead to different sizes and sensitivities. The techniques, however, are much the same.

These kinds of electromagnetic sensors can be thought of as being for three rough categories of measurements:

- a. Distant lightning environments (away from arcs and corona).
- b. Environments near (or in) arcs and corona (lightning "source" region).
- c. Lightning response (measurements of electronic system response (internal)).

Categories a and b optimally use the same kinds of techniques as for the nuclear electromagnetic pulse. Category b requires the use of techniques similar to those used in nuclear source regions, but with some relaxation of the requirements because of the absence of nuclear ionizing radiation and compton source currents.

These types of sensors have already been used for lightning related measurements with considerable success. It is anticipated that they will find widespread application in the lightning community.

REFERENCES

In the interest of brevity the following abbreviations are used:

SSN	sensor and simulation notes
IN	interaction notes
MN	measurement notes

These are part of the note series on EMP and related subjects described in "The Compleat Guide to the Notes", INDEX 1-1, February 1973, by Baum. These have played a prominent role in transient/broadband technology. Listings of these can also be found in the IEEE AP-S Newsletter. Copies of these papers can be requested from the author, from the Defense Documentation Center, Cameron Station, Alexandria, VA 22314, or from the Editor, Dr. Carl E. Baum, Air Force Weapons Laboratory (NT), Kirtland AFB, NM 87117. In addition, these notes are available at many universities and companies doing research in EMP and electromagnetic theory. Other report numbers used are

AFWL-TR Air Force Weapons Laboratory Technical
Report (AFWL-TRs are available from Defense
Documentation Center, Alexandria, VA 22314)
AL Albuquerque Division
EG&G Inc.
9733 Coors Road, NW
Albuquerque, NM 87114

- (1) C.E. Baum, E.L. Breen, J.C. Giles, J.P. O'Neill, and G.D. Sower, "Sensors for Electromagnetic Pulse Measurements Both Inside and Away from Nuclear Source Regions", IEEE Trans. Ant. Prop., AP-26, No. 1, January 1978.
- (2) R.E. Partridge, "Invisible' Absolute E-field Probe", SSN 2, February 1964.
- (3) K. Theobald, "On the Properties of Loop Antennas", SSN 4, February 1964.
- (4) C.E. Baum, "Minimizing Transit Time Effects in Sensor Cables", SSN 6, October 1964.
- (5) ___, "Characteristics of the Moebius Strip Loop", SSN 7, December 1964.
- (6) ___, "Maximizing Frequency Response of a B-dot Loop", SSN 8, December 1964.
- (7) C.E. Baum, "Electric Field and Current Density Measurements in Media of Constant Conductivity," SSN 13, January 1965.
- (8) G.L. Fjetland, "Design Considerations for a Twinaxial Cable", SSN 14, March 1965.
- (9) C.E. Baum, "Radiation and Conductivity Constraints on the Design of a Dipole Electric Field Sensor", SSN 15, Feb. 1965.

- (10) L.E. Orsak and A.L. Whitson, "Electric Field Sensor for EMP Simulators", SSN 18, December 1965.
- (11) C.E. Baum, "Combining Voltage or Current Dividers with Sensor Cables", SSN 19, November 1965.
- (12) ___, "A Technique for the Distribution of Signal Inputs to Loops", SSN 23, July 1966.
- (13) ___, "A Technique for Measuring Electric Fields Associated with Internal EMP", SSN 24, August 1966.
- (14) ___, "The Multiple Moebius Strip Loop", SSN 25, August 1966.
- (15) ___, "The Influence of Radiation and Conductivity on B-dot Loop Design", SSN 29, October 1966.
- (16) ___, "The Single-Gap Cylindrical Loop in Nonconducting and Conducting Media", SSN 30, January 1967.
- (17) ___, "Two Types of Vertical Current Density Sensors", SSN 33, February 1967.
- (18) ___, "Parameters for Some Electrically-Small Electromagnetic Sensors", SSN 38, March 1967.
- (19) ___, "Conducting Shields for Electrically-Small Cylindrical Loops", SSN 40, May 1967.
- (20) ___, "The Multi-Gap Cylindrical Loop in Nonconducting Media", SSN 41, May 1967.
- (21) ___, "A Conical-Transmission-Line Gap for a Cylindrical Loop", SSN 42, May 1967.
- (22) ___, "Some Considerations for Electrically-Small Multi-Turn Cylindrical Loops", SSN 43, May 1967.
- (23) ___, "Some Electromagnetic Considerations for a Rocket Platform for Electromagnetic Sensors", SSN 56, June 1968.
- (24) ___, "Some Considerations for Inductive Current Sensors", SSN 59, July 1968.
- (25) ___, "An Equivalent-Charge Method for Defining Geometries of Dipole Antennas", SSN 72, January 1969.
- (26) ___, "Parameters for Electrically-Small Loops and Dipoles Expressed in Terms of Current and Charge Distributions", SSN 74, January 1969.

- (27) ___, "Electrically-Small Cylindrical Loops for Measuring the Magnetic Field Perpendicular to the Cylinder Axis", SSN 78, March 1969.
- (28) ___, "The Circular Parallel-Plate Dipole", SSN 80, March 1969.
- (29) ___, "Some Further Considerations for the Circular Parallel Plate Dipole", SSN 86, June 1969.
- (30) ___, "The Single-Gap Hollow Spherical Dipole in Nonconducting Media", SSN 91, July 1969.
- (31) ___, "The Circular Flush-Plate Dipole in a Conducting Plane and Located in Nonconducting Media", SSN 98, February 1970.
- (32) ___, "Capacitance and Equivalent Area of a Disk in a Circular Aperture", SSN 106, May 1970.
- (33) C.E. Baum, "Two Approaches to the Measurement of Pulsed Electromagnetic Fields Incident on the Surface of the Earth", SSN 109, June 1970.
- (34) R.W. Latham and K.S.H. Lee, "Capacitance and Equivalent Area of a Spherical Dipole Sensor", SSN 113, July 1970.
- (35) C.E. Baum, "Further Considerations for Multi-Turn Cylindrical Loops", SSN 127, March 1971.
- (36) K.S.H. Lee and R.W. Latham, "Inductance and Current Density of a Cylindrical Shell", SSN 130, June 1971.
- (37) F.M. Tesche, "Optimum Spacing of N Loops in a B-dot Sensor", SSN 133, July 1971.
- (38) P.H. Duncan, Jr., "Analysis of the Moebius Loop Magnetic Field Sensor", SSN 183, September 1973.
- (39) K.S.H. Lee, "Electrically-Small Ellipsoidal Antennas, SSN 193, February 1974.
- (40) C.E. Baum, "A Figure of Merit for Transit-Time-Limited-Derivative Electromagnetic Field Sensors", SSN 212, December 1975.
- (41) H. Whiteside and R.W.P. King, "The Loop Antenna as a Probe", IEEE Trans. Antennas Propagat., pp. 291-297, May 1964.
- (42) A.H. Libbey et al., "Development of Hardened Magnetic Field Sensors", AFWL-TR-69-58, Vol. I and II, June 1969.

- (43) R. Morey et al., "Development and Production of Multi-Gap Loop (MGL) Series EMP B-dot Sensors", AFWL-TR-70-153, February 1971.
- (44) J.K. Travers and J.H. Kraemer, "Development and Construction of Electric Field and D-dot Sensors", AFWL-TR-70-154, March 1971.
- (45) W.R. Edgel, "Hollow Spherical Dipole D-dot Sensor (HSD-4) Development", AFWL-TR-75-77, January 1975 (also AL-1147, January 1975).
- (46) S.L. Olsen, "Asymptotic Conical Dipole D-dot Sensor Development", AFWL-TR-75-263, January 1976 (also AL-1185, September 1975).
- (47) T. Summers, "I-dot Sensor Design and Fabrication", AL-516, November 1970.
- (48) W. Edgel, "I-dot Sensor Design and Fabrication Phase II", AL-678, December 1971.
- (49) J. Harrison, "Fabrication and Testing of a Multi-Turn B-dot Sensor", AL-735, February 1972.
- (50) W. Edgel, "I-dot Sensor Development", AL-921, June 1973.
- (51) ___, "B-dot Sensor Development", AL-952, July 1973.
- (52) S. Olsen, "Flush Plate Dipole D-dot Sensor Development", AL-1100, August 1974.
- (53) W. Edgel, "MGL-6 B-dot Sensor Development", AL-1101, August 1974.
- (54) ___, "Radiation Hardened I-dot Sensor (OMM-1A) for Use in Baum Antenna", AL-1102, August 1974.
- (55) ___, "MGL-S7A B-dot Sensor Development", AL-1104, Aug. 1974.
- (56) ___, "MTL-2 B-dot Sensor Development", AL-1105, August 1974.
- (57) ___, "A Small Radiation Hardened B-dot Sensor (CML-4A)", AL-1106, August 1974.
- (58) S. Olsen, "Sensor MGL-8B Sensor DW", AL-1186, September 1975.
- (59) ___, "MGL-S8 B-dot Sensor Development", AL-1197, Sept. 1975.

- (60) G.D. Sower et al., "Cylindrical Moebius Loop Radiation Hardened B-dot Sensor (CML-6A(R)) Development", AL-1224, June 1976.
- (61) ___, et al., "Cylindrical Moebius Loop Radiation Hardened B-dot Sensor (CML-X3A(R) and CML-X5A(R)) Development", AL-1229, June 1976.
- (62) ___, "Outside Moebius Mutual Radiation Hardened I-dot Sensor (OMM-2A) Development", AL-1232, June 1976.
- (63) ___, "Parallel Mesh Dipole Radiation Hardened E-field Sensors (PMD-1C) Development", AL-1233, June 1976.
- (64) B.C. Tupper et al., "EMP Instrumentation Development", Final Report, SRI Project 7990, Stanford Research Institute, Menlo Park, CA, June 1972.
- (65) C.E. Baum, Ed., "Electromagnetic Pulse Sensor Handbook," EMP Measurement 1-1, June 1971 (original issue).
- (66) ___, "Electromagnetic Pulse Instrumentation Handbook", EMP Measurement 2-1, June 1971 (original issue).

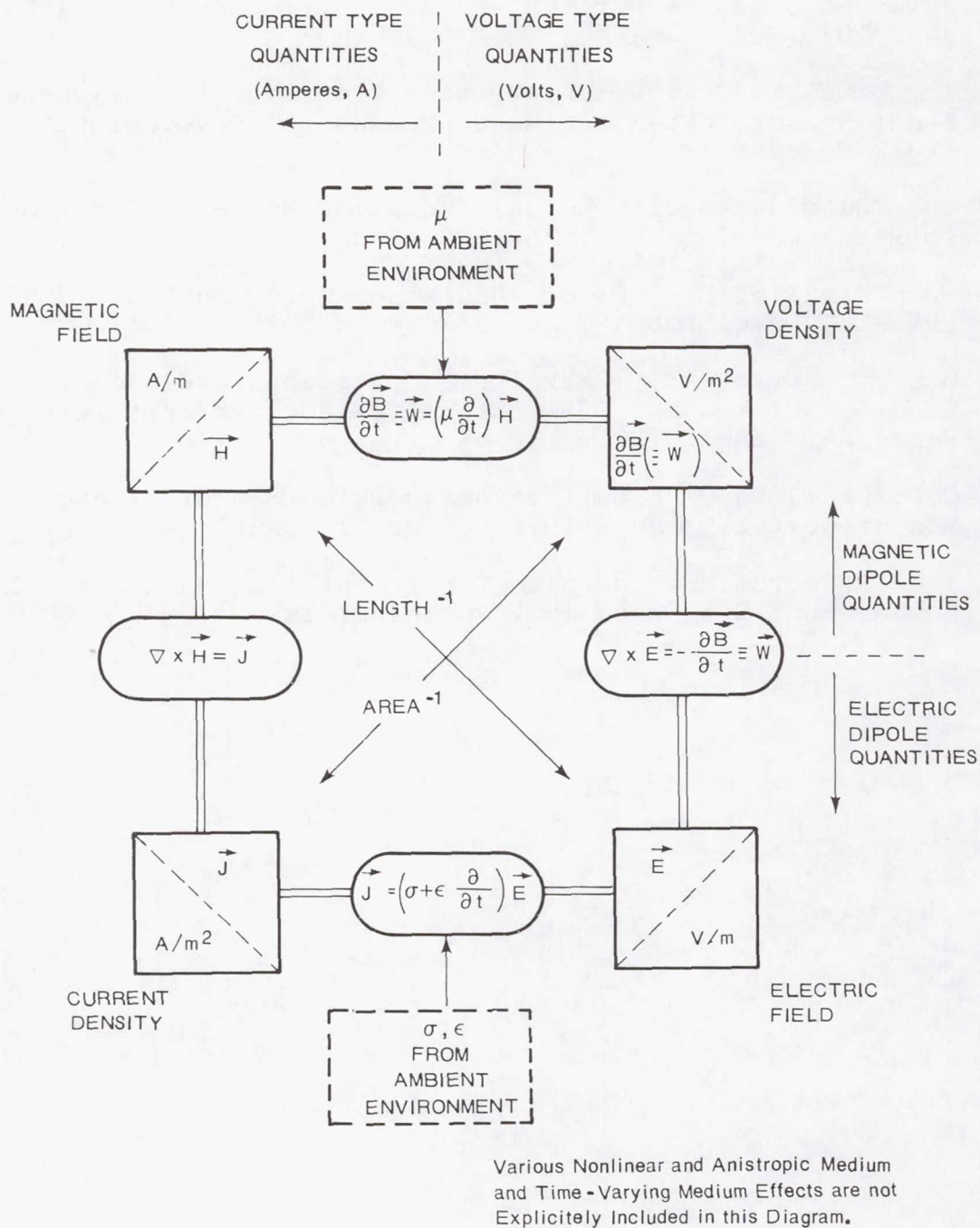
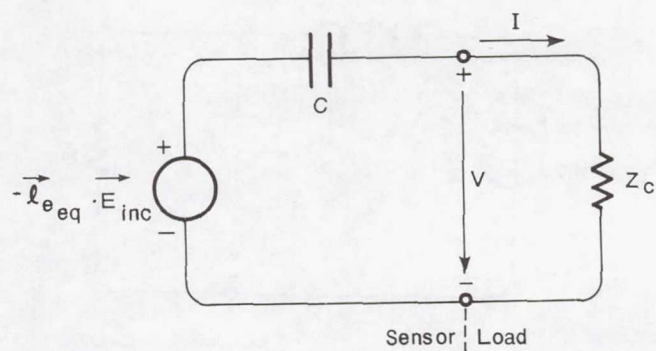
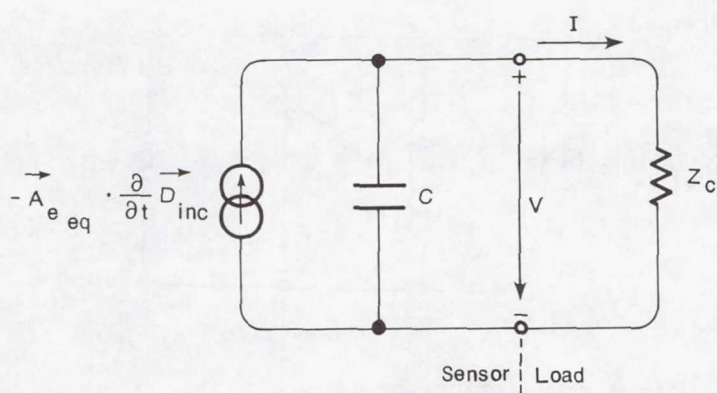


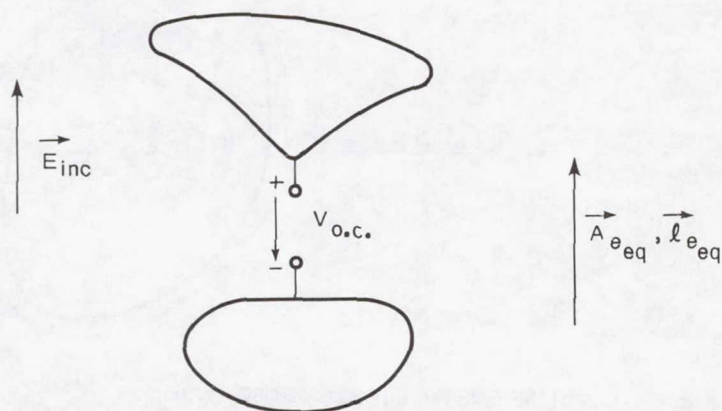
Figure 1.1. Diagram of Basic Electromagnetic Quantities for Source Region EMP Environment and Interaction



a) THEVENIN EQUIVALENT CIRCUIT

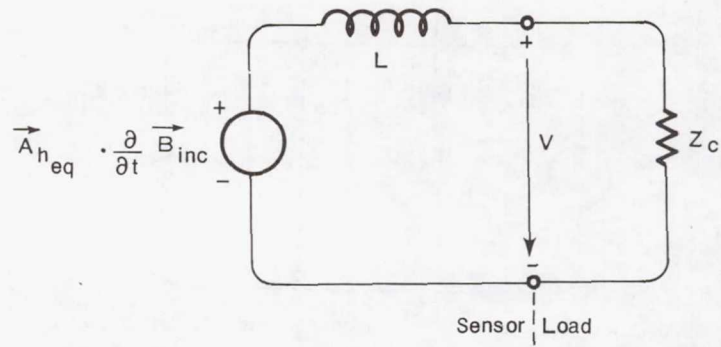


b) NORTON EQUIVALENT CIRCUIT

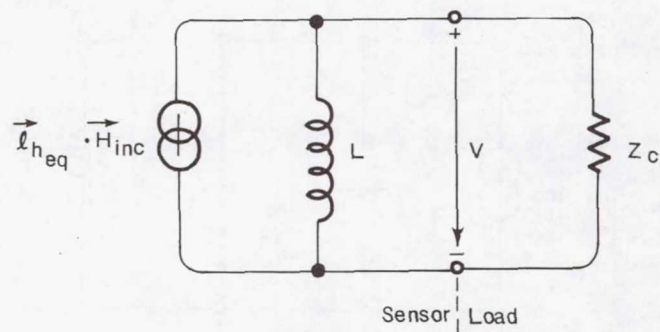


c) ELECTRIC DIPOLE SENSOR

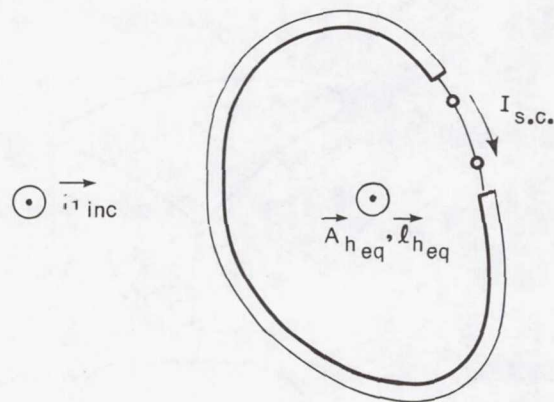
Figure 1.2. Electrically Small Electric Dipole Sensor in Free Space. (a) Thevenin Equivalent Circuit. (b) Norton Equivalent Circuit. (c) Electric Dipole Sensor.



a) THEVENIN EQUIVALENT CIRCUIT

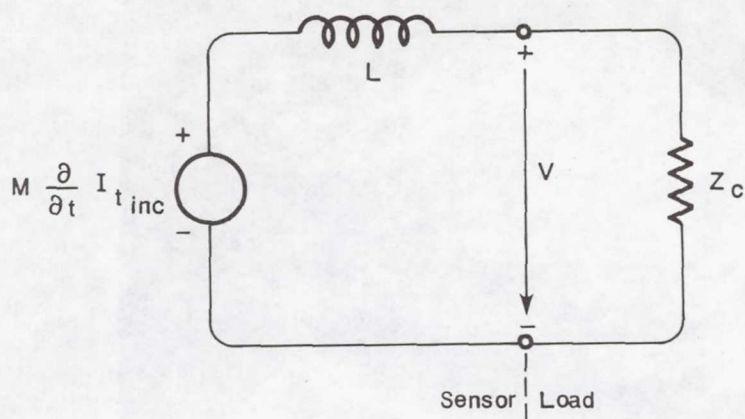


b) NORTON EQUIVALENT CIRCUIT



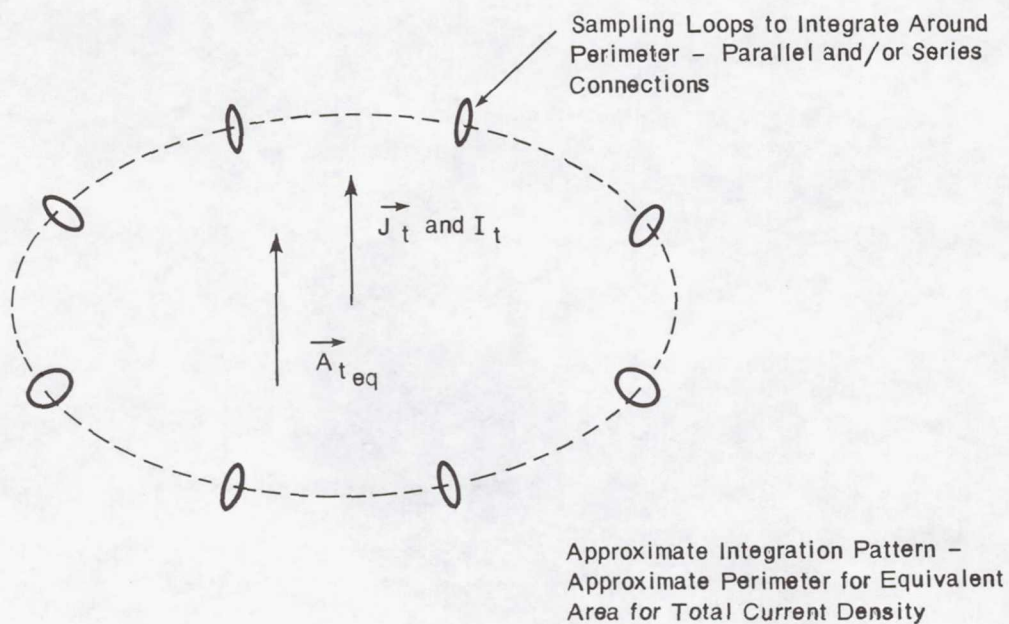
c) MAGNETIC DIPOLE SENSOR (Loop)

Figure 1.3. Electrically Small Magnetic Dipole Sensor in Free Space. (a) Thevenin Equivalent Circuit. (b) Norton Equivalent Circuit. (c) Magnetic Dipole Sensor (Loop).



$$I_{t_{inc}} = \vec{A}_{t_{eq}} \cdot \vec{J}_{t_{inc}} \quad \text{For Measurement of Distributed Current Density}$$

a) NORTON EQUIVALENT CIRCUIT



b) INDUCTIVE CURRENT SENSOR (Multiple Loops)

Figure 1.4. Electrically Small Inductive Current Sensor in Free Space. (a) Norton Equivalent Circuit. (b) Inductive Current Sensor (Multiple Loops)

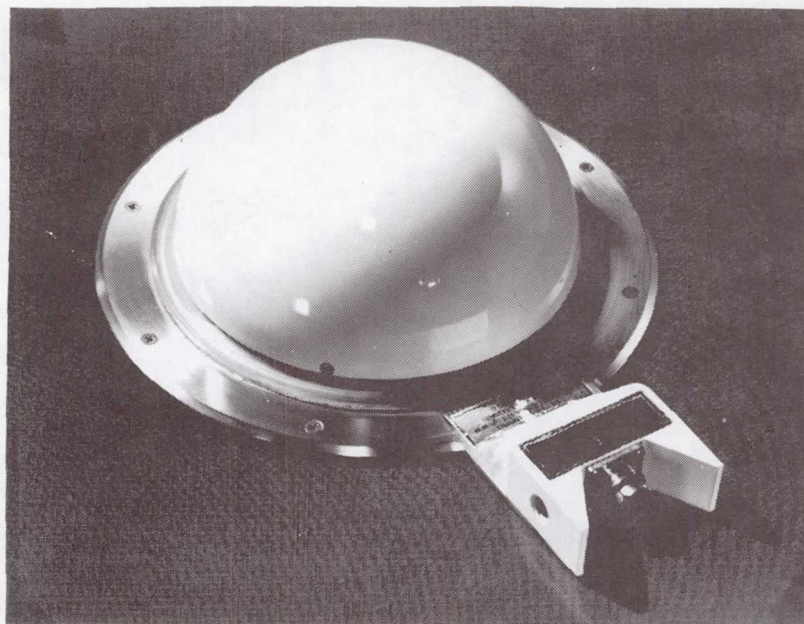


Figure 2.1. Photo of HSD-S1A(R)

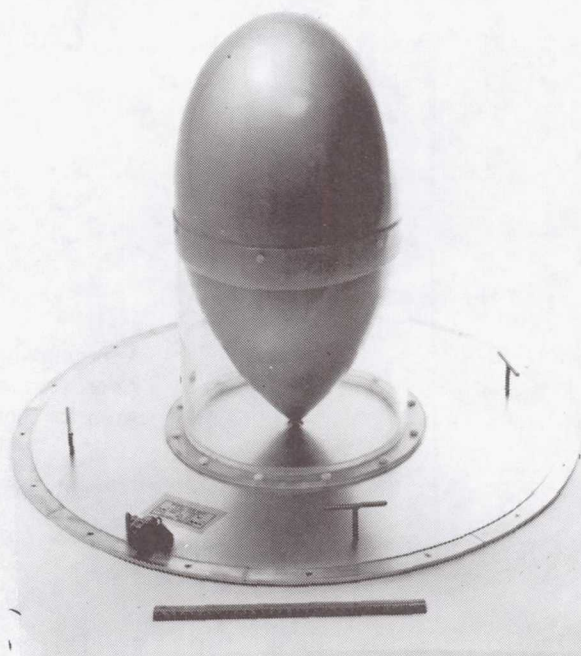


Figure 2.2. ACD-5A(A) D-dot Sensor

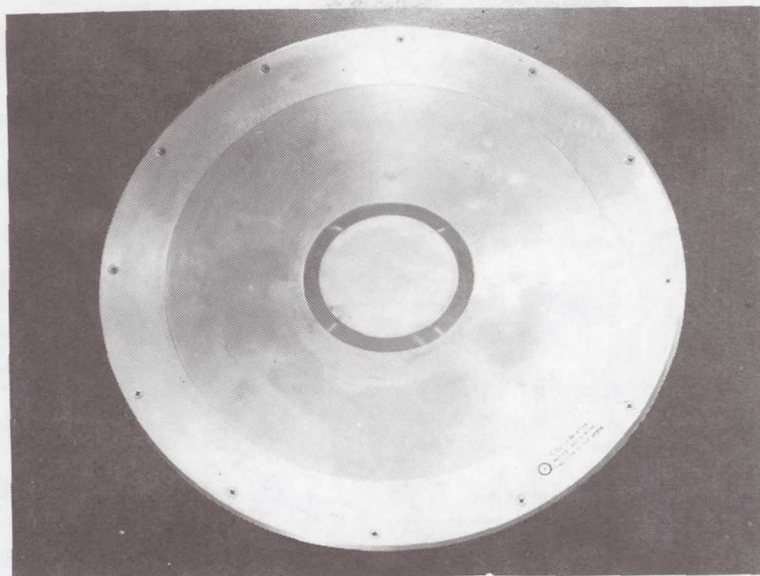


Figure 2.3. Flush Plate Dipole D-dot Sensor

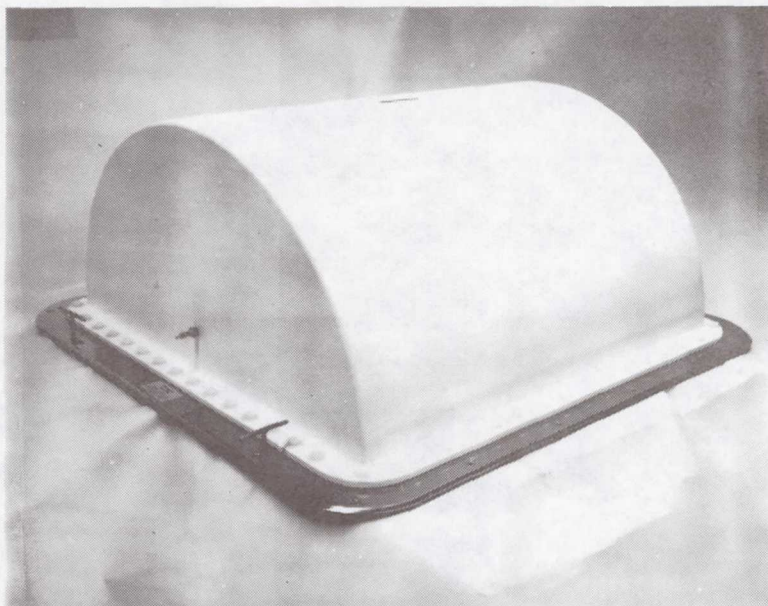


Figure 2.4. Multigap Loop (MGL) B-dot Sensors

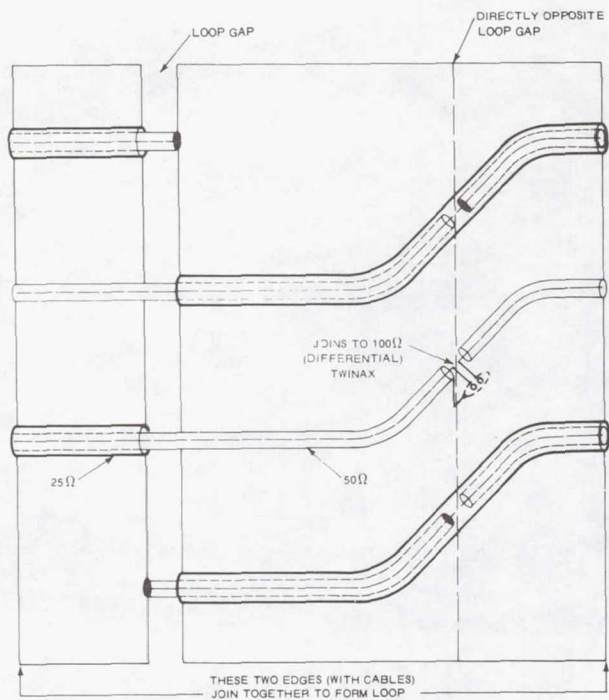


Figure 2.5. OML-1A(A) B-dot Loop Sensor (Expanded Diagram)

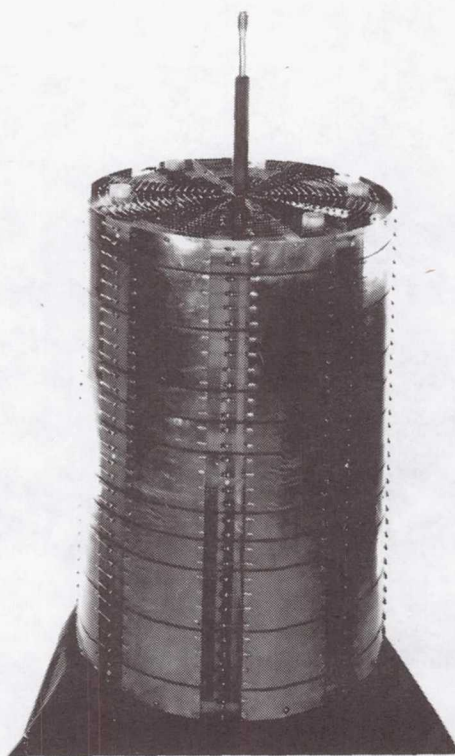


Figure 2.6. MTL-1 Sensor (Coil with Axial Shorts and Conducting Shield in Place)

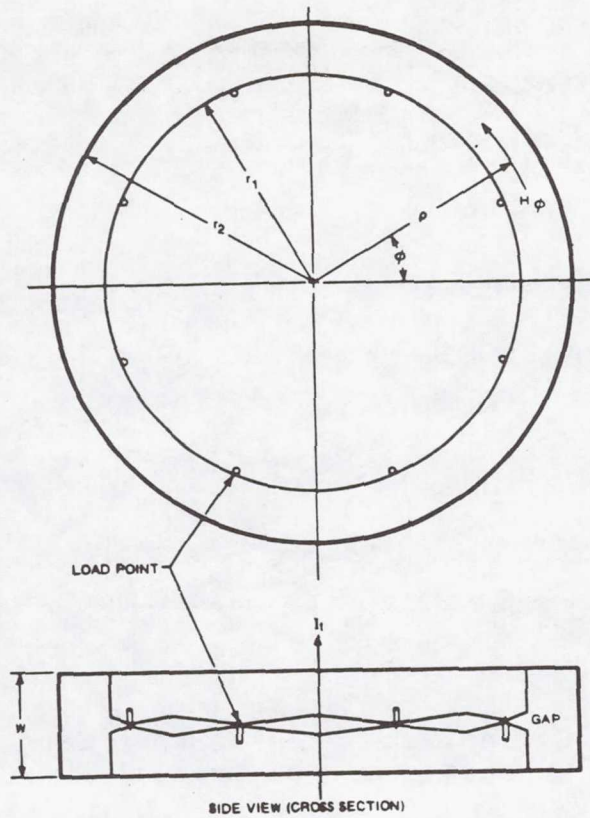


Figure 2.7. Typical CPM Sensor Geometry

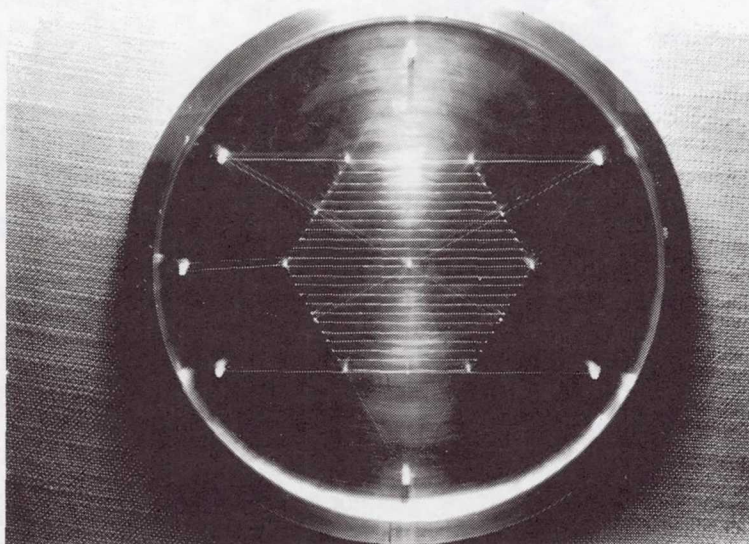


Figure 3.1. Parallel Mesh Dipole (PMD-1A) E-Field Sensor

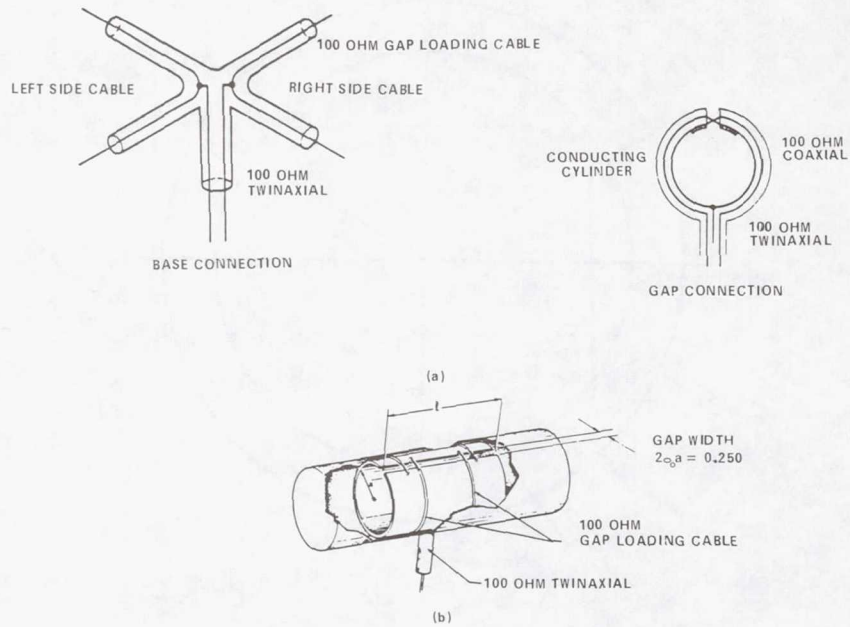


Figure 3.2. Cylindrical Moebius Loop Sensor CML-2B(R)
 (a) Electrical Connections; (b) Typical Loop Configuration

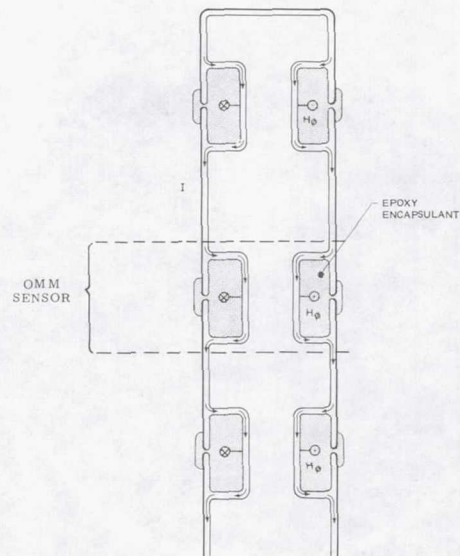


Figure 3.3. OMM-1A Sensor Details

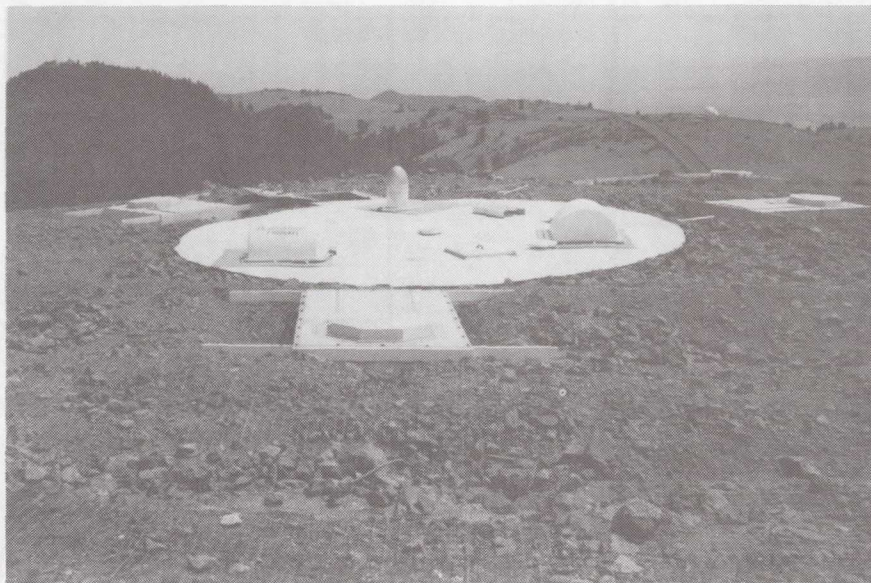


Figure 4.1. Lightning Electromagnetics Measurement Site

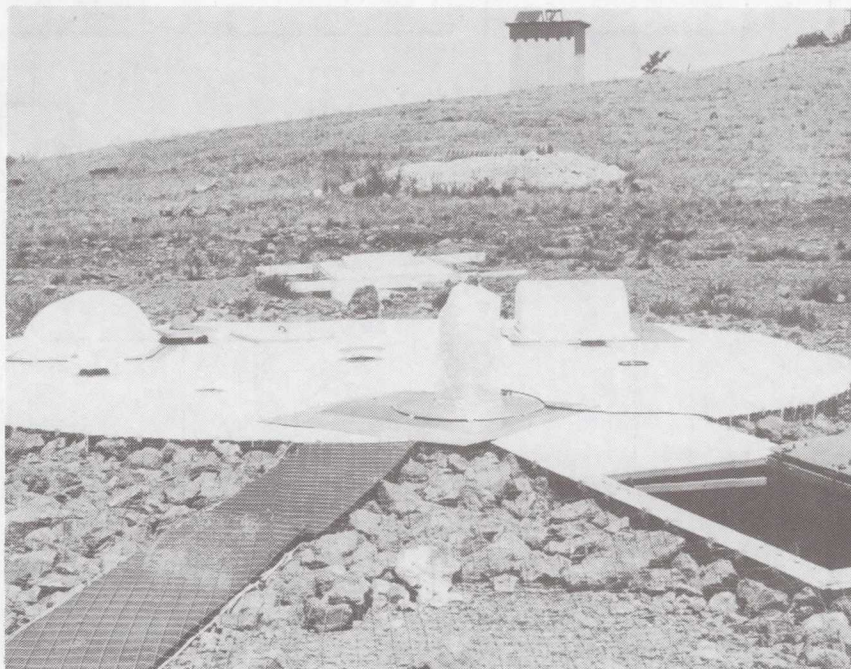


Figure 4.2. Instrumentation Room and Field Sensors

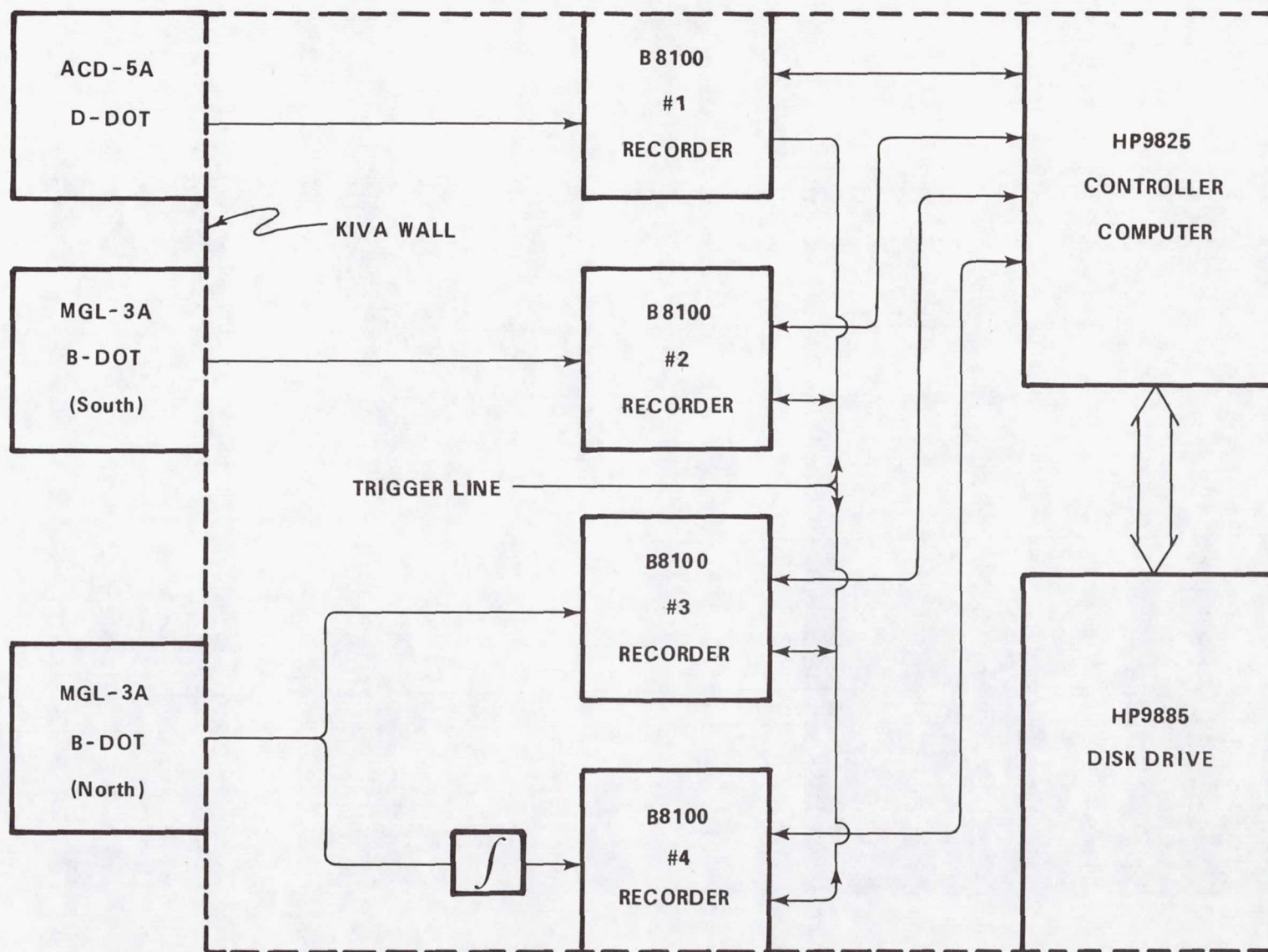


Figure 4.3. Block Diagram of Lightning Electromagnetics Measurement System

EXPANDED INTERLEAVED SOLID-STATE MEMORY FOR A WIDE BANDWIDTH TRANSIENT WAVEFORM RECORDER

Robert M. Thomas, Jr.
NASA-Langley Research Center

INTRODUCTION

This paper describes an interleaved, solid-state expanded memory for a 100 MHz bandwidth waveform recorder. The memory development resulted in a significant increase in the storage capacity of a commercially available recorder. The motivation for the memory expansion of the waveform recorder, which is used to support in-flight measurement of the electromagnetic characteristics of lightning discharges, was the need for a significantly longer data window than that provided by the commercially available unit. The expanded recorder provides a data window that is 128 times longer than the commercial unit, while maintaining the same time resolution, by increasing the storage capacity from 1024 to 131 072 data samples. The expanded unit operates at sample periods as small as 10 ns. Sampling once every 10 ns, the commercial unit records for about 10 μ s before the memory is filled, whereas, the expanded unit records for about 1300 μ s. A photo of the expanded waveform recorder is shown in figure 1.

The selection of the electronic waveform recorder to record snapshots of the electromagnetic waveforms associated with lightning discharges was due to two advantages over storage oscillosopes. The storage oscilloscope limitations concern its time resolution and the characteristics of its triggering process. The time resolution limitation is a window width vs. window precision trade off. In order to get fine time resolution, the display window is short, whereas, if the window is expanded, the resolution is decreased, and hence the frequency response is decreased. For example, if the oscilloscope provides 500 elements horizontally and each element represents 10 ns, then a window of 5 μ s results. If the window is expanded to 500 μ s, then the resolution reduces to 1 μ s per element. The expanded memory electronic waveform recorder, on the other hand, has the equivalent of 131 072 time elements and, hence, can provide a time window of 1.3 ms at a 10 ns resolution. The triggering process of the oscilloscope requires the detection of some part of the waveform before it can be captured, which prevents the capture of the signal prior to the trigger detection. The electronic recorder has a provision that permits the portion of the waveform prior to the trigger event to be recorded.

RECORDER OPERATION

The waveform recorder is a DC to 100 MHz bandwidth instrument which converts an analog input signal to a digital representation and stores the result in an interleaved solid-state memory. The instrument utilizes a high-speed 6-bit resolution analog to digital converter (ADC) to transform the analog input signal to a digital representation. The recorder is operated like an oscilloscope in that the portion of the input signal that is retained is determined by the trigger criteria selected on its front panel controls. The recorder has two record modes, delay trigger and pretrigger, and has provisions for delaying the effect of the trigger, trigger delay. Once information is stored in the instrument, it may be read out in one of three ways: to an oscilloscope, to an x-y recorder, or to an instrument that accepts digital data.

The delayed trigger record mode of operation is similar to that of an oscilloscope with the delayed sweep feature. When the trigger criteria, such as the slope and amplitude, which are preset on the front panel controls are satisfied, the instrument begins storing the digital representation of the input in the memory. When the memory is filled, the recording stops. In the pretrigger mode of operation, however, the instrument stores the input signal representation continuously in an endless-loop fashion until the trigger occurs, at which time the recording stops. By endless-loop is meant that once the memory has been filled, new data is stored by overwriting the oldest stored information. Figure 2 illustrates the difference between delayed trigger and pretrigger for the case of zero trigger delay.

The trigger delay feature allows the user to select the portion of the input signal that is captured relative to the trigger event. Front panel switches allow selection of the number of sample time delays to occur between the detection of the trigger event and the resulting action on the information recorded. For example, if the instrument is sampling at 10 ns per sample and the delay is set to 1000 units, the trigger action is delayed 10 000 ns. In the delayed trigger record mode of operation, this feature is similar to the delayed sweep function of an oscilloscope; namely, the recorded waveform can be delayed in time relative to the trigger. In the pretrigger record mode of operation, the recording is not stopped with the detection of the trigger but continues for the amount of time set in the trigger delay as shown in figure 3. Thus, one may obtain a snapshot of the input waveform that includes events occurring prior to the trigger - a feature that standard oscilloscopic techniques do not provide.

As stated previously, a stored snapshot can be retrieved in one of three ways: as analog outputs suitable for either an x-y plotter or an oscilloscope, or as a digital output suitable for digital instrumentation. The plotter and oscilloscope outputs are produced by sequentially reading the digital data stored in the memory and presenting it to a digital to analog converter (DAC) within the unit. The resulting analog signal and an internally generated analog time base ramp are used to drive the oscilloscope display or plotter. The data is read out at a 1 MHz rate for the oscilloscope and at a slower rate for the pen-type x-y plotter (this latter rate is selectable.) The digital

output is accomplished by the instrument receiving a data request signal from an external source and responding by placing the next data word on the output bus.

The recorder is used in the pretrigger mode for lightning measurements. The recorded snapshot of each lightning event is recorded on an airborne instrumentation magnetic tape recorder so that subsequent events may be captured. The snapshot is encoded into a serial pulse code modulated (PCM) signal prior to recording on magnetic tape. Once the data is transferred to the tape, the digital waveform recorder is placed back in the "endless-loop" record state awaiting the next trigger event.

SYSTEM DESCRIPTION

A description of the general functions performed by portions of the waveform recorder provides background for discussion of the memory expansion. The electronics can be partitioned into the following functional sections: input signal conditioner, ADC, memory, output circuitry, and control and timing as depicted in figure 4. The input signal is received and conditioned based on the criteria provided by the front panel switch settings, such as input signal amplitude range, AC/DC coupling, and signal offset. This conditioned signal is presented to the ADC section which contains a parallel ADC with 6-bit resolution. The signal is quantized by a set of comparators operating in parallel. The outputs of the comparators are converted into a 6-bit Gray code representation of the input signal and then alternately stored into one of two parallel registers under control of the sample rate clock. This design achieves the maximum sample rate of 500 MHz with a 250 MHz sampling clock by using the alternate phases of the clock to steer the digitized data into the two registers. The outputs of the two registers are routed to the memory section, where they are stored in integrated circuit (IC) random access memories (RAM's). The memory section, which will be described more fully later, also contains memory addressing circuitry which manages the sequential storage and retrieval of the digitized data. During the output phase of operation of the waveform recorder, the data is read out of the RAM's and routed to the output section. The output section includes two DAC's which are used to generate output signals for either oscilloscope display or x-y plots of the data. One DAC is used to convert the stored data back to an analog form while the other is used to generate a ramp signal to use as a horizontal sweep for the display devices. The output section also has provision to present the data in digital form. The timing and control section includes circuitry for generating the timing and control signals required by the other parts of the waveform recorder such as circuitry for the detection and delay of the trigger signal; a clock generator from which the sampling clock, the read clock, the output clock, and the timing signals needed by various parts of the system are formed; and circuitry to manage the proper sequencing of the data being output.

Memory Section

The memory section will now be described in more detail. The memory section circuitry may be considered as consisting of four functional areas as depicted in figure 5. These areas are control, address, storage (RAM's), and output. The control circuitry includes the read or write enables for the RAM's, the routing of the read or write clocks, the enabling of the output circuitry during the read state, and other control functions required by the memory section. The address circuitry includes counters that sequentially generate addresses for the RAM's. The storage circuitry includes the RAM IC's, and the output circuitry includes a Gray code to two's complement binary converter and an output buffer.

The memory section is organized as a 32-way interleaved memory in the expanded recorder so that the recorder can sample the input at a faster rate than the RAM IC's operate. Figure 6 illustrates the interleaving by indicating the data paths from the ADC. The nodes (small rectangles) in figure 6 represent 6-bit parallel registers and the lines represent 6-bit wide data paths between registers. The interleaving is accomplished in three stages. The first stage of interleaving (level 1) is performed in the ADC section by the two registers that alternately store the 6-bit Gray code produced by the comparators. Thus, at the 2 ns sample period, each of these registers has a cycle time between new samples of 4 ns. The outputs of these two registers are each routed to four registers as shown to perform the second stage of interleaving (level 2). These registers have a cycle time between new samples of 16 ns. Finally, each of the second-stage register outputs are routed to four more registers to perform the third stage of the interleaving (level 3) providing a 64 ns cycle time between new samples. Thus, new data is stored every 2 ns, but each of the third-stage registers and hence the RAM columns that receive their outputs, have a 64 ns period in which to handle the data routed to them. Figure 7 is a timing diagram which depicts the timing relationship of the data routed to column 0 through the three stages of registers. The bars represent the time period when the data for column 0 is in the respective register while the triangle represents the time when the data is written into the RAM's.

The expanded memory uses a 4096 by 1-bit RAM IC. Each column is composed of six of these IC's providing storage capacity for 4096 data samples. Thus, the 131 072 word memory is achieved using a total of 192 RAM IC's. Before the expansion, the recorder utilized eight columns of six IC's per column or a total of 48 IC's for a total storage of 1024 words. The memory interleaving permits the utilization of a RAM with a 55 ns write cycle period to be used in a memory which is being written into every 2 ns, since each column has a 64 ns period in which to store the data sample routed to it.

The addressing function is accomplished using two separate counters. The first counter (the column counter) is used to control the routing of the data to the appropriate RAM column in sequence while the second counter generates a 12-bit binary address which is shared by all columns. The column counter is a 16-stage twisted ring or Johnson counter which produces 32 distinct, 50-percent duty cycle, evenly space states. This type of counter is used to minimize time delays of the address signals. The 12-bit counter is a 12-stage binary counter,

which advances by an increment of one each time the column counter goes through a complete cycle. For each address value produced by the 12-bit counter, data is sequentially routed to each of the columns by the column counter. In this manner, the writing of data into each of the columns is overlapped or interleaved during the write mode of operation. The same two counters are used to generate the RAM addresses during the read mode of operation. The required output data rate (2 MHz per data point maximum) is significantly slower than the input data rate and hence the read out of data is not interleaved. The data appears as a single merged output train.

Timing and Control Section

Two functions within the timing and control section, the delay counter and the memory tracking counter, will now be described, since they both required modification to be compatible with the expanded memory. The delay counter is used during the write mode of operation to provide delay between the time that a trigger signal is detected and the time when action is taken appropriate to the selected record mode - either delayed trigger or pretrigger. The expanded memory waveform recorder is only used in the pretrigger mode, so the counter delays the time that the write operation ceases. When a trigger signal is detected, the delay counter begins counting the sample clock. The output of the delay counter is compared to the amount of delay set into the front panel delay switches. When the two values match, a signal is generated to stop the write clock and hence to stop the write operation. The capacity of the delay counter was increased by a factor of 100 (from 9990 to 999 000 maximum).

The read operation begins upon completion of the write operation. The memory tracking counter is used to keep track of the amount of data that has been read. Since the waveform recorder does not anticipate cessation of the write operation, the address counters in the memory section are never preset to any particular value. When the write operation does cease, the next memory address is the oldest or first value stored, and the current address is the last item stored. When the read operation begins, the memory address is advanced by one, the memory tracking counter is cleared, and the oldest data item is read out. As each successive data item is read, the memory tracking counter is advanced by one in synchronism with the address generator and when all the data in the memory has been read out, the memory tracking counter will roll over. This roll over is detected and used to signify that the full content of memory has been read. The count capacity of this counter must be the same as the memory capacity in order to detect when the memory has been completely read, so the counter capacity was increased by a factor of 128 to be compatible.

EXPANSION DETAILS

The principal changes to the waveform recorder to achieve the desired expanded capacity were the increase of the memory storage capacity, the conversion of the power supply to 400 Hz at 115 VAC, and the increase in the number of sample times that the trigger may be delayed. The changes were accomplished by:

installing two small printed circuit (PC) cards on two of the existing PC boards in the commercial unit, replacing the existing memory PC board with an interface PC board and adding four wire-wrap boards mounted in a separate chassis, replacing the 60 Hz power supply with a 400 Hz one, and by replacing the 60 Hz fans with 400 Hz ones. The expanded waveform recorder has a memory capacity of 131 072 (2^{17}) 6-bit words instead of 1024, trigger delay selection of from 0 to 999 000 sample times instead of 9990 and can operate in an aircraft environment with 400 Hz power.

The memory capacity increase was accomplished by extending the architecture of the commercial units memory while employing similar concepts. The 4096 by 1-bit HMOS (a high performance metal oxide semiconductor technology) RAM IC was selected over the 128 by 1-bit emitter coupled logic (ECL) RAM IC of the commercial unit because of the combination of storage capacity and write cycle period. The addressing scheme was extended from eight columns to 32 and the register and gating logic was adapted or modified as required by the expanded architecture. Where the commercial unit used solely ECL logic on the memory PC board, the expanded unit utilizes a combination of ECL, transistor-transistor logic (TTL), and HMOS logic. An interface PC board was built which is inserted into the slot occupied by the original memory PC board. The interface board serves the function of connecting the unmodified unit to the expanded memory and it contains the column counter and some of the control gating. In particular, the functions which are the most sensitive to the propagation delays of their signals were placed on this board in order to minimize these delays. The interface PC board has two layers of conductors and it utilizes the stitch-weld technique for interconnecting signals. This construction allows for large ground planes on both sides of the PC board in spite of the large number of interconnections required.

The remainder of the memory is distributed among four wire-wrap frames, which are installed in a separate chassis. Each of these boards contains the circuitry required for eight of the memory columns. In addition, the 12-bit address counter and the eight level one data registers are contained on these boards. Each wire-wrap frame consists of two sections, a TTL section and an ECL section. The TTL section is a two-layer PC board where each layer contains one of the voltage planes associated with TTL circuitry (0 volts and +5 volts). All the HMOS and TTL IC's are inserted on this board. The ECL section is further subdivided into two parts. One part is for ECL IC's while the other part is for ECL to TTL level translator IC's, which make the signal voltages of the two types of logic compatible. The ECL part has three layers (-5.2, -2.0, and 0 volts) and the translator part has four layers (-5.2, -2.0, 0, and +5 volts). The purpose of the multilayers is to control the impedance between the voltage planes and the signal leads minimizing signal propagation delays and reducing reflections. The wire-wrap boards used have provisions for single inline package (SIP) resistor networks so that the termination resistors required by the ECL IC's can be easily accommodated. All the IC's are interconnected using the wire-wrap technique. The four wire-wrap frames are housed in a chassis which is mounted on top of the original waveform recorder. Figure 8 is a photo showing the wire-wrap circuit boards.

The two piggyback PC cards were required for the memory storage capacity increase. One card extends the range of the memory tracking counter from 1024 (2^{10}) to 131 072 (2^{17}). This was accomplished by removing one of the IC's of the original counter and inserting the piggyback card in its place. The other piggyback card was required to extend the range of the delay trigger counter from 9990 to 999 000. This second modification was accomplished in a similar manner in which the function on the piggyback card was inserted in place of an IC.

The power supply changes were required to accommodate the increased load of the additional circuits and the use of aircraft 400 Hz 115 VAC power. The expanded waveform recorder requires about 300 watts of power and weighs about 32 kilograms (not including the power supply, which weighs about 46 kilograms).

RESULTS AND CONCLUDING REMARKS

The original goal of an expanded recorder operating at a 2 ns sample period was not achieved, however, the unit does operate properly at 10 ns. The unit operates at a 5 ns period, but the stored data has scattered errors. At the 2 ns period, the sampling clock is loaded down so much when it reaches the column counter on the interface PC board that the counter does not reliably advance. Hence, the synchronization required between the data coming from the ADC and the RAM's is lost. Further refinements in the IC layout, signal paths, and clock buffering will allow the proper operation of the column counter and further refinements in signal paths and PC layout will eliminate the scattered errors observed while operating at the 5 ns period. Although the stitch-weld PC board system allows the maintenance of ground planes over most of the surface of both sides of the PC board, a multilayer board should be used. Also, a multilayer PC board should be used in place of the four wire-wrap frames. Finally, if ECL 4096 x 1-bit RAM IC's with a 30 ns write cycle time are used instead of the HMOS RAM's, the necessity for translating the signals from ECL to TTL levels would be reduced, the number of IC's used in the memory section would decrease from about 500 to 400, the gating functions would be simplified, the signal path lengths would be reduced, the PC board area would decrease, and the power requirements would decrease. (ECL RAM's of this type were not available when this project was begun.) On the positive side, a usable recorder with a 6-bit amplitude resolution and a 10 ns time resolution that can record a 1300 μ s event has been produced, which is an improvement over previously available recorders.

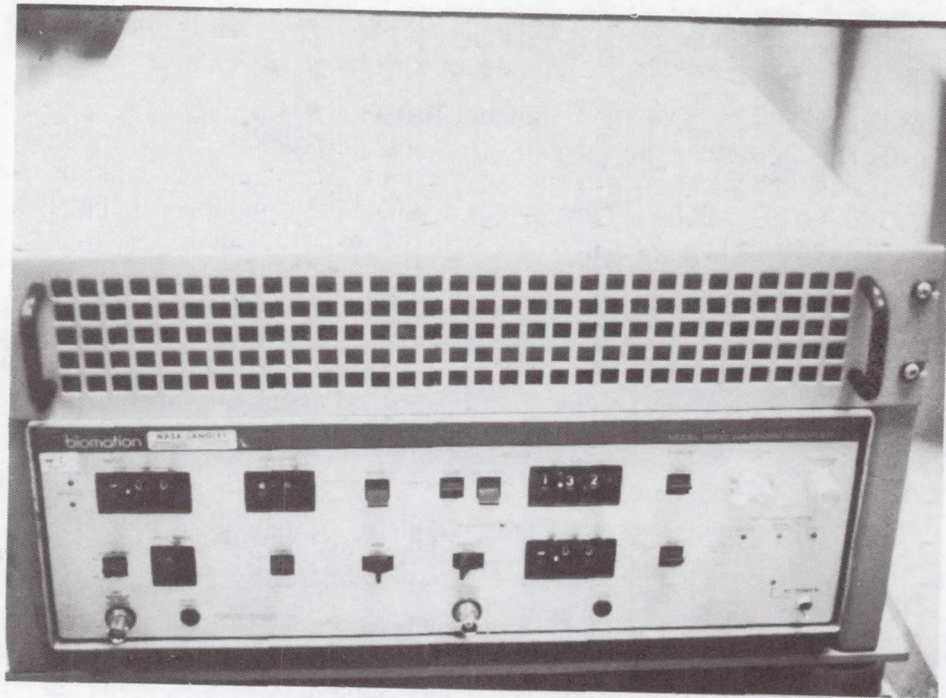


Figure 1.- Expanded waveform recorder.

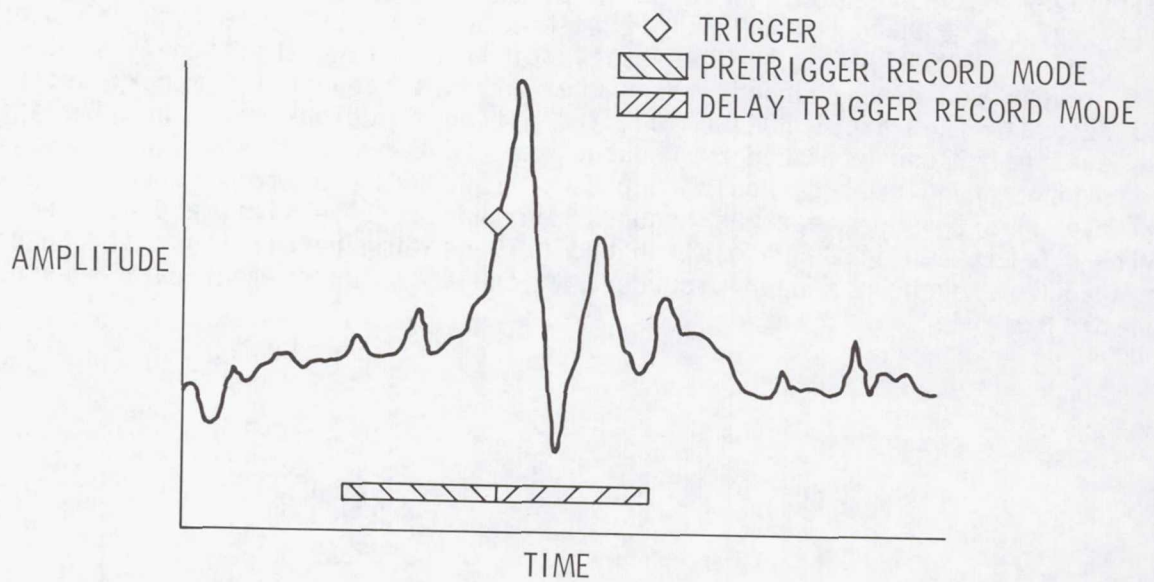


Figure 2.- Pretrigger and delay trigger records.

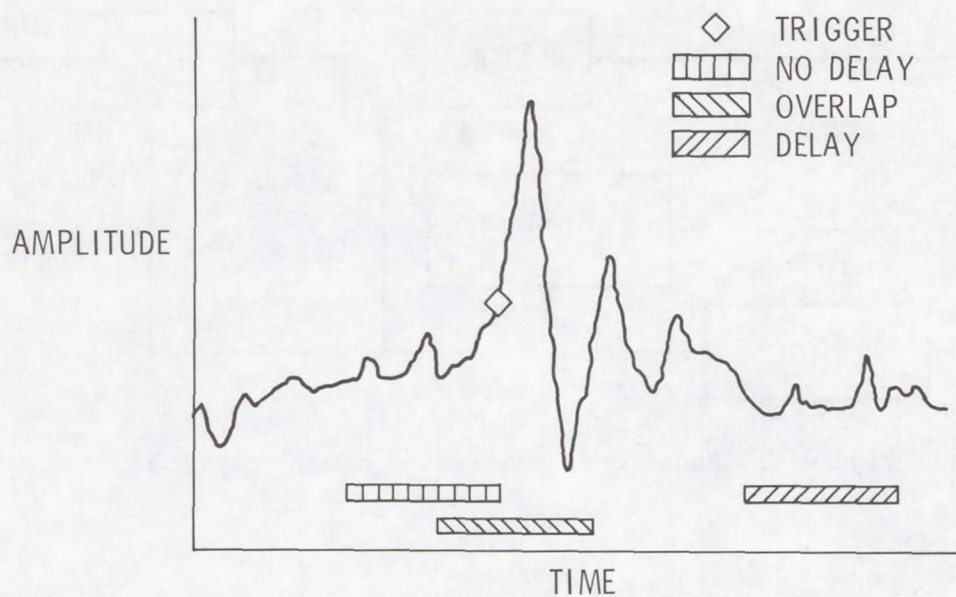


Figure 3.- Pretrigger records using trigger delay.

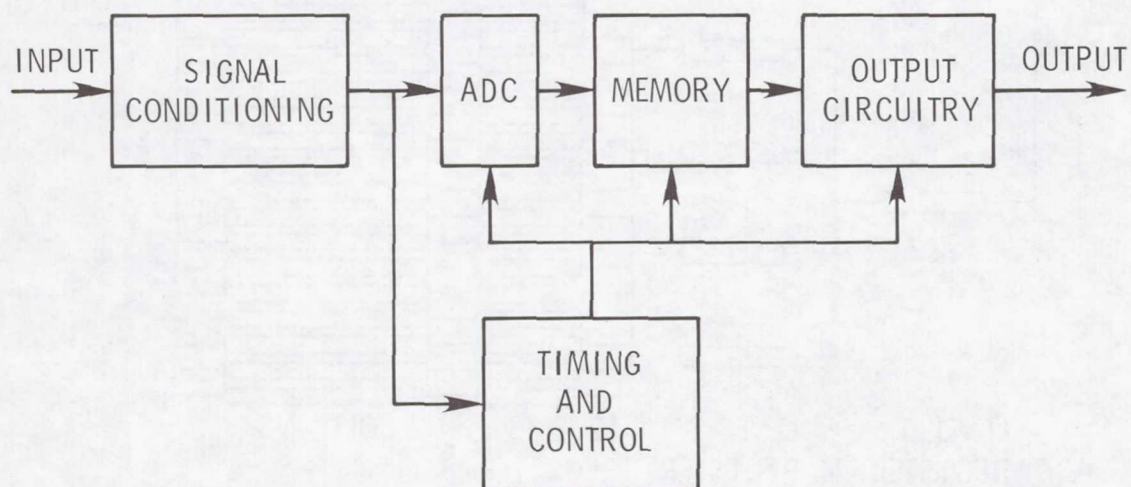


Figure 4.- Functional diagram of waveform recorder.

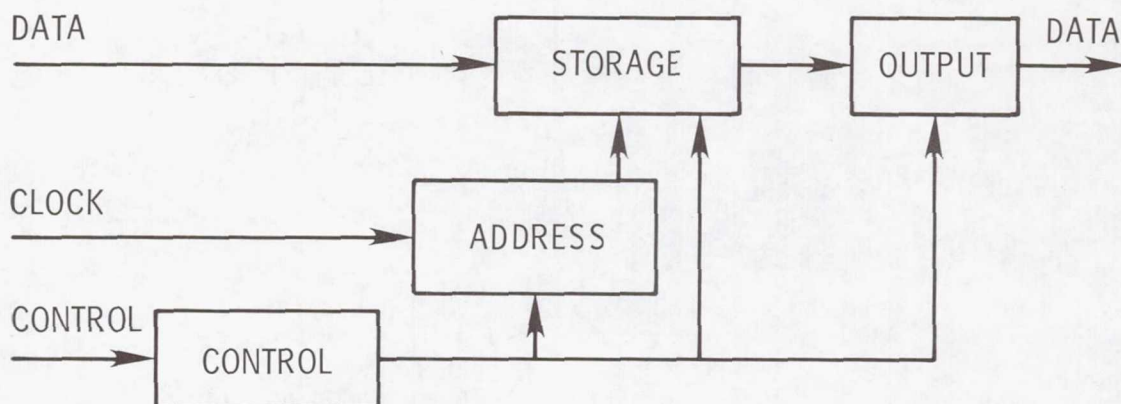


Figure 5.- Functional diagram of memory section.

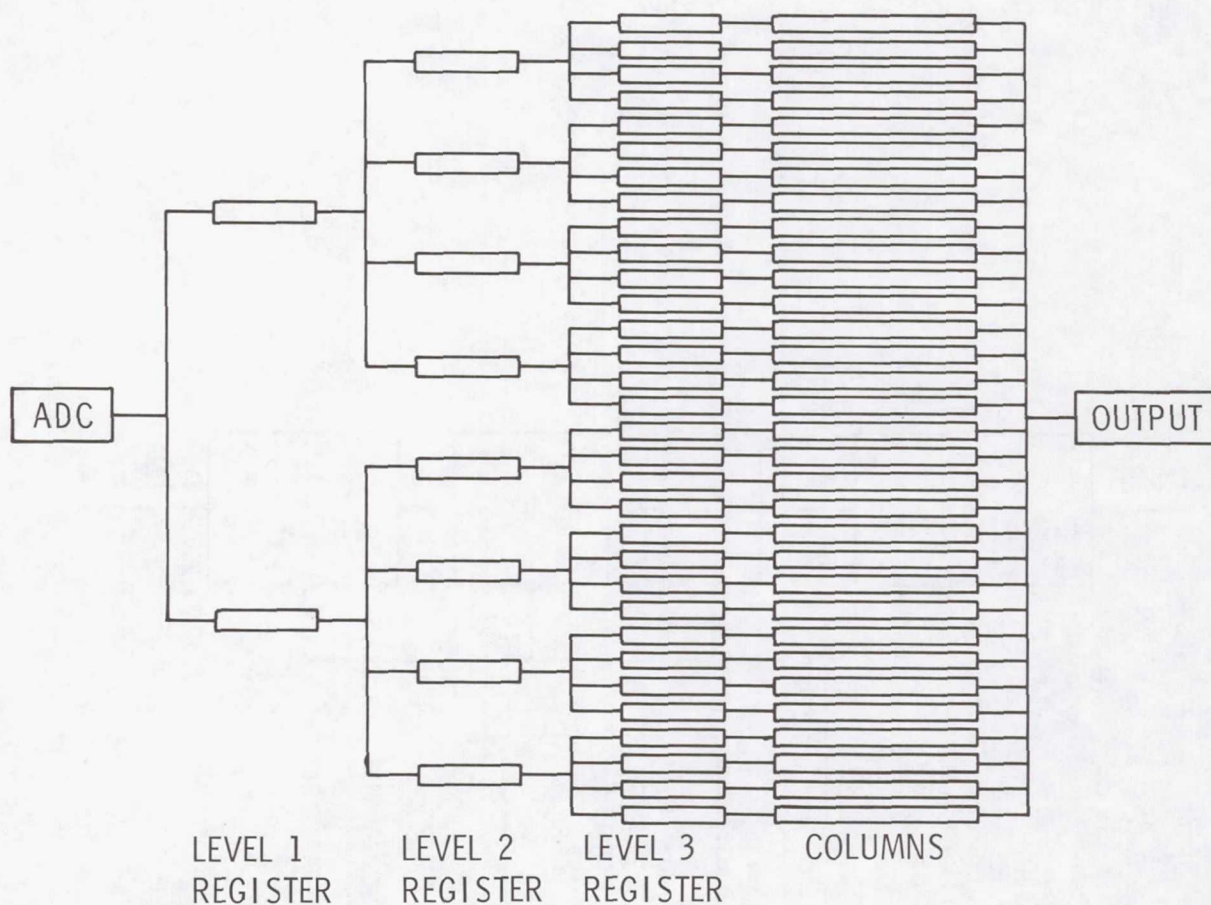


Figure 6.- 32-way interleaved memory.

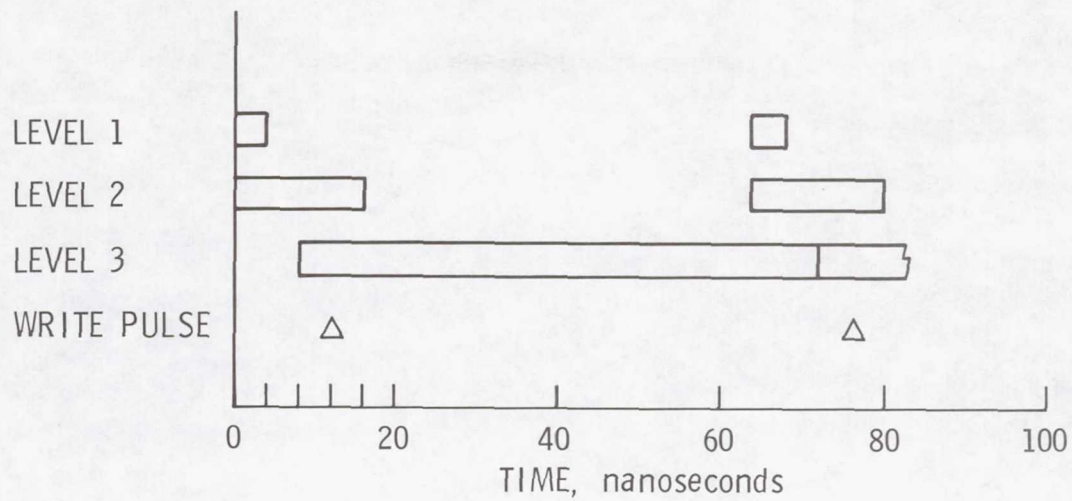


Figure 7.- Column 0 data path timing.

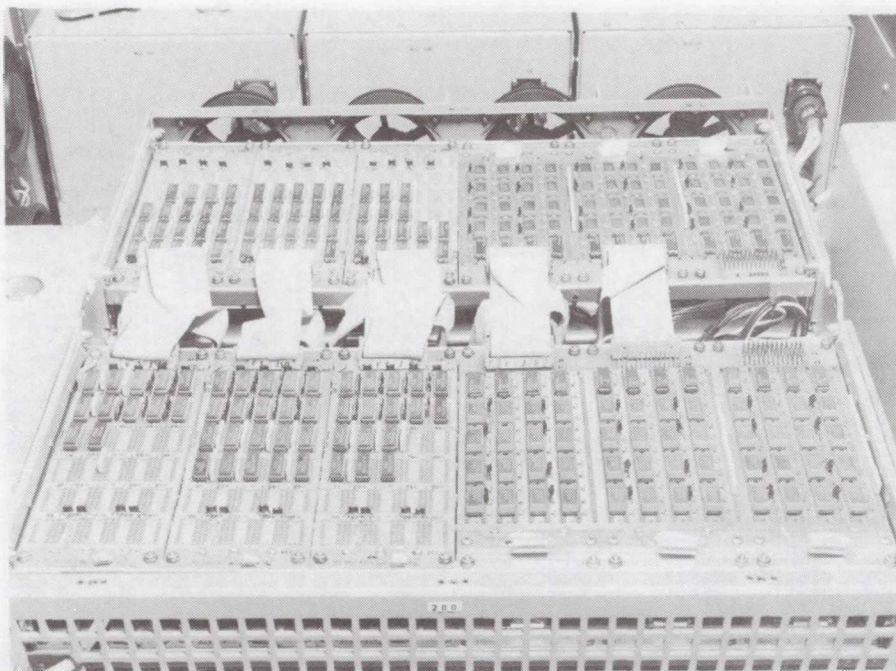


Figure 8.- Top two wire-wrap frames.

Page intentionally left blank

BROADBAND ELECTROMAGNETIC SENSORS

FOR AIRCRAFT LIGHTNING RESEARCH

Thomas F. Trost
Electrical Engineering Department
Texas Tech University

Klaus P. Zaepfel
NASA Langley Research Center

SUMMARY

A set of electromagnetic sensors, or electrically-small antennas, is described. The sensors are designed for installation on an F-106 research aircraft for the measurement of electric and magnetic fields and currents during a lightning strike. The electric and magnetic field sensors mount on the aircraft skin and respond to the exterior fields $\frac{\partial D}{\partial t}$ and $\frac{\partial B}{\partial t}$, respectively. The current sensor mounts between the nose boom and the fuselage and responds to $\frac{\partial I}{\partial t}$, where I is the boom current. The sensors are all on the order of 10 cm in size and should produce up to about 100 V for the estimated lightning fields. The basic designs are the same as those developed for nuclear electromagnetic pulse studies. The most important electrical parameters of the sensors are the sensitivity, or equivalent area, and the bandwidth (or rise time). Calibration of sensors with simple geometries is reliably accomplished by a geometric analysis; all the sensors discussed in this paper possess geometries for which the sensitivities have been calculated. For the calibration of sensors with more complex geometries and for general testing of all sensors, two transmission lines were constructed to transmit known pulsed fields and currents over the sensors.

INTRODUCTION

With increasing use of composites, digital avionics, and digitally controlled fly-by-wire systems, much emphasis has been placed on protecting aircraft, equipment, and personnel from the various effects of lightning. Not only may the digital systems be more susceptible to upset by lightning-induced transients, but the Faraday shield protection created by the metal skin of present generation aircraft will disappear with the use of composites. Strong lightning fields will induce unwanted pulses on wiring that could, at a minimum, produce erroneous information and, at a maximum, destroy critical, stored data without actually destroying the physical structure of the system. With an analog system, interruptions are momentary; but with a digital system,

interruptions may last as long as it takes to reset, reload, or reprogram the system. Clearly, because of the lack of external protection, the line of defense will have to be drawn within the digital system itself by lightning-hardened designs, and these designs need to be tested. However, since very little data exist for lightning generated fields on aircraft, a fundamental prerequisite for solving the problem is the definition of these fields.

The Langley Research Center has undertaken to develop a design process that can produce ultrareliable digital equipments and it has also undertaken a research program to better define the electromagnetic effects of lightning on aircraft which may affect such equipments. To this end, a lightning measurements program has been implemented. An instrumented aircraft will fly into thunderstorms, and recordings will be made of electromagnetic sensors located on the aircraft. Another part of the program will then correlate that data with simultaneously recorded ground-based observations which will give additional information about the properties of the lightning.

The instrumentation system that is being developed has been described in detail at a previous workshop (ref. 1), and a major element in the recording process, the endless-loop digital recorder, is described in detail at the present symposium (ref. 2). The endless-loop digital recorder can store 130 000 data samples at a 10 ns sample interval. This information is then re-recorded at a slower rate in PCM format on a slow analog recorder. A system containing two digital recorders, a video recorder, and a conventional recorder was flight tested during late summer of 1979. Future systems will contain up to twelve channels of such wide-band, digital recording.

As will be seen in their detailed descriptions that follow, the sensors are directional in design; consequently, by placing several of them at various locations and orienting them along expected major axes of field directions, a multidimensional picture of the field of interest can be reconstructed from the recorded data. Some preferred locations of the measurements that need to be made on an aircraft are shown in figure 1. Electric fields are measured near the extremities of the aircraft, and magnetic fields are measured nearer the center of the aircraft. This should give maximum signal output in the presence of electromagnetic resonances. Total current in the nose boom, caused by a direct strike to the boom, will be measured as it flows from the boom to the airframe. In the case of a nearby strike, the three-axes magnetic field measurement in the boom will define the ambient magnetic field with the least amount of aircraft distortion.

SENSOR DESIGN

The sensors that were flown last summer, and will be flown this year, are being designed at Langley Research Center and at the Texas Tech University and built at Langley Research Center. Their locations are shown on the research aircraft, an F-106B, in figure 2. Their designs are based on those of the sensors developed for making nuclear electromagnetic pulse measurements by the Air Force Weapons Laboratory (AFWL), where they are referred to as the multigap

loop (MGL), the flush-plate dipole (FPD), and the outside Moebius mutual-inductance (OMM) loop (ref. 3). The fundamental quantities which they measure are time-rates-of-change of magnetic flux density, electric displacement, and of current; hence, they are called in this paper B-dot, D-dot, and I-dot sensors, respectively. All the sensors are electrically small. The maximum expected values of I-dot, B-dot, and D-dot are as follows: the maximum I-dot is about 10 kA/0.1 μ s; with this current flowing over a fuselage of 1 meter radius, B-dot is 2×10^4 Tesla/s on the surface; the maximum D-dot is 50 A/m², which corresponds to a rate-of-change of E of about 10^5 V/m/0.1 μ s (ref. 4).

D-dot Sensor

The D-dot sensor is an FPD design. It consists of an insulated plate which is mounted flush with a ground plane and is enclosed underneath by a metal cavity. When the sensor is mounted on the aircraft, the aircraft skin serves as the ground plane. A photograph of the sensor is shown in figure 3 and a sketch in figure 4. The plate is loaded by two cables which are connected together at a signal summing point to form a single output. The use of two load points rather than one reduces the relative propagation delay in picking up the field from different parts of the sensor. The boundary condition equating the charge density on the plate to the electric displacement field, D, normal to the plate results in an output current from the plate proportional to the time derivative of D.

Because the bandwidth of an FPD sensor of given dimensions cannot be calculated, prototype testing was a prerequisite. A sensor having a large enough plate to achieve the desired sensitivity was built. The sensor capacitance was measured, and from this the bandwidth determined. In order to optimize the design, various changes were then made, and the capacitance remeasured. The results are summarized in Table I, where the measured capacitance, C, and 3-dB bandwidth, f_0 , are given for three designs and are compared with the capacitance and bandwidth calculated for the case of an infinite cavity (open space under the ground plane). This last case has the maximum possible bandwidth. For the 10.2 cm (4 in.) deep cavity, the bandwidth is close to the maximum: 180 MHz vs 215 MHz; consequently, 10.2 cm appears to be a reasonable depth to use. Unfortunately, the slot is sealed in the final version of the sensor to protect it from the environment, and this addition of dielectric material means a slightly lower bandwidth. A seal consisting of a layer of structural adhesive (Scotch-Weld 2216 clear) was used on the prototype.

The final version of the sensor differs slightly from the prototype as shown in Table I. The cavity is limited in depth to 8.3 cm (3.25 in.) by the geometry of the F-106, and thus the cavity diameter has been increased to 33.0 cm (13 in.) in order to keep the capacitance low. Also, the adhesive has been replaced with silicone rubber (RTV 630), which has a lower dielectric constant (3.2 vs 5.5). The capacitance and the bandwidth of the final version were measured to be 24 pf and 132 MHz.

The bandwidth, f_0 , is calculated from the capacitance by assuming a simple model of the sensor consisting of a current source and a capacitor in parallel and loaded by the 50- Ω line. See figure 5a (the radiation resistance of the sensor is small and may be neglected). The output falls by 3 dB when $1/(2\pi f_0 C)$ equals 50 Ω , which is the expression for f_0 . Also, the sensor rise time, t_r , required to charge the capacitance, C , can be obtained from the formula $t_r f_0 = 0.35$. The total sensor rise time is t_r plus the propagation time for a field crossing the sensor.

The sensitivity, or equivalent area, A_D , of the D-dot sensor can be calculated from the sensor geometry using the formula $A_D = \pi r_1 r_2$ (ref. 5). The value of A_D from the formula is given in Table II, which gives parameters for all the sensors. Alternately, A_D can be measured by exposing the sensor to a known field.

In order to measure A_D , the sensor may be exposed to a D-field with a step change in time. Then the sensor output resulting from the step is integrated and A_D is found from the final value reached by this integral. This process is shown in figure 5. In figure 5b, the D-field is given in terms of the unit step, $u(t)$, and the sensor current source then contains an impulse function, $\delta(t)$. The resulting sensor output voltage is shown in figure 5c. The impulse charges the capacitor instantaneously, followed by an exponential decay. The integral of the output is given in figure 5d. The final value is $RA_D D_0$, from which one obtains A_D . In the section below entitled SENSOR TESTING, the value of A_D is measured in this way, using the leading edge of a pulse propagated over the sensor as the D-field step. The step is, of course, not instantaneous, but is much faster than the response time of the sensor.

B-dot Sensor

An MGL design employing two gaps was chosen for the B-dot sensor. (See figures 6 and 7.) The reasoning behind the design is as follows: The sensor is essentially a semicircular loop on a ground plane and gives an output voltage, from Faraday's law, which is proportional to the rate of change of the magnetic field cutting through the plane of the loop. To reduce the sensitivity of the loop to electric fields normal to the plane, a plate is inserted to short the center of the loop to the plane. This creates two separate loops, each of which requires a gap and a loading cable. In addition, the sensor is made fairly long to lower its inductance (and thus increase its bandwidth) by spreading out the current; so that, in fact, two loading cables are needed along each gap. The two cables have 100- Ω impedances and are connected in parallel to a 50- Ω cable, providing the sensor with two 50- Ω output cables, one from each loop. The cable connections are shown at the lower right in figure 7. The output voltages are of the opposite sign, so that the total output is obtained by subtracting

the two. This is done in a differential amplifier at the load end of the output cables. The arrangement has the advantage that any interfering signal which is picked up equally along both cables will be cancelled out.

The size of the B-dot sensor was chosen large enough for adequate sensitivity and then the inductance and bandwidth corresponding to this size were calculated. The bandwidth was found to be several times larger than required, allowing the final version of the sensor to be fabricated. The inductance of the sensor is given approximately by the following formula (ref. 6, p. 52):

$$L = 1/2 \frac{r^2}{(9r + 10l)} \quad 10^{-6}H = 0.0456 \times 10^{-6}H,$$

where $r = 6.4$ cm (2.5 in.) and $l = 11.7$ cm (4.6 in.). This is the usual formula for a circular loop with the factor $1/2$ added because the sensor is in the form of a semicircular loop on a plane. The resistance, R , loading the loop is 100Ω ($100//100 + 100//100$), so the rise time is given by

$$t_r = 2.2 \frac{L}{R} = 1.00 \times 10^{-9} \text{ s, and the bandwidth is } f_o = \frac{.35}{t_r} = 350 \text{ MHz. The}$$

circuit model is shown in figure 8a.

The sensitivity (equivalent area) of the B-dot sensor, A_B , can be calculated from the geometric area of the sensor loops together with a correction for the effect of the sensor baseplate as is done in reference 6. The result is given in Table II.

A_B can also be measured, using the same technique described above for A_D . The equations are given in figure 8 and are very similar to those in figure 5. The actual measurement of A_B is discussed in the section SENSOR TESTING.

I-dot Sensor

The I-dot sensor is an OMM type and will be used to detect lightning current flowing on the nose boom of the F-106. Figure 9 shows a photograph of the sensor and figure 10 a sketch of a cross-section through the sensor. By Faraday's law, current flowing over the sensor induces a voltage in the small rectangular loop, which is machined circumferentially around the sensor. The gap in the loop is loaded at four points as shown in the cabling diagram in the upper left portion of the figure. The sensor has a differential output similar to the B-dot sensor and, therefore, has good immunity from the pickup of interfering signals on the output cables. Experience with OMM sensors was gained prior to the construction of the F-106 sensor through the construction and testing of two prototype versions.

The bandwidth of the I-dot sensor is determined approximately with the use of a simple circuit model consisting of a voltage source in series with an inductance and a resistance load. For the I-dot sensor, the voltage source is given by $2M \frac{di}{dt}$, where M is the basic mutual inductance of the sensor, and i is the current flowing over the sensor. Because the two outputs are connected across the gap in opposite directions, the sensor has effectively two turns and thus the factor of 2 in the source as shown in reference 7. The inductance in the model consists of two parts: the sensor inductance, L_s , which is somewhat more than $4M$, and the inductance, L_w , of the short lengths cable center-conductor which extend across the sensor gap. The load R is the combined load of the cables, or 100Ω . The value of $L_s + L_w$ is estimated to be $1.1 \times 10^{-8} \text{ H}$. Thus, the 3-dB bandwidth, f_o , is $f_o = \frac{R}{2\pi(L_s + L_w)} \approx 1.5 \text{ GHz}$.

This is much higher than is required for the instrumentation system. The corresponding rise time is .23 ns.

The sensitivity or mutual inductance, M , of the I-dot sensor can be calculated from the formula $M = 2 \times 10^{-7} w \ln \frac{a}{b} \text{ H}$ as shown in reference 7. The result is given in Table II. M can also be measured, and one way this can be done is by connecting a fairly low-frequency sinusoidal source to the sensor. The amount of current flow is measured using a Tektronix CT-2 current transformer. Using the above procedure for frequencies around 10 MHz gives a value of M which is within a few per cent of the calculated value.

TRANSMISSION-LINE SENSOR CALIBRATORS

Two special transmission-line structures were built for testing and calibrating the sensors. A large flat-plate line based on "Design A" of ACHATES Memo 1 (ref. 8) was built for transient and steady-state testing of B-dot and D-dot sensors; and a smaller, coaxial line was built for the transient testing of I-dot sensors.

Flat-Plate Transmission Line

The two conductors of the flat-plate line are a ground plane and an upper plate as shown in figures 11 and 12. Sensors are mounted on the ground plane beneath the upper plate and are illuminated by a TEM field which propagates from one end of the upper plate to the other (mainly between the plate and the ground plane). The ground plane is made of aluminum panels which are taped together with conducting tape to give an overall length of 10.97 m (36 ft.) and

width of 4.88 m (16 ft.). The upper plate is also of aluminum panels, with bolted and taped joints, and is suspended from the ceiling by adjustable nylon cords. The upper plate is angled toward the ground plane and tapered to a point at the input end, where it connects to the coaxial cable (3/8-inch foam dielectric Heliak) from the signal source. At the output end, the upper plate is similarly angled and tapered and is connected to a matched load. The characteristic impedance of the line is 100 Ω .

One can imagine that the line is derived from a 200- Ω line with symmetric upper and lower plates by passing a ground plane through the plane of symmetry, thus eliminating the lower plate and obtaining a 100- Ω line between the ground plane and the upper plate.

Sensors to be tested are positioned on the center line of the ground plane below the first bend in the upper plate. Figure 12 shows the B-dot sensor in place and also the electronics used for transient testing. A Tektronix 109 pulse generator ($t_r = 250$ ps) drives the line with 50-V pulses. The outputs from the sensor are sampled with Tektronix S-4 sampling heads ($t_r = 25$ ps); and the output waveforms, their difference, and the integral of their difference are displayed. The pulse generator also supplies a trigger signal through a tee and an attenuator.

Coaxial Transmission Line

Figure 13 shows the I-dot sensor mounted in the coaxial line for testing. The sensor actually forms an integral part of the line. The center conductor consists of, from left to right, a cone, the sensor, and four heavy-gauge wires like those used on the F-106 to conduct the lightning current between the sensor and the fuselage. In the coaxial line these wires are flared out and fastened to the outer conductor at the right-hand end of the line, thus essentially shortening the line at this point. Because of the short, the line is used for transient testing only. The sensor output cables are passed along the center and out at the right-hand end. The same pulse generator and sampling equipment used on the flat-plate line are used here. The line is 121.9 cm (48 in.) long.

The characteristic impedance Z_c of the coaxial line is roughly 100 Ω . It varies somewhat with position along the line because of the varying radius of the sensor and wires. Thus, various reflections occur along the line, and the field over the sensor gap is not known precisely. Because of this, the line is not used for making accurate checks of the sensitivity of the sensor but only to verify that the sensor output waveforms are reasonable.

SENSOR TESTING

Preliminary testing of the sensors described above was done by examining the time-domain reflectometer (TDR) response of each sensor, using a Hewlett Packard 1415A TDR. Measured TDR waveforms were compared with the expected waveforms, which are predominantly inductive for the B-dot and I-dot sensors and predominantly capacitive for the D-dot sensor. The measured waveforms were satisfactory and reflections at connectors and summing points were small (ref. 9). Further testing of the sensors was then carried out using the transmission-line calibrators.

B-dot Sensor

The B-dot sensor was installed in the flat-plate line as shown in figure 12. The sensor is oriented for maximum sensitivity. The sampling scope displayed the two sensor outputs corresponding to the passage of the leading edge of the pulses over the sensor. The waveforms are shown in figure 14; they are roughly like the calculated B-dot sensor output in figure 8. Notice that the pulse from the front (left-hand) section of the sensor is quite sharp, while that from the rear section is lower in amplitude and broader. This slower response from the rear section of the sensor is apparently due to the fact that the rear section is in the shadow of the front section as far as the high-frequency components of the field are concerned.

Figure 15 shows the total output, that is, the difference of the individual outputs, and the integral of this. Because the sensor output should, ideally, be the derivative of the magnetic field step, its integral should closely approximate the field step. The individual outputs remain somewhat positive after the initial pulses; consequently, the total output contains a weakly positive region following the pulse, and this gives rise to a region of somewhat gradual rise in the integrated output following the initial rapid rise. Thus the 10 to 90-percent rise time, t_r , of the integrated signal is quite long, 3.5 ns. The 10 to 50-percent rise time is only 0.5 ns. The interpretation of these observations leads one to believe that this gradual rise is a basic characteristic of multigap sensors of this type.

The sensitivity, or equivalent area A_B , of the sensor is determined from the integrated output. The final value of the output is equated to $A_B B_0$, as in figure 8d, where B_0 is the value reached by the magnetic field over the sensor. B_0 is related to the pulse generator voltage from a theoretical analysis of the flat-plate transmission line. The result is $A_B = 5.70 \times 10^{-3} \text{ m}^2$, which is in excellent agreement with the calculated value of $5.73 \times 10^{-3} \text{ m}^2$.

The output of the B-dot sensor in figure 15 shows weak oscillations which persist for a long time after the output pulse. These oscillations occur when

there should be no output from the sensor and, therefore, constitute a spurious response which requires further investigation.

If the B-dot sensor is rotated 90° on the ground plane, its output is a minimum and results primarily from electric-field pickup. The total output in this orientation was found to be 32 db down from its value for the previous orientation.

D-dot Sensor

The D-dot sensor was tested in the flat-plate line in the same manner as the B-dot sensor. The output, as observed on the sampling oscilloscope, is shown in figure 16; the integrated output is shown in figure 17. From the final value of the integrated output, the equivalent area of the D-dot sensor was measured to be $A_0 = .0383 \text{ m}^2$. This value is 6.4 percent below the value calculated from theory ($.0409 \text{ m}^2$). The sensor rise time, from figure 17, is 2.4 ns. This corresponds to a 3 dB-bandwidth, f_0 , of 147 MHz, using $t_r f_0 = .35$. Earlier, the bandwidth was determined to be 132 MHz by measurement of sensor impedance. (See Table I.) The difference in the two values gives some idea of the accuracy of the bandwidth determination.

I-dot Sensor

The output waveforms of the I-dot sensor when mounted in the coaxial line were very similar to those of the OMM sensors shown in reference 7, figures 4-5.

CONCLUSIONS

Electromagnetic sensors were designed and constructed for use on a research aircraft. The output waveforms of the I-dot and D-dot sensors were as expected when tested in the transmission-line calibrator. However, a need for some refinements in the design of the B-dot sensor was indicated in order to reduce the weak oscillations that follow the output pulse. Future work on this sensor might also include the use of a more detailed circuit model which includes the mutual inductance between the two sections and the capacitance of the gaps.

Another validation of the sensor and calibrator performance is the reasonable agreement achieved between the two methods used for obtaining the equivalent area (sensitivity) of each sensor. Calculations from sensor geometry, and measurements in the calibrator agree to within several percent. Because the accuracies in the calculations for both methods are approximately equal, using the calibrator in this way does not constitute a conventional laboratory calibration, in which the standard should be an order of magnitude more accurate than the device under test. Although neither method can serve as an accurate

reference for the other, they do serve to validate each other and provide good values of sensor equivalent area.

For the sensors that have so far been developed at Langley Research Center, the geometric approach is the preferred technique. The transmission line technique should be used as the prime calibration technique if sensors of more complex geometries are required.

REFERENCES

1. Pitts, F.L., et al.: In-flight Lightning Characteristics Measurement System. FAA-Florida Institute of Technology Workshop on Grounding and Lightning Technology, Report No. FAA-RD-79-6, March 6-8, 1979, pp. 105-111.
2. Thomas, Robert M.: Expanded Interleaved Solid-State Memory for Wide Bandwidth Transient Waveform Recorder. Symposium on Lightning Technology. NASA CP-2128, 1980.
3. Baum, C.E., et al.: Sensors for Electromagnetic Pulse Measurements Both Inside and Away from Nuclear Source Regions. IEEE Trans. Electromag. Compatibility, vol. EMC-20, no. 1, Feb. 1978, pp. 22-35.
4. Clifford, D.W., et al.: A Case for Submicrosecond Rise-Time Lightning Current Pulses for Use in Aircraft Induced-Coupling Studies. IEEE Symposium on Electromagnetic Compatibility, October 9-11, 1979, San Diego, Calif., p. 143.
5. Latham, R.W.; and Lee, K.S.H.: Capacitance and Equivalent Area of a Disk in a Circular Aperture. Sensor and Simulation Note 106, AFWL, Kirtland AFB, New Mexico, May 1970.
6. Mory, Rex, et al.: Development and Production of Multi-Gap Loop (MGL) Series EMP B-dot Sensors. Tech. Rep. No. AFWL-TR-70-153, Kirtland AFB, New Mexico, Feb. 1971.
7. Radiation Hardened I-dot Sensor (OMM - 1A) for Use in Baum Antenna. Tech. Rep. No. AL-1102, EG & G, Inc., Albuquerque, New Mexico.
8. Chen, Kenneth, et al.: ACHATES Design. ACHATES Memo 1, AFWL, Kirtland AFB, New Mexico, Nov. 5, 1976.
9. Electromagnetic Pulse Sensor Handbook. vol. 1, AFWL, Kirtland AFB, New Mexico, June 1971.

TABLE I.-D-DOT SENSORS

Prototype Designs				
Cavity Depth cm (inches)	Type of Dielectric	C (pf)	f ₀ (MHz)	Fixed Dimensions cm (inches)
7.6 (3)	air	19	168	Plate Diameter: 21.6 (8.5) Cavity Diameter: 30.5 (12.0) Slot width: 1.3 (0.5)
10.2 (4)	air	18	180	
10.2 (4)	Scotch-Weld 2216 (clear)	25	129	
Infinite cavity	air	15	215	
AIRBORNE (F-106) DESIGN				
8.3 (3.25)	RTV 630	24	132	Plate Diameter: 21.6 (8.5) Cavity Diameter: 33.0 (13) Slot width: 1.3 (0.5)

TABLE II.-SUMMARY OF SENSOR PARAMETERS

<u>Type of Sensor</u>	<u>Quantity Measured</u>	<u>Max. Expected Input</u>	<u>Sensitivity³</u>	<u>Rise Time (10%-90%)</u>
Multigap Loop	B-dot	2×10^4 Tesla/s	$5.73 \times 10^{-3} \text{ m}^2$	3.5 ns ¹
Flush-plate Dipole	D-dot	50 A/m ²	$4.09 \times 10^{-2} \text{ m}^2$	2.4 ns ²
Outside Moebius Mutual Inductance Loop	I-dot	10^{11} A/s	$2.13 \times 10^{-9} \text{ H}$.23 ns ³

Notes: ¹Measured (10%-50% rise time is 0.5 ns)

²Measured

³Calculated

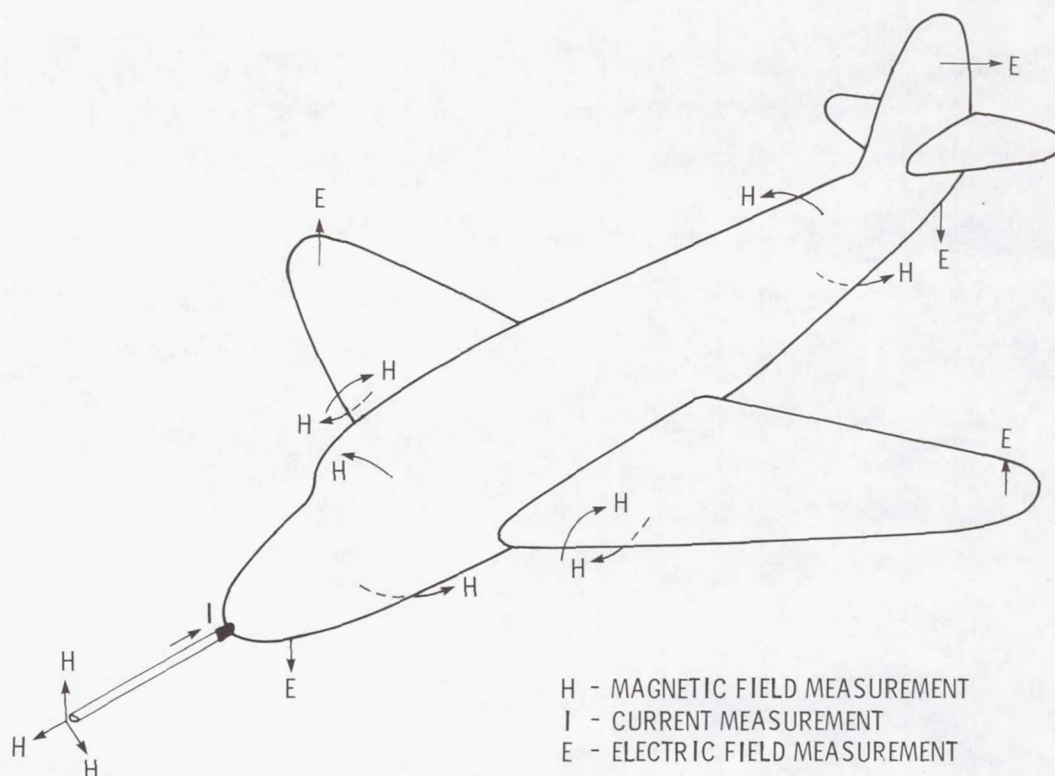


Figure 1. - Preferred measurement locations.

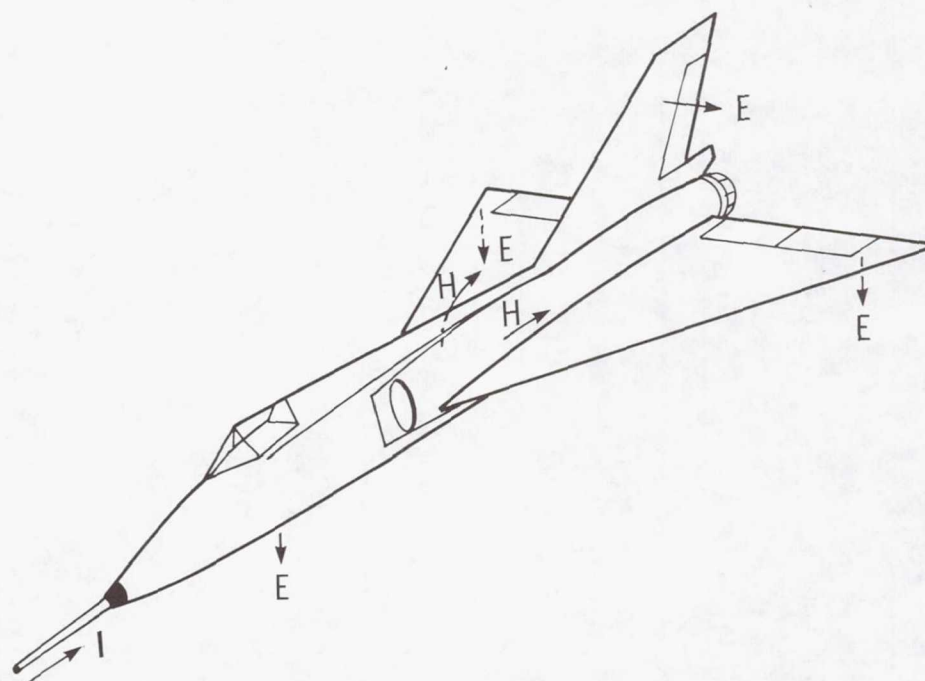


Figure 2. - Measurement locations for 1980.

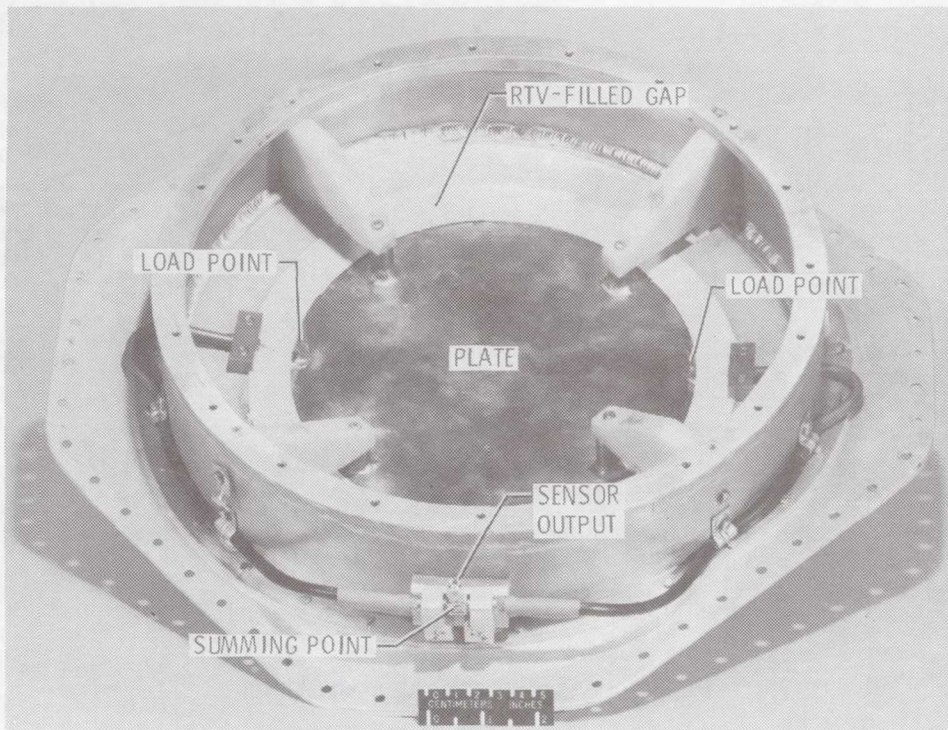


Figure 3. - D-dot sensor mounted to the inside of F-106 fuselage panel. Cavity cover removed.

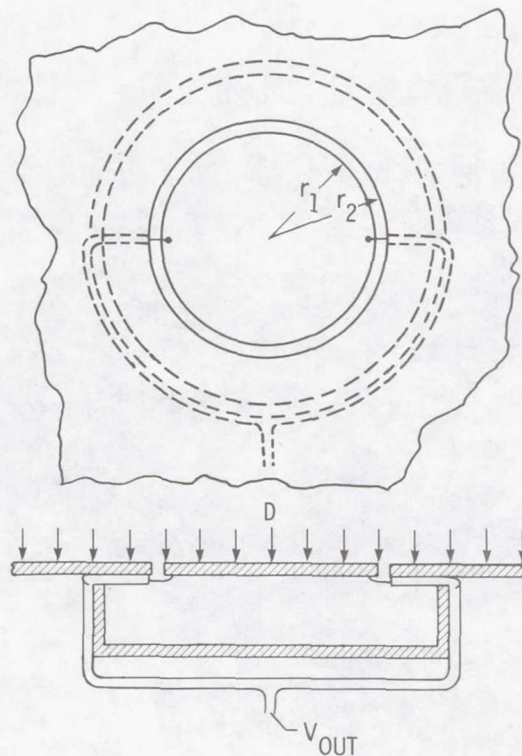
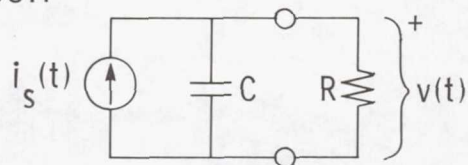
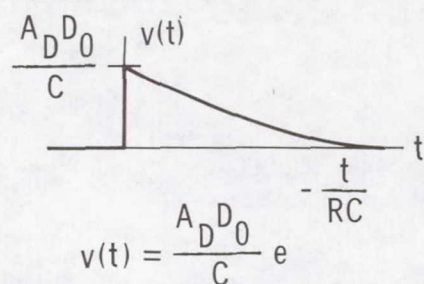


Figure 4. - D-dot sensor

a. CIRCUIT



c. OUTPUT VOLTAGE



b. SOURCE VOLTAGE FOR A STEP D

$$D = D_0 u(t)$$

$$i_s(t) = A_D \frac{dD}{dt} = A_D D_0 \delta(t)$$

d. INTEGRATED OUTPUT VOLTAGE

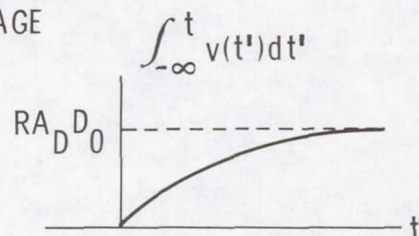


Figure 5. - Summary of D-dot sensor response to a step electric field.

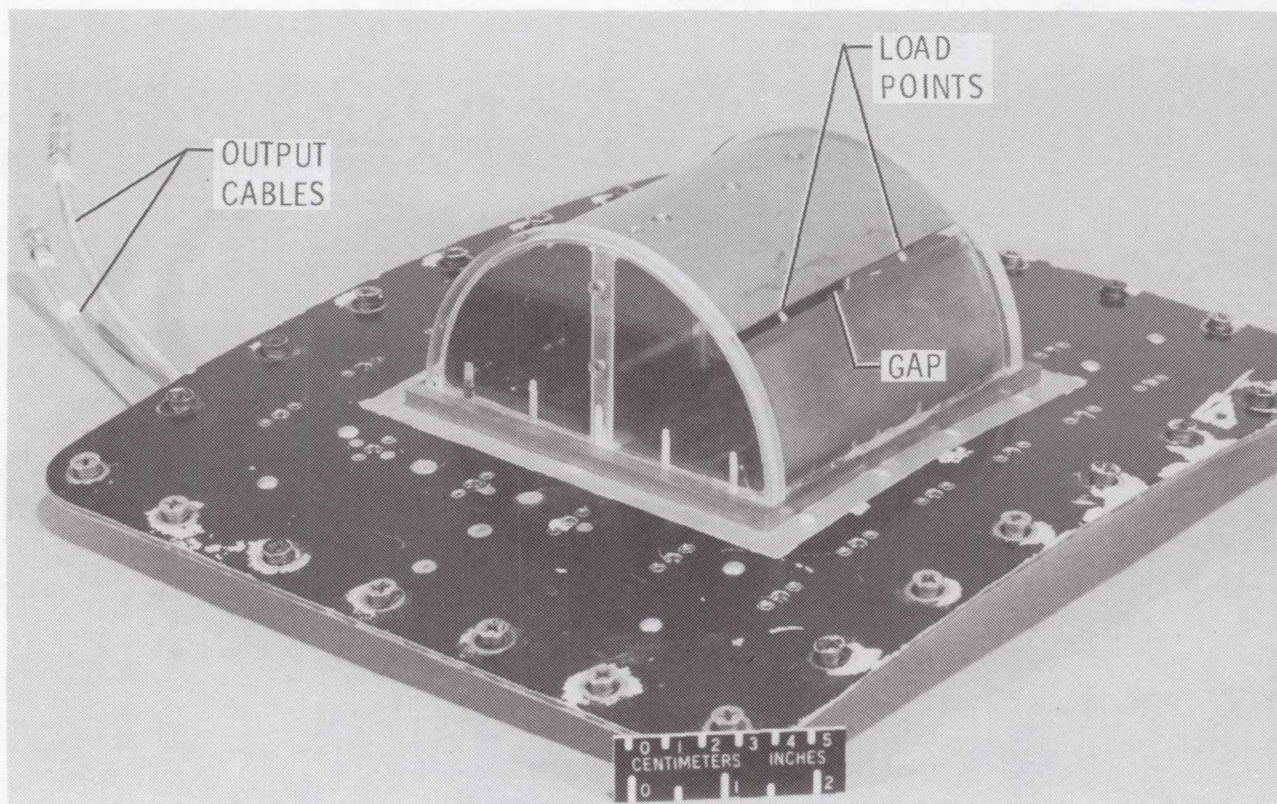


Figure 6. - B-dot sensor mounted on F-106 fuselage panel.

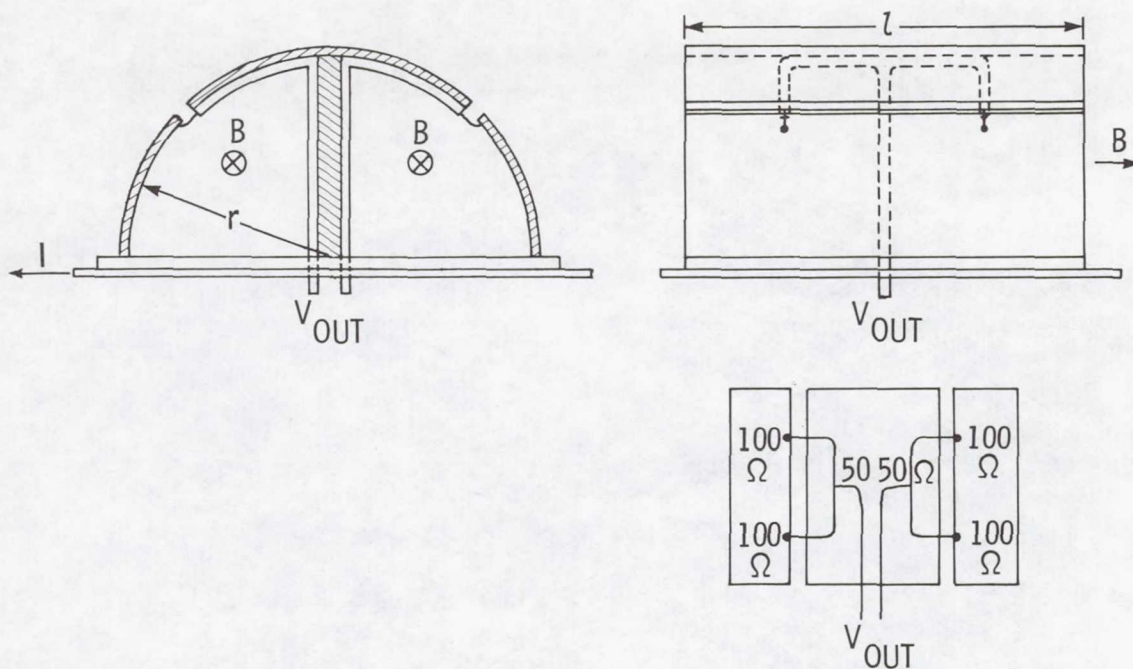
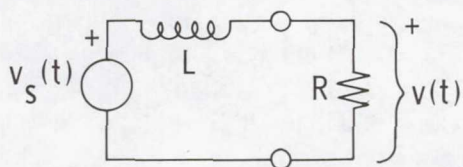
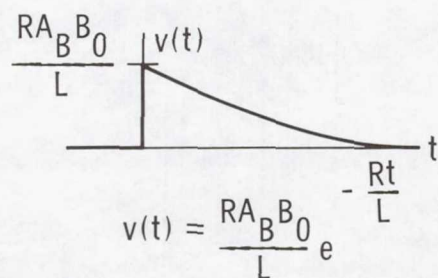


Figure 7. - B-dot sensor.

a. CIRCUIT



c. OUTPUT VOLTAGE



b. SOURCE VOLTAGE
FOR A STEP B

$$B = B_0 u(t)$$

$$v_s(t) = A_B \frac{dB}{dt} = A_B B_0 \delta(t)$$

d. INTEGRATED OUTPUT
VOLTAGE

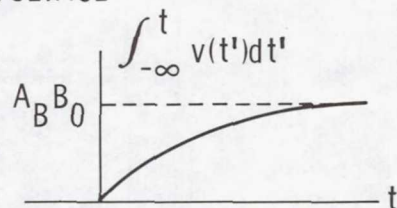


Figure 8. - Summary of B-dot sensor response to a step magnetic field.

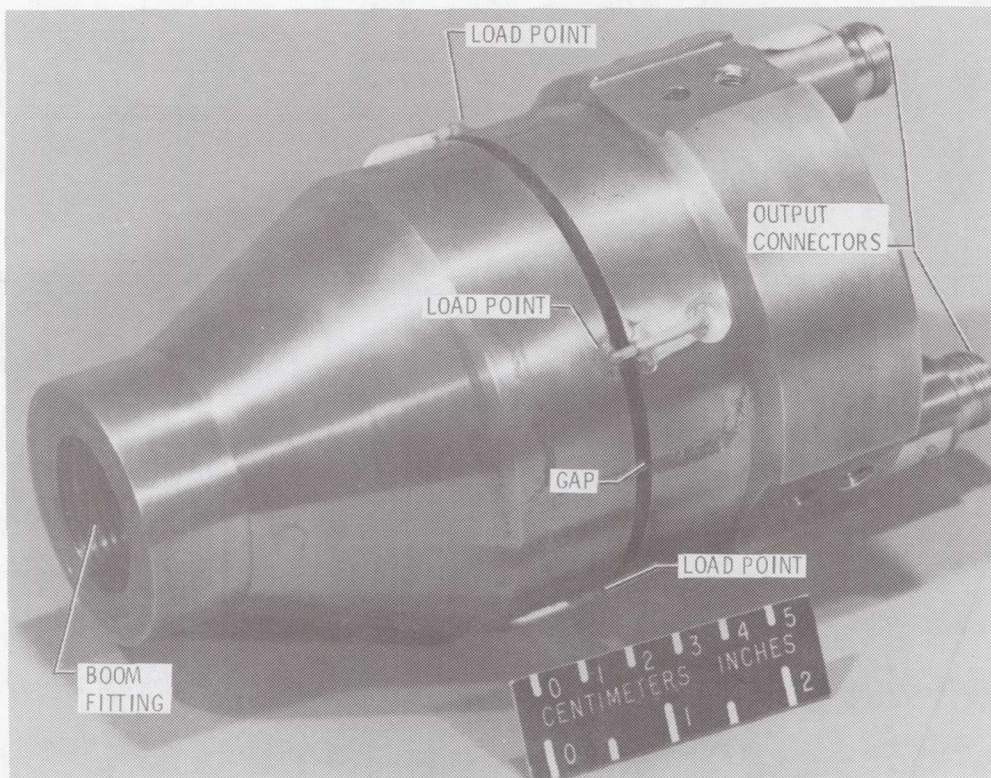


Figure 9. - I-dot sensor designed to be fitted to back of F-106 pitot-static boom.

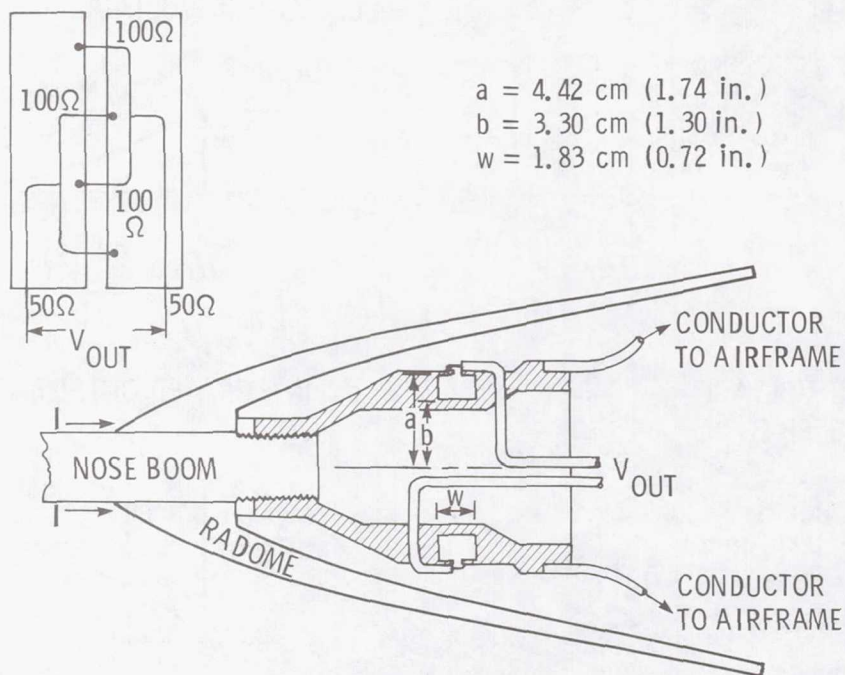


Figure 10. - I-dot sensor mounted inside F-106 radome.

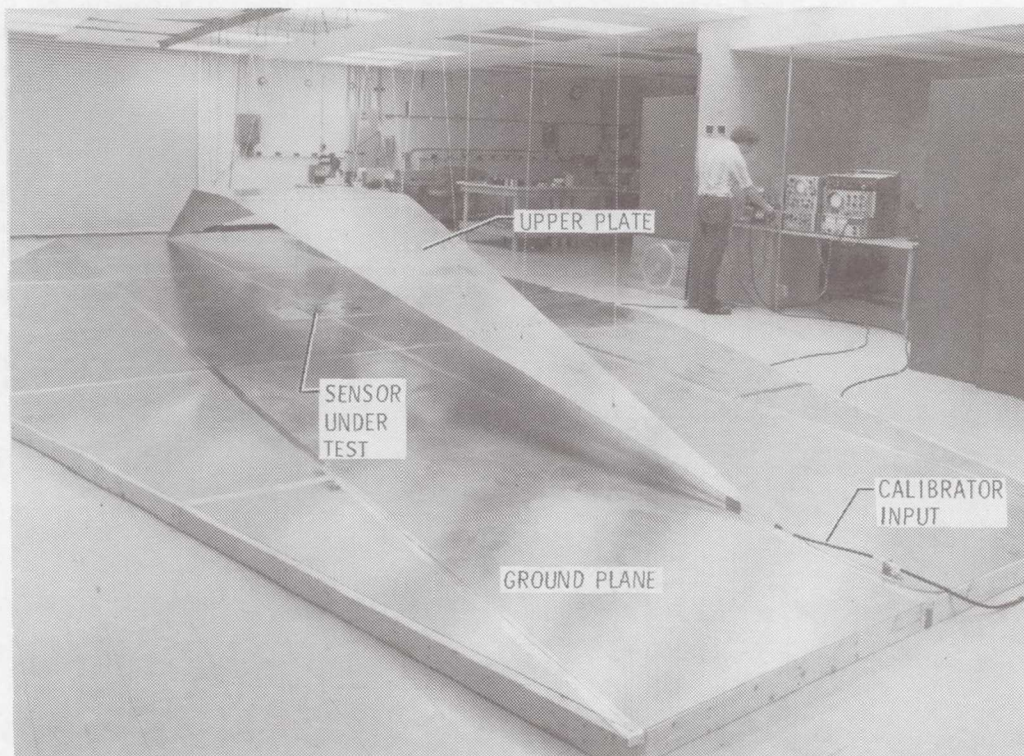


Figure 11. - Flat-plate transmission line calibrator.

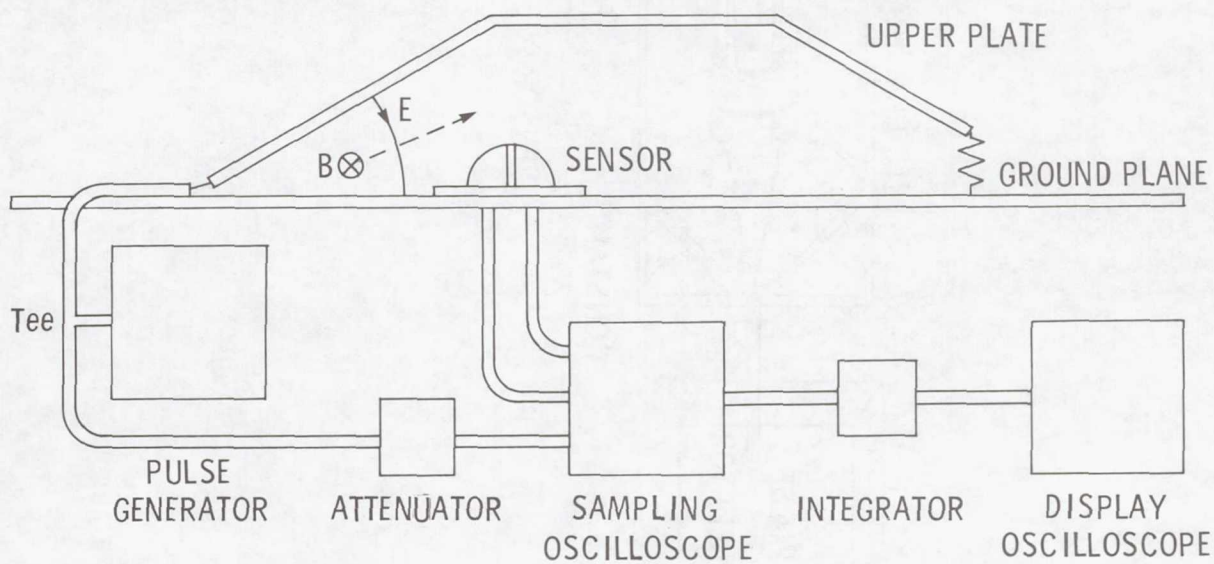


Figure 12. - Flat-plate transmission line with electronics for transient testing of sensors.

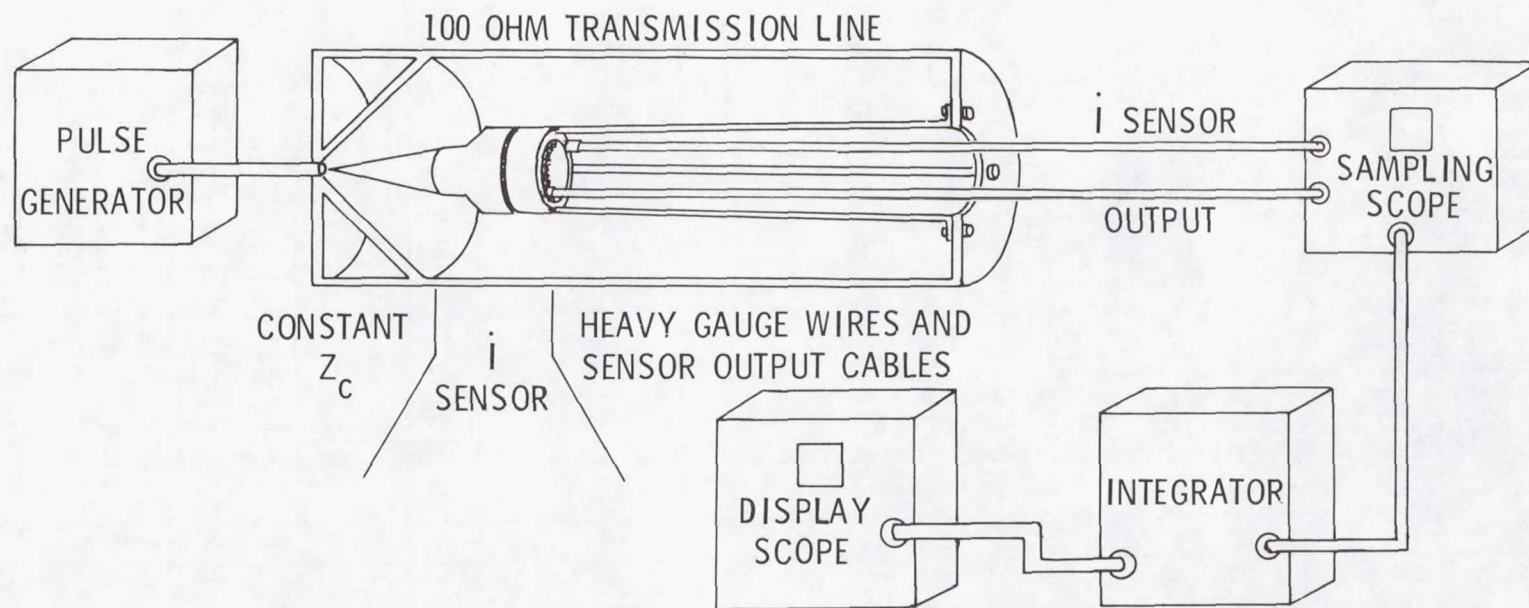


Figure 13. - Coaxial transmission line with \dot{I} -dot sensor and calibration electronics.

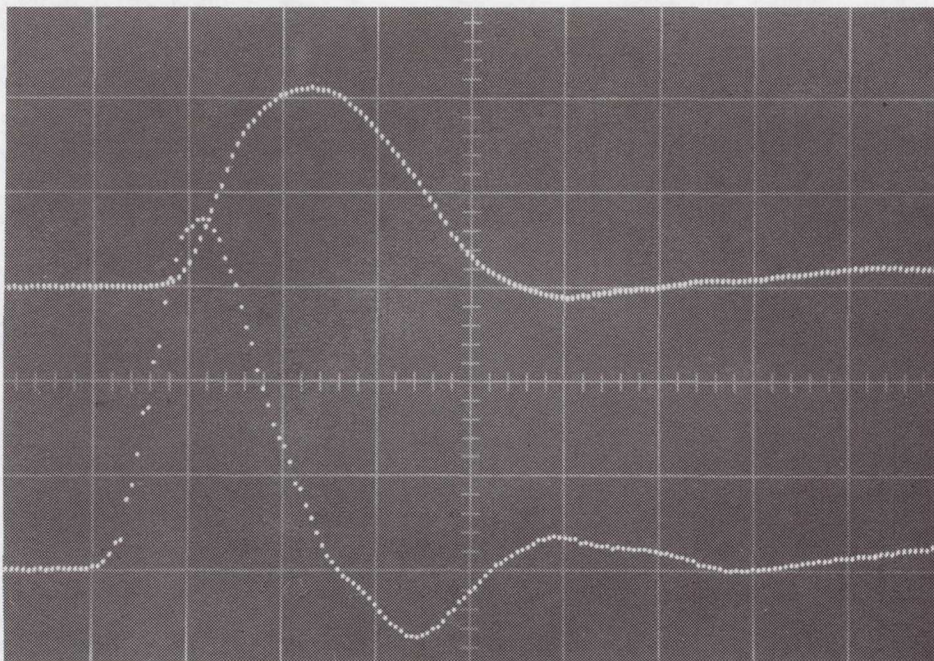


Figure 14. - Outputs of B-dot sensor. Vertical 200 mV/div.; horizontal 500 ps/div. Lower trace from front section of sensor (inverted). Upper trace from rear section of sensor.

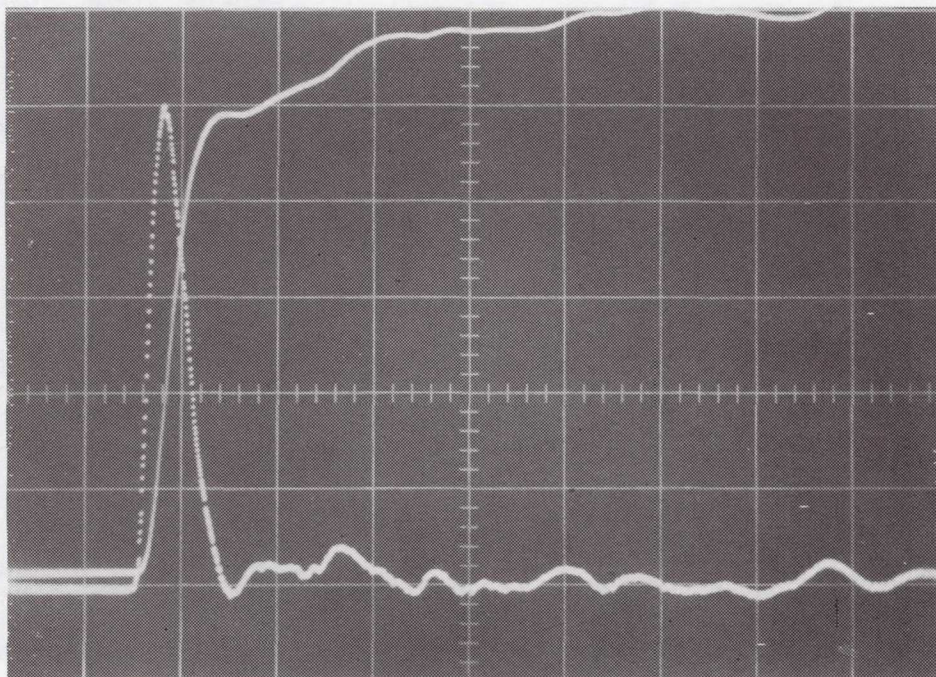


Figure 15. - Total output of B-dot sensor and integrated total output. Horizontal 2 ns/div.

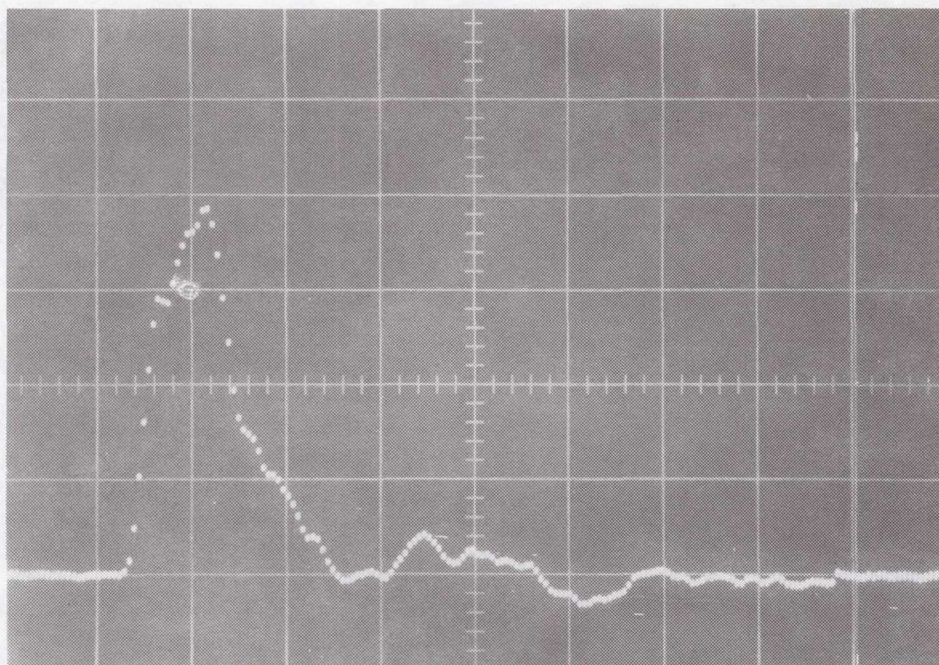


Figure 16. - Output of D-dot sensor. Vertical 100 mV/div.; horizontal 2 ns/div.

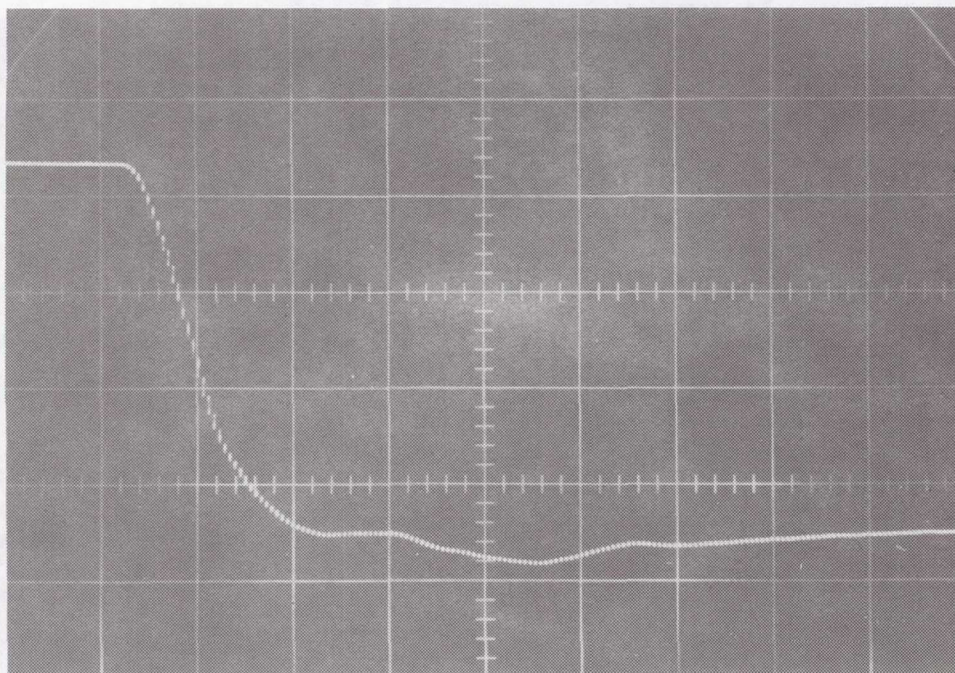


Figure 17. - Integrated output (inverted) of D-dot sensor. Vertical 2×10^{-10} V-s/div.; horizontal 2 ns/div.

AIRBORNE LIGHTNING CHARACTERIZATION

Capt. Robert K. Baum

Air Force Wright Aeronautical Laboratories

SUMMARY

A WC-130 aircraft was instrumented with wideband electromagnetic field sensors and flown near active thunderstorms to obtain data on the characteristics of nearby and direct strike lightning. An electric field ground station and time-of-arrival network provided time correlated data to identify the three dimensional locations of the discharge and the different events in the lightning flash. A description of the sensors, calibration procedures, and recording equipment is presented. Data are presented on return stroke characteristics in the 5 to 50 km range. At the time of this writing, data on the three dimensional source locations are not available for publication.

INTRODUCTION

The present interest in high frequency lightning characterization stems in part from a concern over an increasing susceptibility of modern aircraft to the electromagnetically coupled effects produced by lightning. Aircraft susceptibility is expected to increase with the use of composite materials and more susceptible microelectronics. To compound the susceptibility problem, the high frequency nature of the lightning event is not as yet well defined. For example, transients arising from the pre-attachment stepped leader process or nearby interstroke and intracloud processes may well be as important from a coupling standpoint as the return stroke phase itself. It is of increasing importance, therefore, to obtain a more refined empirical model of the overall lightning event taken from an appropriate base of wideband measurements.

In 1979, the Air Force Wright Aeronautical Laboratories began a joint flight research program with the National Oceanic and Atmospheric Administration to obtain data on the high frequency characteristics of lightning. Objectives of the 1979 phase of the program were: 1) develop a sensor/instrumentation package with linear response and recording capabilities in the 0.1-20 MHz range, 2) develop a ground station recording system capable of providing three dimensional locations of very high frequency (VHF) lightning activity with an accuracy of ± 250 m on a 20 km radius, 3) obtain wideband airborne data on electric and magnetic field characteristics associated with lightning within a 20 km range, 4) obtain and compare corresponding wideband aircraft skin current transients, and 5) correlate ground measurements (VHF source location and electric field) with the airborne data to permit field scaling, channel reconstruction, and isolation of important coupling events.

At this writing, the source location data were being analyzed and correlated with the airborne data. A short description of the ground station apparatus and the approach to be used to analyze the data is presented.

Construction and calibration of the airborne sensors is described since they have not been used in any previous program of this type.

GROUND STATION DESCRIPTION

The ground station was situated at Devil's Garden, Florida. It consisted of two separate systems, one to identify the discharge phase, the other to determine the three dimensional VHF lightning source locations.

Phase Identification

The discharge phase was identified using a low frequency electric field measuring system similar to that described by Fisher and Uman (ref. 1). Two plate antennas and three separate recording channels were used to allow linear sensing over the 80 db dynamic range in electric field levels expected within a 20 km radius of the site.

VHF Source Location

The VHF source location system was similar in concept to the Lightning Detection and Ranging (LDAR) system (ref. 2) with modifications as described by Rustan(ref. 3). The system used provides continuous source location data based on differences in times of arrival (DTOA) of the lightning pulses at widely separated stations. The system consisted of three recording stations and a central site positioned in a Y configuration on a 20 km radius. Two backup recording stations were placed on the same radius to provide redundant data. Antennas at each site consisted of four folded dipoles oriented to provide circularly polarized omnidirectional response. The antenna outputs were passed through a 6 MHz bandpass filter centered at 63 MHz. An envelope detector and a logarithmic amplifier were used to effectively compress frequency and dynamic range of the signal to within limits of the recorder. A complete description of the time domain relationship between the antenna output and the recorded signal has been published by Rustan (ref. 3).

The processed VHF signals received at each site were recorded on separate modified video recorders (in contrast to the LDAR system which re-transmits the signals to a central site). The recorders were tuned to a commercial broadcast station (Channel 11) and a normal video recording was made except that the luminance portion of the composite video signal was replaced with the VHF signal and the audio portion of the signal was replaced with a demodulated IRIG B time code transmitted from the test aircraft (see fig. 1). The recording system was designed to operate automatically when the transmitted IRIG B carrier was detected for a period of 10 seconds.

The Timing System

To provide the required source location accuracy of ± 250 m, the data from each video recorder must be time correlated with a relative error no greater than $\pm 0.1 \mu\text{s}$. This was achieved using the transmitted IRIG B as a coarse absolute time reference (common to all airborne and ground-based data) in com-

bination with the vertical and horizontal sync pulses detected and recorded from the composite video signal. The vertical sync pulse (VSP) occurs every 16.66 ms and was used to identify the beginning of one 'frame' of data from one of the two rotating video record heads. The fine time resolution within a given frame was derived from the chroma reference signal (CRS). The CRS is a 3.58 MHz signal recorded from the composite video signal by separating and heterodyning to 629 kHz. The phase of the CRS is advanced 90 degrees by the occurrence of the broadcast horizontal sync pulse every 65.1 μ s. By passing the CRS through a band-reject filter centered at 629 kHz, the periodic phase shift is seen on playback as a sharp spike occurring nominally every 65.1 μ s. This signal was also used to correct the VHF signal for minor fluctuations in headwheel and capstan speed inherent in the recorders. Figure 2 illustrates the various timing pulses reproduced or derived from the data. Data from the VHF stations were digitized and time correlated using the signals described. VHF source locations were then calculated for selected short intervals corresponding to the airborne recordings using the waveform correlation techniques developed by Rustan (ref. 3).

AIRCRAFT DESCRIPTION

Sensors

The test aircraft was fitted with two single axis sensors to detect free field radiation and a sensor on each wing to detect induced skin currents. The sensors were placed as shown in figure 3. The free field sensors were placed on the symmetry axis of the aircraft (forward upper fuselage) to reduce coupling from symmetric resonances on the aircraft skin. All sensors were designed to have a usable bandwidth of at least 20 MHz.

The vertical component of the incident electric field $E(t)$ was sensed by a parallel plate dipole (PPD) patterned after a design by C. Baum (ref. 4). The sensor consisted of a pair of 0.2 m diameter concentric plates mounted on opposite sides of a common ground plane. Each plate was loaded with an 80 ohm resistive rod in series with a 50 ohm cable matching resistance which served as the signal pickoff point. This configuration resulted in a balanced 100 ohm differential output. The sensor assembly was elevated 0.25 m from the fuselage surface and enclosed in a protective fiberglass fairing. Equivalent height of the sensor (h_{eq}) was calculated to be 0.101 m. Sensor capacitance (C) as derived from reference 4 was 7.1 pF. The equivalent circuit of the sensor is shown in figure 4.

The C_s parameter in figure 4 represents the total stray and distributed capacitance which was found from measurement to be ≈ 1.5 pF. From figure 4, the output voltage of the sensor can be written as:

$$v_o(s) = -R_L C h_{eq} s E(s) \quad (1)$$

where s is the Laplace transform variable, R_L is the load resistance, C is the sensor capacitance, and h_{eq} is the equivalent height of the sensor. Equation

1 is valid provided that:

$$R \ll \frac{1}{2\pi C f_{\max}} \quad \text{and} \quad f_{\max} < \frac{1}{2\pi C(R+R_L)} \quad (2)$$

where f_{\max} is the upper frequency of interest. With the values given, these conditions are satisfied for $f \leq 20$ MHz. Within this frequency range, the sensor responds to the time rate of change of the electric field with a sensitivity constant K_E given by:

$$K_E = RCh_{eq} \approx 7.17 \times 10^{-11} \frac{V-s-m}{V} \quad (3)$$

Since the effects of the sensor mounts and enclosure were not easily calculated, the entire apparatus was tested in a 50 ohm parallel plate transmission line to derive K_E . A continuous wave (CW) test was performed using a sinusoidal signal ranging in frequency from 0.1 to 15 MHz as input to the transmission line. K_E was then calculated from the following time domain equivalent of equation 1:

$$v_o(t) = -R_L Ch_{eq} \frac{dE}{dt} = -K_E \frac{dE}{dt} \quad (4)$$

For sinusoidal excitation in the derivative band of the sensor, equation 4 can be written as:

$$v_o(t) = -K_E \omega A \sin(\omega t) \quad (5)$$

where A is the peak amplitude of the input sinusoid and ω is the radian frequency. When peak readings are taken, equation 5 can be rewritten as:

$$|K_E| = \frac{v_o(t)}{\omega A} \quad (6)$$

K_E was found to be 4.32×10^{-11} V-s-m/V from the CW test, and this was the value used in the data analysis.

The incident magnetic field sensor consisted of a one conductor multi-turn loop patterned after a design by C. Baum (ref. 5). The sensor was a split copper cylinder, 0.635 m in diameter, wrapped with triaxial cable to yield an effective 4 turn loop with an equivalent area A_{eq} of 0.051 m^2 . Sensor inductance of $0.71 \mu\text{H}$ was found from tables developed by C. Baum (ref. 5). From the equivalent circuit shown in figure 5, the sensor output voltage in the complex frequency domain is given by:

$$V_o(s) = A_{eq} s B(s) \quad (7)$$

provided that:

$$R_L \gg R_S \quad \text{and} \quad f_{\max} < \frac{R_L}{2\pi L} \quad (8)$$

For the values given, the self-integrating frequency of the sensor ($R_L/2\pi L$) is marginally greater than the 20 MHz limit of interest. The sensitivity constant for the sensor is simply:

$$K_B = A_{eq} \approx 0.051 \text{ V-s/T} \quad (9)$$

This constant was verified to within $\pm 5\%$ in the parallel plate transmission line, using the CW test technique described earlier.

The two skin current sensors each consisted of a shielded, two turn rectangular half loop (0.027 m high, 0.305 m long) mounted directly on a removable aircraft skin panel. Sensor output was taken from the underside of the panel into a short 100 ohm twinaxial cable. From the loop dimensions, the sensor's equivalent area was calculated to be 0.0165 m^2 . The approximate loop inductance was calculated to be $2.7 \text{ } \mu\text{H}$ from (ref. 7):

$$L = n^2 \mu_o (b+d) \left[\log_e \left[\frac{bd}{a(b+d)} \right] + 0.25 \right] \quad (10)$$

where n is the number of loop turns, b and d are the rectangle dimensions, a is the shield radius and μ_o is the free space permeability.

From Ampere's law and Faraday's law of induction, the induced loop voltage at the sensor output $v_i(t)$ is related to the time derivative of the surface current density J_s on the panel by:

$$v_i(t) = -\mu_o A_{eq} \dot{J}_s \quad (11)$$

where the assumption is made that negligible flux penetrates the underside of the panel.

The sensor equivalent circuit is identical to the magnetic field circuit in figure 5 with the voltage $v_i(t)$ given by equation 11. The Laplace transfer function for the sensor (assuming $r_s \ll R_L$) is given by:

$$v_o(s) = -K_J J(s) \left[\frac{s}{s + R/L} \right] \quad (12)$$

where:

$$K_J = \mu_0 A_{eq} \frac{R_L}{L} \approx 0.723 \text{ A/m-V} \quad (13)$$

The condition ($f_{\max} \ll R_L/2\pi L$) from equation 8 is not met as was the case with the magnetic field sensor, hence the ' $s + R_L/L$ ' term must be retained in equation 12. The resulting time domain relation between the sensor output and the surface current density is therefore:

$$J_s = -\frac{1}{K_J} \left[v_o(t) + \frac{R_L}{L} \int_0^t v_o(t) dt \right] \quad (14)$$

Using this relation, the K_J parameter was verified within $\pm 5\%$ from a CW test similar to the one already described for the electric field sensor.

The transient response characteristics of the sensors were verified in the 50 ohm parallel plate transmission line using a 13.5 V, 12 ns rise step as the input. Figure 6 shows the step input and the corresponding response of each of the sensors. The frequency response plots shown in figure 6 were derived by computing the log magnitude of the Fourier transform of the derivative of each sensor output (a valid technique as long as the excitation function is a good step approximation; i.e. $t_r \leq 15$ ns for 20 MHz).

Recording Equipment

Each sensor output was routed via a short twinaxial cable to a shielded, battery-operated fiber optic link which in turn was connected to parallel digital and analog recording systems. The digital recording system consisted of four Biomation 8100 digital transient recorders which provided threshold triggered records (2048 samples, 10 ns sample interval) of each sensor output. The digital records, together with the acquisition time and aircraft position, were stored on flexible disk. The analog recording system was a multi-channel analog recorder with a bandwidth of 400 Hz to 150 kHz. The continuous analog record was required to identify the particular event in the discharge process which triggered the digital system.

The instrumentation was protected from internal transients and power supply surges through the use of metal enclosures, solid-state transient suppressors and power supply isolation filters. A block diagram of the instrumentation is shown in figure 7.

Timing

The time reference for the entire recording system was taken from the IRIG B time code generated on-board the aircraft. The time code was also transmitted to the various ground sites to permit time correlation between the air and ground data. Resolution of the IRIG B time code, typically limited to ± 0.5 ms

will be improved to $\pm 10 \mu\text{s}$ using correlation techniques on the code waveform after correction for propagation delays.

PROCEDURE

Prior to each flight, functional tests were performed with small loop and dipole antennas driven by a signal generator to insure integrity of the sensor, optic system, and recorders. Sensor outputs were stored and compared daily for any significant variation in signal amplitude or response characteristics. Every two weeks, sensor cabling was disconnected and a signal injected directly into the fiber optic transmitter to insure that the cable insertion losses remained approximately constant. Analog tapes were stripped and degaussed before each flight.

Flights were typically two hours in duration and were taken in the early afternoon when storm activity was verified over the ground site. The aircraft was flown in a 40 km clockwise rectangular pattern around the central site at a nominal altitude of 4 km. The aircraft was restricted from penetrations into developed storm cells although many flights were taken into heavy precipitation areas surrounding the cell area.

Data from the digital system were stored only when a return stroke was visually verified by one of the aircraft observers or when a direct strike appeared to have occurred. When a nearby strike was observed, the approximate range and azimuth were noted for later verification of position data.

RESULTS

Data were obtained from 7 flights in the immediate vicinity of the ground station during the period from 17 August to 28 September 1979. Data from 43 visually verified cloud-ground return strokes were recorded on the airborne analog/digital system and on the VHF source location system. Data from the low frequency electric field antenna site were not usable this year due to operation difficulties. It is anticipated that phase identification can still be accomplished from the low frequency airborne data. Data were also recorded on two separate events believed to have occurred immediately prior to direct aircraft strikes. The direct strike assumption was verified by pilot report and attachment evidence on the aircraft radome. At this time however, the actual phase of the discharge which was recorded is not known. To date, the only data analyzed in detail are the high frequency airborne recordings. The following results are therefore presented without benefit of phase identification or accurate source location.

The high frequency recordings were grouped into three general categories: first return stroke, subsequent return strokes, and unidentified. The last category arises from the substantial number of waveform which were of the same approximate peak amplitude as the return stroke data but were isolated and impulse-like with total duration times on the order of 100-200 ns and were devoid of any of the classic return stroke waveshape characteristics.

First And Subsequent Stroke Characteristics

The return stroke waveforms were classified as first or subsequent based on the characteristics discussed by Weidman and Krider (ref. 8). Figure 8 shows typical first and subsequent return stroke electric field waveforms taken from the data. The first stroke is characterized by a slowly rising (1 to 3 μ s) concave front (F in fig. 8a) sometimes followed by an abrupt fast transition to peak portion (R in fig. 8a) lasting on the order of 100-700 ns. Subsequent strokes are further characterized by the absence of a slow front portion and the relatively smooth and structureless subsidiary peaks (a,b,c in fig. 8b) compared to those of the first strokes.

Front And Fast Transition Times

The 10-90% rise time was calculated for the fast transition portion (R) of the first stroke waveforms. Average R for 22 waveforms was 390 ns. For comparison, the average front plus fast transition time (F+R) was found to be 2.2 μ s. Relative distributions of the two rise times are shown in figure 9. Based on the criteria described earlier, four electric field waveforms were classified as subsequent strokes. Average 10-90% fast transition time for these strokes was 550 ns. The peak electric and magnetic field levels recorded ranged from 13 to 146 V/m and 0.017 to 0.145 A/m respectively, indicating an approximate distance from the aircraft of 5 to 50 km (ref 9).

The average fast transition time quoted for both first and subsequent return strokes are approximately two times slower than those reported by Weidman and Krider (ref. 8). The discrepancy is probably due to several factors. First, the 50 ns resolution claimed for direct interpretation of oscilloscope photographs may be in error since this translates to a horizontal axis distance of only 0.25 mm assuming a 10 cm scope face and 20 μ s sweep. The rise times in this report were computer calculated from the digitized record and have a maximum resolution of two times the sample interval, or approximately 20 ns on a 20 μ s record. Second, the rise times in this report were not corrected for the HF propagation losses over land which was not a factor in Weidman and Krider's data since the propagation was over salt water. Third, and probably most importantly, no standard method exists for defining the beginning of the F and R waveform transition points.

Rise Time Calculation Procedure

In this paper, a consistent method was adopted in which the F and R points were defined by the intersection point of two straight lines whose slopes were given by the best fit straight line through two waveform segments chosen well away from the waveform transition areas. Figure 10 illustrates the method using a first stroke waveform where the F and R points are marked by triangles and the corresponding best fit lines are shown dashed. In the data presented, the best fit lines were computer calculated using the method of least squares but a graphic approximation would be adequate in most cases.

Rise Times and Aperture Coupling

From a standpoint of developing a good model of the aircraft/lightning interaction, at least during the direct attachment return stroke phase, the importance of accurate radiation field rise times cannot be overemphasized. As evidence of this, consider the above ground field equations developed by Uman et al. (ref 10), which describes the time derivative of the magnetic field $dB(t)/dt$ at an altitude z , slant range R , and horizontal range r from the idealized return stroke:

$$\frac{dB(t)}{dt} = \frac{\mu_0 v(t)}{4\pi R} \left[\frac{r}{R^2} i(Z, t-R/c) + \frac{r}{cR} \frac{\partial i(Z, t-R/c)}{\partial t} + \text{Image Terms} \right] \quad (15)$$

where $v(t)$ is the vertical stroke velocity (assumed constant), c is the speed of light and Z is the dipole height above the ground plane. The image term is given by substituting the image slant range R_I and image height $-Z_I$ for R and Z respectively into the first term in equation 16. If $r \geq 3(Z_I + z)$, the image term contribution is approximately equal to the source term, and the Laplace transform of equation 15 (omitting the phase delay term due to the retarded time) is:

$$I(s) \approx \frac{2\pi r c}{\mu_0 v} B(s) \left[\frac{r}{s + c/r} \right] \quad (16)$$

From equation 16, it is apparent that the return stroke current is approximately proportional to the radiation component of the magnetic field provided:

$$R \geq 3(Z_I + z) \quad \text{and} \quad f_{\min} \gg c/2\pi r \quad (17)$$

where f_{\min} is the minimum frequency of interest.

Now consider further the aircraft involved in the return stroke phase of a lightning. After entry and exit points have been established, the channel discontinuities caused by the aircraft are small and the return stroke current passes through the aircraft essentially unperterbed. The return stroke current $i(t)$ results in an average magnetic field tangential to a small aperture and an electric field normal to the aperture given by:

$$h_T(t) = i(t)/2\pi r_{\text{ave}} \quad \text{and} \quad e_n(t) = \rho(t)/\epsilon_0 \quad (18)$$

where r_{ave} is the average equivalent radius of the principal conducting element (i.e. wing, fuselage), $\rho(t)$ is the time varying charge density, and ϵ_0 is the permittivity of air. As discussed by Cabayan (ref. 11), the fields interior to the aperture are proportional to the exterior fields as follows:

$$\begin{aligned} e_N(t) &\propto \left[\frac{1}{R^3} e_N(t) \quad , \quad \frac{1}{R^2} \dot{e}_N(t) \right] \\ e_T(t) &\propto \left[\frac{1}{R^2} \dot{h}_T(t) \quad , \quad \frac{1}{R} \ddot{h}_T(t) \right] \\ h_T(t) &\propto \left[\frac{1}{R^3} h_T(t) \quad , \quad \frac{1}{R^2} \dot{h}_T(t) \quad , \quad \frac{1}{R} \ddot{h}_T(t) \right] \end{aligned} \quad (19)$$

where the primed quantities refer to the interior fields and R is the distance away from the aperture as shown in figure 11. Thus, the aperture coupled fields on the aircraft are dependent not only on the stroke current but also on its first and second derivatives, and the importance of accurate return stroke rise time definition becomes evident. Of course, the rise time can only be used to calculate an average derivative. To the extent that the return stroke average derivative varies from its true instantaneous derivative, the expected aperture coupled fields will be in error. Thus from a coupling standpoint, the best rise time calculation is that which provides derivatives agreeing most closely with the instantaneous derivative.

Peak and Average Derivatives

A comparison was made between the peak instantaneous derivative (D_p) taken from the unintegrated record and the average derivatives calculated from the F+R intervals (D_{F+R}) and the R interval only (D_R) taken from the integrated initial stroke record. From a 15 waveform sample, the following average results were obtained:

$$D_p = 7.9 D_{F+R} \quad \text{and} \quad 2.3 D_R \quad (20)$$

These averages agree well with the work of Weidman and Krider (ref. 8) who estimated peak derivative values 3 to 10 times faster than those inferred by straight line approximation. The distribution of D_p taken from 23 unintegrated electric field records is shown in figure 12 where the values have been normalized to 100 km. (ref. 12). Again, the average D_p of 20.3 V/m- μ s at 100 km are in very close agreement with the estimates by Weidman and Krider (ref. 8). The fast transition derivative D_R is evidently a reasonable approximation to the peak derivative while the D_{F+R} derivative is definitely not suitable for accurate estimation of the peak return stroke derivative.

Peak Return Stroke Derivatives

Given the average observation distance of 20 km and the short record length of 20 μ s, the conditions given in equation 17 were satisfied for the data obtained, and the D_p values were used to infer peak return stroke current derivatives from the time domain equivalent of equation 16:

$$\frac{di(t)}{dt} = \frac{2\pi rc}{vZ_0} \left[\frac{dE(t)}{dt} \right] \quad (21)$$

where Z_0 is the free space impedance (377 ohms), and the quantity ($1/\mu_0 \times B(s)$) has been replaced in equation 16 with the radiation field equivalent term ($1/Z_0 \times E(s)$). If the return stroke velocity $v(t)$ is assumed constant at 1×10^8 m/s (Uman, ref. 10), the peak return stroke derivative inferred from equation 21 ranged from 30 to 150 kA/ μ s with an average value of 100 kA/ μ s.

Unidentified Waveforms

As mentioned earlier, a substantial number of waveforms were recorded which could not be identified as return stroke fields. Since the procedure was adopted to save only those data resulting from visually verified discharges, it must be assumed that these waveforms were associated with the return stroke

process. From the isolated pulse-like nature of the data, one could further assume the data are associated with the preliminary leader formation although this assumption cannot presently be verified.

The pulse amplitudes were in the same range as those found in the return stroke data (10-100 V/m) but were characterized by high frequency content and pulse rise times ranging from 300 ns to 50 ns (or less). Figure 13 illustrates a complete set of typical pulse waveforms taken from the free field and skin current sensors. A more complete analysis of the skin currents and pulse data will be made when phase and source location data are available.

CONCLUSIONS

The average front plus fast transition 10-90% rise time for 22 initial strokes was found to be 2.2 μ s. The average 10-90% rise time for the fast transition portion only was 390 ns. The fast transition times were approximately two times slower than those reported by Weidman and Krider. Peak return stroke current derivatives are important in simulating aperture coupled fields on the aircraft. The peak electric field derivatives calculated from the initial stroke fast transition time averaged 2.3 times lower than the peak derivatives taken directly from the unintegrated sensor output. The electric field peak derivatives averaged 20.3 V/m- μ s when normalized to 100 km; a value in good agreement with estimates of Weidman and Krider. The peak return stroke derivatives inferred from the electric field derivatives, assuming an average 30 kA strike, ranged from 30 to 150 kA/ μ s with an average value of 100 kA/ μ s.

Unidentified pulses were recorded which had peak magnitudes of 10-100 V/m and rise times ranging from 300 ns to 50 ns or less. The pulses are thought to be associated with the return stroke leader process. The high frequency characteristics of the pulses may present a significant coupling source to the aircraft and should be investigated further.

REFERENCES

1. Fisher, R.J. and M.A. Uman, Measured Electric Field Risetimes for First and Subsequent Lightning Return Strokes, J. Geophys. Res., V. 77, No. 3, Jan 1972.
2. Lennon, K., LDAR III - System Description and Performance Objectives, Federal Electric Corporation, RF Systems Branch, Kennedy Space Center, 26 April 1977 (unpublished).
3. Rustan, P.L., Properties of Lightning Derived From Time Series Analysis of VHF Radiation Data, PhD dissertation, University of Florida, 1979.
4. Baum, C.E., the Circular Parallel Plate Dipole, AFWL Electromagnetic Pulse Sensor and Simulation Notes, AFWL EMP 1-6, Note 80, July 1971.
5. Baum, C.E., A Technique for Distribution of Signal Inputs to Loops, AFWL Electromagnetic Pulse Sensor and Simulation Notes, AFWL EMP 1-1, Note 23 Dec 1966.
6. Baum, C.E., Further Considerations for Multiturn Cylindrical Loops, AFWL Electromagnetic Pulse Sensor and Simulation Notes, AFWL TR 73-168, Note 127 April 1971.
7. Grover, F.W., Inductance Calculations, Dover Publications, N.Y., N.Y., 1946.
8. Weidman, C.D. and E.P. Krider, The Fine Structure of Lightning Return Stroke Waveforms, J. Geophys. Res., V. 83, No. C12, Dec 1978.
9. Uman, M.A., R.D. Brantley, Y.T. Lin, J.A. Tiller, E.P. Krider, and D.K. McLain, Correlated Electric and Magnetic Fields From Lightning Return Strokes, J. Geophys. Res., V. 80, No. 3, Jan 1975.
10. Uman, M.A., Y.T. Lin, R.B. Standler, M.J. Master, and R.J. Fisher, Calculations of Lightning Return Stroke Electric and Magnetic Fields Above Ground, Symposium on Lightning Technology, NASA CP-2128, 1980.
11. Cabayan, H.S. and J.E. Zicker, Review of Article "A case for Submicrosecond Rise Time Lightning Current Pulses for use in Aircraft Induced Coupling Studies", by D.W. Clifford, E.P. Krider, and M.A. Uman, Lawrence Livermore Laboratory, University of California, Memorandum No. EMS 80-0016, Jan 17, 1980.
12. Krider, E.P., C.D. Weidman, and R.C. Noggle, The Electric Fields Produced by Lightning Stepped Leaders, J. Geophys. Res., V. 82, No. 6, Feb 20, 1977.

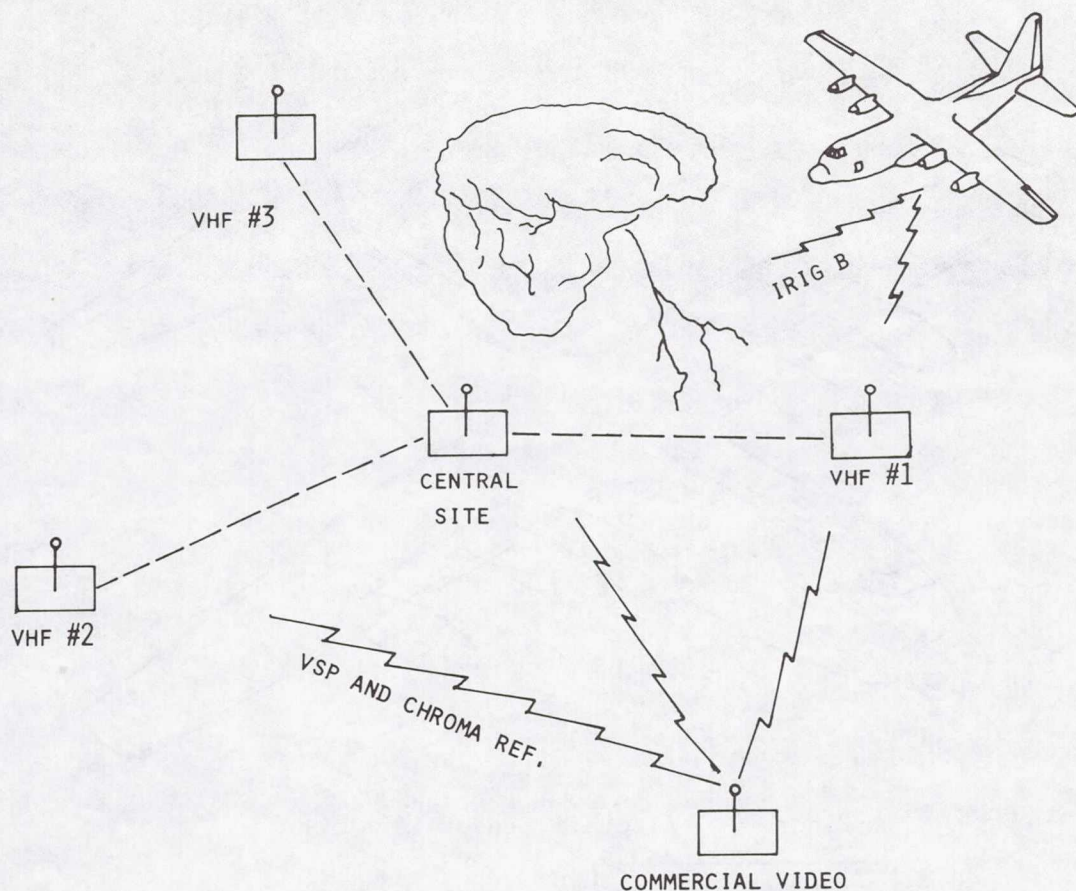


Figure 1. Orientation of Ground Sites and Test Aircraft

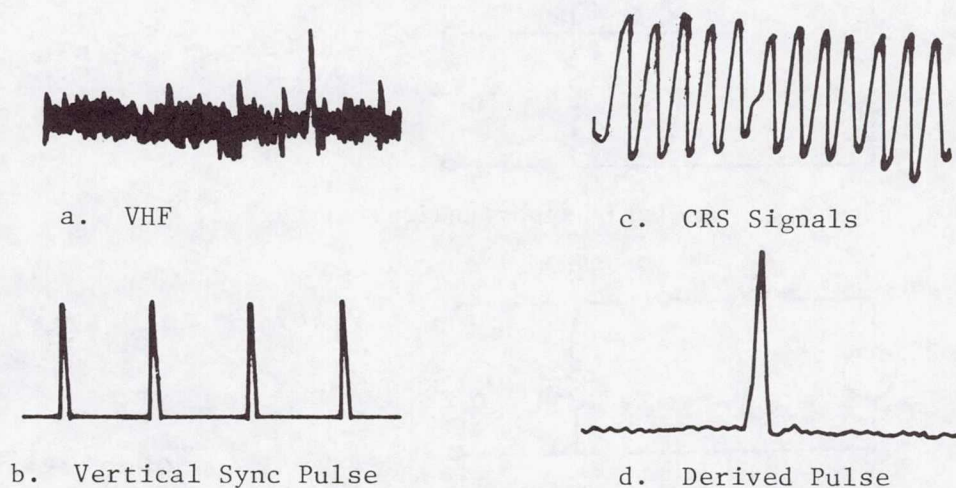


Figure 2. Illustration of Typical VHF Source Pulses & Timing Signals (not to scale)

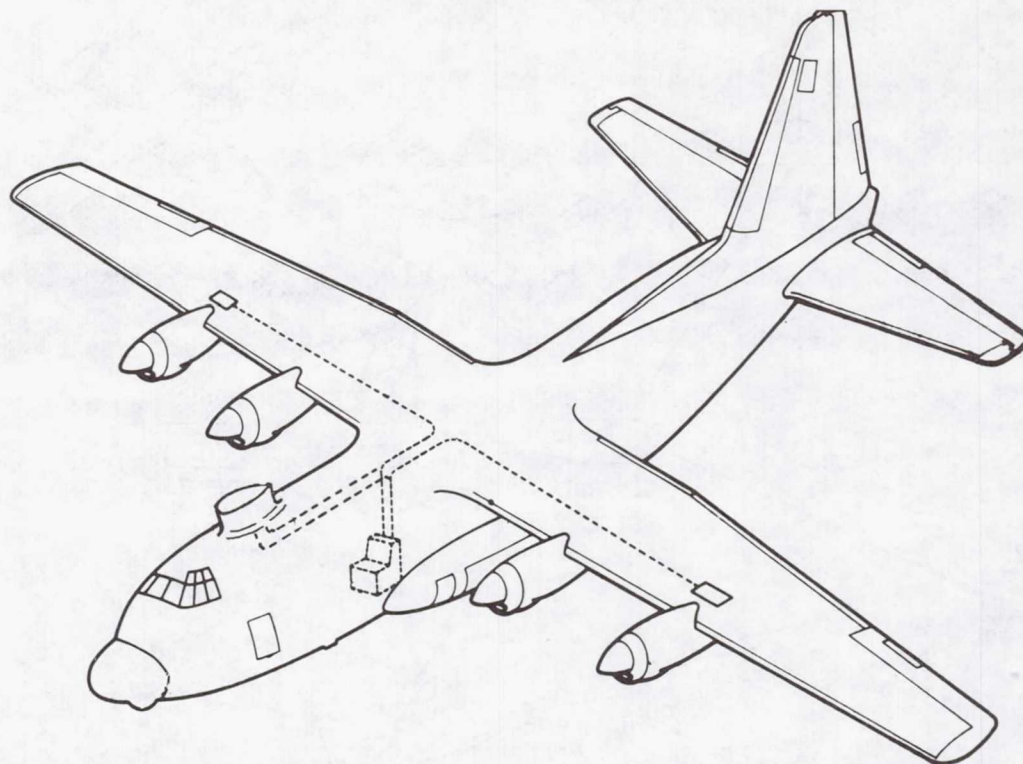


Figure 3. Aircraft Sensor Locations

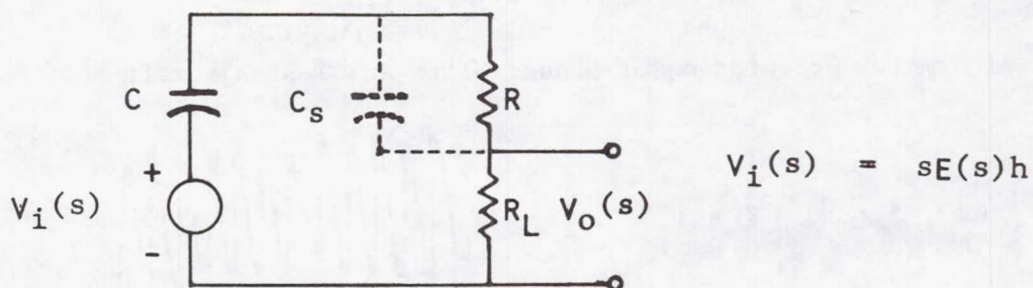


Figure 4. E Field Sensor Equivalent Circuit

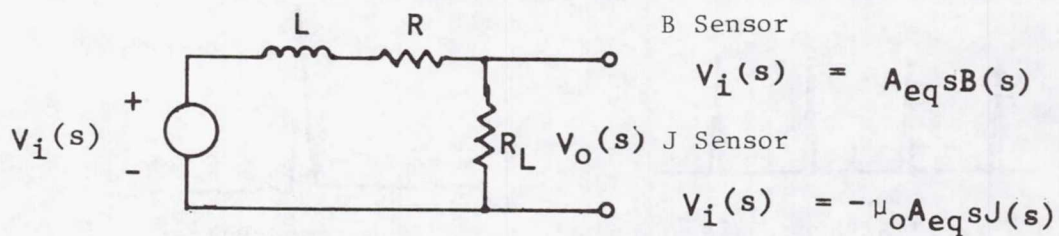
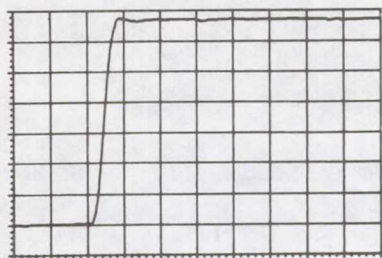
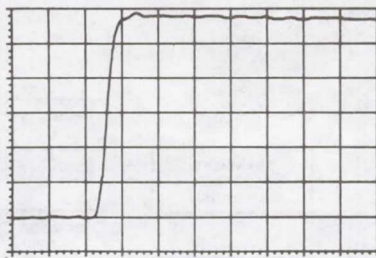


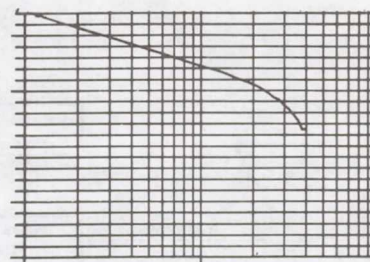
Figure 5. B and J Sensors Equivalent Circuit



Applied Voltage

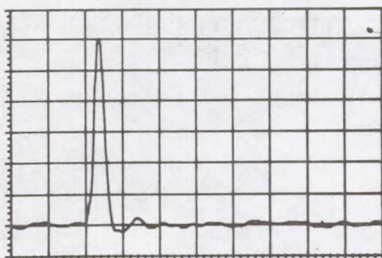


Applied Current

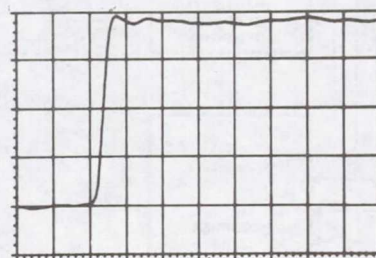


Applied Spectrum

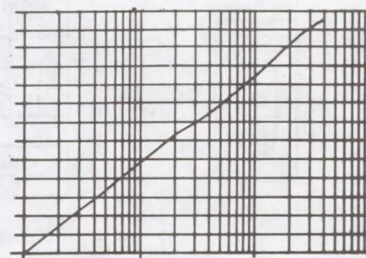
a. Input Characteristics



Output Voltage

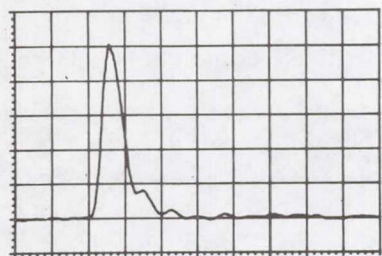


Integrated Output

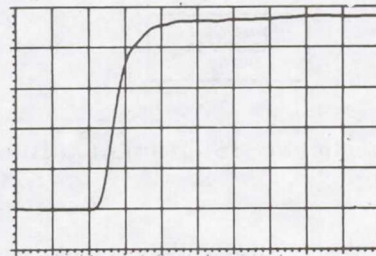


Frequency Response

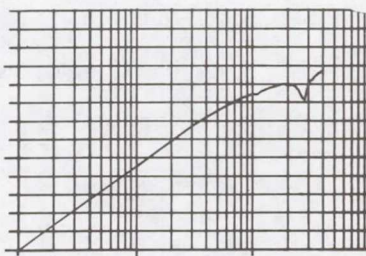
b. Electric Field Sensor



Output Voltage

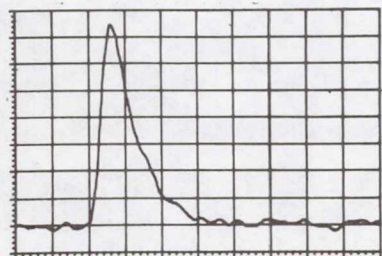


Integrated Output



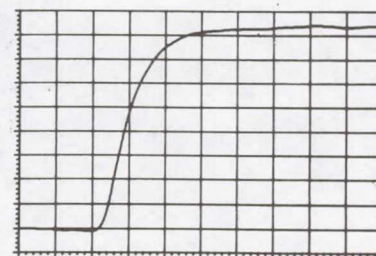
Frequency Response

c. Magnetic Field Sensor



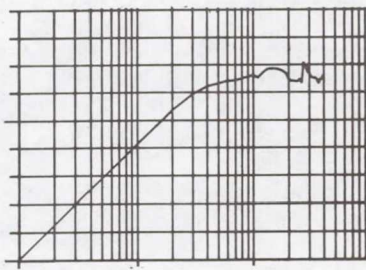
50 nanoseconds/div

Output Voltage



50 nanoseconds/div

Integrated Output



0.1 1.0 10
MegaHertz

Frequency Response

d. Surface Current Sensor

Figure 6. Sensor Response Characteristics

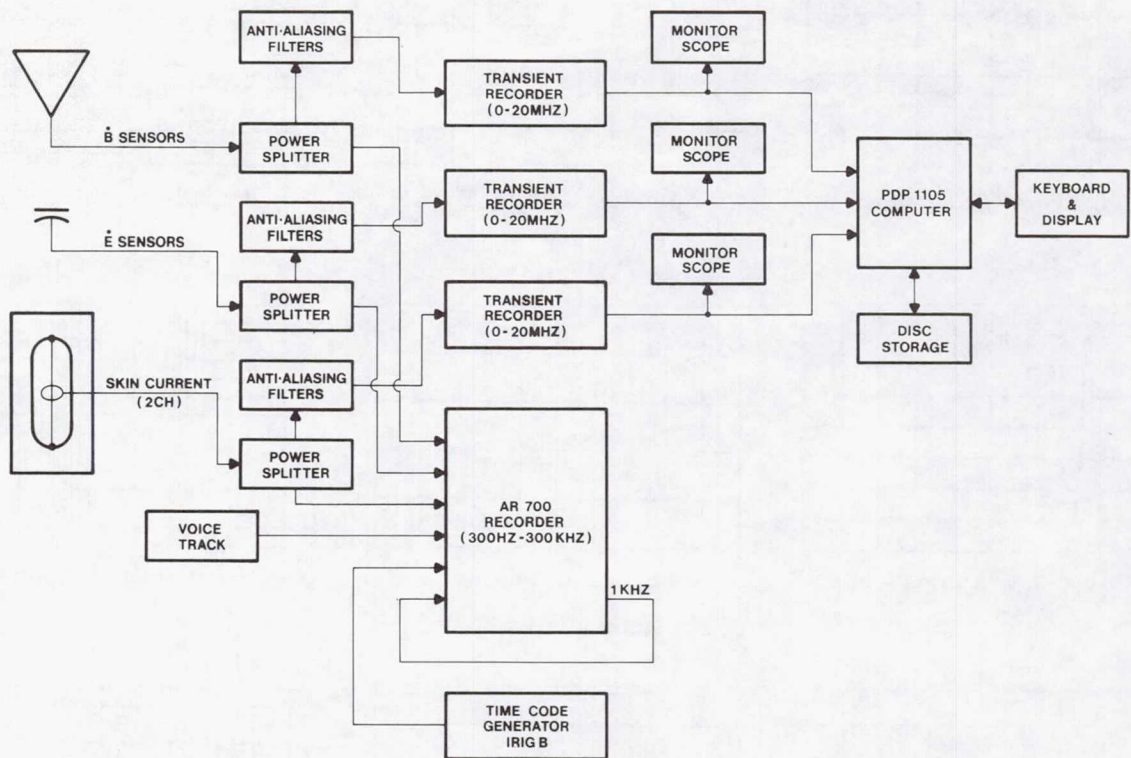
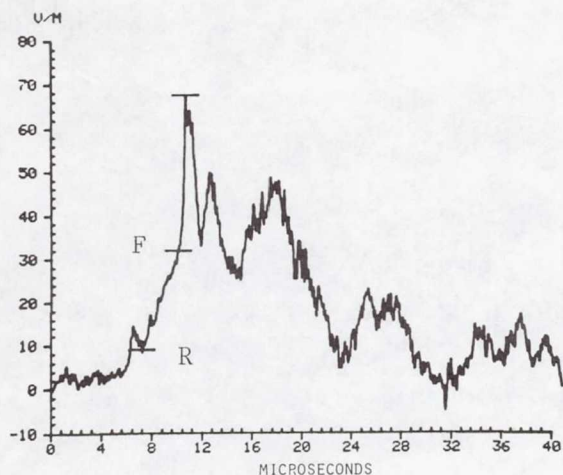
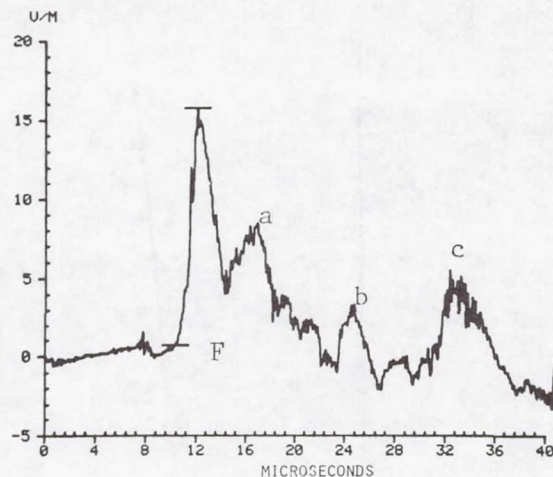


Figure 7. Airborne Instrumentation Diagram

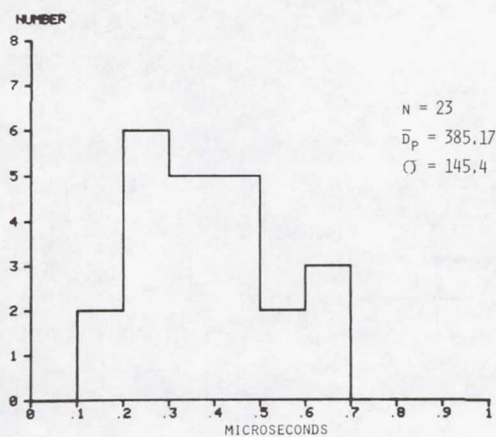


a.

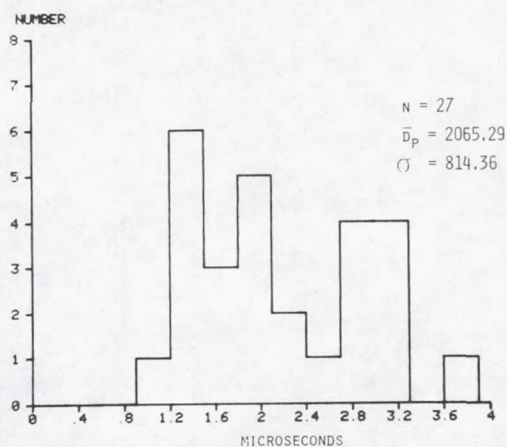


b.

Figure 8. Typical First (a) and Subsequent (b) Return Stroke Radiation Field Waveforms



a.



b.

Figure 9. Distribution of First Stroke Risetimes : (a) Fast Transition Time Only, and (b) Fast Transition Plus Slow Front.

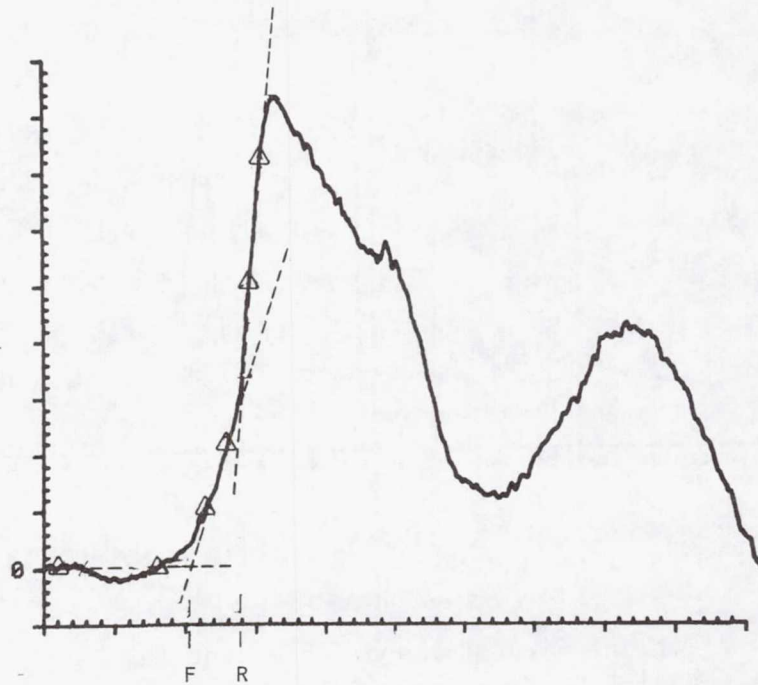


Figure 10. Rise Time Calculation from Best-Fit Segment Intersection

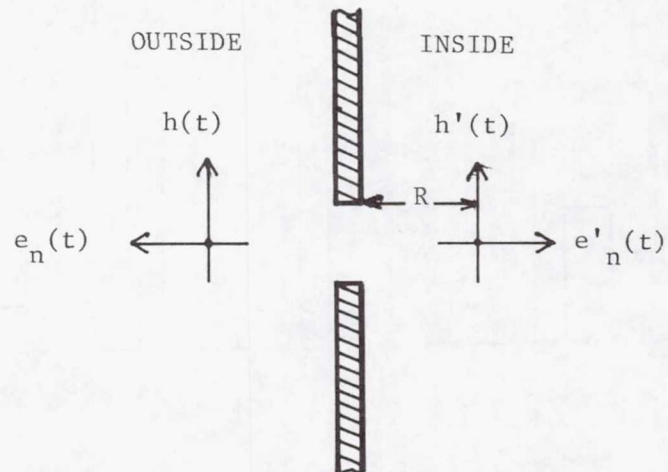


Figure 11. Aperture Geometry

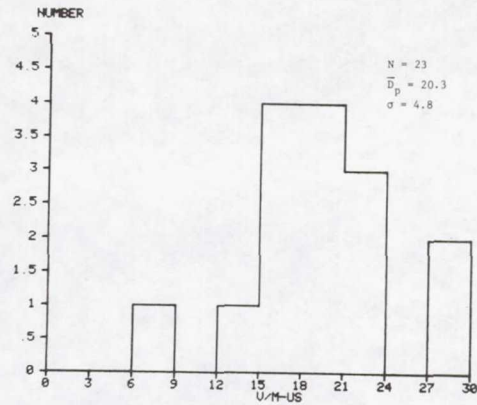


Figure 12. Distribution of Peak Electric Field Derivatives Normalized to 100 km.

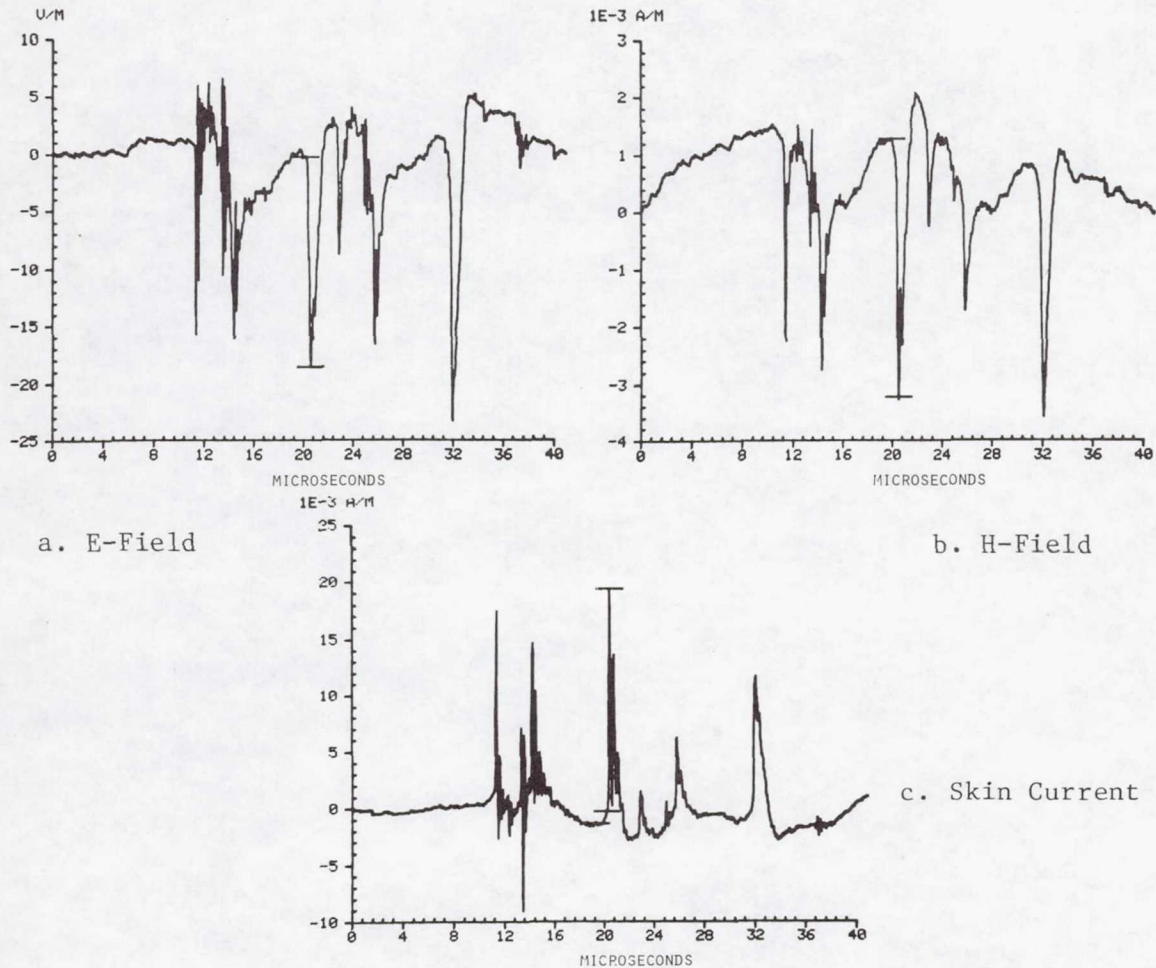


Figure 13. Typical Electric and Magnetic Field Pulse Waveforms and Corresponding Induced Aircraft Skin Current

Page intentionally left blank

MAGNETIC TAPE LIGHTNING CURRENT DETECTORS

Keith E. Crouch
Lightning Technologies, Inc.

W. Jafferis
National Aeronautics & Space Administration

SUMMARY

Development and application tests of a low cost, passive, peak lightning current detector (LCD) found it to provide measurements with accuracies of $\pm 5\%$ to $\pm 10\%$ depending on the readout method employed. The LCD, which was invented at the National Aeronautics and Space Administration, John F. Kennedy Space Center (NASA-KSC), uses magnetic audio recording tape to sense the magnitude of the peak magnetic field around a conductor carrying lightning currents. The test results showed that the length of audio tape erased was linearly related to the peak simulated lightning currents in a round conductor.

Accuracies of $\pm 10\%$ were shown for measurements made using a stopwatch readout technique to determine the amount of tape erased by the lightning current. The stopwatch technique is a simple, low cost means of obtaining LCD readouts and can be used in the field to obtain immediate results. Where more accurate data are desired, the tape is played and the output recorded on a strip chart, oscilloscope, or some other means so that measurements can be made on that recording. Conductor dimensions, tape holder dimensions, and tape formulation must also be considered to obtain a more accurate result. If the shape of the conductor is other than circular (i.e. angle, channel, H-beam) an analysis of the magnetic field is required to use an LCD, especially at low current levels.

BACKGROUND

To design systems that can survive lightning strokes, a knowledge of the magnitude of those lightning strokes must be known. To quote from Lord Kelvin (1824-1907), "I often say that when you can measure what you are speaking about, and express it in numbers, you know something about it; . . ." (ref. 1) But since lightning strikes occur at statistically governed times and places, direct measurements by ordinary means are not capable

of providing enough data to suitably describe the statistical nature of lightning. This has long been recognized along with the need for inexpensive recording devices with which to measure lightning parameters such as the peak current amplitude (ref. 2).

The first such devices used were magnetic links which were introduced in the early 1930's. These devices are small packages of magnetic steel positioned next to a conductor that carried lightning currents (ref. 3). The magnetic field around the conductor will magnetize the steel to an extent dependent on the magnitude of the current. Comparing the magnetized link to laboratory exposed links provides a method of determining the peak current.

The data collected using these magnetic links provided a large portion of the statistical base for present estimates of the lightning peak current distributions.

Other, more sophisticated systems have and are presently being installed to gather more data on lightning (ref. 4).

This paper summarizes work done to calibrate and develop application techniques for a new, passive, peak lightning current detector (LCD). The LCD developed by NASA-KSC was reported in 1976 (ref. 5) and patented in 1978 (ref. 6). The LCD consists of a length of magnetic audio recording tape upon which a reference continuous wave voltage signal has been recorded. When this tape is placed in the magnetic field near a current carrying conductor, that field will change the magnetic domains on the tape.

The magnetic intensity (H) of the field around a conductor is proportional to radial distance (r) and current (i);

$$H = \frac{i}{2\pi r} \quad (1)$$

If the tape is positioned along the radial distance, then the length of tape affected will indicate the current carried by the conductor. The early work has shown that, not only does the principle work, but provides reasonably accurate data at relatively low initial costs.

An LCD is not field (current) direction sensitive, whereas a magnetic link remains magnetized in the direction of the impressed field. Two successive strokes of opposite polarity will leave a magnetization level on the magnetic link which bears no relationship to either peak. Since there is no way a current can reconstruct the reference signal on the magnetic tape, it will always indicate the highest peak current.

APPLICATION OF LCD'S

There are a variety of possible applications where the LCD could provide useful information concerning peak lightning currents in conductors. Data on lightning current magnitudes in telephone cables, radio broadcast towers, power transmission systems, oil well towers, etc., would be very useful in evaluating the lightning protection designs for these systems.

Figure 1 shows a typical mounting for an LCD on a conductor. Figure 2 is a photo of an LCD using a cassette tape installed for calibration tests at Lightning Technologies, Inc. The magnetic tapes are stored in the cassette holder with a portion pulled down inside the tube on the tape carrier. The carrier is positioned so that the flat (width) of the tape is perpendicular to the plane of the conductor. The LCD is shown secured to a conductor by means of a plastic mount and plastic wire ties. Any convenient method of mounting may be used, provided it holds the tube in the desired location and orientation and contains no iron parts that would affect the magnetic fields in the region of the tape.

When an LCD is installed where more than one conductor is present, magnetic fields from the other conductors will affect the results. The effects can be minimized by mounting the LCD so that other conductors are 25 feet or more away and orienting the LCD so that its points out of or away from the other conductors. Measurements using LCDs with spacings less than 25 feet between conductors will require sophisticated means of interpreting the data since analysis of the magnetic fields will be necessary in order to interpret the tape recordings.

Magnetic Tape Types

The magnetic tape utilized in an LCD depends somewhat on the use and required accuracy. The calibration factors for different manufacturers' tapes vary by up to $\pm 10\%$. For many applications, other factors (such as the readout method) will limit the overall accuracy of the LCD and any convenient ferric oxide* tape can be used. When a calibration factor averaged from all tapes tested is used, the results should not be in error by more than $\pm 10\%$.

* Chrome tapes, which are more resistant to change, would exhibit smaller signal erasures for a given current level and, therefore, were not evaluated for these applications.

A more important consideration is the selection of reel-to-reel tapes or cassette tapes. Both give the same technical result, but the difference lies in the readout method. The reel magnetic tape is cut, positioned down one side of the tape carrier and back up the other side, and attached at the top. After exposure, it must be removed and spliced to pieces of reference tape of sufficient length to allow it to be played.

A cassette tape will have the cassette mounted in the top of the tape holder with a portion of the tape pulled down into the tube by the tape carrier. After exposure, the tape is wound back into the cassette, and if desired, notes concerning the exposure could be recorded on the tape (date, time, etc.). The cassette can then be advanced and exposures made so that the entire history of the site can be kept on one cassette. Also, since splices are not needed, the cassette can be played on a battery operated player in the field and the peak current estimates made without going to a laboratory.

Since the reel tapes must be respliced on leader tapes for playback, an external means is needed to insure that a strike has occurred before going through the effort of reading the tape. Checking a cassette tape by playing it in the field eliminates the need for the external indicator.

If a cassette is selected, a quality cassette, such as those manufactured by Maxell (ref. 7) is suggested, since the cassette shell is an integral part of the tape transport system. The tape to head contact pressure is controlled by the pressure pad which is also part of the cassette shell. Also, a shell fastened together with screws rather than glued is preferred since, in case of damage, the tape can be salvaged or repairs made. Tape length should be 60 minutes total or less to avoid working with the very thin tapes used for long playing cassettes (ref. 8).

Reference Signal Recording

The LCD technique depends on being able to detect the length of tape upon which a reference signal has been erased. A typical erasure is shown in figure 3. This sketch illustrates the output of a tape player as it would appear when displayed by an oscilloscope or high frequency strip chart recorder (Visicorder).

From figure 3, it can be seen that the erased portion goes gradually from full reference signal to no signal. The reference signal level must, therefore, be very uniform or consistent to detect where an erasure begins. If for example, the reference were to randomly vary by 20%, then the detection of where an erasure began would be almost impossible. For consistent LCD readings, the reference signal level, when played back, should not vary by more than $\pm 5\%$.

Theoretically, any reference signal level and frequency can be used. However, as a practical matter, if the level is too low, noise will be a problem, and if it is too high, the recorder/player will saturate and/or limit the output. Therefore, the level should be set at a mid-range value, usually specified in the recorder manufacturer's instructions. Most tape recorder/players have the best frequency response in the 100 Hz to 4000 Hz range and so the reference signal frequency selected should fall in this range. For the cassette tests conducted here, 400 Hz, which is close to the musical note Middle C (440 Hz), was selected.

Tape Readback Method

Once a magnetic tape has been exposed to a lightning current magnetic field, a portion of the tape will have been erased. Actually, exposure to the magnetic field magnetizes all the domains on the tape into saturation in the same direction - a DC condition - and the tape player needs a varying magnetic domain pattern - an AC condition - for it to respond. At greater distances and/or lower magnetic intensities, the number of disturbed domains decreases and the original reference signal becomes dominant again.

Measuring the length of tape on which the reference signal is erased requires playing the tape on a player. The speed at which the player operates is quite important and should be known to an accuracy at least greater than the desired measurement error. A length of prerecorded tape can be marked at intervals of 1.5 m and the time between marks measured while the player is operated. A simple marking system consists of placing small length (0.3 cm) of splicing tape over the oxide on the magnetic tape. Care must be taken to insure that the splicing tape adhesive does not cause the magnetic tapes to stick in the cassette. Timed tapes are also commercially available. Battery operated players especially must be checked for speed quite often as they tend to slow down as the batteries wear out.

A relatively simple method for determining the length of erased tape is to measure the time that the reference signal is absent with a stopwatch. Since the human ear responds to logarithmic changes in sound, a VU meter in parallel with a speaker makes the change visually detectable as well as audible. Such a system is shown pictorially and schematically in figure 4.

The volume on the player is adjusted so that the VU meter reads 100% (0 dB) during the reference signal. When the exposed portion of the tape passes, the meter will dip and the time between the 80% points can be measured with a stopwatch. Calibration tests using this method indicate that an accuracy of $\pm 10\%$ is possible when measurements are made using this method.

Low peak currents (less than 7 kA) are hard to measure with this technique because the erasure times (0.1 to 0.5 seconds) approach a person's reaction time, making large errors (100%) quite possible.

More accurate measurements of the erasure time can be made if the output of the tape player is displayed and recorded on an oscilloscope or a strip chart recorder. However, the writing speed of the strip recorder or oscilloscope must be known as accurately as the player speed. The time, or length of tape erased, can then be determined by measurements on the strip chart or oscillogram. Assuming that the player and recorder speeds are known to sufficient accuracy, measurements made with such systems are accurate to within $\pm 5\%$.

Magnetic Tape Holder Effects

In the discussions thus far, the total length of magnetic tape erased has been measured. This represents the distance from where the erasure starts to the bottom of the LCD and back to where the erasure ends on the back side of the tape carrier. So the tape on the backside of the tape carrier is really in parallel with that on the front side and both are erased simultaneously during exposure. The tape erasure distance is $1/2$ of the distance from where the erasure starts to where it stops. Positioning the tape in this manner eliminates the need for determining where the tape reaches the bottom of the LCD. If the tape was only placed on one side of the tape holder, it would have to be spliced at the bottom end and data could be lost during the process.

From equation 1 ($H = i/2\pi r$), it can be seen that for a given current, H is inversely proportional to radial distance, r ; but r is measured from the center of the conductor. So the thickness of the holder bottom plate and $1/2$ of the diameter of the conductor must be added to $1/2$ the length of tape erased in order to compare tapes exposed in different holders and/or on different diameter conductors.

The length of erased tape measured also includes the thickness of the tape carrier. If the tape carrier was infinitely thin, the magnetic tape would fold directly back on itself and no extra tape would be involved, but since it is not, extra tape is required. Even though these dimensions will be small in a well designed holder, they can cause errors at low current levels because the length of the erased tape is short. The effects of the tape holder can be designed out if the tape carrier thickness is made twice the end cap thickness.

Other, less obvious errors can be introduced at low levels if the magnetic tape is not centered over the conductor. These errors will generally be small but questions can be eliminated if guides are provided on the tape carrier and the LCD to insure that the tape is centered over the conductor.

Magnetic Tape Calibration Factors

For many years, peak current accuracies of 5% to 10% will be sufficient and they should use ferric oxide cassette tapes and stopwatch readouts due to the simple procedures involved. It would still be advisable to measure the tape player speed since many inexpensive players, and especially battery operated players will vary more than $\pm 10\%$ from the standard 4.76 centimeters per second (1 7/8 in/s). Also, currents of less than 4 kA cannot be measured accurately by this method and the conductor should not exceed 1.3 cm (1/2 in) diameter.

When the stopwatch times are measured between 80% of reference signal points and the above conditions are met, the magnetic tape calibration is:

$$4.3 \text{ kA/s}$$

If the player is operated at speeds other than standard, the factor must be adjusted accordingly.

For those investigators desiring a more precise measurement, the erasure should be measured by recording the output of the player on an oscilloscope or a strip chart recorder. Again, player and recorder speeds must be known to accuracies better than the desired results. Also, attention must be given to holder and conductor dimensions. The tape formulation also begins to play a part in the readout.

Since the holder and conductor dimensions as well as player and recorder speeds will have to be considered in the measurements, the calibration factors are listed as a function of erased tape length for various measurement points (50%, 80%, and 90%) and manufacturers. The calibration factors are:

	50%	80%	90%
Reel Tapes - Group 1*	2.51 kA/cm	1.95 kA/cm	1.75 kA/cm
Reel Tapes - Group 2*			1.40 kA/cm
Cassette - Group 1*	2.53 kA/cm	1.88 kA/cm	
Cassette - Group 2*	2.53 kA/cm	1.78 kA/cm	

* Group 1 tapes manufactured by Ampex & Maxell; Group 2 tapes manufactured by Scotch and BASF.

The total length of tape erased is determined by multiplying the measurement (strip chart or oscillogram) by the appropriate player and recorder speeds. This length must then be divided by two to account for the tape being folded. Then the distance from the bottom of the tape to the center of the conductor (holder bottom cap thickness + $1/2$ conductor diameter) minus $1/2$ of the tape carrier thickness, must be added to the length. When multiplied by the appropriate above calibration factor, the peak current measured is then determined.

REFERENCES

1. Richards, J. A.; Sears, F. W.; Wehr, M. R.; and Zemansky, M. W.: Modern University Physics, Addison-Wesley Publ. Co., Inc., 1960 p. 2.
2. McEachron, K. V.; and Patrick, K. G.: Playing with Lightning. Random House, 1940, pp. 98-102.
3. Foust, C. M.; and Kuehni, H. P.: The Surge-Crest Ammeter, General Electric Review. Vol. 35, no. 12, 1935, pp. 664-648.
4. Schneider, H. M.; and Stillwell, H. R.: Measurement of Lightning Current Waveshapes on Distribution Systems. IEEE-PES Summer Power Meeting. Vancouver, B. C., Canada July 1979.
5. Livermore, S.: Development of Lightning Current Detector, NASA TR-1482, 1976.
6. Livermore, S. F.: Lightning Current Detector. U. S. Patent 4112357, Sept. 1978.
7. Maxell Corporation of America, 60 Oxford Drive, Moonachie, New Jersey 07074.
8. Clyatt, S. P.: Unpublished Data, NASA-KSC, 1979.

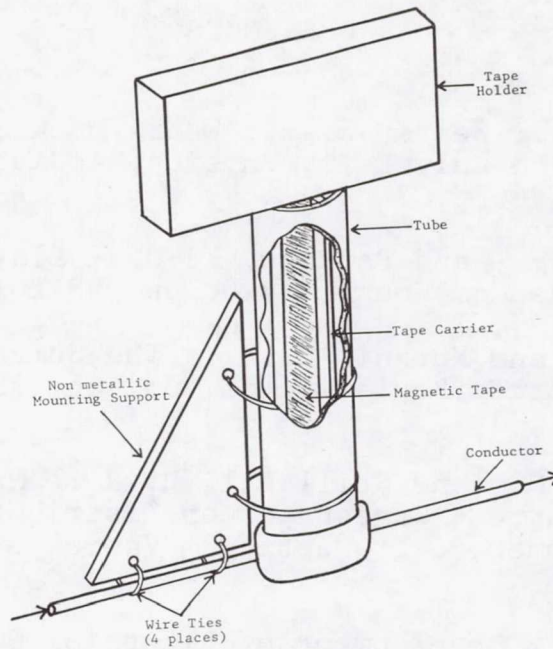


Figure 1.- Typical LCD mounted on a conductor.

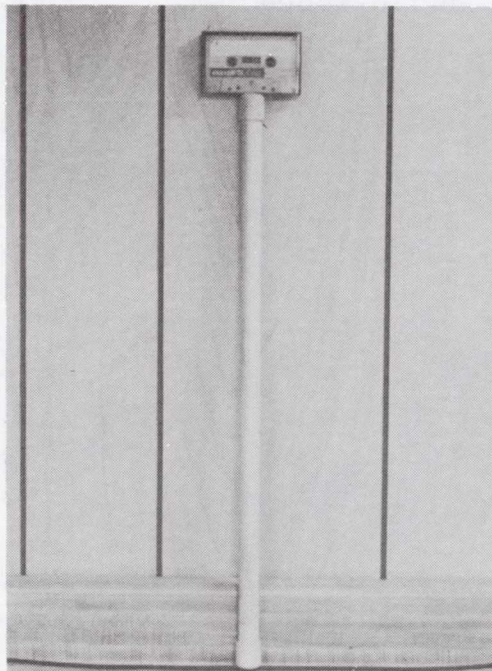


Figure 2.- LCD installed for test at Lightning Technologies, Inc.

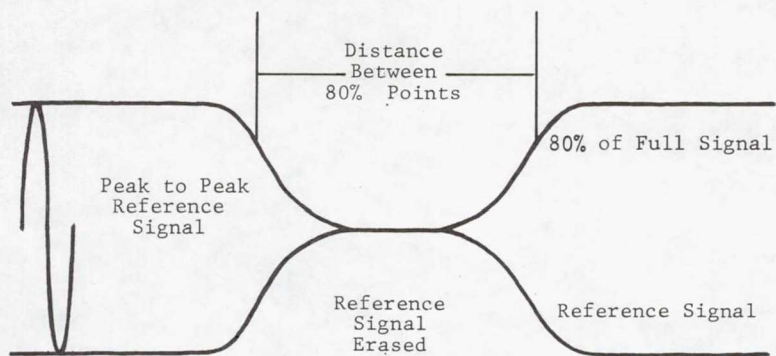


Figure 3.- Typical LCD erasure pattern.

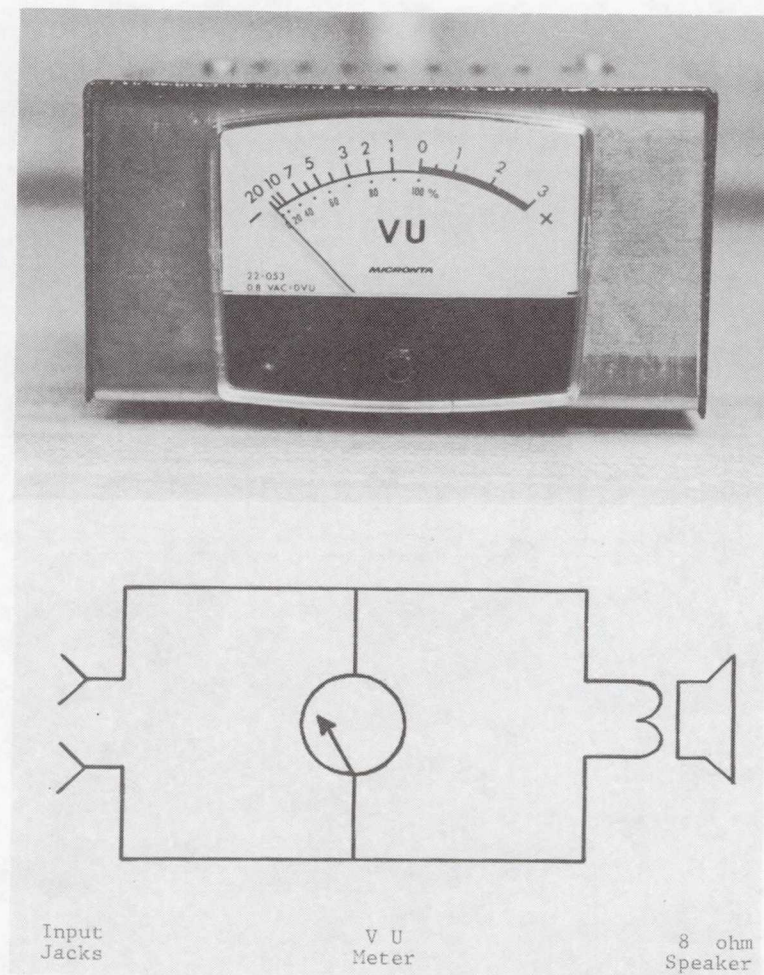


Figure 4.- Magnetic tape playback monitor.

Page intentionally left blank

SESSION III.- LIGHTNING DETECTION AND TRACKING

Page intentionally left blank

A STUDY OF THE COMPARATIVE PERFORMANCE OF
SIX LIGHTNING WARNING SYSTEMS*

Richard L. Johnson and Donald E. Janota
Southwest Research Institute

J. Edmund Hay
Pittsburgh Research Center of USBM

SUMMARY

An analysis of mining explosive accident reports indicate a need for clear and ample warning of approaching electrical storms to reduce injuries/fatalities due to lightning induced premature detonation. During the Spring and Summer of 1979, six lightning warning devices were comparatively evaluated at three test sites. The devices tested were: (1) Flash counter, (2) Corona point, (3) Radioactive probe, (4) Field mill, (5) azimuth/range locator, and (6) Triangulation locator. The test sites were chosen to provide system evaluation under varied thunderstorm conditions. The devices were tested at San Antonio, Texas, Kennedy Space Center, Florida and Langmuir Laboratory, New Mexico. Comparative performance is reviewed in terms of alarm reliability, false alarm and failure to alarm probabilities. Improved lightning warning system requirements and methods of relating warning criteria to explosive hazard are discussed.

INTRODUCTION

The objective of this study is to evaluate the adequacy of electrical storm warning systems and to recommend improvements if necessary. Mine safety standards specify that "when electric detonators are used, charging (of blastholes) shall be suspended...and men withdrawn to a safe location upon the approach of an electrical storm." These federal health and safety standards apply to metal and nonmetal open pit and underground mines, sand, gravel, and crushed-stone operations, surface coal mines, and surface work areas of underground coal mines.

The intent of the safety regulation is clear. Evacuation reduces injuries associated with lightning-induced premature explosions, providing that there is clear and ample warning of approaching lightning storms. Mine accident records indicate a distinct need for improvements in early detection of approaching electrical storms in order to allow sufficient time for workers to withdraw to a safe location. For example, in 1977 there were three fatalities within a month due to two separate accidents: one at a strip mine in Tioga County, Pennsylvania, and two near Van Lear, Kentucky.

*The work described in this paper was supported by the U.S. Bureau of Mines under Contract J0387207.

The Bureau of Mines has sponsored the acquisition and dissemination of information on the characteristics and adequacy of devices and systems designed to give warning of atmospheric electrical activity. It is also within the scope of Bureau of Mines concerns to develop improvements in such devices and systems if necessary. Under the purview of this study, Southwest Research Institute (SwRI) has evaluated six conceptually distinct lightning warning devices in side-by-side tests at three sites. These tests provide directly comparable results under thunderstorm conditions initiated by the three major sources of thunderstorm activity, viz, movement of frontal air masses, convection due to localized surface heating, and unstable air masses due to mountainous terrain (orographic) effects.

A review of previous work in the comparative evaluation of lightning warning systems reveals that a side-by-side study was conducted by the USAF Air Weather Service at Cape Canaveral AFS during the period April-September 1970. Five devices were evaluated in this effort. A prototype device developed by the Air Force Geophysical Laboratory was determined to best satisfy USAF requirements (ref. 1). No copy of the test plan nor details of the results has been located. Of the devices tested, two are currently being manufactured commercially.

A comprehensive theoretical review was done by Cianos and Pierce (ref. 2, ref. 3), using an existing statistical data base of thunderstorm and lightning parameters available in the literature. This effort addressed the general problem of lightning warning. Conclusions and recommendations were made based on the theoretical or projected performance of the systems analyzed.

In other studies, the performance of single sensor types has been evaluated. These include an evaluation of a radioactive probe by Buset and Price (ref. 4), a field mill by the USAF Air Weather Service (ref. 5), an azimuth/range locator by Schneider and Mangold (ref. 6), and a triangulation location system by Vance (ref. 7).

This paper summarizes the results of all known types of lightning warning systems which are commercially available. The results of this effort are directed toward providing a cost effective solution for timely warning of atmospheric electrical activity appropriate to the general mining industry requirement.

EXPERIMENTAL DESIGN

Blasting area vulnerability to lightning is based on two primary conditions. (1) Thunderstorms move into the blasting area, e.g. due to weather front or convective cell movement, (2) a thunderstorm builds up in place over the site. In the first case electromagnetic emanations from the cloud and the lightning discharge can be used to detect storm approach. In the second case, the first sign of danger may be a lightning strike occurring without warning. On relatively clear days thunderstorm activity can be directly observed. However, under overcast conditions, thunderstorms may occur within the area without being detected until cloud-to-ground lightning events are initiated.

Thus, effective lightning warning requires (1) capability to detect storms at a distance resulting in alarm, for example, 30 minutes prior to dangerous approach and (2) capability to detect static buildup in the immediate vicinity of the site. The comparative evaluation of lightning warning systems requires that both capabilities be evaluated in terms of (1) false alarm and failure to alarm rates, and (2) alarm reliability in terms of dangerous electrical energy dissipation in explosive detonators.

To achieve these test goals, the comparative evaluation test was implemented as follows: (1) a survey of all known methods of lightning warning was performed and representative devices were acquired for test, (2) an optical lightning location system was developed to provide proximity data on cloud-to-ground strikes, (3) a detonator simulation circuit was developed which simulates both bridgewire and bridgewire-to-case arcover detonation, and (4) selection of three test sites representative of the prevalent thunderstorm generating conditions. At each site a perimeter of 18 km about the array of sensors was established within which warning indications as thunderstorms approached was monitored. Assuming a mean storm movement of nominally 36 km/hr, this provided a 30 minute warning capability.

Data from the study is analyzed based upon (1) alarm indications from the candidate electrical warning systems, (2) meteorological data from weather radar facsimile, the NWS (16 mm film archive at Asheville, North Carolina), eyewitness observations by the site operating personnel, and lightning flash locations from the photographic sensors. Criteria used for comparative analysis of system performance include alarm reliability, failure-to-alarm rate, and false-alarm rate of the warning systems determined from observed electrical activity and the two detonator simulation records.

LIGHTNING WARNING SYSTEMS

Flash Counter

A lightning flash counter senses the atmospheric radio emission from a lightning discharge (sferic) and indicates the received sferic (flash) rate. The higher the rate, the more intense and/or nearer the proximity of the storm.

A review of the development of lightning flash counters and their utility as warning devices is given by Chalmers (ref. 8). Comparative performance data of the Pierce-Golde, modified Prentice, and a Czechoslovakian flash counter is given by Anderson (ref. 10). The use of a flash counter as a lightning warning device has been advocated frequently, but its primary utility has been in the acquisition of thunderstorm electrical statistics such as ratio of cloud-to-ground versus intracloud discharges, or number of strikes as a function of storm duration, etc.

Corona Point

A summary discussion of the corona point principle is given by Latham and Stromberg (ref. 11). The corona point device is perhaps conceptually the simplest of the lightning warning systems. In paraphrase of Cianos and Pierce (ref. 2), if a sharp point is raised to a height h above a ground plane, the corona current i in the presence of an electrostatic field E and wind speed w is given by:

$$i = ah(E-E_0) (w^2 + c^2 E^2 h^2)^{1/2}. \quad (1)$$

where a and c are constants and

$$E_0 = \text{threshold field to initiate corona} \sim 1 \text{ kv/m.}$$

If the wind velocity is zero, equation (1) becomes

$$i = ah(E-E_0) (cEh).$$

For small field values, $E < E_0$, the corona current is essentially constant. Under the conditions of thunderstorm activity, the wind velocity term is such that $w > cEh$ and equation (1) reduces to

$$i = ah(E-E_0)w$$

Warning levels of corona current should allow for enhanced current due to high wind speeds.

Radioactive Probe

A description of the radioactive probe device is given by McCready (ref. 12). Also summaries can be found in Cianos and Pierce (ref. 2) and Chalmers (ref. 8). In principle, the radioactive probe measures the electrostatic field in the presence of ionizing particle emission. The probe is connected to a conductor. The emitted particles ionize a small volume of air about the probe which brings the potential of the conductor to that of the atmospheric gradient. Potential is estimated by measuring the current through the conductor and using a knowledge of the coupling resistance of the probe to the surrounding air. Commonly used radioactive sources are polonium and tritium.

Field Mill

Field mill devices are described by Uman (ref. 13), Israel (ref. 14), and Chalmers (ref. 8). In paraphrase of Chalmers summary, the field mill device consists of a fixed test plate with a circularly disposed array of conducting surfaces on the fixed plate. By rotating the upper plate, the conducting

elements are alternately exposed to and shielded from the electric field lines between the earth and atmosphere. The upper rotating plate is generally grounded to earth and the conducting elements, which become charged during the exposure cycle and are discharged during the shielding cycle through a resistor-capacitor network. The resulting sinusoidal signal is rectified and measured. The amplitude of the sinusoidal signal is proportional to the charge deposited upon the conducting surfaces and thus proportional to the electric field strength.

Azimuth/Range Locator

Description of an azimuth/range location system are given by Harth and Pelz (ref. 15), Sao and Jindoh (ref. 16) and Ryan and Spitzer (ref. 17). The technique described here is a paraphrase of that proposed by Ryan and Spitzer (ref. 17). The sensor is a conventional crossed loop direction finder with a monopole sense antenna as developed by Watson-Watt and Herd (ref. 18). The receiver is broad band tuned with a center frequency of 50 kHz.

The crossed loops are also quadrature summed to form a composite signal which is compared to a threshold level. Provided the signal exceeds the threshold value, the analog signals from each crossed loop are integrated for a period of 500 microseconds. The integrated signals are then effectively divided by the square of the composite signal, in what is termed a "foldback method," so that the "folded back" signal is smaller in magnitude for a larger received signal and larger in magnitude for a smaller received signal. This signal, then, results in a range estimate which coupled with the directional data, produces a dot on a CRT screen. The points of electrical activity resemble the polar trace of a weather radar CRT.

Triangulation Locator

A review of lightning triangulation location techniques is given by Horner (ref. 19). Recent techniques are reported by Oetzel and Pierce (ref. 20), Cianos, et. al. (ref. 21), Krider and Noggle (ref. 22), Krider, et. al. (ref. 23) and Herman, et. al. (ref. 24). Other techniques reported which have been used are by Lennon (ref. 25), Taylor (ref. 26) and Warwick (ref. 27). The system described herein is a paraphrase of Krider, et. al. (ref. 28).

The direction finding technique described in the previous section, using a crossed loop sensor, exhibits significant directional errors when the magnetic field has an appreciable horizontal component. To overcome this problem, a system has been developed to: (1) discriminate between intercloud and cloud-to-ground discharges, and (2) to gate the direction finder on the initial portion of the cloud-to-ground strike which emits a predominately vertically polarized magnetic field, typically occurring during the first 100 meters of the return stroke channel.

The system consists of two remote DF stations which transmit data to a centralized facility. The function of the central site is to determine a point of intersection of the directional data reported by each remote site. Two sensors are located at each remote site, a crossed loop antenna and a flat plate antenna. The flat plate antenna is used as a sense element to resolve the 180 degree ambiguity of the crossed loop. The system is designed to operate only upon negative cloud-to-ground discharge. If this criterion is met, an angle of arrival is computed. Essentially the cloud-to-ground test is based on two criteria: (1) time to initial peak, typically less than 5 to 10 microseconds, and (2) decay time, approximately 40 microseconds. If these conditions are satisfied, the initial peak value is used to determine the angle of arrival. The 180 degree ambiguity is resolved by the E field flat plate sensor which indicates a positive field change for negative ground discharges and vice versa for positive ground discharges.

Also located at the remote site is a digital processor which computes the angle of arrival of each stroke in the flash, tests the results for agreement, and averages the computations. The digital processor then transmits the result to the central site over a 200-baud land line pair of wires.

At the central facility, the location of the lightning strike is computed from the intersection of the two respective bearings reported by the remote sites. The positional data are output to teletype giving time, northing, easting, number of strokes in the flash and relative signal strength at each of the two sites. Also the position is presented graphically on an X-Y plotter.

SwRI TEST SITE

SwRI is located on the western city limits of San Antonio, Texas. The city is situated in the south-central portion of Texas. Precipitation from April through September usually occurs with thunderstorms, fairly large rainfall amounts occurring in short periods of time. Hail of damaging intensity seldom occurs but light hail is frequent in connection with springtime thunderstorms. During the evaluation period, 1 April - 15 May 1979, 10 thunderstorm events were monitored over a cumulative period of 36 hours. All storms were frontal type thunderstorms, initiated by the movement of large air masses.

The field deployment of the lightning warning sensors at SwRI is shown in Figures 1 and 2. The mobile laboratory is a 25-ft trailer. Mounted atop the trailer are wind speed and wind direction sensors. An interior view of the mobile laboratory is shown in Figure 3.

KENNEDY SPACE CENTER TEST SITE

The Kennedy Space Center (KSC) complex is located on the Atlantic Ocean, with the Banana and Indian Rivers running through the complex. Terrain in the

area is flat, soil is mostly sandy, and elevations in the area range from 5 to 30 m above sea level. The "rainy season" from June through mid-October produces 60 percent of the annual rainfall. The major portion of the summer rainfall occurs in the form of local convective thundershowers. These showers are occasionally heavy and produce as much as 5 to 8 cm of rain. During the test period at KSC, 1 June - 15 July 1979, 22 thunderstorm events were monitored over a cumulative period of 43 hours. The triggering mechanisms for these storms were: (1) movement of frontal air masses, (2) localized convection due to surface heating, and (3) nearby passage of a tropical depression.

A map of KSC is shown in Figure 4 showing the deployment of the mobile laboratory, the three optical locator sites and two direction finding sites used for the triangulation location system.

LANGMUIR LABORATORY TEST SITE

The Irving Langmuir Laboratory for Atmospheric Research provides a base for the study of cloud processes that produce lightning, hail, and rain. The laboratory is located 3.2 km feet above sea level near South Baldy Peak in the Magdalena Mountains of the Cibola National Forest. It is approximately 31 km southwest of Socorro, New Mexico. Solar heating on the mountains of this area causes localized updrafts each day so that convective clouds form over these elevated regions. When the winds are gentle, these clouds often go through their entire life cycle--from the first condensation to full development--and then dissipate over the mountains where they first formed.

During the test period at Socorro, 21 July - 20 August 1979, 16 thunderstorm events were monitored. The cumulative time of observation was 37 hours. While a thunderstorm was in progress on 7 August 1979, lightning struck the corona point device and severely damaged the electronics. Concurrent with the strike, a transient on the AC power line resulted in a failure of the power supply in the field mill electronics.

A map of New Mexico is shown in Figure 5 showing the deployment of the mobile laboratory near South Baldy Peak. The triangulation location system remote electronics were installed at Socorro and Magdalena, New Mexico, with the central facility at the New Mexico Tech campus.

SYSTEM COMPARATIVE PERFORMANCE

To determine the radial coverage of interest which ensures timely mine evacuation, a study was made of simulated premature detonations versus distance to the lightning strike as recorded by the triangulation locator. These data are shown in Figure 6. There were 90 incidences of the all-fire condition, 150 instances greater than the no fire threshold. As shown on the graph, when a premature detonation occurs, the probability is 80 percent that

the lightning strike was at 18 km range or less. This curve cannot be used to infer the probability of premature detonation as a function of distance. Rather, the curve indicates the probability that the strike was within a given distance or less from the sensors given a premature detonation has occurred.

The performance parameters of the LWS's from which comparative performance is derived are the following:

- (1) Mean Warning Time: The time elapsed between first warning and storm arrival at 18 km radius. Positive time implies time before reaching 18 km. Negative time implies time after the storm reaches 18 km radius. Zero mean warning time means alarm first occurred when the storm was at 18 km radius.
- (2) Percent Incidence of False Alarm: The percentage of total alarms for which an alarm was given when no storm event was observable.
- (3) Percent Incidence of Failure to Alarm: The percentage of total storm events within 18 km range for which no alarm was given.
- (4) Percent Valid Alarms: Percent of alarm events for which storm activity was within 18 km range.
- (5) Mean Time to Clear: Time after storm events passed beyond 18 km range to clear the alarm condition of the LWS.

The average warning time of each system is determined as follows: Based upon 18 km radius about the site, a hazard exists when (1) a radar echo of "heavy" (VIP level 3) or more has entered the periphery, (2) thunder is reported by the operator, (3) lightning has been observed, or (4) premature simulated detonation has occurred and 30 minutes is subtracted.

The time to clear was determined by recording the time at which (1) radar echoes of "heavy" (VIP level 3) or more had left the 18 km circle, (2) 30 minutes had transpired since the last premature detonation or (3) the operator was able to visually ascertain that no hazardous condition existed within the area of interest.

RESULTS

Table I is the summary data for the performance of the six systems under frontal storm conditions. The table shows that the corona point device and azimuth/range locator were generally unsuitable for warning. The corona point device indicated warning on the average of 20 minutes after the hazardous conditions were in effect. The device also indicated a clear condition 19 minutes prior to the return of a "safe" condition. Had the alarm threshold been decreased to, say, 10 microamperes, the already high false alarm rate of 27 percent would have significantly increased.

In the case of the azimuth/range locator, the ranging algorithm produced 73 percent false alarms which reduces its effectiveness for use as a warning device in terms of the criteria for this program.

The performance of the remaining four devices is relatively similar with the field mill system exhibiting a somewhat higher false alarm rate than the other four.

Thunderstorms observed during the period 1 June 1979 to 15 July 1979 at KSC, Florida were frontal passages during the early part of the experiment and predominately convective (due to local surface heating) throughout the remainder of the period. The convective cells generally formed south of KSC and moved toward the northeast during their lifetime. The average duration of electrical storm hazard was one hour and forty-two minutes.

The summary data for the six systems are shown in Table II. These data reflect alarm conditions during the period when the test operator was present at the site. The operator received storm information from the Air Weather Service at Cape Canaveral on 45 km alert radius. Data acquisition was initiated when the operator arrived on site. Continual observations as in the San Antonio test were not feasible. Bias (if any) in these data tends to underestimate the false alarm rate and mean alarm times.

Throughout this test, the corona point device exhibited erratic behavior, particularly regarding the lengthy time to reach cleared status. (For example, due to causes unknown this device constantly false alarmed between approximately 7 and 11 p.m. throughout the test). This is primarily attributed to the poor ground provided by the sandy soil at the site. The performance of the flash counter was less favorable than in the San Antonio test. This device required continual adjustments in sensitivity due to its high susceptibility to radio frequency interference. During the experiments at KSC, flash counter false alarm rate measurements were vitiated by the high incidence of coupled extraneous noise and interference.

The three systems exhibiting conventional warning performance during this test were the (1) radioactive probe, (2) field mill device, and (3) triangulation locator.

Thunderstorms observed during the period 21 July 1979 to 20 August 1979 at Langmuir Laboratory, New Mexico, were convective type cells initiated by mountainous terrain. The cumulus buildup generally started over the mountain ridges and was swept eastward or remained stationary over the mountain tops. The average storm hazard duration was one hour and thirty minutes.

Shown in Table III is the summary of system performance for mountainous terrain. The site was operated on a twenty-four-hour basis. The measured data for the azimuth/range locator is more representative of system performance regarding false alarms than reported in Table II. In this case the systems which revealed best overall performance were the radioactive probe, the field mill device and the triangulation locator.

The observations revealed two significant phenomena not observed at the lower altitude test sites; (1) atop the mountain, E fields of 15-20 KV/meter were common; maximum electrostatic fields measured at low altitude were of the order of 1-5 KV/meter; (2) eighty percent of all simulated detonations occurred at the New Mexico site as compared with the two previous sites. This occurred in spite of the fact that numerous cloud-to-ground strikes were observed in close proximity (less than 4 km) at both of the other sites.

CONCLUSIONS

1. The evaluation study has revealed that a truly automated, single site lightning warning system must have the capability of measuring at least three parameters to be effective to 18 km range. The parameters are: (1) electrostatic field, (2) electrical discharge rate (sferics), and (3) atmospheric noise background level. System design must take into account physical and radio frequency environmental factors.
2. The single most important lightning warning statistic requiring improvement is the failure to alarm rate. Improved performance is possible by incorporating an adaptive threshold capability in the warning system.
3. Performance failures of the corona point sensor tested outweigh its potential usefulness as a lightning warning system.
4. The azimuth/range locator tested is not considered to be a useful lightning warning system due to the high false alarm rate.
5. The triangulation locator provided best performance statistics of all units tested. However, this unit lacks capability to sense overhead buildup.
6. Using present technology single point lightning warning can be provided by combining a radioactive probe or field mill, flash counter, and background sensing device capable of adaptive warning threshold adjustment.

REFERENCES

1. AN/GMH-7, Lightning Warning Set (LWS). USAF HQ AWS Sensor Fact Package, Apr. 14, 1978.
2. Cianos, N. and E. T. Pierce: Methods for Lightning Warning and Avoidance. SRI Tech. Rept. 1 May 1974.
3. Pierce, E. T.: Lightning Warning and Avoidance. Volume 2 of Lightning edited by R. H. Golde. Academic Press, N.Y. 1977 pp 497-519.
4. Buset, K. and K. W. Price: Lightning Flash Densities and Calculation of Strike Probabilities to Certain Vulnerable Installations at the Nevada Test Site (NTS). Session 1, paper 9, Proceedings of the 1975 Conference on Lightning and Static Electricity, Royal Aeronautical Society, London 1975.
5. Pittman, D.W.: Production Qualification and Acceptance Test of the Lightning Warning Set AN/GMH-7. USAF Air Weather Service, Oct. 1977.
6. Schneider, J. G. and V. L. Mangold: Ground Evaluation of Lightning Monitoring System (Stormscope). FAA/FIT Workshop on Grounding and Lightning Technology. Mar., 1979, pp 37-42.
7. Vance, D. L.: The Geographical Distribution of Lightning - Forestry and Range Requirements and Interests. Proceedings: Workshop on the Need for Lightning Observations from Space, Feb. 1979, pp 110-113.
8. Chalmers, J. A.: Atmospheric Electricity. Pergamon Press, New York, 1967.
9. Laitinen, L.: Experience with Lightning Flash Counters in Finland. Session III, paper 3, Proceedings of the European Meeting on Lightning Instrumentation at Uppsala University. Nov. 21-22, 1975.
10. Anderson, R. B.: Measuring Techniques. Volume 1 of Lightning edited by R. H. Golde, Academic Press, N.Y. 1977, pp. 458-461.
11. Latham, J. and I. M. Stromberg: Point Discharge. Volume 1 of Lightning edited by R. H. Golde, Academic Press, N.Y. 1977, pp. 100-101.
12. McCready, P. B.: Equipment for Forecasting Lightning Danger in Recent Advances in Atmospheric Electricity edited by L. G. Smith, Pergamon Press, N.Y. 1958.
13. Uman, M. A.: Lightning, McGraw-Hill, N.Y. 1969.

REFERENCES (Cont)

14. Israel, H.: Atmospheric Electricity. U. S. Dept of Commerce, NTS, 1973.
15. Harth, W. and J. Pelz: Eastern Thunderstorms Located by VLF Atmospheric Parameters in Radio Science, Vol. 8, No. 2, Feb. 1973.
16. Sao, K. and H. Jindoh: Real Time Location of Atmospherics by Single Station Techniques and Preliminary Results in Jour. of Atmos. and Terr. Phy., Vol. 36, 1974.
17. Ryan, P. A. and N. Spitzer: Stormscope, U. S. Patent No. 4,023,408, May 17, 1977.
18. Watson-Watt, R. A. and J. F. Herd: An Instantaneous Direct Reading Radiogoniometer in Jour. of the IEE, Vol. 64, 1926.
19. Horner, F.: Radio Noise from Thunderstorms in Advances in Radio Research edited by J. A. Saxton, Volume 2, 1964.
20. Oetzel, G. N. and E. T. Pierce: VHF Technique for Locating Lightning, in Radio Science, Vol. 4, 1969
21. Cianos, N., G. N. Oetzel, and E. T. Pierce: A Technique for Accurately Locating Lightning at Close Ranges in Jour. of Appl. Meteor., Vol. 11, 1972.
22. Krider, E. P. and R. C. Noggle: Broadband Antenna Systems for Lightning Magnetic Fields in Jour. of Appl. Meteor., Vol. 14, 1975.
23. Krider, E. P., R. C. Noggle and M. A. Uman: A Gated, Wideband Magnetic Direction Finder for Lightning Return Strokes in Jour. of Appl. Meteor., Vol. 15, 1976.
24. Herman, B. D., M. A. Uman, and R. D. Brantley: Test of the Principle of Operation of a Wideband Magnetic Direction Finder for Lightning Return Strokes in Jour. of Appl. Meteor., Vol. 15, 1976.
25. Lennon, C. L.: LDAR - A New Lightning Detection and Ranging System (Abstract), EOS Trans., AGU, Vol. 56, 1975.
26. Taylor, W. L.: A VHF Technique for Space-Time Mapping of Lightning Discharge Processes in Jour. of Geo. Res., Vol. 83, 1978.
27. Warwick, J. W., C. O. Hayenga and J. W. Brosnahan: Interferometric Directions of Lightning Sources at 34 MHz in Jour. of Geo. Res., Vol. 84, 1979.
28. Krider, E. P., R. C. Noggle and M. A. Uman: Detection System for Lightning. U. S. Patent No. 4,115,732, Sep. 19, 1978.

TABLE I. - FRONTAL TYPE STORM SUMMARY

DEVICE	AVERAGE WARNING (MINUTES)	FALSE ALARM RATE	FAILURE TO ALARM RATE	ALARM RELI- ABILITY	TIME TO CLEAR (MINUTES)
Radioactive	33	9%	9%	91%	15
Field Mill	40	18%	9%	82%	22
Corona Point	-20	27%	55%	73%	-19
Flash Counter	35	0%	9%	100%	44
Triangula- tion Locator	21	0%	9%	100%	5
Azimuth/ Range Locator	121	73%	0%	27%	109

TABLE II. - KSC STORM SUMMARY

DEVICE	AVERAGE WARNING (MINUTES)	FALSE ALARM RATE	FAILURE TO ALARM RATE	ALARM RELI- ABILITY	TIME TO CLEAR (MINUTES)
Radioactive	28	0%	10%	100%	-8
Field Mill	27	0%	15%	100%	9
Corona Point	-15	0%	80%	100%	22
Flash Counter	32	0%	55%	100%	-18
Triangula- tion Locator	21	0%	6%	100%	-4
Azimuth/ Range Locator	39	0%	5%	100%	17

TABLE III. - MOUNTAINOUS TYPE STORM SUMMARY

DEVICE	AVERAGE WARNING (MINUTES)	FALSE ALARM RATE	FAILURE TO ALARM RATE	ALARM RELI- ABILITY	TIME TO CLEAR (MINUTES)
Radioactive	21	0%	27%	100%	33
Field Mill	50	0%	20%	100%	67
Corona Point	-20	0%	80%	100%	40
Flash Counter	-4	0%	64%	100%	23
Triangula- tion Locator	20	0%	9%	100%	0
Azimuth/ Range Locator	101	82%	0%	18%	117

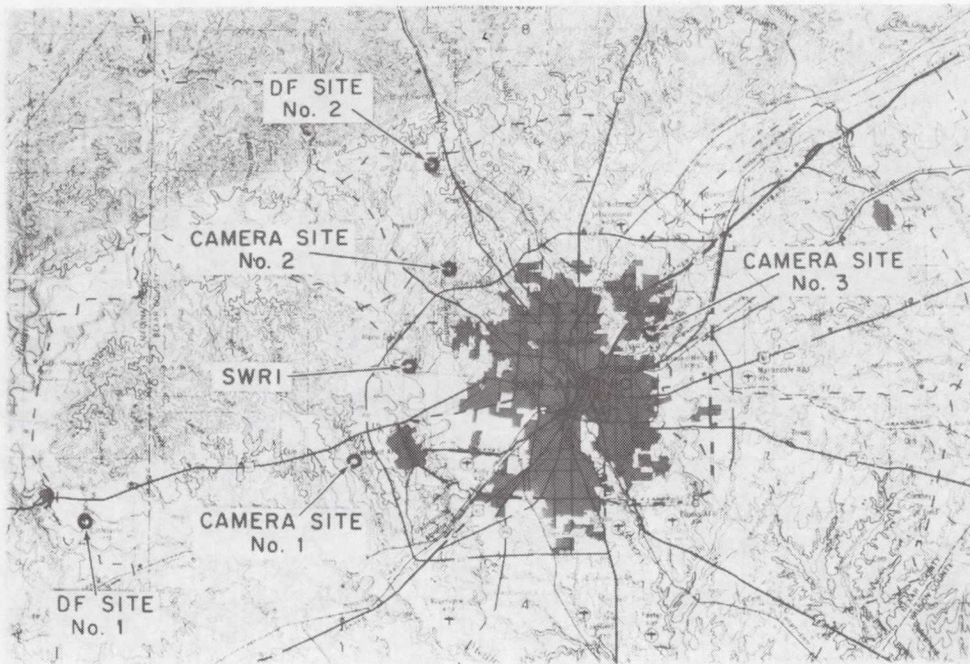


Figure 1.- Southwest Research Institute deployment in San Antonio, Texas.

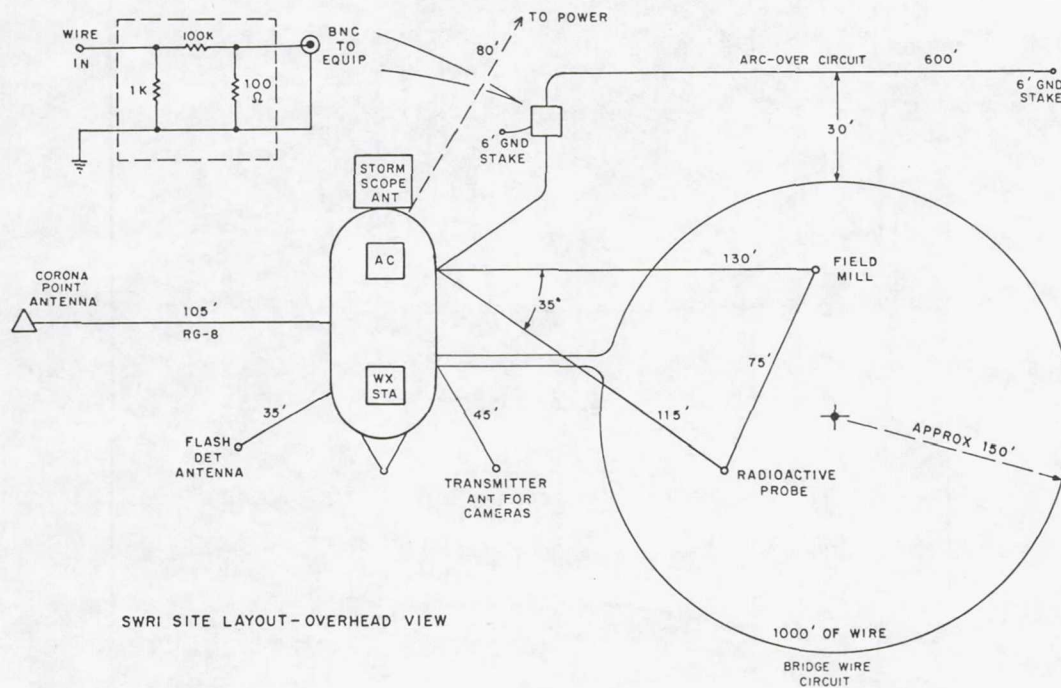


Figure 2.- Southwest Research Institute site layout - overhead view.

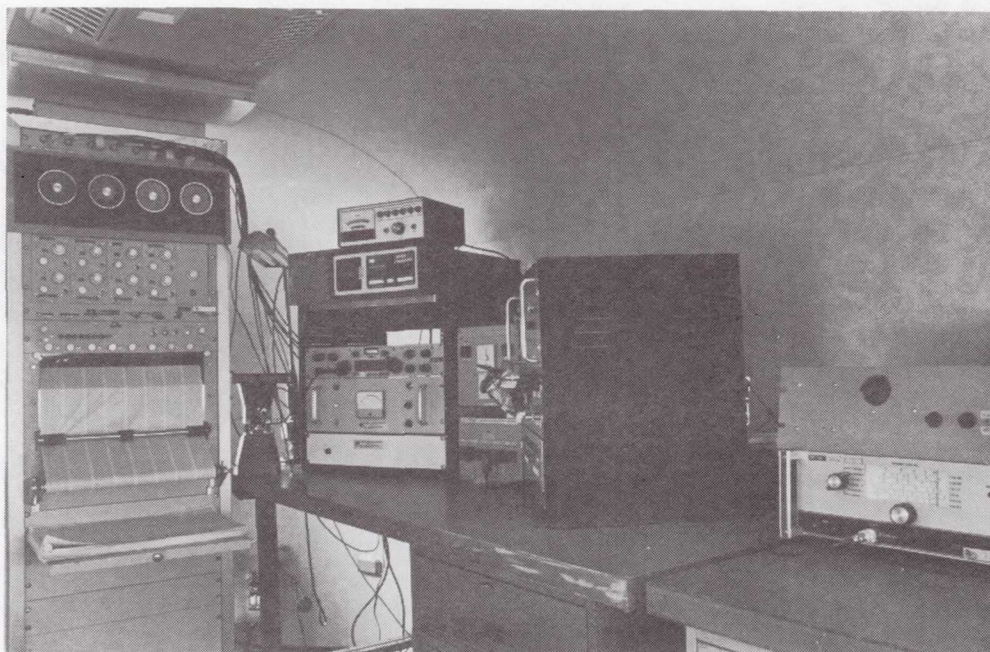


Figure 3.- Interior view of mobile laboratory.

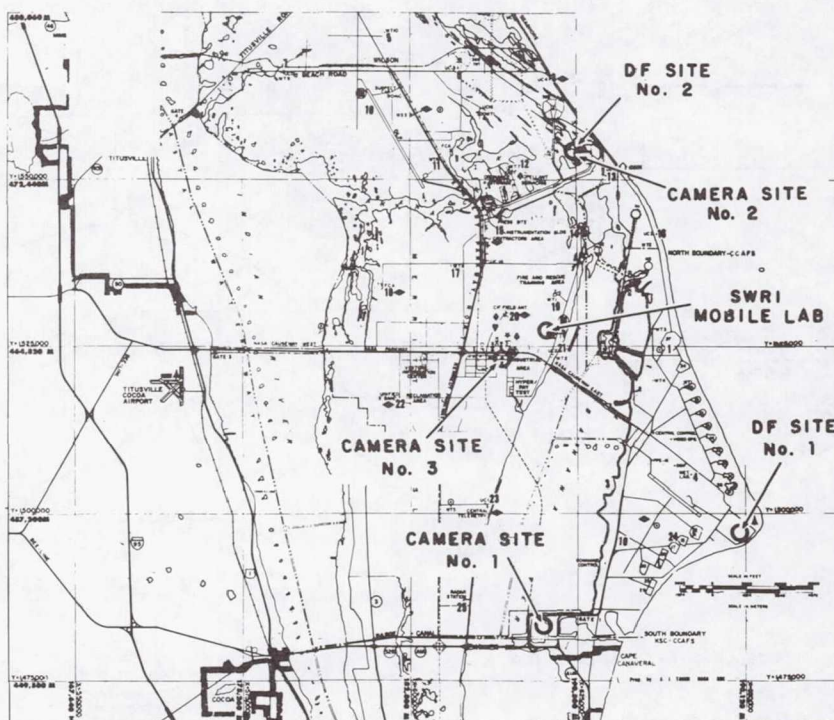


Figure 4.- Kennedy Space Center deployment.

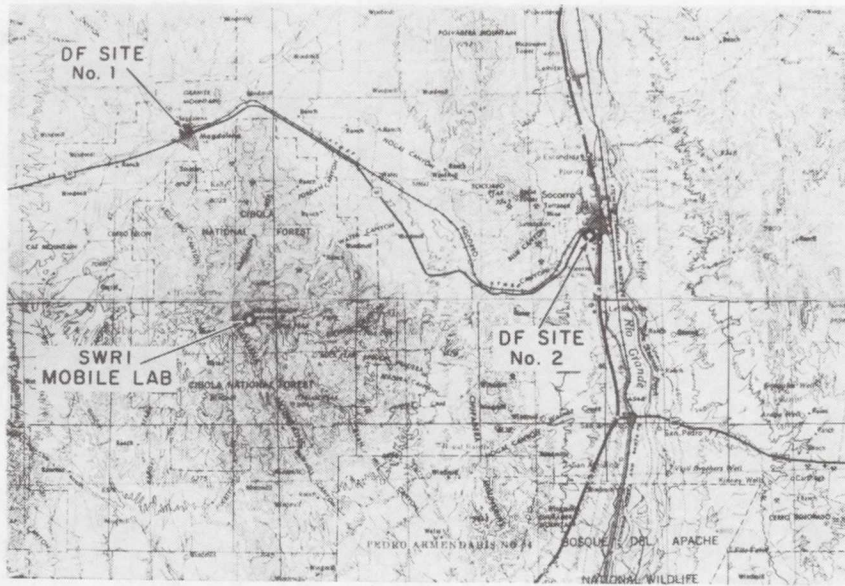


Figure 5.- Socorro, New Mexico deployment.

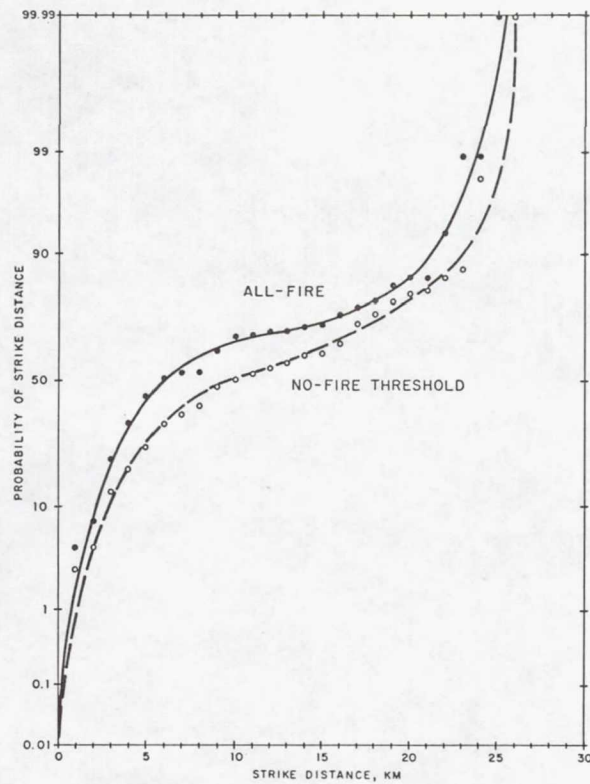


Figure 6.- Lightning strike distance on predetonation.

Page intentionally left blank

AN AUTOMATIC LOCATING SYSTEM FOR CLOUD-TO-GROUND LIGHTNING

E. Philip Krider, Albur E. Pifer, and Martin A. Uman
Lightning Location and Protection, Inc.

SUMMARY

Extensive networks of magnetic direction-finding (DF) stations are currently operating throughout the western United States, Alaska, and Canada to facilitate the detection of lightning-caused forest fires. Similar systems are being used in the Tampa Bay area and Scandinavia to evaluate the effects of lightning on electric power distribution lines, and in South Florida to determine the basic lightning statistics and their relationship to the storm dynamics. Each detection station contains a new, wideband direction-finder that responds primarily to cloud-to-ground lightning and that discriminates against cloud discharges and background noise. Good angle accuracy is obtained by measuring the lightning direction at just the time that the return stroke magnetic field reaches its initial peak. Lightning locations are computed automatically from the intersections of simultaneous direction vectors and/or from the ratio of the signal strengths measured at 2, 3, or 4 direction-finding sites. The development of these systems has proved to be a significant aid in fire management and in lightning research.

INTRODUCTION

Each year lightning starts approximately 10,000 wildland fires in the United States. The lightning fire hazard is particularly serious in remote, unpopulated areas because of the greater difficulty of early detection and suppression. Meteorological satellites and weather radars can identify convective cloud systems and precipitation, but not lightning. Since some clouds produce much precipitation but little lightning, and since others produce lightning but relatively little precipitation, a system which automatically detects and locates the lightning itself is highly desirable. Here we briefly describe a new lightning locating system that has been developed to facilitate the detection of lightning-caused fires.

A typical lightning discharge to ground or flash contains several large current surges or strokes (see Uman, 1969 [ref. 1] for a review of basic lightning phenomena). A flash begins with a faint leader, which proceeds rather slowly from cloud to ground in a series of short luminous steps. When this stepped leader contacts the ground, a very energetic and bright return stroke propagates rapidly back up the ionized path established by the leader. After a pause of 30-50 milliseconds, a dart leader often forms and is followed by another bright return stroke propagating upward. A typical flash to ground contains three or four leader-return stroke combinations, which almost always

transfer negative charge to ground. The currents in return strokes typically rise to peak values of 10-40 kA in 1-10 μ sec or less.

LOCATING SYSTEM

Fig. 1 shows a block schematic diagram of the lightning locating system. Each of 2, 3, or 4 remote direction-finding stations transmits lightning direction and signal strength data to a central position analyzing station. The position analyzer receives data from the remote direction finders, calculates the lightning positions, and outputs the results in real-time to a digital x-y plotter, a magnetic tape recorder, and/or a local data terminal. The system provides the time and location of each discharge, the number of return strokes in each flash, and the peak amplitude of the first return stroke magnetic field.

Direction Finder

Each direction finder (DF) senses the electromagnetic fields radiated by lightning on two orthogonal magnetic-loop antennas and on a flat-plate electric antenna. The bandwidths of the antenna system are wide (approximately 1 kHz - 1 MHz) so that the shapes and polarities of the lightning field waveforms are preserved. The voltage produced by the electronics associated with each magnetic loop is proportional to the lightning magnetic field multiplied by the cosine of the angle between the plane of the loop and the direction of the incoming field. Therefore, the direction of a lightning flash can be determined from the ratio of the signals on the two orthogonal loops, a standard technique in radio direction finding.

In order to optimize accuracy and to eliminate background noise, the DF electronics are designed to respond to only those field waveshapes that are characteristic of return strokes in cloud-to-ground flashes. The DF electronics require the incident lightning field to have a risetime, width, and subsidiary peak structure characteristic of a return stroke. The electric field must have a positive initial polarity (the polarity produced when negative charge is lowered toward ground), and the field overshoot following the initial peak must not be too large relative to the first peak. The risetime and bipolar shape requirements also serve to eliminate very distant (> 400 km) lightning signals because the effects of propagation increase the field risetimes (ref. 2), and distant ionospheric reflections are often large and inverted with respect to the initial ground wave (ref. 3).

In order to provide an optimum detection efficiency over a wide dynamic range, the DF contains both high- and low-gain analog circuits that operate in parallel. The field shape criteria can be different in the high- and low-gain sections because the shapes of near and distant lightning signals are usually different (refs. 2, 4). Since the shapes of first and subsequent stroke fields are also different, the shape criteria are automatically switched to values appropriate for subsequent strokes after the first stroke in a flash is detected.

When a return-stroke field is detected, the magnetic direction is determined at just the time that the radiation field reaches its initial peak. At this time, the stroke current is still within about 100 m of the ground, so that any errors in magnetic direction due to horizontal channel sections and branch currents are minimized (refs. 5, 6), and errors due to ionospheric reflections (ref. 7) are eliminated. Also, by sampling at this time, the magnetic direction indicates the location of the ground contact point rather than some elevated portion of the channel. The angular accuracy of a DF system is typically 1-2 degrees or better (ref. 5), a value which is usually more than adequate to resolve individual cells of electrical activity within larger cloud systems.

A photograph of the DF electronics is shown in figure 2. The system is designed to operate either in a stand-alone mode, often in conjunction with a weather radar, or as part of a larger network with an automatic position analyzer. In the former case, the lightning directions are plotted on an analog x-y recorder on a compass grid with the length of each vector being proportional to the peak amplitude of the first stroke field. Clusters of vectors show the directions and angular extent of individual storm cells, and if weather radar data are available, then the lightning clusters can be used to identify which echos are producing lightning and which echos are not. With some experience, the operator of a single DF system can often estimate an approximate range to a storm using just the average lightning signal strength within a given cell.

A microcomputer subsystem built into each DF digitizes and stores the signals for up to 8 return strokes in each flash to ground, computes the angles to each stroke, and stores the results in a buffer memory for subsequent output. The time, angle, signal amplitude, and the number of return strokes for the most recent flash are shown on a front panel LED display and can be typed on a local data terminal, if desired. Under most conditions, the amplitude of the field at a given range and the multiplicity of return strokes are good indicators of the severity of the discharge. The total number of flashes that are detected each hour, or for an operator-determined time interval, are available for display on the front panel or for typing on command. The DF microcomputer can also transmit the angle and signal strength data for each discharge to the remote position-analyzing station where individual lightning locations are computed automatically in real-time.

Position Analyzer

The position analyzer is a preprogrammed microcomputer system which automatically computes, maps, and records lightning locations in real-time using as inputs the data generated by 2, 3, or 4 DF stations. The date and time are provided by an internal crystal-controlled calendar clock with a battery back-up power supply. In normal operation, the time, azimuth angle, range, and the number of return strokes for the most recent discharge are displayed continuously on a front panel LED display (see figure 3). The time, the lightning location, the number of strokes, and the peak signal strengths (if desired) can be typed on a local data terminal and/or transmitted back to the remote

direction-finding sites. The format of the typed locations can be (i) angle-range with respect to any desired origin with the distance units in kilofeet, kilometers, statute miles, or nautical miles; (ii) North-South and East-West coordinates; or (iii) a latitude-longitude format. The position analyzer can plot lightning locations in real-time on a digital x-y plotter or CRT terminal and can record all lightning data on magnetic tape. The tape-recorded data can be replotted on any of 100 preset map scales or retransmitted back to the remote DF sites. The date, the time, the total number of lightning discharges which have been detected, and a variety of other statistics are stored in the position analyzer memory and are available for output at periodic intervals or on command.

The locations of the DF sites and all other program data are stored in a write-protected magnetic memory that is immune to power outages. The lightning locations are computed by triangulation using simultaneous DF angles or, if necessary (such as when a discharge is near the baseline of a 2-DF system), using the DF angles and the ratio of first-stroke field amplitudes. The locations of all discharges which occur within a preset rectangular region unique to each DF site can be transmitted back to each DF in any desired format relative to a coordinate origin located at the remote site.

The direction finder and position analyzer computers each contain a complete set of test programs which can be used to check all components of the system. The position analyzer continuously monitors the status of all the DF stations and the data links, and automatically types a diagnostic message if the status of any DF unit or a data link changes.

DETECTION NETWORKS

The USDI Bureau of Land Management (BLM) has been operating lightning detection networks in the western U.S. and Alaska since 1976 to facilitate early detection of lightning-caused fires. Currently, the BLM stations are located at the sites shown in figures 4 and 5. Similar networks are also operating in the Northwest Territories, Ontario, Saskatchewan, British Columbia, Quebec, and Alberta for forest-fire detection. In figures 4 and 5, the nominal range of each DF is shown as a circle with a radius of about 400 km (220 nm), although large lightning signals can often be detected at much greater distances. It is estimated that each DF station detects 80-90 percent of all cloud-to-ground flashes within the nominal range. Flashes are not detected if there are unusual fluctuations in the return-stroke field shapes, if the signal amplitudes are below the system threshold, or if the flashes lower positive charge to ground. The solid lines in figures 5 and 6 show the communications lines which are used to connect individual DF stations to position analyzers. Two examples of lightning position maps obtained during 1979 are shown in figures 6 and 7.

CONCLUDING REMARKS

To the best of our knowledge, the stations shown in figures 4 and 5 represent the largest and the most accurate lightning detection networks that have been installed anywhere in the world. These systems have already proved to be a significant aid in wildfire management and in fire weather forecasting. Detection patrols and sometimes even fire suppression crews are now sent directly to those areas where the position analyzers show lightning is occurring. The early warning and improved detection provided by these systems have reduced both the size of fires when first detected and the suppression costs.

Weather forecasters have found the networks to be beneficial because lightning and areas of disturbed weather are identified instantly even in remote areas that are out of radar range. The location, motion, and time-development of storms can often be used to forecast hazards and to improve interpretations of the weather radar displays.

Lightning detection systems similar to those described above are being used in several research projects designed to measure many of the basic characteristics of lightning, the effects of cloud seeding on lightning, and the effects of lightning on electric power distribution systems (refs. 8, 9, 10, 11). In the future, we hope further applications of such systems will help to improve lightning warnings and reduce lightning damage throughout the world.

REFERENCES

1. Uman, M. A.: Lightning. McGraw-Hill, New York, 264 pp., 1969.
2. Uman, M. A.; Swanberg, C. E.; Tiller, J. A.; Lin, Y. T.; and Krider, E. P.: Effects of 200 km propagation on Florida lightning return stroke electric fields. *Radio Science*, vol. 11, pp. 985-990, 1976.
3. Taylor, W. L.: Radiation field characteristics of lightning discharges in the band 1 kc/s to 100 kc/s. *J. Res. NBS*, vol. 67D, pp. 539-550, 1963.
4. Lin, Y. T.; Uman, M. A.; Tiller, J. A.; Brantley, R. D.; Beasley, W. H.; Krider, E. P.; and Weidman, C. D.: Characterization of lightning return stroke electric and magnetic fields from simultaneous two-station measurements. *J. Geophys. Res.*, vol. 84, pp. 6307-6314, 1979.
5. Krider, E. P.; Noggle, R. C.; and Uman, M. A.: A gated, wideband magnetic direction finder for lightning return strokes. *J. Appl. Meteor.*, vol. 15, pp. 301-306, 1976.
6. Herrman, B. D.; Uman, M. A.; Brantley, R. D.; and Krider, E. P.: Test of the principle of operation of a wideband magnetic direction finder for lightning return strokes. *J. Appl. Meteor.*, vol. 15, pp. 402-405, 1976.
7. Horner, F.: Very-low-frequency propagation and direction-finding. *Proc. IEEE*, vol. 104B, pp. 73-80, 1957.
8. Boulanger, A. G.; and Maier, M. W.: On the frequency of cloud-to-ground lightning from tropical cumulonimbus clouds. *Preprints 11th Tech. Conf. Hurricanes and Tropical Meteorology*, Miami Beach, Dec. 13-16, 1977, Amer. Meteor. Soc.
9. Maier, M. W.; Boulanger, A. G.; and Sarlat, J.: Cloud-to-ground lightning frequency over South Florida. *Preprints Conf. Cloud Physics and Atmospheric Electricity*, Issaquah, WA, July 31 - Aug. 4, 1978, Amer. Meteor. Soc.
10. Darveniza, M.; and Uman, M. A.: Lightning studies of distribution lines. *Proc. IEEE Power Engineering Conf. Overhead and Underground Transmission and Distribution*, Atlanta, April 1-6, 1979.
11. Darveniza, M.; and Uman, M. A.: Research into lightning protection of distribution systems equipment for field tests. To be published in *IEEE Trans. Power Apparatus and Systems*. Presented at IEEE Power Eng. Soc. Summer Meeting, Vancouver, July 1979.

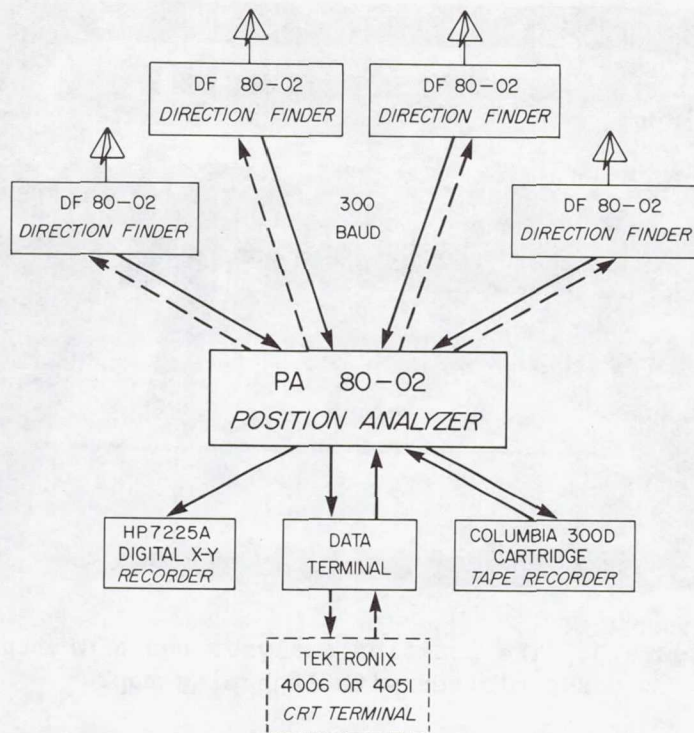


Figure 1.- A block schematic diagram of the lightning locating system.

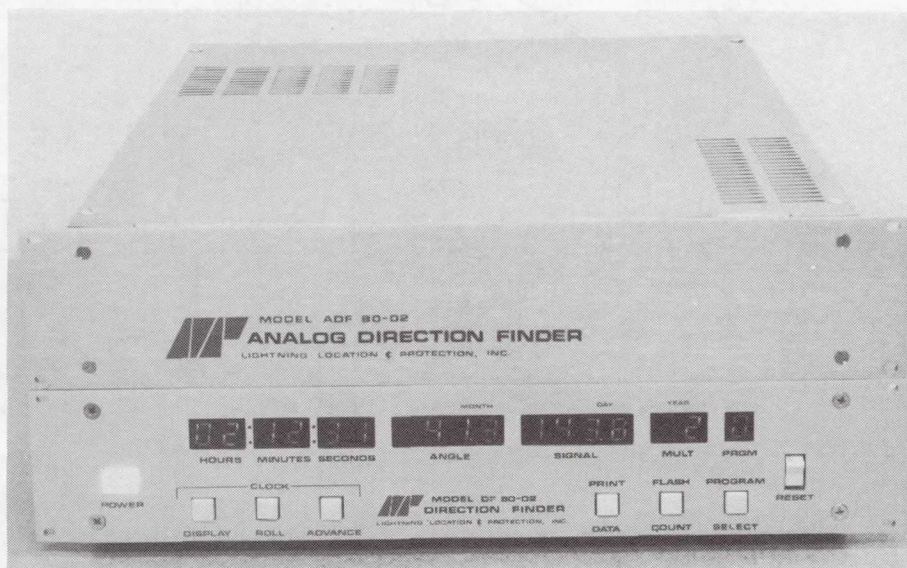


Figure 2.- The direction-finding system electronics.

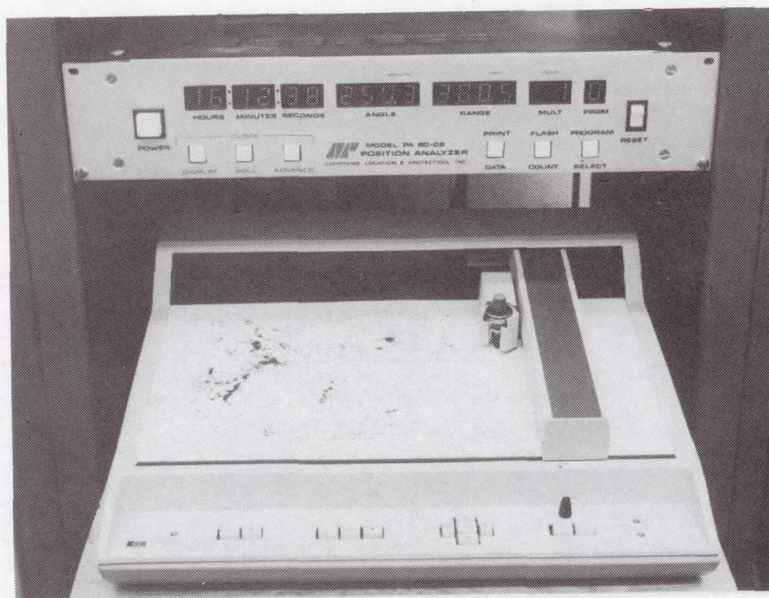


Figure 3.- The position analyzer and a digital x-y plotter with lightning map.

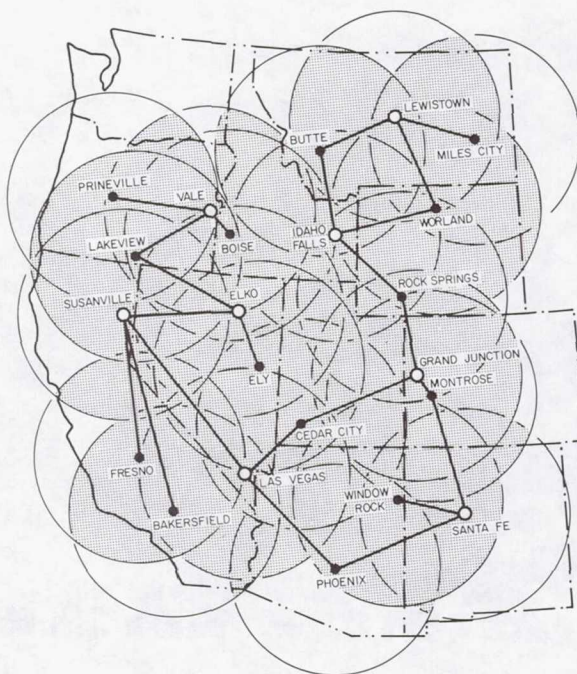


Figure 4.- The locations of direction finders (solid dots) and position analyzers (open circles) in the western U.S.

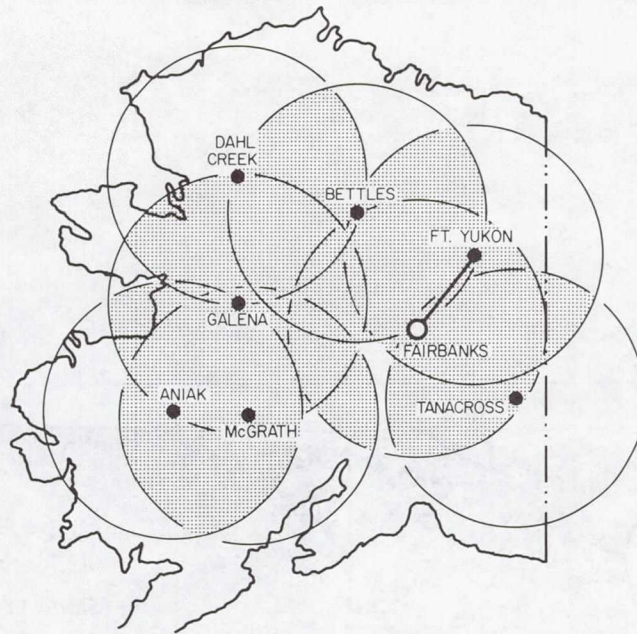


Figure 5.- The locations of direction finders (solid dots) and a position analyzer (open circle) in Alaska.

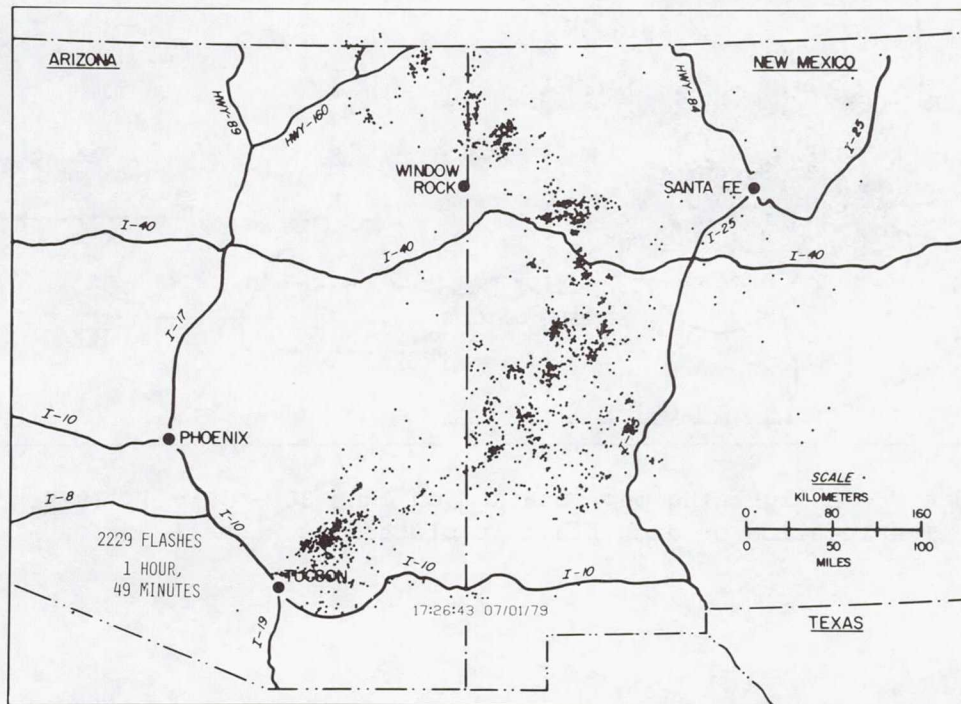


Figure 6.- A lightning position map obtained on July 1, 1979. The location of each flash is plotted as a small dot.

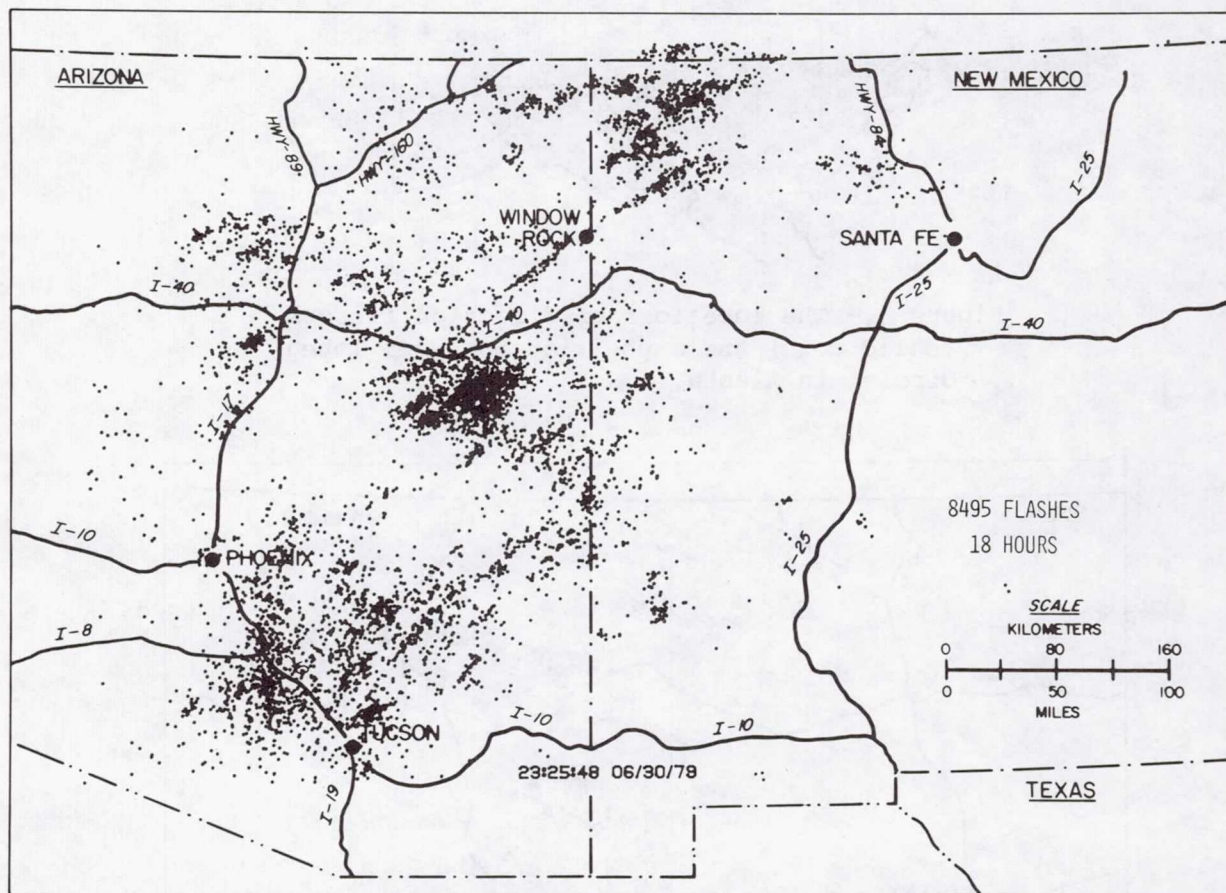


Figure 7.- A lightning map obtained on June 30 - July 1, 1979.
The location of each flash is plotted as a small dot.

A NETWORK OF AUTOMATIC ATMOSPHERICS ANALYSATORS

Josef Schäfer, Hans Volland and Paul Ingmann
Radioastronomical Institute, University of Bonn

Andrew J. Eriksson
National Electrical Engineering Institute, Pretoria

G. Heydt
Heinrich-Hertz-Institut Fuer Nachrichtentechnik, Berlin

SUMMARY

In a new version of the atmospherics analysator of the Heinrich-Hertz-Institute, Berlin, a desktop computer is connected to the analysator. The computer collects all data, makes Gaussian fits to the group time delay data, the spectral amplitude ratio data and the spectral amplitude data of each thunderstorm center, determines its azimuth and stores the appropriate parameters on the internal magnetic tape cartridge. The capacity of the tape cartridge is sufficient to store all parameters which are collected within a time interval of at least one month. Applying a propagation model, the distance of each thunderstorm center is determined in real time, so that the activity centers can be plotted immediately onto a map by means of desktop plotter. Additionally, the data are printed out on the internal paperstrip printer, and also the display of the parameters on an oscilloscope screen is possible. The operation of the system is completely automatic apart from a regular exchange of the tape every month. After copying to a normal computer tape, the digitized parameters can be handled by any large computer. At present, three equipments of this kind are (or are being) installed at Berlin, Pretoria (South Africa) and Tel Aviv (Israel).

METHOD OF MEASUREMENTS

The vertical component of the electric field E_z of a single atmospherics at distance ρ from a receiver can be expressed by a Fourier integral

$$E_z(\rho, t) = \frac{1}{2\pi} \int_{-\infty}^{+\infty} W(\rho, \omega) \hat{E}_z(\rho, \omega) e^{-i\omega t} d\omega \quad (1)$$

where

$$\hat{E}_Z(\rho, \omega) = |E_Z| e^{i\psi} = \int_{-\infty}^{+\infty} E_Z(\rho, t) e^{i\omega t} dt \quad (2)$$

is the Fourier transform of the sferic above a perfectly conducting earth, and

$$W(\rho, \omega) = |W| e^{i\Psi} \quad (3)$$

is the transmission function of the wave guide between earth and ionosphere normalized to the value of free propagation over a perfectly conducting earth.

The atmospherics analyser (ref.1 and 2) of the Heinrich-Hertz-Institute, Berlin, measures the magnitude of the Fourier transform in (1) (spectral amplitude: SA) :

$$|W(\rho, \omega) \hat{E}_Z(\rho, \omega)| \quad (4)$$

of each sferic arriving at a small band receiver (resonance frequency 5 kHz) at an angle of incidence (azimuth) ϕ .

It furthermore measures the ratio of the SA at two frequencies (9 and 5 kHz) for each sferic (spectral amplitude ratio: SAR) :

$$\left| \frac{W(\rho, \omega_1) \hat{E}_Z(\rho, \omega_1)}{W(\rho, \omega_2) \hat{E}_Z(\rho, \omega_2)} \right|, \quad (5)$$

and finally the instrument determines the second derivative of the phase of the Fourier transform in (1) (group time delay: GDD) :

$$\Delta t_{gr} = \frac{\Delta^2 \Phi}{\Delta \omega} = \frac{\Phi(\rho, \omega_1) + \Phi(\rho, \omega_2) - 2\Phi(\rho, \omega_m)}{\Delta \omega} \quad (6)$$

$$\text{where } \Phi(\rho, \omega) = \Psi(\rho, \omega) + \psi(\rho, \omega) \quad (7)$$

is the sum of the phases of W and \hat{E}_z in (1), and

$$\omega_m = \frac{\omega_1 + \omega_2}{2} \quad (8)$$

is the mid frequency ($f_1 = 5$ kHz, $f_2 = 9$ kHz, $f_m = 7$ kHz).

The group time delay Δt_{gr} in (6) is the time difference in the pulse arrival times at the two frequencies 6 kHz and 8 kHz. It is a measure of the dispersion characteristics of the wave guide.

While in the far field, above a perfectly conducting earth, the electric field is directed vertically, the vector of the magnetic field is parallel to the ground and perpendicular to the direction of incidence. Therefore, by using a crossed loop antenna plus a whip antenna, the angle of incidence of each spheric can be determined by conventional direction finding techniques, and the parameters SA, SAR and GDD are obtained by the analyser from the output of the whip antenna.

DATA ANALYSIS AND RECORDING

The probability distribution of the spectral amplitudes SA follows rather closely a logarithmic normal distribution

$$N = \frac{0.174}{\sigma} N_0 \int_S^{\infty} \exp \left\{ - \frac{(\log y - \log \bar{y})^2}{2\sigma^2} \right\} \frac{dy}{y}, \quad (9)$$

where N is the number of spherics exceeding the threshold S , N_0 is the total number within the time interval considered, σ is the root mean square value and

$$\bar{y} = \Lambda e^{-2.65 \sigma^2} ; \quad \Lambda = A |W(\rho, \omega) \hat{E}_0(\rho, \omega)| . \quad (10)$$

A is an amplification factor depending on the receiver characteristics, and \hat{E}_0 is the statistical mean of $|\hat{E}_z|$. Knowledge of Λ allows therefore to determine the transmission function $|W|$ if E_0 is known, or \hat{E}_0 can be determined if $|W|$ is known.

From the theory of VLF propagation, it follows that in the case of the first mode:

$$\Delta t_{gr} \propto \frac{\rho}{f_m^3 h^2} , \quad (11)$$

where h is the virtual height of the lower ionosphere (ref.1). More detailed calculations show that t_{gr} also depends on the azimuth of the incoming signal, on the geographic locations of source and receiver, and on the times of day and season (ref.3 and 10). The GDD measurements allow therefore to determine directly the distance between source and receiver if the propagation conditions are known. In the near field (up to some 100km) of the transmitter, the interference of several modes in the propagation of VLF waves gives rise to some ambiguities in the interpretation of the data. This nonuniqueness can be reduced considerably if the SAR data are used in addition.

In the first mode approximation, SAR like GDD is a linear function of distance:

$$SAR = \alpha_1 + \alpha_2 \rho , \quad (12)$$

where the constants α_1 and α_2 can be taken from model calculations (ref. 10, 11 and 12). However, the deviations of the GDD and SAR from linearity due to higher order modes in the near field are to a certain degree opposite to each other (ref. 11) so that the ambiguity can be reduced and the accuracy of the determination of distance can be increased by taking into account the mean value of both parameters.

In an earlier version of the equipment (ref.1 and 2), the values for the SA, SAR and GDD of each sferic exceeding the threshold of the receiver were displayed against the azimuth as points on an oscillograph screen. Every 5 minutes, a photographic picture of the screen was taken. From the point clusters in

these pictures, the mean direction of incidence and the mean values of the parameters SA, SAR and GDD could be estimated for each center of activity. Some results of the data analysis applying this method are given in ref.1 to 10. The disadvantage of this version was the necessity to determine the parameters by inspection of each picture and to punch the data in order to make them accessible to a computer. The new version of the atmospherics analyser allows completely automatic receiving, analysing and recording of the data. Except from changing the data tape cartridge of a desktop computer once every month and occasional checking of the correct operation, no maintenance is required. The mean azimuth, group delay time difference, spectral amplitude ratio and spectral amplitude of each thunderstorm center are calculated immediately during each period of measurement (in general 20 minutes) and they are printed out and stored on magnetic tape. The use of an external plotter for drawing the thunderstorm centers onto a map is also possible.

Within a time period of 18 minutes (changeable), the calculator collects the data of all incoming pulses. During the next two minutes, four histograms are calculated from the received parameters and Gaussian fits to the peaks are made, so that for each thunderstorm center the azimuth, GDD, SAR and SA are determined. After a possible power interrupt, the calculator reads automatically the whole operation program which is stored on the tape and runs it anew. In case of the occurrence of another error, the program does not stop but - with the aid of a special error recovery routine - tries to eliminate the error and goes on.

RESULTS

Since some years, a somewhat older version of the equipment (using paper tape) is operating at the Berlin station. As an example, Fig.1 shows a comparison of the synoptic data, reported within the time period 3.00 GMT to 6.00 GMT on Aug. 22. 1975 (below) with the calculated atmospherics data for the same time period (above). The distances are calculated a posteriori (not in real time) with a large computer by using the propagation model given by Harth and Pelz (ref.10), only for the GDD, however. That model gives the GDD (and SAR) per 1000 km, depending on the azimuth (more exactly on the horizontal component of the geomagnetic field, perpendicular to the propagation plane) and, in order to distinguish between day and night conditions of the ionosphere, on the elevation of the sun, i.e. on geographic coordinates, time of day and season.

One notices that generally all synoptic reports correspond to sources detected by the atmospherics analyser, whereas, because of the absence or non-function of a weather station (e.g. on the Atlantic Ocean), not all atmospheric sources have their synoptic counterparts. It is obvious, e.g. from the activity centers on the Atlantic Ocean and in the 135° direction, that the direction finding system and the source-finding computer program are quite reliable. The differences in distance for one source arise mainly from the still imperfect

propagation model which takes only the GDD into account. Especially during sunset and sunrise and during disturbed ionospheric conditions, considerable deflexions from model conditions can occur.

These effects can be eliminated, when at least two stations are available for direction finding. Since December 1979, a new station is operating at Pretoria, South Africa, and simultaneously a further new equipment is built up for testing purposes at Bonn, West Germany, which will be installed shortly at Tel Aviv, Israel. The Pretoria station is equipped with a plotter, which (if desired) marks all (or only the largest) atmospheric sources by signs on a map as shown in Fig.2. In the new version, the model values for the GDD and SAR, depending on the parameters mentioned above, are included in the operation program of the desktop computer, so that a real time determination of the distance of activity centers is possible. At this stage of development, the model of Harth and Pelz (ref.10) is used; it can still be optimized, however, during the course of measurements, when a sufficient number of simultaneous recordings from different stations are available.

As an example, Fig.2 (right) shows the printout of the Pretoria and Bonn stations at Jan. 12. 1980, near 4.00 GMT, and, on the left, two of the associated activity centers, one in South America near 10°S , 75°W , at ca. 258° from Bonn and 256° from Pretoria, the other in Middle Africa, near 8°N , 35°E , at ca. 242° from Bonn and 11° from Pretoria. For a better survey, a map containing only the orthodromes and distance circles for the Pretoria station is chosen. While the propagation from South America to both stations is during pure night conditions, the day-night terminator passes the African source near 4.00 GMT. One notices that the bearings are again quite constant, and that the fluctuations in distance for the South American source which is more than 10000 km away are already considerably suppressed. With the exception of one case which is too close, this is generally true also for the African source, although the modelling of the propagation conditions during the day-night transition is rather difficult. This is true in particular in that case, where the propagation path forms a small angle with the terminator.

In order to give a further impression of the operation of the system, another preliminary result is shown in Figs.3a and 3b, where the overall activity recorded by the Pretoria station is plotted within longer time intervals. Each cross symbol marks the location of an activity center. However, the distances are only rough estimates, because, for testing purposes, they were determined by using always a constant model value ($33 \mu\text{sec per } 1000 \text{ km}$) for the GDD only (which is too small during day and too large during night for most directions), so that the sources are partly spread out along the propagation paths (e.g. in South America). Some isolated points are migrated too far away, e.g. north of 50°N in Fig.3b. These effects are eliminated, or at least considerably reduced, when the optimal model is applied. In Fig. 3a, the activity during the time interval from Jan. 24. 1980, 5.45 GMT to Jan. 25. 1980, 5.45 GMT is shown, Fig. 3b shows the accumulated activity for one week, Jan. 25. 1980 to Jan. 31. 1980.

The fact that there are (nearly) no sources observed in the Mediterranean area is due to the blocking out of these sferics (which are not so frequent

during the winter season) by the more active sources in the nearer environment of the station. Generally, the marked South American Sources are detected during night time propagation conditions, which will be emphasized later by the use of different plot symbols for different times of day. On the whole, the range of the method is much larger during night time because of the upward shifting of the lower ionosphere.

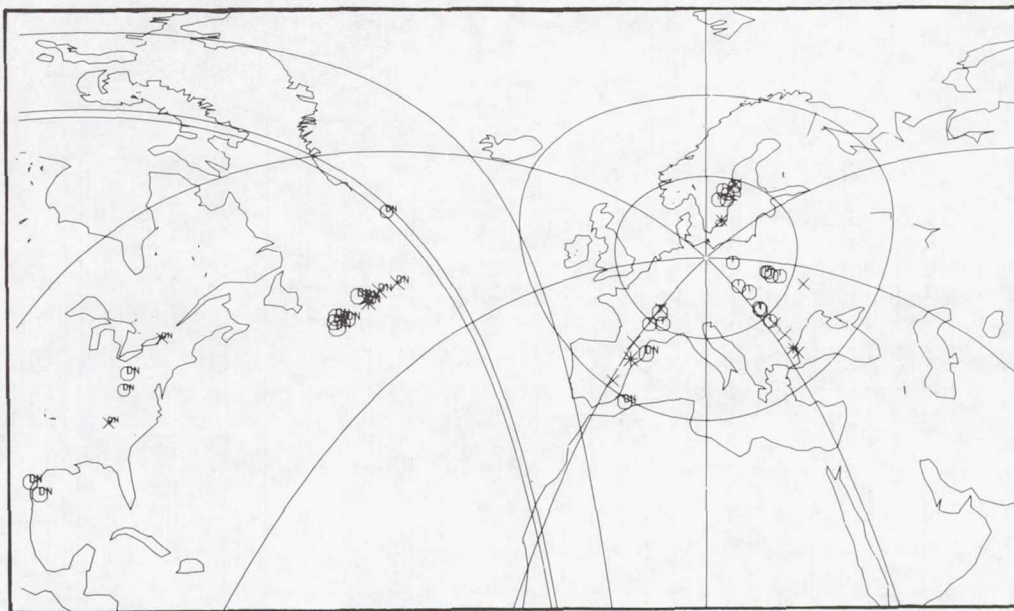
Of course, even after optimizing the propagation model, there will be some deflexions from model conditions caused by ionospheric perturbations which cannot be forecasted. However, as already mentioned, they will be at least partly suppressed by the opposite course of the GDD and SAR parameters. On the whole, an accuracy of direction finding of about 0.5° and of distance determination of about 5% is expected. The reason that not all sources lead to simultaneous bearings from two or more stations (cf. Fig. 2) is firstly due to the possible blocking out of more distant sources by closer and more active sources in the same direction, and secondly to the selection of the few strongest activity centers by the operating program. However, the selection threshold can be modified, and it will also be adjusted to optimal conditions during the course of measurements. Finally, the detection of atmospheric sources is limited by the range of the whole system, depending on azimuth, local time and season (cf. Fig. 3). The minimum distance, where an unambiguous determination of the parameters becomes impossible due to the interference of the higher order modes is ca. 300 km. The maximum distance reaches from a few thousand kilometers for activity centers in the east direction to more than 10000 km for signals from the west direction during night time propagation conditions.

REFERENCES

1. Volland, H.; Heydt, G.; Harth, W.: Statistical Measurement of Spectral Amplitude and Phase of Atmospherics in the VLF Range. AGARD Conference Proceedings No 33. K. Davies (ed), Technivision Services, Slough, England, 55, 1970.
2. Volland, H.: Review of a German Equipment for Locating Thunderstorm Areas. NRL Report 7763, Naval Research Laboratory, Washington, D.C., 361, 1974.
3. Harth, W.: The Delay Time Difference and the Amplitude Ratio of Spectral Groups within Various Propagation Models, NRL Report 7763, Naval Research Laboratory, Washington, D.C., 147, 1974.
4. Frisius, J.; Heydt, G.: Spectral Parameters of the VLF Radio Noise Observed as Functions of Azimuth. Radio Sci. 3, 1004, 1968.
5. Frisius, J.; Heydt, G.: Statistical Analysis of Data from the Atmospherics Analyser. NRL Report 7763, Naval Research Laboratory, Washington, D.C., 381, 1974.
6. Heydt, G.: Observation of Single Storm Complexes with the Atmospherics Analyser. NRL Report 7763, Naval Research Laboratory, Washington, D.C., 420, 1974.
7. Harth, W.: Daily Variations of VLF Atmospherics Parameters for Long-Lasting Thunderstorms. NRL Report 7763, Naval Research Laboratory, Washington, D.C., 462, 1974.
8. Harth, W.: The Propagation of Atmospherics. Electric Processes in Atmospheres. H. Dolozalek and R. Reiter (eds.), D. Steinkopff Verlag, Darmstadt, 663, 1977.
9. Harth, W.; Hofmann, C.A.; Falcoz, H.; Heydt, G.: Atmospherics Measurements in San Miguel, Argentina. J.Geophys.Res. 83, 6231, 1978.
10. Harth, W.; Pelz, J.: Eastern Thunderstorms Located by VLF Atmospherics Parameters. Radio Sci. 8, 117, 1973.
11. Harth, W.: Theory of Low Frequency Wave Propagation. Handbook of Atmospherics. H. Volland (ed.), CRC-Press, Boca Raton, FL., 1981.
12. Volland, H.: Low Frequency Radio Noise. Handbook of Atmospherics. H. Volland (ed.), CRC Press, Boca Raton, FL, 1981.

ATMOSPHERICS-SOURCES:

* $\Delta T=0$; X $\Delta T<1H$; $\odot \Delta T\leq 3H$ 06.00 GMT



OBSERVED FLASHES

LEGEND: < $R=T=0H$; $\square R=T\leq 1H$; $\triangle R=T\leq 3H$

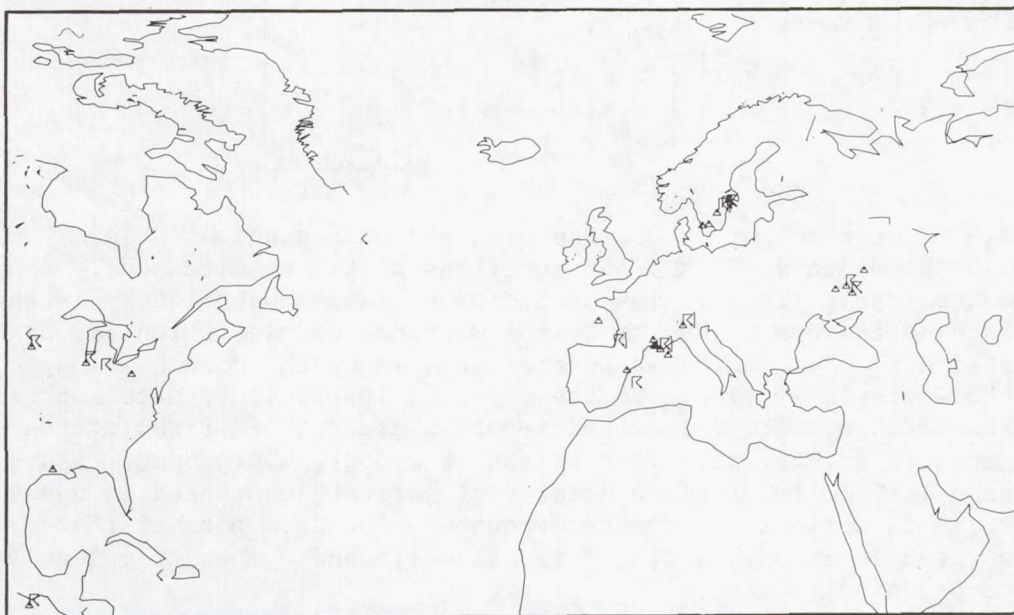


Figure 1.- Comparison of atmospheric sources (above) with synoptic data (below) on Aug. 22, 1975 between 3.00 GMT and 6.00 GMT. Sources within each single period are marked by different signs: $T=0$: 6.00 GMT, $T\leq 1H$: 5.00 GMT to 6.00 GMT and $T\leq 3$: 3.00 GMT to 5.00 GMT. "DN" indicates that the propagation path intersects the day-night boundary which is drawn (above) for both ground and ionospheric level at 6.00 GMT.

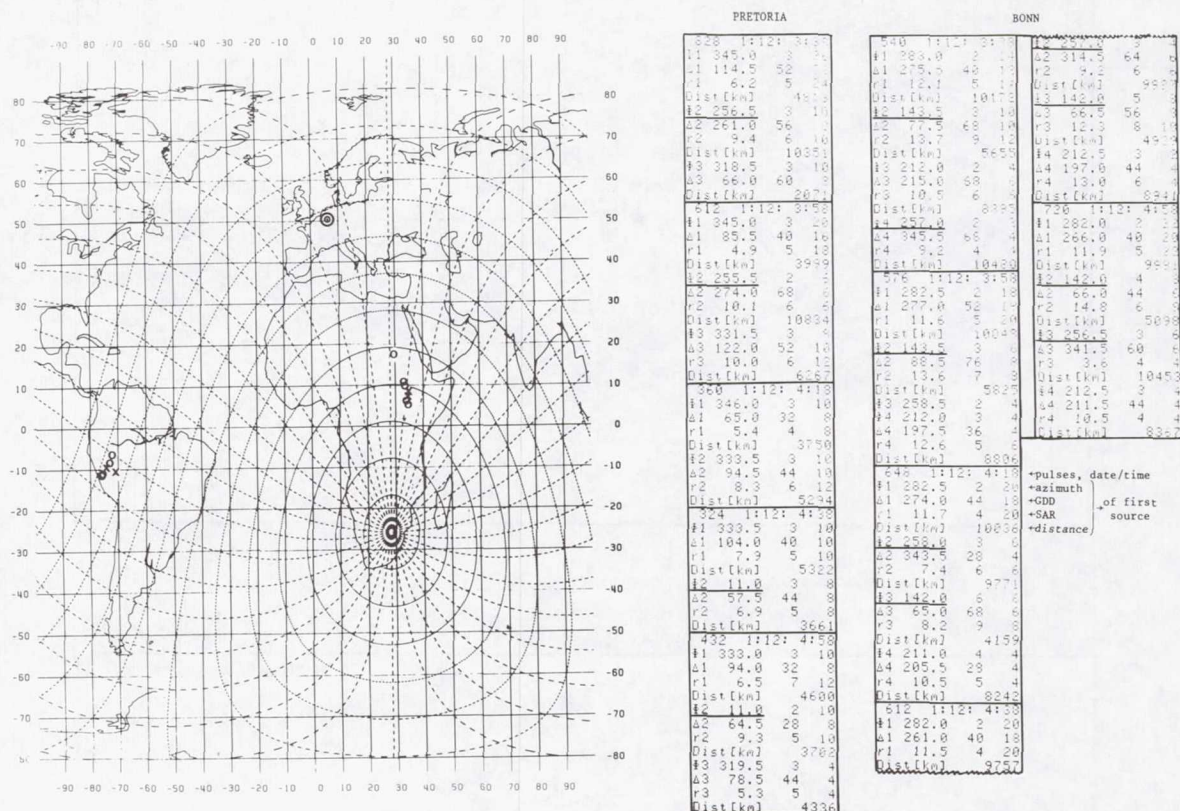


Figure 2.- Printer output of the Pretoria and Bonn stations (right) on Jan. 12, 1980, 3.38 GMT to 4.58 GMT, and locations of two simultaneously recorded sources on a map (left). The orthodromes, dashed with 100 km intervals, are intersected every 1000 km by the distance circles which are dashed with 1° intervals. "O" indicates sources located by the Bonn station, "X" is for the Pretoria station. On the paper strip printout, date and time (GMT) and the total number of received impulses are printed first at the end of each measuring interval. Then azimuth ϕ : ϕ (deg), GDD: Δ (μ sec), SAR:r(dB) and Distance (km) follow for each center of activity, numbered in descending order (SA is optional). The three numbers for each parameter are: mean value (peak location), width of Gaussian fit and number of pulses from that source per minute.

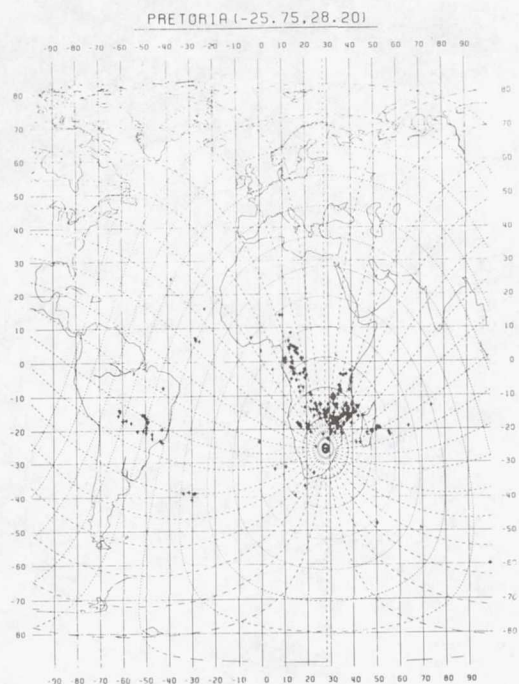


Figure 3a.- Accumulated activity for the time period from Jan. 24, 1980, 5.45 GMT to Jan. 25, 1980, 5.45 GMT. Each sign marks an atmospheric source within one 20 minute measuring interval. The South American Sources, as well as the sources between 10°E , 10°S and 20°E , 10°N in Central West Africa were observed during night time.

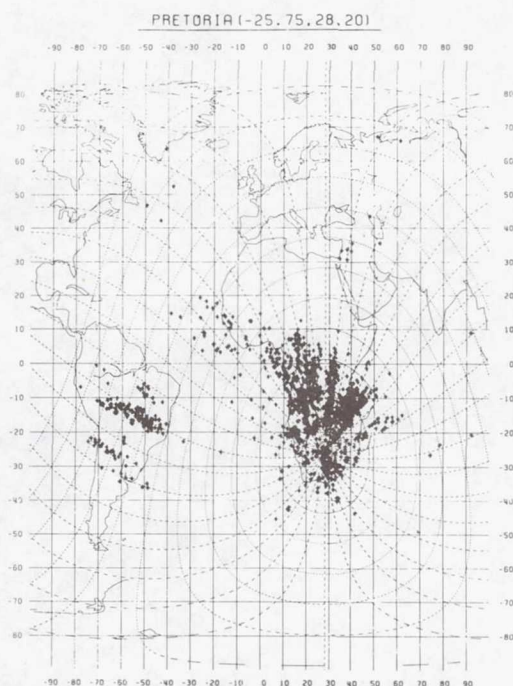


Figure 3b.- Accumulated activity for the time period from Jan. 25, 1980, to Jan. 31, 1980 (one week) recorded by the Pretoria station.

Page intentionally left blank

SESSION IV - LIGHTNING INTERACTION AND SIMULATION

Page intentionally left blank

SHIELD TOPOLOGY IN LIGHTNING TRANSIENT CONTROL

E. F. Vance
SRI International

F. M. Tesche
LuTech, Inc.

ABSTRACT

A formalism in which the interaction of a system with an electromagnetic source is described by sets of scattering, penetrations, and propagation functions will be reviewed and interpreted in the context of the lightning interaction problem. In this formalism, the system is decomposed into simple volumes separated by closed shield surfaces. These surfaces may be nested and interconnected to produce higher levels of shielding and subvolumes within a given level. The interaction analysis uses scattering theory to define current and charge densities on the shield surfaces, in conjunction with the diffusion, apertures and transmission line analysis, to define penetration through shield imperfections and propagation within the protected volume.

Because the protection of electronic circuits from the lightning source is viewed as the use of shields to provide electromagnetic separation of the volume containing the circuit from the lightning source, a rational approach to the treatment of apertures and penetrating signal power or other conductors is to minimize these compromises to the shield. This view also makes questions regarding the grounding of filters and surge arresters irrelevant since the proper use of filters and surge arresters is to close the shield about the conductor (outof-bond or above some threshold voltage).

These and other interpretations of the use of shield topology to implement interference control and decide issues of grounding and shielding are described.

INTRODUCTION

Small-signal electronic circuits, whether they use discrete components or integrated circuits, are susceptible to malfunction or damage caused by transient interference of a few volts or a few tens of milliamperes. On the other hand, transients associated with lightning and switching on power lines and buried communication cables commonly have peak currents of tens of kiloamperes and peak voltages of megavolts. Thus, if small-signal electronic circuits are to be operated by commercial ac power or used in systems that are interconnected by long cables, it is apparent that the structure between the outside cables or

power conductors and the small-signal electronic circuits must be capable of reducing the transient peaks by over 100 dB.

The perfectly-conducting closed shield completely isolates the volume enclosed by the shield from electromagnetic sources outside the shield, as illustrated in Figure 1. Therefore, if we could enclose our electronic system in such a shield, it would be completely immune to lightning, EMP, and other external sources of interference .

However, because such a closed system does not allow electromagnetic signals to enter or leave the system, we must compromise the shield to allow information to flow into and out of the system. Further compromises are usually necessary to supply power to the system and to dispose of waste heat. Doors and access hatches are necessary to allow the equipment to be installed and serviced. If the system requires human operators, many more accommodations must be made. Finally, perfect conductors for large-scale shielding are not yet practical.

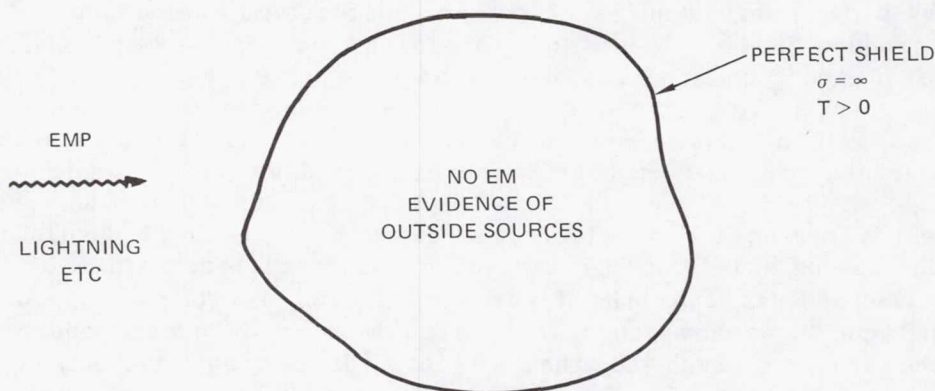


Figure 1.- Electromagnetic isolation with a perfect shield.

Because of these deviations from the closed, perfect shield two or more levels of shielding may be required to protect small-signal circuits from strong sources of interference such as lightning and the EMP. Although one can approach the shielding effectiveness of the ideal shield with arbitrary closeness by using thick metal shields with sophisticated treatments of all conductors and apertures penetrating the shield, in practice such an approach is very costly to implement and maintain. Furthermore, achieving nearly perfect shielding in practical systems is inappropriate because electromagnetic interference of significant amplitude is generated by the system itself.

Thus, we may find that it is indeed more practical to use two or more levels of imperfect shielding. For example, the first shield might be the building or room metal structure, the metal skin of an aircraft, or the hull, decks, and bulkheads of a ship. The second shield is usually the metal equipment cabinets.

Such multilayer shields occur naturally as a part of the structural design in many systems; with a modest interference-control design based on topological concepts, an effective shield system can be developed.

SYSTEM TOPOLOGY AND INTERACTION

Virtually every system is comprised of a number of conducting surfaces which can be used to form an electromagnetic shield.^{1,2,3} Consider, for example, the aircraft. A topological model for an aircraft and its associated electronic equipment might be that shown in Figure 2. The aircraft skin, denoted as surface $S_{0,1}$, is seen to have aperture and diffusive penetrations, as well as points where energy can be injected directly into the interior of the system, (i.e., via deliberate antennas on the aircraft). Additional shielding surfaces, such as $S_{1,2}$ and $S_{2,3}$, which might correspond to shielded equipment racks, black box shielding, coaxial cables, etc., are located in a nested fashion within the first shield. The unprotected region exterior to the aircraft is denoted by V_0 . With our notation, the surface $S_{i,j}$ separates volumes V_i and V_j .

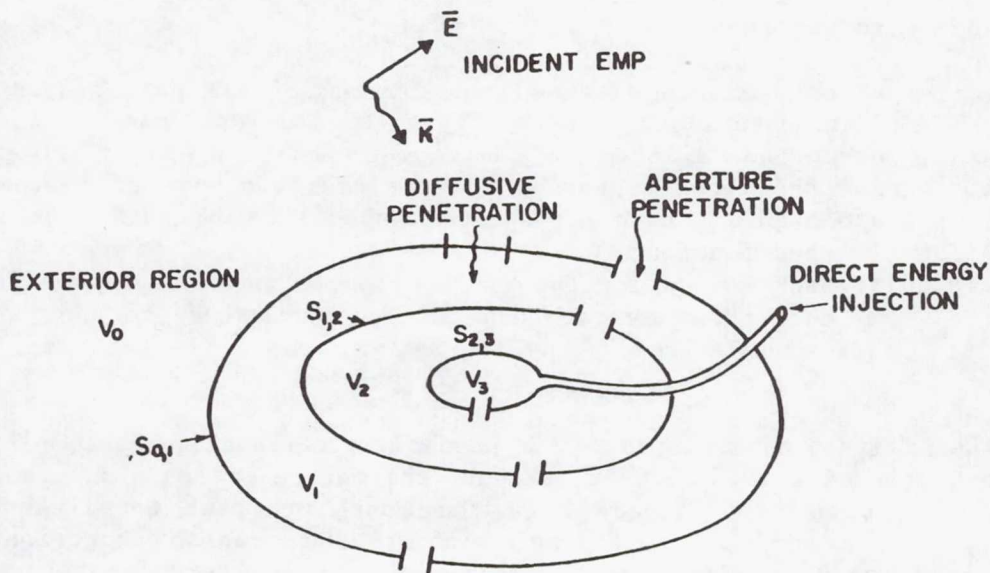


Figure 2.- Simplified shield topology of aircraft.

The interference energy, which is incident on the system from volume V_0 and eventually excites some interior circuits, can be viewed as undergoing a number of interactions with the various surfaces of the system. Energy that penetrates the surface $S_{0,1}$ will then produce fields in the volume V_1 and induce charges and currents on the surface $S_{1,2}$. These currents and charges will cause energy to penetrate into volume V_2 . This process continues sequentially until the energy reaches the circuit level.

An actual aircraft will have additional compartments located inside the $S_{0,1}$ surface but which do not lie within $S_{1,2}$. These cells, such as the bomb bays, wheel wells, and equipment bays, can act much like a shielded enclosure and are often referred to as elementary volumes. The formalism applied to the $S_{j,j}$ surfaces can also be used for these enclosures. Because all of these elementary volumes occupy part of the same principal volume V_j , it is necessary to employ another subscript, k , to distinguish between the various regions. Thus, the k th subvolume within the j th region will be denoted by $V_{j,k}$, with the k subscript dropped if no subvolumes exist. Figure 3 shows a hypothetical example of a more complete version of a shielded system. Within the V_1 region, note that there are four subvolumes denoted by $k = 1, 2, 3$ and 4 . These volumes can be identified as $V_{1,1}, V_{1,2}$, etc. Since a particular volume within a system can be labeled by two indices, j and k , it is convenient to refer to these indices as the longitudinal and transverse shielding numbers, respectively.

In this case, it is necessary to expand slightly the index on the terms $S_{j,j}$ to permit a precise definition of the various surfaces. The surface dividing volumes $V_{j,k}$ and $V_{k,\ell}$, is thus described as $S_{j,k;k,\ell}$. Some of these surfaces are indicated in Figure 4.

The interaction sequence diagram is a diagram of all possible interaction paths from one volume to another in the system topological model. A portion of the interaction sequence diagram for the geometry of Figure 3 is illustrated in Figure 4. The dotted lines represent the configuration of the system and the solid lines are the interaction paths from the outside, V_0 , to various volumes inside. The transfer function for a particular path connecting the $V_{j,k}$ region to the $V_{l,m}$ region is denoted by $T_{j,k;l,m}$. If more than one path exists from one volume to another, superscripts (1), (2), etc., will distinguish between the different transfer functions.

In the analysis of a system, it is necessary to identify the complete interaction sequence diagram. However, because the entire interaction sequence diagram can be quite complicated, only the most important coupling paths are considered. The decision regarding which of the transfer functions may be neglected is reached by examining results of canonical problems which treat a particular aspect of the overall problem (aperture penetration is but one example), or by examining experimental results.

A rigorous formalism has been developed by Baum in which the overall interaction is described in terms of wave scattering functions that define the charge and current density on the shield surfaces.⁴ Within a volume where interference

largely propagates along cables and other conductors, multiconductor transmission line theory can be used to describe energy "tubes." Junctions of these "tubes" can be described with scattering matrices.⁵

PRESERVING SHIELD TOPOLOGY

The essence of interference control is to identify the compromises --particularly the insulated conductors and apertures in the shield topology --and to apply corrective measures. To this end it is useful to keep in mind that complete isolation is obtained with the topologically closed shield. All deviations from the topologically closed surface are then immediately identified as compromises that may require corrective action.

Effective corrective measures preserving the shield in the vicinity of the compromises will be those that tend to close the shield or eliminate the interaction path so that externally-induced currents and charges are confined to the outside surface of the shield.

In the following sections we discuss the corrective techniques for the three principal types of compromises. The categories are, in order of importance, (1) insulated conductors traversing the shield surface, (2) apertures in the shield surface, and (3) imperfectly conducting shield materials.

Propagation Along Conductors

The worst violations of the shield topology are usually insulated conductors that penetrate the shield, since these conductors allow large currents induced outside the shield to propagate into the protected region inside the shield. Figure 5 illustrates the proper method of handling these conductors at the first shield. Note that in each example the proper design causes the large interference currents induced outside the shield to be diverted to the outside surface of the shield, thus preserving the shield topology. In particular, note that grounding conductors should not penetrate shields otherwise they, as well as any other conductor, may allow interference to propagate through the shield.

Power and signal conductors cannot be connected to the shield continuously as can plumbing, waveguides, and grounding conductors, but they can be connected momentarily when a threshold is exceeded (i.e., through a surge limiter) or at all out-of-band frequencies (through a filter). Even in this case, however, it is appropriate to think of the surge limiter or filter as a device for closing the shield about the conductor so that the current remains on the outside surface of the shield.

Only "short-circuit" devices, those that divert the conductor current to the shield, have been illustrated here because at the first level of shielding the interference levels caused by lightning are very large. "Open-circuit" devices, such as chokes and dielectric gaps, must be capable of withstanding

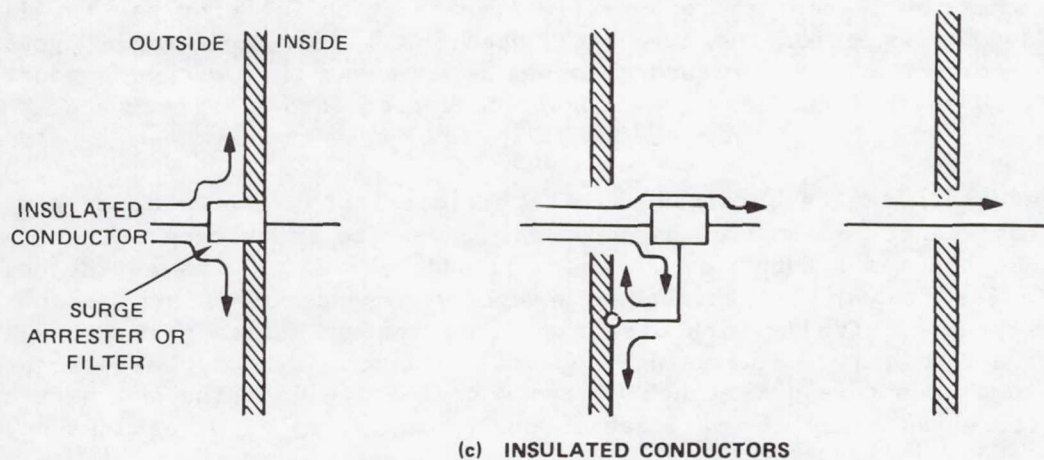
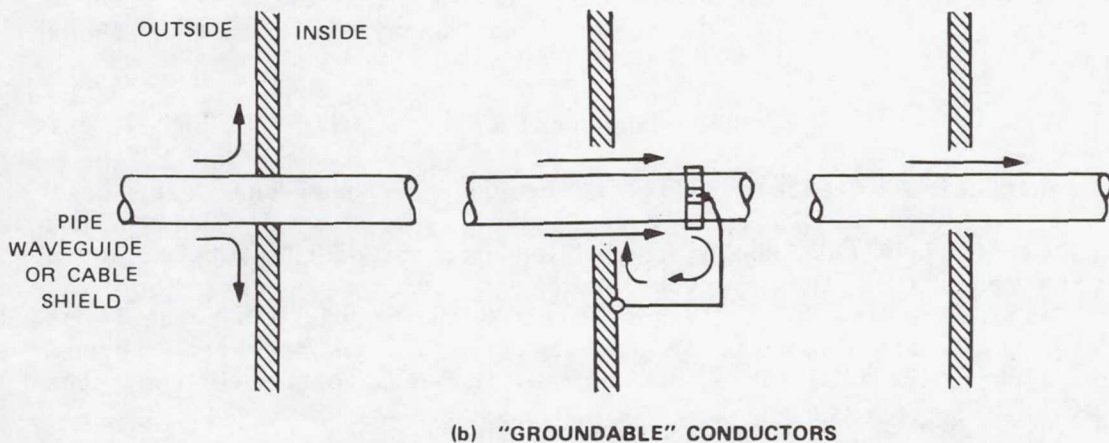
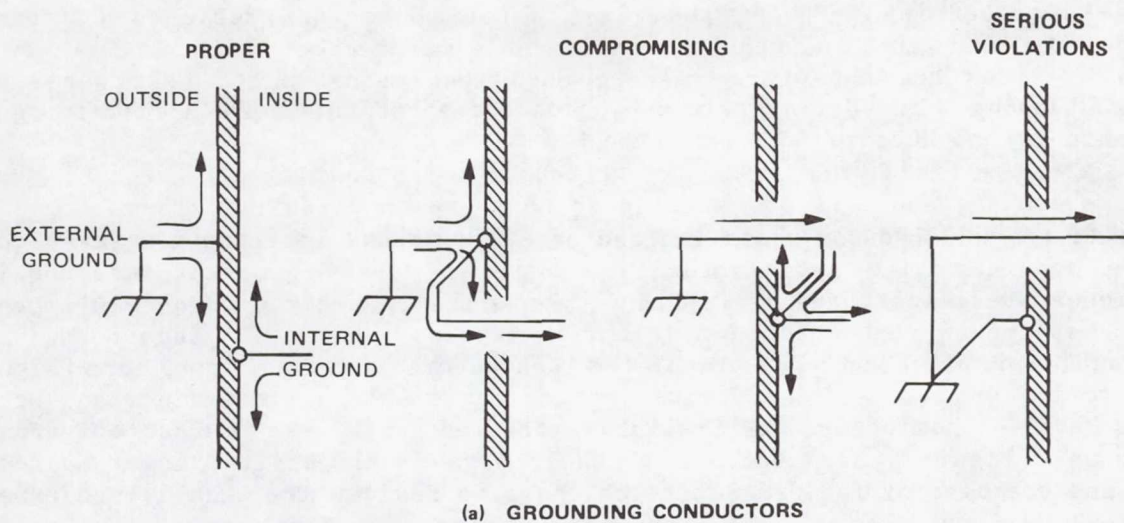


Figure 5.- Shielding integrity near interference-carrying external conductors.

voltages approaching 1 MV at the first shield. Devices designed for these voltages are expensive and require considerable maintenance, whereas the short-circuit devices are cheap and require much less maintenance. For water and sewage plumbing, however, plastic piping can be substituted for metal piping to eliminate the conductor.

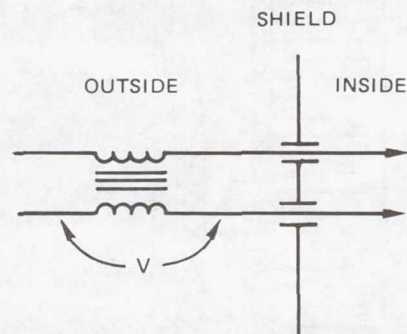
At secondary and tertiary shields where the open-circuit voltages are less severe (i.e., hundreds of volts instead of MV), current-interruption techniques can be applied quite satisfactorily. Several passive current-interruption techniques are illustrated in Figure 6, where the open-circuit voltage impressed across the current-interrupting device is also indicated. Such techniques are usually applied only to insulated conductors such as power and signal conductors; "groundable" conductors such as cable shields, plumbing, and waveguides are economically and reliably treated with the current-diversion approach of Figure 5(b). Because of their higher reliability, lower maintenance, and the ease of failure detection, passive devices are usually preferred. Active devices such as gas tube or solid-state surge limiters must be tested periodically to ascertain that they function, since their failure is often not apparent during the normal functioning of the system. Furthermore, these non-linear devices tend to regenerate the high-frequency spectrum that the shield excludes.

Aperture Control

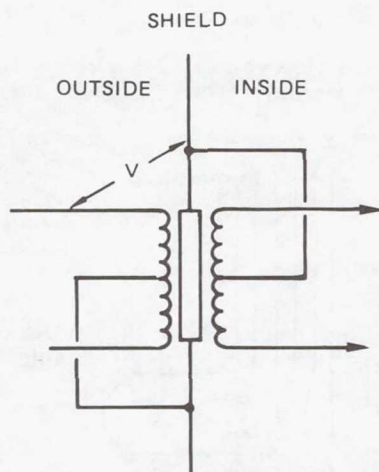
The penetration of external fields through apertures that are small compared to a wavelength is illustrated in Figure 7. As shown in Figure 7(a), part of the electric field that would otherwise terminate on the outside surface of the shield penetrates the aperture where it may induce charge on internal cables. Similarly, some of the magnetic field that would otherwise be bounded by the surface current in the shield is permitted to penetrate through the aperture, link an internal cable, and thereby induce a voltage in the cable [see Figure 7(b)].

If a given area of wall opening is subdivided into, say, ten small openings having the same total area, the penetrating fields at an interior point will be about $1/\sqrt{10}$ as large for the ten small openings as for the single opening. Thus, one common treatment for such openings is to cover them with a conducting screen or mesh so that the large opening is converted into a multitude of small openings.

More reduction can be obtained with sacrifices in optical transparency and increased resistance to air flow by adding thickness to the screen. Each small aperture then becomes a tube through the wall and behaves as a waveguide beyond cutoff. Fields transmitted through a waveguide beyond cutoff are attenuated approximately exponentially with distance along the guide, so that very large attenuation may be achieved by using many small tubes welded or brazed together in a honeycomb structure. Sketches of the magnetic field in the vicinity of a single aperture, an array of small apertures, and an array of waveguides beyond cutoff are shown in Figure 8.

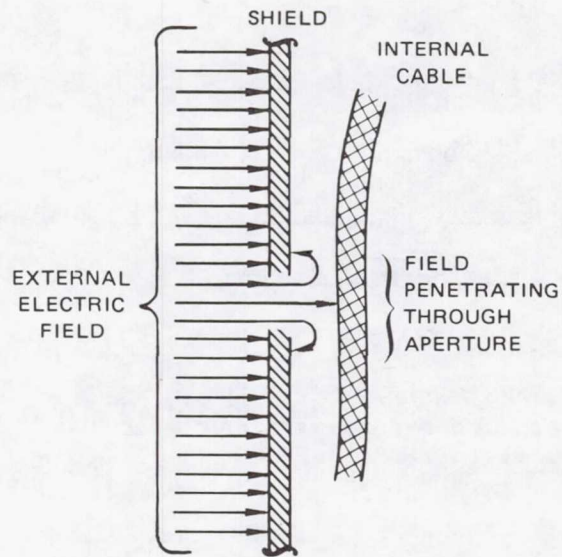


(a) BIFILAR CHOKE AND FEEDTHRU CAPACITORS
(passes dc and ac)

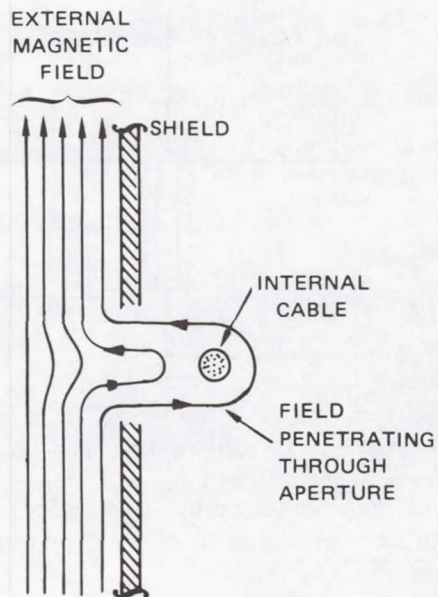


(b) ISOLATION TRANSFORMER (ac only)

Figure 6.- Passive current interruption techniques
for penetrating conductors.

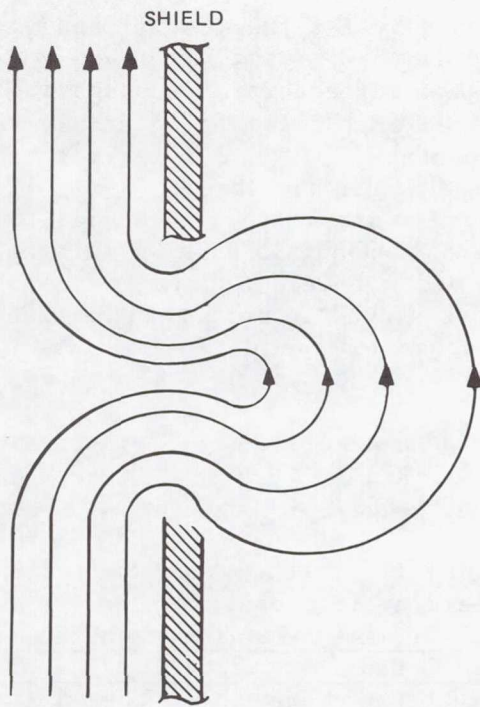


(a) ELECTRIC FIELD

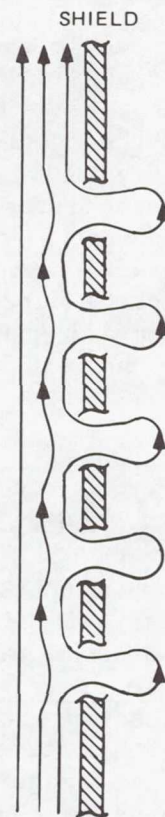


(b) MAGNETIC FIELD

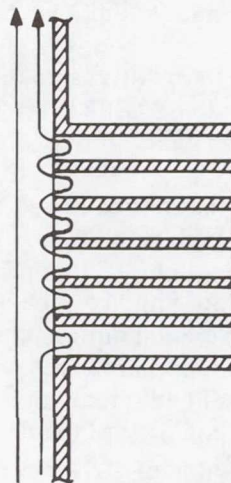
Figure 7.- Electromagnetic penetration of small apertures.



(a) SINGLE APERTURE



(b) MANY SMALL APERTURES



(c) ARRAY OF WAVEGUIDES
BEYOND CUTOFF

Figure 8.- Magnetic field penetration of apertures.

Diffusion Through Shield Walls

Continuous, closed sheet-metal shields are by far the most effective electromagnetic shields because they severely limit the penetration of energy in the spectrum above $f\delta = (\pi\sigma d^2)^{-1}$ and they are good reflectors of propagating waves throughout the spectrum. Because the duration of the lightning stroke current is frequently longer than the shield time constant, $\tau_s = \mu\sigma d^2$, for most shielding materials diffusion of lightning fields through the shield is significant. Nevertheless, it is estimated that a 20-kA direct stroke to a 10-m-dia., 0.5-mm-thick spherical aluminum shell would induce only about 15 V in an internal wire parallel to the current path, providing it did not melt a hole in the shield. The rise time of the induced voltage would be slowed to more than 3 μ s, even if the stroke current had zero rise time, because of the diffusion time of the shield.

SHIELD DESIGN CRITERIA

Since we cannot provide ideal shields in practice, we must develop some rational basis for determining how much shielding is necessary. We can readily specify a minimum shielding criterion: the minimum shielding required is that necessary to prevent damage to equipment enclosed (protected) by the shield. That is, the first level of shielding should be good enough so that lightning, EMP, and other external sources cannot cause insulation breakdown or other unacceptable damage to equipment in the protected volume. There is little benefit in using a poorer shield because with it the equipment would be damaged anyway.

The minimum shield thus prevents damage to the protected system but it does not prevent degraded performance caused by the residual interference penetrating the shield. Hence, digital circuits may be upset and analog circuits may suffer poor signal-to-noise ratio (SNR). To eliminate these effects, more shielding than the minimum specified above will be required.

In analog circuits the SNR is determined by signal strength and the resultant strength of the noise (1) generated in the circuit, (2) generated by other equipment in the protected space, and (3) generated outside the protected space, penetrating the shield, and coupling to the circuit. The best we can achieve with improvement in the shield is to reduce the noise from external sources to a level at which it is negligible compared to the circuit and internal noise. The cost of making the shield any better than that required to make the externally-generated noise negligible is not justified by a possible improvement in performance, because circuit performance is now determined by internal and circuit-generated noise, not by externally-generated noise.

A similar rationale can be used to specify shielding for digital circuits. Because the signal is a pulse, however, we are concerned with impulsive interference rather than the noise spectrum. For the digital circuit, therefore, we may argue that the shield is sufficient if the peak voltage (or current) induced

on a protected signal conductor by external sources is small compared to that induced on the conductor by internal sources. That is, if the shielding is such that the peak interference is determined by internal, rather than external, sources adding more shielding does not produce the desired benefit of improved circuit performance.

At the second shield this implies that both the internally-generated and the attenuated, externally-generated interference must have peak values smaller than the logic level of the digital circuit. Thus, it is assumed that transients with peak values equal to or greater than the logic level can produce a logic error. In evaluating the internally-generated interference level, however, we may overlook internal interference synchronized with the logic train; such coherent interference can often be rejected by digital circuits even if it is larger than the circuit logic level.

Also inherent in the criterion for reducing externally-generated interference to a level below the internally-generated interference is the assumption that the system will perform satisfactorily in the normal internal environment. If, in fact, the system will not tolerate the normal internal environment, as is sometimes the case, one must first (1) improve the internal environment, or (2) improve the system tolerance. Regardless of which of these courses is pursued, however, the shielding criterion for controlling externally-generated interference is the same --only the levels change.

ALLOCATION OF SHIELDING

The advantage of these shielding criteria is that they place rational bounds on the amount of shielding required at any level. At the first level of shielding, which may be of primary interest to facility designers, these criteria have particular importance. If the first shield is designed to make externally-generated interference smaller than internally-generated interference, then any equipment that can tolerate the internally-generated interference will also tolerate the external transients. For ground-based systems operated from commercial electric power, peak transient voltages of 500 to 1,000 V are common. Such transients may be generated by lightning and by switching in the power distribution system. Similar transients may be produced inside a facility by high-current devices (rectifiers, water heaters), solenoid-actuated equipment (time clocks, vending machines), and by starting and stopping large motors. Therefore, the requirements that the first shield limit interference from external sources to levels comparable to those generated internally is not usually overly restrictive.

At the second level of shielding, usually the electronic equipment case, the interference must be further reduced until it is smaller than the logic levels used in the electronic circuits. Since these levels are typically between a fraction of a volt and a few volts, the second shield must be capable of reducing the interference induced on small-signal conductors by sources outside the shield to a fraction of a volt. This requirement is again not overly

restrictive because the severity of the environment outside the second shield has already been limited by the first shield. In fact, the second shield will ordinarily be specified by the electronic equipment manufacturer, and the shielding requirement is merely a specification that the equipment should operate reliably in the ambient environment to which it will normally be subjected.

Exceptionally noisy intermediate environments may be produced by high-power transmitters, large rectifiers, diathermy equipment, etc., inside the facility. It is often desirable to reduce the interference produced by these machines to avoid procuring special high-tolerance equipment for a facility. Two topologically different approaches to controlling such sources are depicted in Figure 9. In the first approach, the first shield is distorted to exclude the offending source, thus preserving the moderate intermediate environment with one shield. In the second approach [Figure 9(b)] a separate shield is provided to confine the offending source. The same principles are used to design the confining shield (shield 1B) as are used to design the facility shield (shield 1A) except the source is inside shield 1B, while it is outside shield 1A.

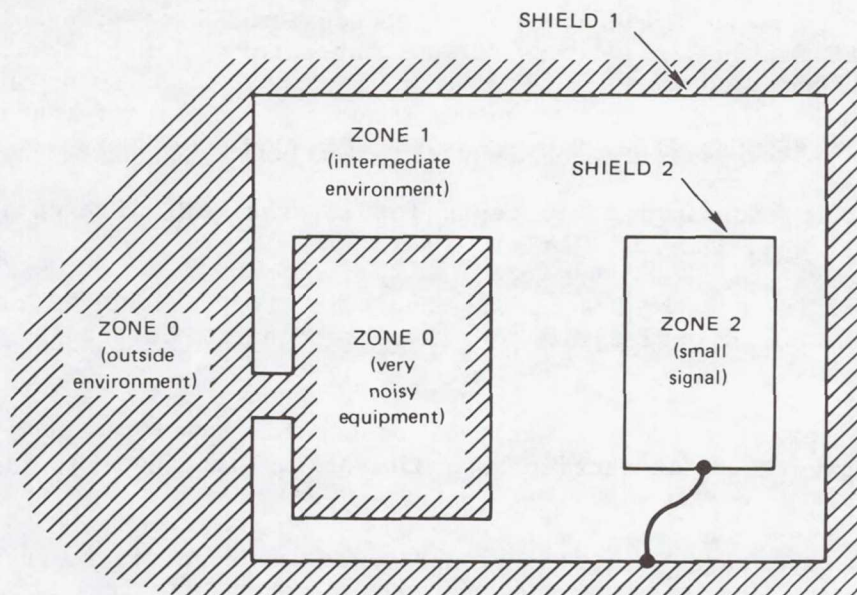
CONCLUSIONS

Interference control is primarily a matter of providing adequate shielding barriers between the interference sources and potential victim circuits, since interfering signals of a given amplitude and spectral content will produce similar undesirable effects regardless of the source. The goal of both interference control and electromagnetic compatibility work is to limit the amount of undesirable signal that reaches a victim circuit to levels that the circuit can tolerate without impaired performance. In the EMP and lightning environment the source is outside the space to be protected, while in the general EMC case the source may be either outside or inside this space. The shield in either case is used to separate the source from the protected space.

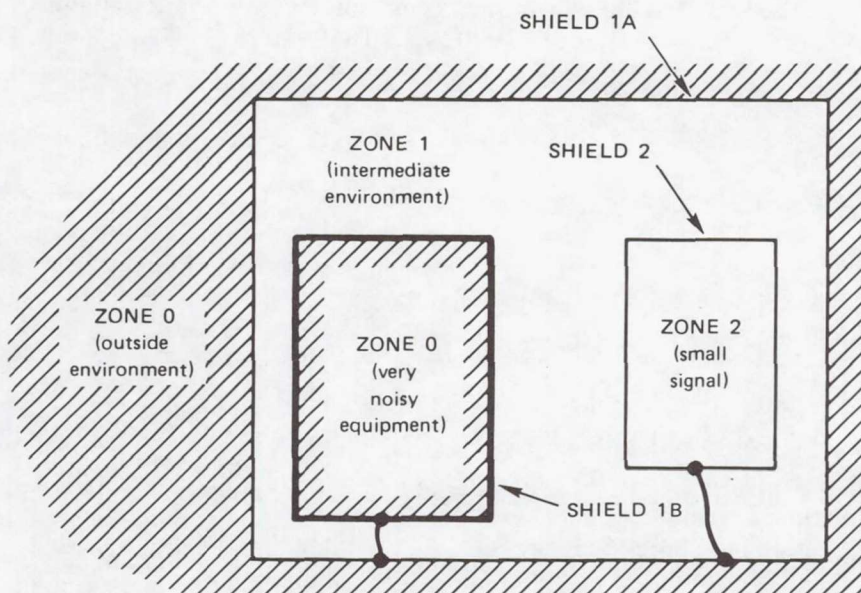
A systematic approach in interference control has as its foundation identification of the topology of the shielding surfaces. The integrity of these shield surfaces is to be preserved in spite of requirements for insulated power and signal conductors to pass through the shield, or of requirements for doors, access hatches, etc., to be cut in the shield wall. Much of interference control technology is, therefore, devoted to

accommodating these compromises of the shield without unnecessarily degrading the shield's ability to separate the internal environment from the external environment.

Finally, a rationale has been developed for determining how much shielding is necessary for a given interference source based on the insulation strength inside the shield and the expected tolerance of the victim equipment. Thus the shield must at least reduce the interference level to that which the insulation can withstand, but it need not reduce the interference to much below the ambient interference level generated in the protected region by internal equipment.



(a) NOISE SOURCE EXCLUDED BY FIRST SHIELD



(b) NOISE SOURCE CONFINED BY SEPARATE SHIELD

Figure 9.- Methods of treating very noisy equipment in a facility.

REFERENCES

1. Baum, C. E.: How to Think About EMP Interaction. Proceeding of the 1974 Spring FULMEN Meeting, Air Force Weapons Laboratory, April 1974.
2. Vance, E. F.: Shielding and Grounding Topology for Interference Control. Interaction Note 306, AFWL, Kirtland AFB, NM, April 1977.
3. Tesche, F. M.: Topological Concepts for Internal EMP Interaction. IEEE Trans. A.P., vol. EMC-20, February 1978, pp. 60-64.
4. Baum, C. E.: The Role of Scattering Theory in Electromagnetic Interference Problems. P. L. E. Uslenghi, ed., Electromagnetic Scattering, Academic Press, 1978.
5. Baum, C. E., et al.: On the Analysis of General Multiconductor Transmission-Line Networks. Interaction Note 350, AFWL, Kirtland AFB, NM, November 1978.
6. Stansberry, C. L.: EMP, Lightning, and Power Transients: Their Threat and Relationship to Future EMP Standards. Unpublished Technical Note, Defense Communications Agency, Washington, D.C., November 1977.
7. Martzloff, F. D. and Hahn, G. J.: Surge Voltages in Residential and Industrial Power Circuits. IEEE Transactions on Power Apparatus and Systems, "vol. PAS-89, no. 6, July/August 1970, pp. 1049-1056.

THE SEM DESCRIPTION OF INTERACTION
OF A TRANSIENT ELECTROMAGNETIC WAVE
WITH AN OBJECT

L. Wilson Pearson
Department of Electrical Engineering
University of Kentucky
Lexington, KY 40506

Donald R. Wilton
Department of Electrical Engineering
University of Mississippi
University, MS 38677

SUMMARY

The Singularity Expansion Method (SEM) was proposed by Baum in 1971 as a means for determining and representing the transient surface current density induced on a scatterer by a transient electromagnetic wave. The resulting mathematical description of the transient surface current on the object is a particularly robust one because of its simplicity and because of its straightforward physical interpretation. The data required to represent the electromagnetic scattering properties of a given object constitutes a relatively small set. Experimental methods have recently been developed for the determination of the SEM description, so that it is realistic to characterize in an approximate fashion even objects so complex in shape as aircraft. It appears feasible to characterize the surface current induced on aircraft flying in proximity to a lightning stroke by way of SEM. To determine the means -- indeed the feasibility -- of using SEM to characterize currents induced due to a direct strike by lightning is in need of further study.

INTRODUCTION

The development of the Singularity Expansion Method (SEM) occurred in 1970-71 in the context of nuclear EMP coupling prediction. The method was proposed by Baum in 1971 [1] and has been extensively elaborated upon by him and by other workers in the years since. A relatively complete bibliography is available in [2] and [3] taken collectively. Although the development of SEM was motivated by a transient application, it can be applied to frequency-domain scattering problems, as well. Frequency-domain applications for SEM have emerged only recently -- particularly in the context of phenomenological interpretation of shielding penetration [4].

The principal distinguishing feature of the SEM approach is the characterization of electromagnetic scattering for a given object in terms of complex natural resonances -- poles -- in the Laplace transform plane. Each conjugate pole-pair constituent of the SEM description contributes an exponentially decaying sinusoidal constituent in the time-domain expansion of the current

induced on the object. Thus, the transient response is given in terms of a summation of damped sinusoidal functions of time. The weighting associated with each sinusoid depends on the field exciting the object and on the observation point at which the surface current is observed.

Mathematically, the SEM representation comprises an infinite number of complex pole-pairs. In practice, however, the band limitation of the waveform of the excitation field renders all but a finite number of pole constituents negligible. Indeed, the method is most efficient when applied with excitation spectra which embrace no more than the first few resonances of the structure.

In this presentation, we discuss the SEM representation and its interpretation. This discussion is supported by simple examples pertaining to thin cylindrical structures. The alternative methods available for obtaining the description for a specific structure are presented, and limitations of their applicability are discussed. Finally, the use of SEM in predicting lightning interaction with aircraft is discussed both in the nearby and direct-strike cases. The issues deserving study in order to provide the tools for the direct-strike case are delineated.

THE SEM DESCRIPTION

Mathematical Statement of the Description

We are concerned with the surface current induced on a conducting object immersed in a lossless medium and excited by an incident wave $\bar{E}^{inc}(\bar{r}, t)$, which may be either transient or time-harmonic in character. The generic configuration is shown in Figure 1. The singularity expansion for the surface current is written in the Laplace transform (complex-frequency) domain as a pole series:

$$\tilde{J}(\bar{r}, s) = \sum_n \sum_i \left[\frac{\beta_{ni}}{s - s_{ni}} - \frac{\beta_{ni}}{s_{ni}} \right] < \bar{C}_{ni}(\bar{r}) ; \tilde{E}^{inc}(\bar{r}, s) > \bar{J}_{ni}(\bar{r}), \quad (1)$$

where

$\bar{J}_{ni}(\bar{r})$ represents the "natural modes" for the object,

$\bar{C}_{ni}(\bar{r})$ represents the coupling vectors,

$\{s_{ni}\}$ is the set of poles associated with the object, and

$\{\beta_{ni}\}$ are normalization constants whose value is associated with the normalization chosen for \bar{J}_{ni} and \bar{C}_{ni} .

The Laplace transform frequency variable is s and tildes (\sim) denote Laplace transformed quantities. The summation indicated in (1) is doubly indexed.

The notation is used to indicate that associated with the n^{th} surface eigenmode for a given object is a collection of poles $\{s_{ni}\}$. That is, the index i distinguishes among the poles associated with a given eigenfunction of the object. The origin of these associations by eigensets is described by Baum [5].

The bracket notation used in (1) indicates a symmetric product integrated over the surface of the object in question as follows:

$$\langle \bar{C}(\bar{r}) ; \bar{E}(\bar{r}) \rangle = \iint_{\text{object}} \bar{C}(\bar{r}) \cdot \bar{E}(\bar{r}) dS. \quad (2)$$

If either of the entries in the symmetric product depends on more than one independent variable, then the integration in (2) is implicitly understood to be over the spatial variable common to both entries.

If the representation (1) is derived from a symmetric operator, then the coupling vectors are identical to the natural modes, i.e.

$$\bar{C}_{ni}(\bar{r}) = \bar{J}_{ni}(\bar{r}).$$

Since all conducting scatterers may be characterized by an electric field integral equation -- i.e. in terms of a symmetric operator -- the modes may always be used as coupling vectors, provided the β_{ni} normalization constants are chosen to be consistent with this usage.

It is convenient, for interpretive purposes, to consider incident fields which are "factorable". Namely, fields which can be written in the form

$$\tilde{\bar{E}}^{\text{inc}}(\bar{r}, s) = \tilde{f}(s) \tilde{\bar{E}}_0(\bar{r}, s), \quad (3)$$

where $\tilde{f}(s)$ is a factor having to do with the time history/spectrum of the incident waveform, while the only frequency dependence of $\tilde{\bar{E}}_0(\bar{r}, s)$ occurs in the context of propagation. For example, if the incident field is a linearly polarized transient plane wave propagating in a direction given by the unit vector \hat{p} and with a time-history $f(t)$,

$$\tilde{\bar{E}}^{\text{inc}}(\bar{r}, s) = \tilde{f}(s) \left[\bar{E}'_0 e^{-s\hat{p} \cdot \bar{r}/c} \right], \quad (4)$$

and the term in brackets is identifiable as $\tilde{\bar{E}}_0(\bar{r}, s)$.

The factorable incident field form and the presumption of a symmetric operator formulation render (1) to be

$$\tilde{J}(\bar{r}, s) = \tilde{f}(s) \sum_n \sum_i \beta_{ni} \left[\frac{1}{s - s_{ni}} + \frac{1}{s_{ni}} \right] < \bar{J}_{ni}(\bar{r}); \tilde{E}_0(\bar{r}, s) > \bar{J}_{ni}(\bar{r}). \quad (5)$$

A frequency-domain expansion follows from (5) when one sets the complex frequency variable to values on the $j\omega$ axis:

$$\tilde{J}(\bar{r}, j\omega) = \tilde{f}(j\omega) \sum_n \sum_i \beta_{ni} < \bar{J}_{ni}(\bar{r}); \tilde{E}_0(\bar{r}, j\omega) > \left[\frac{1}{j\omega - s_{ni}} + \frac{1}{s_{ni}} \right] \bar{J}_{ni}(\bar{r}). \quad (6)$$

The form (6) is conveniently interpreted in terms of "difference vectors" in the complex plane in the manner often used in control systems theory for the graphical construction of Bode plots. We develop this concept with the aid of Figure 2. We use the terminology "complex difference vector" to indicate the vector portrayal of the difference in two complex numbers in the s -plane. This terminology differentiates from the spatial "vector" of which we normally speak. We endeavor to interpret (6) for a fixed value of the frequency variable ω . Clearly, the denominator factors $j\omega - s_{ni}$ are complex difference vectors, as indicated in Figure 2 -- one difference term resulting from each pole embraced in the summation in (6). Because the complex differences appear in the denominator in (6), it is clear that the terms associated with shorter complex difference vectors in the figure dominate in the summation. A resonance interpretation, thus, is evident: a frequency value near a pole results in an emphasis of that pole term and its associated mode relative to other terms in the summation and relative to its value when the frequency is further from it. This relationship is illustrated in Figure 2b.

The singularity expansion for the case of a transient excitation results from the Laplace transform inversion of (5). The result may be written as

$$\bar{J}(\bar{r}, t) = u(t) \sum_n \sum_i \beta_{ni} \eta_{ni}^{(x)} \tilde{f}(s_{ni}) \bar{J}_{ni}(\bar{r}) e^{s_{ni}t}, \quad (7)$$

where $\eta_{ni}^{(x)}$ indicates a generic coupling coefficient form, and results from the time domain interpretation of the factor

$$< \bar{J}_{ni}(\bar{r}); \tilde{E}_0(\bar{r}, s) >$$

in the Laplace inversion process. Different coupling coefficient forms may be defined to account for different forms of the spatial part of the incident wave. For example, planewave coefficients, cylindrical wave coefficients, spherical wave coefficients, etc. There are several other mathematical nuances which allow one to choose other aspects of coupling coefficient forms. Baum delineated several of these in his original description of SEM [1], and Pearson, Wilton and Mittra have added some insights into the origins of different forms [6].

We introduce two alternative planewave incidence forms here to indicate the nature of these alternatives. A Class 1 form may be written

$$\eta_{ni}^{(1)} = \langle \bar{J}_{ni}(\bar{r}) ; \bar{E}'_0(\bar{r}) e^{-s_{ni} \hat{p} \cdot (\bar{r} - \bar{r}_0)/c} \rangle \quad (8)$$

and a Class 2 form as

$$\eta_{ni}^{(2)}(t) = \langle \bar{J}_{ni}(\bar{r}) ; \bar{E}'_0(\bar{r}) e^{-s_{ni} \hat{p} \cdot (\bar{r} - \bar{r}_0)/c} \rangle_{I(t)}. \quad (9)$$

The time dependence of the Class 2 form stems from the limiting of the domain of integration to an "illuminated region" which expands across the object behind the incident wavefront as indicated in Figure 3. It is evident that the Class 2 form becomes constant and equal to the Class 1 form as the wavefront clears the object.

The reference vector \bar{r}_0 denotes the space-time origin for the incident wave representation, i.e., a point in space which lies on the wavefront at $t = 0$. A useful restriction on (8) and (9) is to choose \bar{r}_0 to be the first point of contact of the incident wavefront with the object as shown in Figure 1. Mathematically, this \bar{r}_0 is such that

$$\hat{p} \cdot \bar{r}_0 = \min_{\bar{r}} \hat{p} \cdot \bar{r}.$$

This results in a current response on the object beginning at $t = 0$.

The time invariance of the Class 1 coupling coefficient is a convenient feature. Its use can lead to active equivalent circuit forms representing the energy-collecting properties of a loaded scatterer or antenna [7,8,9]. However, it has been shown that the Class 1 coupling coefficient places arduous requirements on the accuracy and completeness of the SEM data [10,4].

Example of SEM Data - Straight Wire Scatterer

The SEM quantities for a straight-wire scatterer may be derived from a numerical model for the structure based on the method of moments [11]. Tesche first carried out this analysis, and his results are reported in [12,13].

The poles which have been computed for a straight wire whose length to diameter ratio is 100 are given in Figure 4. The second quadrant poles are shown: third quadrant conjugate companions exist, as well. The arcs connecting poles indicate their association with a given eigenvalue for the integral equation from which they were derived. These groupings, conjectured by Wilton for the wire, were reported in [14]. This is the commonality associated with the index n . It is seen that increasingly high-ordered eigenvalues have more poles associated with them.

The well-known resonance behavior of the wire is seen to be associated with a "layer" of poles lying quite near the $j\omega$ axis. A subsequent frequency-domain expansion example illustrates this clearly.

Modes associated with selected poles are displayed in Figures 5, 6, and 7. Figures 5 and 6 show modes associated with first layer poles for several different eigensets. Notice, in particular, that they are quite nearly sinusoidal in character; although one cannot ignore the appreciable imaginary parts of these modes, particularly for the higher-ordered eigenvalues. Figure 7 shows the modes associated with the fourth eigenset poles. (Only the modes corresponding to second quadrant poles are given: The complete eigenset comprises conjugate modes associated with the conjugate poles, too.) It is particularly noteworthy that all of the modes associated with this fourth eigenvalue have four "half-cycles" associated with them, though the relative prominence of them shifts from mode to mode.

The final constituents of the SEM description for the structure are the normalization constants β_{ni} . Since they provide no physical insight into the behavior of the structure they are not reproduced here. The interested reader is referred to references [13] or [4] for their tabulation.

Specimen Results from SEM Computations

We present two examples of SEM computation for the straight wire structure whose SEM characterization is described above. This structure is chosen because of its relative simplicity and because the results derived are relatively familiar and are readily interpreted.

We first consider the computation of the input admittance frequency response for a thin symmetric dipole antenna. This is modeled with SEM by using the frequency-domain expansion (6) and particularizing the incident field to a localized electric field at the center of the structure across the feed gap. Since a center-fed structure is considered, the symmetric products between this field and the current natural modes which are odd functions of z (even-indexed eigensets) are zero.

The result of an input admittance computed from the Singularity Expansion (6) for the current on this structure is given in Figure 8. The familiar admittance behavior characteristic to a dipole antenna is evident. Each of the odd-indexed first layer poles contributes a resonance to the response. The even-indexed poles do not, because the zero coupling products indicated above delete them from the series. Nine first layer poles were used in the computation of the results in Figure 8. A tailing off of the reactive component of admittance is seen above the fourth resonance (seventh pole). This occurs because the truncation of the series has delete constituents of the admittance which begin to be significant for normalized frequency values much larger than even on the scale in the Figure.

Figure 9 shows a transient current waveform computed at the center of a

wire scatterer with (7) and using the Class 2 coupling coefficient (9).

A plane wave with Gaussian time-history excites the wire at 30 degrees off broadside. The solid line exhibits the current response which is characteristic of the structure and indeed has been validated by other computational methods. The dashed line, on the other hand, departs appreciably from the correct value in the early time, though it is indistinguishable from the solid curve in the late time. The solid line is computed using a Class 2 coupling coefficient while the dashed line uses the Class 1. The departure of the latter is due to acute sensitivity of the Class 1 form to errors in pole location in the early time as we indicated previously.

METHODS FOR OBTAINING SEM DESCRIPTIONS

Analytical Determination

Perhaps the most satisfying mathematical derivation of the Singularity Expansion proceeds by way of an eigenfunction analysis of an integral equation description of the scatterer. Baum carries out this development in [5], and it may be found in [6]. However, the formal procedure can be carried out for only a few structures, in practice. The structure must conform or approximately conform to a separable coordinate system.

The separability requirement appears to limit analytical determination of SEM quantities to two geometries: the perfectly conducting sphere and the thin wire loop. The latter structure is, in fact, tractable only through approximation. The sphere was first in the light of SEM in [1] while the loop was treated by Umashankar and Wilton [15].

These analytical results have proven useful in only a few practical applications; and, consequently, we do not present details here. On the other hand, these two example structures, being amenable to analytical SEM treatment, have proven immensely useful to theorists in discerning and verifying the mathematical concepts of SEM.

Numerical determination of the SEM characterization can be determined through the use of numerical methods applied to Laplace transform domain integral equations describing the structure's electrical response. In particular the method of moments described by Harrington [11] has proven particularly useful. For example, the straight wire results in the previous section were determined by moment method modeling. A variety of other structures have been SEM-characterized using this approach. In the present context, perhaps the most germane work is that of Crow, *et. al.* [16]. Their work on SEM characterization of multiple wire structures can be extended to the determination of SEM quantities for wire models of aircraft. A study is presently under way by Pearson and his coworkers in developing SEM descriptions for cylinders which are sufficiently thick to approximate missiles.

The approach used in numerical determination of SEM quantities is to search for the poles of the structure in question and then to determine the

rest of the quantities. The method of moments reduces an integral equation formulation for current on the object to an approximately equivalent matrix equation

$$[\tilde{M}(s)] [\tilde{I}(s)] = [\tilde{E}(s)], \quad (10)$$

where the $[\tilde{I}(s)]$ vector is the new current-related unknown, $[\tilde{E}(s)]$ is a vector characterizing the excitation field; and $[\tilde{M}(s)]$ is a matrix approximation to the integral operator. The current vector thus is

$$[\tilde{I}(s)] = [\tilde{M}(s)]^{-1} [\tilde{E}(s)]. \quad (11)$$

We observe that a pole of $[\tilde{I}(s)]$ results whenever $[\tilde{M}(s)]^{-1}$ is singular, or, equivalently for

$$\det [\tilde{M}(s)] = 0. \quad (12)$$

Therefore, poles may be obtained by computing $\det [\tilde{M}]$ as a function of s and systematically searching for the pole values s_{ni} such that

$$\det [\tilde{M}(s_{ni})] = 0. \quad (13)$$

The natural modes follow as homogeneous solutions to the matrix equation at a pole:

$$[\tilde{M}(s_{ni})] [\tilde{I}_{ni}] = 0. \quad (14)$$

A homogeneous solution, of course, exists because of the zero determinant (13).

Baum describes these concepts thoroughly in [2] and Singaraju, et.al. describe extremely effective means of locating the poles [17].

Some aspects of the numerical approach which ultimately dictate its range of applicability should be pointed out. First, the frequency range over which poles may be determined is limited. The method of moments requires roughly 72 unknowns per square wavelength of surface area of the scattering object under consideration. This practically limits the method to determining the first few resonances of the object. It is evident, for example, that wire structures may be more thoroughly characterized than structures with surfaces. On the other hand, for many excitation spectra, a few resonances will suffice. The second principal limiting aspect of the numerical approach is interrelated with the first. Namely, the numerical determination of the SEM quantities is computationally expensive. It is quite evident from the generality in which the SEM characterization applies, that one possesses a tremendous amount of information -- albeit compactly represented -- once the characterizing quantities are in hand. One must expect to pay a computational cost commensurate with the information value obtained. For example, the pole location procedures of [17] are particularly efficient relative to other alternatives available. Even so, to determine, say the first ten resonances of a structure, might involve from a few to several thousand evaluations of the moment matrix and its determinant.

Experimental Determination

Concomitant with the size limitation of the numerical approach is a limitation on the geometric complexity of objects which can be characterized. On the other hand, the utility of the SEM description in many contexts hinges on the characterization of complex-shaped objects, for example, aircraft.

Van Blaricum and Mittra were the first to recognize the utility to SEM of the determination of pole content is a transient waveform [18]. A great deal of related work by many workers has proceeded in this area since they introduced the concepts. Recently, Pearson and Roberson [19] portrayed an approach where an approximate SEM description of a reasonably complex object may be obtained experimentally using pole identification concepts. Figure 10 portrays, generically, a suitable experimental configuration. The small arrows represent, schematically, small probes which sample the local transient surface current components excited on an object when the object is illuminated by a known transient field. A systematic reduction of the data obtained from a multiplicity of these probes scattered over the object leads to a rough approximation to the SEM description.

An experimental implementation of this scheme using ground-plane symmetry was reported by Pearson and Lee only recently [20]. Figure 11 displays the first four even function current modes experimentally determined for a thin cylinder taken from [20]. Tesche's results described previously herein are displayed for comparison. The highest-ordered mode displayed (mode 7) is only crudely determined. This is due to the fact that the excitation spectrum was quite weak at the frequency associated with this mode, thereby leading to poor signal-to-noise ratio for this mode. The techniques of [20] are presently limited to ground-plane measurements. This restricts their applicability to twofold-symmetric objects and precludes the recovery of one of the two symmetry classes of modes [19]. Work has recently begun to develop miniaturized transient telemetry methods so that the measurements may be made in a free-field environment, thereby lifting these restrictions.

APPLICATION OF SEM TO LIGHTNING INTERACTION PROBLEMS

Lightning Stroke in Proximity to an Aircraft

The application of SEM concepts to the prediction of currents induced on an aircraft by radiation from a stroke of lightning is straightforward. So long as the lightning channel is a few aircraft dimensions removed from the aircraft, the energy transfer will be almost solely due to radiation, and a direct application of (7) is proper. In principle, one simply chooses the (presumably known) electric field radiated by the lightning stroke and incorporates it into the incident field dependent entries in the expansion. If one attempts to apply the SEM description in this context, the dominant issue is likely to be the development of the SEM quantities which describe the aircraft in question. If bulk current information suffices in the user's application, then the wire equivalent structure models elaborating upon those in [16]

conceivably can be computed. Requirements for more detailed data would likely force one to apply experimental techniques such as those in [19] and [20]. Indeed, one might conduct more carefully detailed measurements in regions of highest interest on the aircraft surface.

If the lightning stroke is quite near to the aircraft, the resulting arc channel will exhibit tight electromagnetic coupling with the aircraft, and the resonance behavior will be that of the aggregate structure. This phenomenology is substantially more complex, of course. For example, the aggregate structure resonances are a function of the relative orientation of the two constituent structures. Wilton and his associates are exploring techniques for deducing the SEM description of electromagnetically-coupled aggregate structures from the SEM descriptions of the constituent geometries. The degree of success achievable through this approach is not known at this writing. It is conceivable, for example, that its viability will hinge on highly-accurate SEM data for the constituent structures. For complex-shaped structures, high accuracy is likely to be unachievable. The approach, on the other hand, can potentially provide an economical means of treating multiple orientations of aggregate structures.

Direct Strike Lightning Modeling

To use SEM to model the surface current response of an object subject to a direct lightning strike is somewhat problematical. The reason is that the lightning arc channel and the object must be viewed as a single structural unit and the resonances and modes of this unit determined. It is quite evident that the multiplicity of orientations and attachment points of the arc channel lead to requirements for the computation and/or measurement of potentially prohibitive quantities of data. At best, one could hope to treat only a few generic configurations. It is unlikely that the substructure aggregate approach referred to in the previous subsection can be applied to this case because of the conductive coupling of the two structures.

CONCLUSIONS

The Singularity Expansion approach to the prediction of the electromagnetic transient surface current response excital on aircraft and missiles in the presence of a lightning strike is a potentially powerful tool. Because of its complex resonance approach to the representation, SEM provides both a compact description and one which is readily interpreted, physically.

Practical SEM descriptions may be derived either through numerical computation or through measurement and data reduction methods. The numerical approach is costly to apply for complex-shaped objects, while the experimental approach involves some compromise in data accuracy and detail.

The further development of a substructure aggregate approach to determining the SEM description of tightly-coupled bodies is likely to provide a tool helpful in predictions of responses where a lightning stroke occurs near an aircraft. Some further consideration is in order relative to a simple SEM approach to the problem of direct lightning strike.

REFERENCES

1. C. E. Baum, "On the Singularity Expansion Method for the Solution of Electromagnetic Interaction Problems," EMP Interaction Note 88, Air Force Weapons Laboratory, Kirtland AFB, NM, December 1971.
2. C. E. Baum, "The Singularity Expansion Method," Ch. 3 in Transient Electromagnetic Fields, L. Felsen, ed., Springer-Verlag, New York, 1976.
3. C. E. Baum, "Toward an Engineering Theory of Electromagnetic Scattering: The Singularity and Eigenmode Expansion Methods," Ch. 15 in Electromagnetic Scattering, P.L.E. Uslenghi, ed. Academic Press, New York, 1978.
4. L. W. Pearson, "Applications of the Singularity Expansion Method," Short Course Notes, "Numerical and Asymptotic Methods in Electromagnetics and Antennas," Syracuse University, Sept. 1979.
also available as University of Kentucky Electromagnetics Research Report 79-3, September, 1979.
5. C. E. Baum, "On the Eigenmode Expansion Method for Electromagnetic Scattering and Antenna Problems, Part I: Some Basic Relations for Eigenmode Expansions, and their Relation to the Singularity Expansion," EMP Interaction Note 229, Air Force Weapons Laboratory, Kirtland AFB, NM, January 1975.
6. L. W. Pearson, D. R. Wilton, and R. Mittra, "Some Implications of the Laplace Transform Inversion on SEM Coupling Coefficients in the Time Domain," in preparation.
7. C. E. Baum, "Single Port Equivalent Circuits for Antennas and Scatterers," EMP Interaction Note 295, Air Force Weapons Laboratory, Kirtland AFB, NM, March 1976.
8. G. W. Streable and L. W. Pearson, "On the Physical Realizability of Broadband Equivalent Circuits for Wire Loop and Dipole Antennas," Electromagnetics Research Report 79-1, University of Kentucky, May 1979.
9. L. W. Pearson and D. R. Wilton, "On the Physical Realizability of Broadband Lumped Parameter Equivalent Circuits for Energy-Collecting Structures," Electromagnetics Research Report 79-2, University of Kentucky, July 1979.
10. L. W. Pearson, D. R. Wilton, F. Hsu, and R. Mittra, "Conditions of Validity for Class 1 and Class 2 SEM Coupling Coefficients," 1978 Fall Radio Science Meeting, University of Colorado, Boulder, CO, October 1978.
11. R. F. Harrington, Field Computation by Moment Methods, MacMillan, New York, 1968.

12. F. M. Tesche, "On the Singularity Expansion Method as Applied to Electromagnetic Scattering from Thin Wires," EMP Interaction Note 102, Air Force Weapons Laboratory, Kirtland AFB, NM, April 1972. See also IEEE Trans. Ant. & Prop., v. AP-21, 1973.
13. F. M. Tesche, "Applications of the Singularity Expansion Method to the Analysis of Impedance Loaded Linear Antennas," EMP Sensor & Simulation Note 177, Air Force Weapons Laboratory, Kirtland AFB, NM, May 1973.
14. D. R. Wilton and L. W. Pearson, "Analytical Properties of Some SEM-Derived Quantities," USNC/URSI National Radio Science Meeting, Boulder, CO, Nov. 1979.
15. K. R. Umashankar and D. R. Wilton, "Transient Characterization of Circular Loop Using Singularity Expansion Method," EMP Interaction Note 259, Air Force Weapons Laboratory, Kirtland AFB, NM, August 1974.
16. T. T. Crow, B. D. Graves, and C. D. Taylor, "The Singularity Expansion Method Applied to Perpendicular Crossed Wires," IEEE Trans. Ant. & Prop., v. AP-23, No. 4, pp. 540-546, July, 1975.
17. B. K. Singaraju, D. V. Giri, and C. E. Baum, "Further Developments in the Application of Contour Integration to the Evaluation of Zeros and of Analytic Functions and Relevant Computer Programs," EMP Mathematics Note 42, Air Force Weapons Laboratory, Kirtland AFB, NM, March 1976.
18. M. L. Van Blaricum and R. Mittra, "A Novel Technique for Extracting the SEM Poles and Residues of a System Directly from its Transient Response," IEEE Trans. Ant. & Prop., v. AP-23, no. 6, pp. 777-781, November 1975.
19. L. W. Pearson and D. R. Roberson, "The Extraction of the Singularity Expansion Description of a Scatterer from Sampled Transient Surface Current Response," IEEE Trans. Ant. & Prop., v. AP-27, no. 2.
20. L. W. Pearson and Y. M. Lee, "An Experimental Investigation of the King Surface Current Probing Technique in a Transient Application," University of Kentucky Electromagnetics Research Report 79-4, December, 1979.

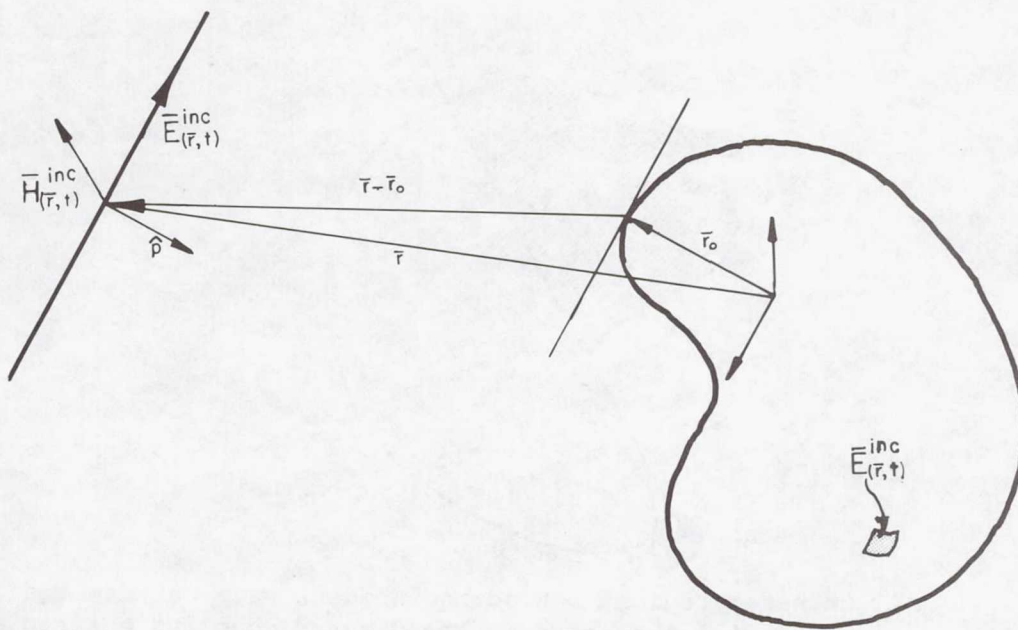


Figure 1.- Generic configuration of a scattering object illuminated by an incident field. A localized "incident" field as shown by the surface patch can model the feeding field of an antenna.

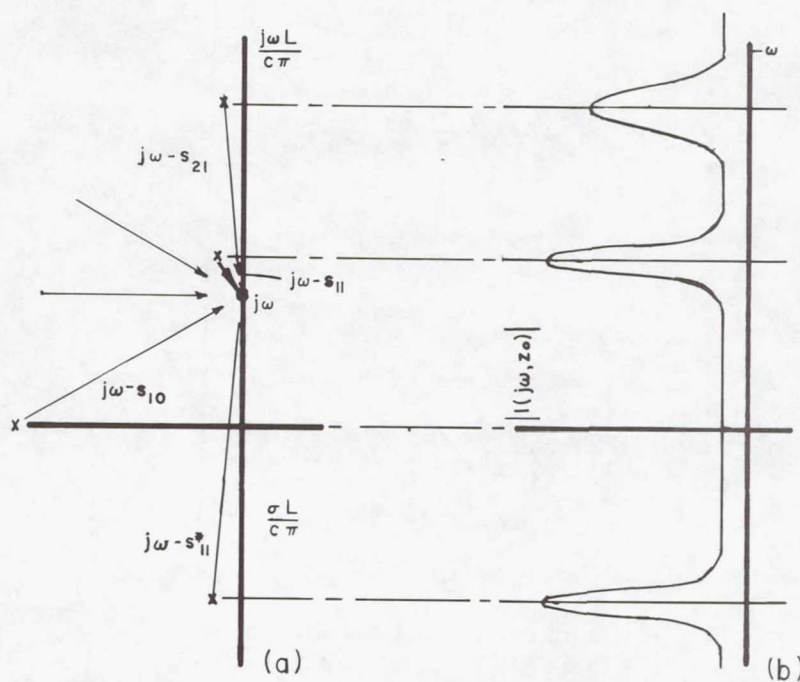


Figure 2.- (a) Complex difference vector interpretation of the relationship between frequency-domain resonance and pole locations in the complex frequency plane. (b) Resonant peaks corresponding to (a).

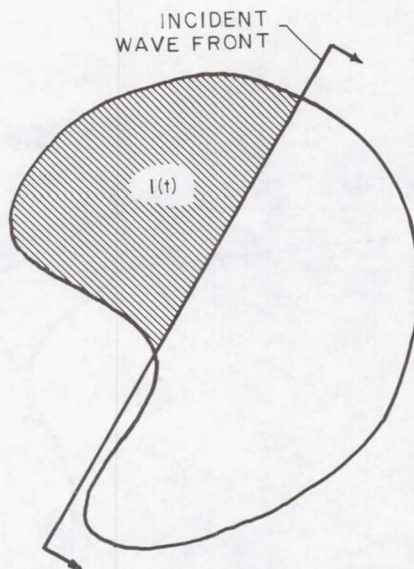


Figure 3.- The "illuminated region" behind an incident wave defines the domain of the symmetric product integration in the Class 2 coupling coefficient form.

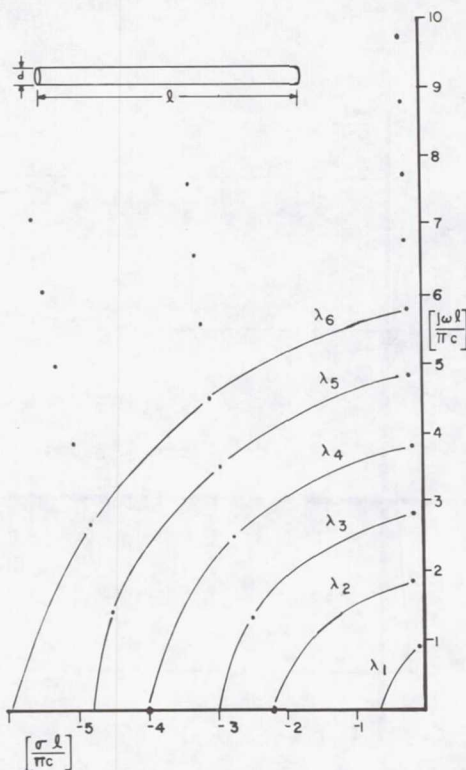


Figure 4.- Second quadrant members of eigensets of poles for a 100:1 cylinder. The poles along a given arc, along with their (third quadrant) conjugate mates comprise an eigenset.

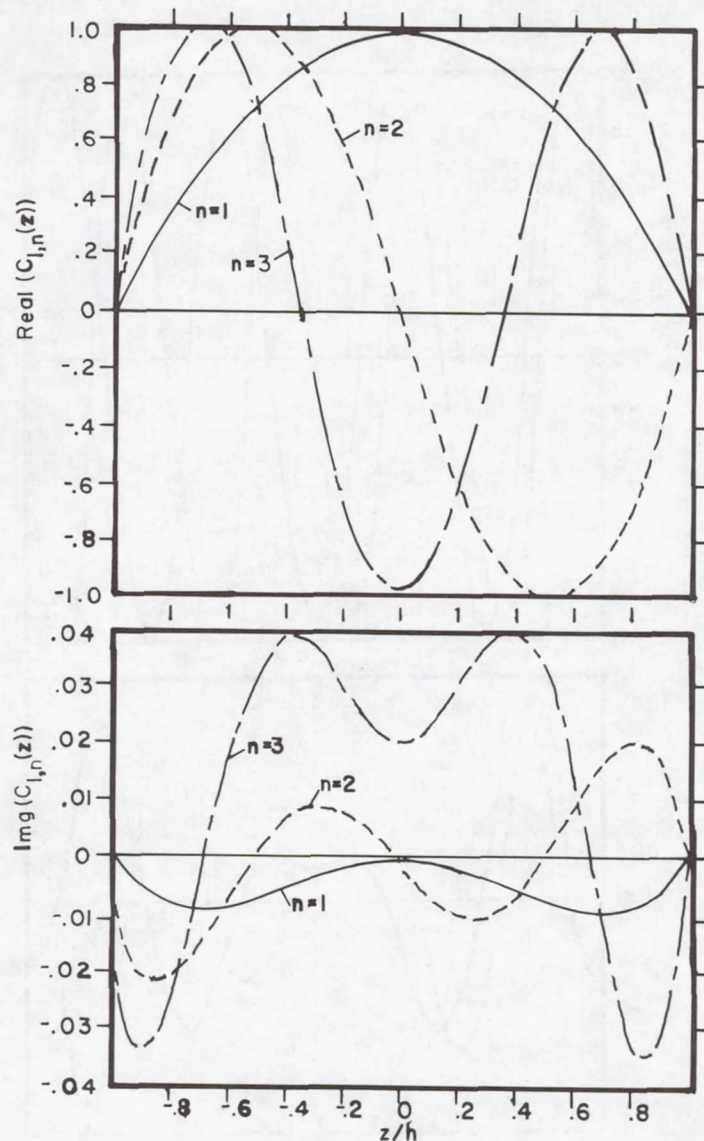


Figure 5.- First layer modes associated with eigensets 1, 2 and 3 for the 100:1 cylinder. The modes associated with corresponding third quadrant poles are conjugate to these.

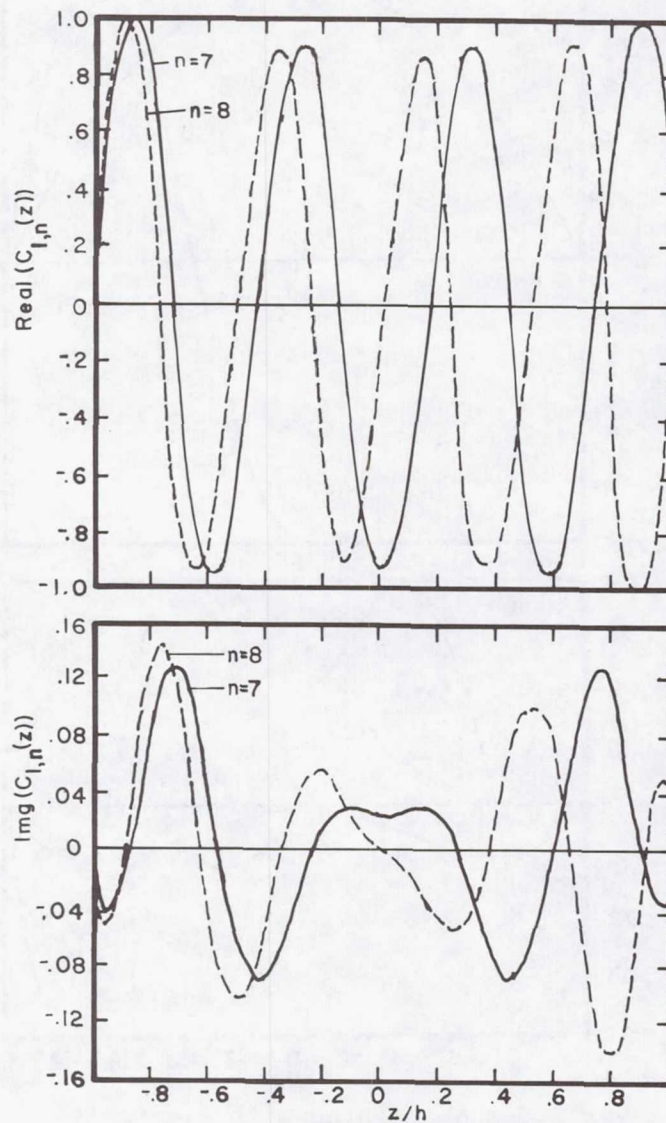


Figure 6.- First layer modes associated with eigensets 7 and 8 for the 100:1 cylinder. The modes associated with corresponding third quadrant poles are conjugate to these.

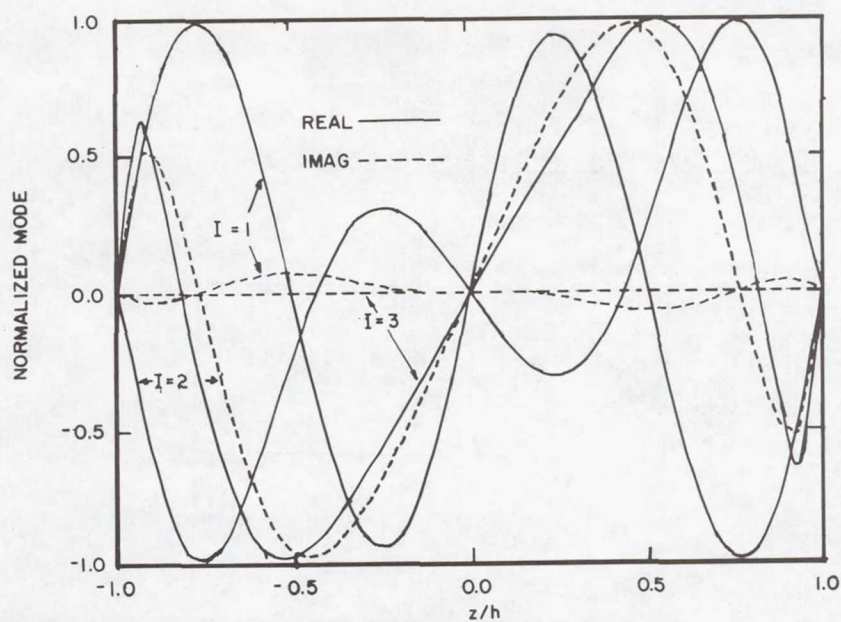


Figure 7.- Modes associated with each of the second quadrant poles in the fourth eigenset for the 100:1 cylinder.

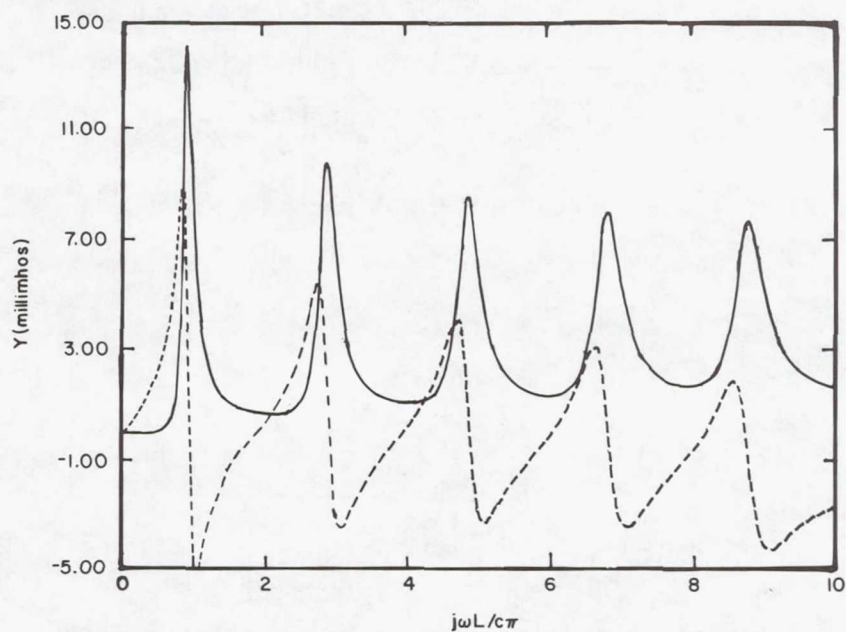


Figure 8.- Input admittance for a 100:1 center-fed dipole antenna as computed by the frequency-domain singularity expansion.

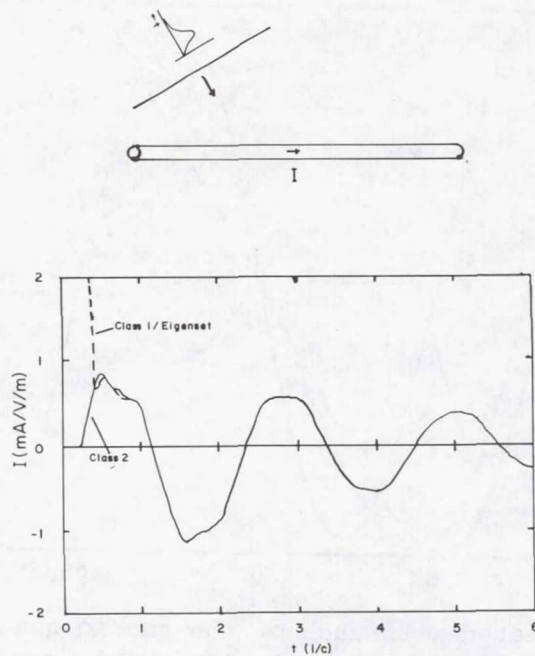


Figure 9.- Current induced on a 100:1 cylindrical scatterer as observed at the center. The incident wave is a plane wave with Gaussian time history.

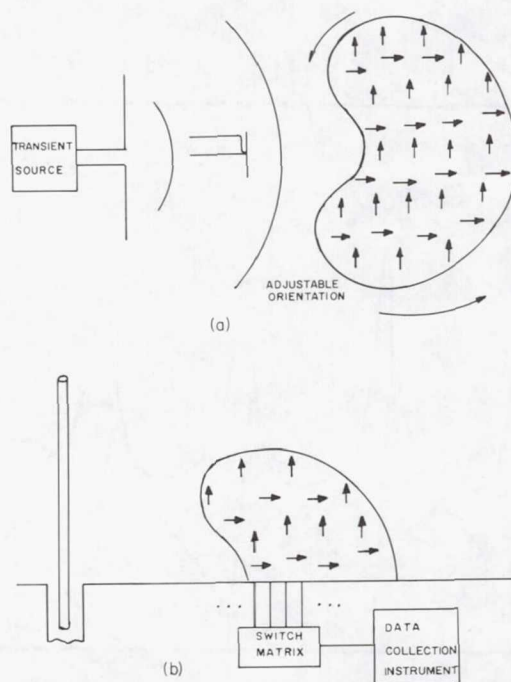


Figure 10.- (a) Schematic representation of measurement configuration through which approximate SEM description may be derived. The arrows represent local surface current probes. (b) Image plane realization of (a).

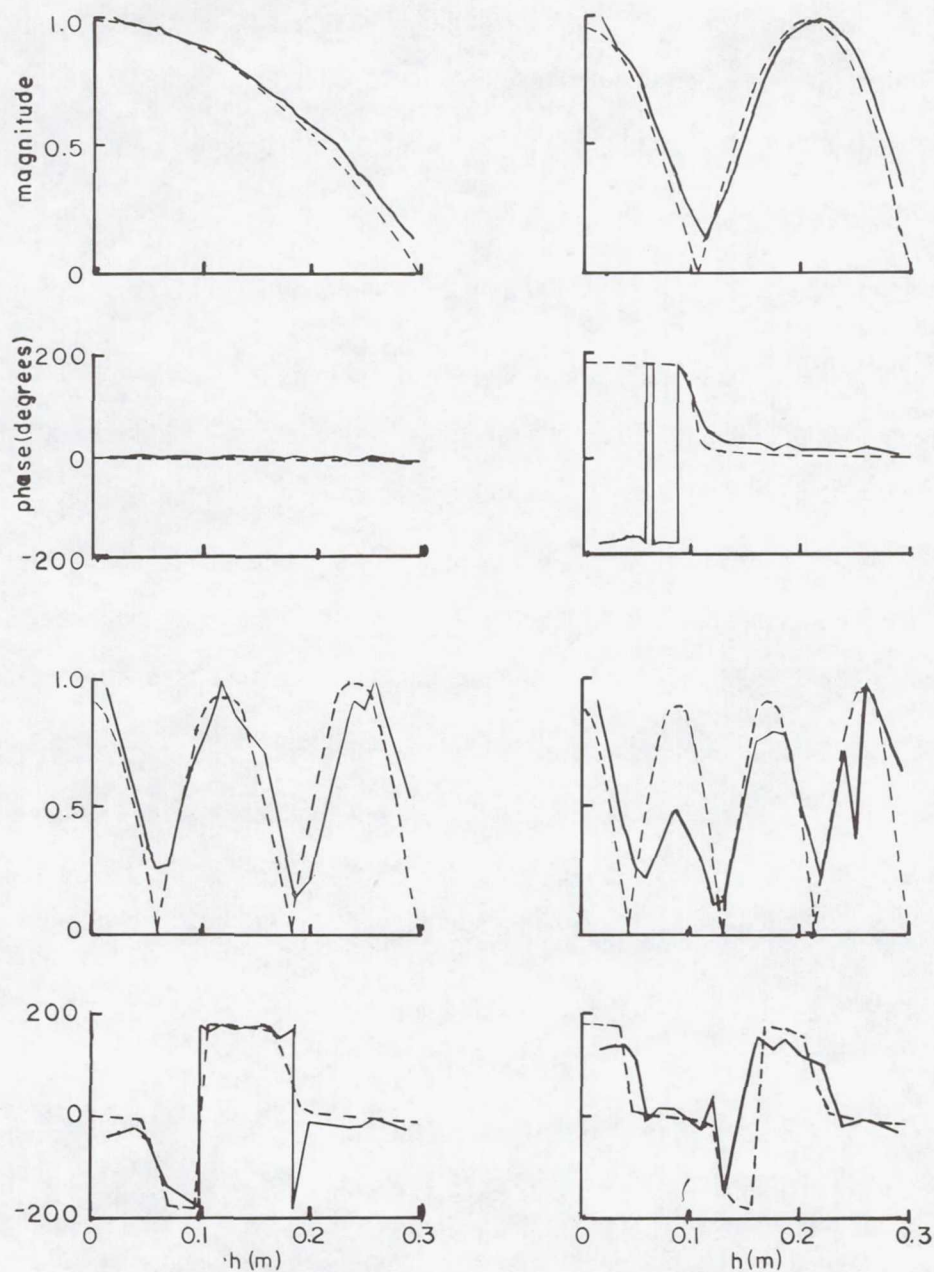


Figure 11.- First four even function first layer natural modes determined for the straight wire through measurement from [20]. The excitation spectrum for the fourth of these was quite small, leading in the noisy result.

Page intentionally left blank

TRANSIENT CORONA EFFECTS ON A WIRE OVER THE GROUND

Kenneth C. Chen
Air Force Weapons Laboratory
Kirtland AFB, New Mexico 87117

ABSTRACT

Investigations pertaining to nuclear EMP effect on VLF/Trailing Wire antennas have revealed new features of corona effects. Previous experimental results on transmission lines with corona under $E_{\max} < 80 \text{ kV/cm}$ recorded in the nanosecond time-frame are analyzed. A nonlinear macroscopic model describing the experimental results is obtained.

INTRODUCTION

VLF/Trailing Wire Antennas (TWA) are employed by certain types of military aircraft for command, control, and communication during a nuclear war. Examples of these aircraft are the E-4 (Airborne Command Post), EC-135, and TACAMO (ref. 1). As a result, the VLF/TWA on these aircraft are designed to survive exposure to a severe nuclear electromagnetic pulse (EMP) environment. These VLF/TWA are also exposed to lightning strikes during normal missions. There are various types of TWA. The E-4 and TACAMO employ a dual-wire antenna. The upper and lower wire are 1.2 km and 7.2 km respectively in length, and both wires have a radius of 2 mm. The angle between the upper and lower wire is approximately 6° . The EC-135 has a single wire antenna with wire radius 2 mm and wire length 8.5 km.

In order to gain a preliminary understanding of the induced voltage and current on the TWA, the Air Force Weapons Laboratory (AFWL) conducted an airborne test (ref. 2) over the Vertically Polarized Dipole I Simulator Facility (VPDI). The upper wire of the TACAMO TWA was extended to 1,000 ft and exposed to a peak electric field two orders of magnitude less than the peak field of a nuclear EMP. The induced electric field around the wire was found to be approximately equal to the breakdown electric field of the surrounding air. Therefore, corona phenomenon is an important factor in determining the voltage and current induced on the antenna.

This work discusses a model to account for corona effects on transmission line modes. Experimental data obtained at Kaman Science Test Facility under an AFWL contract (refs. 3 and 4) are used to verify the model. Although the basic microscopic processes taking place during a corona have been a subject of much study (refs. 5 and 6) and are well understood, the recording of responses in a nanosecond time-frame reveals new features of corona effect.

Since AFWL/KSC's corona work has not been previously reported in the literature (ref. 4), this work includes a brief but self-contained discussion of the experimental setup and the basic findings of that work. The problem of a wire driven by a high voltage input is discussed. This problem can be studied in three transient stages: (1) wire without corona, (2) corona onset, (3) macroscopic nonlinear modes. Finally, the main findings and limitations of this work are given, and future research subjects are listed.

SYMBOLS

$C(Q), C_o, C$	line capacitance
c	the speed of light
e	electronic charge, 1.6×10^{-19} coul
$E(t)$	time domain electric field
I, I_o	line current
$[I]$	discontinuity in line current
L	line inductance
\ln	logarithm to base e
\log	logarithm to base 10
n, n_o	electronic density, number per centimeter cubed
p	pressure in mm-Hg
Q, Q_o	line charge, 1 coul/m
$[Q]$	discontinuity in line charge
Q_1	charge deposition due to corona, coul/m
ρ	polar coordinate with origin at the center of the wire
ξ	advanced time, $t + \frac{x}{v}$
η	retarded time, $t - \frac{x}{v}$
$\sigma(x,t)$	hypersurface of discontinuity
γ_o	wire radius
γ_c	equivalent corona radius

t	time
τ	ξ or η
V	line voltage, Volt/m
V_B, V_D	sensor output in Volts
$[V_B], [V_D]$	discontinuity in sensor output
$v(Q), v_o, v$	propagation velocity
v_d	electron mobility
x	net ionization frequency
χ	coordinate along the wire

AFWL/KSC CORONA EXPERIMENT

The AFWL perceived the importance of the corona effect on wires, designed a corona test configuration, and funded Kaman Science Corporation to set up the test facility and obtain test data pertaining to wire with corona. The major contributor to the design of the test setup and measurement techniques was Carl Baum. Phil Book was responsible for physically performing the experiment and obtaining the test data. This section includes discussions of (1) the test facility, and (2) typical data.

Test Facility

The schematic diagram of the overall layout of the test facility is given in figure 1. The ground plane was comprised of plain weave copper wire cloth (No. 16 mesh size) spot-soldered at 10 to 15 cm intervals to form an overall surface area about 9.6 m wide by 70 m long. Five measuring stations, where electric and magnetic field sensors were located to record the corona effect, are shown in the diagram. Cable conduits containing a pair of Rg-8/U size cables were routed from the measuring stations to the instrumentation trailer. Each of the test conductors was suspended 1 meter above the ground plane with nylon cord fastened to the wood support structures. Test conductors were terminated in their characteristic impedances so as to minimize the reflection from the end of the line. High-power, low-inductance metal film resistance manufactured by Carborundum Company was used. Table 1 shows physical and geometrical properties of the test conductors and the measured termination resistance used during the test. A charged line high voltage pulser was used to drive the test conductor with respect to the ground. The charge was stored in a 190 ft coaxial cable (RG-220/U), and a pneumatic switch was used to trigger the spark gap. The pulser used could deliver up to a 90 kV 20 ns rise-time pulse to a 500 ohm load. The signal recording instrumentation consisted of a

Textronix type R454 oscilloscope equipped with type C-40 cameras. Pulse measurements were made with test cables to characterize the recording instrumentation. The recorded camera trace was formed to have a rise time of less than 5 ns. Model MGL-S5A(A) B and model HSD-S3A(R) D sensor of Baum (ref. 7) were used to measure the field at the ground plane. They were located symmetrically on both sides of the conductor centerline and separated by 0.86 m.

Test Data

Time-domain responses of the electric and magnetic field sensors were recorded for different voltage levels, polarities, and test conductor materials. The scope of the test data is listed in table 2. Examination of the time-response sensor data for various test conditions showed that all of the tests produced results with essentially similar characteristics. Therefore, bare copper wire at only one nominal input voltage level 80 kV will be discussed. Figures 2 and 3 show time-domain sensor outputs at all five stations for a nominal input test voltage of 80 kV. To convert from sensor outputs to line charge and line current, one uses the following formulas:

$$Q = \pi h \left[1 + (x/h)^2 \right]^{-1} 2 \times 10^{-6} V_D \quad (1)$$

$$I = h \left[1 + (x/h)^2 \right]^{-1} 2.5 \times 10^3 V_B \quad (2)$$

Notice that the time-domain responses show basically three distinct time regions. Region 1 is the early-time part, which has identical waveforms at all stations. In this time region, corona has not yet occurred. Region 2 is characterized by a dip (except at Station 1) in the signal strength, which indicates the onset of corona. Region 3 starts when the signal strength reaches a minimum value.

CORONA MODEL

Models which can describe the three time regions of the time-domain responses noted previously are derived in this section. Simple models which interpret the basic features of each region have been constructed. Region 1 does not require further modeling, since a lossless transmission line will suffice to explain the phenomenon. Region 2 requires microscopic considerations. The basic mechanism is Townsend's electron avalanche, which is followed by the saturation brought about by the reduction of the electric field due to the presence of the positive ions around the wire. Finally, in Region 3 the remaining positive ions and electrons around the wire modify the line capacitance in a nonlinear way such that a nonlinear transmission line is formed. Alternatively, a time-dependent line capacitance, determined from the electron avalanche, can be adopted. In this work, nonlinear transmission line theory and the corona onset will be discussed.

NONLINEAR TRANSMISSION LINE THEORY

A Formal Solution

Let us consider a transient voltage pulse to be applied at one end of the wire. As the electric field near the wire surface exceeds that required for electron avalanche, positive ions and electrons start to accumulate around the wire. The corona setup mechanism in the test configuration as discussed before is a microscopic process, which will be discussed in the next subsection. For the analysis in this subsection we shall assume that the corona onset happens very quickly, and that the general input waveform varies much more slowly in time. There may be cases where these assumptions do not hold. In those circumstances a microscopic calculation cannot be avoided.

Assume that a cloud of positive ions or electrons has been set up around the wire. We then write the transmission line equations as

$$\frac{\partial Q}{\partial t} = - \frac{\partial I}{\partial x}, \quad L \frac{\partial I}{\partial t} = - \frac{\partial V}{\partial x} \quad (3)$$

The nonlinearity enters through the assumption that the line capacitance is a nonlinear function of the line charge of the form $C(Q) = Q/V$. The presence of positive ions and electrons leads to the nonlinear capacitance. The purpose of this subsection is to show that this pair of equations has a simple nonlinear solution form, which enables us to understand and explain the test data.

The solution to equation (3) is

$$Q = Q(\tau), \quad I = I(\tau) \quad (4)$$

with

$$\tau = t \mp x/v(Q), \quad v(Q) = \{f(Q)\}^{1/2}, \quad f(Q) = \frac{1}{L} \frac{d}{dQ} (Q/C) \quad (5)$$

Nonlinear Line Capacitance

As an example of how the line capacitance can be a function of line charge, let us assume that the corona onset occurs instantaneously, and the electrons and positive ions are generated instantaneously. Furthermore, we assume an instantaneous transport of charges. As a result, the region around the wire will have an electric field greater than some breakdown electric field E_{bd} . This region is bounded by the surface $\rho = \gamma_c$. Here

$$\gamma_c = \frac{V}{E_{bd}} \quad (6)$$

The Gauss theorem requires that the electric field is zero within $\rho < \gamma_c$, and all line charges are situated on the surface $\rho = \gamma_c$. A simple electrostatic

consideration gives

$$C = \frac{2\pi\epsilon_0}{\ln\left(\frac{2h}{\gamma_c}\right)} \quad (7)$$

The larger the γ_c , the greater the deviation of Q away from the value assumed by the wire without corona. As a result, $\gamma_c = \gamma_c(Q)$.

A Linear Approximation to $v(Q)$

Let us assume a linear approximation to the velocity $v(Q)$, one obtains from equation (5)

$$\frac{Q}{C} - \frac{Q_0}{C_0} = Q L \bar{v}^2 \quad (8)$$

with

$$\bar{v}^2 = \frac{v_0^2 + v_0 v + v^2}{3} \quad (9)$$

The derived formula will now be applied to an example using the test data results. The value of line charge for bare copper wire at a nominal driving voltage of 80 kV is shown in figure 2 from \dot{D} sensor output at all five stations. A simple formula for $v(Q)$ applicable to the data is

$$v(Q) = \frac{1}{\left(\frac{\Delta\tau}{\Delta x} + \frac{1}{c}\right)} \quad (10)$$

where

Δx = the distance between two stations

$\Delta\tau$ = the difference in arrival time of the same signal strength as measured from the wavefront, or the retarded time

c = the speed of light

Formulas (1) and (10) are used to obtain figure 4. From equations (7) and (9) it can be shown that

$$\gamma_0 = \text{initial corona radius} \approx 1.15 \text{ mm} \quad (11)$$

$$\gamma_c = \text{equivalent corona radius} \approx 4.36 \text{ mm} \quad (12)$$

Here we have calculated the corona radius corresponding to $Q = 112 \times 10^{-8}$ coul/m. As shown in figure 2 this value of Q corresponds to the time of about 200 ns from onset of the corona. We can perform a simple microscopic calculation on the approximate maximum distance that electrons can travel during this time interval as follows

$$d_{\max} \sim \int_0^{200 \text{ ns}} v_d dt \approx 0.1 \text{ mm/ns} \times 200 \text{ ns} = 20 \text{ mm} \quad (13)$$

If one attempts to calculate the equivalent corona radius based on a linear transmission line theory (ref. 4), the numerical value for this radius turns out to be a factor of 10 greater than that given by equation (12). This shows the advantage of a nonlinear model in giving a more reasonable result, which is consistent with a microscopic calculation.

Propagation of Discontinuities

As discussed earlier, one can consider the corona setup as a process which occurs very rapidly. The effect on the response waveform can be looked upon as a discontinuity. It is well known that a nonlinear wave with amplitude-dependent wave velocity can create this type of discontinuity. Let the surface of discontinuity in the hyperspace be $\sigma(x,t) = \text{constant}$. The velocity of the discontinuity $v = \frac{dx}{dt}$ is given by

$$\frac{\partial \sigma}{\partial t} + \frac{\partial \sigma}{\partial x} \frac{dx}{dt} = 0 \quad (14)$$

Let $Q = Q(\sigma)$, $I = I(\sigma)$. Then with the first equation of (3) we obtain

$$\frac{dQ}{d\sigma} \frac{dx}{dt} - \frac{dI}{d\sigma} = 0 \quad (15)$$

Integrating across the surface of discontinuity yields

$$v[Q] - [I] = 0 \quad (16)$$

Applying the same technique to the second equation of (3) one obtains

$$v L[I] - \frac{1}{C} [Q] = 0 \quad (17)$$

Therefore,

$$v = \frac{[I]}{[Q]}, \quad C = \frac{1}{v^2 L} \quad (18)$$

An examination of figures 2 and 3 for time domain responses at Station 2 shows that $[V_B] \sim 6$ mV and $[V_D] \sim 9$ mV correspond to the reduction of signals associated with corona onset. These values can be used in equations (1), (2), and (18) to calculate the velocity associated with these discontinuities as follows

$$v = \frac{[I]}{[Q]} \approx 3.98 \times 10^8 \frac{[V_B]}{[V_D]} \approx 2.65 \times 10^8 \text{ m/sec} \quad (19)$$

Note that the calculated value of the velocity is very sensitive to the measurement errors. The calculation shown here is only to illustrate the non-linear theory.

THE CORONA ONSET

It is difficult if not impossible to use a macroscopic theory to calculate accurate time-domain waveforms right after corona onset. To achieve this requires accurate time-dependent electron and positive ion distributions around the wire. Since a detailed microscopic calculation is not the objective of this work, discussions will be limited to the determination of the corona onset time.

In order to understand the time domain waveform as shown in figure 2, it is important to examine the microscopic processes leading to the corona onset. The ambient electrons, ever present because of cosmic rays, etc., which are accelerated by the electric field, start the avalanche processes. As an example, we calculate the corona onset for Station 2 from data obtained in Station 1. The electric field measured at Station 1 can be used to calculate the electric field near the wire to give

$$E(t) \sim \begin{cases} \frac{5\gamma_0 t}{\rho} \text{ kV/cm} & , \quad 0 < t < 16 \\ \frac{\gamma_0}{\rho} (64 + t) \text{ kV/cm} & , \quad 16 < t < 30 \end{cases} \quad (20)$$

Equi-electric field lines for $E = 50$ kV/cm and 60 kV/cm are shown in figure 5 to indicate what field level the wire is exposed to. From the electron mobility formula

$$v_e = (3.92 + 0.263 E/p) \times 10^{-2} \text{ mm/ns} \quad (21)$$

where the electric field is in Volt/cm. The electron trajectory is described by

$$-\frac{d\rho}{dt} = 0.0392 + 0.0173 \frac{\gamma_o t}{\rho}, \quad 0 < t < 16 \quad (22)$$

where γ_o is the wire radius in mm, ρ is the location of the electron in polar coordinate in mm, and t is in nanoseconds.

Electron trajectories provide a vivid picture of how electrons are drawn to a positive wire. In figure 5 these trajectories up to 16 ns from the wavefront are shown. It is more important to determine how the electron density increases along the trajectory. Note that the Townsend avalanche formula (8) can be approximated by

$$\ln \frac{n}{n_o} \sim \int_{t_o}^t 760 \times 10^{0.9 + 3.25 \log \frac{E(t)}{p}} dt, \quad t < 16 \quad (23)$$

In evaluating the above integral, one can conveniently use a linear approximation for the trajectory. Let us pay special attention to electrons that arrive at the wire surface at $t = 14$ ns. The differential equation for the trajectory can be used to give

$$\frac{\gamma_o t}{\rho} \sim t_f \left(1 - \frac{t}{14} - 0.24 t\right) \quad (24)$$

Substituting equations (20) and (24) into equation (23) gives

$$N \approx N_o \times 10^6 \sim 10^9 \text{ No/cm}^3 \quad (25)$$

Let us calculate the charge deposition per meter based upon the electron density obtained. The charge deposition per meter due to corona is designated by $Q_1(\eta)$, which is

$$\begin{aligned} Q_1(\eta) &= en2\pi\gamma_o \int_{\gamma_o}^{\infty} e^{-\frac{v}{v_d}(\rho - \gamma_o)} d\rho \\ &= en2\pi\gamma_o \frac{v_d}{v} \\ &\approx 1.2 \times 10^{-11} \text{ coul/m} \end{aligned} \quad (26)$$

here we have used $e = 1.6 \times 10^{-19}$ coul, $\gamma_o = 1.15$ mm, $n = 10^9 \text{ No/cm}^3 = 10^{16} \text{ No/m}^3$, $v/v_d = 10^5 \text{ m}^{-1}$.

One can show from a perturbation calculation that the change in current waveform is given by

$$\Delta I(\eta) = - \frac{x}{2} \frac{\partial Q_1(\eta)}{\partial \eta} \quad (27)$$

with η = the retarded time. As an estimate, let us assume

$$\frac{\partial Q_1(\eta)}{\partial \eta} \approx \frac{v}{2} Q_1(\eta) = 0.12 \text{ A} \quad (28)$$

Here one-half of the avalanche frequency has been used. Therefore, equation (27) gives

$$\Delta I(\eta) = - 0.72 \text{ A} \quad (29)$$

This should coincide with the start of a dip in the waveform, which is the corona onset.

CONCLUDING REMARKS

A macroscopic nonlinear model is proposed for a transmission line with corona. The model not only accounts for overall waveform, but also describes the sharp changes in the waveform associated with the corona onset. Since the detailed structure of the waveform right after the corona onset depends on the electric field in a complicated manner, a universal solution is hard to obtain, and is not attempted. The experimental data and the resulting model are limited by the low voltage level at which the experiment was performed. At a higher voltage level, which has not yet been determined, the streamers can emanate from the wire; the effect on the line voltage (or line charge), and line current can be considerably different from the case considered here. Furthermore, the higher the electric field intensity, the faster are the electron avalanche process; the sharp changes in the waveform associated with the corona onset will be sharper and will appear as discontinuities. A continuation of both experimental and theoretical work is required. Experimental investigations in the following three areas will be the most useful to the overall understanding of wires with corona: (1) further experimentations at higher voltages to determine the effect of streamers, (2) determination of the optical spectrum of corona and streamers, (3) investigations of acoustic effect, which may be the byproducts of the avalanche electrons. Theoretical work in determining how to apply the present results and the results from the suggested investigations to the trailing wire antenna (TWA) problem is most challenging. These results and other related work (refs. 9 and 10), can then lead to a successful simulation of TWA under the most severe EMP or lightning environments.

As of now, basic features of current and charge waveform on wires with corona at $E_{\text{max}} < 80 \text{ kV/cm}$ can be described by a model using simple equivalent corona radius. This corona radius can be estimated to be about 15% of the

maximum distance electrons can travel. Alternatively, if accurate experimental data are available, one can deduce the equivalent corona radius from the data with simple procedures described in this work. However, more studies are required before one can conclude that a quantitative understanding has been achieved for wires with corona.

REFERENCES

1. Marin, L.; Castillo, J. P.; and Lee, K. S. H.: Broad-Band Analysis of VLF/LF Aircraft Wire Antennas. IEEE Trans. Antennas and Propagation, vol. AP-26, 1978, pp. 141, 1978.
2. Castillo, J. P.: AFWL TACAMO Testing. AFWL-TR-78-110, Nuclear Technology Digest, August 1978.
3. Book, P. S.; and Price, H. J.: A Transmission Line Corona Experiment. AFWL Interaction Notes, Note No. 313, October 1976.
4. Book, P.S.: Study of Corona in a Transmission Line Test Facility. AFWL Interaction Notes, Note No. 369, November 1978.
5. Cobine, J.D.: Gaseous Conductors. Dover Publications, N.Y., 1941.
6. Lam, J.: Theoretical Study of the Electrical Corona on a Long Wire. AFWL Interaction Notes, Note No. 305, June 1976.
7. Baum, C. E.; Breen, E. L.; Giles, J. C.; O'Neill, J.; and Sower, G. D.: Sensors for Electromagnetic Pulse Measurements Inside and Away from Nuclear Source Regions. IEEE Trans. Antennas and Propagation, vol. AP-26, pp. 22, 1978.
8. Buntschuh, C.; Salkins, B.; and Gilden, M.: Nanosecond Pulse Breakdown Study. AFWL Pulsed Electrical Power Dielectric Strength Notes, Note 18, vol. I, pp. 18, February 1963.
9. Landau, L. D.; and Lifshitz, E. M.: Fluid Mechanics. Addison-Wesley Publishing Company, 1960.
10. Baum, C. E.; Castillo, J. P.; and Marin, L.: A Simple Way of Simulating the EMP Effects of VLF/LF Dual-Wire Antenna on the E-4B. Miscellaneous Simulator Memos, Memo No. 14, November 1977.

TABLE 1.-THEORETICAL AND NOMINAL TRANSMISSION LINE TERMINATIONS

<u>Test conductor</u>	<u>Terminal resistance</u>	
	<u>Diameter (mm)</u>	<u>Measured (ohms)</u>
Copper tube	9.525	393
Cu antenna wire	4.064	393
Al antenna wire	4.064	393
Bare Al wire	4.115	393
BeCu wire	2.305	447

TABLE 2.-SCOPE OF TEST DATA

<u>Type</u>	<u>Test conductor diameter (mm)</u>	<u>Test voltages for raw data (kV)</u>
Copper tube	9.525	-30, -80, 30, 40, 50, 60, 70, 80, 90
Cu antenna wire	4.064	-60, -70, -80, -90, 60, 70, 80, 90
Al antenna wire	4.064	-60, -80, 60, 80
Bare Al wire	4.115	-60, -70, -80, -90, 60, 70, 80, 90
BeCu wire	2.305	-40, -50, -60, -70, -80, -90, 40, 50, 60, 70, 80, 90

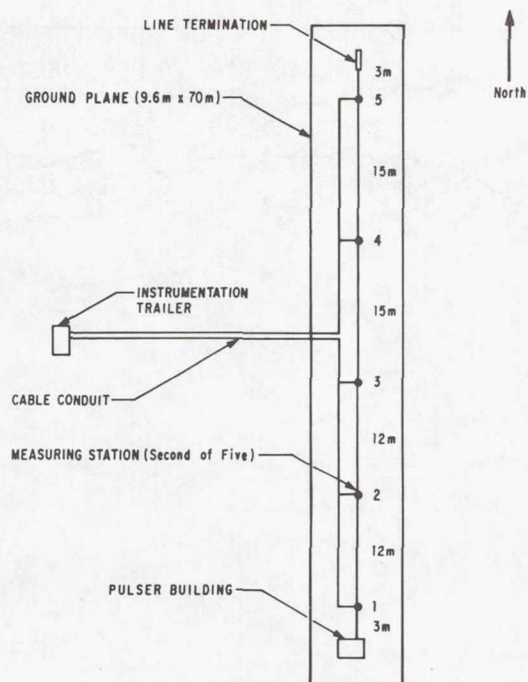


Figure 1.- Schematic diagram of the test facility.

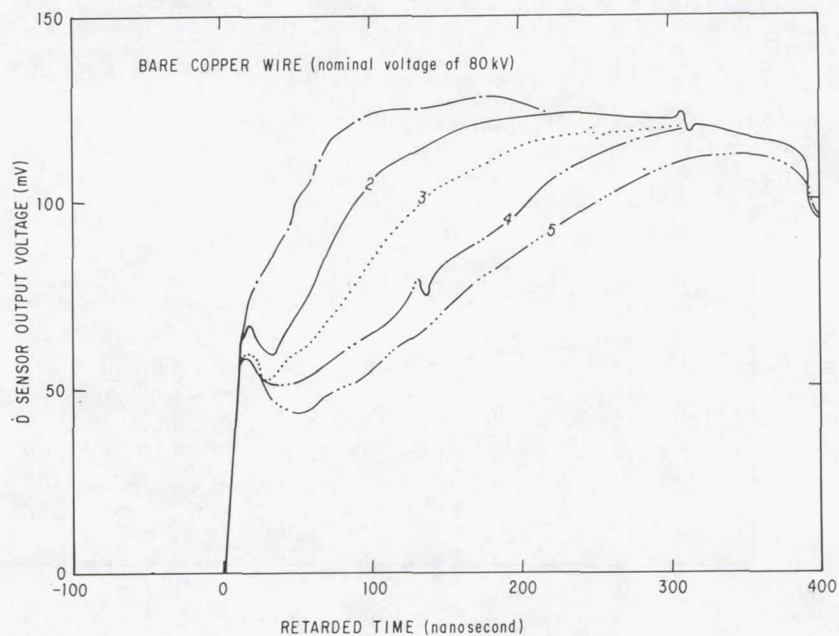


Figure 2.- \dot{D} sensor output voltages.

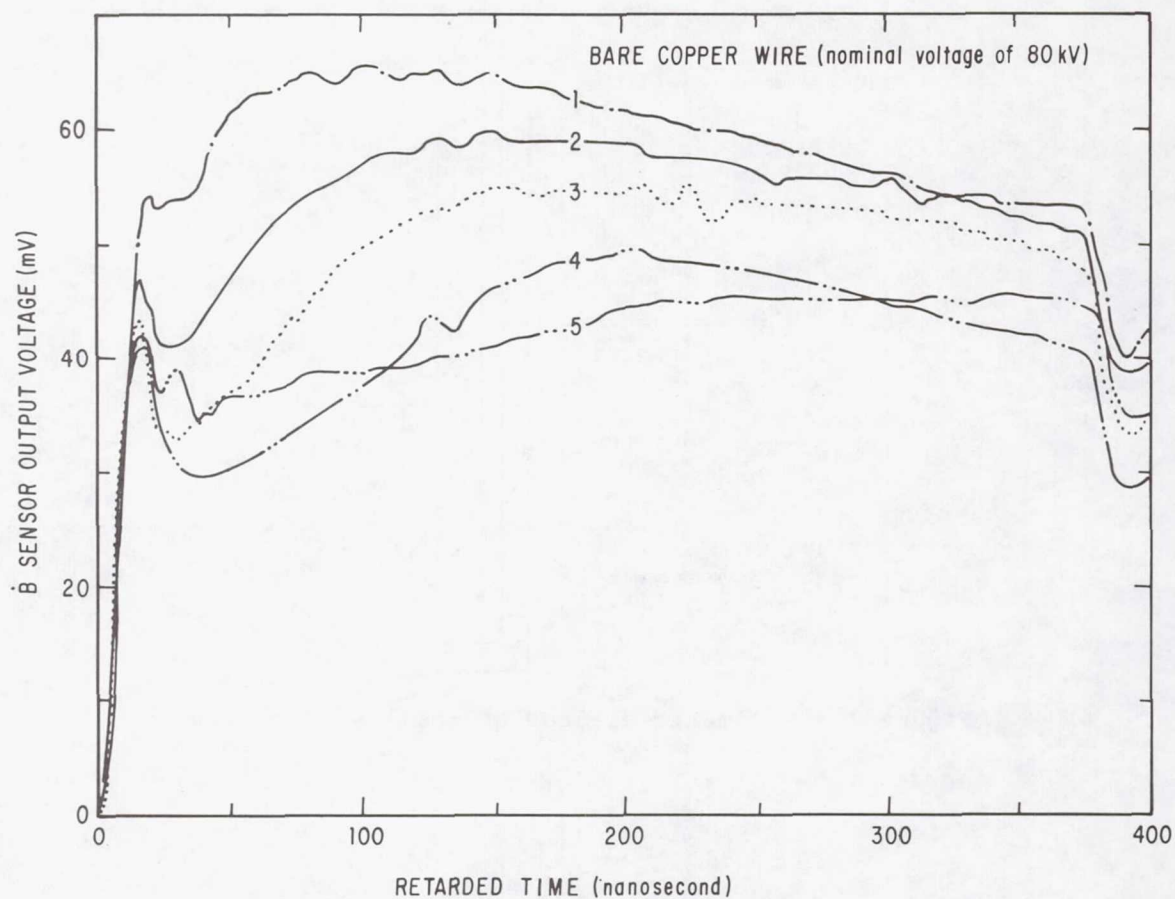


Figure 3.- B sensor output voltages.

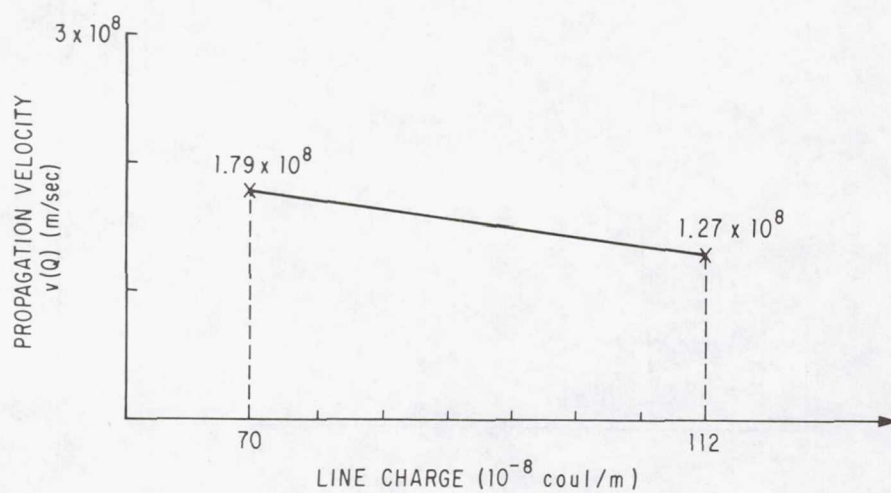


Figure 4.- Approximate propagation velocity $v(Q)$.

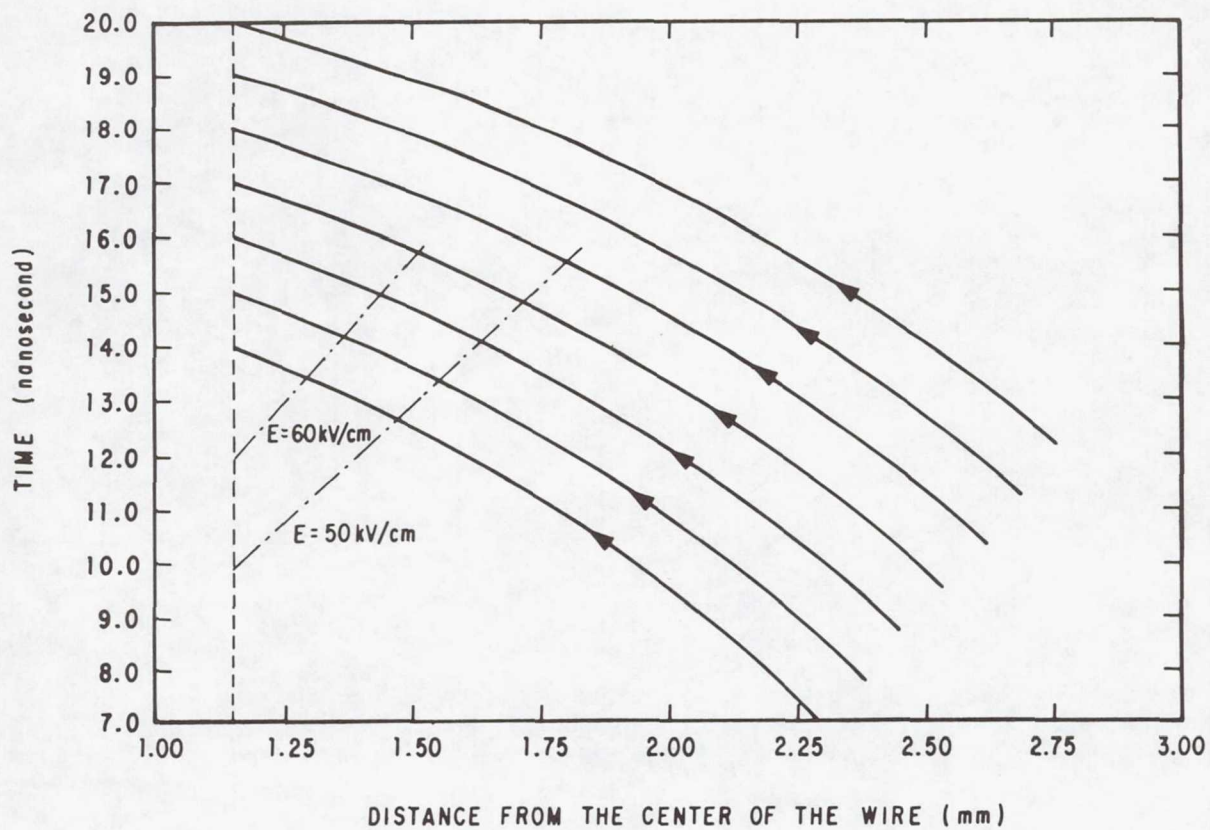


Figure 5.- Electron trajectories around the wire.

Page intentionally left blank

SIMULATION OF ELECTROMAGNETIC ASPECTS OF LIGHTNING

Carl E. Baum
Air Force Weapons Laboratory

ABSTRACT

In testing complex electronic systems for their vulnerability to lightning interference and electrical damage, it is necessary that the test include a simulation. For a simulation one requires that the experimental conditions be sufficiently close to the true physical environment that valid conclusions can be drawn concerning the response in such a criterion environment. Present commonly used test procedures, particularly for the direct-strike case, are in general not simulations. For the case of distant lightning, commonly used EMP simulation techniques are applicable with some modification in the sources (pulsers).

Electromagnetic processes peculiar to the direct-strike case are reviewed with respect to their implications for lightning electromagnetic simulation. At low frequencies (quasistatic) there are important surface-charge-density and corona effects in addition to the surface-current-density effects. At resonant frequencies the frequency-spectral content of the excitation and properties of the arc (attachment, detachment, time history, spatial distribution, resistance, etc.) are significant. Of great complexity in all this are the nonlinear aspects of the arc and corona around the system of interest. The complexity of these various processes requires rigor in the simulator design. Potential simulation concepts are presented and their relative merits are discussed.

I. INTRODUCTION

In an engineering discipline concerned with the reliable performance of some complex electronic system in an intense electromagnetic environment, there comes the question of the demonstration of the performance in such an environment. Such a system is in general so complex that one cannot have a complete understanding of its response to such an environment from first-principle calculations. While one may be able to calculate whether or not the signals at some electronic elements are sufficient to cause failure, some is not good enough (even though the information can still be useful). Given some definition of the mission of the system (in the electromagnetic environment) one must be able to determine whether or not the mission will be accomplished in the presence of the environment. This requires that there be no failures (in the mission accomplishment sense) in any of a certain subset of the electronic elements; such electronic elements (black boxes, subsystems, etc.) are usually referred to as mission critical. More importantly it is required that one know that there be no such failures with high confidence. There are possible

exceptions to this stringent a requirement if sufficient redundancy is built into the system, but this is a more complicated question. In general the system complexity and the possibility (or even probability) that there are important signal paths which are not even identified (even implicitly) in the formal statement of the system design (blueprints, etc.), makes a reliance on first-principle analysis usually untenable for system vulnerability assessment.

Since system-level testing (experimentation) is required for high confidence assessment, the question arises as to what is an adequate test. One might think of an arbitrary electromagnetic stimulus as a test, but what assurance would one have that the system response would bear any significant relationship (for assessment) to its response in the real environment of interest. For the test to be useful it should be reasonably closely related to the real environment of interest and this relationship should be quantitative. Ideally this real environment is summarized in the form of a valid criterion. Paraphrasing an earlier definition (ref. 6),

A lightning electromagnetic criterion is:

a quantitative statement of the physical parameters of the lightning environment relevant to the electromagnetic response of a system of interest in a volume of space and a region of time and/or frequency extended to contain all physical parameters having a non-negligible influence on any of the electromagnetic response parameters.

Normally one will have to state some range or bounds of the parameters, and the time functions (waveforms) and/or frequency spectra may be specified in simplified analytic form, a form which, however, should quantitatively include all relevant environmental parameters.

To test to such a criterion in a way which is quantitatively related to it requires a special kind of test referred to as a simulation. For lightning (electromagnetic) simulation the definition of nuclear electromagnetic pulse (EMP) simulation can be adapted (ref. 7).

Lightning (electromagnetic) simulation is an experiment in which the postulated lightning exposure situation is replaced by a physical situation in which:

1. the lightning sources are replaced by a set of equivalent sources which to a good approximation produce the same excitation (including reconstruction to the extent feasible) to the total system under test or some portion thereof as would exist in the postulated nuclear environment, and
2. the system under test is configured so that it reacts to sources (has the same Green's function) in very nearly the same way and to the same degree as it would in the postulated lightning environment.

A lightning (electromagnetic) simulator is a device which provides the excitation used for lightning simulation without significantly altering the response of the system under test by the simulator presence.

Lightning (electromagnetic) simulation naturally divides into types according to the types of lightning environments to be simulated. If the system of interest is sufficiently distant from the lightning stroke and its associated ionization, the simulation problem is somewhat simplified due to the ability to separate the incident and scattered fields at the system; this case is briefly discussed later. A much more difficult case is that of a direct lightning strike to the system because of the complex electromagnetic field structure, the time-varying electromagnetic properties (conductivity, etc.) of the lightning arc and corona around the system, and the nonlinear properties of the lightning arc and corona. This latter case is very important because of both the intense electromagnetic fields present and the poorly understood nonlinear and time-varying electromagnetic parameters of importance in this lightning source region. These source-region phenomena are of fundamental importance to the lightning simulation problem (for the direct strike); some of the implications of these phenomena for simulator design are discussed in this note.

There is a fundamental limitation in how far we can go in designing a lightning (electromagnetic) simulator; namely one must know what he is to simulate. The detailed physical processes of the lightning arc and corona are poorly quantitatively understood. How then does one simulate it? One can try to have "real" arcs and corona, but how can one be sure that all the relevant physical parameters have been properly controlled. In a direct-strike situation such questions can be very important, while for distant strokes the problem can be reduced to the locally incident electromagnetic fields and electromagnetic properties of the local materials. Particularly in the direct-strike situation the reader should note that the present considerations concerning a lightning simulator are based on the current limited understanding of the lightning arc and corona. As our understanding of the lightning physics becomes more detailed, more rigorous design constraints may be placed on the simulator.

II. SIMULATION OF DISTANT LIGHTNING

If, as indicated in figure 2.1, the lightning arc is distant from the system of interest, the lightning interaction is greatly simplified. Let S be a closed surface bounding an interior volume V which contains the system of interest. For simplicity let the system be in "free space" such as an in-flight missile or aircraft.

Let all the current and ionization associated with the lightning arc be outside S (i.e., not in V). Then the field equivalence principle can be invoked by noting that the incident field in V (in the absence of the system) is determined by imposing the tangential components of the original \vec{E} and \vec{H} on S via equivalent electric and magnetic surface current densities on S (refs. 8,11). These equivalent currents also give zero fields outside S . Having referred the

incident fields to equivalent sources on S, note that the incident fields are somewhat decoupled from the lightning arc. We do not need to understand the details of the lightning arc if we have sufficient knowledge of the incident fields (say by measurement of such fields).

Introducing the system into V there are now scattered fields which propagate away from the system through S. These fields can scatter from the lightning arc (in general a nonlinear process) and in turn rescatter from (interact with) the system thereby changing the system response. To avoid this interaction of the system with the lightning arc one can require that the system be sufficiently far from the arc that the interaction via the multiply scattered waves be sufficiently small as to be insignificant. In this latter approximation the system can be considered as responding to the lightning incident fields in a manner decoupled from the arc physical processes.

In this case of the system distant from the lightning arc the simulation problem is greatly simplified. The problem becomes similar to that found in many EMP simulation problems in which the system is away from the source region. Referring to figure 2.1 the equivalent sources on S can be approximately synthesized with sets of electric and magnetic dipoles to correspond to any desired incident field (consistent with Maxwell's equations with no sources in V). This is the PARTES simulation concept which is quite general, but perhaps complex to implement (ref. 8).

If the system is sufficiently distant from the lightning arc that the incident fields can be considered as an approximate plane wave, then the problem further simplifies. The high-altitude EMP (below the source region) is also approximated as a free-space plane wave; various EMP simulator types produce an approximation of this type of field (ref. 7). One of the most applicable types is the guided wave or TEM-transmission-line simulator constructed with parallel plates and conic sections for launch and/or termination of the wave. Note, however, that while the spatial forms (plane waves) are common between the cases of distant lightning and high-altitude EMP, the temporal forms (waveforms) are not the same. Thus while the simulator proper (electromagnetic-field-forming structure (waveguide, antenna, etc.)) can be used for both simulation problems, one needs different waveforms with different frequency spectral contents; this can be achieved by the use of different sources (pulsers, etc.) to drive the simulator proper. Hence some EMP simulators can also be used for lightning simulation for the case of distant lightning provided there are changes in the driving sources.

The discussion here has centered on the case of an in-flight system distant from lightning because of the simplifications thereby introduced. Similar considerations apply to the case of a system on or near the earth surface. If the system is sufficiently distant from the lightning stroke a plane-wave approximation can still be made, except that the ground reflection should also be included. This problem is also encountered in the case of the high-altitude EMP incident on systems near the ground surface. A commonly used simulator for this type of EMP is a hybrid EMP simulator shaped as an impedance loaded arch (half loop) connected to the earth with a generator in one position in the arch (ref. 7). This simulator includes the incident and reflected waves at the

ground surface, but again for application to the simulation of distant lightning the required waveforms are different requiring a modification in the simulator sources.

III. SIMULATION OF DIRECT-STRIKE LIGHTNING

A more interesting and more difficult type of lightning (electromagnetic) simulation is that concerned with a direct strike including arc attachment to and detachment from the system and corona surrounding the system. Since in general the stimulus is larger than that from distant lightning, the direct-strike case is important to understand and design against.

The first and fundamental problem to observe is that the system is in contact with the nonlinear and time-varying source. As such the separation into incident fields followed by system response discussed in the previous section is no longer applicable. A surface S surrounding the system as in figure 2.1 now has current passing through S into (and out of) V . The problem no longer separates into incident and scattered fields. The system is in the source and influences the evolution of the lightning arc. The interaction of the fields with the system is in turn influenced by the nonlinear, time-varying arc which can change the electromagnetic properties of the system (e.g., natural frequencies), and by the nonlinear, time-varying corona which can influence the response of the external penetrations (apertures and antennas) on the system.

Subsequent sections of this note consider some of the important aspects of the interaction of direct-strike lightning with the system, and the implications of the processes for lightning simulator design. Beginning with the recognized low-frequency current effects, the lightning interaction and simulator design are extended to include charge (more generally normal-current-density) effects and the associated corona. Then the arc-conductance effects are considered as well as the interaction of peripheral parts of the simulator with the test object. The inclusion of all these effects leads to a more rigorous simulator design.

IV. QUASISTATIC (LOW-FREQUENCY) CONSIDERATIONS

Consider first the case that wavelengths of interest are large compared to the exterior system dimensions; this is the low-frequency or quasistatic regime. For this part of the lightning interaction problem one can think of the current flowing through and charge on the aircraft as producing responses which are separable from each other, at least as an approximation.

While the magnetic fields associated with the lightning-arc current flowing on the system surface can penetrate through a metallic surface at sufficiently low frequencies, this type of penetration is usually not of dominant significance because the shield inductance and resistance (of the basic metal)

make a low-pass filter with a very low roll-off frequency. (Note that for some composite materials with conductivities much lower than those of typical metals this magnetic distributed type of penetration can be of greater significance.) For typical systems such as aircraft the important penetrations are generally more discrete (spatially localized) in nature; they include apertures, antennas, and various direct conductive penetrations such as power, signal lines, mechanical control cables, etc. For the present discussion consider the cases of small apertures and antennas as illustrated in figure 4.1.

Consider, as in figure 4.1A, the case of small apertures. In the linear approximation the fields inside an exterior conducting system surface (at positions not near the aperture) are derived from equivalent dipole moments at the aperture. By an equivalent dipole moment is meant that vector quantity which, when substituted in the formulas for fields in free space (ref. 9), approximately gives the correct fields over a volume of space of interest, at least in the low-frequency asymptotic form for positions not close to the aperture. In this sense we can write

$$\tilde{\vec{p}}_{a\text{eq}}(s) = \tilde{\vec{P}}_{a\text{eq}}(s) \cdot \tilde{\vec{D}}_{\text{s.c.}}(s) = \epsilon_0 \tilde{\vec{P}}_{a\text{eq}}(s) \cdot \tilde{\vec{E}}_{\text{s.c.}}(s)$$

\equiv equivalent electric dipole moment

$$\tilde{\vec{m}}_{a\text{eq}}(s) = \tilde{\vec{M}}_{a\text{eq}}(s) \cdot \tilde{\vec{H}}_{\text{s.c.}}(s) = \frac{1}{\mu_0} \tilde{\vec{M}}_{a\text{eq}}(s) \cdot \tilde{\vec{B}}_{\text{s.c.}}(s)$$

\equiv equivalent magnetic dipole moment

(4.1)

$s \equiv \Omega + j\omega \equiv$ complex frequency or Laplace-transform variable

\sim indicates Laplace transformed quantity (for, in general, two-sided Laplace transform)

where the subscript s.c. (\equiv short circuit) indicates the electromagnetic fields on the system exterior with the aperture closed (shorted). These short-circuit fields can also be related to the corresponding surface current and surface charge densities via the unit outward-pointing normal vector $\hat{\vec{I}}_{S_s}$ to the system boundary surface S_s as

$$\begin{aligned} \vec{E}_{\text{s.c.}} &= \frac{1}{\epsilon_0} \rho_{\text{s.c.}} \hat{\vec{I}}_{S_s} \\ \vec{H}_{\text{s.c.}} &= -\hat{\vec{I}}_{S_s} \times \vec{J}_{\text{s.c.}} \end{aligned} \quad (4.2)$$

Assuming for the foregoing that the system exterior (outside S_s) is free space with

$$Z_o = \frac{\mu_o}{\epsilon_o} \approx 377 \, \Omega \quad (\text{wave impedance}) \quad (4.3)$$

$$c = \frac{1}{\sqrt{\mu_o \epsilon_o}} \approx 3 \times 10^8 \, \text{m/s} \quad (\text{speed of light})$$

one can make some observations concerning the relative magnitudes of the electric and magnetic types of aperture penetration. Considering the case of an open aperture (say a circular hole) first note that the equivalent polarizabilities

$$\vec{\tilde{P}}_{a \text{ eq}}(s) \equiv \vec{I}_s \vec{I}_s \vec{\tilde{P}}_{a \text{ eq}}(s) \quad (\text{equivalent electric polarizability}) \quad (4.4)$$

$$\vec{\tilde{M}}_{a \text{ eq}}(s) \equiv \left[\vec{I} - \vec{I}_s \vec{I}_s \right] \cdot \vec{\tilde{M}}_{a \text{ eq}}(s) \quad (\text{equivalent magnetic polarizability})$$

have units (meter)³, making them some kind of equivalent volumes. Furthermore an open hole (perhaps covered with an insulator) has polarizability components of order d^3 where d is a characteristic dimension of the aperture (say the radius of a circular hole). Specifically the dominant components of the electric and magnetic polarizabilities of an unloaded circular aperture are about equal, and frequency independent for wavelengths $\lambda \gg d$.

For the case that the short-circuit electric field is the same magnitude as Z_o times the short-circuit magnetic field, i.e., for

$$|\vec{\tilde{E}}_{s.c.}(s)| \approx Z_o |\vec{H}_{s.c.}(s)| \quad (4.5)$$

and assuming (as above) comparable equivalent aperture polarizabilities, i.e.,

$$|\vec{\tilde{P}}_{a \text{ eq}}(s)| \approx |\vec{\tilde{M}}_{a \text{ eq}}(s)| \quad (4.6)$$

where for dyads (or matrices) the magnitude $||$ is the 2 norm (or spectral or euclidean norm) (ref. 10), then we have from (4.1)

$$|\vec{\tilde{P}}_{a \text{ eq}}(s)| \approx \frac{1}{c} |\vec{\tilde{m}}_{a \text{ eq}}(s)| \quad (4.7)$$

provided $\vec{\tilde{H}}_{s.c.}$ is oriented approximately in a direction corresponding to the largest components of $\vec{\tilde{M}}_{a \text{ eq}}$. This result (4.7) is precisely that for making the far fields (r^{-1} terms) in the dipole formulas comparable for both electric and magnetic dipoles (ref. 5). The near fields (r^{-2} and r^{-3} terms) are dominantly electric for electric dipoles and magnetic for magnetic dipoles. Thus, for a significant class of apertures, comparable short-circuit exciting fields (related by Z_o as in (4.5)) give comparable fields penetrating the aperture.

Now consider direct-strike lightning. Figure 4.2 illustrates the case of some elongated object of radius a (with length $\gg a$) which might represent a missile or aircraft. Let arc 1 first attach to one end followed by arc 2 detaching from the other end. For quasistatic (slow time variation) considerations with current I flowing through the system we have a typical short-circuit magnetic field on the system surface

$$H_{s.c.} \approx \frac{I}{2\pi a} \quad (4.8)$$

The corresponding short-circuit electric field can be estimated by noting that an arc leaving the system surface occurs when the breakdown electric field of air has been exceeded. This implies an electric field of

$$E_{s.c.} \approx 3 \text{ MV/m} \quad (4.9)$$

or a little less because of the system's operating altitude. Letting

$$a \approx 1 \text{ m} \quad (4.10)$$

let us consider two cases:

Case 1:

$$I \approx 200 \text{ kA}$$

$$H_{s.c.} \approx 30 \text{ kA/m} \quad (4.11)$$

$$\frac{E_{s.c.}}{H_{s.c.}} \approx 100 \Omega$$

Case 2:

$$I \approx 20 \text{ kA}$$

$$H_{s.c.} \approx 3 \text{ kA/m} \quad (4.12)$$

$$\frac{E_{s.c.}}{H_{s.c.}} \approx 1000 \Omega$$

These cases of interest then give quasistatic E/H ratios on the system surface comparable to Z_0 . Thus the quasistatic electric and magnetic fields are of comparable importance for penetration through a class of apertures.

For this result the effect of corona on the polarizabilities has not been included. Our estimate of the quasistatic electric field in (4.9) is based on streamers (arcs) leaving S_s . One form of such breakdown can be considered a corona around much of S_s . One can readily show that the magnetic-field change

associated with bounded variations in air conductivity around local perturbations of S_g (such as apertures) is small in the quasistatic (low-frequency) limit (ref. 2). Basically a bounded conductivity change over a small region does not significantly alter an external magnetic field provided the skin depth (or diffusion depth) in the region is large compared to the size of the region. However, the case for the electric field is quite different. The air conductivity σ directly combines with the electric field \vec{E} producing the current density \vec{J} ($= \sigma \vec{E}$). The low-frequency local continuity of the current density clearly indicates that changes in σ change \vec{E} in a comparable way. This change in σ can then change the equivalent electric dipole moment and the corresponding electric polarizability by changing the charge distribution in the vicinity of the aperture, including in the air as well. Note that the nonlinear (and poorly known) character of the corona near the aperture significantly complicates the problem and requires the analysis to be conducted in time domain. It may be interesting to view this electric response in terms of the total current density

$$\vec{J}_{t.s.c.} \equiv (\sigma + \epsilon \frac{\partial}{\partial t}) \vec{E}_{s.c.} \quad (4.13)$$

which includes the local corona conductivity.

The case of electrically small antennas on S_g is indicated in figure 4.1B. Analogous to the aperture-penetration formulas (4.1) one has the linear response of such antennas as

electric:

$$\begin{aligned} \tilde{V}_{o.c.}(s) &= -\tilde{E}_{s.c.}(s) \cdot \tilde{\ell}_{eq}(s) \\ \tilde{I}_{s.c.}(s) &= -s\tilde{D}_{s.c.}(s) \cdot \tilde{A}_{eq}(s) \end{aligned} \quad (4.14)$$

magnetic:

$$\begin{aligned} \tilde{V}_{o.c.}(s) &= s\tilde{B}_{s.c.}(s) \cdot \tilde{A}_{eq}(s) \\ \tilde{I}_{s.c.}(s) &= \tilde{H}_{s.c.}(s) \cdot \tilde{\ell}_{eq}(s) \end{aligned} \quad (4.15)$$

for open-circuit voltage and short-circuit current. Note that the electrically small antennas are usually characterized by equivalent lengths (or heights) and equivalent areas. While these are generally functions of frequency, simple electric- and magnetic-dipole antennas have frequency-independent equivalent lengths and areas in the electrically small regime (ref. 4). In the quasistatic regime of the system the direct-strike lightning current is important for magnetic antennas, and the lightning charge is important for electric antennas.

Note that as in the case of apertures the corona in the vicinity of the antenna needs to be considered. The effect of corona conductivity on the response of magnetic antennas is not of first-order importance at low frequencies

(ref. 2). It is, however, of fundamental importance to the response of electric (or current-density) antennas (refs. 1,3).

Noting the importance of both current and charge at low frequencies on the system of interest, one might attempt to simulate this part of the direct-strike lightning environment as illustrated in figure 4.3. The technique indicated in figure 4.3A is currently commonly employed, but note that as used it gives a large current with a (relatively) small voltage on the system. Beyond present practice, various types of impedance loading in the leads connecting to the pulse generator (and various impedances with the pulse generator) can be used to tailor the driving waveform and the response of the system by controlled loading of the system exterior.

The complementary simulation for the low-frequency charge is indicated in figure 4.3B. This charge or voltage simulation raises the potential of the system relative to some ground reference, such as a ground plane. This can be thought of as a high-impedance simulation in contrast to the low-impedance simulation for current. The capacitance of the system with respect to the ground reference is used to determine the required voltage (V) needed to produce the desired total charge (Q) on the system.

For both the current and charge quasistatic simulation one should be careful of lead placement and proximity of the system of interest to other objects (such as buildings, earth, etc.) because these all influence the distribution of the surface current and charge densities on S_S . In other words one should minimize what is referred to as the simulator/test-object interaction (ref. 7). Combining the two quasistatic techniques one might have a somewhat more complete simulation as indicated in figure 4.4. Here one has two sources V_1 and V_2 with associated impedances \tilde{Z}_1 and \tilde{Z}_2 together with a ground reference to establish the desired V and I on the system at low frequencies.

Note that, while our discussion in this section has been centered on the quasistatic regime for the system, the nonlinear character of the lightning arc and corona on S_S limits one's ability to completely separate the quasistatic regime from the higher-frequency regime. The early-time and resonant response all affect the lightning arc and corona which in turn influence the quasistatic response.

V. EXTERIOR SYSTEM RESONANCES

It is well known that typical electromagnetic scatterers resonate in a manner characterized by damped sinusoids in time domain. These complex natural frequencies s_α are poles in the complex-frequency or s plane. Generalizing on this observation has led to the singularity expansion method (SEM) for the representation of the electromagnetic scattering process for linear (and to date time invariant) scatterers. There is a considerable literature now developed to which the reader may refer (refs. 13,14). We are not concerned here with the general theory, but are concerned with some of its implications for the lightning external interaction and corresponding lightning simulation.

Consider an integral equation of the general form (ref. 14)

$$\left\langle \tilde{\tilde{Z}}(\vec{r}, \vec{r}'; s) + \tilde{\tilde{Z}}_{\ell}(\vec{r}, s) \delta(\vec{r} - \vec{r}') ; \tilde{\tilde{J}}(\vec{r}', s) \right\rangle = \tilde{\tilde{E}}_s(\vec{r}, s)$$

$\tilde{\tilde{E}}_s(\vec{r}, s) \equiv$ source or incident electric field

$\tilde{\tilde{Z}}_{\ell}(\vec{r}, s) \equiv$ impedance loading (such as lightning arc) (5.1)

$\tilde{\tilde{J}}(\vec{r}, s) \equiv$ response current density

$\tilde{\tilde{Z}}(\vec{r}, \vec{r}'; s) \equiv$ impedance kernel

with \langle, \rangle indicating the domain of integration (the region over which the current density (or at least its relevant portion) exists).

Ignoring for the moment the nonlinear and time-varying character of the air conductivity in the lightning arc, let us approximate the impedance loading by the reciprocal of the air conductivity (times the dyadic identity). Without the arc one can find the exterior natural frequencies of the system from

$$\left\langle \tilde{\tilde{Z}}(\vec{r}, \vec{r}'; s_{\alpha}^{(0)}) ; \vec{j}_{\alpha}^{(0)}(\vec{r}') \right\rangle = \vec{0}$$

$\vec{j}_{\alpha}^{(0)}(\vec{r}) \equiv$ natural mode without arc (5.2)

$s_{\alpha}^{(0)} \equiv$ natural frequency without arc

where \vec{r}, \vec{r}' is here only over the system. In the moment method (MoM) (ref. 12) the impedance kernel is converted into a matrix ($\tilde{\tilde{Z}}_{n,m}(s)$) which allows one to find the natural frequencies from

$$\det \left((\tilde{\tilde{Z}}_{n,m}(s_{\alpha}^{(0)})) \right) = 0 \quad (5.3)$$

Now including the arc conductivity in an approximation as linear and time-invariant, we have a new equation for natural frequencies as

$$\left\langle \tilde{\tilde{Z}}(\vec{r}, \vec{r}'; s_{\alpha}^{(1)}) + \tilde{\tilde{Z}}_{\ell}(\vec{r}, s_{\alpha}^{(1)}) \delta(\vec{r} - \vec{r}') ; \vec{j}_{\alpha}^{(1)}(\vec{r}') \right\rangle = \vec{0}$$

$\vec{j}_{\alpha}^{(1)}(\vec{r}) \equiv$ natural mode with arc (5.4)

$s_{\alpha}^{(1)} \equiv$ natural frequency with arc

with \vec{r}, \vec{r}' over the system plus arc. In general one does not expect the set of $s_{\alpha}^{(1)}$ to equal the set of $s_{\alpha}^{(0)}$ given their different defining equations. Furthermore, as the arc conductivity is varied the natural frequencies $s_{\alpha}^{(1)}$ will in general also vary. Similar observations can be made concerning the natural modes $\vec{j}_{\alpha}^{(1)}(\vec{r})$ and the amplitudes of these resonances known as coupling coefficients.

In order to have the $s_{\alpha}^{(1)}$ be correctly included in the simulation it is in general necessary that the arc conductance per unit length be properly included in the simulation. At least near the system, then, the leads from the pulse generators in figures 4.3 and 4.4 can be impedance loaded to approximate some desired arc conductance per unit length. If the lead lengths from their connections to the system are sufficiently long one can get at least some of the natural frequencies and natural modes (on the system) to approximate those appropriate to the desired arc conductance per unit length.

One should regard this arc-conductance part of the simulation as a necessary condition in the resonance regime of the system. It is not in general a sufficient condition because of the nonlinear and time-varying character of the real lightning arcs. In addition there is the corona surrounding the system under direct-strike lightning conditions which may also have some influence on the resonance-region response. To include these nonlinear and time-varying conductivities in the simulation may require a very realistic simulation with "real" current levels, voltages, and surrounding atmosphere with arcs and corona.

VI. MAKING SIMULATION A "PART" OF A LONG LIGHTNING ARC

Previous sections have considered some of the aspects of the interaction of direct-strike lightning with electronic systems from the viewpoint of simulating such aspects with pulsers and impedances directly connected to S_s . However, such simulation is limited by the nature of the lightning arc, especially in its nonlinear and time-varying characteristics. This is further complicated by the limited state of quantitative knowledge concerning the detailed physical processes in the arc and the resulting conductance per unit length, tortuosity, etc.

A possible approach to lightning simulation which at least partly avoids some of these difficulties consists in constructing an arc in air and letting this arc attach to and detach from S_s . This arc is generated by an appropriate high-voltage pulse generator with impedance loading as illustrated in figure 6.1. The arc might be initiated at some high-voltage electrode, propagate toward the system of interest (perhaps meeting streamers from the system), attach to the system, charge the system, detach from the system, propagate toward a return conductor (such as a ground plane), and close to the return conductor, thereby completing the current path through the pulse generator.

This type of simulation might be referred to as dual-arc lightning simulation, referring to the two arcs connected to the system in figure 6.1. How

closely this simulates the direct-strike lightning phenomenon depends potentially on various physical parameters. The arcs should be sufficiently long to simulate the important aspects of the natural phenomenon. For the simulation of in-flight conditions for the system (as for an aircraft or missile) one may wish to control the local air density, water-vapor content, etc. Clearly what is required for the environmental details can be a rather complex question.

A less complete form of the type of simulation in figure 6.1 would use only one arc in air. One might have an attachment single-arc simulation by electrically connecting the system to the return conductor to the pulser (through perhaps some distributed impedance). An alternate approach would be a detachment single-arc simulation obtained by connecting the system to the high-voltage electrode in figure 6.1 (again perhaps with special impedances). Both of these techniques allow charging of the system (with resulting large electric fields). However, the sequential charging and discharging in the non-linear, time-varying arc manner is not fully accomplished.

VII. SUMMARY

As one may now realize, there are several possible improvements that can be incorporated into lightning testing to make the test a simulation. Associated with various identifiable physical processes in the lightning interaction with electronic systems, one can formulate corresponding constraints on the simulator design. While this leads to improved simulator designs, this is not necessarily complete because of the limited understanding of the lightning physical processes by the scientific/engineering community. For distant lightning, except for some waveform questions, the simulation problem is similar to a class of EMP simulation and thereby relatively well known. For direct-strike lightning the situation is quite complex and little understood by comparison.

For direct-strike lightning one can consider the physical processes involved to develop simulator design. Quasistatic considerations lead to the importance of both current and charge on the system, thereby requiring the simulator to produce large voltage as well as large current. In the resonance region SEM considerations lead to the requirement of simulating the lightning arcs in both geometry and impedance properties, at least near the system. Both low frequencies and resonance frequencies require that the non-arc conductors and other objects be positioned away from the system under test so as to not undesirably modify the system response. At high frequencies (short wavelengths compared to system dimensions) the problem is very messy making it difficult to identify specific aspects of the simulation associated with this regime.

By successively imposing the various constraints on lightning simulation one can progressively improve the realism of the simulation. Given the state of lightning understanding at a given time (such as the present) one can design a simulator which is consistent with this understanding. Such understanding already indicates that considerable improvement in lightning simulation is needed as discussed here. However, there is still the fundamental need of obtaining an adequate understanding of the lightning electromagnetic environment.

REFERENCES

1. Baum, C. E.: Radiation and Conductivity Constraints on the Design of a Dipole Electric Field Sensor. Sensor and Simulation Note 15, February 1965.
2. Baum, C. E.: The Influence of Radiation and Conductivity on B-Dot Loop Design. Sensor and Simulation Note 29, October 1966.
3. Baum, C. E.: Two Types of Vertical Current Density Sensors. Sensor and Simulation Note 33, February 1967.
4. Baum, C. E.: Parameters for Some Electrically-Small Electromagnetic Sensors. Sensor and Simulation Note 38, March 1967.
5. Baum, C. E.: Some Characteristics of Electric and Magnetic Dipole Antennas for Radiating Transient Pulses. Sensor and Simulation Note 125, January 1971.
6. Baum, C. E.: Extrapolation Techniques for Interpreting the Results of Tests in EMP Simulators in Terms of EMP Criteria. Sensor and Simulation Note 222, March 1977.
7. Baum, C. E.: EMP Simulators for Various Types of Nuclear EMP Environments: An Interim Categorization. Sensor and Simulation Note 240, January 1978, and IEEE Trans. on Antennas and Propagation, January 1978, pp. 35-53, and IEEE Trans. on Electromagnetic Compatibility, February 1978, pp. 35-53.
8. Baum, C. E.: The PARTES Concept in EMP Simulation. Sensor and Simulation Note 260, December 1979.
9. Baum, C. E.: Emerging Technology for Transient and Broad-Band Analysis and Synthesis of Antennas and Scatterers. Interaction Note 300, November 1976, and Proc. IEEE, November 1976, pp. 1598-1616.
10. Baum, C. E.: Norms and Eigenvector Norms. Mathematics Note 63, November 1979.
11. Love, A.E.H.: The Integration of the Equations of Propagation of Electric Waves. Phil. Trans. Roy. Soc. London, ser. A, vol. 197, 1901, pp. 1-45.
12. Harrington, R. F.: Field Computation by Moment Methods. MacMillan, 1968.
13. Baum, C. E.: The Singularity Expansion Method, in L. B. Felsen (ed.), Transient Electromagnetic Fields. Springer-Verlag, 1976.
14. Baum, C. E.: Toward an Engineering Theory of Electromagnetic Scattering: The Singularity and Eigenmode Expansion Methods, in P.L.E. Uslenghi (ed.), Electromagnetic Scattering. Academic Press, 1978.

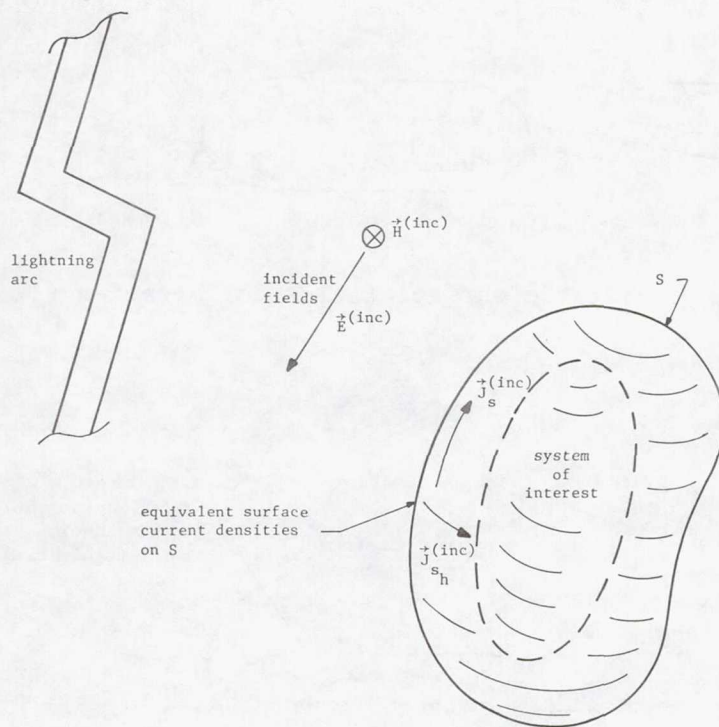


Figure 2.1.- Fields incident on system away from lightning arc.

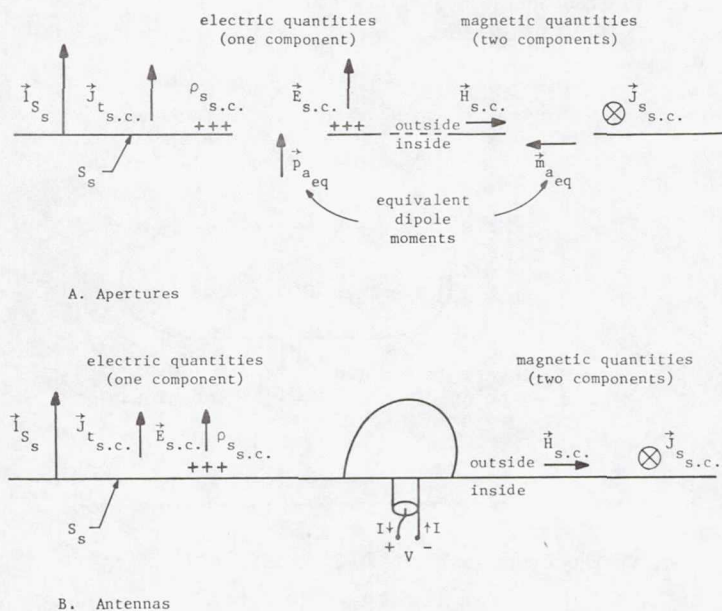


Figure 4.1.- Quasistatic interaction mechanisms for small penetrations.

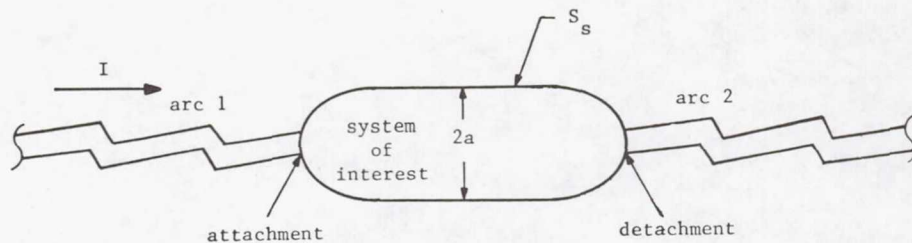
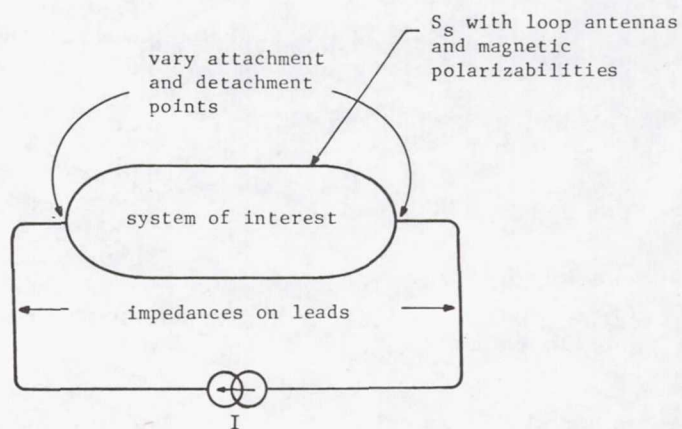
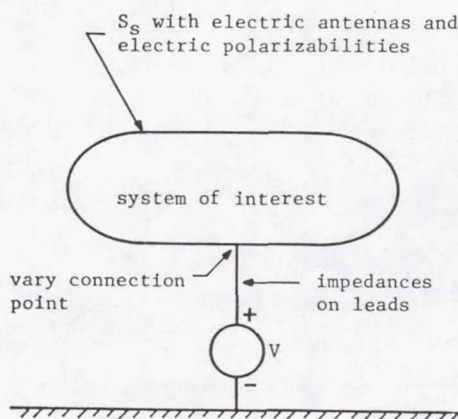


Figure 4.2.- Quasistatic surface fields for direct-strike lightning.



A. Current (or tangential magnetic field)



B. Charge (or normal electric field)

Figure 4.3.- Current and charge low-frequency simulation.

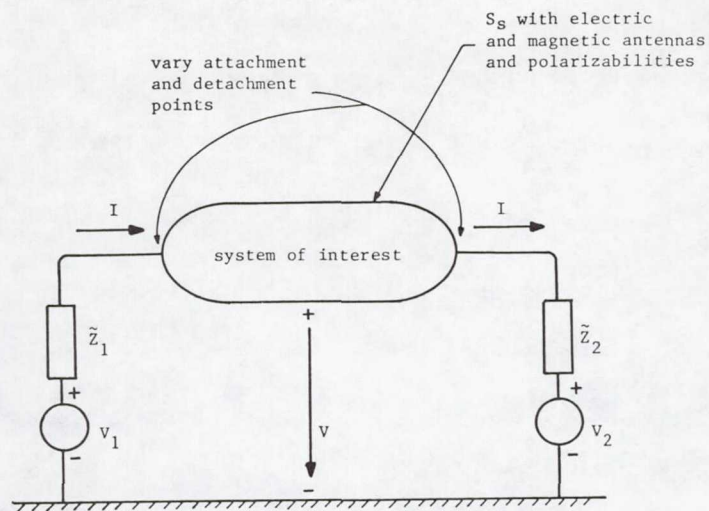


Figure 4.4.- Combined current and charge low-frequency simulation.

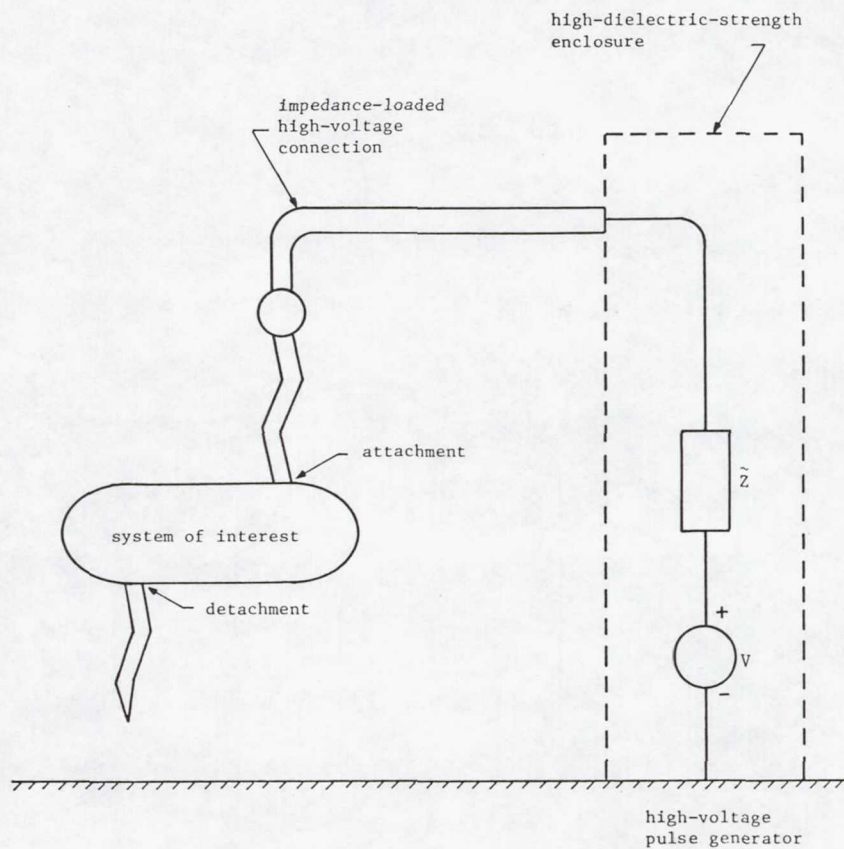


Figure 6.1.- Dual-arc lightning simulation.

Page intentionally left blank

SESSION V - PROTECTION OF GROUND SYSTEMS

Page intentionally left blank

A UNIVERSAL PROCEDURE FOR EVALUATION AND APPLICATION OF SURGE-PROTECTIVE DEVICES

Bernhard I. Wolff
General Electric Company, Semiconductor Products Department
Syracuse, N.Y.

SUMMARY

First of all the source, nature, and frequency of occurrence of transients must be identified. A representative standard test wave should be chosen for proof testing. The performance of candidate suppressor devices then can be evaluated against the withstand goals set for the equipment. The various suppressors divide into two classes of generic behavior. The key to a universal procedure for evaluating both classes lies in representing transients as quasi-current sources of defined current impulse duration. The available surge current is established by the Thevenin equivalent transient voltage and source impedance. A load line drawn on the V-I characteristic graph of the suppressor quickly determines the clamping voltage and peak current. These values then can be compared to the requirement. The deposited energy and average power dissipation for multiple transients also can be calculated.

It may be possible to improve the protective level at a sensitive circuit by use of two suppressors in a cascade network. A series impedance is necessary to provide a degree of isolation between the primary and secondary suppressors. The method is illustrated with a design example for motor vehicle alternator load dump suppression.

INTRODUCTION

Until the last decade or two surge suppression was not a problem which touched the activity of many circuit and equipment designers. Most electron tubes and electro-mechanical devices were relatively large and rugged, and exhibited high inherent immunity to surge damage or upset. Surge protection was the business of specialists concerned mainly with equipment or personnel exposed to the effects of direct lightning strikes. Adequate protection usually was obtainable with well designed spark gaps incorporating resistive elements to limit follow current from the power source. However, the micro-circuit revolution has changed all that. With these sensitive devices the effects are felt of transient disturbances appearing locally at relatively low levels. Transient suppression then becomes a necessary phase of design.

It is the purpose of this paper to outline the basic procedure that is used in evaluation and application of suppressor (surge-protective) devices.

Although reactive and resistive elements also may be used effectively as variables as will be seen, the active suppressor element is usually the centerpiece of design. Because of the variety of transients that may occur depending on the environment, and the different properties of candidate suppressors, the selection of a suitable device isn't necessarily a routine matter. However, certain steps are basic to the evaluation process. These are familiar to experienced suppression designers but the presentation here may be of benefit to the newcomer. These steps will be illustrated with some examples involving variable-resistance and discharge type behavior suppressor devices, and the areas where these different devices are incomparable will be indicated.

REPRESENTATION OF THE TRANSIENT ENVIRONMENT

One of the difficulties encountered in dealing with transients is that different kinds of transients tend to occur in different environments. Worse, in some environments no two transients are likely to be identical. Nonetheless, it usually is possible to make reasonable generalizations about their characteristics. For example, the pioneering inquiry of reference 1 into the nature of transients on ac power lines in indoor residential or commercial locations produced the oscillograph of Figure 1. This was obtained by triggering the oscilloscope when transients above a preset level occurred over a 24 hour period. The bright white central band in the figure was produced by the sinusoidal ac power voltage while the transient waveforms appear above it. As evident, none of these seem likely to be identical in amplitude or waveshape.

Despite detail differences from actual transients it should be sufficient for simulation purposes to define standard waves that are suitable for proof testing of equipment. A waveform can be chosen that is representative of those typically observed. Also, a peak amplitude can be chosen that generally will not be exceeded. Indeed, this is the procedure that was used to adopt the test waves and amplitudes of the IEEE 587.1 Guide (reference 2). The oscillatory open-circuit voltage waveform of Figure 2 is deemed to represent transients observed on long branch circuits in the indoor environment, and is recommended for use in designing surge-protective systems.

For locations at or near the ac service load center the additional waveform like Figure 3 is recommended. This is the familiar $8 \times 20 \mu\text{S}$ impulse current waveform traditionally used for testing station-class and secondary arrestors located in the outdoor environment. The choice of this current wave for the IEEE location category B derives from simulated lightning tests and from field experience with surge-protective devices. When subjected to a current waveform of this shape the voltage waveform response of a typical suppressor is as shown in the oscillogram of Figure 4. Note that the voltage rises toward crest value much more rapidly than the current and that the impulse duration (decay time to 1/2 of crest value) is longer for voltage than for current. The test wave of Figure 2 also is recommended by the IEEE for location category B but due to a lower peak current and shorter effective

impulse duration it deposits much less energy in the suppressor. The test wave of Figure 3 therefore is more severe with respect to the size of suppressor that is required to withstand it.

Another popular test wave is the current impulse of dimensional shape $10 \times 1000 \mu\text{S}$. This wave is considered representative of lightning remnants; i.e., a composite of individual strokes within a lightning flash where the wave has been smoothed and stretched by effect of lightning arrestors upstream in the transient propagation path. Such a wave also might be representative of the discharge of energy stored in inductances such as transformers and relay coils. Because of their long-standing popularity the $8 \times 20 \mu\text{S}$ and $10 \times 1000 \mu\text{S}$ current waves both have been adopted as standard test waves in IEEE test specification for gas tube, metal-oxide-varistor, and avalanche diode suppressors. See references 3, 4, and 5. However, many other test waves are in use which are considered representative of specific environments, or which have been adopted to satisfy specific proof-testing objectives.

A complete description of the expected transients also must include the frequency of their occurrence. In the case of lightning and its related switching disturbances the frequency will vary widely with geographic location. The probable occurrence of transients of a given level of severity also will vary with the exposure of the incoming electrical service to lightning strikes. A building fed by long overhead lines has an extreme exposure compared to one that is fed by an underground distribution system. Data on expected rates of occurrence are presented in IEEE 587.1. Other kinds of environments or those which combine the effects of internally and externally generated transients must establish their own transient waveforms, amplitudes, and rates of occurrence. It should be recognized that an excessive margin in the specification over and above the actual need may add little to reliability while leading to a cumbersome design with excessive cost.

In the final specification of the surge simulation all the essential parameters of the surge must be included. This is illustrated by Figure 5. The open circuit transient voltage V_{TH} of Figure 5a) determines the dielectric stress that will be applied to an unprotected equipment. By addition of a suppressor as in Figure 5b) the transient is suppressed to a protective voltage level within the design withstand capability. However, the suppressor is thereby subjected to a current stress. This current will be limited by the impedances in the transient source and wiring. If V_{TH} alone is specified without a value for source impedance, or without specifying transient peak current, the suppressor selection problem is left without sufficient information to solve it. Also, since the ability of a suppressor to withstand the current impulse depends on the duration of the impulse, this parameter too must be specified and controlled in testing.

CHARACTERISTICS OF SUPPRESSORS

The suppressor evaluation and application process suffers from a near embarrassment of riches in the variety of devices available. These operate on several different physical principles but their terminal behavior can be regarded as falling into two distinct classes. By definition, devices in the variable-resistance (varistor) class exhibit a terminal voltage that increases nonlinearly and monotonically with current over a wide range. Devices operating on the reverse junction breakdown principle such as silicon avalanche diodes fall into this category along with metal-oxide-varistors. The protective voltage level of all such devices can be approximated as a function of current by a two-term equation. (See reference 6). The parameters of this equation may vary somewhat with device technology and size but the model is the same.

The second class of devices exhibit what may be called discharge type behavior. This class includes not only gas discharge tubes and air gap sparkover devices but also certain solid-state circuits with "crowbar" action. These devices are typified by a V-I curve that includes a region in which voltage drops sharply after a threshold value is exceeded. Consequently, these devices also tend to draw follow-current from the power source after the surge has passed. Except for systems in which the follow-current is sufficiently limited in amplitude and duration a fixed or variable resistance element then is usually employed in series.

The response of voltage and current versus time for a typical varistor device subjected to an $8 \times 20 \mu\text{s}$ current stimulus was shown in Figure 4. The response of the "crowbar" circuit device of Figure 6 is shown by the oscillogram of Figure 7. A comparison of the Figures 4 and 7 clearly shows the difference in voltage behavior. However, although the voltage of the discharge behavior device drops to a low level the protective level seen by the equipment is the peak voltage at which breakover occurs. In these examples the observed protective levels are roughly the same; i.e., somewhat over 300V. Note also that the current waveforms are not a function of the class of suppressor. Therefore, devices which may seem incomparable due to differences in voltage behavior may be aptly compared when current amplitude and impulse duration are used as the basis.

One aspect in which nearly all suppressors seem incomparable is that of their terminology. Although various IEEE and JEDEC standards plus the practices of industry have brought about a considerable degree of uniformity in the terms used within a device family the different technologies tend to use different terms to describe the same test parameters. The comparative glossary of Table I is offered as a guide to relate some of the device terms most frequently used to the system designers' terminology.

OPERATING POINT DETERMINATION

The determination of the suppressor operating point has two principal objectives: a) to find the protective level provided by the suppressor, b) to find the peak current of the pulse that passes through the suppressor. This process is relatively easy for devices of the discharge type. Assuming that the voltage rate-of-rise is fixed a gas tube will fire at approximately the same voltage regardless of the peak value of the current pulse. The breakover voltage of a solid-state circuit also is essentially unaffected by peak current. The protective level then can be found from design data sheet values. Also, since both devices have a relatively low voltage drop when in the conducting state the peak pulse current is approximately the same as a short-circuit value. This is easily computed from test circuit parameter values V_{TH} and R_{TH} of Figure 5A. Of course, this simple analysis assumes that a series follow-current limiting resistance is not used.

In the case of variable-resistance type devices the determination of operating point values is not the same trivial procedure. Because the device clamping voltage increases monotonically with current the values must be found by a simultaneous equations solution procedure. Writing the equation for the sum of voltages in Figure 5 , and the behavioral equation for the suppressor (from reference 6) gives respectively:

$$V_C = V_{TH} - R_{TH}I \quad (1)$$

$$V_C = KI^\beta + R_S I \quad (2)$$

where:

V_C is the suppressor clamping voltage

V_{TH} is the Thevenin equivalent peak voltage of the transient

R_{TH} is the Thevenin equivalent source impedance of the transient

I is the peak surge current

K is a suppressor constant similar to nominal breakdown or varistor voltage

β is the characteristic of suppressor nonlinearity, $0 < \beta < 1$

R_S is the suppressor internal series bulk resistance.

(It should be noted that the model of equation (2) assumes that reactive elements of the device or application circuit are not significant. In practice, uncontrolled lead inductance may greatly affect clamping voltage results see reference 7, pages 84-85, and reference 8.)

A general solution this system of equations is faced with two practical problems. First, limit values for device parameters β , R_S may not be given on manufacturer's data sheets. Secondly, even if available the equations are not directly solvable by simple analytical means since they are not homogeneous of degree one. However, two other procedures can be used to find solutions which are satisfactory for engineering purposes without resort to computer programs.

An approximate solution can be calculated by noting that the power law term KI^β approaches the numerical value of the constant K as the value of parameter β approaches zero. That is, the device is treated as ideally non-linear and constant in voltage except for the drop across internal resistance R_S . This is a reasonable assumption for most avalanche diodes especially if the expected operating point is only incrementally different from a specified test point. The procedure is illustrated by the following example.

Consider the case of a JEDEC type 1N5665 diode. This device of 200V nominal breakdown voltage is specified to have a maximum voltage of 287V at 5.2A (reference 9). available data sheets do not include a limit value for R_S , but from measurements of reference 6 it appears that a value on the order of 1.2 ohms would be reasonable for purposes of illustration. This number first can be used to impute a value for the KI^β term so that equations (1) and (2) can be solved simultaneously. By rearrangement and substitution into (2):

$$KI^\beta = V_C - R_S I = 287 - 1.2(5.2) = 281 \text{ V}$$

For this example assume that the test uses the 100KHz wave of IEEE category A where $V_{TH} = 6000\text{V}$ and effective $R_{TH} = 30 \text{ ohms}$. Using equations (1) and (2) the solution for I and V_C at the peak operating point gives:

$$V_{TH} - R_{TH} I = KI^\beta + R_S I$$

$$6000 - 30I = 281 + 1.2I$$

$$I = 183\text{A}$$

By substitution in (2)

$$V_C = 281 + 1.2(183) = 501\text{V, maximum}$$

The second procedure for operating point solution requires no a priori knowledge of a behavioral model or its parameter values. Instead, the maximum clamping voltage curves which are provided on the data sheets of many manufacturers are utilized to obtain fast and accurate answers. This is shown in figure 5B which illustrates the maximum clamping voltage curve of a typical metal-oxide-varistor. The solution for I and V_C at the peak operating point is obtained by a graphical analysis. A load line representing equation (1) is drawn on the graph where the varistor maximum V-I characteristic curve represents equation (2). The intersection of the load line with the V-I curve gives the solution. Note that the load line is a curve, rather than straight, when the graph has log-log coordinates.

As a concrete example consider the case of a commercial type metal-oxide-varistor, V130LA10A or equivalent. Reference 7, page 118, shows the maximum V-I characteristic graph for this type. Suppose that a load line is drawn representing IEEE 587.1 category B where the parameters of the transient generator are $V_{TH} = 6000V$, $R_{TH} = 2.0$ ohms. The operating point values at the junction of the clamping curve and load line will be $V_C = 600$ V maximum, $I = 2700$ A, as seen by inspection. The value of $V_C = 481V$ at 2800A measured on a device specimen (see reference 6) is well within this maximum limit.

When the operating point has been determined the designer can compare the predicted values against the goals set. The checklist should include the following:

- a) Does the suppressor satisfy the desired protection level?
- b) Does the peak current fall within the rated capability of the suppressor for the specified waveform?
- c) Does the rated capability encompass include the expected number of surge occurrences over the equipment life?
- d) If the goals are not satisfied has the trade-off been explored between suppressor capability and equipment design withstand level?
- e) If a practical, economic combination of suppressor and equipment protection need seems unattainable, does the surge specification accurately reflect genuine field application conditions?

ENERGY DEPOSITION

When the peak voltage and current of the suppressor have been determined it will be possible to calculate the energy deposited in a variable-resistance type suppressor. By definition this energy is the product of instantaneous voltage and current integrated over time. Hence it is a function of waveshape and impulse duration. The integration procedure is cumbersome to perform since the integration feature is not generally available in the surge generation equipment itself. Therefore, some approximate estimation procedure accurate enough for engineering purposes is desired.

Reasonably good estimates of deposited energy can be obtained from the relation:

$$W = KV_c I_p \gamma \quad (3)$$

where:

W is the energy in joules

K is a form factor unique to the waveshape

γ is the current impulse duration in seconds as defined in Figure 3

V_c , I_p are as defined previously

The basis for equation (3) is that V_c varies very little for a wide variation of I , especially if the exponential characteristic of nonlinearity, β , has a value approaching zero. Values below 0.1 or especially below 0.04 provide a good approximation to the ideal. Then V_c is regarded as a constant in the calculation while the form factor K is associated with the current waveshape.

The form factors for some frequently encountered waveshapes have been compiled (reference 7, page 39) and are reproduced in figures 8 and 9. Form factors for other waves can be derived from composites of those shown. For example, the $8 \times 20 \mu S$ current wave of Figure 3 can be regarded as a quarter-sine wave on the front followed by an exponential decay. Using the values shown in the figures an approximate form factor constant for the $8 \times 20 \mu S$ wave can be computed as:

$$K\gamma = K_1\gamma_1 + K_2\gamma_2$$
$$K = \frac{(.64/2)(8) + 1.4(12)}{20} = .97$$

In the case of gas discharge tubes and crowbar circuits it is obvious that calculation by equation(3) is inapplicable because of the large change in voltage after device turn-on. Indeed, variable-resistance and discharge class devices are incomparable on an energy basis. Furthermore, energy rating can be misleading as an indicator of the comparative merit of different varistor types. The energy deposited depends on the V-I characteristic of the suppressor; the better the suppressor, the lower the clamping voltage, and the lower the energy given the same peak current and waveshape. Therefore, current withstand ratings are the appropriate basis for evaluating the withstand capability of all types of suppressors.

CASCADE SUPPRESSION OF MOTOR VEHICLE LOAD DUMP TRANSIENTS

The preceding sections have discussed the principles of application for single suppressors. This section will illustrate the potential for improving the protective level by using suppressors in cascade. The example is that of protection against the load dump transient in motor vehicles.

Electronic circuits in motor vehicles are subject to a number of electrical transients but load dump is of the greatest damage potential (reference 10, p.58). The source of this transient may be illustrated by the simplified vehicle electrical circuit of Figure 10. Normally, the vehicle battery acts as an excellent sink for power line transients, but it is subject to inadvertent disconnection as a result of terminal corrosion or other causes. Then, when a vehicle electrical load is removed, such as by turning off the rear window heating element, a significant transient is produced on the power line. This occurs during the interim between load switch-off and restoration of normal voltage regulation and is manifested as a positive-going voltage transient. In the worst case the load is itself a badly discharged battery drawing maximum

alternator amperage. When the connection to it is interrupted a voltage transient of 80V peak or more can be produced.

Attempts have been made to arrive at an industry standard for expressing the shape of the transient. Also, Circuits have been devised for simulating the load dump transient in bench test equipment without recourse to a vehicle or its alternator based charging system. (reference 11, Fig 5.2). Unfortunately, this has characterized the load dump transient in terms of peak voltage and duration in the unsuppressed condition only. (See Figure 11. In any event, that simulator is today considered by the industry to be inadequate in severity.

Although this earlier circuit provided an indication of damage exposure for unprotected electronics it didn't directly give the crucial information for suppressor application. Both the peak current and current impulse duration must be accurately simulated. Bench tests using typical alternators of 70-90A rated output suggest that the load dump transient may in fact approach 50A peak current, have an effective impulse duration of about 33mS, and deposit about 90 joules of energy in a commercial type V24ZA50B metal-oxide-varistor. It is necessary, therefore, to devise a simulator circuit with appropriate component values to simulate these two conditions: a) the open circuit peak voltage that can damage sensitive components, and b) the peak current and impulse duration that will evaluate the protective level and energy withstand capabilities of the suppressor.

The simplified equivalent circuit of Figure 12 shows the suggested simulator circuit and its component values. When the storage capacitor C1 is charged to 94V an open circuit peak voltage of 85V is produced at the output terminals. It does not matter that the open circuit voltage duration is longer than that produced by an unsuppressed alternator load dump. What does matter is that the simulator surges suppressor specimens with a peak current value corresponding to the alternator load dump, and that it has a current impulse duration which deposits the corresponding energy.

The operating point values of suppressors VUT1, VUT2 in Figure 12 can be found by graphical analysis. It is first assumed that the population of available suppressors can be sorted by the user so that those with superior clamping are separated. Thus, though VUT1 and VUT2 are of similar type VUT2 has a lower maximum V-I characteristic as shown in Figure 13. Note that this V-I graph uses linear coordinates for simplicity. The condition for equality in the branches of the circuit of Figure 12 is given by the relations

$$V_{C1} = V_{C2} + I_2 R_A = V_{TH} - I_T R_{TH} \quad (4)$$

$$I_T = I_1 + I_2 \quad (5)$$

where the isolation resistor between VUT1 and VUT2 is designated by R_A ,

where all terms are as previously defined, the subscripts 1, 2 indicate the respective suppressor, and I_T is the total current. The voltage sum $V_{C2} + I_2 R_A$ is shown on Figure 13 by the heavy dashed line, while the load line and suppressor maximum V-I characteristics are the solid heavy lines indicated. To find the graphical solution the lightly dashed line of voltage V_{C1} must be placed so that equations (4) and (5) are simultaneously satisfied. The values found are very close to those observed in Figures 14 and 15, where maximum limit suppressor specimens were tested in the load dump circuit. Note that clamping voltage $V_{C2} = 38V$ is substantially improved over the 46V that would occur with a single suppressor like VUT1.

The energy deposited in each suppressor can be estimated by equation 3. In Figure 15 it is important to observe that the current impulse duration of the secondary suppressor has been "stretched" by the nonlinear effects of the primary. Therefore, the sharing of surge energy will be different than expected from the peak current values alone. Calculations give approximate energies of

$$W_1 = 1.4(44)(30)(.03) = 55 \text{ Joules}$$

$$W_2 = 1.4(38)(15)(.05) = 40 \text{ Joules}$$

CONCLUSIONS

The simulation of transients by surge generators with appropriately chosen open circuit voltage, source impedance, and current impulse waveshape is an effective tool in protection design. Suppressor devices of various technology types can be evaluated by this procedure at both the analytical and laboratory proof testing stages. However, if the surge impedance is not defined, or implied by a short-circuit current value, there is insufficient information to determine either the protective level provided by a suppressor or its ability to withstand the surge.

The use of two suppressors in a cascade network can significantly improve the protective level even if the value of the isolating impedance is relatively small. However, the energy deposited in the secondary suppressor will be greater than expected due to the pulse "stretching" effect of the primary.

REFERENCES

1. Martzloff, F.D. and Hahn, G.J., "Surge Voltage in Residential and Industrial Power Circuits," IEEE PAS 89, 6, 1049-1056 (July/August 1970).
2. Guide on Surge Voltages in AC Power Circuits Rate Up to 600V, Final draft, May 1979. Document P587,1/F prepared by Working Group 3.4.4 of the Surge Protective Device Committee, Power Engineering Society, IEEE.
3. Test Specifications for Gas Tube Surge Protective Devices, IEEE Standard 465.1-1977.
4. Test Specifications for Varistor Surge Protective Devices, Sixth Draft, May 1979. Document P465.3/D5 prepared by Working Group 3.3.6 of the Surge Protective Device Committee, Power Engineering Society, IEEE.
5. Test Specifications for Avalanche Diode Surge Protective Devices, Third Draft, October 1979. Document P465.4/D2 prepared by Working Group 3.3.6 of the Surge Protective Device Committee, Power Engineering Society, IEEE.
6. Wolff, B.I., "Analyzing Surge Protective Devices within a Common Framework," Federal Aviation Administration-Florida Institute of Technology Workshop on Grounding and Lightning Technology, FAA-RD-79-6, March 6-8, 1979, Melbourne, Florida, U.S. Dept. of Transportation, Washington, DC 20590.
7. Transient Voltage Suppression Manual, Second Edition, General Electric Company, Auburn, NY, 1978.
8. Clark, O.M., and Pizzicaroli, J.J., "Effect of Lead Wire Lengths on Protector Clamping Voltages," Federal Aviation Administration-Florida Institute of Technology Workshop on Grounding and Lightning Technology, FAA-RD-79-6, March 6-8, 1979, Melbourne, Florida, U.S. Dept. of Transportation, Washington, DC 20590.
9. Transient Absorption Zener 1N5629 Thru 1N5665 and 1N5907, Siemens Company, Iselin, NJ.
10. Preliminary Recommended Environmental Practice for Electronic Equipment Design, New York, Society of Automotive Engineers, 1974.
11. Electromagnetic Susceptibility Test Procedures for Vehicle Components (except Aircraft), New York, Society of Automotive Engineers, 1974.
12. IEEE Standard Dictionary of Electrical and Electronic Terms, IEEE Std 100-1977, New York, John Wiley & Sons, Inc., 1977.

TABLE I A COMPARATIVE GLOSSARY OF SUPPRESSION TERMS⁶

Design Tests ¹	Variable Resistance Devices		Discharge Behavior Devices	
	Avalanche Diode ²	Metal-Oxide-Varistor ³	Gas Tube ⁴	Solid-State Crowbar ⁵
test voltage	breakdown voltage	varistor voltage	dc breakdown voltage	reference voltage
protective level	clamping voltage	clamping voltage	impulse breakdown voltage	breakover voltage
rated voltage	standoff voltage	rated voltage	holdover voltage	repetitive peak off-state voltage
withstand current	peak pulse current	peak single pulse transient current	single impulse discharge current	non repetitive peak on-state current
withstand energy	peak pulse power*	single pulse transient energy	NA	NA

* nearest equivalent

NA - no applicable term

NOTES: 1. Defined in IEEE Std 100-1977 (see reference 12)

2. Defined as per IEEE Std 465.1-1977 (see reference 3)

3. Defined as per IEEE draft P465.3/D6 (see reference 4)

4. Defined as per IEEE draft 465.4/D2 (see reference 5)

5. Defined as per JEDEC publication No. 77B, January, 1978

6. Device data presented under these terms may not be comparable due to differences in the strict definitions and test methods.

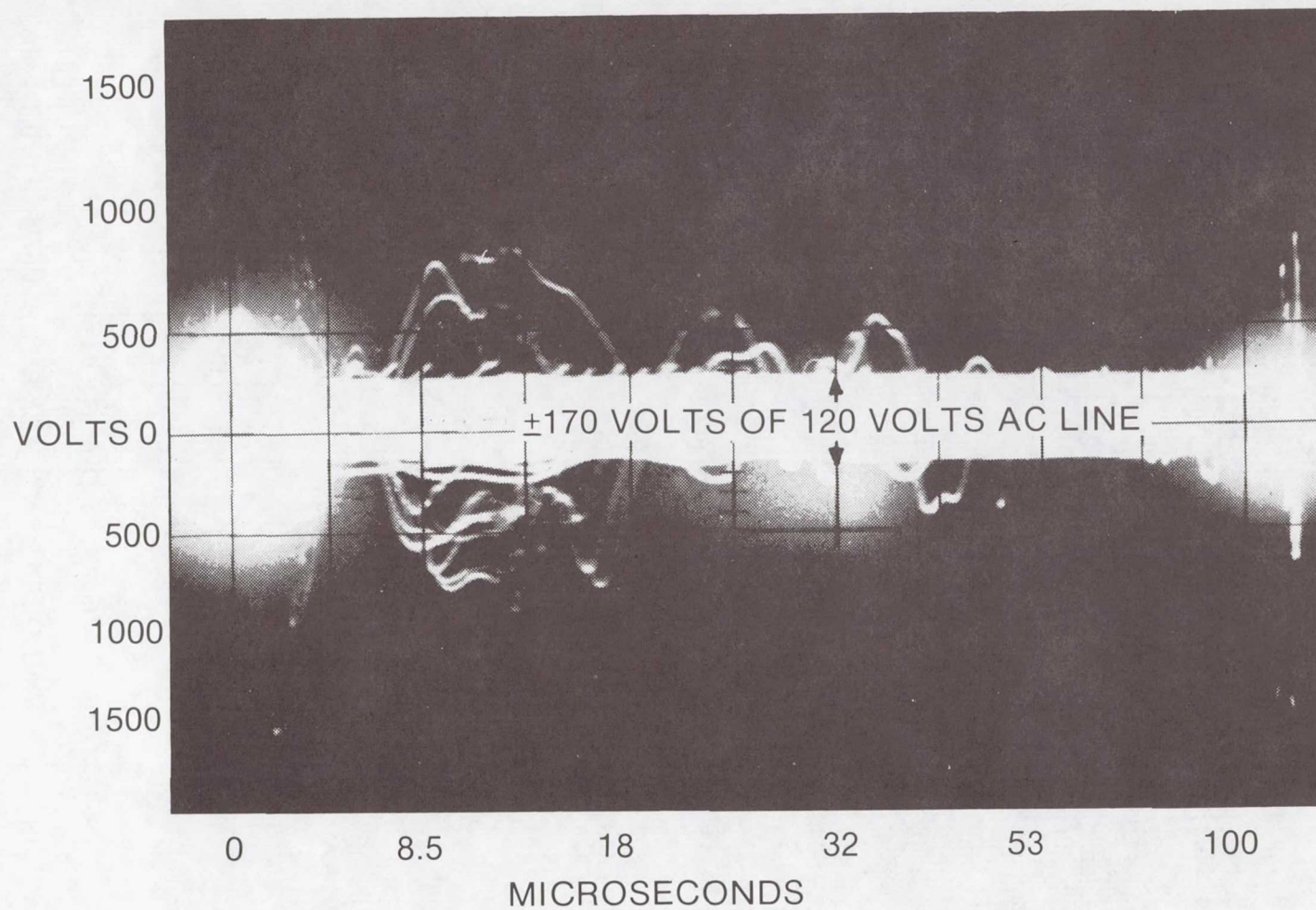


Figure 1.- Oscilloscope recording of a household power line (24 hours).

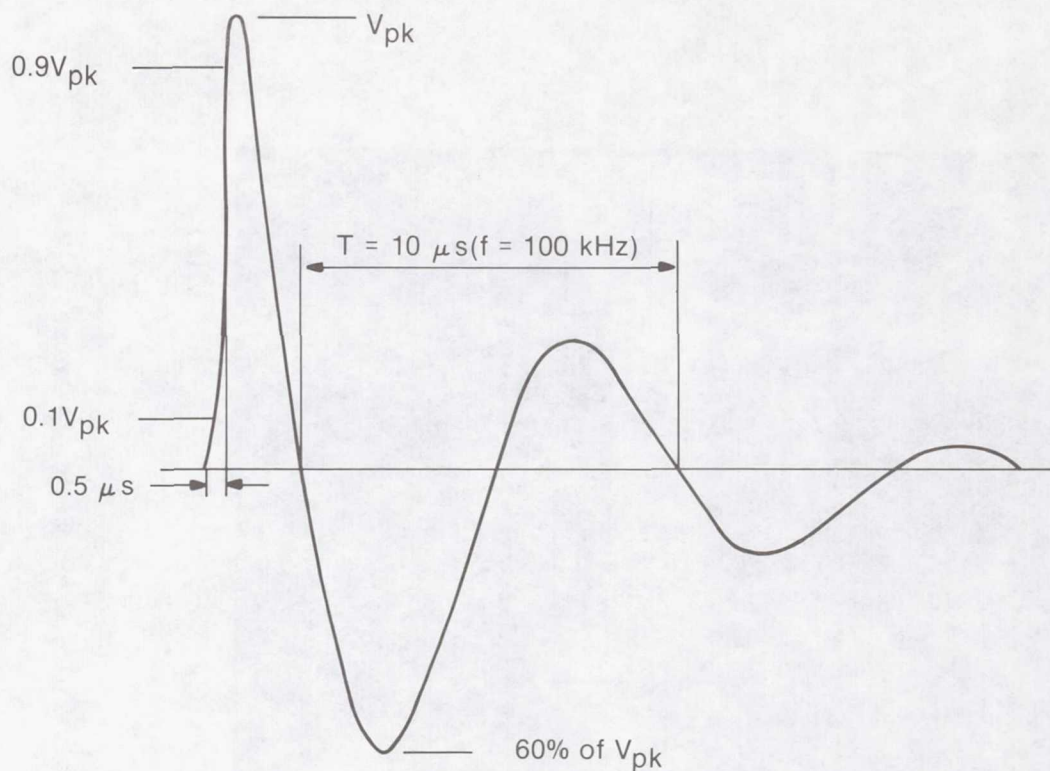


Figure 2.- 100 kHz ring wave (open-circuit voltage).

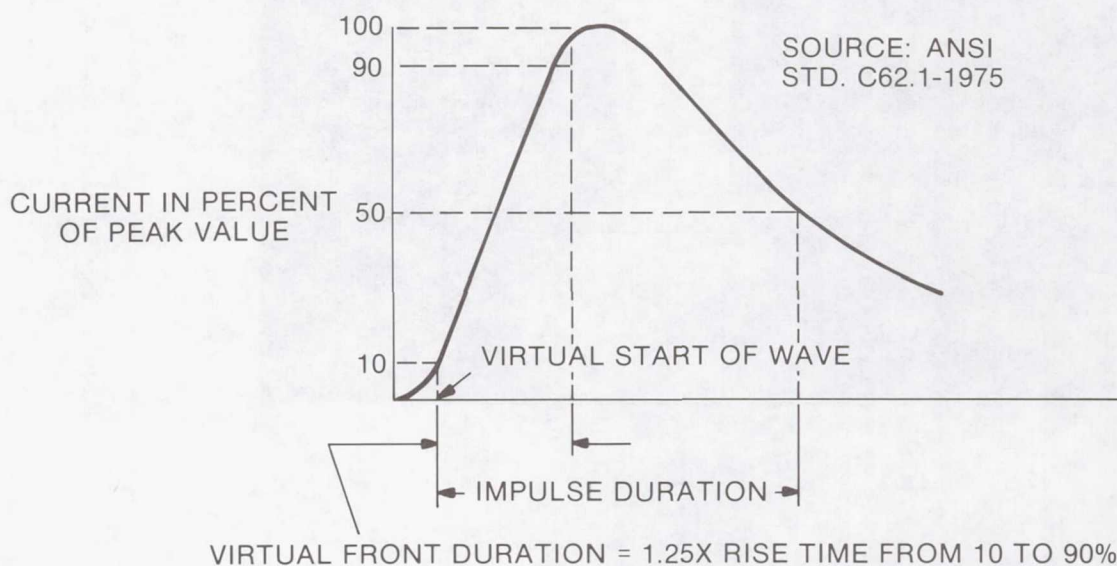
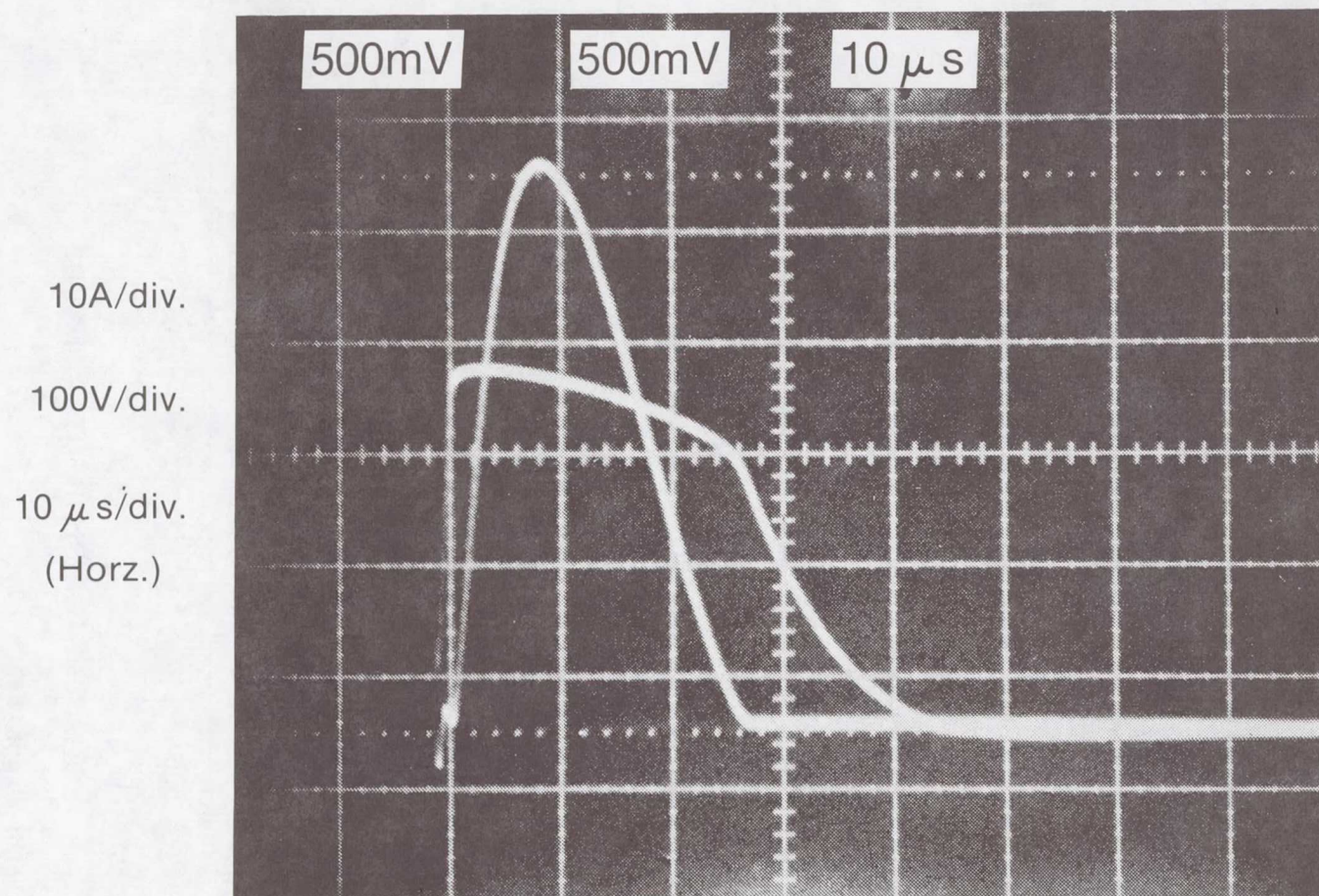
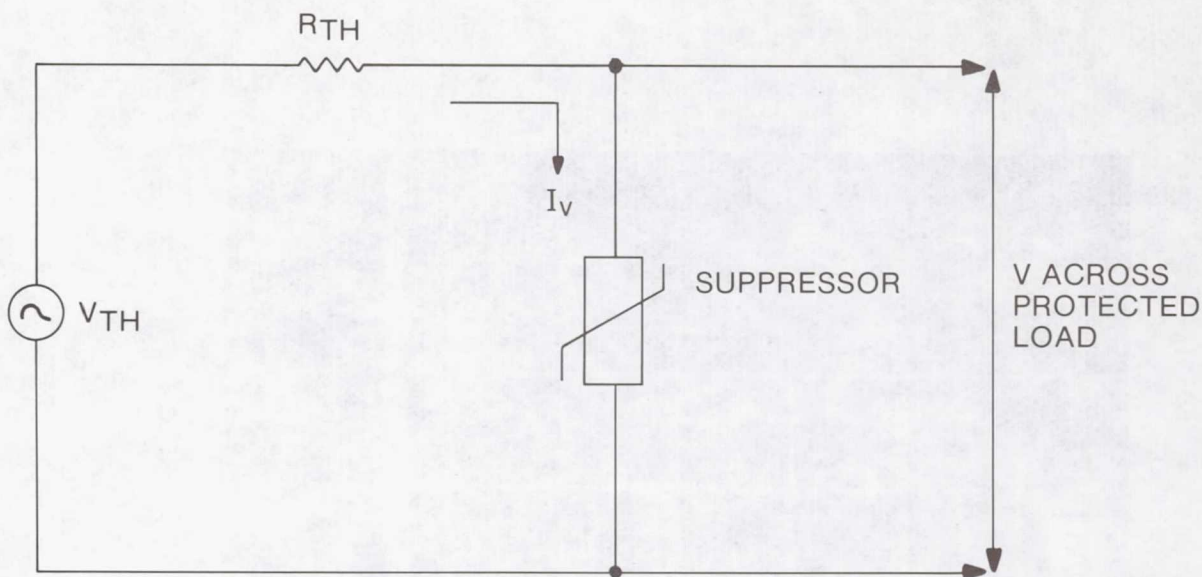


Figure 3.- Peak current test impulse wave. $8 \mu\text{s}$ front duration $\times 20 \mu\text{s}$ (impulse duration) except as noted.

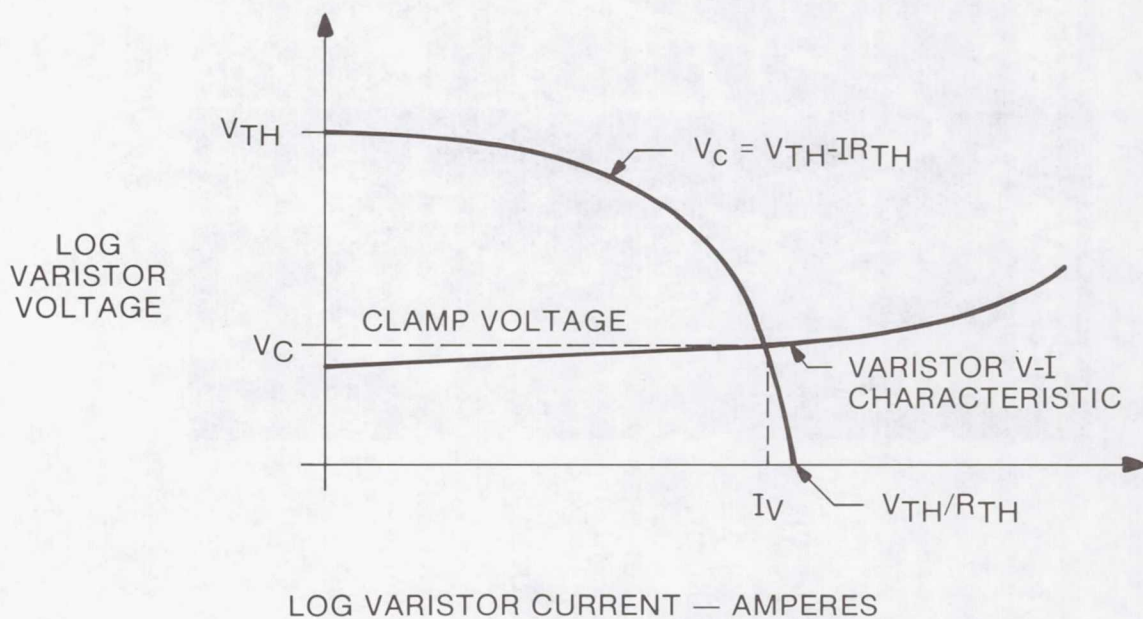


8 x 20 TEST WAVE, I_p -50A, V_C -315V

Figure 4.- Test response of typical varistor.



(a) Equivalent circuit of suppressed surge.



(b) Graphical analysis to determine peak V, I .

Figure 5.— Two steps for evaluating protection requirements.

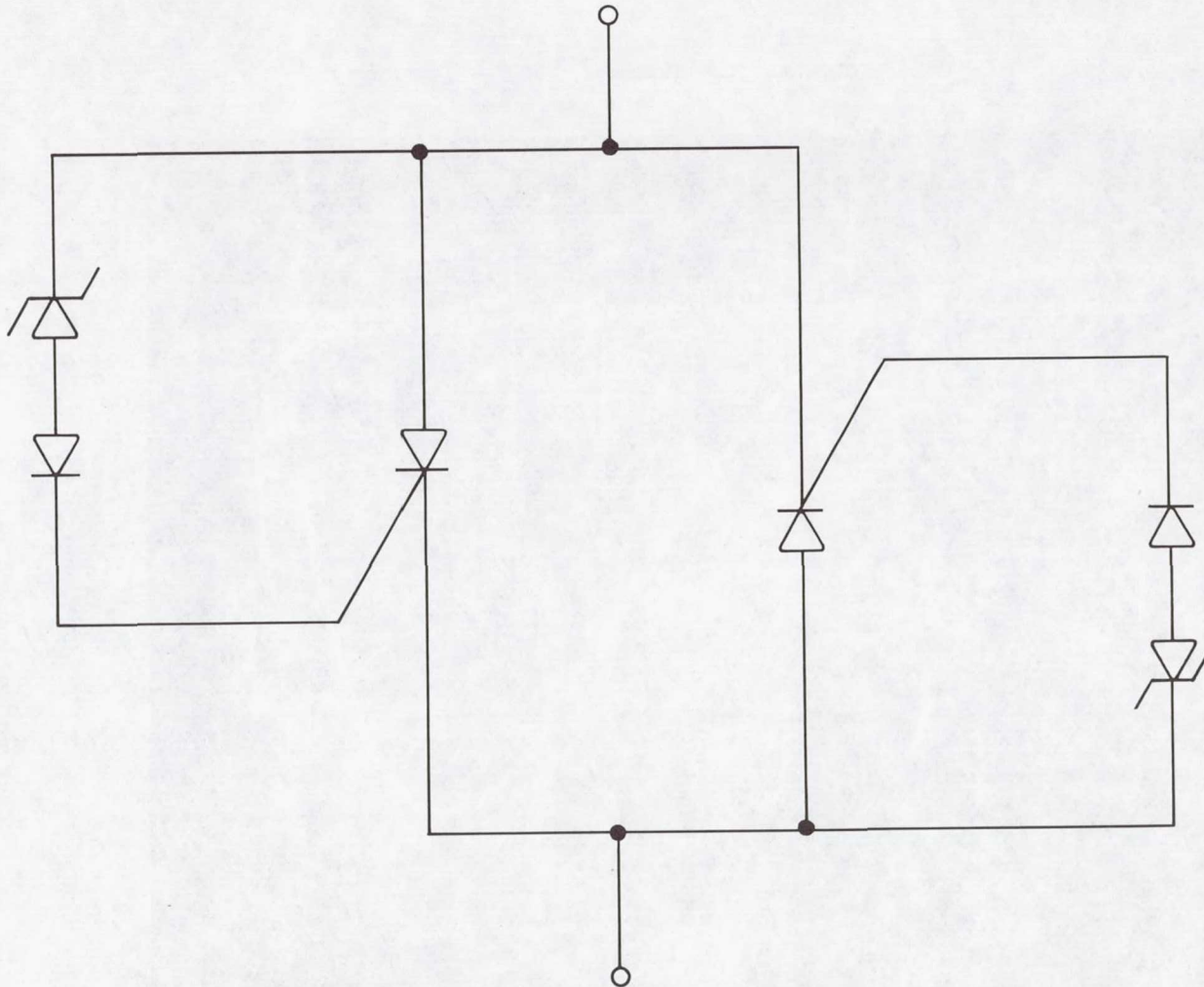


Figure 6.- Crowbar functional circuit.

100A/div.
100V/div.
10 μ s/div.
(Horz.)

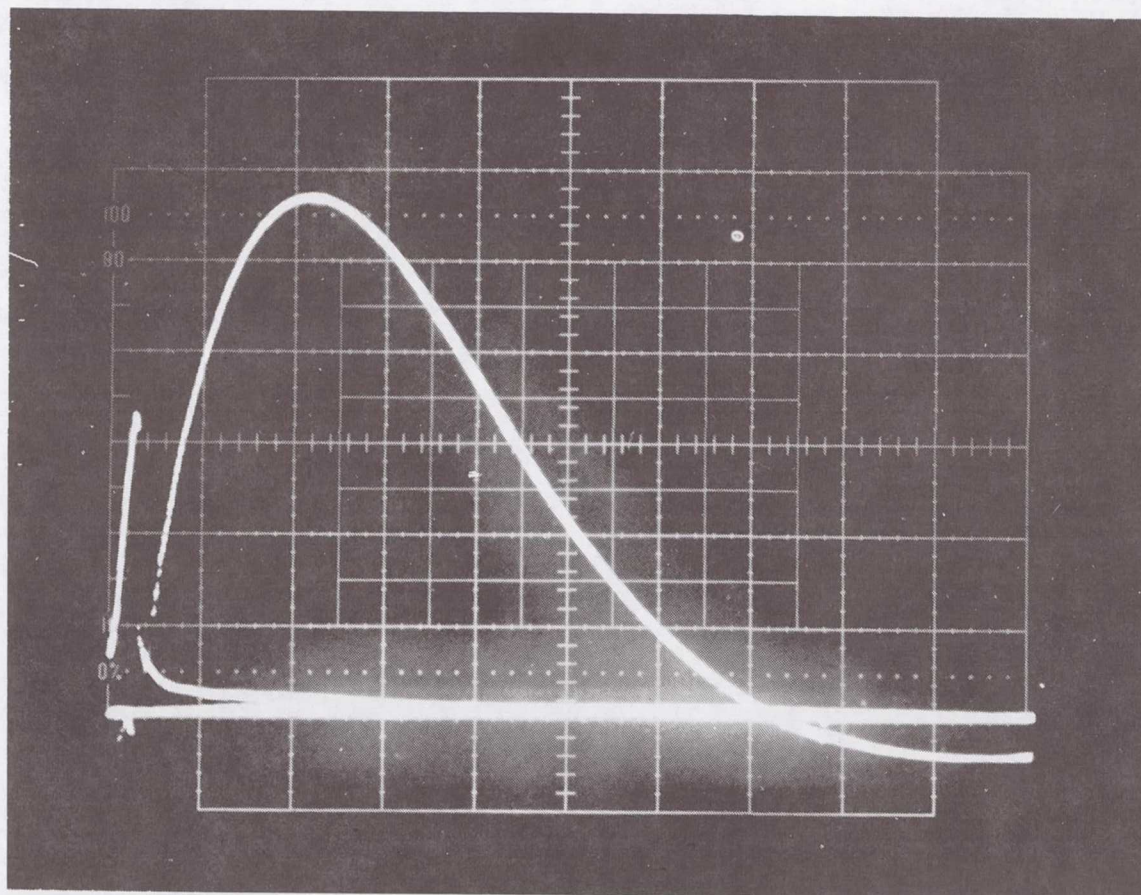


Figure 7.- Test response of crowbar.

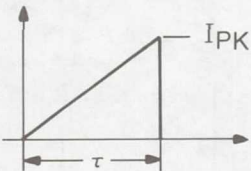
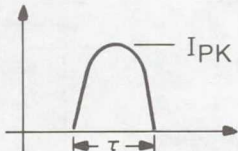
WAVE SHAPE	EQUATION	K
	$I_{PK} \left(\frac{t}{\tau} \right)$	0.5
	$I_{PK} \sin \left(\frac{\pi}{\tau} t \right)$	0.637

Figure 8.- Form factor constants of simple waves.

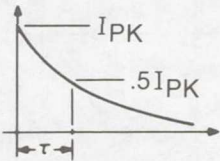
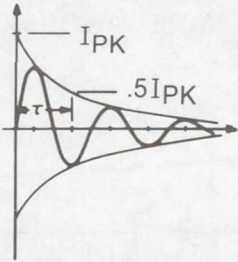
	$I_{PK} e^{-t/1.44\tau}$	1.4
	$I_{PK} \sin (\pi t) e^{-t/\tau}$	0.86

Figure 9.- Form factor constants of decaying waves.

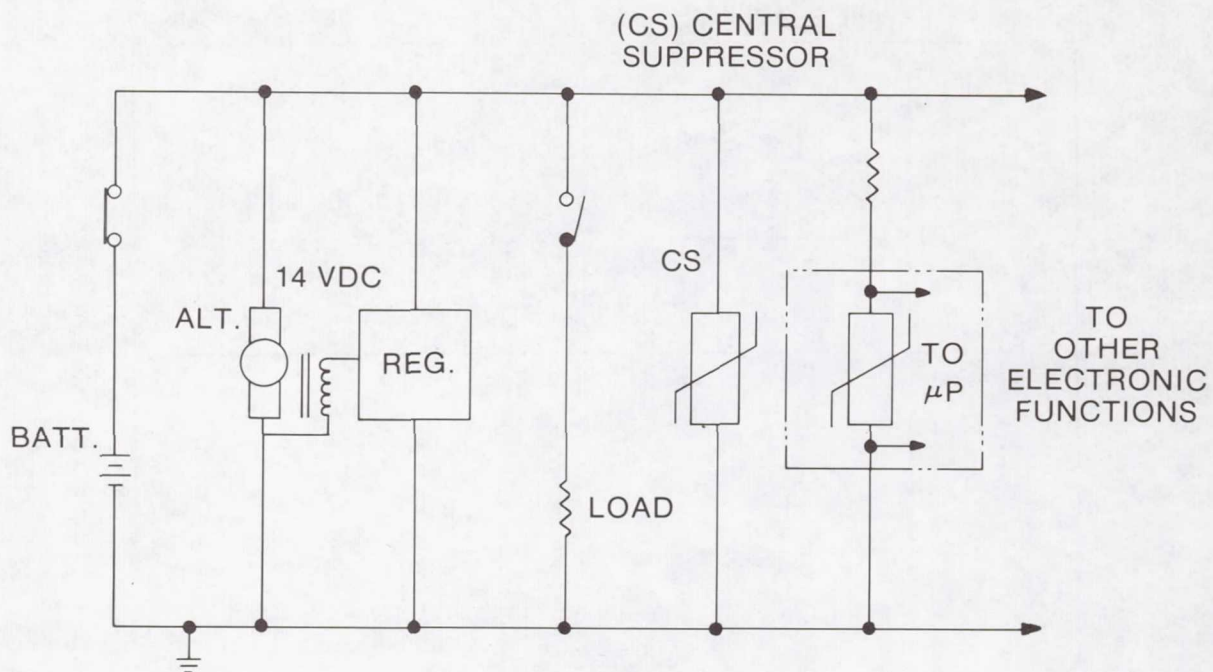


Figure 10.- Simplified electrical circuit of motorcar.

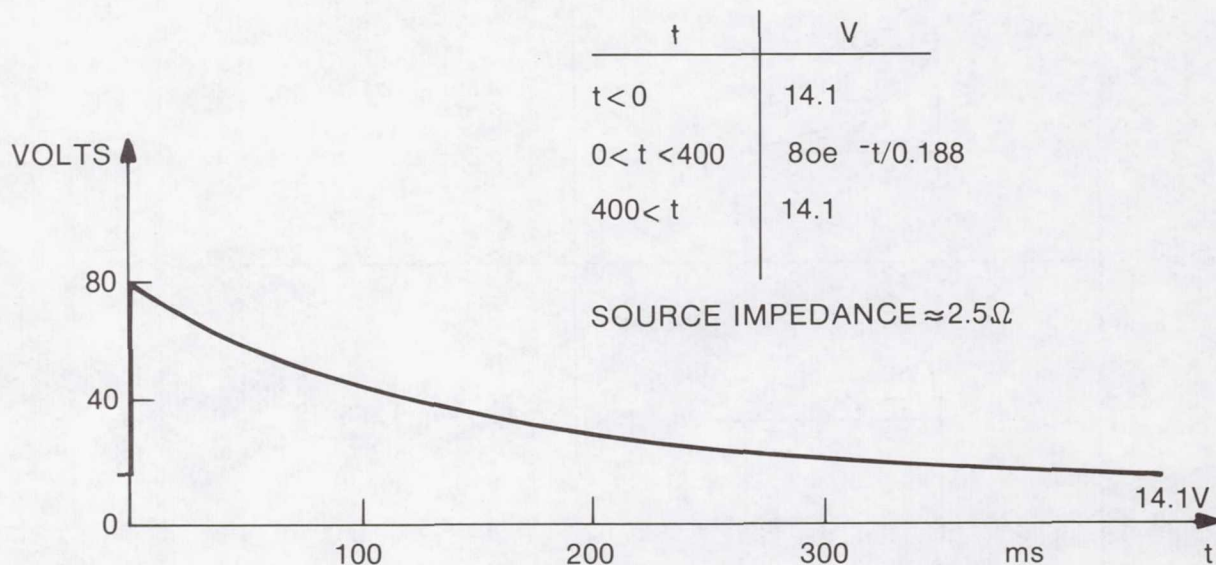


Figure 11.- Load dump transient (unsuppressed) from SAE proposed procedures.

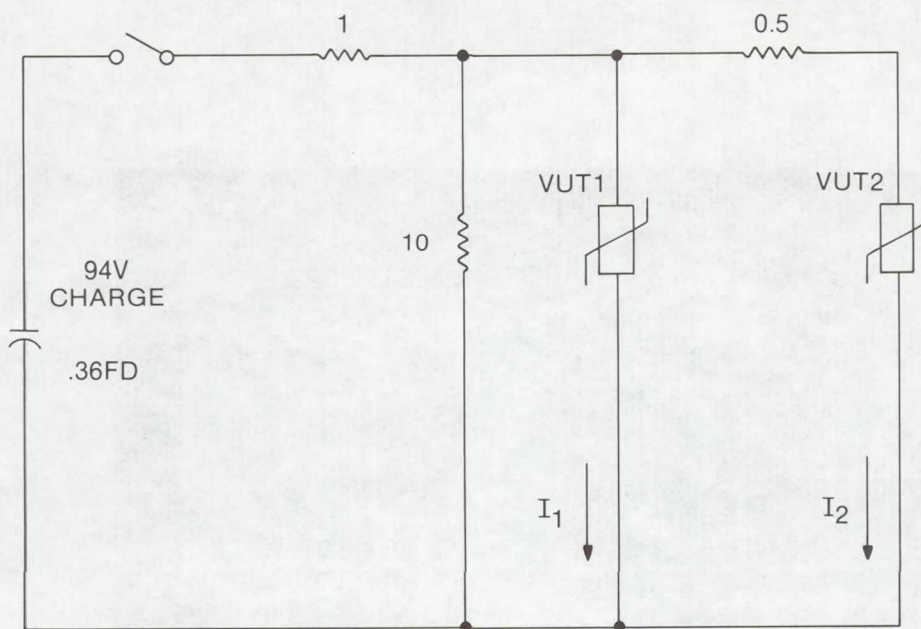


Figure 12.- 85V load dump test circuit.

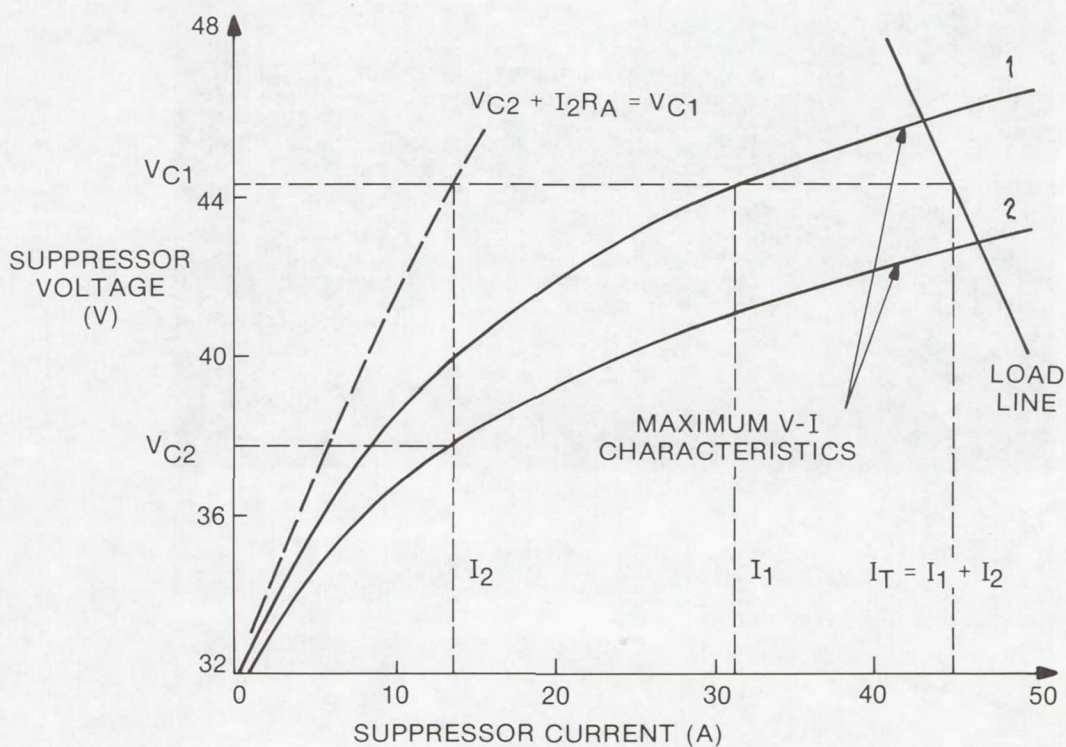
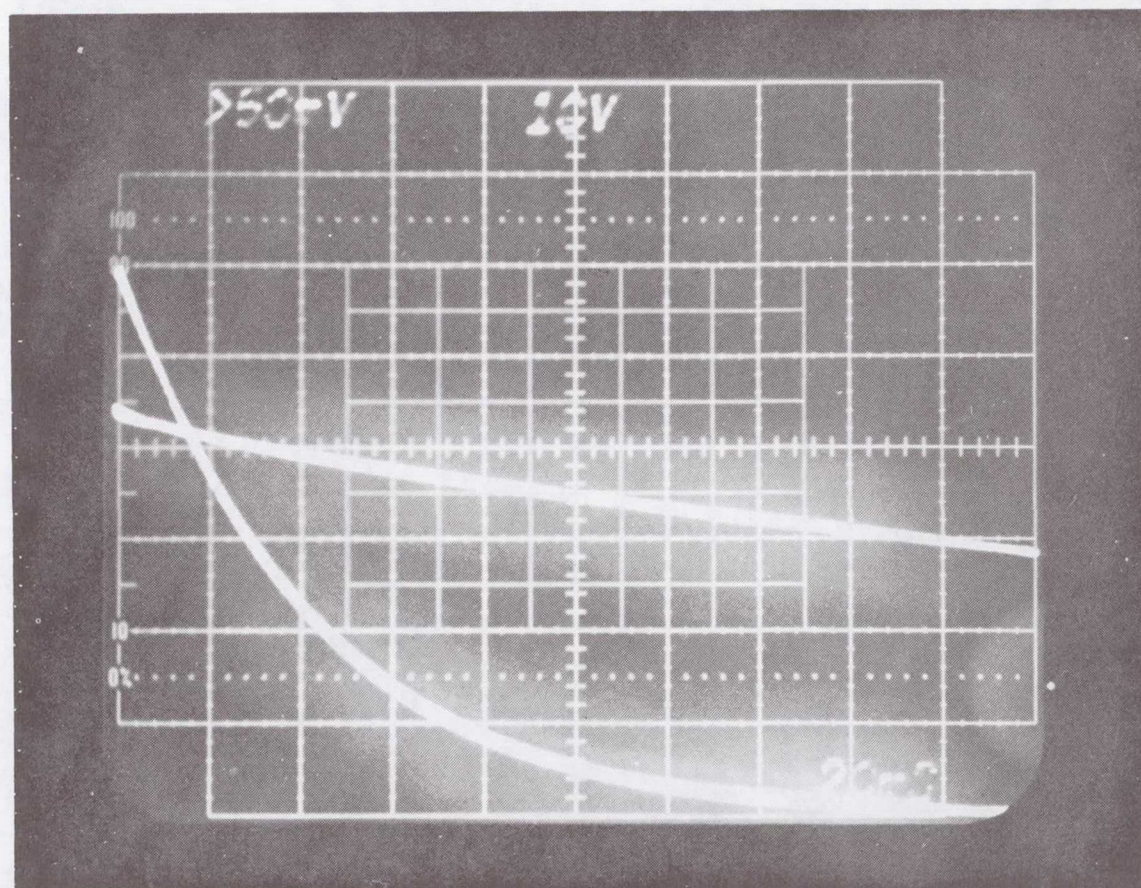


Figure 13.- Graphical analysis to find V,I.

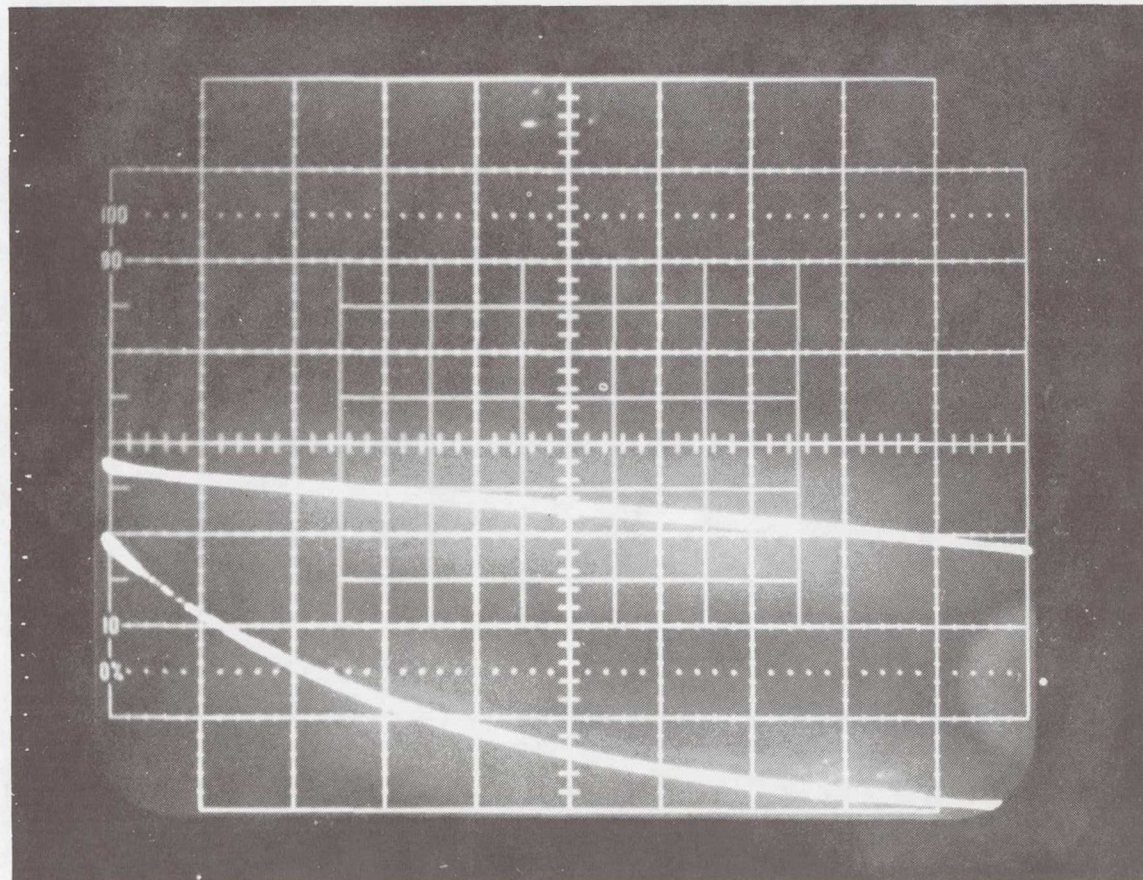
5A/div.
10V/div.
20ms/div.
(Horz.)



I_p -30A, V_C -44V

Figure 14.- Response of central suppressor.

10V/div.
5A/div.
20ms/div.
(Horz.)



I_p -15A, V_C -38V

Figure 15.- Response of secondary suppressor.

Page intentionally left blank

CONDUCTIVE SURGE TESTING OF CIRCUITS AND SYSTEMS

Peter Richman
KeyTek Instrument Corp.

SUMMARY

Techniques are given for conductive surge testing of powered electronic equipment. Dealt with first are the correct definitions of common and normal mode.

Testing requires not only spike-surge generators with a suitable range of open-circuit voltage and short-circuit current waveshapes, but also appropriate means -- termed couplers -- for connecting test surges to the equipment under test. Key among coupler design considerations is minimization of "fail positives" resulting from reduction in delivered surge energy due to the coupler.

Also included is some mention of back-filters and the lines on which they are necessary; plus ground-fault and ground potential rise considerations, as well as a method for monitoring delivered and resulting surge waves.

INTRODUCTION

Years of effort by a number of organizations have resulted in several generally-accepted, standard spike-surge test waves. Different waves have been specified for several of the most important application areas. These include waves for simulating typical ac power line spike transients (refs. 1 and 2), and for testing telecommunications lines and protectors both in the U.S. (refs. 3 and 4) and internationally (ref. 5). While specialized areas may require variations in these waves or even totally different ones (refs. 6 and 7), the mainstream -- most electronic equipment -- can generally be addressed by one or more of the new standards.

Some of the newer waves (refs. 1 and 7) are designed to test not just for susceptibility (upset or malfunction), but also for vulnerability (damage). For this reason they are relatively long impulses, implying the need for coupling and filtering effectiveness at levels well beyond what has been necessary heretofore.

SYMBOLS

C	capacitor (used for wave coupling), uF
$e(t)$	general expression for a time-variant voltage, volts
$e_{IN}(t)$	input signal, volts
$e_{OUT}(t)$	output signal, volts
E	peak of surge wave, volts
$i(t)$	general expression for a time-variant current, amperes
$I(s)$	Laplace transform of $i(t)$
L	inductance, Henries
Q	quality of a resonant circuit, non-dimensional
R	load resistance, ohms
t	time, independent variable, secs
t_a	time of first zero-axis crossing of a capacitor-coupled impulse wave, secs
t_x	time of intersection of a wave with a fixed voltage level V, secs
$t_{.5 IN}$	time for decay to 50% of peak for a network input impulse, secs
$t_{.5 OUT}$	time for decay to 50% of peak for a network input impulse, secs
s	the Laplace operator
T	exponential decay wave time-constant, secs
V	fixed clamping voltage, volts
W _o	energy, total deliverable by a surge wave to a load resistance R, joules
W	energy, total actually delivered by a circuit to a load resistance R, joules

W+ energy, total actually delivered by the positive
 portion of a wave to a load resistor R, joules

W- energy, total actually delivered by the negative
 portion of a wave to a load resistor R, joules

COMMON AND NORMAL MODES

Except in the unlikely event that ground is used as a return path, equipment inputs and outputs are usually ungrounded two-terminal-ports. Elsewhere in the system, one line of each such pair may be connected to ground. However, in view of line inductance, for spike surges it is safest to treat this distant ground connection as the high impedance it usually is.

Thus in most surge test situations, at least two essentially ungrounded lines are involved, with the one that may be connected via line impedance to a remote ground referred to as "low". In addition, there exists the local ground, connected via some other line or conduit impedance to a perhaps different but equally remote ground. The situation is shown, highly-simplified, in figure 1.

One of the major sources of upset or damage due to surge is the circuit involving equipment local ground, or common, and one or both of the input lines. Surge currents seeking earth can usually pass with least resistance and inductance via the ground; thereby causing significant ground potential rise. The effect can produce extreme potentials between local ground -- or common -- and either or both lines of the pair. This is in fact the original, and now only the alternative, definition (ref. 8) of "common-mode"; i.e., signals applied not to both sides of the input pair in common, but rather from any one or more leads to common, or ground.

The reason for stressing this correct definition of common mode, is that experience has shown that the terminal pair at which surges can be most damaging is often the one composed of input or output low, and ground. This is one of the three common modes for a typical "two-terminal-port". The remaining ones are from high to ground (or common), and finally from high and low simultaneously -- perhaps less ambiguous usage than "in common" -- to ground.

SURGE TEST WAVES: IMPULSIVE AND OSCILLATORY

Figure 2 shows an oscillatory wave and figure 3 an impulse, in each case accompanied by conventional definitions (refs. 1 and 12).

Oscillatory surge waves, with effective Q's ranging from 2 or 3 to 20 or 30, are often found in measurements in actual equipment. Some test waves are therefore specified as oscillatory (refs. 1, 2 and 6). However, impulse waves have also been measured (refs. 9 and 10) and generally can convey higher energy content per surge. In addition, in view of flashover-imposed peak voltage limitations in low voltage systems, frequencies on the order of one or just a few kHz must be postulated for oscillatory waves with enough energy to simulate, in the laboratory, damage that has actually occurred; at which point the distinction between impulsive and oscillatory becomes academic. This blurring is particularly true in light of the low Q's, typically 2 to 4, of many measured "oscillatory" waves. Their first overshoot is often no more than 30 to 40% of first peak amplitude. This can be not too dissimilar from the overshoot obtained by capacitance coupling a unidirectional impulse wave for test purposes.

Impulses have also historically been chosen to test surge protectors (refs. 4 and 11), and hence find application in vulnerability, or damage testing, when energy in the tens or even hundreds of joules must be delivered to simulate field situations in which protectors may be involved.

COUPLING THE TEST SURGE WAVES

Wave-coupling requirements are minimal for some of the standard surge waves, particularly for fractional or low-joule oscillatory surges like the IEEE/UL, 100 kHz damped cosine (refs. 1 and 2), or the IEEE power sub-station 1 MHz damped cosine (ref. 6). The low energy levels and oscillatory nature of such waves, make them most suitable for upset rather than damage evaluations. These characteristics also imply small coupling capacitors, typically in the range below one, or at most just a few microfarads, to couple the test surge; even for rather heavy loads. This still holds true, for example, for loads drawing 15 to 30 amperes from a 115 V ac power line, with implications of only a few ohms load impedance. The 1.2 x 50 impulses of the newest IEEE ac power line guide

(ref. 1), the 10 x 700 impulses now standard in international telecommunications (ref. 5), and the 10 x 1000 impulses of U.S. telecommunications (refs. 9 and 10), all require more complex and sophisticated approaches both to coupling and to filtering the surge test waves. And so, surely, will the 4 x 200 (or longer) waves implied for power lines by a recent EPRI study (ref. 7). The 4 x 200, if it eventuates, will be even more difficult to couple than the still longer telecommunications waves, since ac load impedances are likely to be lower than telecom loads -- just a few ohms for heavy equipment. The combination of low load impedance with relatively long waves implies that coupling capacitors will be huge; and ac lines are seldom as suitable as candidates for gas-tube surge coupling as are telecom lines and others.

All of the long impulse waves carry tens or hundreds of joules. It is therefore important to use these waves with couplers that don't reduce their energy appreciably.

Figure 4 shows a variety of multi-line surge couplers.

CAPACITIVE SURGE COUPLING

The simplest coupler, conceptually, is probably a capacitor. It is suitable for cases in which surged lines can operate normally with the capacitor in place, when the surge isn't present.

The circuit of figure 5 shows a series capacitor, C, coupling the exponentially-decaying impulse, $E \exp(-t/T)$, to a shunt load R. From the surge standpoint, of greatest interest for even this extremely simple circuit are the energy implications.

The input wave is:

$$e(t) = E e^{-t/T} \quad (1)$$

The Laplace circuit equation is:

$$I(s) (R + 1/Cs) = E/(s + 1/T) \quad (2)$$

from which the output may be solved for as:

$$e_{OUT}(t) = E \left(\frac{RC}{RC - T} \right) (e^{-t/T} - T e^{-t/RC}) \quad (3)$$

The axis crossing, t_a , is found by setting equation (3) equal to zero and solving for t . It is:

$$t_o = T \left(\frac{RC}{RC - T} \right) \ln (RC/T) \quad (4)$$

(In the limit, for $RC = T$, t_a is also equal to T .)

The energy the input wave would deliver to R with C shorted is:

$$W_o = \int_0^{\infty} (1/R) e^2(t) dt \quad (5)$$

which, when solved, yields:

$$W_o = E^2 T / 2R \quad (6)$$

Total energy delivered to R by the actual output wave of equation (3) is

$$W = \int_0^{\infty} (1/R) e_{OUT}^2(t) dt \quad (7)$$

which yields

$$W = (E^2 T / 2R) \left(\frac{RC}{RC + T} \right) \quad (8)$$

Finally, the fraction of W_o delivered, from equations (6) and (8), is:

$$W/W_o = RC / (RC + T) \quad (9)$$

Similar calculations for the energy W_+ delivered by the (+) portion of the e_{OUT} wave -- i.e., integrating from 0 to t_a -- and the energy W_- delivered by the (-) portion, give results included in the numeric summary that follows.

Conclusions are summarized in Table I for this circuit. Specifically, if the RC time constant is equal to the decay time constant, then W/W_o -- the ratio of total energy delivered to R , to what would be delivered if C were either infinite or a short circuit -- is $1/2$. Thus half the total available wave energy will be undelivered for this case. Further, the energy W_+ contained in the positive-going portion of the delivered wave, will be only .43 times the total available energy.

Increasing the value of the coupling capacitor improves the situation, but a dramatic increase -- by perhaps 10 to 1 -- is necessary before, as shown in Table I, even 85% of the available energy can be furnished to R during the positive-going portion

of the delivered wave. Also note the results of undersizing C. If RC is reduced only by half, to $.5T$, then just 29% of the available wave energy will be delivered on the positive peak.

Other characteristics of the energy transfer from the impulse wave through the capacitor are also shown in Table I. The axis-crossing, t_c , is given (it is equal to T if RC equals T .) The time to 50%^a of peak, usually taken as a crucial duration measurement for an impulse, is given in ratio form as $t_{.5 \text{ OUT}}/t_{.5 \text{ IN}}$. The table shows that this duration ratio tracks, very nearly, the ratio W/W_o of delivered to available wave energy. Finally, the energy in the overshoot, W_- , is related to W_o in the ratio W_-/W_o .

The implications of the figures of Table I are clear. To couple a typical 50 μs duration impulse to a power system will require on the order of a 100 to 150 μs time constant to deliver a credible portion of the available wave energy. If the system being surged consumes 15 A at 115 V, say, its impedance will be $115/15$ or about 8 ohms, ignoring inductance. Obtaining a 150 μs time constant under these circumstances will require about a 20 μF capacitor, presumably at six to eight kV, to deliver a typical 6 kV surge (ref. 1). Such capacitors imply large filter inductors and capacitors for the L-C filter that will keep the surges from reaching unsurged power lines. As a result, it may be difficult even to turn the circuit breaker on to activate such a power line, in view of the heavy capacitance loads such filters imply. Electronic or thermal time delays, or variable transformers, may be required to turn on line power.

The simple capacitor can do a fine job of surge coupling; provided it is large enough, and provided that the implications of its large value on the surge-decoupling filter are taken into account. Generally, the capacitor value C should be of such a size that RC, the (load) x (capacitance) time constant, is in no event less than T , the impulse wave decay time constant; and preferably $2T$. It should also go without saying that the capacitor must have a voltage rating equal to the largest peak expected for the test surge, plus the maximum opposite-polarity voltage that can exist on the driven line at the time of the surge. Any lower rating will risk capacitor failure in the event the driven load breaks down, and the impulse source is stiff enough to charge the capacitor to almost the full impulse peak.

GAS-TUBE SURGE COUPLING

More complex couplers use gas tubes, alone or in combination with clamping surge protectors, to surge higher-impedance lines which can't operate normally when shunted with large capacitors.

While the gas tube couplers of figure 4 have the advantage of connecting the surge source only when the surge exists, they have various disadvantages as well. Foremost among them is the fact that a gently-sloping surge front, as may be specified for a particular simulation, will be turned into a super-steep, nanosecond edge when the gas tube conducts. This severe waveform alteration is shown in figure 6.

Clamping protectors are often used in series with gas tubes as shown in figure 4, to allow disconnect after the surge even if there is voltage above the gas-tube arc potential "standing" regularly on the line being surged. The series clamping protectors, however, will have the effect of reducing energy applied to the test piece since they remove the lowest, heavy energy-bearing portion of the decaying exponential. This is true as well if the clamping protector is used alone, without the gas tube, to couple the surge. Figure 7 shows the clipping effect.

For the wave $E \exp(-t/T)$ shown in the figure, clipped off below V , the delivered energy to a load R is reduced to 68% of available for $V/E = .1$ "Available" energy, W_o , is taken to be the energy of the unclipped wave delivered to a load R , again given by equation 7, as $W_o = E^2 T / 2R$. Actual energy delivered may be found in a manner similar to that used to solve for the capacitor-coupled case, and the ratio likewise can be determined to be:

$$W/W_o = 1 - 4(V/E) + (V/E)^2 (3 + 2 \ln(E/V)) \quad (10)$$

If $V/E = .2$, less than half of the available energy is delivered -- 45% to be exact. A value for V/E of .1, is a typical situation for a 300 to 350 V varistor coupling a 5 to 6 kV wave; at full current, the varistor will require on the order of 600 to 700 V. At lower surge peaks, such as the 3 kV recommended for some surging by IEEE (ref. 1), the same varistor will constitute 20% of peak voltage, i.e. $V/E = .2$, and over half the available energy will be undelivered. It is particularly worth noting that even if the surge peak is readjusted to deliver the original desired peak voltage to the load, clipping off the lower "tail" of the exponential will still leave energy errors about equal to half the errors cited above.

ISOLATING AND SURGING THE EQUIPMENT UNDER TEST

Figure 8 shows the basics for a system to apply normal-mode surges to an Equipment Under Test (EUT). The situation depicts application of test waves to the ac lines powering the EUT, but it could as easily be to any other input or output line pair, so long as surge filters are interposed between the EUT and the lines' destination.

Common-mode surging, between any line(s) and ground, is accomplished in analogous manner, by connecting the surge generator Lo to ground, and employing a multi-line coupler if more than one line is to be surged in common mode.

As shown in figure 8, the ac line to be surged is first applied to an isolation transformer, to provide ground fault isolation. This transformer in no way assists in filtering the surge from the input, it merely makes possible use of the large filter capacitors necessary to reduce the surge at the input, while still retaining the possibility of using a ground fault circuit interrupter (GFCI) in the power line. If a GFCI is not in place or is not required, the transformer may be omitted.

(It should be noted that during the surge test, ac power to the EUT cannot be monitored by a GFCI; so suitable precautions should be taken to operate without one. Even if a GFCI is in place at the input, and an isolation transformer is used as shown, unbalance current in the transformer secondary won't be measured as such by the primary GFCI.)

The ac is then connected to a surge back-filter, consisting in its simplest form of two series chokes -- one in each line of the pair -- and a total of three capacitors between them and to ground, as shown.

The surge is applied at this point, with no connection mandatory between points A and B in the figure tying the surge generator low to the ground of the EUT, although at least a clamping protector between them is an excellent precaution. The most important point is that continuing grounds from the EUT to other equipment must be disconnected as shown, along with the local EUT ground; in effect, the EUT must become the end of the line for ground. This implies that the case or cabinet of the EUT may rise to a high surge potential during the test. Suitable precautions must be taken, as indicated later on in connection with figure 9.

The connection between points A and B may be made directly, although an ungrounded-output surge generator as such is still far preferable, so that it may be grounded at this point only, if at all. Of course for common-mode surging, the connection must be omitted between A and B, as must be the protector.

Note that all ground and low lines in the figure are shown as series impedances. This is done to emphasize the fact that if a surge travels via one of them, it will generate a large resulting ground potential rise -- possibly as great or even greater than the applied peak surge voltage.

MONITORING WITHIN SURGED EQUIPMENT

There may be excellent reasons for monitoring the results of the applied surge, deep within the EUT, to find the peak voltage reached across a particular component or circuit for example, or its specific breakdown mode. Figure 9 shows a recommended monitoring scheme, which further illuminates some of the considerations touched on in the preceding section in regard to ground and isolation of other signals to and from the EUT.

The most important point to be made in connection with figure 9 is the requirement for a barrier surrounding the EUT, to provide safety and a guarantee against flashover to any other object. This barrier may be simply sufficient separation -- including from the floor, which must be presumed to contain conduit or other metal. Alternatively, the entire barrier can be physical insulation. In either case, it should be complete, except where penetrated for insertion of input or output lines, and measurement probes; and it should be safe for a peak voltage equal to at least twice the peak of the incident test surge. (Circuits in breakdown can oscillate at high rf frequencies, and can thereby increase applied peaks by a factor approaching two.)

All other lines must be removed from the EUT; or if it is not possible to do so, then they must be surge-back-filtered like the lines actually being surged; since if flashover occurs within the EUT, it may be conducted to any port.

Monitoring is accomplished, as indicated, most readily on a differential basis. This enables use of safely grounded oscilloscope or peak detectors, with high voltage probes that have no ground leads attached. "Ground" within the EUT may not be ground at all, and the scope (or peak detectors) should not generally be connected to it.

Probes with safe peak-voltage margin for at least twice the applied surge peak should be employed. Ordinary low-voltage scope probes are unsafe, even if the resulting circuit peak voltages are thought to be just a few hundred volts; since under fault conditions an internal EUT flashover or other malfunction may apply enough voltage to destroy the probe, the monitor device input circuits, and possibly even other equipment, if it can once enter the laboratory ground system via this route.

Of course, elimination of other input and output lines, or even altering their impedance and so on with filters, may give a less than totally realistic result for surge response. However, nothing short of surging with actual lightning or the other physical phenomena being simulated can eliminate this conceptual limitation. Until generation of such natural phenomena becomes both necessary and practical, the suggested methodologies stand as a reasonable and generally successful approach.

As a final point, oscilloscope (or other monitor) common-mode and noise rejection should be carefully checked. This is best accomplished with both inputs first monitoring the total input surge, and then EUT ground; to insure that oscilloscope readings aren't unduly limited by noise.

CONCLUDING REMARKS

Spike-surge testing of powered electronic equipment has become practical, with the advent of quantitative specifications on standard waves for a variety of different situations. Led by this quantitative approach, it is now possible to couple without undue losses, to calculate, and even to measure the energy levels involved in test surges. Results include increased understandings of failure modes pertinent to specific equipments, waves and so on.

Methods for applying the surges have been developed for normal and all forms of common-mode, along with coordinated filtering to prevent them from reaching unsurged lines. Equally important has been evolution of a simple, safe approach to monitoring surge results deep within the equipment under test, for diagnostic purposes, without jeopardizing the over-all system or laboratory ground system.

REFERENCES

1. Guide on Surge Voltages in AC Power Circuits Rated up to 600V. IEEE Designation: Standard 587-1980 (in publication).
2. Standard for Ground-Fault Circuit Interrupters. Underwriters Laboratories Designation: UL 943, Dec. 1972, plus amendments.
3. Connection of Telephone Equipment to the Telephone Network. Federal Communications Commission Designation: Docket 19528 Part 68.
4. Standard Test Specifications for Gas Tube Surge-Protective Devices. IEEE Designation: IEEE Standard 465.1-1977.
5. Protection: Tests on Power-Fed Repeaters Using Solid State Devices in order to Check the Arrangements for Protection from External Influence. CCITT (International Telegraph and Telephone Consultative Committee of the International Telecommunication Union) Designation: Volume IX, Recommendation K.17, 1977, Geneva.
6. Guide for Surge Withstand Capability. Designation: IEEE Standard 472-1974.
7. Study of Lightning Current Magnitude Through Distribution Arresters. Designation: EPRI (Electric Power Research Institute) EL-1140, Project 1141 Final Report, Sept. 1979.
8. IEEE Standard Dictionary of Electrical and Electronics Terms, Wiley-Interscience, 1977, p. 114.
9. Bennison, E., Ghazi, A. J. and Ferland, P.: Lightning Surges in Open Wire, Coaxial and Paired Cables. IEEE Trans., Vol. COM-21, Oct. 1973, pp. 1136-1143.
10. Bodle, D. W. and Gresh, P. A.: Lightning Surges in Paired Telephone Cable Facilities. BSTJ, Monograph 3846, Vol. 40, March 1961, pp. 547-576.
11. Standard Techniques for Dielectric Tests. Designation: IEEE Standard 4-1978.
12. Standard for Surge Arresters (Lightning Arresters) for Alternating-Current Power Circuits. IEEE Designation: Standard 28-1972.

RC/T	t_a/T	$\frac{t(.5OUT)}{t(.5IN)}$	W/W ₀	W ₊ /W ₀	W ₋ /W ₀
.1	.3	.1	.09	.09	.01
.5	.7	.3	.33	.29	.04
1	1	.5	.5	.43	.07
2	1.4	.6	.67	.58	.08
10	2.6	.9	.91	.85	.05

Table I.
EFFECT OF CAPACITOR COUPLING
ON IMPULSE PARAMETERS

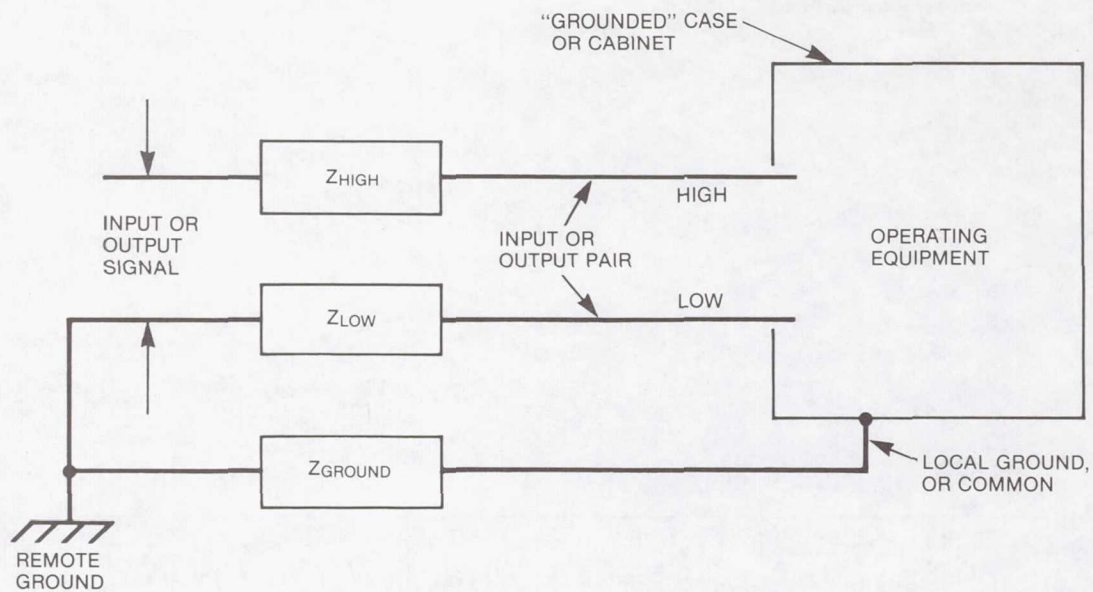


Figure 1.- Typical input or output line pair to/from operating equipment.

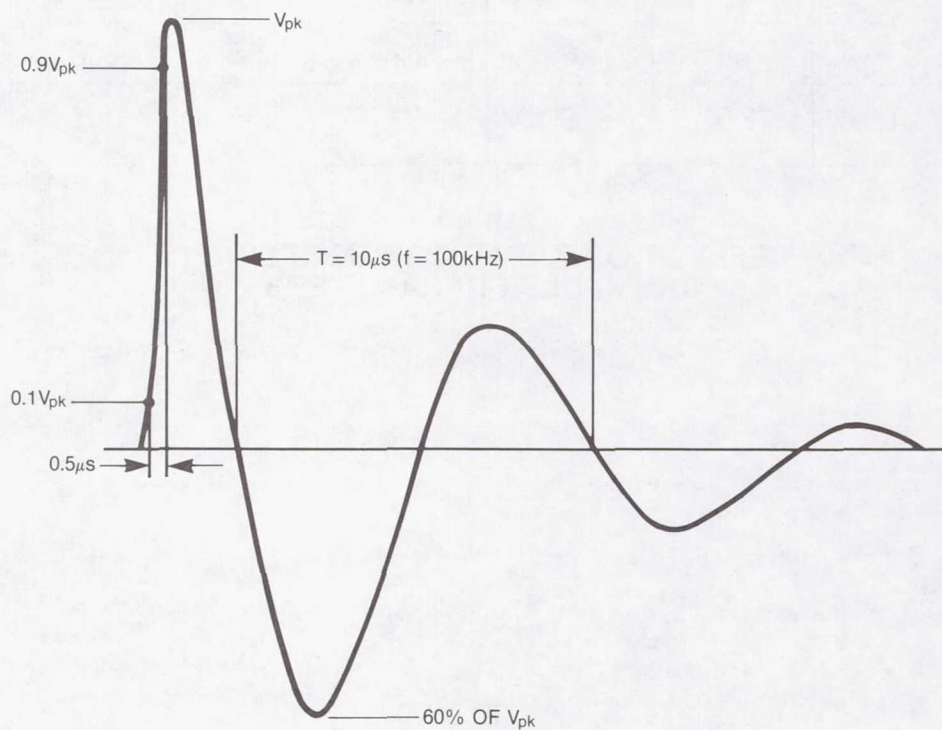


Figure 2.- Specification for standardized 100 kHz "ring" wave from reference 1.

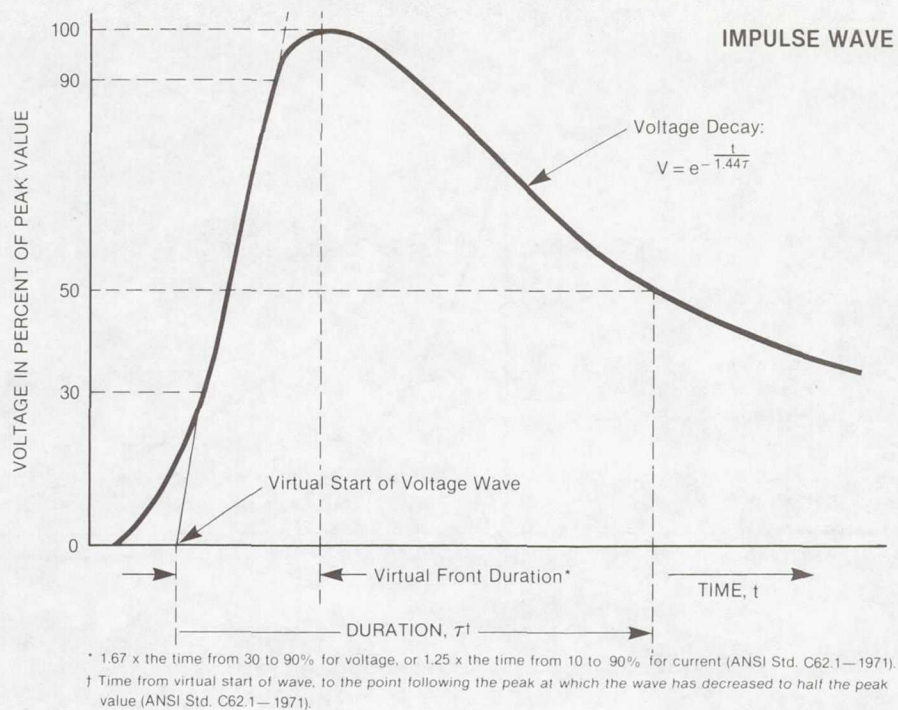


Figure 3.— Specification for standardized impulse wave from reference 12.

CONDITIONS	COUPLER	APPLICATION NOTES
1. LOW-Z LINES (POWER, ETC.)	<p>SURGE-RATED CAPACITORS</p>	$\left(\frac{V_{oc}}{I_{sc}} \right) C \geq \text{WAVE DURATION}$ (UNLESS LINE Z IS KNOWN)
2. HI-Z LINES WITH STANDING $V < 10$ TO 15 V AND NO SIGNIFICANT CURRENT CAPABILITY	<p>COMMON ELECTRODE MULTI-ELECTRODE GAS GAP</p>	APPLIED SURGE EDGES MAY BE STEEP DUE TO GAS-TUBE TURNON
3. HI-Z LINES WITH STANDING $V > 10$ TO 15 V (REPEATERS, ETC.)	<p>SILICON AVALANCHE DEVICES</p>	AVALANCHE $V >$ CIRCUIT STANDING VOLTAGE
4. SAME AS (3)	<p>VARISTORS</p>	VARISTOR CLAMP $V >$ CIRCUIT STANDING VOLTAGE

Figure 4.— Multi-line surge couplers.

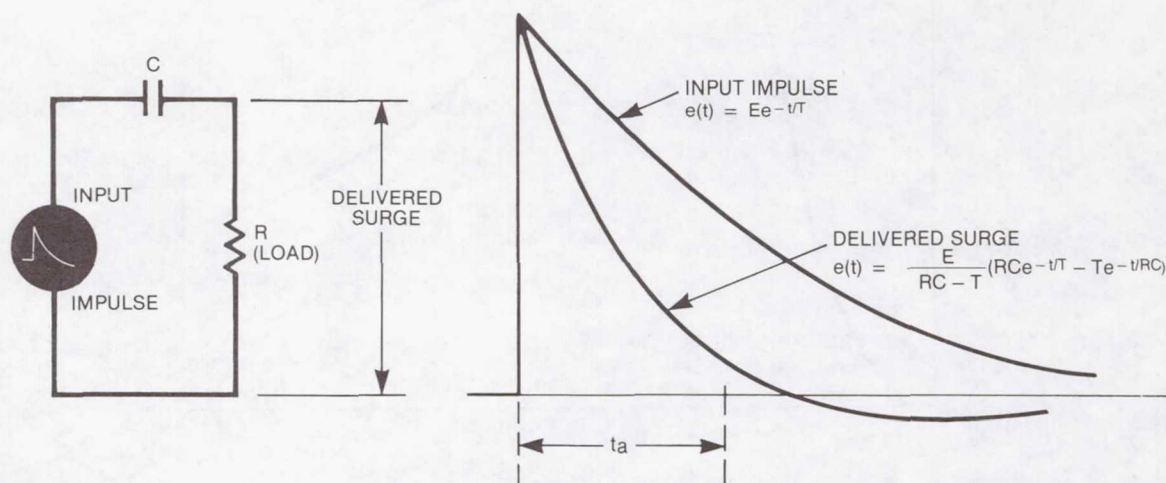


Figure 5.- Capacitor-coupled impulse.

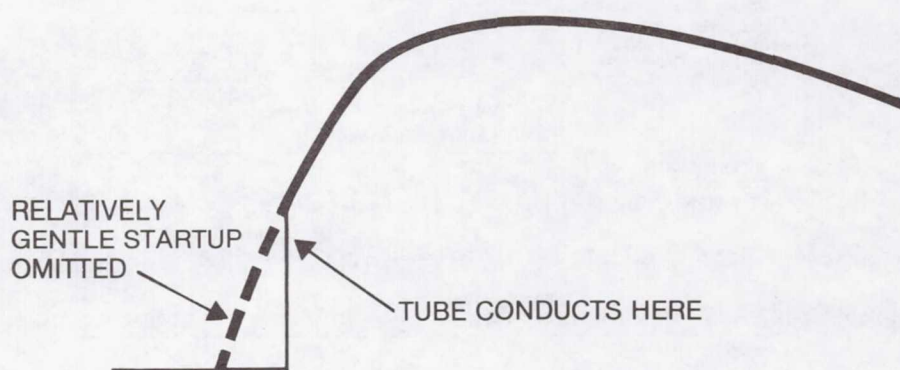


Figure 6.- Gas-tube coupler modification to leading edge of classic 10×1000 wave.

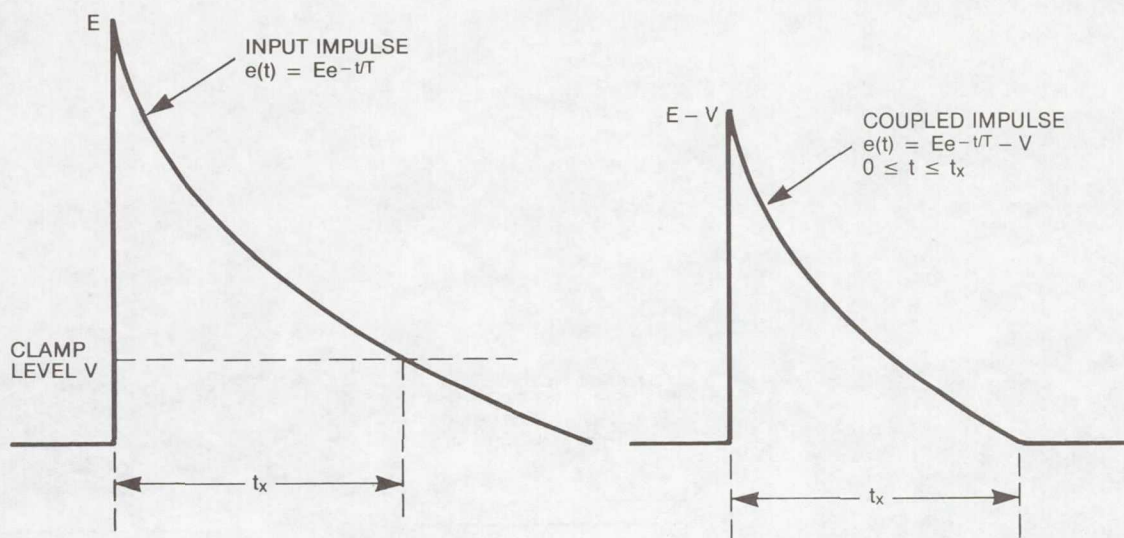


Figure 7.- Low-end "chop" due to use of varistor or silicon suppressor in surge coupler.

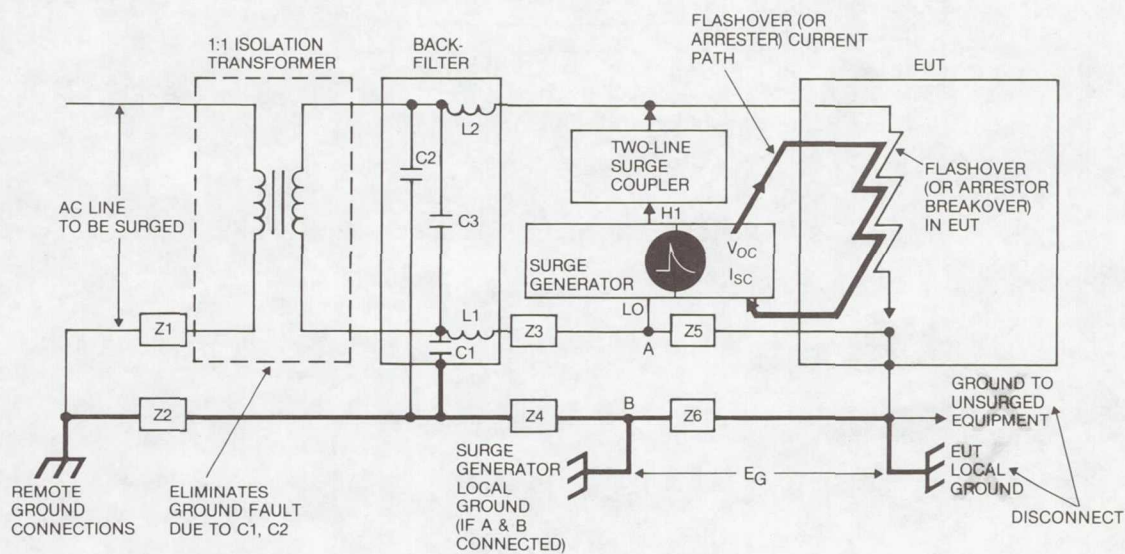


Figure 8.- Normal-mode surge testing.

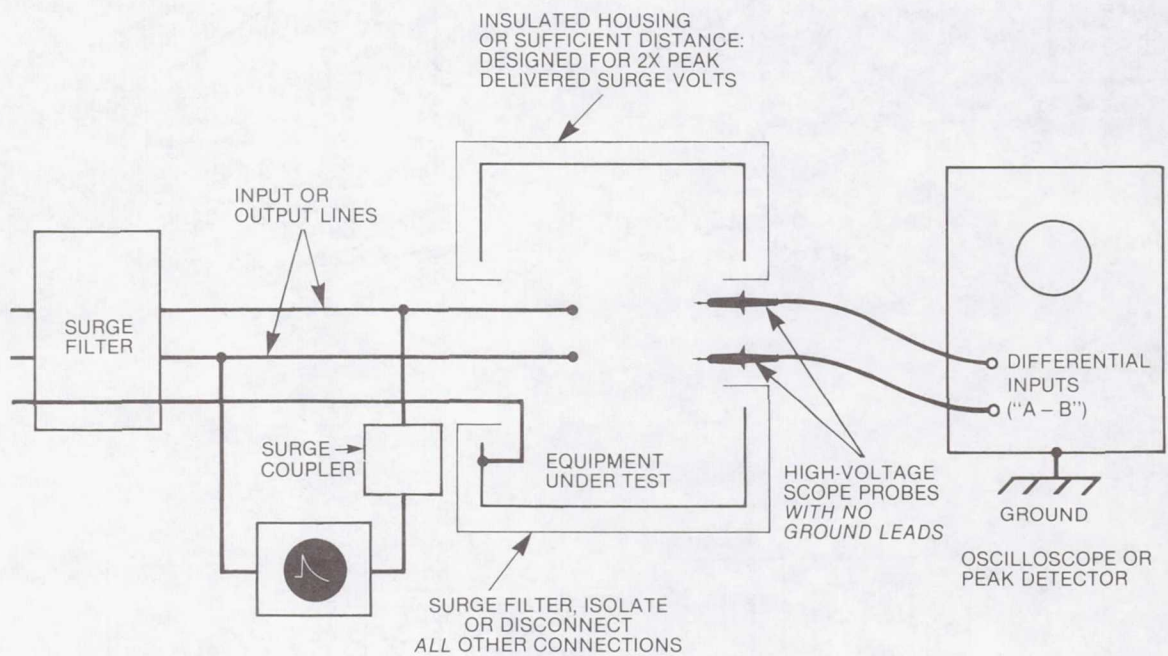


Figure 9.- Monitoring within surged equipment.

RESPONSE OF SURGE PROTECTION DEVICES TO FAST RISING PULSES*

I.N. Mindel
IIT Research Institute
Chicago, IL

SUMMARY

Two types of lightning protection modules incorporating "leadless" (pill type) Zener like devices were evaluated with regard to their ability to suppress EMP induced transients. Two series of tests were performed to evaluate the ability of these modules to react to fast rate of rise ($> 1\text{Kv/ns}$) transients, and the attenuation introduced and the ability to limit damped sinusoid pulses which may be induced due to an EMP resulting from a nuclear detonation.

INTRODUCTION

The Federal Aviation Administration (FAA) was responsible for the design and fabrication of two types of lightning protection modules incorporating "leadless" (pill type) Zener like devices, (GSI TransZorbs). These devices were designed to protect electronics/electrical equipments against lightning induced surges. Since the characteristics of lightning induced surges are markedly different than EMP induced transients, it was of interest to determine the performance of these modules to EMP induced transients.

Lightning induced transients from a nearby lightning stroke are characterized by rates of rise on the transient wavefront of the order of a few hundred to a few thousand volts per microsecond, (Figure 1). Often they are a single pulse transient. Since lightning is a point discharge phenomena, these signals are induced over a limited (local) portion of the system.

The electromagnetic pulse (EMP) resulting from a high altitude nuclear detonation is, on the other hand, essentially a plane propagating electromagnetic (EM) wave. This EMP being generated in the ionosphere illuminates extremely large areas on the earth's surface nearly simultaneously, and consequently illuminates the entire system of interest nearly simultaneously. The EM wave couples to any conducting element in the system (i.e., the cables,

*The work reported herein was sponsored by the FAA and conducted under contract No. S-79-01001 between IITRI and the Florida Institute of Technology.

antennas, and the system structure itself). The rate of rise of the free field EMP is of the order of five thousand volts per nanosecond, (Figure 1). The induced signals resulting from this EMP normally take the form of a damped sinusoid waveform where the ring frequency is determined by the system geometry (self resonances) or a single transient. The rate of rise of the wavefront of the first cycle of such a damped sinusoid is of the order of one to five thousand volts per nanosecond, (Figure 2).

The increased rate of rise for the EMP induced versus lightning induced signals is extremely important because of the difference in spectral content of the two. Due to the higher frequency content associated with the EMP induced signals, the parasitic inductances and capacitances of the terminal protection modules and solid state devices are far more important to the overall module performance.

MODULE CONSTRUCTION

As stated there were two types of terminal protection modules to be evaluated. One module was designed for use in high frequency coaxial circuits whereas the second was designed for lower frequency hard wired data systems utilizing multiconductor paired cables, for example.

The coaxial module construction is depicted in Figure 3. The coaxial module is a modified type 'N' coaxial tee. It was modified to house a "pill" type zener device. Contact to the zener device is achieved by means of a conical spring of approximately six (6) turns.

The 5-port module utilizes the same type zener device as the coaxial module. Again, contact to the diode is achieved by a conical spring of three turns as shown in Figure 4. The lower end of the spring contacts a quarter inch copper ground bus which is common to all five ports.

In the preliminary evaluation of these modules, it was the inductance of these springs which was of primary concern for the fast rise time pulse response.

TEST PROGRAM

Two series of tests were performed on the two types of terminal protection modules to be evaluated. The first series of tests utilized a pulse source with a fast rate of rise wavefront. The objective of this first series was to define the turn up voltage of the module, and secondly the device, due to the parasitic inductance associated with the module. It must be noted that the turn up voltage is rate of rise dependent.

The second series of tests utilized a damped sinusoid as a driving waveform with the basic frequency of the sinusoid being 1, 10 and 100 MHz. The objective of this series of tests was to determine the minimum clamp voltage

due to the stray inductance and secondly, the device performance (i.e., the insertion loss) due to shunting of the signal by the device capacity.

The test setup, instrumentation, and test procedure for each of these series of tests are discussed in this section.

Pulse Tests

The test setup for the pulse test series is depicted in block diagram form in Figure 5.

The pulser is an IITRI designed and fabricated unit capable of producing a square pulse of adjustable length and with a fast rate of rise on the pulse wavefront. A pulse duration of 300 nanoseconds was selected for both series of tests. The pulse amplitude and rate of rise varied somewhat for the two test series due to reflections in the system.

The series 50 ohm resistor is provided to minimize reflections, and limits the discharge current through the device in the module under test.

The module under test consisted of the basic coaxial tee module and the 5-port module. Test configurations for each module included; (1) the module empty (open circuited), (2) the module short circuited by a brass plug with the spring removed, (3) the module plus a brass dummy diode with the spring inserted, and (4) the module housing the TransZorb device(s) in its normal configuration.

The open circuit configuration provides measuring the pulse incident on the device under test. The shorted module with the spring removed provides for determining the effects of the stray inductance in module less spring inductance. With the spring inserted and the module short circuited, (a dummy brass slug of the same dimensions as a TransZorb) provides for determining the effect of the spring inductance. Finally, the module housing the TransZorb(s) provides for determining the module plus device performance under normal conditions.

The 40 dB attenuator was a thru line type provided in the circuit to limit the voltage input to the scope. It was switched in or out depending on the voltage present across the terminals of the module under test.

The termination provides for a matched system again to minimize reflections back to the module under test. The scope is a standard Tektronix laboratory scope with a 300 MHz bandwidth so as not to distort the pulse measurement.

Damped Sinusoid Tests

The principal difference between the pulse test series setup and the damped sinusoid test series setup is the driving source. This driving source is shown in block diagram form in Figure 6.

The driving source consists of an RF source tuned to the desired frequency which for this assessment was selected to be 1, 10, and 100 MHz. This RF sinusoidal signal is modulated by an exponentially decaying pulse developed by a square wave pulse generator and a pulse shaping network. The network capacitance is selected so the resulting damped sinusoidal pulse decays to 50 percent of the initial cycle in six (6) to eight (8) cycles. Modulation of the RF is performed by the double balanced mixer.

The damped sinusoid is then amplified to the desired level by a preamplifier and a final amplifier. The 100 watt final amplifier produces an output signal of approximately 140 volts peak to peak. This signal is then used to drive the module under test.

The remaining components of the test system are the same as for the pulse test series except that the 40 dB attenuator is no longer required.

TEST RESULTS

Diode Characteristics

Four diodes (TransZorbs) were made available by the FIT and the FAA for use on this program. The characteristics of these devices of interest to this program are summarized in Table 1.

The GZ 60316 B device was the only low capacitance device tested, and reported on in this paper. The low capacitance is obtained by fabricating the device as a zener junction in series with a pair of parallel low capacitance silicon junction diodes. Being the only low capacitance device it is the only one which could be expected to have a reasonable insertion loss above 1 MHz. As will be seen, it exhibits large insertion loss (shunting) due to the capacitance at 100 MHz. The characteristics of this device of interest are:

Breakdown voltage 6.66 - 8.14 volts @ 10 ma
Clamping voltage (max) 12 volts
Polarity - Unipolar
Junction capacitance 250 pf

The TransZorb is of the pill type (i.e., leadless) which removes the lead inductance problem.

Pulse Tests

The pulse test series consisted of diode tests in both the coaxial tee and 5-port modules. In addition, tests of each of the modules with a dummy diode (brass slug of the same dimensions as the diode) were performed.

Coaxial Tee Module

The driving pulse waveform for the coaxial tee module test is presented in Figure 7a. From Figure 7a, the pulse amplitude can be seen to be 1700 volts. From Figure 7a, the rate of rise of the leading edge of the pulse can be seen to be approximately 1100 volts/nanosecond. The pulse duration was 300 nanoseconds.

Figure 8a shows the performance of the module under short circuit conditions, (i.e., with a dummy diode in place). The figure shows the result when a single simulated diode is utilized with the short cap and longer (more turns) spring. In this configuration the turn up voltage is approximately 780 volts and the half amplitude pulse duration is approximately 2 nanoseconds. This turn up voltage is due to the inductance of the conical spring.

The result of the single diode (type GZ 41116 L) is shown in Figure 8b. As can be seen from this figure, the turn up voltage is approximately the same (780 volts) as for the single dummy diode - large spring case (Figure 8a). The clamping voltage is undiscernable for the GZ 60316 B diode because of the vertical scale sensitivity employed. No pulse stretching at the half amplitude points is apparent. This indicates that the inductance associated with the diodes is insignificant and the total turn up voltage is due to the inductance associated with the module and spring.

5-Port Module

The driving pulse waveform for the 5-port module tests is presented in Figure 7b. From this figure, it can be seen that the pulse amplitude reaches approximately 2300 volts with a rate of rise of the pulse wavefront of approximately 1500 volts/nanosecond.

The same series of tests were performed for the 5-port module as for the coaxial tee module. Inserting the spring with a simulated brass diode results in a voltage drop of 225 volts and a pulse duration at the half amplitude points of 1.5 nanoseconds, Figure 9a. It should be noted that the spring inductance does contribute appreciably to the voltage drop, but it is significantly less than for the coaxial tee module due to its shorter length.

Tests of the 5-port module with the TransZorb devices shows the turn up voltage is primarily due to the module spring. The results of the tests with the GZ 41116 L diode indicate a turn up voltage of 225 volts, clamp voltage of a few volts, and pulse duration at half amplitude points of approximately 1.6 nanoseconds, Figure 9b.

Coaxial Tee Module

The results of the damped sinusoid tests on the coaxial tee module incorporating a single TransZorb, type GZ 60316 B, are presented in Figure 10. These tests were performed at three frequencies of the input signal: (1) 1 MHz, (2) 10 MHz, and (3) 100 MHz. Only data at 1 MHz and 100 MHz are presented.

The driving signal level was 60 volts at 1 MHz and 100 volts at 10 and 100 MHz. These were the maximum drive available with minimum distortion from the amplifier. The decay of the signal (damping) was controlled to 6 or 8 cycles to the 50 percent level.

The test results for the GZ 60316 B diode (unipolar) show good clamping action at the 12 V level in the reverse breakdown direction at 1 MHz, Figure 10a. At 10 MHz, the zener action is apparent but the signal level was reduced (10 volts) due to signal shunting the junction capacitance. At 100 MHz, no zener action takes place due to shunting by the junction capacitance and the voltage drop in both directions is due to the spring inductance, Figure 10b. At 1 and 10 MHz, the voltage drop in the forward direction is due to the spring inductance.

5-Port Module

The 5-port module was also tested using damped sinusoid driving signals at frequencies of 1, and 10 MHz.

The voltage drop across the module with the spring is lower than in the case of the coaxial modules, Figure 9a. This is due to less total inductance as was also seen in terms of the turn up voltage during the Pulse Test Series. Voltage drops without the spring of 0.6 and 1.5 volts at 1 and 10 MHz, respectively.

Tests using the GZ 60316 B diode were very similar to those discussed previously, Figures 11a and 11b. Good clamping action with little or no capacitive shunting was observed at 10 MHz. At 10 MHz, source signal loss due to the junction capacitance shunting the signal is observed.

CONCLUSIONS AND RECOMMENDATIONS

Based on the data presented on Pulse Test Series, it can be seen that the inductance of the spring and module for both the coaxial modules and the 5-port module results in a significant voltage turn up. For fast rising (1-5 Kv/ns) pulses, this voltage may range from a few hundred volts to the kilovolts range, especially in the case of the coaxial module which has more inductance. The duration of this voltage spike is very short for the TransZorbs tested (2 nanoseconds or so). This voltage spike is that which would appear at the load terminals. This duration of voltage spike is in the short pulse regime for semiconductor junction damage. That is, the failures to be expected in most cases for pulses this short, are voltage breakdown type failures. The levels measured would not result in failures for many semiconductor devices. Devices which are very sensitive to voltage breakdown failures, such as unprotected insulated gate field effect transistors, might experience some problems, however. It should also be noted that the spike level was essentially independent of the TransZorb utilized. This was because the spike was due to the high frequency currents through the spring. The large capacity associated with these diodes tends to shunt the high frequency components (the diode appears as a short to the high frequencies), resulting in large high frequency currents. This spike may be lower for lower capacity devices.

Tests of both the coaxial and 5-port modules indicate that the GZ 60316 B TransZorb could be used in circuits operating up to about 10 MHz with a reasonable insertion loss. High capacitance devices should not be used in RF circuits above approximately 1 MHz if the insertion loss is to be controlled.

If circuits employ highly voltage sensitive devices where the spike voltages reported here may be troublesome, the inductance of all modules would have to be reduced. Some reduction in the spring inductance could be achieved by using a spring with fewer turns and less total length. Another and better approach would be the use of a low inductance flat spring. These modifications could easily be incorporated in the present modules at a minimum expense.

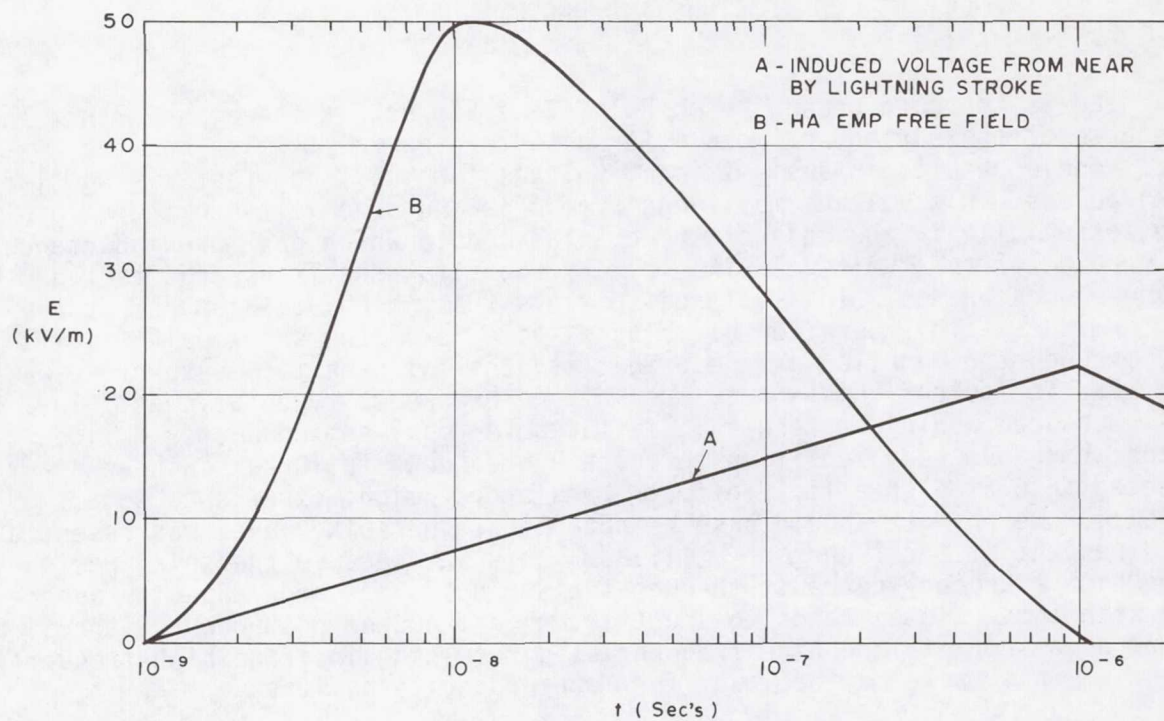


Figure 1.- Lightning and EMP waveforms.

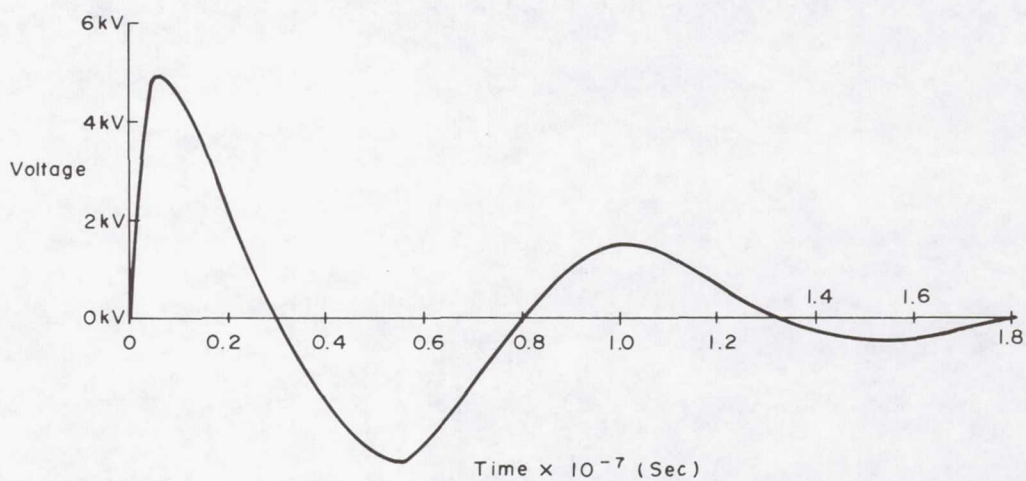


Figure 2.- Typical EMP induced signal.

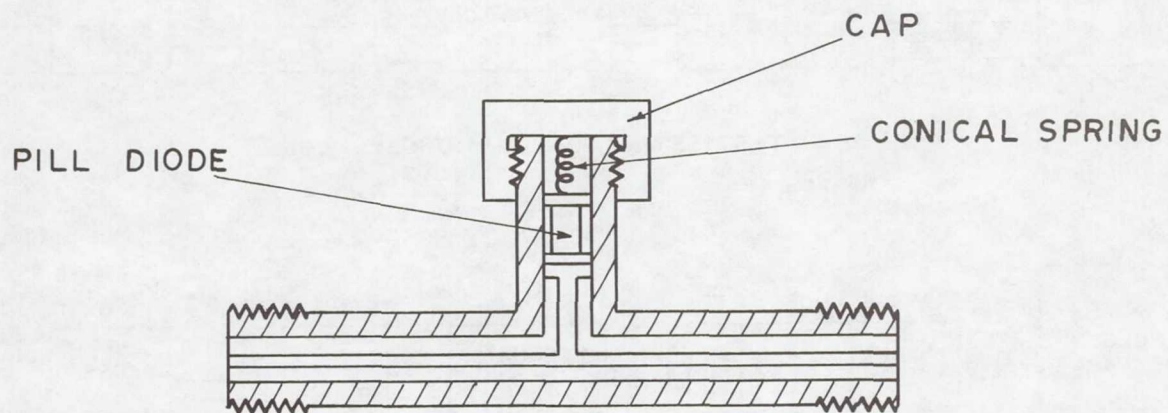


Figure 3.- Coaxial module (cutaway).

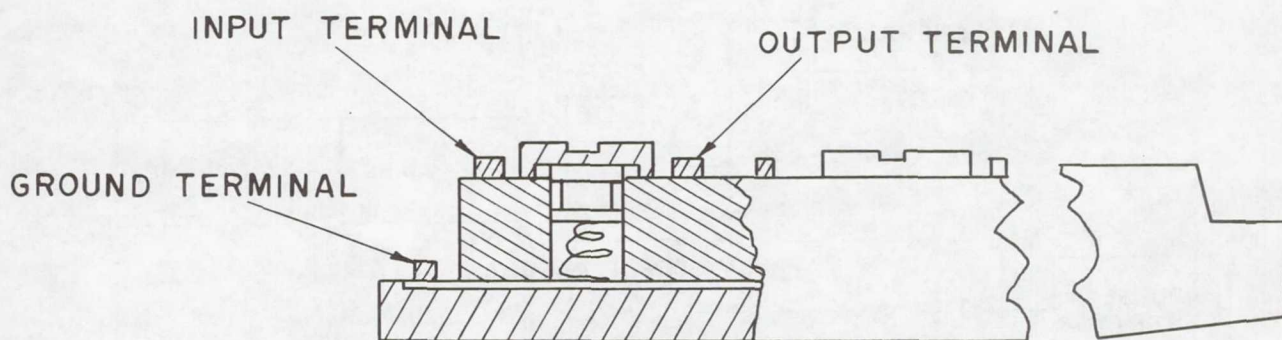
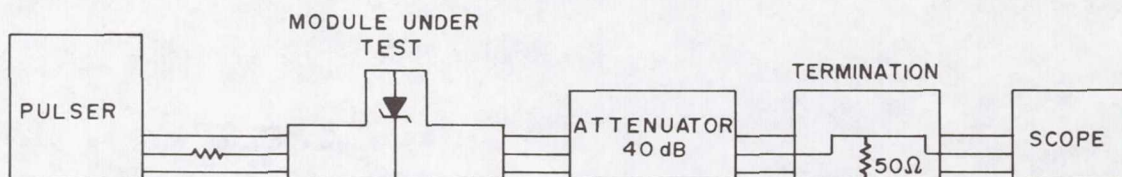
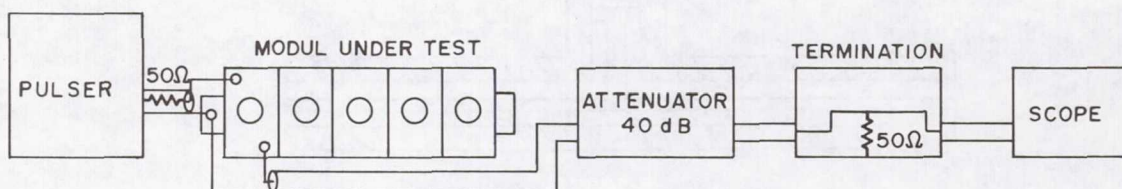


Figure 4.- 5-port module (cutaway).



5A. TEST SETUP COAXIAL MODULE



5B. TEST SETUP 5-PORT MODULE

Figure 5.- Pulse test series test setup.

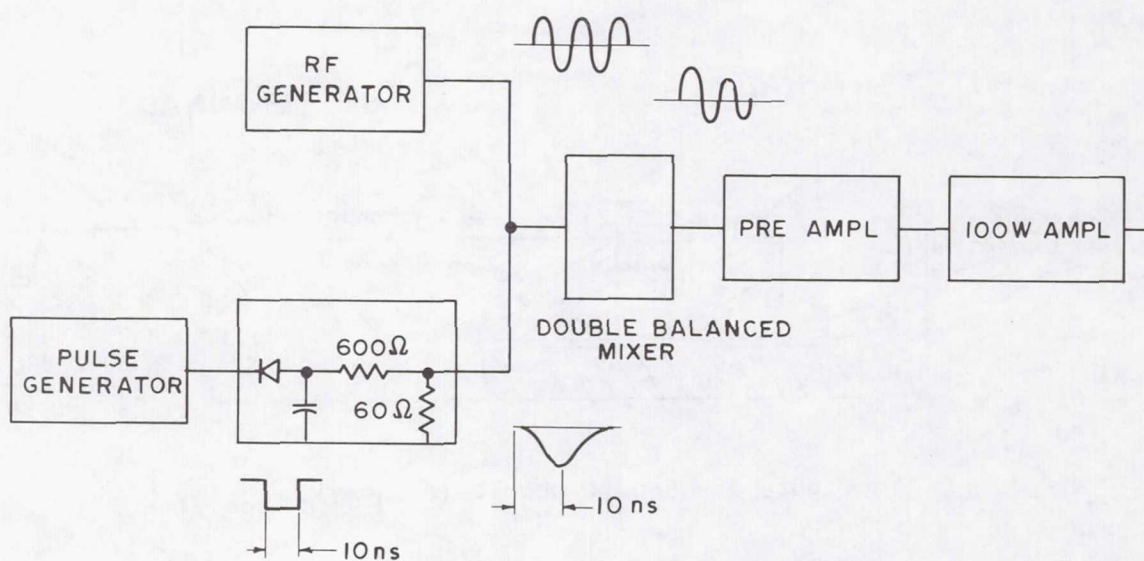
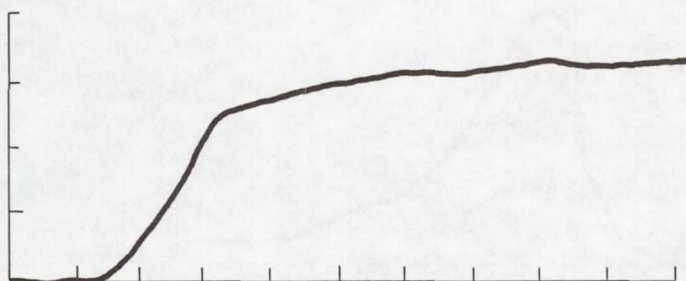
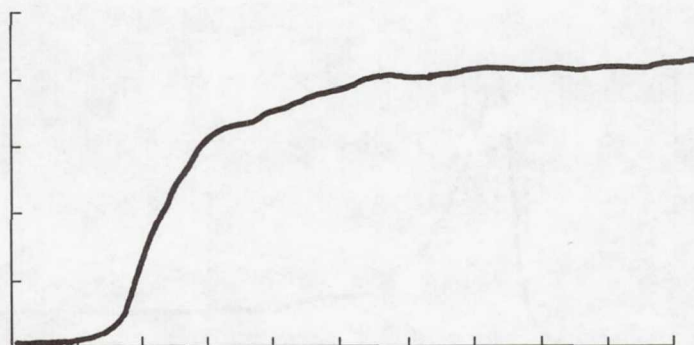


Figure 6.- Damped sinusoid source.



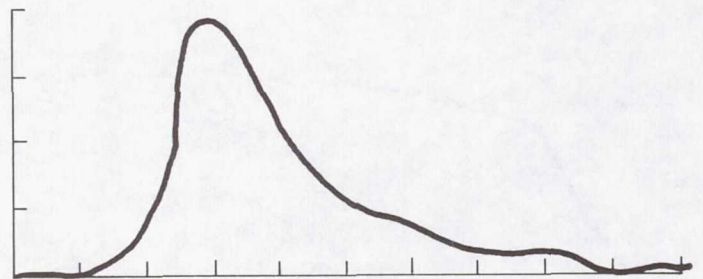
VERTICAL SCALE 500 VOLTS / DIV
HORIZONTAL SCALE 1 ns / DIV

Figure 7a.- Driving pulse - coax module.



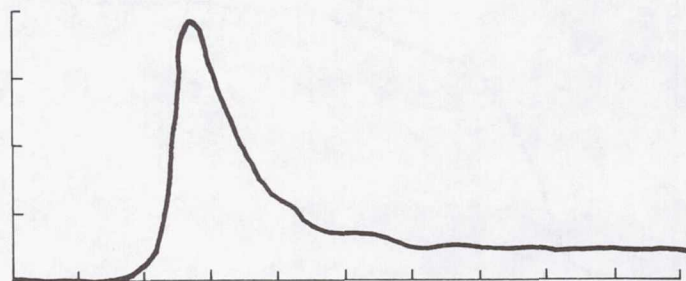
VERTICAL SCALE 500 VOLTS/DIV
HORIZONTAL SCALE 1 ns/Div.

Figure 7b.- Driving pulse 5-port module.



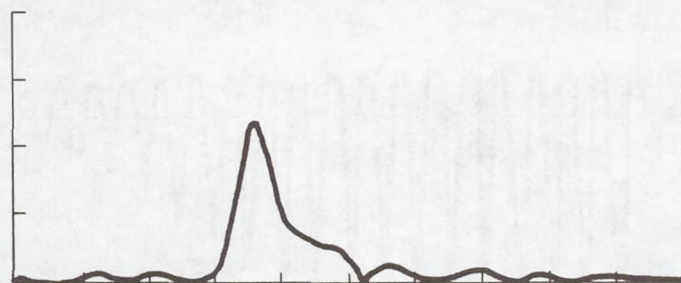
ONE DUMMY DIODE - LARGE SPRING
VERTICAL SCALE 200 VOLTS/DIV
HORIZONTAL SCALE 1 ns/DIV

Figure 8a.- Coaxial tee module - short
circuit conditions.



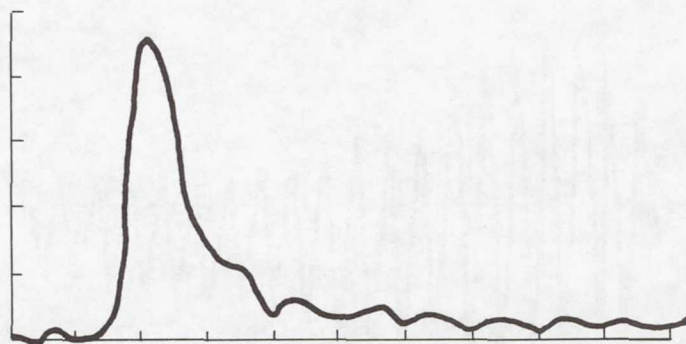
VERTICAL SCALE 200 VOLTS/DIV
HORIZONTAL SCALE 2 ns/DIV

Figure 8b.- Coaxial tee module -
GZ 41116 L TransZorb.



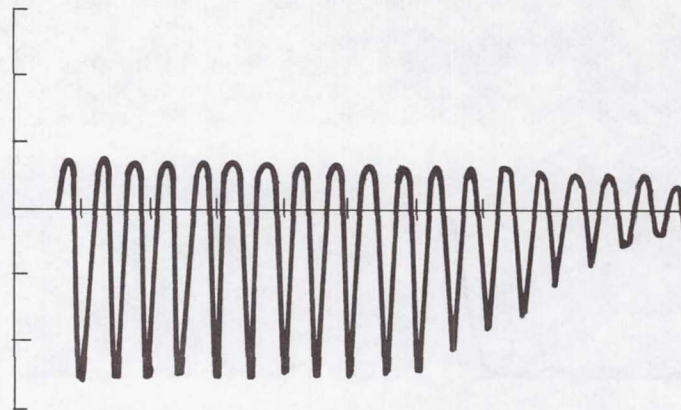
VERTICAL SCALE 100 VOLTS / DIV
HORIZONTAL SCALE 2 ns / DIV

Figure 9a.- 5-port module - brass plug with spring.



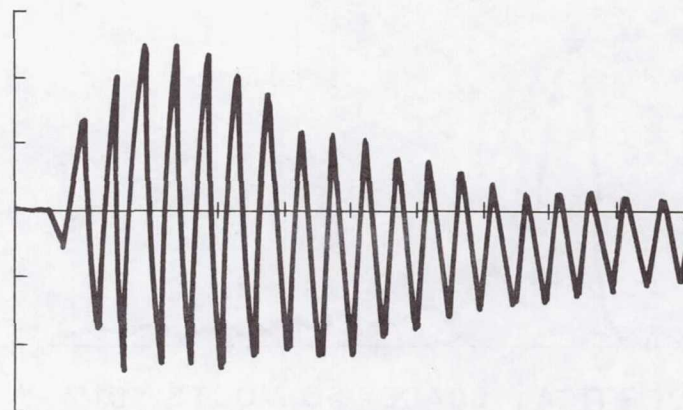
VERTICAL SCALE 50 VOLTS / DIV
HORIZONTAL SCALE 2 ns / DIV

Figure 9b.- 5-port module -
GZ 4116 L TransZorb.



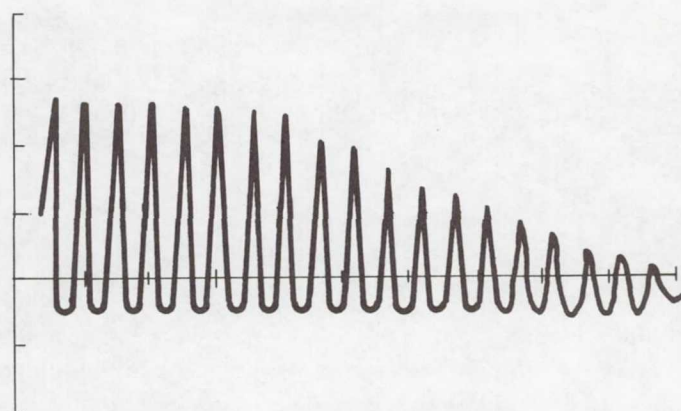
VERTICAL SCALE 5 VOLTS/DIV
HORIZONTAL SCALE $2 \mu\text{s}/\text{DIV}$

Figure 10a.- Coaxial tee module -
GZ 60316 B TransZorb - 1MHz.



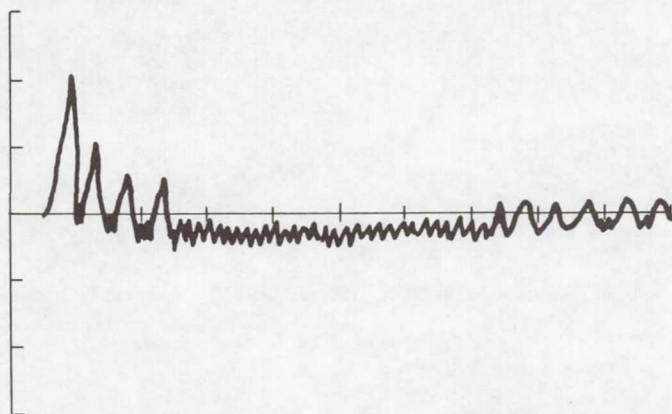
VERTICAL SCALE 10 VOLTS/DIV
HORIZONTAL SCALE $20 \text{ ns}/\text{DIV}$

Figure 10b.- Coaxial tee module -
GZ 60316 B TransZorb - 100 MHz.



VERTICAL SCALE 5 VOLTS / DIV
HORIZONTAL SCALE $2 \mu s$ / DIV

Figure 11a.- 5-port module -
GZ 60316 B TransZorb - 1 MHz.



VERTICAL SCALE 5 VOLTS / DIV
HORIZONTAL SCALE $0.2 \mu s$ / DIV

Figure 11b.- 5-port module -
GZ 60316 B TransZorb - 10 MHz.

Page intentionally left blank

SESSION VI - LIGHTNING AND STATIC INTERACTIONS WITH AIRCRAFT

Page intentionally left blank

DIRECT EFFECTS OF LIGHTNING ON AN AIRCRAFT DURING INTENTIONAL PENETRATIONS OF THUNDERSTORMS

Dennis J. Musil and John Prodan

Institute of Atmospheric Sciences
South Dakota School of Mines and Technology
Rapid City, South Dakota 57701

INTRODUCTION

An armored T-28 aircraft was struck by lightning on two different days while participating in the 1979 Severe Environmental Storm and Mesoscale Experiment (SESAME) in Oklahoma. The T-28, which is specially armored and instrumented, was making intentional penetrations of thunderstorms and was struck twice on 30 May 1979 and once on 5 June 1979. Various degrees of damage, mainly in the form of large burn spots and holes, resulted to the aircraft.

T-28 SYSTEM

The T-28 is a low-wing monoplane with a radial engine and tricycle landing gear (Fig. 1), which has been modified to make safe intentional penetrations of thunderstorms and hailstorms. The aircraft is owned by the State of South Dakota and is operated by the Institute of Atmospheric Sciences (IAS) at the South Dakota School of Mines and Technology. The modifications made to the aircraft (ref. 1) included the armoring of all leading edges, such as the cowlings, wings and tail, with aluminum thick enough to withstand hailstones up to about 7.5 cm in diameter. The original bubble canopy was replaced with a strengthened one which included a 2 cm thick acrylic plastic windshield. In addition, a larger engine and stronger propellor were installed and the rear seat area and interior compartments were stripped to make room for the instrumentation and data collection system.

The T-28 is equipped with an elaborate instrumentation system (Table 1) which emphasizes observations of the cloud microphysics, but also provides measurements of temperature, pressure, vertical air motion, turbulence, and other quantities of interest. The most notable items in the system include a hail spectrometer developed by the IAS (ref. 2), a Particle Measuring System (PMS) Forward Scattering Spectrometer Probe (FSSP), a PMS two-dimensional (2-D PMS) Optical Array Spectrometer (ref. 3), and a special particle camera (ref. 4) developed for photographing hydrometeors in flight. The main feature of the

data acquisition system is that it has the capability of sampling over virtually the entire hydrometeor spectrum, as well as making a distinction between the liquid and solid phases of water.

The main purpose of the development of the T-28 system was to obtain previously unavailable observations from the interiors of thunderstorms and hailstorms on a routine basis. To date, the T-28 has made over 400 penetrations of active thunderstorms and hailstorms while participating in various field programs in Colorado, Florida, and Oklahoma. Although the T-28 system has never been instrumented for electrical measurements, the severe nature of the lightning strike damage and the somewhat unusual circumstances surrounding the strikes, make it worthwhile for reporting to the scientific community. Furthermore, the hydrometeor measurements provide a data source never before obtained during lightning strikes.

DESCRIPTION OF LIGHTNING STRIKES AND DAMAGE

On 30 May 1979, the T-28 was struck twice by lightning while penetrating a weak to moderate thunderstorm. Four penetrations were made on this day between 0850-1100 CST. The first strike occurred at about 092322 during Penetration 1, and the second strike occurred at 100030 during Penetration 4. Nominal penetration altitude was about 6.3 km MSL, which corresponded to a temperature of about -15C.

The pilot's visual observations of the strikes were that the bolt in each case appeared to strike the hub of the propellor and moved immediately out to the propellor tips in sort of an explosive flash without noise, which resulted in a single ring of visible electricity. Then the lightning moved 10-15 cm inboard of the propellor tips forming a second ring with a lattice structure of visible electricity between the rings. Some streamers extended radially outward from the propellor tips. The physical sensation of the experience was a bump or jolt, similar to that of running over a dead animal on the highway with an automobile.

Visual damage to the aircraft consisted of numerous burn spots and holes, especially along the trailing edges of the aircraft. In some cases, the metal vaporized in shapes that appeared like teeth marks in the flaps, ailerons, rudder, and elevator sections of the wings (Figs. 2 and 3). The largest vaporizations were of the order of 1 x 3 cm. Some rivets were fused and, in some cases, holes about 3-4 mm occurred in the skin of the aircraft, such as the top of the right flap (Fig. 4) and the left side of the aircraft. Each blade of the propellor had a vaporized burn area on the trailing edge near the tip.

Later examination of the research data from this flight showed that there were no apparent adverse effects on the data from the lightning strikes. The pilot's recorded comments made during the penetrations also noted a static squeal in the radios which began approximately 25 sec prior to each

strike and lasted until near the time of each strike. Additional examples of the damage will be shown during the oral presentation of the paper.

A single lightning strike occurred on the aircraft on 5 June 1979 while penetrating a smaller echo which was part of a much larger storm complex. The strike occurred at 111308 CST during Penetration 3, which had a nominal altitude of 4.6 km MSL, which corresponds to a temperature of about -2C. A total of eight penetrations were accomplished on this day.

The strike was visually observed by the pilot as he was making a visual scan of the wing static discharge wicks during a period of static buildup in the communications equipment. The static squeal began approximately 30 sec prior to the time of the strike and ended near the occurrence of the strike. The main lightning channel appeared to terminate on the right wing tip lightning rod, although several other streamers were noted in the right wing tip area. Post-flight inspection revealed 12 cm of metal missing from the tip of the lightning rod, several (6-7) small pits ahead of the lightning rod, one large (5-7 mm diameter) welded spot 5-8 cm aft of the small pits, and burning and pitting on one propellor blade. Once again, later examination revealed no apparent adverse effects on the data being gathered.

Over 400 penetrations have been accomplished with the T-28 system in past field seasons in Colorado and Florida, as well as the penetrations in Oklahoma as a part of SESAME. The only apparent lightning damage other than that described here, has been an occasional pinhole-type burn mark. The static buildup which occurred in conjunction with each strike is a common occurrence during many penetrations, even in quite small convective clouds that have not reached the cumulonimbus stage of development.

The lightning strikes described here were unusual in the sense that each storm being penetrated did not appear to be very active by comparison with other storms that have been penetrated with the T-28, both in Oklahoma and other parts of the country. Several have had an even greater visible electrical nature and many were stronger in terms of vertical velocity and reflectivity. Since past lightning problems have been very minor, there is a suggestion that the Oklahoma clouds may be different, at least those clouds where the aircraft was struck by lightning. Since the T-28 hydrometeors over virtually the entire spectrum, it is worthwhile to examine some of the observations made near the times of the lightning strikes.

OBSERVATIONS NEAR THE TIME OF THE LIGHTNING STRIKES

Some of the pertinent observations made within ± 10 sec of the lightning strikes described in the preceding section are shown in Table 2. All of the lightning strikes occurred during morning hours when normal convective activity is usually not so strong. In fact, the storms being investigated were not particularly strong on either day.

On 30 May, during the penetrations on which the strikes occurred, the peak updrafts measured 14 and 16 m s^{-1} , while the downdrafts were -9 and -14 m s^{-1} . The first lightning strike on 30 May occurred near the center of the cloud, while the minimum downdraft occurred near the end of the penetration. The peak updraft was just outside the 10 sec limit imposed in Table 2. The second strike occurred when the aircraft was on a north-northeast heading through the cloud and was approximately 30% through the penetration. The extreme vertical velocities on this penetration occurred about 6 min after the strike within a few km of the end of the penetration.

The storm on 5 June was much weaker than the storm on 30 May. The T-28 was approximately 65% through the penetration on which the lightning strike occurred. The downdraft reported in Table 2 was the minimum for the penetration, while the maximum updraft, which was only 6 m s^{-1} , occurred about 1 min prior to the strike.

A cursory check of the radar data for each day showed that the storm on 5 June had tops at about 8.2 km MSL, while the storm on 30 May had tops that were in excess of 11 km MSL. Reflectivity structure in each storm was relatively weak as convective activity goes. The maximum reflectivity in either case was only about 45 dBz, with the highest values found near the ground.

Spot checks from the foil impactor data showed the hydrometeors to be of the order of 1-2 min with concentrations of several hundred l^{-1} . The imprints had a splattered appearance and looked somewhat fragile, indicating low density hydrometeors. The clouds on both days were noted for their lack of liquid substance, at least at the altitudes where the T-28 was penetrating. The predominant habit was rimed particles as indicated by the 2-D PMS probe.

The data presented here are only preliminary at this time. An analysis of the data is currently underway and results will be given in more detail during the presentation of the paper.

SUMMARY

This paper has presented some effects of lightning on an aircraft during intentional penetration of thunderstorms in Oklahoma during SESAME 1979. The damage which has been described was quite severe, especially considering the relatively weak nature of the storms that were penetrated. There were no adverse effects noted in the data being gathered by the T-28 at the time of the lightning strikes.

The hydrometeor concentrations near the times of the lightning strikes were not unusual; in fact, they were quite similar to those found in other parts of the country. The variety of ice crystal habits was greater in the Oklahoma storms, but any relationship between the hydrometeors and the lightning strikes is unknown at this time. Effects are not apparent in the data analyzed so far. The analysis work is continuing.

REFERENCES

1. Sand, W. R.; and Schleusener, R. A.: Development of an armored T-28 aircraft for probing hailstorms. *Bull. Amer. Meteor. Soc.*, 55, 1974, pp. 1115-1123.
2. Spahn, J. F.; and Smith, P. L., Jr.: Some characteristics of hailstone size distributions inside hailstones. *Preprints 17th Conf. Radar Meteor.*, Seattle, Amer. Meteor. Soc., 1976, pp. 187-191.
3. Knollenberg, R. G.: Three new instruments for cloud physics measurements: the 2-D spectrometer, the forward scattering spectrometer probe, and the active scattering aerosol spectrometer. *Preprints Intn'l. Conf. Cloud Physics*, Boulder, Colorado, Amer. Meteor. Soc., 1976, pp. 554-561.
4. Cannon, T. W.: A particle camera for powered aircraft. *Preprints Intn'l. Conf. Cloud Physics*, Boulder, Colorado, Amer. Meteor. Soc., 1976, pp. 572-575.

TABLE 1		
T-28 Instrumentation Complement		
Variable	Instrument	Range of Measurement
<u>State:</u>		
Static Pressure (Altitude)	Rosemount 1301-A-4-B Ball Engineering EX-210-B	0 to 15 PSI 0 to 27,000 ft (8.2 km) MSL
Total Temperature	Rosemount 102AU2AP, platinum wire NCAR Reverse Flow, diode	-25 to +25°C -25 to +25°C
<u>Hydrometeors:</u>		
Cloud droplets	Johnson-Williams LWC Particle Measuring Systems FSSP	<50 μm dia (liquid only); 0 to 6 g m^{-3} 3 to 45 μm dia; adjustable
Rain, graupel, snow	Williamson Foil Impactor Particle Measuring Systems OAP-2D Cannon Particle Camera (alternates with hail spectrometer)	1 to 20 mm dia 31 to 1000 μm Approx. 50 μm up
Hail	IAS Laser Hail Spectrometer (alternates with Cannon camera)	4.5 to 50+ mm dia
<u>Aircraft Navigation & Performance:</u>		
Attitude	Servomechanisms TR541 angle-of-attack vane Pitch (Humphrey vertically-stabilized accelerometer) Roll (Humphrey vertically-stabilized accelerometer)	-15 to +15° -50 to +50° -50 to +50°
Navigation	IAS Heading indicator NARCO UDI-2ARD DME CESSNA 400 DME NARCO MK12 VOR (2 units) NARCO NAV-122 VOR	0 to 360° magnetic 0 to 100 n mi 0 to 100 n mi 0 to 360° from 0 to 360° from
Performance	Ball Engineering 101A variometer (rate-of-climb) Rosemount 1301-D-1-B dynamic pressure (ind. airspeed) NCAR True Airspeed Computer Humphrey SA09-D0101-1 vertically- stabilized accelerometer Giannini 45218YE manifold pressure	-6000 to +6000 ft min^{-1} (-30 to +30 m s^{-1}) -3 to +3 PSI 0 to 250 knots (128 m s^{-1}) -1 to +3 g's 0 to 50+ in Hg

TABLE 2						
Observations Made Near the Time of the Lightning Strikes						
Date	Time [CST]	Altitude [m MSL]	Temp [°C]	Max Updraft [m s ⁻¹]	Min Downdraft [m s ⁻¹]	LWC [gm ⁻³]
30 May	092322	6211	-14.4	12	-6	<0.1
30 May	100030	6334	-15.4	8	0	<0.1
5 June	111308	4660	-2.2	4	-5	<0.1

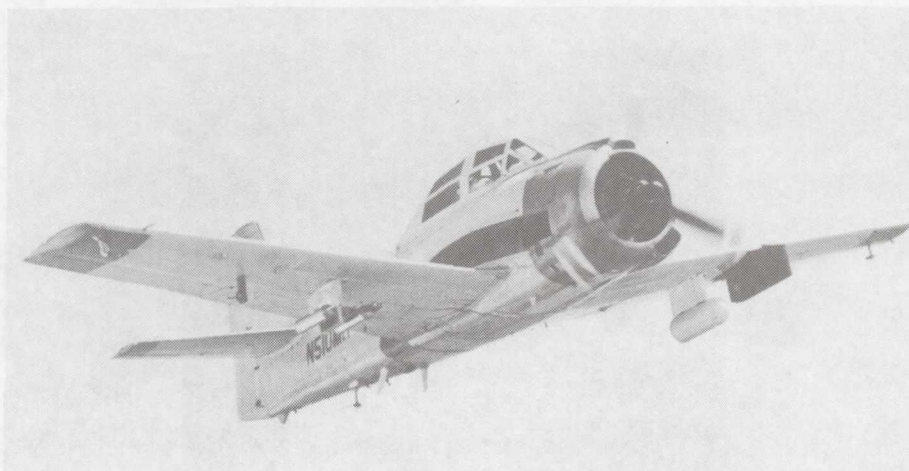


Figure 1.- View of armored T-28 aircraft in flight. Cannon camera device consisting of white pod housing film transport, rotating mirror and control electronics, and black flash system is shown on the aircraft's left wing. The reverse flow temperature device (with exhaust ports) is outboard from the Cannon camera. The FSSP and 2-D Particle Measuring Systems probes are shown on the pylon of the right wing, with the foil impactor located between the probes. Outboard from these instruments are the angle-of-attack and the Johnson-Williams Liquid Water devices. (Photo by Roger Rozelle - AOPA Pilot Magazine)

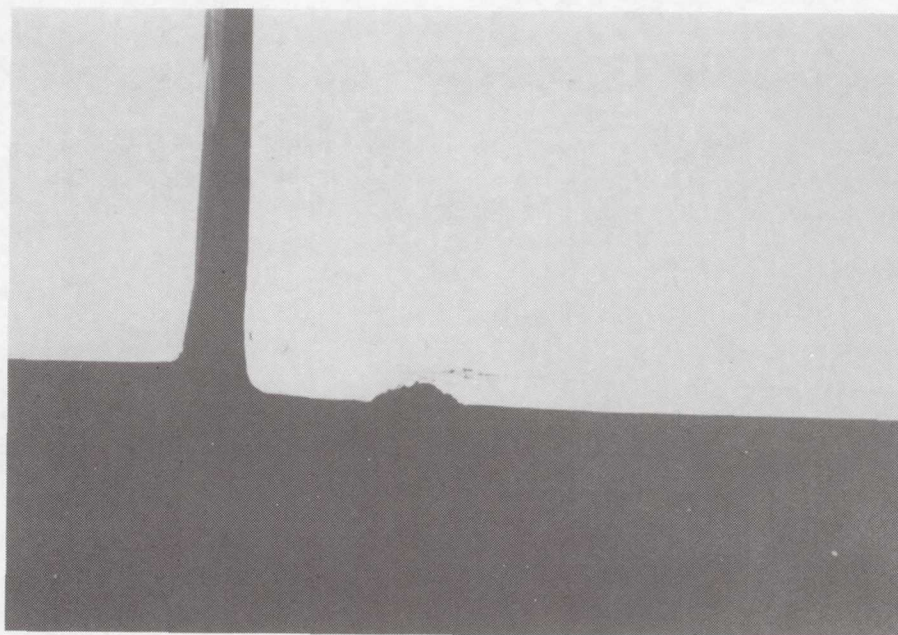


Figure 2.- Lightning damage on aileron.

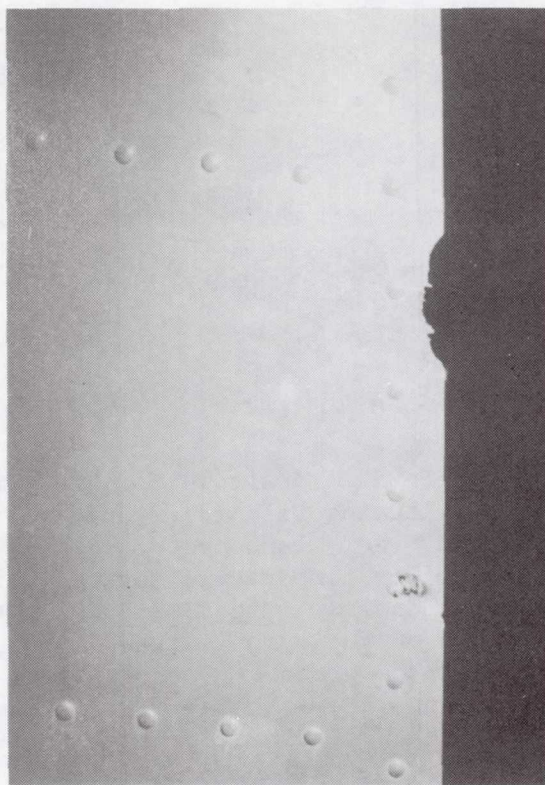


Figure 3.- Lightning damage on vertical stabilizer.



Figure 4.- Hole from lightning on aileron.

STATE-OF-THE-ART METHODS FOR COMPUTING

THE ELECTROMAGNETIC INTERACTION OF LIGHTNING WITH AIRCRAFT

F. J. Eriksen and R. A. Perala
Electro Magnetic Applications, Inc.

John C. Corbin, Jr., ASD/ENAMA
Wright-Patterson AFB, Ohio 45433

INTRODUCTION

The electromagnetic interaction of lightning with aircraft is assuming more importance for modern and future aircraft because of new technological developments which include the use of fly-by wire systems, graphite-epoxy composite structures, and low level integrated circuit devices. It is therefore desirable to determine a cost effective means for computing external surface currents and charges and internal wire voltages and currents when the aircraft interacts with a lightning event. This interaction event is quite complex because it includes the case when the aircraft is attached to the leader or return stroke channel as well as when the aircraft is in the near or far fields of a nearby stroke.

Several electromagnetic interaction codes have been developed to predict the response of an aircraft illuminated by a nuclear electromagnetic pulse (NEMP). Various mathematical techniques have been used and include finite differencing, solution of the electric or magnetic field integral equations, and others. They are varied in their complexity and accuracy, and are usually written to solve the problem of an aircraft in free space illuminated by a plane wave. The objective of the study to be presented in this paper is to evaluate and summarize existing NEMP coupling codes and methods in view of their potential application to the lightning/aircraft interaction event. The differences between NEMP and lightning interaction with aircraft are discussed and critical parameters peculiar to lightning are examined. The results of this study may then be used to identify an optimum external and internal coupling approach which adequately describes the lightning/aircraft interaction event.

IMPORTANT FEATURES OF THE LIGHTNING ENVIRONMENT

Electromagnetic field intensities produced by lightning events (either near-miss or attached stroke) can be larger than those produced by a high altitude nuclear burst (NEMP). However, the lightning processes are generally slower than nuclear processes (~50 ns vs. ~10 ns). The net effect is that

* This work is supported by the U.S. Air Force, AFFDL, under Contract Number F33615-79-C-3412.

derivatives associated with lightning events can be larger than those associated with NEMP, although perhaps not most of the time. In the following discussion of the lightning environment, attention will be focused on the fields during leader attachment, the fields during return stroke current flow in the aircraft, and the effect of a non-linear air conductivity on these fields.

The threat to an aircraft from an attached stroke begins when the aircraft enters a high ambient static field region, typically on the order of 10-100 kV/m. The effect of this field is to polarize the aircraft. The next event is the formation of a stepped leader which propagates from the cloud toward the aircraft. As this leader approaches, its high potential causes the aircraft to polarize further until the fields at the extremities become large enough to produce corona and streamers. The stepped leader attaches to one of these streamers and charge flows onto the aircraft in much the same manner as a current source charges a capacitor. This charging may last for as long as several hundred nanoseconds. The aircraft will continue to charge until normal electric field levels on the aircraft surface exceed air breakdown levels (~ 1 to 3 MV/m). When this happens, corona and streamers again form at various locations on the aircraft surface, and eventually, at least one of the streamers will form the continuation of the stepped leader which propagates to the earth's surface. Electric field changes during this charging time may exceed 10^{13} (V/m)/sec. We note that despite the importance of $\partial E/\partial t$ few measurements or calculations have been performed to evaluate this parameter quantitatively.

After the stepped leader has passed through the aircraft and attached to a streamer near the ground, a large return stroke current flows up the channel towards the aircraft. During this process, the return stroke "drains" the charge out of the corona sheath which surrounds the leader channel. When the return stroke reaches the aircraft, charge from corona regions on the aircraft is also drained into the channel, and in this sense the aircraft may be viewed as an extension of the ionized leader channel.

The threat from the attached stroke current arises from magnetically induced EMFs in the internal wiring of the aircraft. Magnetic fields internal to the aircraft arise either by diffusion or by penetration through apertures. The diffusion coupled internal voltages are independent of $\partial i/\partial t$ due to a relatively long diffusion time, but the aperture coupled fields are not limited and are proportional to $\partial i/\partial t$. An estimate of $\partial i/\partial t$ can be made using information on radiation field risetimes. Recent data show the maximum values of $\partial i/\partial t$ are probably in the range of 3×10^{11} to 10^{12} amps/sec.

Finally, the values of the fields near the aircraft surface will be affected by the conductivity of the surrounding air. Because the fields will often be large enough to ionize air, a proper coupling model should include this effect. In particular, the charging and discharging times for the aircraft are determined by air breakdown effects. The non-linearity of these processes has important implications in the choice of an external coupling model.

EXTERNAL COUPLING MODELS

In this section we review nuclear electromagnetic pulse (NEMP) external coupling models. In contrast to other reviews (ref. 1) NEMP methods are considered specifically from the point of view of lightning/aircraft interaction problems. A good summary of the NEMP literature can be found in IEEE Transactions (ref. 2) devoted exclusively to these problems.

For our purposes, the external coupling problem is the determination of the exterior surface charge and surface current distributions induced on an aircraft either by the electromagnetic fields which occur during a lightning electromagnetic pulse (LEMP), or, by the direct transfer of charge which occurs during an attached lightning event.

The first method we will discuss uses a finite difference approximation to solve Maxwell's equations (differential form). Two approaches have been developed, one by Taflove and Brodwin (ref. 3) and another by Holland and others (ref. 4). The latter is embodied in a computer code called THREDE. The two approaches differ slightly in their treatment of boundary conditions but for all practical purposes are the same. THREDE has been used more extensively to analyze the pulse responses of aircraft, whereas Taflove's method has been applied to the sinusoidal response of various inhomogeneous systems. Examples of the physical resolution obtained with THREDE are shown in Figures 1 and 2. Studies of the NEMP response of the B-52, A6 and F111 (refs. 5, 6), and of the lightning response of the ADCA (ref. 7), have been made using THREDE. Taflove's work has been restricted to a few missile-like structures (ref. 8).

Three-dimensional versions of finite difference codes require large computer storage and are expensive if applied to any reasonable sized problem. However, the method has the special advantage of being able to treat inhomogeneities and non-linearities in a straightforward way. Most other modelling approaches are restricted to linear problems.

Integral equation methods generally involve either the electric field integral equation (EFIE), the magnetic field integral equation (MFIE), or both. The two methods, EFIE and MFIE, tend to be used for mutually exclusive kinds of geometry (ref. 9). The EFIE, for example, is most often used in modelling thin, cylindrical shapes such as antennas, or flat, open surfaces, although recently Wilton has developed an efficient way of treating closed surfaces (ref. 10). The MFIE on the other hand is used for large, closed surfaces such as spheres or fat cylinders.

EFIE methods we have reviewed are: 1) the Antenna Modelling Program (AMP) (ref. 11), 2) WIRANT (ref. 12), 3) Ohio State Code (ref. 13), 4) CHAOS (ref. 14), 5) the Thin-Wire Time-Domain Code (TWTD) (ref. 15), and 6) Wilton's method for surfaces. All of the codes except for Wilton's incorporate the thin-wire approximation, that is, currents and charges are assumed to reside on thin, wire segments and only axial currents are assumed to exist for each segment.

To model a surface, therefore, these codes must analyze a wire grid representation of the surface. An example of a wire grid model using WIRANT is shown in Figure 3. Wire grid modelling is known to have basic limitations especially at low frequencies (ref. 16). Although an intelligent choice of this grid reduces the low frequency error, the problem remains significant because lightning fields have a substantial component in the low frequency regime. In addition to the wire grid modelling problem, all the codes except TWTD solve the coupling problem in the frequency domain and so must determine the pulse response by Fourier convolution. Thus, only linear problems can be addressed easily by the majority of the EFIE methods.

Work using the MFIE method has been reported by: 1) Bennett (ref. 17), 2) Perala (ref. 18), and 3) Sancer (ref. 19). Sancer has studied a model aircraft, shown in Figure 4, which has elliptical cross-section members. His method uses a variable patching scheme to represent the aircraft surfaces. Bennett's and Perala's work have been applied mostly to simple geometric shapes such as spheres and cylinders. Bennett's work has been aimed at determining radar cross-sections. Although his results for far-fields compare favorably with other methods and with experiments, we note that far-field calculations are not always sensitive to the near-field effects required in a coupling analysis. Perala has determined the surface currents on a cylinder with a length to diameter ratio of about unity. Perala and Bennett use MFIE for solution in the time domain, although neither approach is easily adaptable to non-linear or inhomogeneous problems. Sancer's work is in the frequency domain and so is limited to linear problems.

Efforts to integrate both EFIE and MFIE solutions have resulted in several hybrid codes. One hybrid code, called AMP2 (ref. 20), uses the EFIE thin-wire code AMP and appends a MFIE solution to treat surfaces. An improved version of AMP2 is called the Numerical Electromagnetic Code (NEC) (ref. 21). Both AMP2 and NEC have been used for problems such as the determination of radiation patterns from antennas near conducting objects. Another hybrid code, used by Bennett, is based on the MFIE and appends an EFIE solution for thin planar surfaces. With this code, far-field responses have been calculated for aircraft shaped objects such as those in Figures 5(a)-(d). Measurements on scale models have agreed well with these calculations (ref. 22).

A somewhat unique approach called the singularity expansion method (SEM) (ref. 23) has been developed by Baum and others. It was recognized that the damped sinusoidal response of many aircraft to NEMP excitation implied a frequency domain response consisting of a few simple poles. This way of writing the response summarized the NEMP/aircraft external coupling in a concise and elegant way, and calculations have been performed using integral equation formulations to get the poles and residues directly. However, SEM calculations are done in the frequency domain and pulse responses must be determined by Fourier convolution. Thus SEM can treat only linear problems.

Two other methods have been considered. In one method, parallel wire segments have been used to model surfaces (ref. 24), and the current distribution in the wires, as would result from an attached stroke, has been determined by a combination of resistive and inductive effects. Such a model is

useful for determining the low frequency B-field penetration of surfaces, either by skin diffusion or through apertures, and has been used successfully by Burrows (ref. 25) to predict B-field induced voltages in a lightning simulation. A second method which is currently under investigation represents a surface by an equivalent circuit with current or voltage sources. Provided that reasonable representations of surfaces can be found, the method would have several advantages, namely: 1) simplicity of model construction, 2) well developed computer algorithms for numerical solution, and 3) the ability to include non-linear effects in a simple manner.

The accompanying Table I compares most of the external coupling methods discussed in this section. For each method we have listed information on the computer requirements, the user orientation, the model accuracy, the frequency limits of the code, what aircraft have been studied, and under a heading of special requirements, whether the code can treat non-linear problems, whether it can analyze an attached stroke, whether it can incorporate the near fields possible in LEMP, and whether it can treat surface current injection (lightning simulation). Although THREDE is a large code, and is restricted to lower frequencies, it can treat non-linearities and inhomogeneities. WIRANT is a smaller code, but has the low frequency difficulties of wire grid models and can only treat linear problems.

INTERNAL COUPLING METHODS

We have also investigated NEMP internal coupling models, that is, methods for calculating the voltages and currents on electrical/electronic wiring inside the aircraft given the distribution of external surface current and charge. Fields from the external surface penetrate the aircraft skin through apertures (e.g., windows), deliberate antennas, cracks and seams in the aircraft skin, and by diffusion directly through the skin. For any penetration, the coupling of the fields to the internal wiring can be represented by equivalent sources that depend on the geometry of the penetration on the external fields. In principle, multiconductor transmission line theory can be used to predict the voltage and current levels at points remote from the coupling region; however, because of the difficulty in modelling aircraft wiring precisely, a more efficient method might be to statistically predict voltage and current levels.

References to general internal coupling problems, apertures, deliberate antennas, and multiconductor transmission line theory can be found in the IEEE Transactions devoted to NEMP (ref. 2). Our discussion here will be concerned with apertures, deliberate antennas, field penetration through cracks and seams in the aircraft skin, and multiconductor transmission line theory.

Apertures

We will denote by the word "aperture" penetrations such as cockpits,

windows, doors, wheel wells, bomb bays, slots, and other openings such as occur behind extended control surfaces, but exclude cracks and seams for a separate discussion. Several articles describing the calculation of fields behind apertures appear in reference 2 , and Brittingham (ref.26) has written a review of this subject.

A general aperture problem, shown in Figure 6, includes a screen S in which the aperture A appears, and an enclosure E behind the aperture with conductors C_i inside the enclosure. The problem is to calculate the fields inside the enclosure and the currents on the conductors C_i when an electromagnetic field is incident on A from outside.

Among the most sophisticated methods are ones based on integral or integro-differential equations for the unknown fields or currents. This type of solution can be applied to very general physical shapes, although finite computer memories limit the numerical solution to simple shapes such as slots. In the following, we discuss six internal equation methods for treating aperture problems. All six solve the problem in the frequency domain.

In one method developed by Butler and Umashanker (ref.27), coupled integral equations are derived for the current on a single finite wire segment located behind an arbitrarily shaped aperture in a plane conducting screen. The equations have been solved numerically in the case of a slot aperture, and extensive results have been given for current distributions on the wire as a function of wire length, slot length, wire position, and wire orientation.

Umashanker and Wait (ref. 28) have also performed calculations for a wire-slot geometry, however the wire had infinite length and they derived an integro-differential equation as the basis of their solution. The problem was solved numerically using a moment method to obtain the aperture fields and wire current as a function of wire diameter and position.

A third method, Rahmat-Samii and Mittra (ref.29) has been applied to an aperture in a plane, conducting screen, backed by a second plane to form a planar wave guide. Coupled integral equations have been derived for the fields using the Green's function for the waveguide region. A numerical solution has been performed for a square ($\lambda/2$) aperture. The fields in the aperture and in the waveguide have been calculated at one frequency.

In a fourth method, Seidel, Dudley and Butler (ref. 30) have treated the problem of an aperture in a plane, conducting screen, with a rectangular enclosure behind the aperture and a wire inside the enclosure. Coupled integral equations are derived for this geometry and a numerical solution obtained for the current on the wire. Unlike the previous methods, however, the aperture is approximated by the dipole moments of Bethe theory.

A general integral equation has been written by Umashanker and Baum (ref. 31) for an arbitrary aperture in a plane, conducting screen with an arbitrary conductor behind the screen. The equations are cast in a form which gives the poles and residues required in the singularity expansion method. Numerical

calculations have been performed for the fields in an aperture alone, for the fields in a region between a screen (no aperture) and a wire, and for a wire behind a slot aperture. The numerical work also includes the response of the current in the wire to a NEMP pulse excitation.

Also, we note that large apertures may be treated as a part of the external coupling calculation. Finite difference or wire grid codes are capable of modelling cockpits or radomes. For example, WIRANT (ref. 32) has been used for such internal coupling problems. Also, Armour (ref. 33) has used the code CHAOS for calculating the internal response of a cavity excited by an aperture. Like WIRANT, CHAOS requires the construction of a wire grid model of the cavity surface, and so these models are likely to have limitations at low frequencies. The models do have the flexibility of treating arbitrarily shaped cavities, however, without a major change in the solution method.

Another method which is much simpler is Bethe's small hole theory. In a treatment originally due to Bethe (ref. 34), an aperture can be approximated by electric and magnetic dipoles. The dipole moments depend upon the aperture shape and upon the short circuit fields, that is, the fields on the surface of a plane, infinite screen with no aperture. Expressions for the equivalent moments of various shaped apertures have been calculated, and computer programs are available for calculating the penetrating fields. Bouwkamp (ref. 35) has improved the theory by including the effects of higher orders of the parameter " ka ". The method has the advantage of being very simple; however, it is limited to 1) apertures that are small compared to a wavelength, 2) fields far from the aperture, 3) apertures in plane, infinite screens, and 4) it does not include effects of enclosures behind the aperture.

Another relatively simple method uses longitudinal wire segments to represent the surface of cylindrically shaped objects, and calculates the B-field for a cross-section of the object using two dimensional magnetostatic theory. The method has been used by Burrows (ref. 36) to calculate fields inside a cockpit and the calculated fields compare favorably with measurements of the pulse response of wire loops in the cockpit of a full-size fuselage. Although the method is restricted to low frequencies where the magnetostatic solution is valid and to geometries for which the 2D wire models can be used to predict 3D fields, the model has the advantage of being able to treat apertures with arbitrarily shaped enclosures. Furthermore, the solution is valid in a frequency range where lightning has an important component.

In summary, methods for calculating fields behind aperture-perforated screens are not nearly as well developed as methods for external coupling analysis. For example, little information on the computer requirements of any of the codes is available, there is little experimental work to compare results to, and the methods are limited mostly to canonical shapes. Cavity backed apertures can only be solved with great difficulty for a full frequency range.

Deliberate Antennas

Deliberate antennas also form a penetration of the aircraft skin. Air-

craft antennas may include loop, half-loop, blade, slot, horn, and other aperture antennas for VHF and UHF; they may include wire, notch, loop, shunt and probe antennas for HF; and may include slot, loop and wire antennas for LF and VLF use. The response of the antenna to NEMP or lightning is usually represented by Thévenin or Norton equivalents as derived from the equivalent circuit of the antenna. The parameters of the Thévenin or Norton equivalent depend on the geometry of the antenna and on the external surface currents and charges. Some antennas have been tested in a NEMP simulator (ref. 37) and most of the ones listed above have been analyzed theoretically (ref. 38).

As an example, consider the blade antenna shown in Figure 7(a). The antenna operates in the frequency range 225-400 MHz, has a high frequency equivalent circuit as shown in Figure 7(b), and a Thévenin equivalent as shown in Figure 7(c). Because the coaxial transmission line segments inside the antenna are nearly short circuits at the frequencies important to NEMP or lightning, the equivalent circuits shown in Figures 8(a,b) are more useful for NEMP or lightning analysis (ref. 38).

Joints and Seams

Joints and seams between panels on aircraft can provide a significant point of entry if not properly designed and manufactured. In terms of coupling, a seam is characterized by its transfer impedance Z_S (ohm·m) or its reciprocal, the transfer admittance Y_S (mho/m). The voltage V_S developed across a seam by a current density J_S (A/m) flowing normal to the seam is estimated according to

$$V_S(\omega) = J_S(\omega) Z_S(\omega).$$

In practice, $Z_S(\omega)$ is usually measured for flat panels in a laboratory. If there are cables behind a seam, this equation can be used to estimate the value of a discrete voltage source which excites the cable. It is an estimate because the exact voltage impressed on the cable depends upon its distance from the seam and upon the geometry of the internal cavity which is behind the seam. For inductive seams, a more fundamental measure of leakage is in terms of the magnetic polarizability per unit length, m . The polarizability is independent of the geometry of enclosures or cavities, and the transfer impedance can be computed from m if the geometry is known.

The seam transfer impedance depends upon the direction of current density flow across the seam. Practically speaking, it has been found that the coupling through a seam for current flowing parallel to the seam is on the order of 20 dB less than that for the orthogonal case (ref. 39). The parallel case can usually be ignored.

Diffusion

Until recently, diffusion of currents through the aircraft skin has usually been of negligible consequence because the skin has been made of

highly conducting metals. However, future (and some present) aircraft rely heavily on composite materials for their skins. These materials have much lower conductivities ($\sim 10^4$ mho/m for graphite epoxy) than metals and diffusion may be an important mechanism, especially for the low-frequency content of the lightning return stroke.

For an infinite flat plate with surface current density $J_s(\omega)$ on one side, the electric field on the other side $E_{INS}(\omega)$ is given by

$$\frac{E_{INS}(\omega)}{J_s(\omega)} = Z_T(\omega) = \frac{\eta}{\sinh \gamma d}$$

where η is the material intrinsic impedance, γ is the material propagation constant, and d is the material thickness. Thus, once the material properties and surface current density are known, the diffused electric field can be easily computed. Strictly speaking, the above relationship is true only for an infinite flat plane. For panels of aircraft shape, the internal electric field is the solution of a boundary value problem which must include the effects of the structure shape and geometry. However, the above relation can be used to provide estimates of the internal fields in order to make engineering judgments.

Internal Propagation

Once electromagnetic fields penetrate into the aircraft interior by means of apertures, diffusion, or seams, they excite the internal wiring which in turn propagates the energy to other parts of the aircraft. In particular, the problem confronting the analyst is to predict the voltages, currents, powers, and energies incident on black box connector pins.

The common approach to this problem is to model the aircraft wiring as single or multi-conductor transverse electric and magnetic (TEM) transmission lines. In doing this for N wires over a ground plane on reference conductors, one must solve the so-called telegrapher's equations:

$$\begin{aligned} \frac{\partial}{\partial x} [V(x,t)] + \frac{\partial}{\partial t} [L(x)] [I(x,t)] + [R(x)] [I(x,t)] &= [V_s(s,t)] \\ \frac{\partial}{\partial x} [I(x,t)] + \frac{\partial}{\partial t} [C(x)] [V(x,t)] + [G(x,t)] [V(x,t)] &= [I_s(x,t)] \end{aligned}$$

with the following definitions:

- $[V(x,t)]$ - the $N \times 1$ matrix of voltages on each of the N wires.
- $[I(x,t)]$ - the $N \times 1$ matrix of currents on each of the N wires.
- $[C(x)]$ - the $N \times N$ Maxwell capacitance matrix in farads/meter.
- $[L(x)]$ - the $N \times N$ inductance matrix in henries/meter defined by $[L(x)] = \mu \epsilon [C(x)]^{-1}$ with μ the permeability, ϵ the permittivity of the surrounding homogeneous medium.
- $[R(x)]$ - the $N \times N$ diagonal wire resistance matrix in ohms/meter.
- $[G(x,t)]$ - The $N \times N$ conductance matrix in mhos/meter defined by

$[G(x,t)] = \frac{\sigma(x,t)}{\epsilon} [C(x)]$ with $\sigma(x,t)$ the conductivity of the surrounding medium.

$[V_S(x,t)]$ - the $N \times 1$ matrix in volts/meter of distributed voltage sources on each of the N wires defined by $V_S(x,t) =$

$$\frac{\partial}{\partial t} \int_0^h B_z(x,y,t) dy, \text{ with } h \text{ the height above}$$

the ground plane and B_z the z -component of the magnetic flux density with all the wires absent.

$[I_S(x,t)]$ - the $N \times 1$ matrix in amperes/meter of distributed current sources on each of the N wires defined by $I_S(x,t) =$

$$-C_{ig}(x) \left(\frac{\sigma(x,t)}{\epsilon} + \frac{\partial}{\partial t} \right) \int_0^h E_y(x,y,t) dy, \text{ with } E_y$$

the y -component of the electric field with all the wires absent.

These equations assume that 1) the fields are TEM only, 2) the line losses are small (ie, $RI < L \frac{\partial I}{\partial t}$ and $GV < C \frac{\partial V}{\partial t}$), and 3) the spacings between the conductors

and the distances to the ground plane are much smaller than the wavelength of the highest significant frequency. Coordinates x , y , and z are such that the transmission line lies along the x axis, and y is normal to the reference plane. The telegrapher's equations can be solved in either the time (ref. 40) or frequency (ref. 41) domains. These equations can be easily and accurately solved in homogeneous media once the inductance and capacitance matrices and the source functions are known. With real cables in aircraft, however, it is often quite difficult to obtain this data. For example, it is a difficult matter to determine in which cable bundle a particular wire runs, where in the bundle the wire is positioned, and what the load impedances on the wire may be. Aircraft to aircraft variations can be significant, with the result that if a rigorous, deterministic approach is applied, every aircraft would have to be analyzed on an individual basis. Also, for a real aircraft cable, the cable geometry with respect to the reference plane and nearby objects changes along its length, such as at positions where the cable branches or where it passes through a bulkhead. Thus the real problem in multiconductor cable propagation is not the mathematics but obtaining accurate input data.

In view of the above difficulty, an alternate approach is to model a multiconductor cable bundle as one bulk cable and determine the bulk cable current by single wire transmission line theory. The actual pin voltages and currents due to a particular wire in the bundle may then be determined statistically from the bulk cable current. This approach has not yet been rigorously demonstrated as being viable, but it is attractive because it eases the analyst's burden in determining the input data. It also would enable one to determine the vulnerability of an aircraft fleet in a statistical

basis. The disadvantage is that the statistical distributions need to be obtained by extensive analysis and testing.

CONCLUSIONS

A review of electromagnetic coupling methods with particular application to lightning has been accomplished. It is clear that the external coupling problem is better understood than the internal coupling problem. In particular, the solution of the coupling to cables within arbitrary shaped cavity backed apertures is a formidable problem. In addition, the internal cable propagation problem has the practical difficulty of determining the exact input data necessary for solution.

The external coupling problem for lightning is complicated by the fact that the attachment process is non-linear. This implies that frequency domain solutions and solutions dependent upon linear operator theory cannot be used for this part of the problem, unless it can be treated in a piecewise linear fashion. Otherwise, time domain solutions are required. In this case, a finite difference approach or a time domain circuit modelling technique would be appropriate.

REFERENCES

1. Baum, Carl E., "Emerging Technology for Transient and Broad-Band Analysis and Synthesis of Antennas and Scatterers," IEEE Proceedings, Invited Paper, v. 64, p. 1598 (1976); Bevensee, R.M., James N. Brittingham, F.J. Deadrick, T. N. Lehman, K. Edmund, and A. J. Poggio, "Computer Codes for EMP Interaction and Coupling," IEEE Transactions on Antennas Propagation, AP-26, p. 156 (1978); Miller, E.K., R. M. Bevensee, A. J. Poggio, R. Adams, F. J. Deadrick and J. A. Landt, "An Evaluation of Computer Programs Using Integral Equations for the Electromagnetic Analysis of Thin-Wire Structures," AFWL Interaction Notes, LLL, Livermore, CA; Miller, E. K., and J. A. Landt, "Direct Time-Domain Techniques for Transient Radiation and Scattering," Lawrence Livermore Laboratory, University of California, Livermore, CA, UCRL-52315, July 1, 1976.
2. IEEE Transactions on Antennas and Propagation, AP-26, 1978; IEEE Transactions on Electromagnetic Compatibility, EMC-20, 1978.
3. Taflove, A., and M. E. Brodwin, "Numerical Solution of Steady-State Electromagnetic Scattering Problems using the Time Dependent Maxwell's Equations," IEEE Transactions on Microwave Theory and Techniques, MTT 23, p. 623 (1975).
4. Holland, Richard, Larry Simpson, and R. H. St. John, "Techniques for Solving Large 3-D EMP Problems;" - presented at IEEE Conference on Nuclear and Space Radiation Effects, Santa Cruz, CA, July 1979; Holland, Richard, "THREDE: A Free-Field EMP Coupling and Scattering Code," IEEE Nuclear Science, 4 December 1977.
5. Kunz, Karl S., and Kuan-Min Lee, "A Three-Dimensional Finite-Difference Solution of the External Response of an Aircraft to a Complex Transient EM Environment: Part I - The Method and Its Implementation," IEEE Transactions on Electromagnetic Compatibility, EMC-20, p. 328 (1978).
6. Kunz, Karl S., and Kuan-Min Lee, "A Three-Dimensional Finite-Difference Solution of the External Response of an Aircraft to a Complex Transient EM Environment: Part II - Comparison of Predictions and Measurements," IEEE Transactions on Electromagnetic Compatibility, EMC-20, p. 333 (1978).
7. Perala, R. A., K. Lee and R. Cook, "Induced Effects of Lightning on an All Composite Aircraft," Proceedings of Third Symposium and Technical Exhibition on Electromagnetic Compatibility, Rotterdam, Holland, May 1-3, 1978.
8. Taflove, Alan, "Time Domain Solutions for Electromagnetic Coupling," RADC-TR-78-142, Rome Air Development Center, Griffiss Air Force Base, New York, June 1978.
9. Mittra, R., "Integral Equation Method for Transient Scattering," Topics in Applied Physics, v. 10, ed. by L. B. Felsen (Spring-Verlag, New York, 1976) pp 73-128.

10. Wilton, D. R., S. S. M. Rao, and A. W. Glisson, "Electromagnetic Scattering by Surfaces of Arbitrary Shape," private communication.
11. Selden, E. S., and G. J. Burke, "Antenna Modeling Program, Composite User's Manual," MB-R-74/46, M. B. Associates, San Ramon, CA 94583.
12. Straw, D. F., M. O'Byrne, and S. Sandberg, "Electromagnetic Coupling Analysis of a Learjet Aircraft," AFFDL-TR-78-121, Wright-Patterson AFB, September, 1978.
13. Richmond, J. H., "An Integral-Equation Solution for TE Radiation and Scattering from Conducting Cylinders," Electromagnetic Pulse Interaction Note 201, ed. by C. E. Baum, AFWL, April 1973; Richmond, J. H., "Radiation and Scattering by Thin-Wire Structures in the Complex Frequency Domain," Electromagnetic Pulse Interaction Note 202, ed. by C. E. Baum, AFWL, Kirtland AFB, NM, May 1974; Richmond, J. H., "Computer Program for Thin-Wire Structures in a Homogenous Conducting Medium," Electromagnetic Pulse Interaction Note 203, ed. by C. E. Baum, AFWL, Kirtland AFB, NM, June 1974; and Richmond J. H., "Computer Program for Thin Wire Antenna Over a Perfectly Conducting Ground Plane," Electromagnetic Pulse Interaction Note 204, ed. by C. E. Baum, AFWL, Kirtland AFB, NM, October 1974.
14. Chao, Hu H., and Bradley J. Strait, "Computer Programs for Radiation and Scattering by Arbitrary Configurations of Bent Wires," Electromagnetic Pulse Interaction Note 191, ed. by C. E. Baum, AFWL, Kirtland AFB, NM, September 1976; Chao, Hu H., and Bradley J. Strait, "Computer Programs for Radiation and Scattering by Arbitrary Configurations of Bent Wires," AFCRL Scientific Report No. 7, Contract F19628-68-C-0180, Syracuse University, Syracuse, NY, September 1970.
15. Miller, E. K., A. J. Poggio, and G. J. Burke, "An Integro-Differential Equation Technique for the Time-Domain Analysis of Thin-Wire Structures," Journal of Computational Physics, v. 12, p. 24 (1973).
16. Sancer, M. I., "Fundamental Errors Associated with the Gross Modelling of the Physical Features of Metallic Enclosures," Interaction Note 298, ed. by C. E. Baum, AFWL, Kirtland AFB, December 1976.
17. Bennett, C. Leonard Jr., and Walter L. Weeks, "A Technique for Computing Approximate Electromagnetic Impulse Response of Conducting Bodies," Purdue University School for Electrical Engineering, Lafayette, IN, June 1968; Bennett, C. Leonard Jr., and Walter L. Weeks, "A Technique for Computing Approximate Electromagnetic Impulse Response of Conducting Bodies," Electromagnetic Pulse Interaction Note 222, ed. by C. E. Baum, AFWL, Kirtland AFB, NM, June 1968; Bennet, C. L., "S3T-CLB," in Electromagnetic Computer Codes Newsletter, ed. by R. M. Bevensee, LLL, Livermore, CA, v. 3, p. 15, April 1976.
18. Perala, Rodney A., "Integral Equation Solution for Induced Surface Currents of Bodies of Revolution," IEEE Transactions on Electromagnetic Compatibility, EMC-16, p. 172, August 1974.

19. Sancer, M. I., Scott Siegel, and A. D. Varvatsis, "Formulation of Electromagnetic Pulse External Interaction Above a Lossy Earth/Comparison of Numerical Results with Experimental Data for Limiting Cases," Electromagnetic Pulse Interaction Note 354, ed. by C. E. Baum, AFWL, Kirtland AFB, NM, October 1978.
20. M. B. Associates, "Antenna Modeling Program, Supplementary, Computer Program (AMP2)," MB-R-75/4, M. B. Associates, San Ramon, CA 94583.
21. Burke, G. J. and A. J. Poggio, "Numerical Electromagnetic Code (NEC), Method of Moments, Volume I - Program Description Theory," Electromagnetic Pulse Interaction Note 363, ed. by C. E. Baum, AFWL, Kirtland AFB, NM July 1977; Burke, G. J., A. J. Poggio, J. C. Logan, and J. W. Rockway, "Numerical Electromagnetic Code - A Program for Antenna System Analysis," Third Symposium on Electromagnetic Compatibility, Rotterdam, Holland, May 1979, p. 39; Burke, G. J., A. J. Poggio, J. C. Logan, and J. W. Rockway, "Numerical Electromagnetic Code (NEC)," Fourth Symposium on Electromagnetic Compatibility, San Diego, CA, October 1979, p. 46; Burke G. J., and A. J. Poggio, "Numerical Electromagnetic Code (NEC) - Part I, Part II, Part III," Navelix Technical Document 1L, ELEX 3041, Naval Electronic Systems Command, San Diego, CA, July 1977.
22. Bennett, C. L. and Gerald Ross, "Time-Domain Electromagnetics and its Applications," IEEE Proceedings, v. 66, p. 299 (1978); Bennett, C. Leonard, "The Numerical Solution of Transient Electromagnetic Scattering Problems," in Electromagnetic Scattering, New York: Academic Press (ed. P. Uslenghi), 1978; Bennett, C. L., H. Mieras, S. L. Teeter and J. P. Toomy, "Low EM Signature Response Techniques," RADC-TR-78-287, Griffiss AFB, NY, March 1979.
23. Baum, Carl E., "On the Singularity Expansion Method for the Solution of Electromagnetic Interaction Problems," AFWL Interaction Note 88, December 1971; Baum, Carl E., "The Singularity Expansion Method," in Topics in Applied Physics, v. 10, ed. by L. B. Felsen (Springer-Verlag, Berlin, 1976), Chapter 3.
24. F. A. Fisher, "Analysis and Calculations of Lightning Interactions with Aircraft Electrical Circuits," AFFDL-TR-78-106, Wright-Patterson AFB, OH, August 1978.
25. Burrows, B. J. C, P. Pownall and C. A. Luther, "Induced Voltage Programme," CLSU Memo No. 34, Culham Lightning Studies Unit, Culham Laboratory, Abingdon, December 1975.
26. Brittingham, J.N., "A Literature Review of EMP Effects on Apertures," UCID-17321, Lawrence Livermore Laboratory, Livermore, CA, November 1976.

27. Butler, Chalmers M., and Korada R. Umashanker, "Electromagnetic Excitation of a Wire Through an Aperture-Perforated, Conducting Screen," Electromagnetic Pulse Interaction Note 251, ed. by C. E. Baum, AFWL, Kirtland AFB, NM, June 1975.
28. Umashanker, Korada R., and James R. Wait, "Electromagnetic Coupling to an Infinite Cable Placed Behind a Slot Perforated Screen," Electromagnetic Pulse Interaction Note 330, ed. by C. E. Baum, AFWL, Kirtland AFB, NM, June 1977.
29. Rahmai-Samii, Y., and R. Mittra, "A New Integral Equation Solution of Electromagnetic Aperture Coupling and Thin Plate Scattering Problems," Electromagnetic Pulse Interaction Note 224, ed. by C. E. Baum, AFWL, Kirtland AFB, NM, February 1975.
30. Seidel, D. B., D. G. Dudley, and C. M. Butler, "Aperture Excitation of a Wire in a Rectangular Cavity," Electromagnetic Pulse Interaction Note 345, ed. by C. E. Baum, AFWL, Kirtland AFB, NM, June 1977.
31. Umashanker, Korada, R., and Carl E. Baum, "Transient Electromagnetic Characterization of Arbitrary Conducting Bodies Through an Aperture-Perforated Conducting Screen," Electromagnetic Pulse Interaction Note 343, ed. by C. E. Baum, AFWL, Kirtland AFB, NM, March 1978.
32. M. C. Vincent, W. L. Curtis, J. R. Gozinsky, W. P. Hanson, J. L. Lin, E. I. Piatkowski, and B. E. Smith, "EMP Response of the B-1 Aircraft for Inadvertent Penetration Coupling, Volume I," AFWL-TR-75-164, Kirtland AFB, Albuquerque, NM, July 1975.
33. Garthwaite, F. G. L. and T. W. Armour, "Electromagnetic Penetration Through Large Apertures and the Prediction of Cavity Fields by Means of Wire Grid Modelling," AWRE, Aldermaston, Reading, UK, April 1980.
34. Bethe, H. A., "Theory of Diffraction by Small Holes," Physical Review, v. 66, p. 168 (1944).
35. Bouwkamp, C. J., "Diffraction Theory," Repts. Prog. in Phys., v. 17, p.35 (1954).
36. Burrows, B. J. C., C. Luther and P. P. Pownall, "Induced Voltages in Full Size Aircraft at 10" A/S," 1977 IEEE International Symposium on Electromagnetic Compatibility, Seattle, WA, August 1977.
37. Coe, R. J., and W. L. Curtis, "Deliberate Antenna Modelling Study," D224-10025-1, Boeing Company, Seattle, WA, October 1973.
38. Liu, T. K., and K. S. H. Lee and Lennart Marin, "Broadband Responses of Deliberate Aircraft Antennas, Part I," Interaction Note 228, ed. by C. E. Baum, AFWL, Kirtland AFB, Albuquerque, NM, May 1975.

39. Whitson, A. L. and E. F. Vance, "Bolted Lapped-Joint EMP Shields," DNA 4472F, Defense Nuclear Agency, Washington, DC, 20305, June 1977.
40. Merewether, D. E., "A Numerical Solution for the Response of a Strip Transmission Line over a Ground Plane Excited by Ionizing Radiation," IEEE Trans. Nuc. Sci., Vol. NS-18, No. 5, August, 1971; Merewether, D. E., and P. Trybus, "A Time Domain Solution of Multiconductor Transmission Line Coupling Problems," AMRC-R-21, Mission Research Corporation, January 1974.
41. Paul, C. R., "Frequency Response of Multiconductor Transmission Lines Illuminated by an Electromagnetic Field," IEEE Transactions on Electromagnetic Compatibility, EMC-18, 183, (1976).

TABLE I

	THREDE (Fin. Diff.)	PERALA (MFIE)	BENNETT (MFIE and MFIE/EFIE)	WIRANT (EFIE)	AMP (EFIE)	NEC (EFIE/MFIE)	TWTD (EFIE)	WIRE MODEL
COMPUTER REQ.	CDC 7600 30x30x30 (ab) 45 kg SCM 1 M8 LCM 15 MIN	CDC 6600 290 PATCHES (CYLINDER) 240 kg 1 HOUR		CYBER 174 147 UNKNOWN (ANTENNA) 175 kg 5 SEC/FREQ	CDC 6500 200 SEGS (ANTENNA) 150 kg	CDC 6600 80 SEGS and PATCHES (SATELLITE) 16 SEC/FREQ	CDC 7600 60 SEG (ANTENNA) 370 kg	
USER ORIENT.	SOME DOC REQ'S USER TO CHOOSE GRID AND OUTER BOUNDARY	LITTLE DOC	SOME DOC	NOT AVAIL- ABLE (PROPRI- TARY)	EXCELLENT DOC	EXCELLENT DOC	GOOD DOC	SOME DOC
	Time Dom.	Time Dom.	Time Dom.	Freq.Dom.	Freq.Dom.	Freq. Dom.	Time Dom.	
MODEL ACCURACY	TYP GRID 30x30x30 MAX GRID 50x50x50	TYP 290 PATCHES FOR A FAT CYLINDER	TYP 54 PATCHES FOR 1 M RAD SPHERE	THIN WIRE APPROX. MOMENT METHOD TYP 150- 200 SECS. MAX	THIN WIRE APPROX. MOMENT METHOD	SAME AS AMP PLUS PATCHES FOR MFIE. IMPROVED "I" EXPANSION + JCT. CONDX FROM AMP.	THIN WIRE APPROX. MOMENT METHOD MAX 60 SEGS.	20-30 WIRE MODEL OF SURFACE CURRENT DIV. BY RES OR INDUCT EFFECT
AIRCRAFT STUDIED	B52, A6, F111, ADCA	NONE	MIG 21 AIRCRAFT MODELS	F111, 747 LEARJET, YC14, B1, AWACS P3		STICK MODEL 29 SEGS. (2 SECS/FREQ)	747 STICK MODEL	HAWKER HUNTER
S Non- P Linear	YES	NOT EASILY	NOT EASILY	NO	NO	NO	NO	
E Attached								
C Stroke	YES	NOT EASILY	NOT EASILY	YES	YES	YES	YES	YES
R Near								
E Fields	YES	YES	YES	PROBABLY	YES	YES	YES	
Q SCIT	YES	NOT EASILY	NOT EASILY	YES			YES	

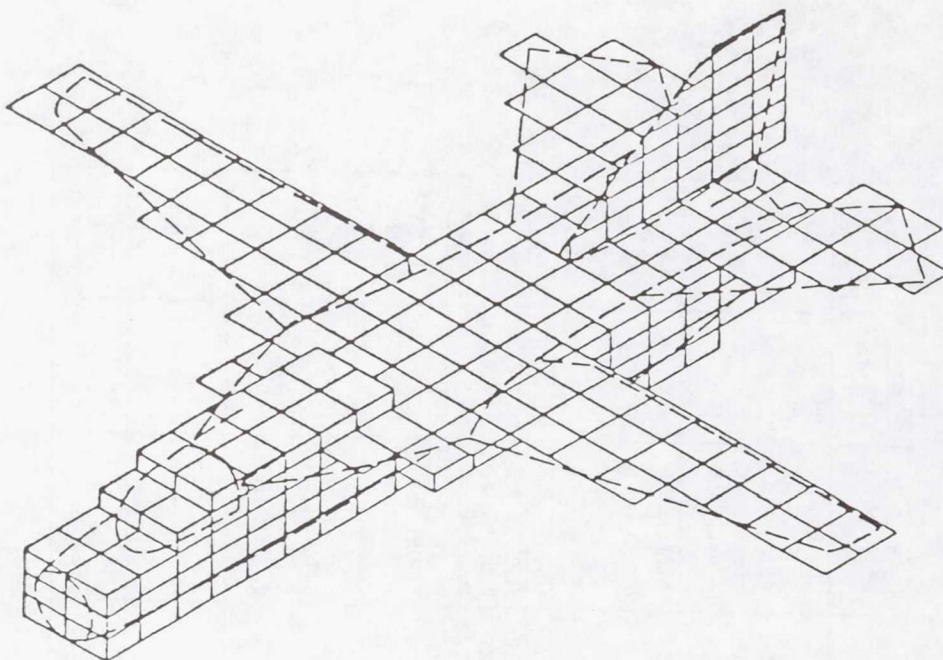


Figure 1.- F111 model using $30 \times 30 \times 30$ grid.

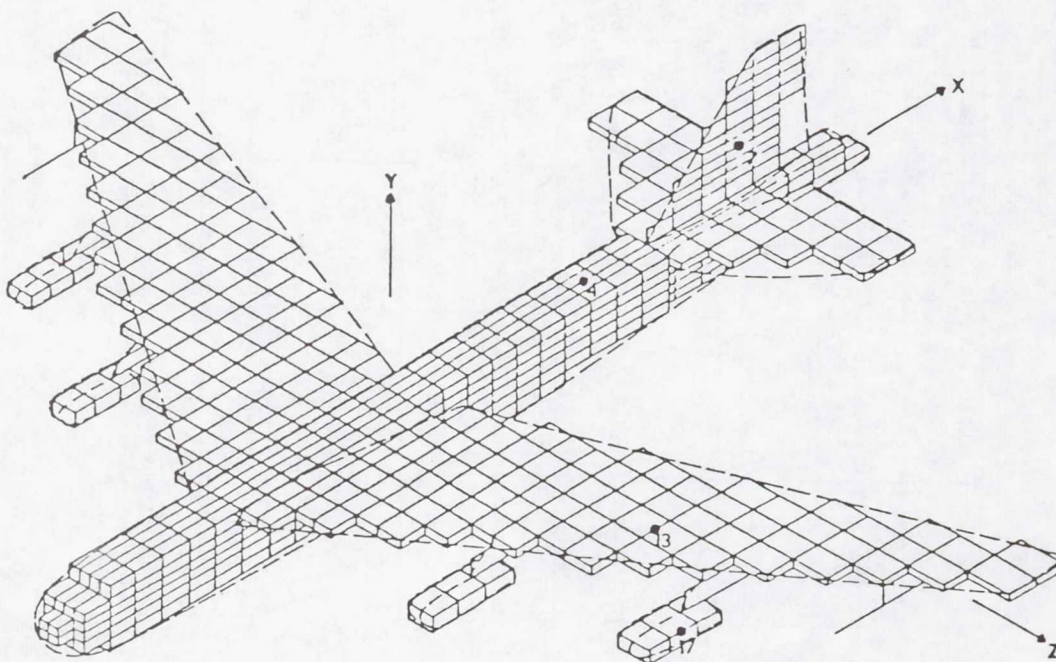


Figure 2.- B52 model using $50 \times 50 \times 50$ grid.

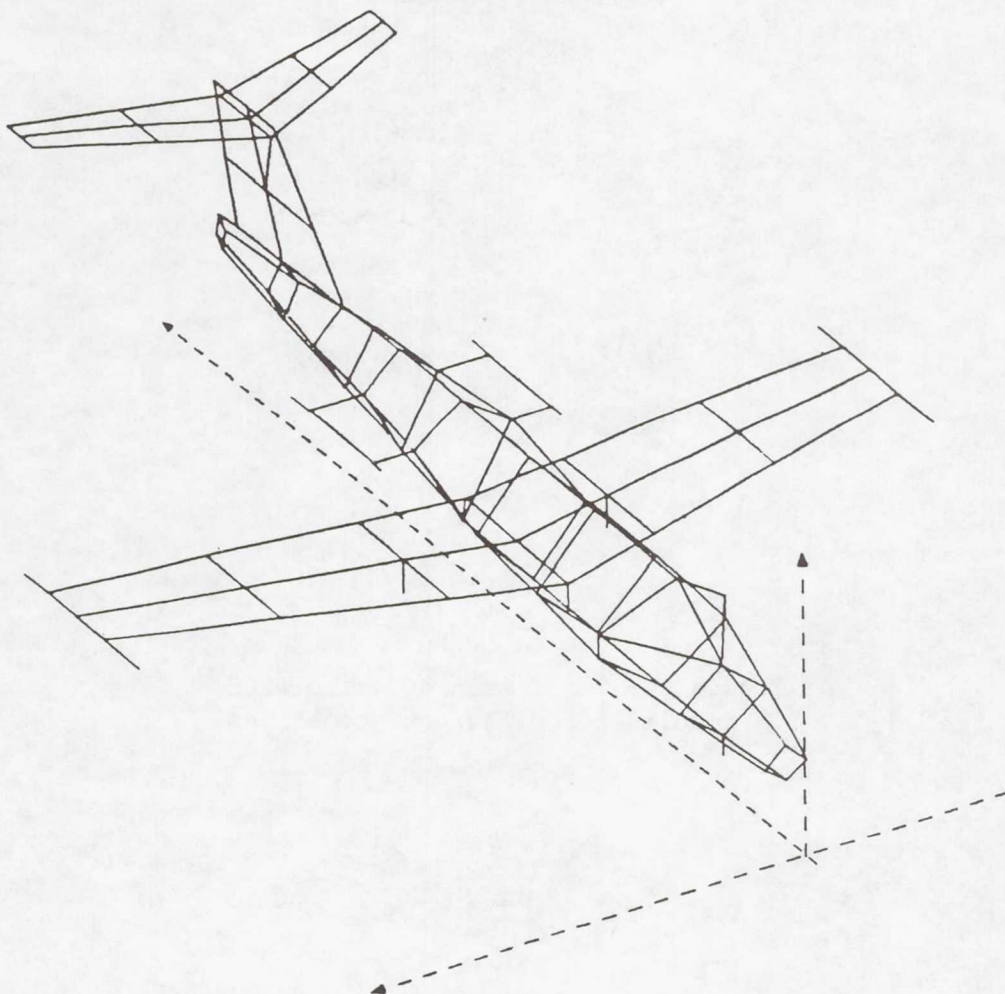


Figure 3.- Wire grid model of a Learjet.

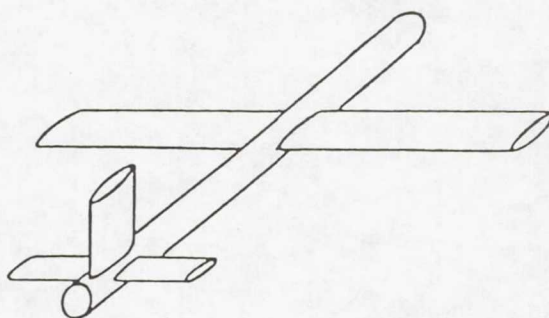


Figure 4.- Model used for MFIE solution by Sancer.

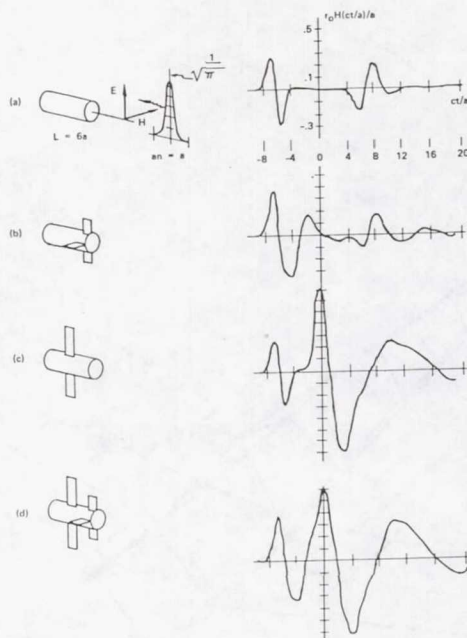


Figure 5.- Comparison of calculated results for different geometries.

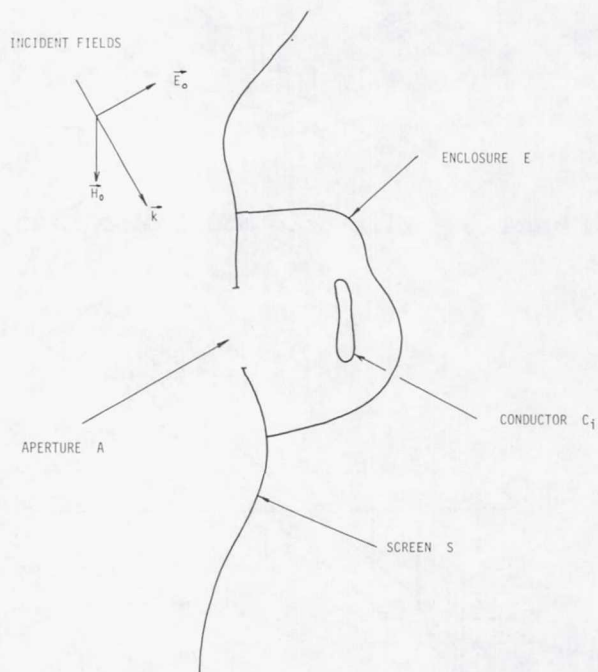


Figure 6.- General aperture coupling problem.

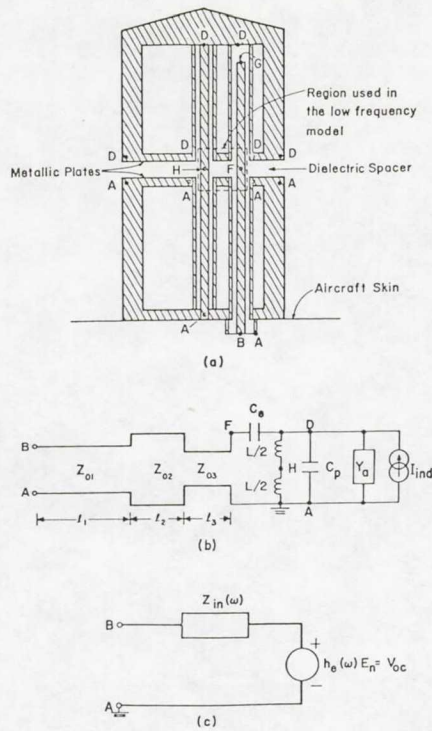


Figure 7.- Equivalent circuit of blade antenna (ref. 38).

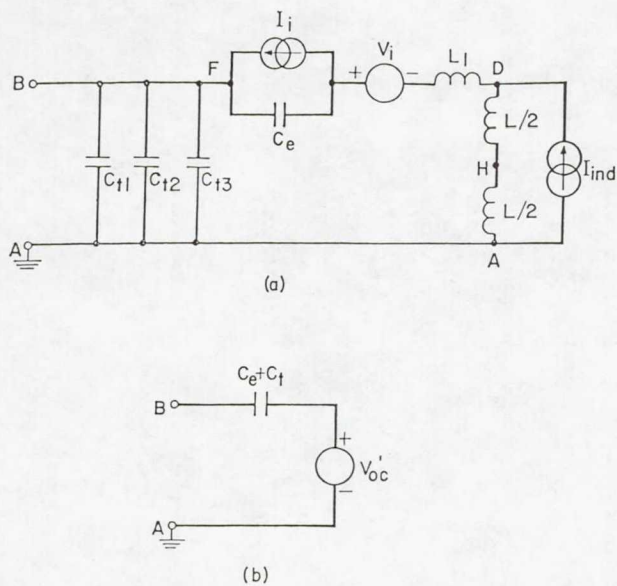


Figure 8.- Low frequency equivalent circuit of blade antenna (ref. 38).

Page intentionally left blank

ANOTHER LOOK AT AIRCRAFT-TRIGGERED LIGHTNING

D.W. Clifford
McDonnell Aircraft Company
St. Louis, Missouri 63166

ABSTRACT

There is positive evidence that a rapidly moving aircraft charged to high potentials by triboelectric processes can trigger lightning discharges by passage through freezing precipitation. The freezing zone in a nonstormy rain cloud is shown to be an electrically volatile region because of the potent charge exchange mechanisms which are active in agitated mixtures of supercooled water droplets and ice. Several intensifying effects are suggested which can be produced by the passage of an aircraft through this precipitation, resulting in a highly-ionized wake which acts like a trailing conductor. If weak charge centers are present in the cloud, the ionized wake acts to short out the gradient field resulting in very high potentials at the aircraft. The high potentials explain the electrical activity at the aircraft described by pilots, including intense corona, sparks and radio interference terminating in a loud discharge. Lightning strikes to naval aircraft towing gunnery targets at the end of long steel cables are described, showing that the same triggering mechanism may be involved in those cases. Recommendations are made to include triggering experiments in government flight programs now in progress.

INTRODUCTION

There has been much debate on the question of whether or not an aircraft can, by its presence, trigger a lightning strike which otherwise would not have occurred. There are positive indications that a conducting body in an electrified environment can initiate lightning. Fitzgerald¹ presented evidence in the Rough Rider Program that the presence of an aircraft produced lightning strikes. Pilots have contended for many years that aircraft either trigger lightning or they experience static discharge.² Several workers have been able to initiate lightning to ground by firing rockets into charged clouds.^{3,4} However, these experiments required grounded wires attached to the rocket, resulting in a different electrostatic situation from that of an isolated aircraft.

Shaeffer⁵ addressed the question of aircraft-initiated lightning by examining the localized electric field enhancement in the region of an aircraft. He showed that the intensification of the local field acted to extend the electrical region of influence of the aircraft to a distance of one-body diameter from the aircraft. Since the length of a lightning channel may be several kilometers, this small intensification would not be expected to have much influence on triggering a strike. Shaeffer also showed that aircraft engine exhaust ionization levels are too low to be a factor in triggering lightning.

This paper will take another look at the possibility of aircraft-triggered lightning. The problem will be addressed from a different point of view than the previous efforts, however. Lightning strike reports and pilot observations from military and commercial aviation experience will be used to work back to the atmospheric conditions where lightning usually strikes aircraft. Those atmospheric conditions will then be examined to determine any unique features which could lead to possible interaction effects with an aircraft which in turn could lead to the production of triggered lightning.

THE LIGHTNING VERSUS STATIC DISCHARGE CONTROVERSY

Many experienced pilots have consistently held that most reported aircraft lightning incidents are not true lightning strikes, but rather discharges of electrical energy accumulated on the aircraft by triboelectric charging. In a 1965 United Airlines report entitled "UAL Turbojet Experience with

Electrical Discharges,"² the practical experience of numerous pilots, with many thousands of hours of flying experience, was summarized and reported as they responded to questions about their experience with lightning. To supplement the testimony of the commercial pilots, there are also many incident reports from military operations reporting electrical discharge phenomena.

Both commercial and military pilots almost unanimously agree that there are two distinct classes of lightning observed in flight. The most common variety usually occurs while flying in precipitation at temperatures near freezing. This type is preceded by a buildup of static noise in the communication gear and the presence of corona (St. Elmo's fire). The buildup may continue for several seconds until a violent discharge occurs. The discharge terminates the static and corona, but the process may repeat itself if flight through the precipitation continues.

The second variety occurs abruptly with no warning, and is usually described as more severe. It is always encountered in or near thunderstorms, in contrast to the former variety which is more likely to be experienced in precipitation that has no connection with thunderstorms. The slow buildup strike reports typically indicate no visible lightning in the vicinity and no radar indication of thunderstorms anywhere in the region. Pilots tend to believe that the slow buildup type of discharge is not a true lightning strike but either a discharge of excess static charge built up on the aircraft by flying through the precipitation, or some sort of triggered discharge produced by the catalytic presence of the aircraft. They say that this nonthunderstorm type of discharge outnumbers the other by anywhere from two to one to ten to one. Both kinds can create a brilliant flash and a report which can be heard throughout the airplane. The abrupt type may cause a louder report and usually produces more damage.

The response of scientists to the pilots' static discharge theory has been universally negative. They insist that insufficient charge can be stored on an aircraft to produce a discharge which looks and sounds like lightning. Scientists are even more emphatic that insufficient energy could be contained in such a static charge buildup to produce any visible evidence such as burn marks, pitting or other damage on the aircraft. Nor have any satisfactory explanations been offered to show how an aircraft could trigger lightning. Yet, the pilots continue to insist that the aircraft is either discharging or triggering a discharge, and that the discharges do manifest themselves by bright noisy arcs and (not all pilots are sure about this) visible damage. The controversy has been characterized as "a difference in view between scientists of long standing and pilots of long sitting."

LIGHTNING MISHAP WEATHER STATISTICS

Most of the reports of lightning or electrical discharge of the type preceded by corona and radio static have involved aircraft flying through some sort of precipitation or suspended ice particles, usually near freezing temperature. In contrast, strikes of the sudden type often occur outside clouds, or in clouds with no precipitation, but always in the vicinity of thunderstorms. There are some cases of aircraft flying near thunderstorms, apparently in high cross-field regions, which have experienced buildup of corona prior to lightning strikes. Except for one special case, however, these slow buildup incidents are rare in comparison to the type involving precipitation. The special case involves aircraft towing long electrical conductors, such as naval gunnery targets, on the end of long steel cables. A disproportionately large number of strikes have occurred to such tow aircraft. These incidents will be discussed in more detail later because they bear directly on the triggering process which will be postulated in this paper.

Before examining some specific in-flight incidents in detail, a review of lightning strike weather statistics will be of value. Where no attempts have been made to differentiate between the different types of discharge, the weather statistics show tendencies to the type of conditions described by the pilots for the slow-type discharge. Figure 1 shows the temperature distribution for lightning strikes to aircraft and Figure 2 shows the environmental conditions related to clouds, precipitation and

turbulence at the time of 214 strikes reported by Fisher and Plumer.⁶ In over 80 percent of the strikes reported, aircraft were within a cloud and were experiencing precipitation and some turbulence. In addition, as can be seen from Figure 1, the vast majority of the reported incidents occur at temperatures near the freezing level. These statistics are often shrugged off as incidental to the thunderstorm environment which actually causes the strike. However, a thorough evaluation of the synoptic conditions and localized weather circumstances by Harrison,² in the case of the UAL strikes, and Trunov⁷ in a summary of USSR incidents, confirm that thunderstorm activity usually is not present at the time of the event.

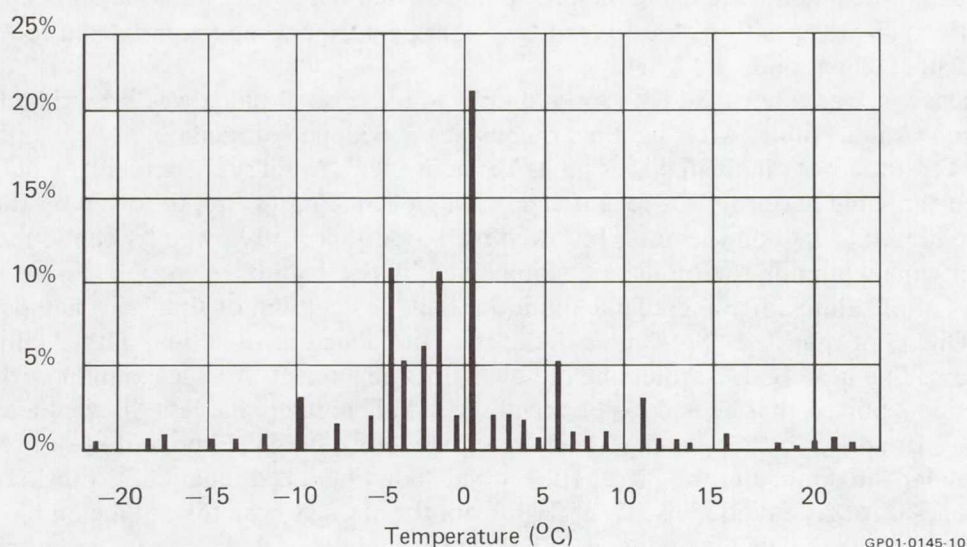


FIGURE 1
LIGHTNING STRIKES TO AIRCRAFT AS A FUNCTION OF TEMPERATURE

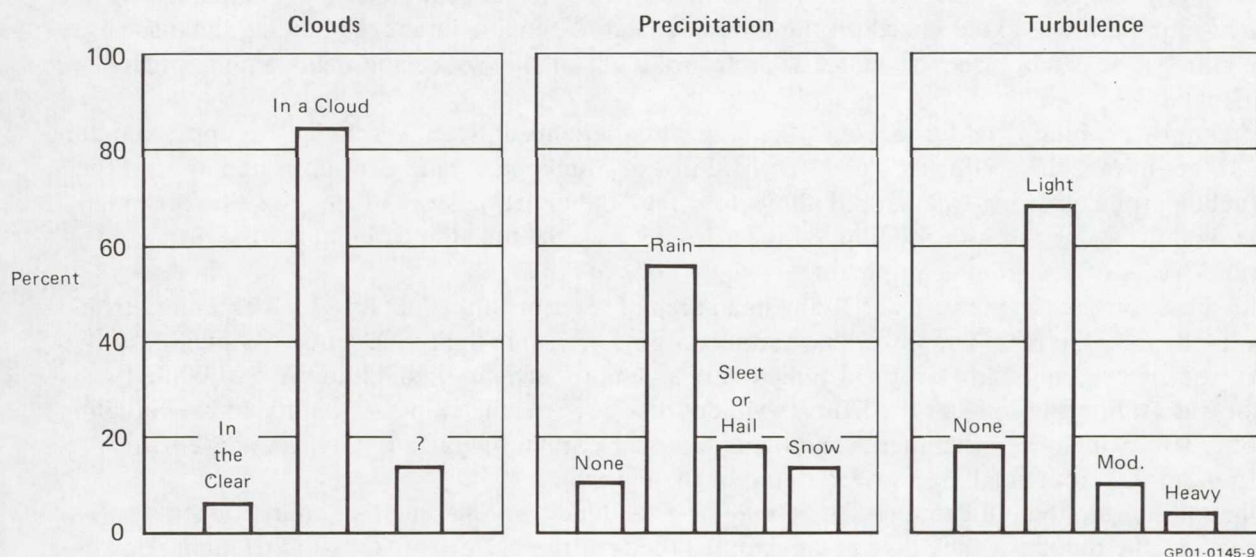


FIGURE 2
ENVIRONMENTAL CONDITIONS AT TIME OF STRIKE

PILOT DESCRIPTIONS OF LIGHTNING INCIDENTS

Some examples of both commercial and military incidents illustrating the slow buildup type of lightning strike follow. The commercial reports are taken from Reference 2.

The first case involves a Boeing 727 which experienced five discharge/lightning strikes in a 20-minute period in the Niles holding pattern at Chicago. "The discharges began at 13,000 feet with temperature -10°C , IAS 250 knots, occasional brief moderate turbulence, and occasional moderate rain mixed with ice. VHF interference existed with buildup of intensity and slight rise in pitch just before the strike/discharge. The third or fourth strike/discharge was forecast by the flight crew several seconds before occurrence using the precip-noise-pitch rise. Strikes/discharges occurred only during conditions of precipitation, and four of them during a time when precipitation rate was increasing and had reached moderate level.

Strikes/discharges were identified by a loud "boom" and a blue flash. It was a daytime flight and St. Elmo's fire was not visible. After landing, there was no evidence of damage."

In another report, a pilot indicated that he had experienced several such incidents which had always followed the same pattern. "There is first a display of St. Elmo's fire, followed by the formation of a large luminous ball on the nose, followed by a loud report, followed by the sound of a broken HF antenna whipping the fuselage, accompanied by the odor of ozone."

The reports of St. Elmo's fire and a large luminous ball, or "column of fire," on the nose is not uncommon. One pilot reported "St. Elmo's fire 20 feet out ahead of the nose." Other pilots have reported "beams like headlights" projecting out ahead of the aircraft. A Chicago pilot with over 20 years experience reported that he had experienced several of these discharges. All were associated with St. Elmo's fire prior to the electrical discharge. "The more the St. Elmo's fire prior to the discharge, the louder the boom and the bigger the burned spot where it discharges." Another pilot reported that he "actually saw the discharge flash from the aircraft nose toward a cloud."

These somewhat dated (1965) commercial pilot reports are supported by more recent military incidents which are largely unpublished. The following incidents are typical of many on file.

A fighter had been in and out of cumulus clouds and had been experiencing light turbulence. At 4000 feet, 180 knots, gear and flaps down, engine anti-ice on, the aircraft again entered clouds. Radio static increased in intensity for approximately 30 seconds. A loud snap accompanied by a bright blue flash was experienced on the port side near the engine intake. Following the discharge, the radio static disappeared. The aircraft later broke out of the clouds and made an uneventful VFR landing.

In another military fighter incident, the aircraft experienced "static discharge" at approximately 5000 feet in rain clouds during a night flight. Prior to discharge, a blue glow appeared around the refueling probe, growing to an arc of about four feet and emitting sparks three to four feet in length. The final discharge temporarily blinded the pilot. Damage to the aircraft included the outage of several pieces of electronic equipment.

In a case at sea, the aircraft was flying in an area of intermittent overcast which extended from sea level to 20,000 feet. There were no thunderstorms or visible lightning. While passing 5,000 feet, the airspeed indicator dropped to zero and a bank of advisory lights illuminated. While the pilot was attempting to reset the lights, a violent discharge occurred in the vicinity of the refueling probe, after which the instruments and lights resumed normal operation. After an uneventful carrier landing, four small holes were found in the radome.

In considering the pilot reports, there may be a tendency among scientists to discount some aspects of the reports if they do not conform to the traditional lines of scientific thought. However, since alertness and objectivity are trademarks of pilots, particularly senior commercial pilots, their reports should be accorded a high degree of credibility. It should also be recognized that most pilots have a better practical understanding of meteorological phenomena than do most desk-bound, or

even laboratory-bound scientists. Therefore, for the sake of this discussion, it is assumed that the pilots' reports are accurate representations of the actual incidents, to the best of their ability to describe them, although the reports are sometimes incomplete and leave many questions unanswered.

Notice that the pilots, both commercial and military, generally refer to this slow buildup type of event as a static discharge. Most pilots feel that when the static and corona buildup precede the flash, then it is a static discharge or a triggered discharge and not a natural lightning strike. Of the 89 experienced commercial pilots who expressed an opinion in the United Airlines survey, 66 thought there were indeed two different phenomena experienced: 1) electrical discharge of the aircraft, and 2) actual lightning. Of the remaining 23, 21 thought that the only type involving aircraft is the electrical discharge. Two pilots felt that the only type encountered is natural lightning.

In considering these pilot reports and opinions, it is apparent that usually the pilots can only report general impressions of what they remember. From their position in the cockpit, they can often only report a flash of light and an audible report, although sometimes they can tell on which side of the aircraft the flash emanated. In modern commercial jets, the pilot cannot even see the wings from the cockpit. They are certainly not in a position to know whether there was truly only one arc from the aircraft to a cloud. If the aircraft actually discharged, there would presumably be only one arc. However, in the case of natural lightning, the aircraft is only a small segment of the channel, so there must be arcs both to and from the aircraft. Therefore, in the cases where aircraft damage is reported at two different positions on the aircraft, such as nose and tail, or both wing tips, then the physical evidence indicates that the aircraft was actually struck by lightning. There are many cases, however, where damage can only be found at one point, and in many others, no damage at all is found. Therefore, the damage reports do not, in themselves, rule out some sort of static discharge event.

STATIC DISCHARGE CONDITIONS

If the pilots' contentions of static discharge are to be considered objectively, physical processes must be considered which could lead to the observed electrical behavior of the aircraft just prior to the discharge. The behavior includes increasingly intense radio static and corona (St. Elmo's fire), often intensifying to the point that the corona extends for several feet in front of the aircraft and is often accompanied by short discrete sparks up to three feet in length. An artist's concept of this electrical activity is shown in Figure 3.

If static discharge is producing these effects, it appears that mechanisms or processes must be postulated which would explain how more charge could be stored on or around the aircraft than is predicted by simple electrostatic calculations. This requirement is the crux of the issue because it can easily be shown that if sufficiently high aircraft potentials can be reached, then all of the pilot-observed phenomena can be expected to occur. Even substantial damage could be produced if potentials of several million volts could be built up on the aircraft, because discharge energy is proportional to the square of the voltage driving the discharge.

If higher than expected concentrations of charge cannot be stored on or around the aircraft, then static discharge of the aircraft cannot be the cause of the observed flash. If that is the case, then an alternative solution must be found to explain the apparent involvement of the aircraft in the production of the discharge.

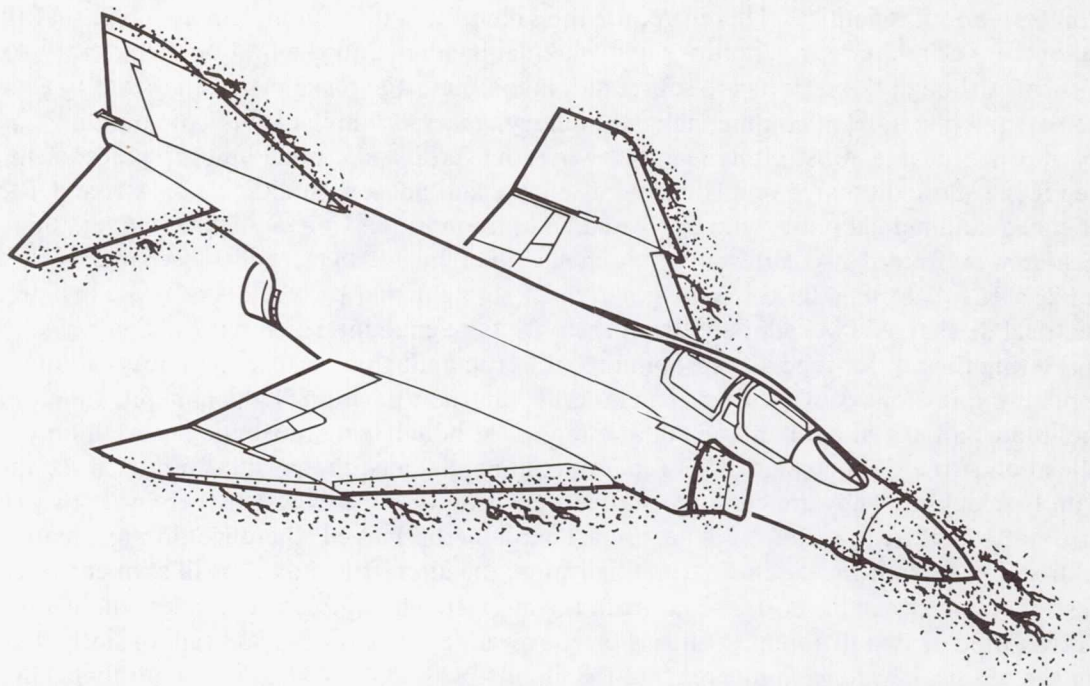


FIGURE 3
ELECTRICAL ACTIVITY DESCRIBED BY PILOTS
JUST BEFORE DISCHARGE OCCURS

GP01-0221-7

Triboelectric Charging

Triboelectric charging (the exchange of charge produced by precipitation particles impacting the aircraft) appears to play a major role in this process and, therefore, some of its general characteristics will be briefly reviewed. Certainly the process of triboelectric charging is widely known, if not widely understood. A reasonable amount of literature has been produced on the subject, much of which is well summarized by Nanevicz in Reference 8. It is accepted that charging rates are a function of precipitation particle concentration, precipitation type, effective frontal area of the aircraft and velocity of the aircraft. However, the physical mechanisms and processes involved in static electrification are not well understood.

Nanevicz gives the precipitation charging current to a vehicle by

$$i = q_p c v A_{\text{eff}}$$

where

- q_p = charge per particle
- c = particle concentration
- v = aircraft velocity

A_{eff} = effective intercepting area of aircraft.

The various parameters in the equation and their interdependencies have been studied analytically, in the laboratory and in flight, and are generally understood for the operating regimes of current aircraft. Typical values of particle parameters for an aircraft operating in the subsonic flight regime are given in Table 1 for two cloud types.

The studies of aircraft charging discussed by Nanevicz provide some insights into the basic charging processes involved. However, in practical charging calculations, Nanevicz suggests the use of the experimental results shown in Table 2. These values lead to total aircraft charging currents of a few hundred microamps, although values as high as three milliamps have been measured in flight.

TABLE 1
PRECIPITATION PARTICLE PARAMETERS

Cloud Type	q_p pico Coulomb	C_3 m
Cirrus	1 - 10	2×10^4
Thunderstorm Anvil	1 - 35	5×10^4

GP01-0221-1

TABLE 2
PEAK CHARGING RATES ENCOUNTERED
WITH KC-135 PROTOTYPE

Cloud Type	Peak Charging Rate (μ amp/sq ft)
Cirrus	5 to 10
Strato Cumulus	10 to 20
Frontal Snow	30

GP01-0221-2

The triboelectric charging rates quoted by Nanevicz for ice particles and water droplets are values measured presumably at temperatures away from the freezing level. The maximum charging rates thus quoted are for ice crystals, which do indeed produce visual displays of windshield streamering and corona. However, no violent or abrupt discharges are reported in cold ice crystals as they are in precipitation at the freezing level.

The presence of corona (St. Elmo's fire) and radio interference in moderate amounts is to be expected in precipitation, because charge will build until the potential of the aircraft causes the electric field strength at the sharpest points on the aircraft to exceed the breakdown strength of air. At the operational altitude, temperature and humidity, the breakdown potential of air may be a fraction of that at sea level. When that condition is reached, sharp points around the extremities (the highest field regions on the aircraft) will go into corona. Intense corona is a strong generator of electromagnetic radiation. Receivers operating in the proper frequency regimes will, therefore, be affected, resulting in radio interference or static.

Aircraft Electrical Parameters

It is thought, however, that the presence of the corona discharge should restrict the further buildup of charge on the aircraft beyond the level of a few thousand microcoulombs maximum, a quantity too low to produce the discharge effects described by the pilots. In Reference 5, cited earlier, Shaeffer examined the field effects of a small fighter aircraft (F-4) and a large bomber (B-52). Shaeffer estimated that a charge of 200 microcoulombs (μ C) for the F-4 and 3000 μ C for the B-52 represent the maximum charge these vehicles can hold (at sea level) before the electrical fields at the extremities become high enough for charge loss mechanisms (corona) to occur. For example, a net charge of 200 μ C on the F-4 results in a field of 20 kV/cm at the pitot mast.

Aircraft capacitance, potential, and electrostatic energy for the estimated vehicle net charge values are shown in Table 3. Since the aircraft capacitance is very small, it does not take much charge to raise the vehicle to a very significant level. The charge transferred by a current of three mA in one second ($3,000 \mu\text{C}$) raises the B-52 potential to more than two million volts. Potentials of this magnitude have been measured on research aircraft in the USSR.⁷

TABLE 3
AIRCRAFT ELECTRICAL PARAMETERS

	B-52	F-4
Capacitance	1310pF	420pF
Estimated Maximum Net Charge	3000 μC	200 μC
Vehicle Potential	$2.3 \times 10^6 \text{ V}$	$4.7 \times 10^5 \text{ V}$
Electrostatic Energy	3400 J	47 J

GP01-0221-3

The limiting factor on stored charge and potential is the breakdown strength of air at the high field regions of the aircraft. Charge loss from corona at the extremities will balance the incoming charge from triboelectric charging at some equilibrium value. It can be assumed that the first onset of radio static is concurrent with the first breakdown of air at the sharpest point (highest field region) on the aircraft. The fact that the intensity of the corona builds higher and higher over a period of several seconds indicates that the first onset of corona does not stop the buildup of charge on the aircraft. There is a limit to how fast charge can be removed from a given point by corona discharge. Therefore, it can be expected that charge will continue to build up on the aircraft until a potential is reached where enough corona sources are produced to balance the charging current.

If the aircraft were stationary, one could argue that a cloud of space charge would quickly accumulate around the corona points, reducing the field at the points, and allowing additional potential buildup on the aircraft. With an unlimited source of charge, a corona sheath could be formed around the aircraft whose outer dimensions would be such as to reduce the average field intensity at the surface of the sheath to the point that no further air ionization occurs. This situation would be analogous to the corona sheath around a lightning stepped leader. The capacitance and charge content of such a system (0.1 coulomb of charge per meter of length) could far exceed the values for an aircraft alone, and could produce the type of activity described by the pilots. However, in order to build up and maintain the corona sheath in a high-velocity air stream, continuous corona activity would have to be so intense as to continually break down virgin air as the previously ionized molecules are swept away.

The currents required to sustain the intense electrical activity described are estimated to be in the ampere range, based upon comparisons with natural lightning leader processes and with laboratory high-voltage machines. Normal triboelectric charging rates are many orders of magnitude lower than this. Normal charging processes could not produce corona extending more than a few millimeters from the surface. The charge removed by one corona pulse (about 10^{-9} coulombs) equals that normally deposited by 10-100 impacting particles.⁸ The corona pulse rate is determined by the

potential gradient at the surface, which can in turn be affected by how fast space charge is swept away by the windstream.

In order for the charging rate to reach the levels required to sustain the described electrical activity, a dramatic increase in the magnitude of one or more of the terms in the charging equation must occur. The frontal area of the aircraft is fixed and the velocities at which the activity is observed are within a relatively narrow range, though increased velocity does intensify the effects somewhat. Therefore, either the charge deposited per particle, or the density of particles must increase. There is evidence that the effects are more predominant in heavy precipitation, but the *volume* density of particles cannot conceivably increase more than one order of magnitude from the maximum values quoted in Table 1. However, the *number* density could increase dramatically if the droplet size were reduced accordingly by some dispersion mechanism. Such a mechanism would be imposed by Rayleigh instabilities if the droplets were highly charged. A liquid droplet cannot be charged beyond the Rayleigh limit or the internal electrical forces will overcome surface tension forces, causing it to break into smaller pieces. If droplets could somehow attain a very high charge content, they would disperse into a fine mist (aerosol) of charged droplets.

Chalmers⁹ cites calculations by Lueder indicating charge densities as high as 0.2 coulombs per cc of supercooled water. If such charge concentrations could exist, the maximum stable droplet size would be of the order of one μ or less because of the Rayleigh limit. Chalmers cites Twomey's calculations which indicate that a 300- μ ice crystal could be charged high enough to produce corona from its surface (70,000 V/m) by impact with a single one- μ supercooled water droplet. That same charge could presumably be imparted to an aircraft impacting the same droplet.

Nanevich quotes a normal raindrop concentration of 5×10^4 per cubic meter (Table 1) in thunderstorms. Raindrop sizes are normally considered to be in the millimeter diameter. Assuming the equivalent mass density per cubic meter of one-micron supercooled water droplets, charging rates in the hundreds of amperes can be calculated for an aircraft flying at 100 meters per second, (with a 10-meter² effective frontal area). Such high rates are difficult to accept in practice, but then so are the pilots' descriptions of electrical activity on the aircraft which we assume to be accurate.

If such high charging rates can be experienced in flight through supercooled water droplets, the right combination of atmospheric conditions must only occur on rare occasions, since such high charging rates have not been measured in any experimental programs.

TRIGGERING CONDITIONS

An alternative mechanism which might explain the observed activity is suggested by laboratory discharge phenomena and by strike incidents involving aircraft towing long conductors.

Laboratory Discharges

The observances of St. Elmo's fire extending for several feet and one- to two-meter discrete sparks around the aircraft can only be explained by aircraft potentials of millions of volts relative to the surrounding air. These effects can be demonstrated in the laboratory by attaching a model aircraft to the output of a very high voltage DC power supply, as shown in Figure 4. As the output voltage is increased sufficiently, the model will begin to emit corona at the sharpest points. If the voltage is raised higher, the corona will intensify and more corona points will be produced. As the potential is raised still further, small discrete instantaneous discharges into the air may be produced and the model may be engulfed in a glow of plasma, particularly at reduced pressures. If the voltage is raised further, eventually a loud spark discharge will be produced to (or toward) the nearest grounded object. Figure 5 illustrates this process for a test where voltage was limited to 100 kV.

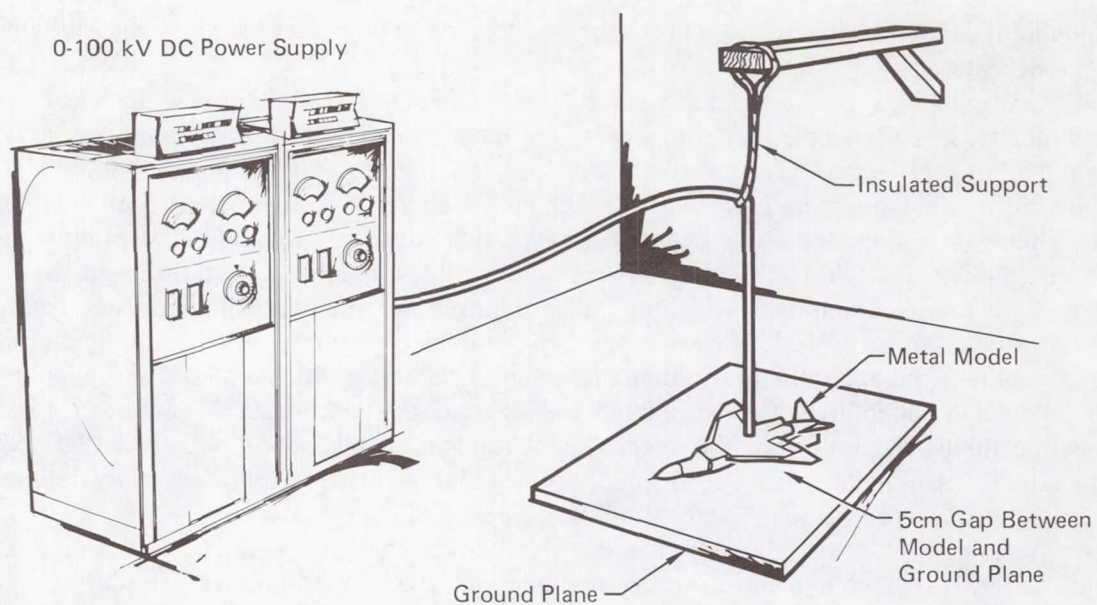


FIGURE 4
AIRCRAFT CORONA EXPERIMENTAL ARRANGEMENT

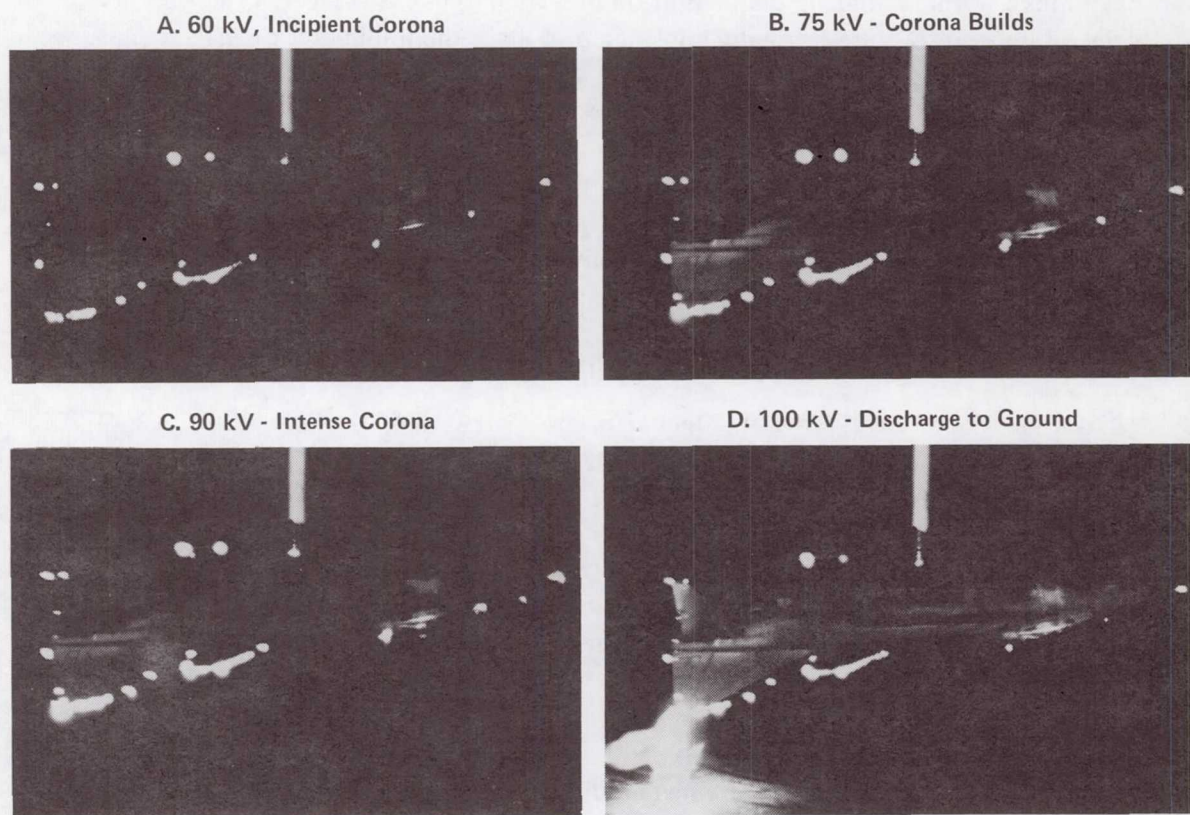


FIGURE 5
CORONA FROM MODEL AIRCRAFT IN LABORATORY EXPERIMENT

In this situation, there is an unlimited amount of charge available to raise the model to the high potential level and to maintain it there despite the corona discharge process. The actual charge required for this laboratory experiment is very small; about a milliamp of current is required to maintain the heaviest corona prior to discharge (assuming a maximum voltage level of 75-100 kV). For an aircraft in flight, however, the corresponding current might be in the hundreds of milliamp range or higher, as mentioned previously.

Based on the similarity of the observed aircraft electrical activity to the DC power supply case, and because of the difficulty in postulating an extraordinarily large amount of static charge around the aircraft in the presence of aerodynamic flow, a triggering process which approximates the power supply condition is desirable to explain the observed electrical activity reported by the pilots.

Aircraft Towing Long Conductors

An interesting series of flight incident reports involve electrical discharges to Navy aircraft towing gunnery targets on the end of long steel cables. The pilot reports bear a remarkable resemblance to the commercial incidents described previously, except for the weather conditions at the time of the strike. In these cases, the reports of outside observers are available because the incidents involve aircraft flying in formation with the tow aircraft at the time of the event. The incidents are unique in that they involve aircraft towing long electrical conductors extended as far as 15,000 to 18,000 feet behind the aircraft. At least ten such events have been reported in the last few years.

In the first case to be examined, the tow aircraft and the chase plane were flying at 3,000 feet in light rain, but they were flying toward a thundercloud. The pilot in the lead plane reported "static electricity" discharging from his refueling probe. His wingman also observed discharges emitting from the front of the drop tanks and the *forward* section of the vertical stabilizer on the lead aircraft. Approximately 20 seconds later the discharges were terminated by a "large electric arc discharge from the refueling probe." The wingman noted that the discharge caused the aircraft to have a "halo effect" with smaller static discharges emitting from all surfaces of the aircraft. (This halo effect following a discharge has also been observed in laboratory experiments.¹⁰) The incident was reported as static electrical discharge with lightning strike unlikely.

In another case, the lead plane was observed to experience St. Elmo's fire initially on the nose refueling probe. The intensity increased, with arcing noted up and down the probe by the pilot. "The aircraft soon became engulfed with the static discharge which immediately resulted in a large explosive sound." The pilot experienced minor shock but there were no other problems.

In another multiple aircraft incident, both the crew members of the lead aircraft and the chase plane pilot observed a six- to eight-foot blue-white electrical charge buildup forward from the radome tip. Approximately ten seconds later, a brilliant flash of light and a loud report occurred. Lightning was not observed to strike the aircraft by the chase pilot. He observed that the arc discharge *from* the aircraft, through the towed conductor.

The similarity of the electrical activity described during the commercial incidents which occurred while flying through freezing precipitation and the military incidents involving long trailing conductors is inescapable. The similarity leads to the consideration that ionization or charging processes may be taking place in the wake of aircraft flying in precipitation which could produce the same effect as a trailing conductor. In order to show that such a highly conducting wake might be produced, the electrical processes involving clouds, ice and water in the freezing zone will be reviewed.

Electrification Processes in Freezing Rain

It was emphasized earlier that the reported electrical discharges generally occur in precipitation at or near the freezing level. The investigator might reasonably question what is unique about this region compared to other precipitation zones, i.e., what extraordinary charging activity could be produced in this environment?

In studies of cloud charging mechanisms, it is notable that the presence of supercooled water drops is an essential element in many of the viable theories of cloud charging. These theories, which closely predict the charging rates and polarities actually observed in clouds, involve freezing, glazing, or riming processes where the latent heat of supercooled water droplets is released upon impact with ice particles.

Pure water in small quantities has a low probability of freezing spontaneously until its temperature is lowered to -40°C , the Schaefer temperature¹¹. However, microscopic analysis of hailstone structure shows that the layers of riming and glazing indicate that most supercooled droplets are frozen at temperatures lower -15°C . As shown in Figure 1, the weather statistics for lightning strike incidents indicate that most strikes to aircraft occur at temperatures between -10°C and $+1^{\circ}\text{C}$. Griffiths¹² found that corona currents cannot be drawn from ice crystals colder than -18°C because the surface conductivity drops too low below this temperature.

The electrical properties of water and ice, particularly in turbulent mixture, are extremely complex. No definite laboratory experiments have been conducted which provide a solid basis for confirming or disproving the various charge separation theories. Chalmers¹³ provides an extensive review of experiments investigating the electrical effects of freezing, riming, glazing and the effect of electrical fields on freezing. The experiments he reports include the work of Workman and Reynolds, Mason and Maybank, Evans and Hutchinson, Latham and Mason, Lueder, and Twomey.

Chalmers notes that in many of these experiments with supercooled water droplets, extraordinary charge exchange rates are measured. He cites the calculations of Lueder⁹ which indicate that supercooled water can yield 0.2 coulombs of charge per cc. In experiments where ice crystals as well as water droplets are present during the freezing process, exceptionally high charging rates are observed which tend to support Lueder's calculations. Chalmers also notes that the many variables present in these experiments make it almost impossible to model them analytically. These variables include the presence of impurities, air bubbles, mixed physical states, bursting and splintering of ice crystals, and many others. Because of these many variables, it has been very difficult to develop theories describing a consistent pattern of charging behavior in the complex freezing zone. The many experiments which have been attempted, both in the laboratory and aloft, have only shown that very substantial charging rates can be experienced in this region.

In 1972, Dawson¹⁴ briefly reviewed the principal charging mechanisms, noting those that could in some way be involved in aircraft electrification mechanisms. He notes that the most interesting aspect of electrification studies involving ice and water is not that charge separation can readily occur, but that charge can be separated in so many ways. He expresses surprise that aircraft workers assume that the highest charging rates are in frozen ice crystals, rather than in the freezing zone where the most active charge mechanisms are known to exist.

The major charging mechanisms that could in some way be involved in aircraft electrification include:

- a. Thermoelectric effects - Whenever two surfaces of ice of similar impurity content at different temperatures come into temporary contact, charge transfer occurs and a potential difference is developed between the surfaces. Thermoelectric effects may result from asymmetric rubbing contact or breakup of fragile crystals. Dawson notes that the most important

source of temperature difference between ice crystals in a cloud results from the latent heat of fusion released by the freezing of supercooled drops colliding with ice crystals, thus intensifying the thermoelectric effect as the warmed crystals collide with colder ones.

- b. Freezing potentials - Rain and cloud drops are dilute solutions of salts, and when dilute solutions freeze, they produce freezing potentials, i.e., the ice becomes charged with respect to the water. Typical salt concentrations in coastal waters are in the right range to result in very potent charging rates.
- c. Riming - Surfaces undergoing riming with large enough supercooled drops become highly charged by a mechanism which has never been fully explained. Riming always produces charging of the rimed surface, including aircraft.
- d. Glazing - Chalmers¹³ notes that electrical effects accompanying glazing are complicated by effects due to water and ice impacts. For water which is not supercooled, it has long been known that impact with ice gives a positive charge to the ice and a negative charge is carried off. Chalmers¹⁵ notes that Meinhold found a strong negative charge to be produced on the surface of an aircraft flying through a cloud of supercooled water droplets, while glazing was taking place. However, no further information is available on that 1951 German work.
- e. Electrical effects of melting - Chalmers decries the lack of definitive experiments on the electrical effects of melting, noting that the experiments which have been conducted imply that the process is sensitive to impurities, among them carbon dioxide. The experiments also suggest that the presence of airflow may be a large factor in explaining the large charging rates observed in clouds at the melting level. If, for example, molten snow forms water drops big enough to be shattered by an air stream, the actual process would correspond to that of splashing, a process known to generate large charge transfer rates.

The point of this review is to establish that varied and sometimes surprisingly intense charge exchange mechanisms can be active in a field of suspended ice crystals and supercooled water droplets. For the sake of the following discussion, one might envision that the particles represent an electrically volatile medium with a complex mixture of mobile and relatively immobile charge carriers; sort of a quasi-plasma. (In addition to the ice and liquid particles, a high concentration of microscopic particles and ionized vapor is probable).

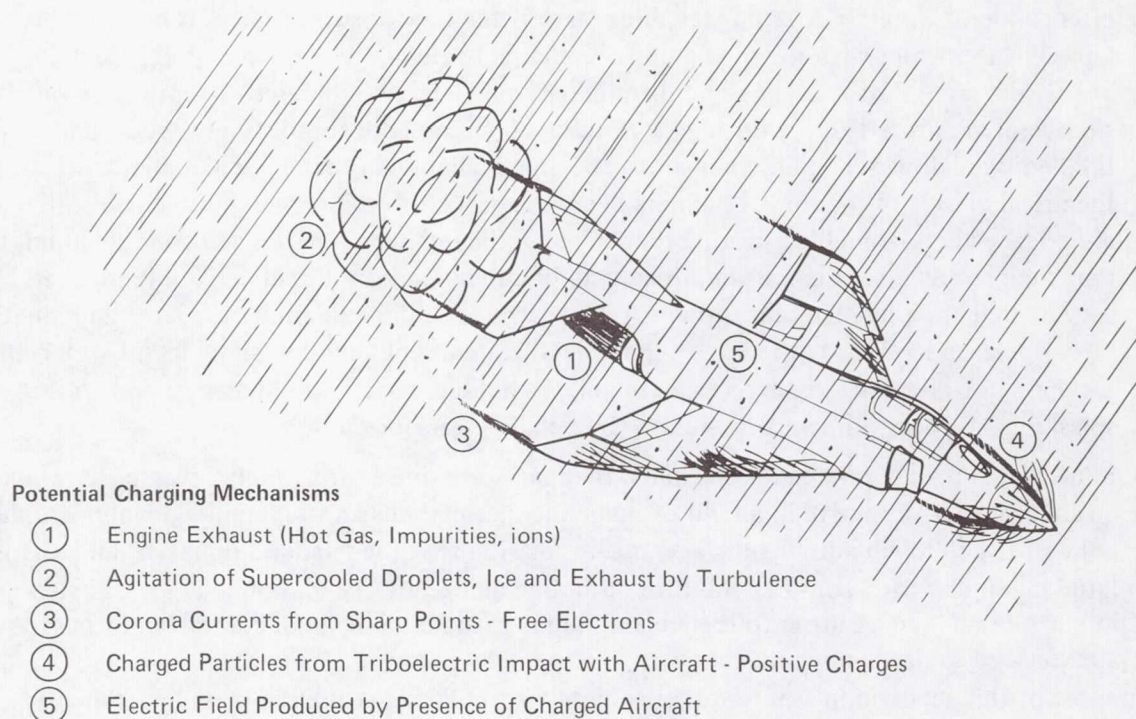
In support of this scenario, it is interesting to note that radar signatures of rain clouds display what is called the "bright band" phenomenon at the freezing level. Chalmers¹⁶ reasons that the reflections are more intense at this level because (a) water reflects better than the ice above, and (b) the water drops are not dropping as fast at this level as they are at lower levels. However, pilots know that there is usually some turbulence at the freezing level (an interesting fact in itself), leading to the conclusion that there is always charge exchange taking place there. That means that there is also a higher concentration of ionized particles and vapors there, including possibly ice particles emitting corona, which could increase the reflectance of electromagnetic waves. Perhaps, then, the radar "bright band" phenomenon might be an indicator of the electrical volatility of this cloud region (which may be more intense at some times than at others). Unexplained radar bright zones are also observed in thunderclouds.

Although there may be intense charge exchange activity going on at the freezing level in apparently stable cloud systems, there is no visible electrical activity because there is no effective mechanism for large-scale charge separation. The strong updrafts present in thunderheads are not present in the cloud systems being considered, so they exhibit only weak concentrations of net charge.

Aircraft Passage Through Freezing Rain

Now, it is interesting to speculate about the possible effects of a large, highly-charged mass of metal, passing at high speeds through this electrically-volatile field of suspended ice crystals and supercooled water droplets, leaving in its wake a turbulent exhaust of hot gasses and contaminants.

As the aircraft passes through this freezing layer, it introduces several perturbing effects, as illustrated in Figure 6. First, it produces intense turbulence in its wake, generated by both aerodynamic and engine exhaust effects. The turbulence will persist for periods up to several minutes, and will expand into a large volume around the flight path. This turbulence, which is a function of aircraft velocity, can be expected to intensify the charge exchange processes in the wake of the aircraft, as it mixes and agitates the various ingredients in the wake.



GP01-0221-10

FIGURE 6
PASSAGE OF CHARGED AIRCRAFT THROUGH FREEZING RAIN

The second effect is produced by the high electric field surrounding the aircraft. Through conventional triboelectric charging, the aircraft will build up a negative charge of at least hundreds of kilovolts. Thus, the presence of an intense electric field is assured, both at the aircraft/particle impact interface and in the regions around the aircraft where charge exchange between particles is taking place. Chalmers¹⁷ cites experimental evidence showing that charge exchange mechanisms can be intensified by a factor of 100 in a 30-kV/meter field. The high potential of the aircraft might also serve to effectively enlarge its aerodynamic size in the charged environment by accelerating charged particles already present at the freezing level toward or away from the aircraft, depending upon the polarity of charge on the particle. One effect would be to add to the turbulence produced.

Another perturbing influence is the presence of the aircraft as a catalytic agent in the charge exchange process. The results of several laboratory experiments noted by Chalmers were discounted as being useful in the development of cloud physics theories because of the presence of apparatus in the test volume which was thought to influence the results. For example, he reports¹⁸ that Pruppacher investigated the effect of an electric field in causing freezing of supercooled drops. His conclusions were that an effect exists only when there is a solid surface present, and so electric fields are not a factor in actual clouds in the atmosphere. For the aircraft case, however, this effect may be important.

Another perturbing effect is the introduction of turbulent hot exhaust gases containing various chemical contaminants into the freezing zone. The hot gases can produce charge exchange by melting frozen particles and can greatly intensify the thermoelectric effect by providing a source of warm particles in a freezing environment. The presence of contaminants can intensify the charging rates produced by melting. Also, contaminants such as sodium along with low pressure wake regions, can enhance photoionization processes which are involved in streamer formation¹⁹.

Finally, the coulomb repulsion or attraction of the aircraft on the particles may introduce a charge separation mechanism. The polarity of charge is not randomly distributed on all particles. Rather, there is a definite categorization of charge according to particle size and state. For example, ice particles tend to be charged positive and water particles negative. Larger ice particles are positively charged and small ones negatively. (The counterflow of these particles produced by the aircraft potential field may be another intensifying factor in the charging process.) However, whether there might be a net charge separation effect over long distances is difficult to determine. The fact that particles will be charged differently according to size and type implies, however, that there will be some net movement and separation of charges, however small that might be. If enough accelerated charge exchange occurs in the aircraft wake, however, large-scale charge separation may not be required to produce the circumstances necessary to trigger a discharge through the freezing layer.

Ionization Levels

As mentioned earlier, the effects of ionization levels in the aircraft wake produced by the engine exhaust were investigated⁵ as a possible lightning triggering mechanism. It was concluded that the ion concentrations in the exhaust are too low, in themselves, to have an effect. In this case, however, the exhaust ions are supplemented by the ionized corona streaming from the charged aircraft, the charged particles resulting from collision with the aircraft, and the ionized particles and vapors resulting from the various charge exchange mechanisms produced in the turbulent wake.

Table 4 lists charge concentration values in various media as reported by Shaeffer⁵ in his study of engine exhaust ionization levels.

Using Nanevicz's values from Table 1 for particle charge and density, charge concentrations in thunderstorm anvils are calculated to be in the 10^5 - 10^7 charges/cm³ range, one to two orders of magnitude higher than the values quoted by Shaeffer for engine exhausts. However, these charges are not free electrons.

These values can be compared to ground-based measurements of charges on falling rain droplets cited by Chalmers¹⁸. Charge densities of 2×10^6 per cm³ were measured by collecting falling rain droplets. However, related experiments showed that with a 30-kV/m field applied, drop fragmentation occurred resulting in 2×10^9 charges per cm³ of water collected.¹⁷

TABLE 4
A COMPARISON OF ELECTRON CONCENTRATION VALUES

Electron Concentration In	Quantity (e/cm ³)
Free Atmosphere	10 ⁻¹⁰ to 10 ³
Jet Exhaust	10 ³ to 10 ⁵
Rocket Exhaust	10 ¹²
Lightning Streamer Head	10 ¹²

GP01-0221-4

Chalmers also cites the work of Twomey and of Lueder⁹ (mentioned earlier) regarding charging processes involving ice crystals and supercooled water. Twomey observed that an ice particle cannot hold a charge greater than that which would give it a surface potential gradient of 70,000 V/m if it were spherical; he pointed out that a 300-micron ice particle could be charged to more than that by a single impact with a one-micron supercooled water droplet, based on Lueder's figure for supercooled water of -0.2 coulomb per cc (1.2×10^{18} charges/cm³). Using these values, Twomey calculated values for charge exchange in thunderstorms which agree quite well with measured values. If Lueder's value of 1.2×10^{18} charges/cm³ of supercooled water is correct, the ionization levels in the agitated wake of an aircraft flying through supercooled droplets could conceivably approach or even exceed the levels of ionization in a lightning streamer.

In regard to the earlier mention of the bright band radar signature at the freezing level, plasma physicists use the following simple equation to determine the penetration frequency of RF beams into plasmas, where f is the penetration frequency and n is the ion concentration in charges/cm³.

$$f = 9000 \sqrt{n}$$

Weather radars operate around 2.9 gigahertz or 2.9×10^9 hertz. Solving for the ion concentration necessary to reflect this frequency,

$$n = \frac{f^2}{8.1 \times 10^6} = \frac{8.4 \times 10^{18}}{8.1 \times 10^6} \approx 1 \times 10^{12} \text{ ions/cm}^3$$

If the bright band phenomenon is due to ionization at the freezing level, then ion concentrations of at least 10^{12} /cm³ must exist.

The contribution from corona currents flowing from the aircraft might also be considered as significant. Discharge rates as high as three mA were reported by Nanevich⁸ in ice crystals. One might conservatively estimate that values 10-100 times this level might be experienced flying through supercooled droplets. A discharge current of 100 milliamps from a few discrete corona points would bleed 6×10^{17} free electrons per second into the wake. At a speed of around 200 knots (10⁴cm/sec), 6×10^{13} electrons per centimeter of path length would be discharged. The triboelectric particles producing the charge on the aircraft would deflect off of the aircraft into the slipstream, separated by some distance from the corona stream, thus preventing instant charge neutralization.

Air Conductivity

Although very high charge densities can be postulated in the wake, unless the charges are mobile enough to move freely in an external field, the wake cannot act as a conductor. The charges are essentially frozen in a dielectric medium. The conductivity of air is normally lower in a cloud than in open air because the moisture droplets capture the free vapor ions and prevent them from moving in the external field. It must be assumed, therefore, that the same condition will exist in the wake and the charges will be attached to relatively immobile ice particles or water droplets.

Under laboratory conditions, the electrical breakdown of a block of solid dielectric material containing a large concentration of frozen internal charges will occur at a lower applied voltage than a similar block of material with no charges imbedded. The fields around the individual charges add to the externally applied field, resulting eventually in a spark discharge through the volume of material as the applied voltage is increased. For example, Griffiths¹² demonstrated a 20 percent reduction in the external field required to produce corona from ice crystals if they were initially charged to nominal values.

In order to further enhance the conductivity in the wake, the charge density must be so high that significant free charges are constantly being liberated by corona from ice and water particles. This condition could conceivably exist based upon Twomey's calculation that 300μ ice particles could be charged to corona threshold levels (70,000 V/m) by a single impact with a 1μ supercooled water droplet. Dawson¹⁹ reasons that this process may result in a dynamic equilibrium of corona generation and reattachment which could explain the unusually high conductivities measured by Evans (Arizona) in Dropsonde measurements of clouds at the freezing level. In this environment, the propagation of high voltage streamers from the aircraft may be significantly enhanced.

Streamer Generation

The physical mechanisms leading to spark discharges involve the generation of streamers from an electrode into the surrounding atmosphere or toward a nearby concentration of charge. The streamers are weakly ionized filamentary channels which are produced when the charge density at a point passes a critical level. Streamers are initiated from a Townsend avalanche processes which relates to the buildup of a space charge in an applied external field.²⁰ When the charge density reaches the critical level, photoionization of the adjacent air in the direction of the applied field allows the charge volume to grow in that direction. The requirement for propagation is related to the ratio of field strength to pressure, E/P .

At sea level, field strengths of about 30 kV/cm are required to initiate streamers, but at altitudes of several thousand feet, the field strength required is less. Once a streamer is formed, the electric field required for continued propagation is much smaller. Phelps²¹ has shown that an ambient field of 7 kV/cm is sufficient for continued streamer propagation at sea level. Most lightning researchers feel that natural lightning can be triggered by large scale ambient fields of 3-4 kV/cm.¹¹ Streamers may gain energy from the ambient field. However, they can propagate in zero field regions if they gained sufficient initial energy.²²

Since streamers, once initiated from the aircraft, can propagate in low field regions, any amount of free charge in the wake added to the external field gradient might allow streamer propagation through the wake in relatively low ambient fields. The streamer would then provide a sufficient concentration of free electrons to act as a conductor and compress the external field.

Streamers, unlike corona pulses, are not short-lived pulses. They propagate at a rate of a few tenths of a meter per microsecond as long as charge is available at the source to sustain the field at the tip at the level needed to continue propagation. In order for streamering activity to reach the levels necessary to produce the observed effects, it would be necessary for the potential of the aircraft to be sustained at a high level by triboelectric processes and for the charge density and distribution in the wake to be high enough to allow continuous streamer propagation from the charged aircraft over a period of several seconds. An ambient electric field would aid the process.

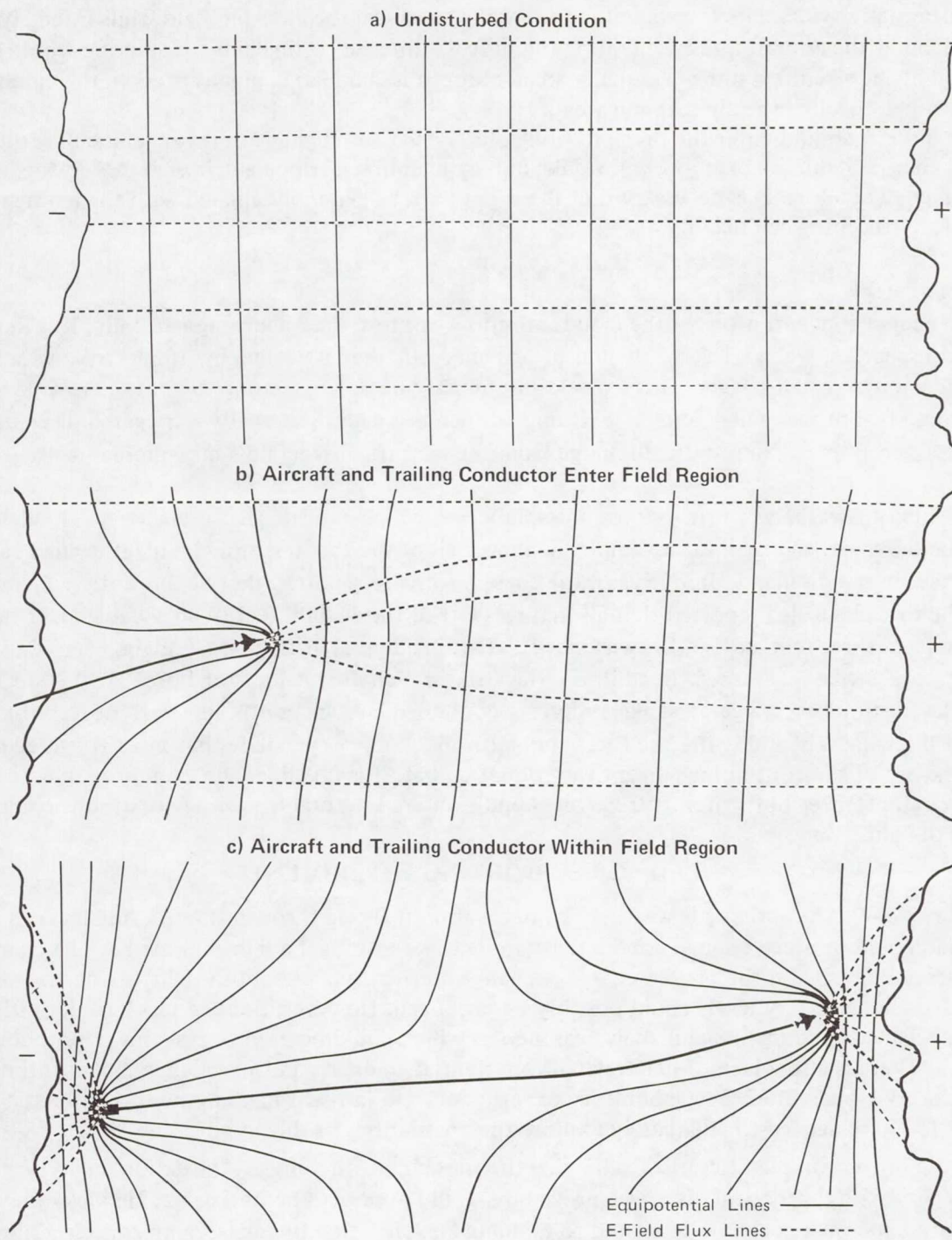
INTENSIFIED FIELD DISCHARGE HYPOTHESIS

Potential gradients in rain clouds are probably on the order of a few thousand volts per meter. Airborne measurements in stormy clouds have shown that large localized horizontal gradients exist at the freezing level.²³ Although they are very rare, a few measurements have been made in non-stormy clouds showing that horizontal gradients also exist there.²⁴ It is reasonable to expect that pockets of charge should exist in rain clouds since the precipitating droplets carry charge (usually of one polarity) to earth, leaving a net charge in localized regions of the cloud. Potential gradients normally measured in electrically active clouds (visible lightning) are in the tens of kilovolts per meter, with at least one measurement of 340,000 V/m at the surface of an airplane just before it was struck by lightning.²³ However, the principal concern here is nonstormy clouds since most of the slow buildup of events occur where no visible lightning is present. It is assumed that the presence of potential gradients on the order of 20 to 30 kV/meter or higher will signal the production of some natural lightning. Therefore, we will consider ambient potential gradients on the order of 10 kV/m or lower.

Pierce²⁵ has investigated the requirements for initiation of lightning to elevated structures and other man-made disturbances of the atmosphere. He concluded that the usual values of ambient electric fields are on the order of 10 kV/meter to trigger lightning and the voltage discontinuity between the object initiating lightning and adjacent atmosphere is about 10^6 V. He concludes that structures must be at least a few hundred meters high to trigger lightning.

Consider now the case of an aircraft towing a gunnery target at the end of a 15,000-foot (5,000-meter) steel cable. If the aircraft and target enter a region with a 10-kV/meter gradient with the flight path aligned with the maximum gradient, the long tow cable will essentially short out the gradient field, concentrating the equipotential field lines at the front end of the aircraft. This effect is illustrated by the sketch in Figure 7. If the full length of the 5,000-m cable entered the field region, a 50-million volt potential would be developed at the ends of the cable. Long before such a potential could be established, however, intense corona currents would develop at the aircraft with other manifestations of high electric fields such as streamering and periodic short spark discharges. In fact, the exact conditions described by the pilots could be expected.

In such a case, the intense field at the aircraft would be in the direction ahead of the aircraft. Therefore, the corona and streamering would be projecting ahead of the aircraft as described. Recall the tow-target incident where the chase pilot described corona and streamering issuing from the forward edge of the vertical stabilizer, rather than the trailing edge. As the potential increases further, it is reasonable to expect that leaders will emanate from the aircraft forward the charge centers, resulting in an abrupt discharge between the pockets of atmospheric charge which generated the field, with the aircraft and cable constituting the principal current path.



GP01-0221-11

FIGURE 7
ELECTRIC FIELD COMPRESSION BY AIRCRAFT WITH TRAILING CONDUCTOR

Now it can be seen how an aircraft with a conductive wake in freezing precipitation could trigger a lightning strike. If the conductivity of the wake is sufficiently enhanced by corona and

streamering activity, charges can migrate in the wake to cancel the external field, thus intensifying the field at the aircraft and accelerating the process. Intense corona and streamering would be produced at the aircraft leading eventually to an abrupt discharge as charge centers in the cloud are discharged through the aircraft and wake.

If the aircraft should enter the precipitation zone so that the flight path is perpendicular to the gradient field, no unusual charging will result; only conventional triboelectric charging effects will be observed. Therefore, it is necessary that the flight path be generally aligned with the ambient field before triggering can occur.

Discharge Effects

If the charge concentrations in the clouds are too weak to trigger lightning naturally, it is likely that the discharges, when triggered, would be less energetic than a normal lightning strike which is energetic enough to self-trigger. There would presumably be no continuing currents or restrikes, but there would be both arc entry and arc exit points since this event is actually a triggered discharge within a cloud rather than a static discharge from the aircraft. Fitzgerald's measurements¹ suggest this view.

There are other aspects of the pilot reports, however, which indicate that even triggered lightning may produce severe damage. For example, in almost all of the tow target incidents, the steel cable was parted by the discharge. In one case, the chase pilot who reported that he did not see lightning strike the tow plane also reported that all that was left of the 18,000 feet of steel cable after the discharge was "a three-mile puff of brown smoke"! This incident is difficult to explain, even if a full-threat natural strike is assumed. In addition, the strike which downed an Air Force KC-130 in 1978 fit the description of a triggered strike and yet it contained enough continuing current to burn a hole through the wing skin and ignite the fuel vapors. Brook et. al.²⁶ speculate that most triggered strikes to ground are of the continuing current variety. Of course, it is possible, and even probable, that in certain circumstances both aircraft triggering conditions and natural triggering conditions could be right at the same time.

NEED FOR SUPPORTING EXPERIMENTS

The crux of this hypothesis is whether or not an aircraft flying through the freezing layer in a rain cloud could produce enough conductivity in its wake to trigger a lightning strike. The charge concentration levels and the proven charge exchange mechanisms present in the freezing zone indicate that the necessary levels could possibly be produced. However, there is a lack of definitive charge exchange experiments and analytical models which could be used to test this hypothetical situation. There is also a lack of data related to potential gradients and space charge concentrations in nonstormy clouds. Both new laboratory experiments and in-flight measurements conducted in the freezing level are needed to adequately explore the possibilities of this hypothesis.

Because of the complexities of the charging theories and of the physical situation, analytical modeling of the hypothetical discharge procedure would appear to be untenable. However, new laboratory experiments can be suggested to evaluate air ionization under freezing zone conditions. Excellent opportunities for in-flight measurements and triggering experiments are afforded through the current Air Force and NASA lightning research flight programs.^{27,28}

Since the lightning mishap statistics indicate that the bulk of aircraft strikes occur in freezing precipitation with no thunderstorm activity present, it seems reasonable to orient at least a part of the flight programs to seeking out the freezing zone in nonstormy precipitation clouds. Flights at different velocities and in different synoptic conditions should produce electrical charging conditions

and, perhaps, discharges that could be interpreted as lightning. Ideally, the research aircraft should be equipped with field mills to help discover the highest field regions and align the flight path with them.

Pilot reports from the UAL study indicated that they felt that aircraft velocity was an important factor in producing the discharges. In fact, some pilots were sure that they could prevent a discharge by throttling back the engines when the corona and static conditions begin to build. Of course, this action affects most of the parameters postulated as ionization mechanisms. Aircraft potential, wake turbulence and engine exhaust levels are all affected. Therefore, flight experiments should be conducted over a wide range of aircraft velocities.

Flight research planners might also want to consider equipping their aircraft with target towing equipment allowing them to tow a trailing conductor up to 20,000 feet behind the aircraft. These measures might be more logical (and safe) than flying into active thunderstorms in an attempt to experience lightning strikes to the aircraft.

Another useful addition to the flight programs would be to equip them for electrostatic charging measurements similar to those made by Nanevich and co-workers in their research flights. Aircraft charging rates need to be measured in the freezing zone, regardless of whether discharges are produced or not, for P-static design information. The other instrumentation already on the aircraft needs to be adequate to measure external field gradients and parameters of discharges if they should occur.

It was noted in the UAL report that the new static dischargers being used on modern aircraft may be effective in reducing the static charge buildup and possibly the frequency of violent discharges. If so, the fact that the new dischargers maintain the aircraft at a lower potential could affect the postulated intensified charging processes since the presence of an electric field was a possible influencing factor. At any rate, the effect of static dischargers could also be investigated in the flight programs. It would be desirable to conduct flights with the vehicle potential maximized by incorporating corona suppression measures (no static dischargers and coating sharp points at extremities with insulators) and with corona maximized with multiple dischargers installed for minimum vehicle potential.

CONCLUDING DISCUSSION

The statistics of environmental conditions existing at the time of lightning strikes to aircraft indicate that the majority of incidents occur in clouds containing precipitation at the freezing level. A survey of UAL and USSR incidents reveal further that most of the reported incidents are not in the vicinity of thunderstorms. Most often there is no visible lightning in the area before the incident.

Both military and commercial pilots report that some electrical discharges do occur without warning, but usually only near thunderstorms. Most discharges are preceded by a buildup of electrical corona and radio interference. The pilots generally describe the latter variety as a static discharge, rather than a lightning strike. Very similar electrical discharge activity is described in strikes to military aircraft towing long conductors.

Although scientists have long discounted the pilots' static discharge contentions, the similarity of the described incidents to certain high-voltage laboratory experiments prompted re-evaluation of the in-flight reports. An examination of the triboelectric charging and discharging mechanisms led to the conclusion that charge loss mechanisms must limit the charge buildup on the aircraft to potentials much lower than those that would be required to produce the observed corona and sparking activity, unless dramatically higher charging rates could be postulated.

In the search for alternative charging mechanisms which would be consistent with the pilots' reports, it was noted that extraordinary charge exchange rates can be produced in mixtures of ice particles and supercooled water droplets. Such an environment is sometimes present at the freezing level in precipitation clouds where the discharges usually occur. It was therefore postulated that the passage of a highly-charged aircraft might intensify the concentration of ionized particles and vapors in the wake of the aircraft to the point that the condition simulated the Navy aircraft towing a long conducting cable. In both cases, intense electrical activity at the aircraft preceded a violent (or at least abrupt) discharge.

In both cases, it was postulated that weak pockets of charge exist in the clouds of insufficient potential to trigger lightning naturally. Relatively weak gradient fields (as low as a few thousand volts per meter) are sufficient to generate potentials at the aircraft which could produce the observed activity, if the flight path is aligned with the field. Further increase in the potential at the aircraft would logically produce a large spark discharge to the air or to a charged region of the cloud through streamer processes.

It has been shown by laboratory experiments that bright loud discharges can be produced at fairly low energy levels. Even the energy stored on a large aircraft at two million volts (3400 joules, Table 3) is sufficient to produce noticeable surface effects such as pitting and loud discharge. If high enough potentials are generated by the trailing conductor to trigger a discharge, low-level damage is certainly possible and even severe damage may be produced by unexplained processes.

In summary, the following observation is offered. Lightning is a spectacular phenomenon and is logically associated in our minds with thunderstorms where it is usually observed. Consequently, when lightning strike incidents are reported by pilots, regardless of the weather conditions they report at the time of the strike, scientists and researchers still tend to associate the report with thunderstorm activity. However, it is just as true, though not as obvious, that strange and unusual electrical activity can also be produced in nonstormy clouds. Frictional charging mechanisms are constantly being manifested around us in our daily lives. It should not be surprising then, that unusually intense electrical activity can be generated under certain unusual atmospheric conditions.

Apparently, some number of the reported strikes are undeniably natural lightning. These unpredictable incidents appear to be unavoidable, although some other triggering mechanism may eventually be discovered to explain their frequency of occurrence. These strikes appear to be more lethal than the slow buildup variety. It is interesting that flight statistics⁶ show that about 20 percent of lightning incidents result in some damage and the UAL pilots² estimate that 20 percent of the strikes are the abrupt thunderstorm type.

Assuming for the time being that nothing can be done about the natural lightning events, immediate attention should be focussed on the possibility of triggering lightning in freezing precipitation. It is strongly recommended that future flight programs be structured to investigate the electrically fertile freezing zone of nonstormy rain clouds. If it is shown that discharges can be produced by flight in the freezing layer, then the statistics of aircraft/lightning mishaps may need to be revised and the discharge threat redefined to account for the triggered discharge parameters. Perhaps, more importantly, new flight restrictions can be defined or wake neutralization schemes might be developed to prevent this type of discharge and greatly reduce the lightning strike incidents to aircraft.

REFERENCES

- 1 D. R. Fitzgerald, "Probable Aircraft Triggering of Lightning in Certain Thunderstorms," *Monthly Weather Review*, 95 (1967), p. 835
- 2 H. T. Harrison, "UAL Turbojet Experience With Electrical Discharges," *UAL Meteorology Circular No. 57* (January 1967)
- 3 M. M. Newman, J. R. Stahmann, J. D. Robb, E. A. Lewis, S. G. Martin, and L. V. Zinn, "Triggered Lightning Strokes at Very Close Range," *J. Geophysical Research*, 72 (1967), p. 4761
- 4 R. P. Fieux, C. H. Gary, B. P. Hutzler, A. R. Eybert-Berand, P. L. Hubert, A. C. Meesters, P. H. Perroud, J. H. Hamelin, and J. M. Person, "Research on Artificially-Triggered Lightning in France," *IEEE Transactions on Power Apparatus and Systems*, Volume PAS-97, No. 3 (May-June 1978), pp. 725-733
- 5 J. F. Shaeffer, "Aircraft Initiation of Lightning," 1972 Lightning and Static Electricity Conference, USAF Report AFAL-TR-72-325 (December 1972)
- 6 F. A. Fisher and J. A. Plumer, "Lightning Protection of Aircraft," NASA Reference Publication 1008 (October 1977)
- 7 O.K. Trunov, "Conditions of Lightning Strike on Air Transports and Certain General Lightning Protection Requirements", 1975 Lightning and Static Electricity Conference, Culham Laboratory, England. April 1975
- 8 J. E. Nanevicz, "Static Electricity Phenomena: Theory and Problems," Conference on Certification of Aircraft for Lightning and Atmospheric Electricity Hazards, ONERA-Chatillon, France (September 1978)
- 9 J. A. Chalmers, *Atmospheric Electricity*, Pergamon Press, Second Edition, Oxford (1967), pp. 419-420
- 10 P. J. Sharp, "Static Electrification of Windscreens and Canopies," 1975 Lightning and Static Electricity Conference, Culham Laboratory, England (April 1975)
- 11 J. Latham and I. M. Stromberg, *Lightning-Volume 1, Physics of Lightning*, edited by R. H. Golde, Chapter 4, Academic Press, London, New York, San Francisco (1977), pp. 99-117
- 12 R. F. Griffiths, "The Initiation of Corona Discharges From Charged Ice Particles in a Strong Electric Field," *J. of Electrostatics*, 1 (1975), pp. 3-13
- 13 Chalmers, *Atmospheric Electricity*, pp. 64-85
- 14 G. A. Dawson, "Ice Crystal Electrification," 1972 Lightning and Static Electricity Conference, USAF Report AFAL-TR-72-325 (December 1972)
- 15 Chalmers, *Atmospheric Electricity*, p. 80

- 16 Ibid, pp. 71, 333
- 17 J.B. Matthews and B.J. Mason, "Electrification Produced by the Rupture of Large Water Drops in an Electric Field," *Quart. J.R. Met. Soc.* 90 (1964) pp. 275-286
- 18 Chalmers, *Atmospheric Electricity*, p. 78-84
- 19 G.A. Dawson, "Pressure Dependence of Water-Drop Corona Onset and Its Atmospheric Importance," *J. Geophysical Research*, 74 (1969), p. 6859-6868.
- 20 L. B. Loeb, *Electrical Coronas*, University of California Press, Berkeley and Los Angeles (1965)
- 21 C. T. Phelps, "Field-Enhanced Propagation of Corona Streamers," *J. Geophysical Research*, 76 (1971), p. 5799
- 22 G. A. Dawson, "The Life Time of Positive Streamers in a Pulsed Point-to-Plane Gap in Atmospheric Air," *Z. Physik*, 183 (1965), p. 172
- 23 R. Gunn, "Electric Field Intensity Inside of Natural Clouds," *J. Appl. Phys.*, 19 (1948), pp. 481-484
- 24 Chalmers, *Atmospheric Electricity*, p. 346
- 25 E. T. Pierce, "Triggered Lightning and Some Unexpected Lightning Hazards," 138th Annual Meeting of the American Association for the Advancement of Science, Philadelphia (December 1971)
- 26 M. Brook, C.R. Holmes, and C.B. Moore, "Lightning and Rockets: Some Implications of the Apollo 12 Lightning Event", *Naval Research Reviews*, April 1970
- 27 R. K. Baum, "Airborne Lightning Characterization," FAA/NASA/FIT Symposium on Lightning Technology, Hampton, Virginia (22-24 April 1980)
- 28 F.L. Pitts, M.E. Thomas, R.E. Campbell, R.M. Thomas, K.P. Zuepfel, "In-Flight Lightning Characteristics Measuring System," FAA/FIT Workshop on Ground and Lightning Technology, Mar (1979) Report FAA-RD-79-6

SESSION VII - OPEN FORUM ON PROTECTION OF GROUND SYSTEMS

Page intentionally left blank

SESSION VIII - AIRCRAFT LIGHTNING PROTECTION DESIGN AND TESTING

Page intentionally left blank

F-5F SHARK NOSE RADOME LIGHTNING TEST*

George W. Scott
Northrop Corporation,
Aircraft Group,
Hawthorne, CA

SUMMARY

A unique F-5F radome with a geometry similar to a Shark Nose profile was tested with a high voltage Marx generator, 1.2×10^6 volts. The purpose was to demonstrate the effectiveness of the lightning protection system with currents from 5×10^3 amperes or greater. An edge discontinuity configuration is a characteristic feature in the forward region of the radome and occasionally serves as an attachment point. The results of nineteen attachment tests at various aspect angles with an air gap of one meter indicated that no damage occurred to the dielectric material of the radome. The test proved the effectiveness of the lightning protection system.

INTRODUCTION

Lightning strikes to in-flight aircraft continues to present a serious threat to the safety of aircraft flying near or in cumulonimbus clouds. The probability is high for a lightning strike to attach to the nose pitot boom of a fighter aircraft in this type of weather condition. Another surface area that can constitute a point of direct stroke attachment on the radome is the edge discontinuity near the nose section of the Shark Nose radome. The configuration of this radome is in contrast to the conventional ogive design of the F-5E aircraft, and presented a challenge to the engineers for the installation and testing of a lightning protection system.

To reduce the hazards of the environmental effects of lightning, four segmented lightning diverter strips were attached on the radome surface. The diverters guide a lightning current, rather than conduct it. Applications of this technique include the F-5E, B-52G, and F-16. The pitot heater wires on the F-5F radome are protected by a copper grounding tube, similar in concept to the F-16 radome assembly.

The Shark Nose lightning protection system was designed to prevent:

- a. The vaporization of heater wires during the transfer of lightning current from the pitot boom to the aircraft structure.
- b. The penetration of lightning current through the radome wall to heater wires or other metallic components.
- c. The coupling of high electrical impulses into the heater wiring circuit which may cause various types of electrical/avionics system's malfunctions.

*Performed under Air Force Contract

The simulated high voltage lightning attachment tests were conducted to determine the effectiveness of the lightning protection system and to evaluate any structural deformation in the radome assembly.

Radome lightning testing is normally performed in two stages. The first stage is to perform a lightning attachment study at low current values to determine the paths of lightning discharge to the radome for various angles of approach of the lightning strike. The second stage is to perform high current testing (200KA) on any path that lightning current followed during the attachment test. For the Shark Nose radome, the copper tube and diverter strips were the intended paths for the lightning current to follow. In previous radome system tests, these items were previously shown to be capable of handling the 200KA test current level. The purpose of this laboratory test was to demonstrate that the diverter strip placement and copper tube mounting design are adequate to divert lightning currents to one of these items. An additional requirement was to measure the level of lightning induced voltages in the pitot heater circuit. This voltage was not to exceed 500 volts.

To conduct the test, simulated lightning strikes from a 1.2×10^6 volt Marx generator were directed at the radome from various angles in azimuth and elevation at an airgap of one meter.

RADOME CONFIGURATION

Figure 1 illustrates the front and side views of the Shark Nose radome. The geometrical design is unusual when compared to the long, slender fuselage forebody generally required by the aerodynamicists for an advanced fighter aircraft. As can be observed from the drawing, the F-5F radome has the characteristics of a broad nose, similar to the profile of a shark's nose. The elliptical design was an asset for the alignment of the copper tube, containing the heater wires. The tube was oriented along the edge in the H plane of the cross section ellipticity. Studs are attached to the tube and extend through the radome wall. This feature presented minimal interference with the radar transmission.

The precise location of the segmented strips and the copper tube in relation to the pitot nose helped to insure a successful lightning attachment test.

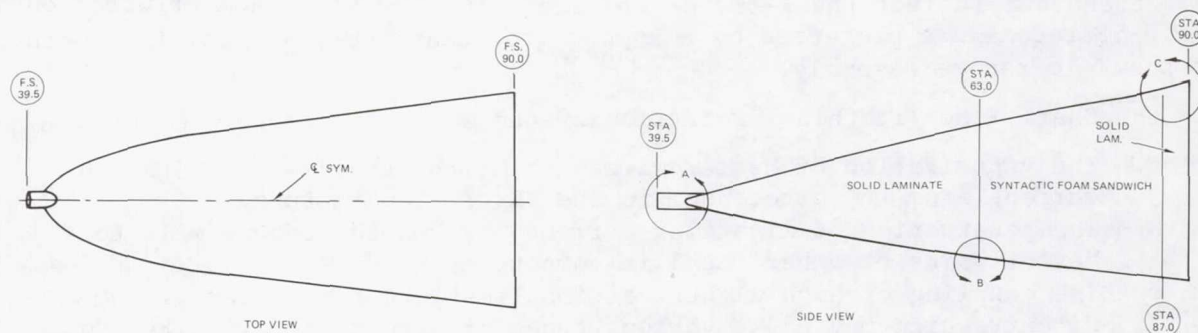


FIGURE 1. RADOME CONFIGURATION

The segmented strips function on the principle that an ionization channel is established over the resistively connected metal segments during the pre-strike phase (high voltage) of the lightning strike. The size of the metal segment is less than one-eighth at the highest operating frequency of the antenna housed within the radome. The metal segments are fabricated on a dielectric substrate which is bonded to the radome wall. The radial spacing of the strips is a function of the metallic components inside the radome and their clearances from the radome wall. Because of the high dielectric strength of the radome wall, the segmented strips were spaced 45° radially around the elliptical surface and extend about one-half the length of the radome. The strips were adequate to conduct at least one 200KA, Action Integral of $2 \times 10^6 \text{A}^2\text{-sec}$ lightning current without excessive damage or erosion.

The pitot probe grounding tube was one-quarter-inch copper tube with 0.035-inch walls. The copper tube was satisfactory from the standpoint of induced voltage, temperature rise, and elongation. The copper tube insures that the voltage induced in the heater circuits is just the IR drop caused by the lightning current flowing along the grounding tube. The amplitude of this voltage is dependent mainly on the amplitude of the lightning current and, to a lesser extent, the frequency of the lightning current.

Figures 2 and 3, reflect the configurations of F-5E and F-5F lightning protection systems. In the former design, plastic data lines were used in pitot boom installations because metal tubes degraded antenna performance. At least one of the segmented strips was extended forward to make connection with the pitot boom to provide an external lightning current path from the pitot boom. In addition, an isolation design was incorporated in the pitot boom heater wiring to prevent the main lightning current from traveling in these wires.

The copper tube in the latest design radome provided the IR drop as opposed to the inductance, $-L \text{ di/dt}$, which would have sent a large pulse into the electrical system.

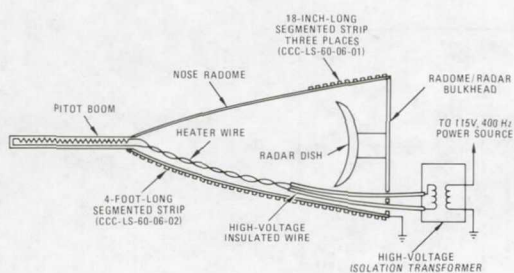


FIGURE 2. UNGROUNDED PITOT BOOM ISOLATION DESIGN ON F-5E

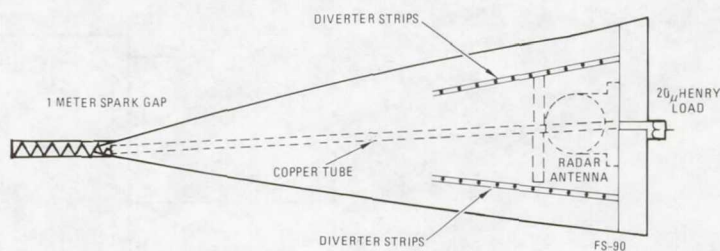


FIGURE 3. GROUNDED PITOT TUBE HEATER WIRES AND SEGMENTED STRIPS ON SHARK NOSE RADOME (F-5F)

TEST FACILITIES

Northrop's Lightning Laboratory is 40x40x40 ft. and is adequate for testing selected full-scale avionics components. The special screen room prevents spurious signals from interfering with recording instruments.

Northrop used a Marx generator (designed by Pulsar Assoc., Inc.) to produce a 1.2-megavolt output. It can deliver up to a six-foot-arc through air, with a (damped) peak follow-through current of about 8,000 amperes. The characteristics of this impulse generator fit the "Engineering Test Voltage Waveform C" description of the SAE Committee AE4L Report (Lightning Test Waveforms and Techniques for Aerospace Vehicles and Hardware), June 20, 1978, paragraph 3.3.2.1. The delay time of flashover is adjusted to between one and three microseconds (two microseconds, ± 50 percent) as a function of the airgap length and operating voltage of the generator.

This voltage impulse generator has 35 stages with each stage of capacitance charged to 40KV (± 20 KV) and switched in series by 35 triggered spark gaps. The generator includes built-in series damping resistors of 2 ohms per stage. The generator inductance is strongly dependent on the test load placement. Typically, a series loop inductance of 10 to 15 microhenries can be obtained. For such inductance, the Marx circuit is quite near to critical damping. Therefore, the load current will not oscillate. A single current pulse of 2000 to 9000 amperes peak current can be delivered to the load. The di/dt of the current wavefront will average 33 kiloamperes per microsecond, depending on the inductance of the discharge loop. The output polarity is reversible by reversing the power supply charging connections. Its pressurized spark gap switches provide low-jitter electronic triggering and provide a wider range of operating voltages than can be obtained from older style atmospheric exposed-gap switch designs.

Figure 4 shows a simple Marx generator circuit. This circuit has three capacitors. The output pulse has a peak voltage three times the individual charge voltage on each capacitor. The charge voltage is supplied through a single-ended charge circuit (one polarity is grounded). The charging current is supplied through charging resistors to each of the capacitors. The charging resistor's role is to isolate the several capacitors and switches from each other during discharge. When the Marx generator has reached full charge, erection is initiated by closure of one of the switches.

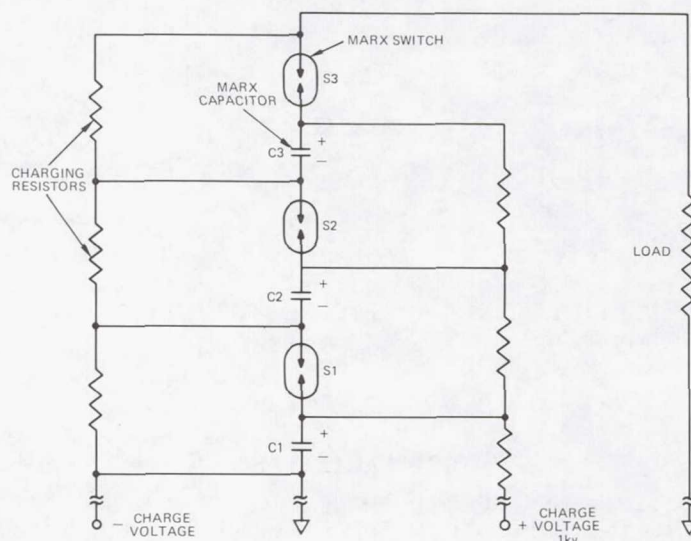


FIGURE 4. MARX CIRCUIT - SINGLE-ENDED CHARGE

An important refinement and the basis for this generator is the "balanced" charging technique. Each stage capacitor is broken out into two components. Each stage capacitor represents two discrete capacitors (or banks of parallel capacitors) connected in series. This feature permits the junction of the two capacitors to be considered a neutral point, and allows each stage capacitor to be charged with a balanced circuit, that is, with a plus and a minus charge voltage on either side of the neutral. The advantage of this circuit is that during the charge cycle of the generator, the absolute D.C. voltage present with respect to the outside environment is cut in half. In Northrop's high voltage generator, each stage is charged to a maximum 40,000 volts. Because of the balanced charging circuit, each stage is charged to +20,000 and -20,000 volts, with respect to the ground. Corona is reduced and the life of the insulators is increased. Another advantage is the capability to monitor the current flowing in the neutral chain. If the generator is operating correctly, this current should be zero, or nearly zero, during a normal charge cycle. A meter on the console monitors this current. If the current through this neutral chain is not zero, it may be an indication that a mechanical problem exists in the generator system.

Figure 5 illustrates the Marx generator in a preliminary test with an F-5 Basic Conical Radome.

Figure 6 shows the side view of the full-scale Shark Nose radome during the test phase.

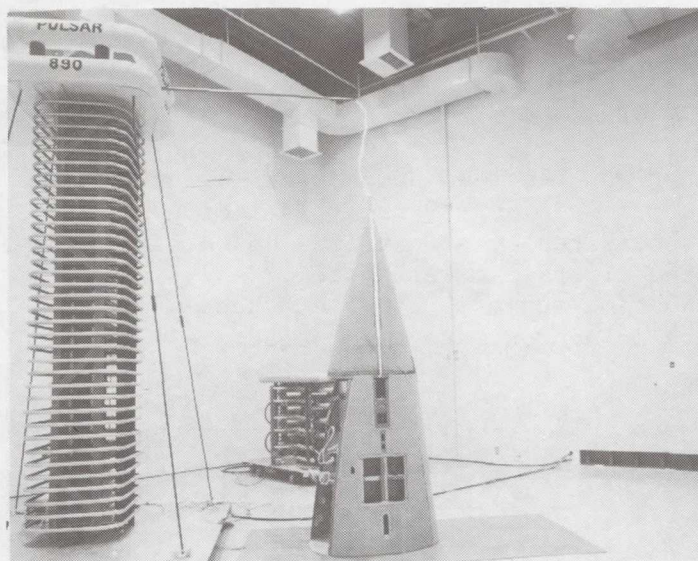


FIGURE 5. PRELIMINARY TEST USING
F-5E BASIC CONICAL RADOME

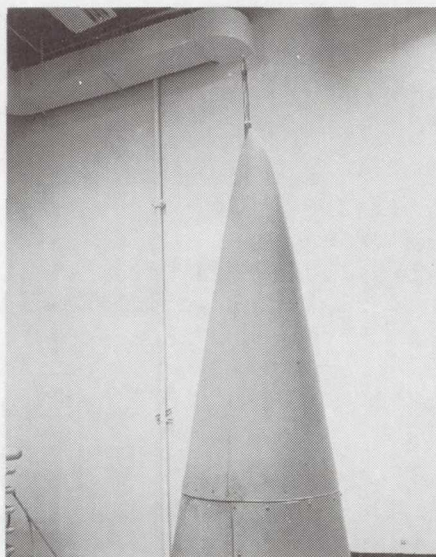


FIGURE 6. SHARK NOSE RADOME
ILLUSTRATING COPPER EDGE VIEW.
STUDS ON RADOME SURFACE HOLD
COPPER TUBE IN PLACE

TESTING TECHNIQUES

The radome test article is shown in Figure 7. The radome console was rotated at 60°, 120°, and 300° azimuth angles for corresponding elevation angles of the electrode of 0°, 15°, 30°, 45°, 60°, and 75° (radial vectors were measured from the center of F.S. 90). The electrode was positioned 1 meter from the surface of the radome. The test plan required sixteen shots, one for the vertical and five for each of the remaining azimuth angles.

Figure 8 shows the block diagram of the attachment test. In all phases of the test, the electrode was at positive polarity. This polarity produces the most profuse streamering from ground objects in or on the radome.

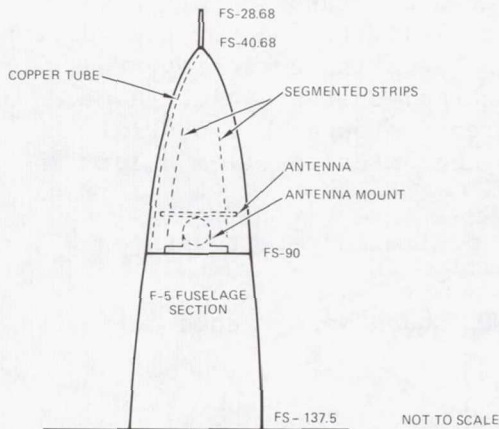


FIGURE 7. RADOME TEST ARTICLE
(TOP VIEW)

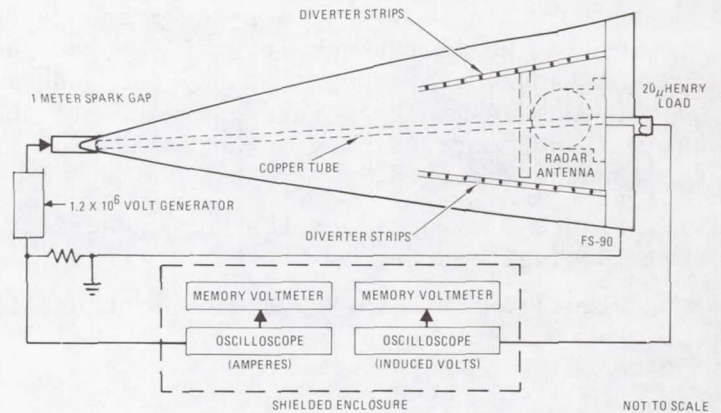


FIGURE 8. BLOCK DIAGRAM
OF IONIZATION TEST

DISCUSSION OF RESULTS

The current from the Marx generator was recorded on an oscilloscope. The exponentially decaying sinusoidal waveform in Figure 9 is typical of a high voltage test. The induced voltage was measured by a Tektronix 485 oscilloscope through a 20 μh load which simulates the aircraft power system. A typical scope result is shown in Figure 10. No time scale is shown on these drawings, but the current and induced voltage are in approximate time phase.

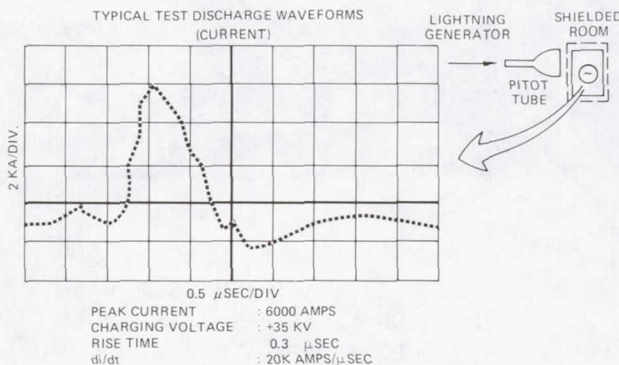


FIGURE 9.

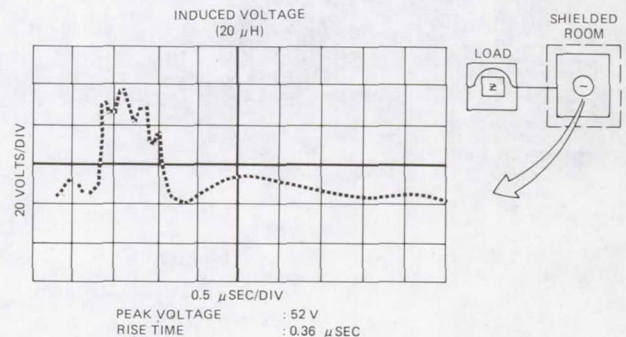


FIGURE 10.

For the 0° , 15° , and 30° elevation angles, the electrode was suspended at the 12 o'clock and approximately at the 1 and 2 o'clock positions, respectively. The lightning attachment probe was pointed to the pitot tube in all cases. The azimuth orientation had no effect on the ionization path, Figure 11. The energy was conducted through the copper tube.

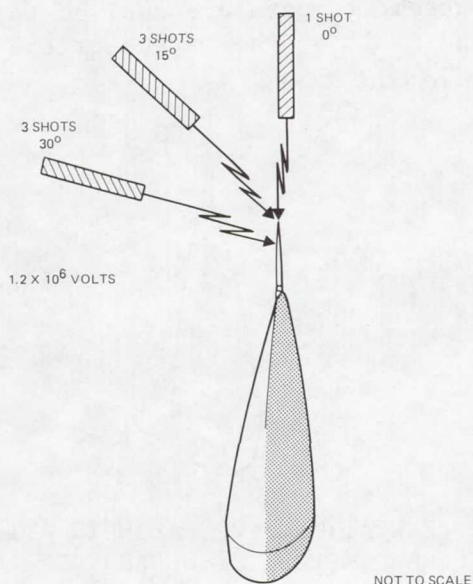


FIGURE 11. 0° , 15° , 30° (ELEVATION ANGLES) AND 60° , 120° , 300° (AZIMUTH ANGLES) ATTACHMENT STROKES

The 45° elevation and 60° azimuth test resulted in the lightning striking the radome near the segmented strip and then forming an ionization channel down the segmented strip, Figure 12.

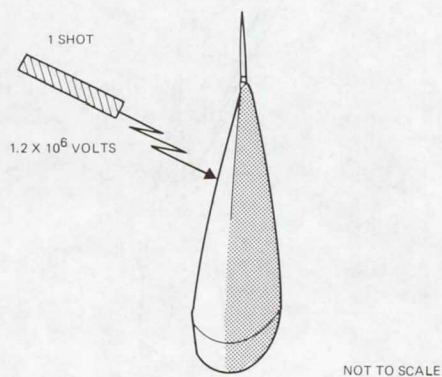


FIGURE 12. 45° ELEVATION, 60° AZIMUTH ATTACHMENT SHOT

When the electrode discharged in the 45° elevation and 120° azimuth (edge side), the lightning attached to the edge and flashed over to the diverter strip (Figure 13). A streamer attempted to move toward the pitot probe. This phenomenon indicates a return strike from the radome. At the point of impact, a small cavity (pencil point size) was observed. A close inspection revealed no puncture through the radome. The core temperature of air sparks can reach 10,000 degrees C. This extreme temperature applied to a small surface area for a fraction of a microsecond could be the cause for the small blemish. It did not occur on other phases of the test.

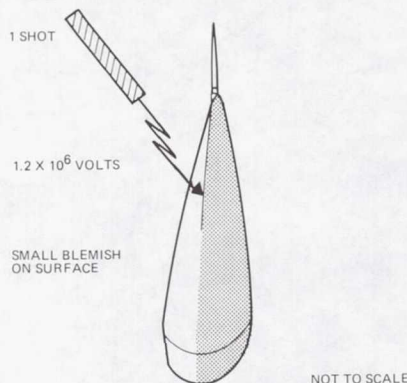


FIGURE 13. 45° ELEVATION, 120° AZIMUTH ATTACHMENT STROKE
(EDGE OPPOSITE COPPER TUBE)

Figure 14 illustrates the test configuration when the electrode was at 45° elevation and pointed at the copper tube edge of the radome (300° azimuth). The ionization was channeled down the metal tube. No anomalies were observed when the lightning stroke attached to the copper tube edge.

When the attachment points were at 60° and the radome was oriented at 60°, 120°, and 300° azimuth, the copper tube edge conducted the energy as in the previous experiments.

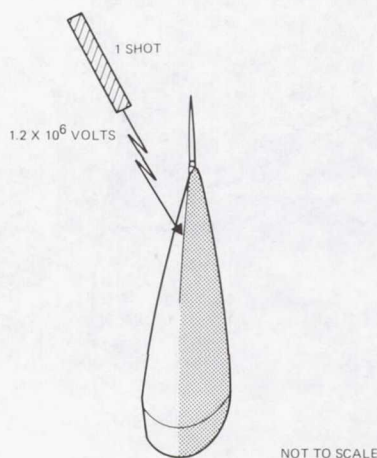


FIGURE 14. 45° ELEVATION, 300° AZIMUTH ATTACHMENT STROKE
(COPPER EDGE)

The 75° elevation of the electrode with the 60°, 120°, and 300° azimuth positioning for the radome resulted in all the lightning strokes attaching to the F-5 fuselage section. Figure 15 shows the attachment area.

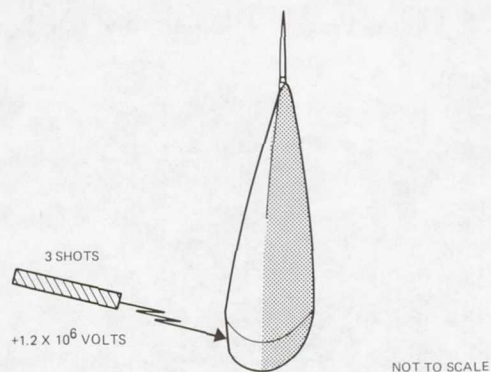


FIGURE 15. 75° ELEVATION, 60°, 120°, 300°
AZIMUTH ATTACHMENT STROKES

A total of 19 high voltage tests were made and the data for 16 attachment points were used to determine the effectiveness of the segmented strip placement and copper tube mounting design for diverting the current from the radome.

CONCLUSIONS

In the test series, the lightning protection system of the F-5 Shark Nose radome diverted lightning strikes from several aspect angles. The four segmented strips intercepted a strike before streamers emanating from internal conductors had time to puncture the radome wall. The copper tube used in the lightning protection design for the pitot tube system conducted the current to the grounded fuselage pedestal when the spark gap was oriented towards the edge of the aluminum studs.

The edge opposite the copper tube attracted the lightning strokes when the electrode was pointed in this area. The flashover occurred from the edge to the diverter strips and the current was channeled to the metal base.

A thorough visual inspection after each attachment test revealed no delamination to the dielectric material or damage to the lightning protection system.

REFERENCES:

1. Amason, M.P., Cassell, G.J., & King, J.T., Segmented Diverted Strip Protection System Lightning.
2. Test Program for AF High Temperature Aircraft Radome, Douglas Report No. MDC J6313, Brinswich Contract No. DVI-10407 and DVI-10449, Jan. 74.
3. Lightning Test Wave Forms and Techniques for Aerospace Vehicles and Hardware, report of Society of Automotive Engineers (SAE) Committee AE4 on electromagnetic compatibility, Special Task Force F, May 1976.
4. Lightning Qualification Test Techniques for Aerospace Vehicles and Hardware, report of SAE Committee AE4L, June 1978.

Page intentionally left blank

ANALYSIS AND MEASUREMENTS OF LOW FREQUENCY LIGHTNING COMPONENT
PENETRATION THROUGH AEROSPACE VEHICLE METAL AND GRAPHITE SKINS

John D. Robb
Lightning & Transients Research Institute

Ta Chen
Texas Instruments

INTRODUCTION AND SUMMARY

An analysis of the shielding properties of mixed metal and graphite composite structures has illustrated some important aspects of electromagnetic field penetration into the interior. These include: (a) that graphite access doors on metallic structures will attenuate lightning magnetic fields very little; conversely, metal doors on a graphite structure will also attenuate fields from lightning strike currents very little, i.e., homogeneity of the shield is a critical factor in shielding and (b) that continuous conductors between two points inside a graphite skin such as an air data probe metallic tubing connection to an air data computer can allow large current penetrations into a vehicle interior. The true weight savings resulting from the use of composite materials can only be evaluated after the resulting electromagnetic problems such as current penetrations have been solved, and this generally requires weight addition in the form of cable shields, conductor bonding or external metallization.

APERTURE COUPLING

The basic concept of electromagnetic shielding is that Stokes type counter currents are setup in an exact but generally unknown pattern which produce interior electromagnetic fields that will cancel any fields from an external source. This mechanism requires that for shielding to occur, the counter currents, which would be set up as if there were no aperture, need to be established essentially without distortion of the current pattern in the conducting cover over an aperture. To shield properly, an aperture in a metal aircraft must therefore be covered with a metal skin with good peripheral bonding which allows the unimpeded establishment of the counter currents. Because a graphite door has a resistivity several thousand times as high as surrounding metal, the lightning current flows around a graphite door, not through it and therefore couples large magnetic fields into the interior. Bethe theory permits an estimate of the interior fields for large cavities (ref. 1), i.e., cavities large compared to one access door dimension. It is based on the analogy to a magnetic dipole equivalent to the current concentrations around the edge of the aperture.

Conversely a graphite aircraft skin would require a graphite access door to allow the establishment of the proper counter current patterns across the aperture and across the aperture boundaries which are required for proper shielding. A metal door in a graphite skin would distort the normal current flow (which would exist without an aperture) and thus also leak magnetic field into the interior. The pattern of current flow in a metal skin through a door with a resistivity 10 times higher for the DC or quasi static case is shown in Figure 1.

Because the lightning energy lies primarily below one megahertz corresponding to a 300 meter wavelength, a typical aircraft aperture would have dimensions which would be a small fraction of a wavelength and the problem may be thought of as primarily quasi static. As may be seen in Figure 1, the current flows essentially around the door.

The horizontal flow pattern shows the electric field lines and represents the current flow pattern for the metal skin with a high resistance door such as one of graphite. It should be noted, however, that this solution to the LaPlace equation also applies to the inverse situation; a high resistance skin such as graphite with a metal door, except that in this case the flow would be vertical and the lines shown would be equipotentials rather than electric field lines.

Measurements on a loop sensor inside a graphite access door illustrate the relatively low attenuation provided as shown in Figure 2. The interior magnetic field is only reduced a few db when an open aperture is covered with a graphite door.

The analysis thus indicates the importance of homogeneity in external skins. Graphite access doors in a metal aircraft are ineffective shields unless they are covered with metallic coating and metal doors in a graphite skin leak magnetic fields into the interior nearly as badly as does an opening with no door.

CONDUCTION THROUGH INTERNAL CONDUCTORS IN AN AEROSPACE VEHICLE

Conduction currents through the interior of an aluminum vehicle can be relatively large. Calculations confirmed by measurements on actual avionics equipment located in a totally enclosed shield (corresponding to the equipment bay of a commercial transport aircraft), have shown currents of the order of a thousand amperes. This represents only about one-half percent of a total lightning current of 200,000 amperes but is well beyond the currents that equipment cases were designed to withstand. With graphite, the penetration currents become even larger.

Skin effect is not too significant as only the low frequency components of the natural lightning waveform pass into the interior. The slight reduction in the effective rise time of the driving potential on the inside of the skin as a result of skin effect can be introduced in the driving function of the equation to correct the result but in most cases it is not large.

Analysis

A simple calculation, following the analysis of Hillan (ref. 2), permits a determination of the interior currents as follows. As shown in Figure 3, the equivalent circuit may be represented as a two branch circuit with a constant current source, a reasonable approximation for lightning. The driving source, ignoring skin effect is the lightning current in the skin. The internal magnetic field from the skin current can be ignored for cylindrical shapes and is not large for typical polygonal shapes of aircraft structures. The current passing through the interior is determined by both the ratio of internal conductor resistance to skin resistance, the DC case and by the internal wire inductance as indicated below.

$$L \, di/dt + RI = Ir_1$$

where

r_1 = skin resistance

r_2 = internal wire resistance

R = skin and wire resistance

L = internal wire inductance

I = lightning current

and where I is of the form

$$I = A (e^{-at} + e^{-\beta t})$$

$$a = 10^5/\text{sec}$$

$$\beta = 10^6/\text{sec}$$

$$A = 225,000$$

Solving the differential equation gives a slightly complex expression.

$$I(t) = r_1 I_0 / w \cdot (e^{-wt} - (w_1/w_2)) (e^{-\beta t} - e^{-Rt/I} (1 - w_1/w_2)) \quad (1)$$

where

I_0 = the lightning current

R = total resistance, skin(r')
joint resistance and (r)
internal circuit resistance

a = lightning wave tail time constant

b = lightning front of wave time constant

L = internal circuit inductance

x = -a + R/L

y = -b + R/L

This expression has been solved in terms of I_0 , the lightning current, R, L and a normalizing function $f_1(t)$ plotted in Figure 4 for easy use in determining internal currents.

$$I(t) = I_0 (r_1/R) \times f_1(t) \quad (2)$$

where $f_1(t)$ may be determined from the graph of Figure 4.

Practical Application

This simple analysis permits one to estimate the percentage of current penetrating a vehicle interior and although it is generally a low percentage of the total current, the current traveling through a specific piece of equipment may be substantial. Several thousand amperes may be a small percentage of a 200,000 ampere lightning strike but this current magnitude can have a substantial effect when passing directly through a piece of electronic equipment. For example, one may consider the current passing from a pitot tube located near the nose of an aircraft via metal connecting tubing into an air data computer. Whereas most equipment cases are fairly well shielded from external fields, they are not designed to withstand currents of several thousand amperes.

In applying this approach to a specific example, all that is needed is the skin resistance which is typically 100 microhms, nose to tail or wing tip to wing tip, for an early piston engine aircraft or a modern wide body metal jet transport, and the resistance and inductance of the connection between the two interior points on the skin. This internal path, of course, does include in its path, the avionics equipment. The inductance of the conductor may be determined from the formula for a conductor over a ground plane.

$$L = (60/c) \times \ln(4 h/d)$$

where

L = inductance

c = speed of light

h = height over ground plane

d = diameter of conductor

The spacing over the ground plane (the skin) or over an equipment rack will vary somewhat but because the inductance varies as the logarithm of the spacing, it can be approximated and still give reasonable answers for the current magnitudes.

Metal Skin Vehicles

As a specific example, we will assume the following constants for the pitot tube to avionics black box connections shown in Figure 3. Assume a run of 1/4 inch copper tubing 10 meters in length spaced an average distance of 8 inches over the skin or equipment rack.

Assuming that the pitot tube has a flange to skin joint resistance of 2.4 milliohms, a metal skin resistance of 0.100 milliohms, for a total skin path resistance of 2.5 milliohms (r') and a total tubing resistance for the path from the pitot tube to the avionics equipment of 7.5 milliohms (r), we find a total tube-over-ground-plane plus skin loop resistance of 10 milliohms (R). For the assumed tubing diameter of 1/4 inch and a spacing of 8 inches, the inductance would be about one microhenry per meter or 10 microhenries for the 10 meter length of run. This results in an R/L ratio of

$$R/L = 10 \times 10^{-3} / 10 \times 10^{-6} = 10^3$$

$$f_1(t) = .042$$

For a 200,000 ampere high current cloud to ground type natural lightning strike as specified in MIL-B-5087B with a slightly modified 2 x 50 microsecond waveshape (2 microseconds to crest, 50 microseconds to half value), we find using Figure 4 and equation (2) that a current of about 2800 amperes penetrates a metal skin into the avionics equipment case.

$$\begin{aligned} I'(\text{metal}) &= I_o (r'/R) \times f_1(t) \\ &= 2 \times 10^5 (.0025/.0075) \times (.042) \end{aligned}$$

$$I'(\text{metal}) = 2800 \text{ amperes}$$

Graphite Skin Vehicle

For graphite, the skin resistance would be about 2000 times greater or 200 milliohms and the penetration current would be

$$R/L = 202.5 \times 10^{-3} / 10 \times 10^{-6} = 20,000$$

$$f_1(t) = 0.26$$

$$I'(\text{graphite}) = I_o (r'/R) \times f_1(t)$$

$$I'(\text{graphite}) = 2 \times 10^5 \times (202.5 \times 10^{-3} / 10 \times 10^{-6}) \times 0.26 = 50,142$$

The results indicate a current of 50,142 amperes passing from a side mounted pitot tube or total temperature probe through the connecting aluminum tubing directly into an air data computer case which is solidly bonded to the internal ground as an exit point for the lightning stroke.

The results show that while large currents pass through conductors connected across the interior of a metal skinned vehicle, very large currents pass through one with a graphite skin.

CONCLUSIONS

Investigations of some of the practical aspects of lightning electromagnetic pulse penetration of graphite skins for aircraft has shown that

- o Graphite access doors in a metal vehicle skin or a metal door in a graphite skin result in negligible shielding of the low frequency magnetic field in the lightning current waveform.
- o Large currents can penetrate the interior on conductors exposed to the exterior such as the tubing from an pitot tube to an air data computer.

REFERENCES

1. Bethe, H.A., Phys. Rev. 66 163 (1944).
2. Hillan, A.B., "Currents and Fields Created Inside a Conducting Ordnance Capsule by a Lightning Strike," AWRE, United Kingdom, Hero Congress, 1961.

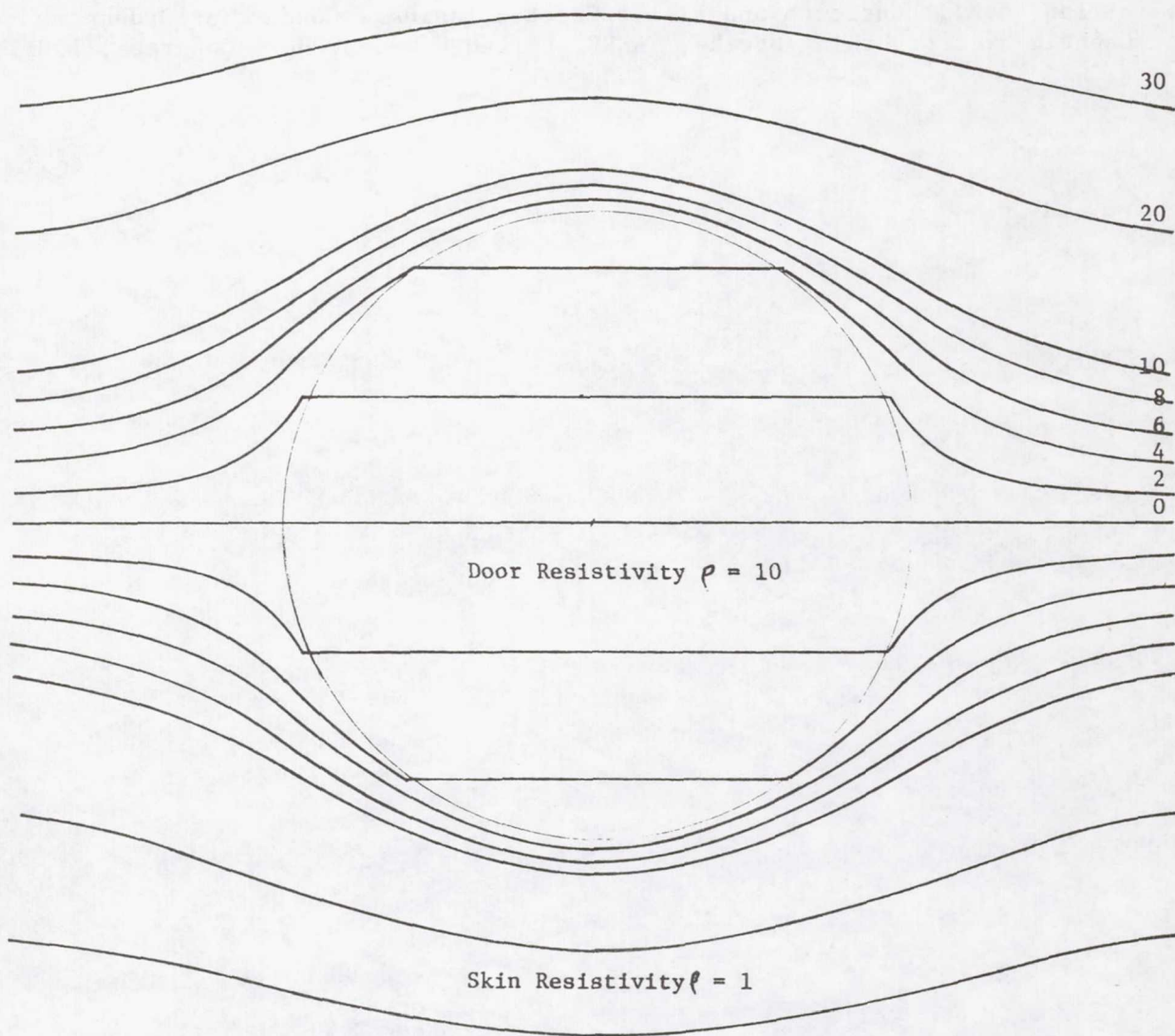


Figure 1.- Solution to LaPlace equation shows current flow through and around door for resistivity difference of ten to one.

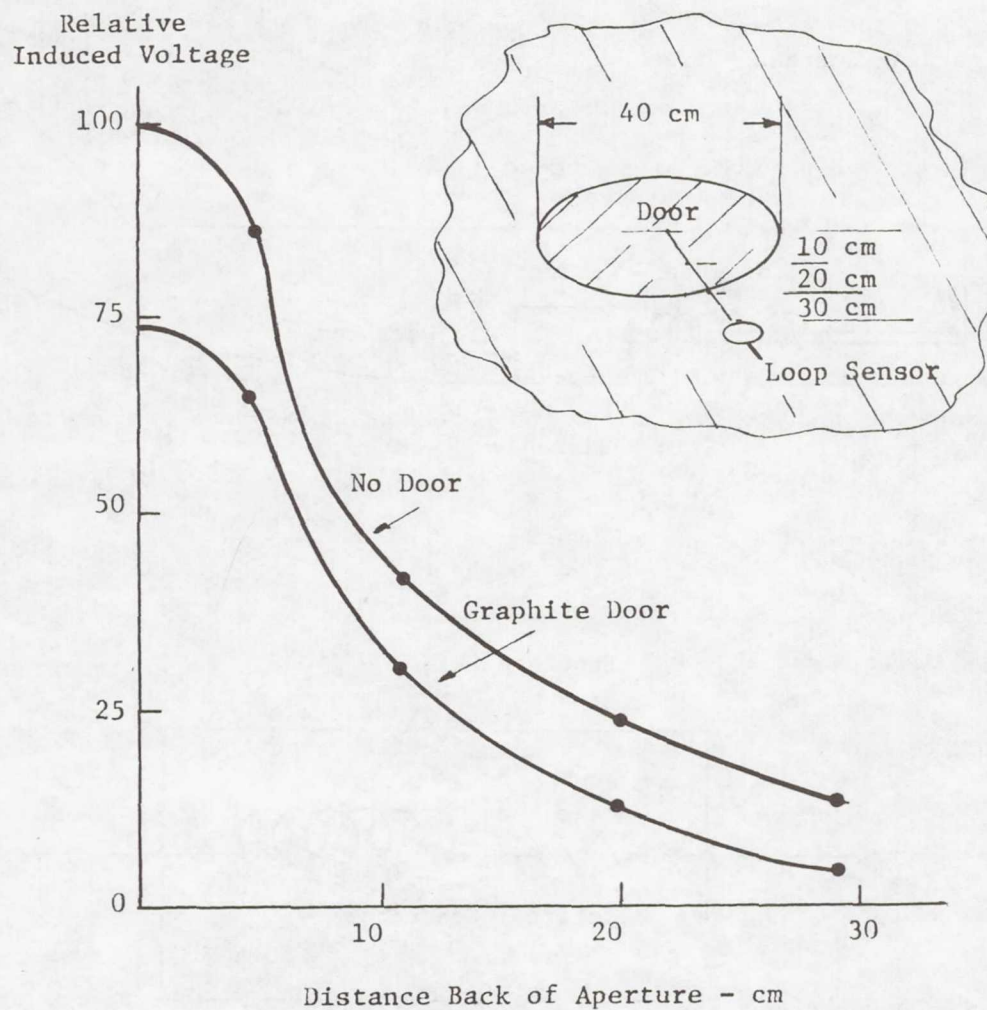


Figure 2.- Induced voltages on loop sensor behind graphite access doors show little attenuation.

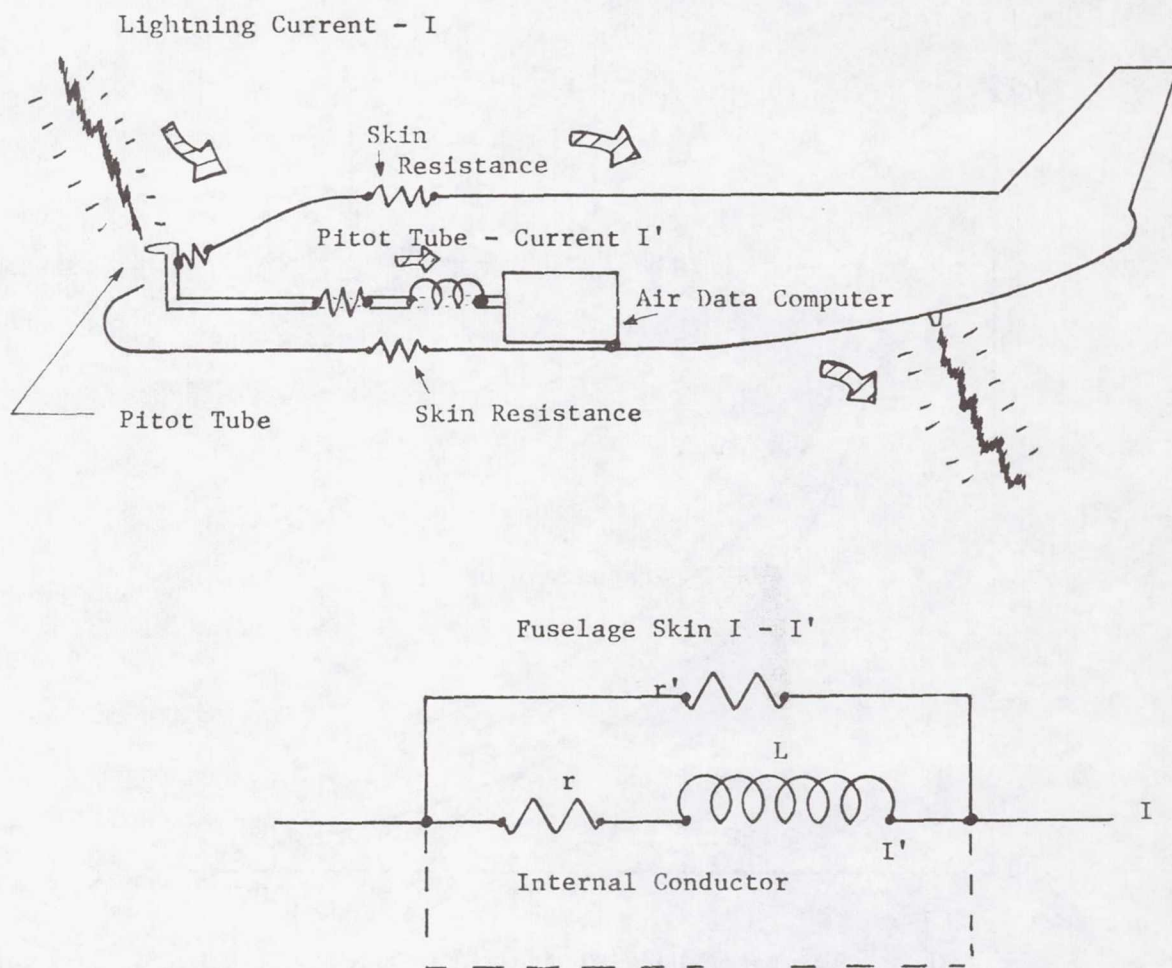


Figure 3.- Diagram of current flow in skin and interior conductor with equivalent circuit.

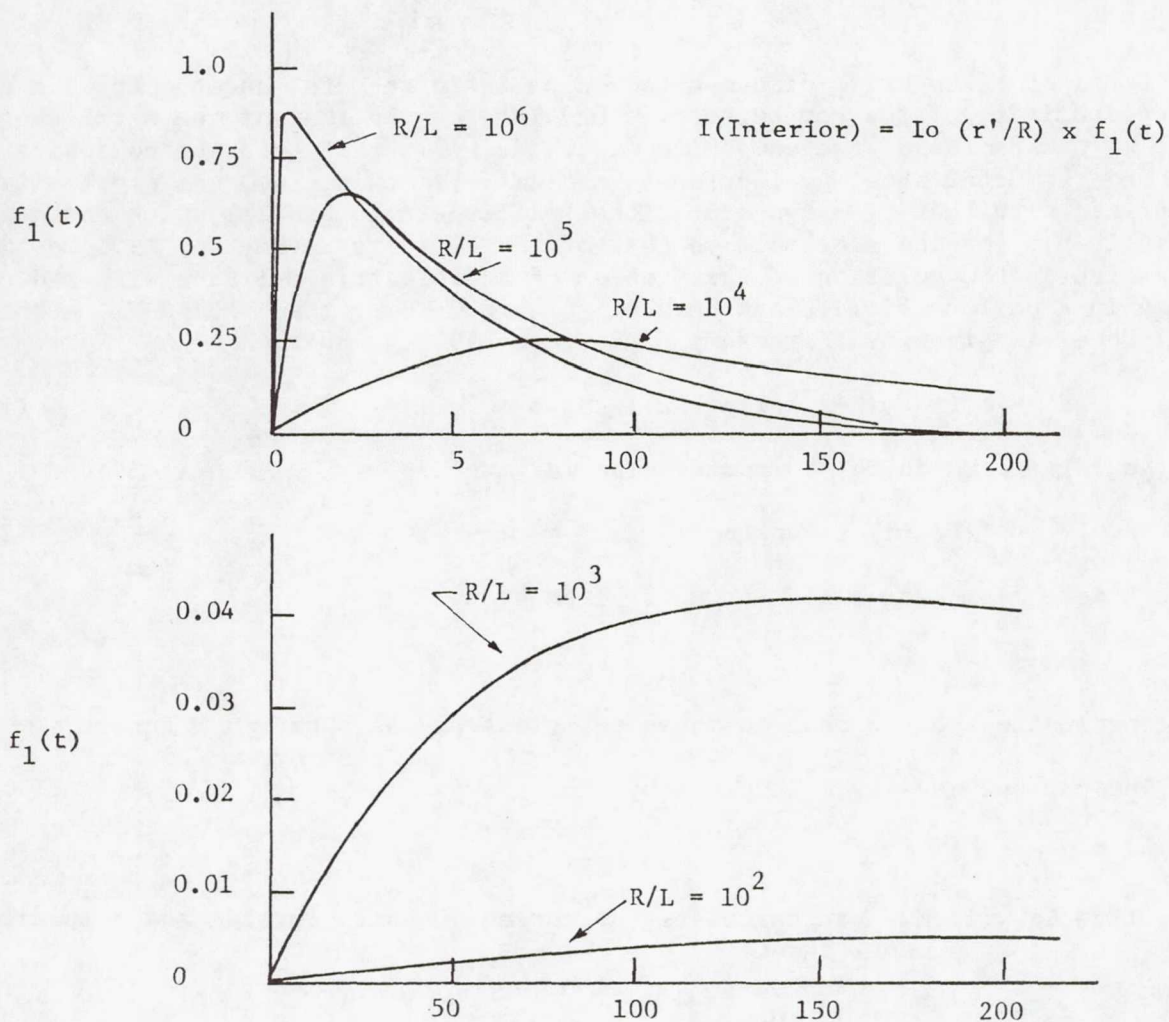


Figure 4.- Graph of current fraction passing through aerospace vehicle interior conductor as a function of R and L .

APPENDIX I

CURRENT AROUND A COMPOSITE DOOR

INTRODUCTION

Consider a composite disc mounted on an infinite metal sheet. Let σ_c be the conductivity of the composite disc and let σ_m be that of the metal sheet. Let b be the radius of the composite disc. We will treat both the composite disc and the metal sheet as isotropic mediums. In this case, the problem is isomorphic with that of a two dimensional electrostatic problem, with the conductivity playing the same role as that of the capacity E (Smythe, 1950, p. 231). In particular the solution of the problem of a dielectric cylinder with radius b placed in a uniform field E can be applied here. Thus, the voltage V_m in the metal sheet is given by (For example, Smythe, 1950, p. 68):

$$V_m = E (r - (k-1/k+1) (b^2/r)) \cos \theta \quad (1)$$

And the voltage V_c in the composite disc is given by

$$V_c = (2E/k+1) r \cos \theta \quad (2)$$

where E is the ambient field and k is given by

$$k = \sigma_c / \sigma_m \quad (3)$$

The coordinates systems used in these equations are as shown in Figure 1.

The current density \vec{J} is given by

$$\vec{J} = \sigma \nabla v \quad (4)$$

Thus, from Eq. (1), we can calculate the current density outside the composite disc (i.e., in the metal sheet)

$$J_m = J_{mx} U_x + J_{my} U_y \quad (5)$$

Where U_x and U_y are the unit vectors in the x and y directions respectively and

$$J_{mx} = (V_m / x) = J_0 (1 - (k-1/k+1) (b^2(y^2-x^2))/(x^2+y^2)^2) \quad (6)$$

$$J_{my} = 2 J_0 (k-1/d+1) (b^2 xy / (x^2+y^2)^2) \quad (7)$$

where $J_0 = \sigma_m E$ is the ambient current density and

$$x = r \cos \theta \quad (8)$$

$$y = r \sin \theta \quad (9)$$

Inside the composite disc, the current density is given by

$$J_c = J_{cx} U_x \quad (10)$$

$$J_{cx} = \sigma_c (2E/(k+1)) \quad (11)$$

$$J_{cy} = (2J_0 k/(k+1)) \quad (12)$$

$$J_{cy} = 0$$

STREAMER FUNCTION

The streamer function u is given by the conjugate function of v , that is

$$(\partial u / \partial y) = - (\partial v / \partial x) \text{ and } (\partial u / \partial x) = (\partial v / \partial y)$$

In the domain of the metal sheet, we have

$$u_m = -E (r + (k-1/k+1)(b^2/r)) \sin \theta \quad (13)$$

Figure 2 gives a numerical example.

MAGNETIC FIELD

Since the ambient current density J_0 produces no field in the inside of the metal sheet we subtract J_0 from Eq. (5), so that the current responsible for the leakage magnetic field is given by

$$J = J_m - J_0 u_x$$

or

$$\begin{aligned} J_{mx} &= J_{mx} - J_0 \\ &= -J_0 (k-1/k+1) (b^2(y^2-x^2)/(x^2+y^2)^2) \\ J_{my} &= 2 J_0 (k-1/k+1) (b^2 xy/(x^2+y^2)) \text{ in the metal sheet} \end{aligned} \quad (14)$$

$$\begin{aligned} J_{cx} &= J_0 (2k/(k+1) - 1) \text{ in the composite disc} \\ J_{cy} &= 0 \end{aligned} \quad (15)$$

The streamer lines of the current \vec{J}' is shown in Figure 3.

The leakage magnetic field at any point P is given by

$$\vec{B} = (\mu/4\pi) \nabla \times \iint_S (\vec{J}' dA/R) \quad (16)$$

Where dA is the element area, R is the distance between P and dA . \vec{J}' is

given by Eq. (14) and (15) and the surface integral is over the whole x-y plane. Numerical integration is too involved to be given here. However, a few qualitative conclusions can be drawn by inspection of Figure 3 and Eq. (14) and (15).

a. The total amount of current is given by the total current through the disc or

$$I't = 2b \times J_0 (2k/k+1 - 1) \quad (\text{see Eq. (15)}) \quad (17)$$

and the shortest path around the current is $4b$ (around the thickest part of the disc). Therefore the maximum field intensity can be estimated as

$$H = (I't/4b) = (i_0/2) (2k/k+1 - 1) \quad (18)$$

For example

$$J_0 = 30,000 \text{ amp/meter}$$

$$k = 0.1$$

we have

$$H = 12,000 \text{ amp/meter}$$

b. All field lines are perpendicular to x - axis, i.e., perpendicular to the ambient current density. Thus maximum coupling occurs when the loop area is parallel to the ambient current density as shown in Figure 4.

c. The overall magnetic field pattern resembles that of a dipole field. The two poles are approximately located at the top and the bottom of the composite disc as shown in Figure 5.

d. The streamer function of "leakage current" I' is given by

$$U_m = - (k-1/k+1) (b^2/r) \sin \theta$$

Note that if we replace K by $1/k$, we get

$$\begin{aligned} U_m(1/k) &= - (1/k - 1)/(1/k + 1) (b^2/r) \sin \theta \\ &= - (1-k/1+k) (b^2/r) \sin \theta \\ &= - U_m(k) \end{aligned}$$

That is if we mount a metal disc on a composite sheet, the leakage field will be exactly the same as that of a composite disc mounted on a metal sheet, except that the field direction is reversed.

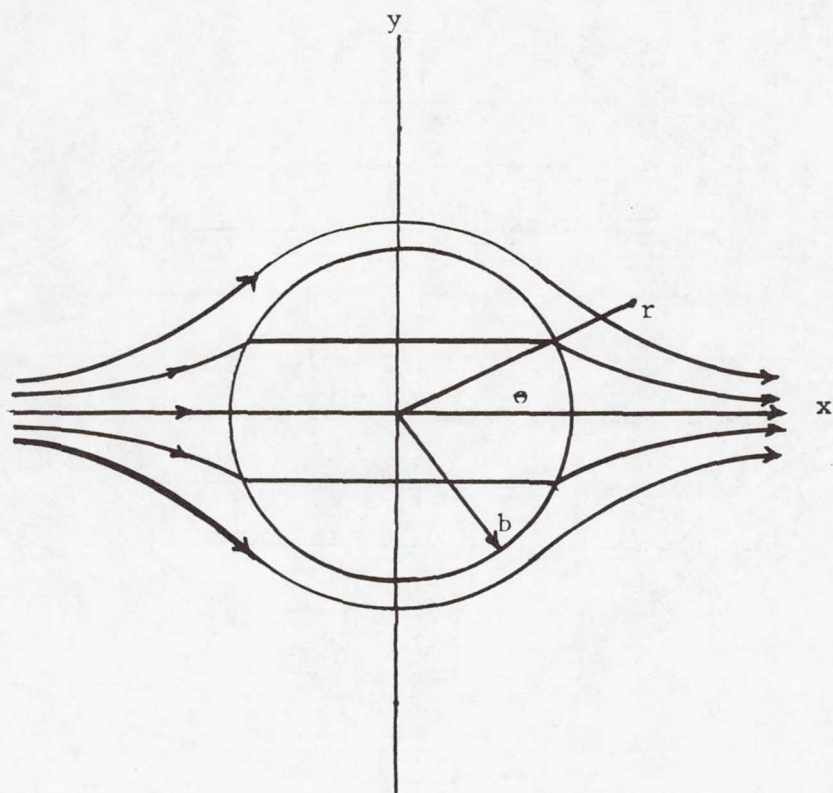


Figure 1.

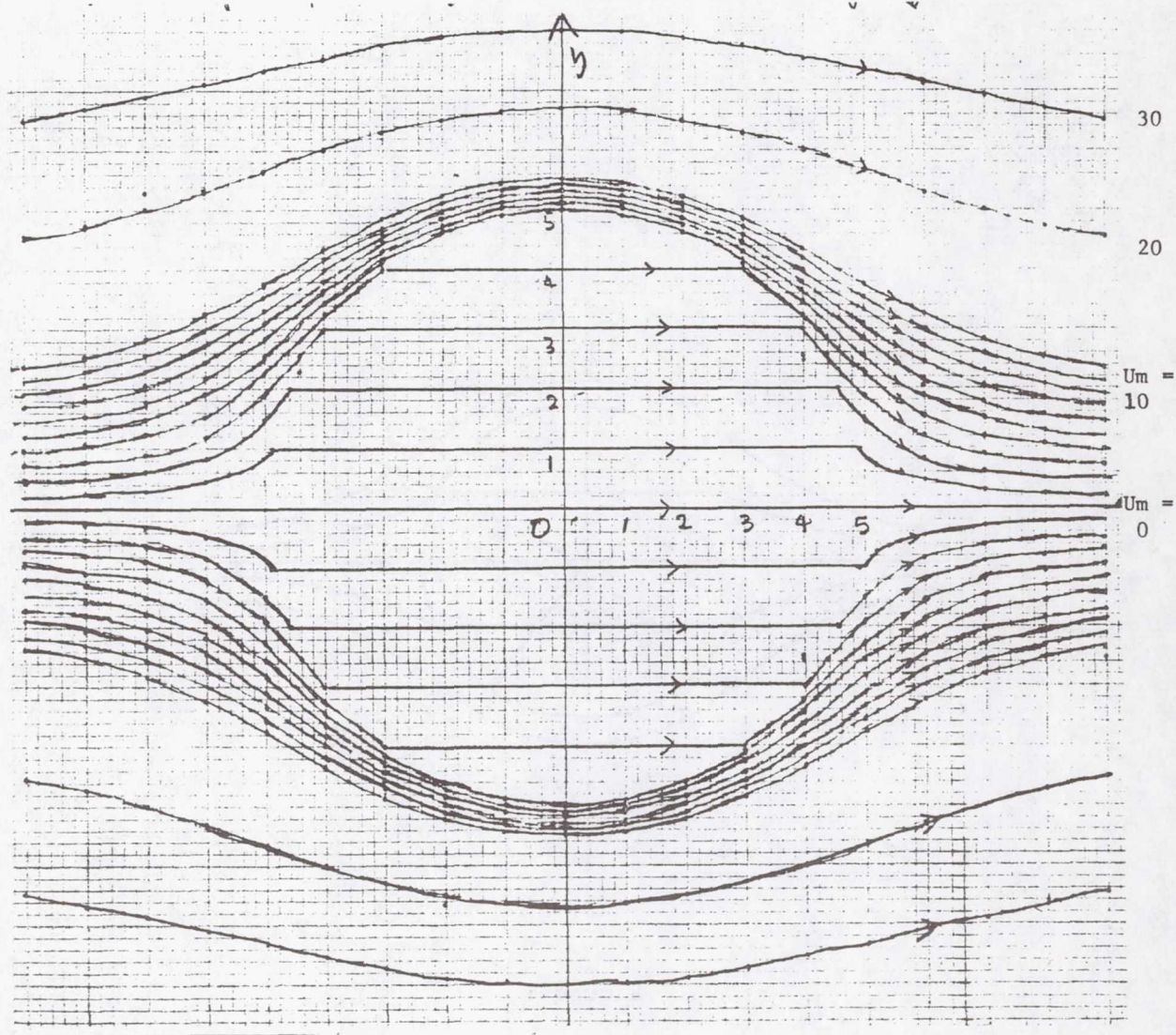


Figure 2.

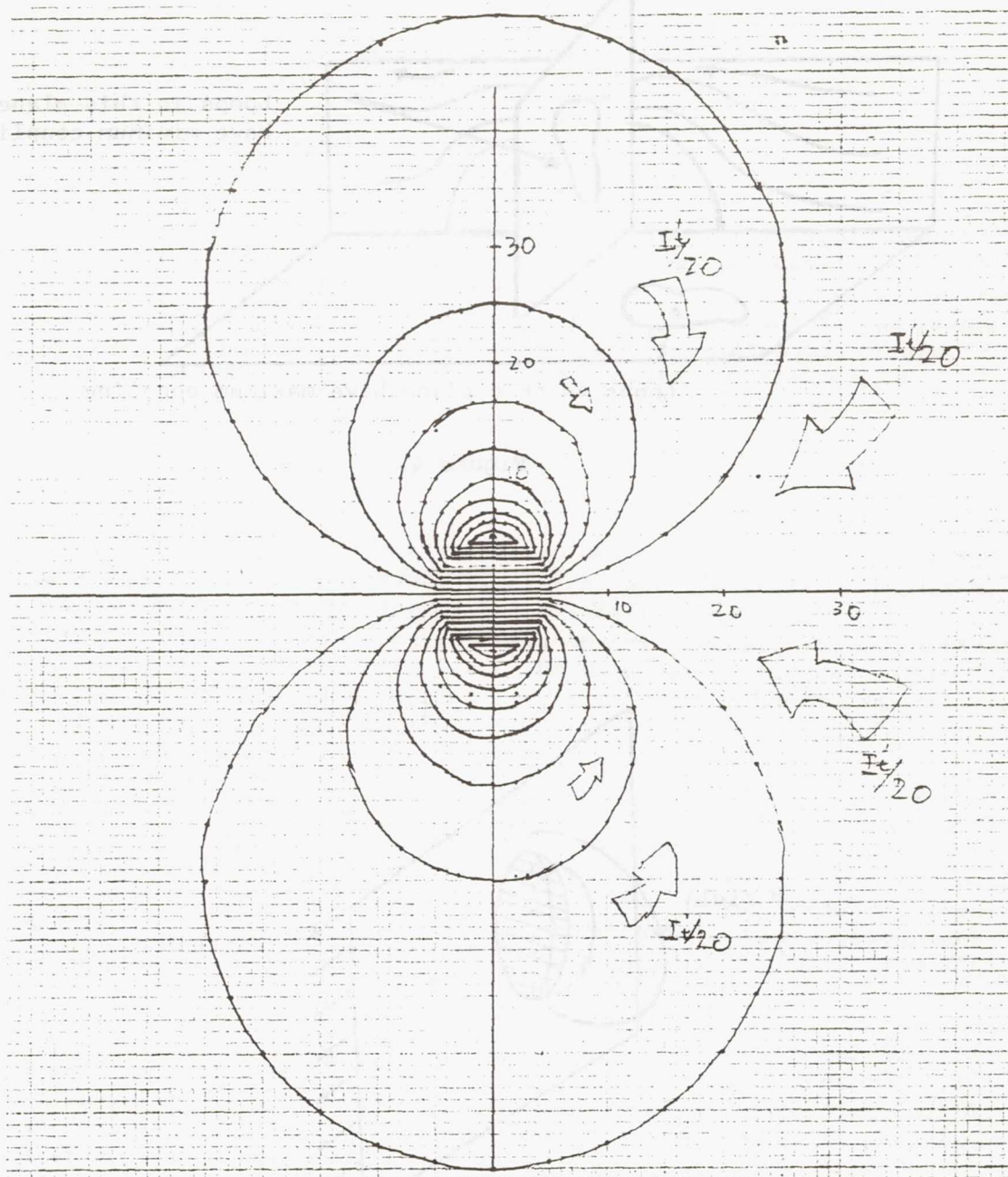


Figure 3.- Current responsible for the leakage.

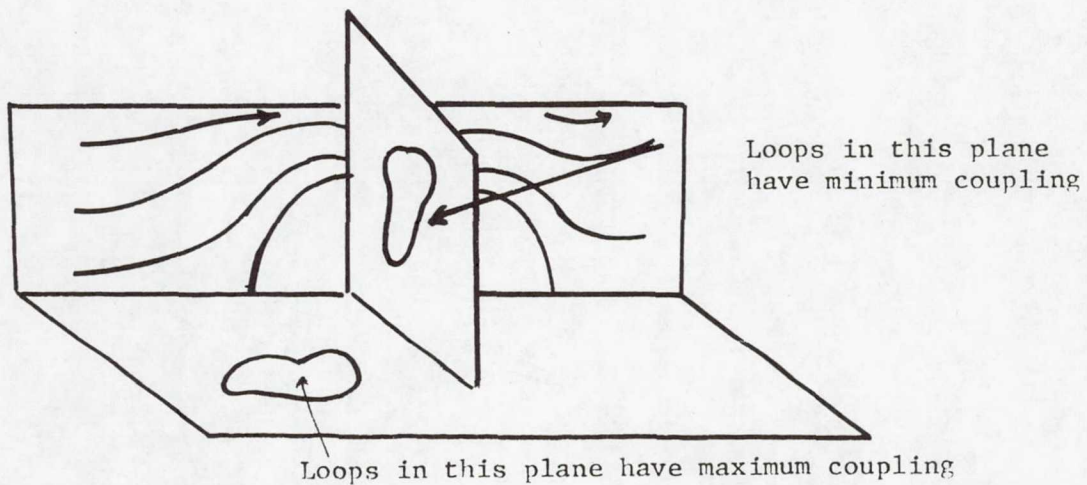


Figure 4.

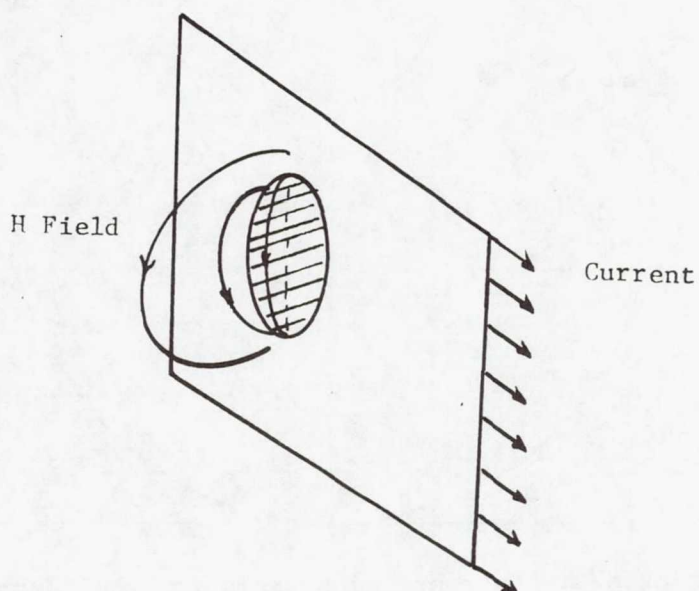


Figure 5.

FULL SCALE LIGHTNING TEST TECHNIQUE

Lawrence C. Walko
Air Force Wright Aeronautical Laboratories

John G. Schneider
Technology/Scientific Services, Inc.

SUMMARY

A test technique has been developed for applying a full scale mean value (30 kiloampere peak) simulated lightning return stroke current on a complete flight ready aircraft to assess the threat of lightning to aircraft electrical circuits. Computer-aided generator design was used to establish the parameters of the test system. Data from previous work done on development of low inductance current return paths determined the basic system configuration.

INTRODUCTION

Tests have been conducted on aircraft to determine the level of voltages and currents induced into the various electrical and electronic circuits as a result of lightning current flowing on the aircraft's surface (ref. 1,2,3). The results of these tests are used to evaluate the severity of the lightning threat to the integrity of the circuits. The majority of the tests have been done at low simulated lightning current levels with the induced results extrapolated up to full threat levels of 200 kiloamperes (kA) peak.

One of the aircraft that has been subjected to this simulated lightning test is the YF-16 aircraft (ref. 4,5). The F-16 aircraft has been designed to sustain a full threat lightning strike without incurring effects impacting safety-of-flight. Preliminary tests were used to determine the amplitude of lightning induced energy on F-16 FCS circuits. The induced energy levels observed on internal wiring were then extrapolated to full threat levels and this threat, with some additional safety margin, was used to establish FCS design criteria.

Having incorporated design changes into the aircraft, a final qualification was to be performed on a production equipped aircraft. This test would involve the direct injection of an average full scale lightning current impulse (30 kA) through an F-16 aircraft to observe the effect of this impulse on the flight control system.

This paper describes the steps taken to realize a system that could accomplish this qualification test. It was the responsibility of the Flight Dynamics Laboratory of the Air Force Wright Aeronautical Laboratories to provide the test set-up, high current impulse generation and measurement equipment and personnel to carry out this test.

THE LIGHTNING SIMULATION TEST CONFIGURATION

Applied Current Waveshape

The typical Lightning Simulation Test (LST) configuration is a series R-L-C circuit which consists of a current impulse generator (a capacitor bank) waveshaping resistors, current return path(s) and the test article as shown in figure 1. The circuit parameters are chosen so that, including the characteristics of the test specimen, the impulse current flowing through the circuit has a unipolar, double exponential, waveshape. Such a waveshape is described by the following equation (ref. 6) and illustrated in figure 2.

$$i(t) = \frac{V}{kL} e^{-at} \sinh(kt) \quad (1)$$

$$a = \frac{R}{2L} \quad (2)$$

$$k = \left(a^2 - \frac{1}{LC} \right)^{1/2} \quad (3)$$

where $i(t)$ is time varying current through the circuit, amps, V is capacitor charge voltage, volts, L is circuit inductance, henries, R is circuit resistance, ohms, and C is circuit capacitance, farads.

The rise time (t_r) of the LST waveform is defined by the intercept of a line drawn between the 10% and 90% points on the front of the waveform and the maximum value of the current. The decay time (t_d) is defined by the time at which the current decays to 50% of its maximum value.

For analysis purposes using equations 1 through 3 the circuit capacitance is assumed to be that of the impulse generator, the circuit resistance is that of the waveshaping (damping) resistance, and the inductance is that of the test specimen and return path.

The problem that has to be dealt with is the selection of circuit component values that give the desired waveform and that are readily available.

CIRCUIT COMPONENTS

Current Return Path

One of the major factors in obtaining a 30 kA or higher peak current is the overall inductance of the test circuit. If the test is simulating a nose-to-tail lightning strike a large part of the total circuit is the aircraft and the current return lines back to the impulse generator. Previous tests using lower peak currents were done with total circuit inductances of between 15-17 microhenries (μH) with return leads placed under the aircraft or a number of

parallel strung wires returning on both sides of the aircraft (ref. 2). The high peak current impulse needed for the full scale tests would be difficult to achieve if the same type of return leads were used.

Burrows has investigated the problem of the inherent high inductance of such a physically large test circuit (ref. 7). To preserve the free space magnetic field configuration around the aircraft he suggests two contrasting designs for the return conductor system. A single return conductor kept well away from the aircraft (10 fuselage diameters) would minimize field distortion but would not reduce total inductance. A coaxial return system as shown in figure 3 would allow for an evenly distributed field and a much lower inductance; this would allow a higher current peak magnitude and would improve the di/dt value of the applied wave.

The final configuration chosen for the return paths was a system of aluminum sheets, 1.2 m wide and 3.7 m long (4 ft. wide and 12 ft. long), bolted together and supported to provide four parallel paths, 14.6 m long (48 ft.). The sheets were placed as shown in figure 4, two above and two below the wings. In order to have a practical test set-up, access to the aircraft and especially the cockpit area could not be hindered by the impulse circuit configuration. It was decided to space the aluminum sheets 1 m from the surface of the aircraft to provide this access. The approximate inductance of this configuration was calculated using the equation (ref. 8):

$$L = 0.2(\log_e r_1/r_2)\mu H/m \quad (4)$$

where r_1 is the radius of a complete circular tube return path and r_2 is the radius of the aircraft fuselage. The inductance of the return path was calculated to be approximately 4 μH .

Optimum Generator Design

Capacitors rated at 2.8 microfarad (μF), 60 kilovolts (kV) each were available for the impulse generator. Given this known capacitance and the calculations for the return path inductance, the problem now was one of determining the configuration of the impulse generator.

From the statistical evidence of the natural characteristics of lightning and standard test waveforms (ref. 9), a lightning attachment simulation requires the current discharge to have the following specific properties:

$$\begin{aligned} I_p &= 30 \text{ kA (peak current)} \\ t_r &= 2 \mu s \pm 20\% \text{ (10-90 rise time)} \\ t_t &= 50 \mu s \pm 20\% \text{ (50\% tail time)} \end{aligned}$$

Since the peak current I_p is critical to the simulation in a full scale test, the R, L, and C parameters shown in figure 1 are varied to achieve a maximum peak current for a given aircraft configuration while maintaining the required waveform tolerances.

Using an existing computer program (GEN FIX) which solves the series R-L-C circuit equations (e.g. equation 1) values of resistance and capacitance were derived which would satisfy the test waveform requirements. As a baseline for the test configuration, a generator capacitance of 9 μF , a peak current of 30 kA, a charge voltage of 120 kV, a 2 μs front time, and a resistance of 3 ohms were derived. The tail time of 50 μs to half value was compromised in order to obtain the peak current and the front time. Tail time was reduced to 25 μs . Also, the generator would have to be at least a two-stage Marx to have a charge voltage of 120 kV.

Another computer program, ICOM, (ref. 10) was used to optimize the test configuration. ICOM is an acronym for Interactive Computer Optimization Methods, which is a collection of fifty-six FORTRAN subroutines and functions which utilize numeric techniques to provide solutions to a wide class of optimization problems. The results of that program are presented here to illustrate the problem of obtaining a realistic design, given certain component and system parameters.

To maximize the applied peak current (I_{max}) for this exercise the following constraints were given:

$$\begin{aligned} L &= 4 \mu\text{H} \\ C &= 80/n^2 \mu\text{F} \\ V &= 50n \text{ kV} \\ t_r &= 2.6 \mu\text{s} \\ t_t &= 25 \mu\text{s} \end{aligned}$$

where n = number of series Marx stages.

The circuit was modeled using a lumped parameter RLC circuit. The Kirchhoff voltage equation for the lightning simulation test model at time $t = 0_+$ is:

$$0 = \frac{1}{C} \int_0^t i(t) dt - V + Ri(t) + L \frac{di}{dt} \quad (5)$$

In order to determine the mathematical relationship between the dependent variables t_r and t_t and the independent variables R, L, and C the time derivative of equation 5 was taken:

$$0 = \frac{1}{C} i(t) + R \frac{di}{dt} + L \frac{d^2i}{dt^2} \quad (6)$$

From this time derivative equation a discrete state-space approximation was made. The peak current I_{\max} was then optimized as a function of the R, L, and C parameters using numeric techniques.

The following optimal constrained solutions were found for two and three stage generators:

Stage	I_{\max} (kA)	R(OHM)	L(μ H)	C(μ F)	t_r (μ s)	t_t (μ s)
2	36.35	2.42	4.0	11.6	2.56	25.2
3	42.35	3.11	5.2	9.0	2.55	25.1

In two stage configuration, L is minimized, R is decreased until the t_t constraint is encountered at which time C is increased to allow further reduction in R while maintaining a feasible solution. This process continues until the t_r constraint is approached due to the low R value. At this point, the optimal constrained solution has been reached since further increase in C causes the t_r constraint to be violated and further decrease in R causes the t_t constraint to be violated. Notice that C has not approached the upper single stage constraint of 20 μ F.

In three stage configuration, L is not placed at the lower constraint as might be expected. This result can be explained as follows:

The three stage configuration allows a higher discharge voltage, but forces an upper constraint on C of 9 μ F. The solution proceeds as in the two stage case, R being decreased and C increased to maintain t_t feasibility. However, the constraint on C is encountered before R can be decreased sufficiently to take full advantage of the t_r constraint; the configuration is, in other words, capacitance limited. The solution in this case is to increase L which in turn increased t_t , thus allowing R to again be reduced until the t_r constraint is finally encountered. It is interesting to note that near the optimum, the partial derivative of the objective function with respect to R is approximately 15 times greater than the partial derivative with respect to L. This fact allows L to be increased to feasible values while obtaining a net improvement in objective function by decreasing R.

RESULTS AND DISCUSSION

The impulse generator used for the full scale tests consisted of a two-stage Marx, each stage consisting of six 2.8 μ F capacitors connected in parallel for a total capacitance, per stage, of 16.8 μ F. In the charging mode the two stages were charged in parallel but at opposite polarities using a \pm 50 kV DC power supply. Each stage was charged through a charging resistance of 500 k Ω . The Marx generator configuration results in a total capacitance of 8.4 μ F. A damping resistance of 3 Ω was placed at the output of the generator.

The generator was triggered through a spark gap between the two stages using a previously designed pneumatic system (ref. 11). The generator discharge was then transferred through input and return spark gaps to the aircraft and return path conductors. Figure 5 is a schematic of the generator and figure 6 is a photograph of the actual generator.

The impulse generator for the full scale lightning simulation test achieved a peak current of 32.6 kA with a rise time of 2.55 μ s. The four conductor, aluminum sheet return path with the F-16 aircraft yielded an actual overall inductance of 3.5 μ H. This compares with previous multiple wire return paths and aircraft configurations with total inductance in the range of 15 μ H.

The data acquisition equipment needed to make valid induced voltage and current measurements on aircraft electrical circuits must operate under what may be major adverse facility effects from the firing of the high current capacitor banks. This acquisition equipment exists today (ref. 11) in the form of shielded breakout boxes and fiber optics data links to insure minimal noise pickup formerly associated with coaxial and triaxial cables.

REFERENCES

1. Skouby, C.D. and Smith, G.R.: Survivable Flight Control System (SFCS) Lightning Susceptibility Evaluation. AFFDL-TR-75-160, February 1976.
2. Mangold, V.L. and Walko, L.C.: Lightning Transient Research on an F-111E Aircraft. AFFDL-TR-78-1, February 1978.
3. Plumer, J.A.; Fisher, F.A.; and Walko, L.C.: Lightning Effects on the NASA F-8 Digital-Fly-By-Wire Airplane. NASA CR-2524, March 1975.
4. Plumer, J.A.: YF-16 #1 Lightning Transient Analysis Test Report. General Dynamics Rep. 16PR051, June 1975.
5. Mangold, V.L. and Walko, L.C.: YF-16 #2 Lightning Transient Analysis Test Report. AFFDL-TM-76-104-FES, September 1976.
6. Condon, E.U. and Odishaw, H.: Handbook of Physics. Second Edition, McGraw-Hill, 1958.
7. Burrows, B.J.C.: Induced Voltage Programme Theoretical Considerations of Whole Aircraft Tests. Culham Lightning Studies Unit Memo No. 42, Culham Laboratory, England, May 1976.
8. Grover, F.W.: Inductance Calculations Working Formulas and Tables. D. Van Nostrand Co., Inc., 1946.
9. Lightning Test Waveforms and Techniques for Aerospace Vehicles and Hardware. SAE Aerospace Recommended Practice (Pending), June 1978.
10. Baum, R.K.: Development and Application of an Interactive Computer Optimization Program. M.S. Thesis, Utah State University, 1979.
11. Walko, L.C. and Seymour, T.J.: New Techniques for the Measurement of Natural and Simulated Lightning Phenomena. Presented at the IEEE International Symposium on Electromagnetic Compatibility. San Diego, CA, Oct. 1979.

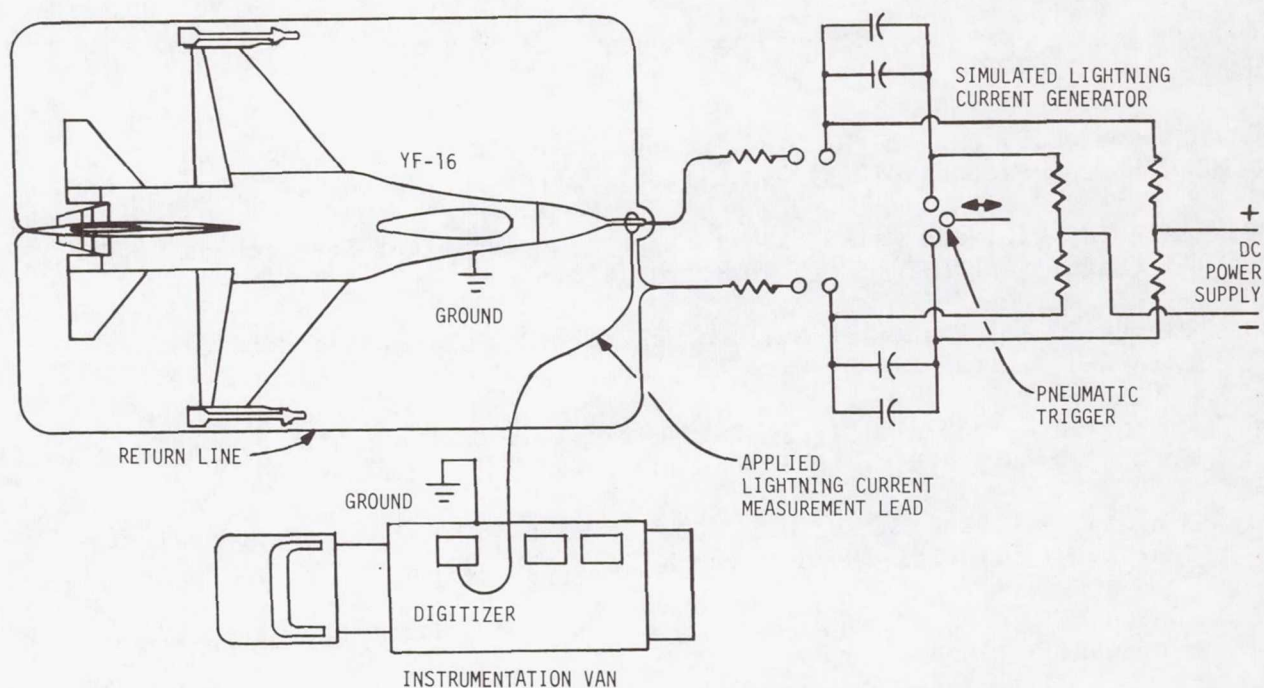


Figure 1.- Lightning simulation test configuration.

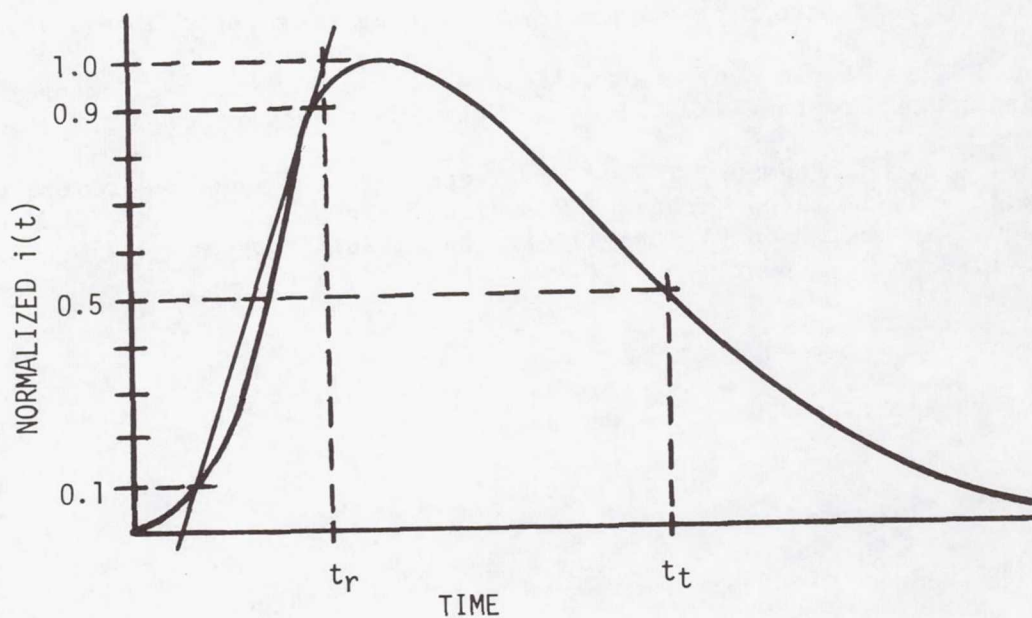


Figure 2.- Unipolar test waveform.

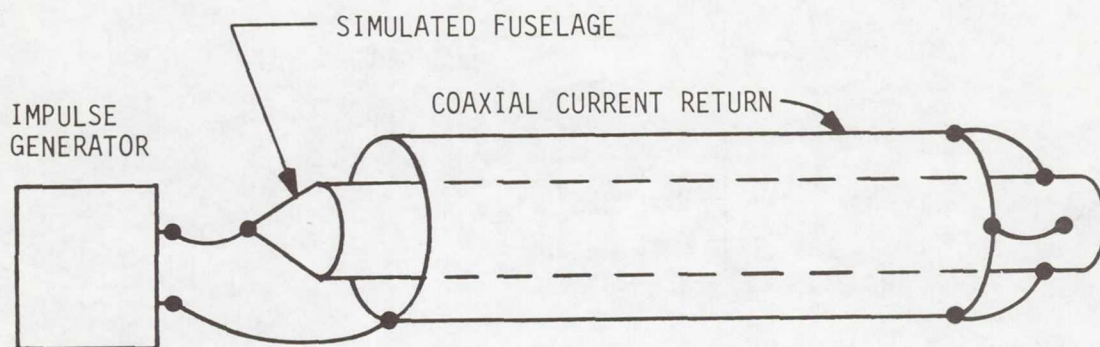


Figure 3.- Ideal test circuit with coaxial current return.

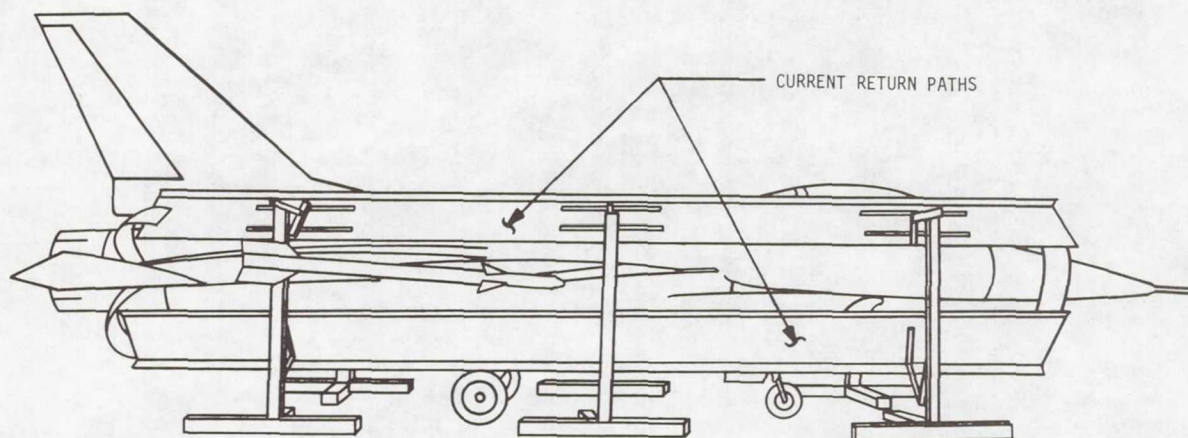


Figure 4.- Full scale test setup showing current return path configuration.

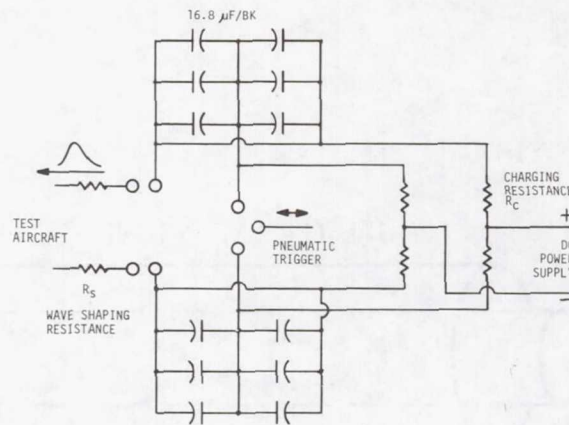


Figure 5.- Schematic of full scale test impulse generator.

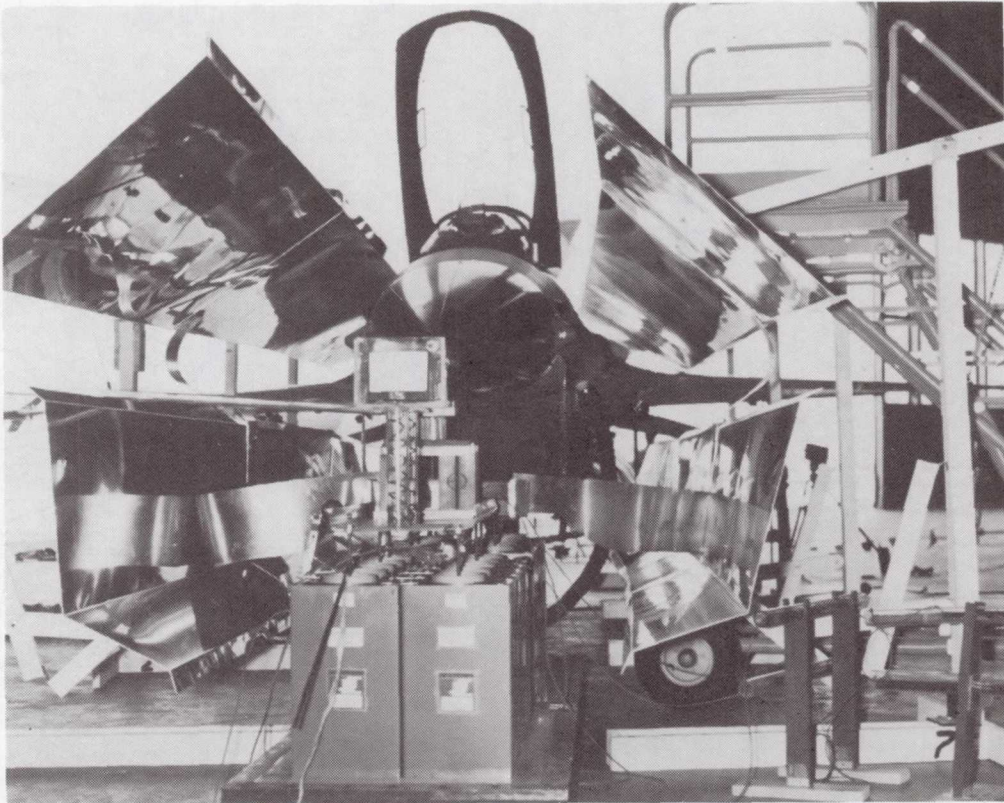


Figure 6.- Actual test setup on F-16 aircraft.

SESSION IX - OPEN FORUM ON SIMULATION AND TESTING

1. Report No. NASA CP-2128 FAA-RD-80-30		2. Government Accession No.		3. Recipient's Catalog No.	
4. Title and Subtitle LIGHTNING TECHNOLOGY				5. Report Date April 1980	
				6. Performing Organization Code	
7. Author(s)				8. Performing Organization Report No. L-13666	
9. Performing Organization Name and Address NASA Langley Research Center Hampton, VA 23665				10. Work Unit No. 505-44-13-02	
				11. Contract or Grant No.	
				13. Type of Report and Period Covered Conference Publication	
12. Sponsoring Agency Name and Address National Aeronautics and Space Administration Washington, DC 20546 and Florida Institute of Technology Melbourne, FL 32901 and Department of Transportation Washington, DC 20590				14. Sponsoring Agency Code	
15. Supplementary Notes					
16. Abstract This report is a compilation of papers presented at the 1980 Symposium on Lightning Technology held at the NASA Langley Research Center April 22-24, 1980. It includes papers concerning lightning phenomenology, measurement, detection, protection, interaction, and testing.					
17. Key Words (Suggested by Author(s)) Lightning and aircraft interactions Lightning instrumentation Lightning phenomenology Lightning protection Lightning detection Lightning simulation			18. Distribution Statement Unclassified - Unlimited Subject Category 47		
19. Security Classif. (of this report) Unclassified	20. Security Classif. (of this page) Unclassified	21. No. of Pages 465	22. Price* \$14.50		